Morphological convergence and dental simplification in myrmecophagous placentals

Sérgio Ferreira-Cardoso

THÈSE POUR OBTENIR LE GRADE DE DOCTEUR DE L'UNIVERSITÉ DE MONTPELLIER

En Biologie de l'Evolution

École doctorale GAIA

Institut des Sciences de l'Evolution de Montpellier

Morphological convergence and dental simplification in myrmecophagous placentals.

Présentée par Sérgio FERREIRA-CARDOSO

Le 29 Novembre 2019

Sous la direction de Frédéric DELSUC et Lionel HAUTIER

Devant le jury composé de

Anjali GOSWAMI, Professor, The Natural History Museum, London	Rapporteur
John NYAKATURA, Junior Professor , Humboldt Universität, Berlin	Rapporteur
Allowen EVIN, Chargée de Recherche, Institut des Sciences de l'Evolution de Montpellier	Examinateur
Frédéric DELSUC, Directeur de Recherche, Institut des Sciences de l'Evolution de Montpellier	Directeur de thèse
Lionel HAUTIER, Chargé de Recherche, Institut des Sciences de l'Evolution de Montpellier	Co-directeur de thèse
Guillaume BILLET, Maître de Conférences, Muséum National d'Histoire Naturelle, Paris	Invité
Thomas LEHMANN, Research Associate, Senckenberg Forschungsinstitut und Naturmuseum	Invité
Anthony HERREL, Directeur de Recherche, Muséum National d'Histoire Naturelle, Paris	Examinateur et Président du jury

UNIVERSITÉ DE MONTPELLIER

Index

Introduction

In biology, convergence is a phenomenon characterized by the evolution of similar features without direct common ancestry. Similar selective pressures may result in identical phenotypes evolving independently in two or more lineages. Once seen as exceptional, convergent evolution is today considered as pervasive (McGhee, 2011). In part, cases of convergence can be explained by how organisms develop under the laws of physics, how they originate from a single cell, and how their organization is coded and transmitted to the next generation (developmental constraints). On the other hand, some phenotypes are functional in nature, while others constitute lethal conditions that cannot survive (functional constraints; McGhee, 2001, 2006). Life is therefore limited to the intersection of developmentally and functionally viable forms (McGhee, 1999), limiting phenotypic variation and leading to similar responses under convergent selective pressures providing evolutionary replicates (Losos, 2017).

Among countless examples of evolutionary convergence, one of the most striking is that of ant- and termite-eating placental mammals (Redford, 1987). The ecological convergence towards dietary specialization was accompanied by numerous adaptations at the morphological, physiological, behavioral, and genetic levels (Redford, 1981; Redford & Dorea, 1984; McNab, 1985; Rose & Emry, 1993; Delsuc *et al.*, 2014; Emerling *et al.*, 2018). Extant strict myrmecophagous placentals eating more than 90% of termites and/or ants include five lineages: anteaters, the giant armadillo, pangolins, the aardwolf, and the aardvark (Fig. 1; Redford, 1987). Most of these species, historically classified as Edentata (except the aardwolf; see 'Phylogenetic background'), show numerous convergently evolved morphological characters, such as tooth reduction/loss, elongated snouts, vermiform sticky tongues, and strong claws and forelimbs for digging into social insect nests (Rose & Emry, 1993; Davit-Béal *et al.*, 2009; Casali *et al.*, 2017; Goździewska-Harłajczuk *et al.*, 2018; Ferreira-Cardoso *et al.*, 2019).

Cranial traits constitute the most defining characteristics of myrmecophagous placentals (Gaudin *et al.*, 1996; Gaudin & Branham, 1998; Reiss, 2001). This is mostly due to the plasticity of the mammalian feeding apparatus and to its role in the several adaptive radiations of the group (Hiiemae, 2000; Schwenk, 2000). This adaptive evolution of the placental skull, combined with conserved developmental processes, resulted in a compartmentalization of the skull in small adaptive units, or modules (Olson & Miller, 1958; Cheverud, 1982a; Goswami, 2006; Porto *et al.*, 2009). These developmental modules often translate into sets of highly correlated traits (phenotypic modules), with a main functional role, an underlying genetic and developmental basis, and a fair degree of independence within an organism (Raff, 1996; Wagner,

1996; Klingenberg, 2005). Under a certain adaptive landscape (e.g., dietary specialization), variational properties such as trait correlation and modularity were suggested to increase the amount of change in the direction of selection (evolvability; Riedl, 1978; Hansen & Houle, 2008; Marroig *et al.*, 2009). The unique cranial phenotype associated to myrmecophagy is, therefore, an example of the trade-off between facilitation and constraint of morphological variation in the context of a functionally and physiologically demanding dietary regime.

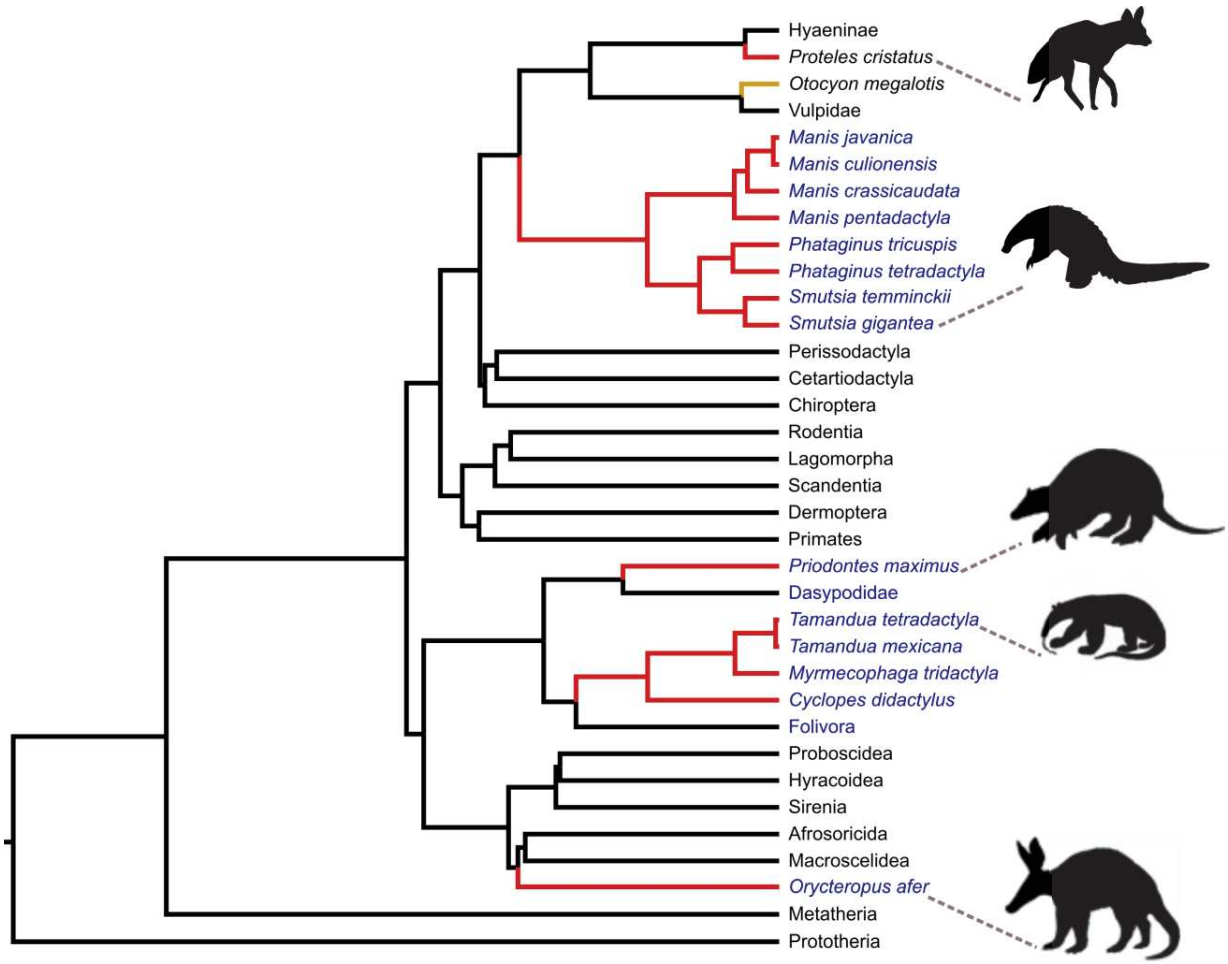

Figure 1 – Molecular-based phylogenetic relationships of extant mammals with emphasis in myrmecophagous placentals. Tree topology and branch lengths obtained from Timetree.org (Kumar *et al.*, 2017). Divergence times (branch lengths) were adjusted for pangolins (Gaubert *et al.*, 2018), xenarthrans (Gibb *et al.*, 2016), and afrotherians (Meredith *et al.*, 2011). Branches colored in red indicate myrmecophagous species; the branch colored in yellow indicates a non-obligate myrmecophagous species; tip labels in blue indicate clades previously historically ascribed to the Edentata.

Ant- and termite-eating placentals have sparked the interest of several studies for more than a century, mainly related to their tooth development (Gervais, 1867; Rose, 1892; Röse, 1892; Martin, 1916; Anthony, 1934a; Davit-Béal *et al.*, 2009), and their loss of chewing abilities and evolution of modified masticatory and hyoid apparatus (Owen, 1856; Reiss, 1997; Endo *et al.*, 1998, 2007, 2017; Naples, 1999a). Despite all the drawn attention, the use of modern geometric morphometric methods is yet to be undertaken on the skull of myrmecophagous placentals, while it could enable to assess the phenotypic variation patterns (e.g., Cheverud, 1982, 1995; Hallgrímsson *et al.*, 2004; Drake & Klingenberg, 2010). Such methods can also provide new insights into ontogenetic patterns (Cheverud, 1982b; Klingenberg, 2016) and systematics (Palci & Lee, 2018). Additionally, the advent of X-ray µ-computed tomography (µCT) and enhanced-contrast scanning protocols now allows performing non-destructive analyses to explore osteological and soft-tissue traits at an unprecedented scale and precision.

The feeding apparatus of myrmecophagous placentals provides a particularly interesting framework to study morphological convergence associated with ecological adaptations. The developmental processes involved in skull formation are well-documented and modular parcellation and its relationship to functional constraints is established for several model and non-model placental species. Moreover, part of these developmental processes, such as face/rostrum elongation, tooth development, or bone-muscle interaction, underlies most of the convergent phenotypic traits associated to myrmecophagy. The myrmecophagous skull thus offers a case study of morphological convergence.

Methodological framework

A set of different methods was used in order to perform the four studies presented in the different chapters of this thesis. A detailed 'Materials and methods' section is provided for each chapter and, therefore, I here provide only the broad outline of my methodological approach.

Data acquisition

First, and foremost, I visited five of the largest natural history collections in the World, including the Natural History Museum (London), the Musée Royal de l'Afrique Centrale / Koninklijk Museum voor Midden-Afrika (Africa Museum; Tervuren), the Museum für Naturkunde (Berlin), the American Museum of Natural History (New York), and the National Museum of Natural History (Washington, DC). Additionally, I borrowed osteological and wet specimens from the Muséum National d'Histoire Naturelle

(Paris), and the Museum of Vertebrate Zoology (Berkeley). Each visit consisted in between one and two days of comparative anatomy work, followed by the placement of three-dimensional (3D) homologous anatomical landmarks (types I and II; Fig. 2). This last step was performed with a Revware MicroScribe M digitizer (accuracy: 0.0508 mm). The number of landmarks placed varied between 85 and 119, according to the clade considered. In total, I landmarked 703 specimens belonging to myrmecophagous species, and some non-myrmecophagous outgroups, including sloths, armadillos, hyenas, bears, and foxes.

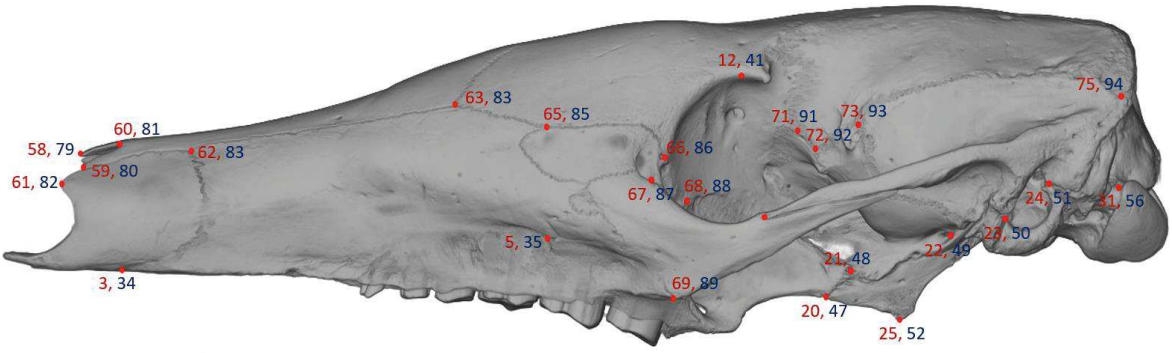

Figure 2 – Volume rendering of a µ-computed tomography scanned skull of *Orycteropus afer*, in lateral view. Points and numbers are examples of the types of landmarks used. Colors indicate left and right side bilateral landmarks.

I used µ-CT to obtain high-resolution image stacks of the skeletal parts of 130 specimens of myrmecophagous species. The µ-CT scanning was performed in two different facilities: i) the Microtomographie-RX, part of the Montpellier Ressources Imagerie (MRI) at the Institut des Sciences de l'Evolution (Montpellier) – equipped with an EasyTom 150 x-ray µ-CT scanner; and ii) the µ-CT laboratory of the Museum of Natural History (London) – equipped with a Nikon Metrology HMX ST 225. All resulting data was subsequently processed using Avizo (FEI), Fiji (Schindelin *et al.*, 2012), and MorphoDig (Lebrun, 2018). These softwares were used to compress the data and generate three-dimensional surfaces (e.g., Ferreira-Cardoso *et al.*, 2017; Martinez *et al.*, 2018).

Lastly, I dissected the heads of six specimens of anteaters stored at the Institut de Sciences de l'Evolution (Montpellier) and at the Institut Pasteur de Guyane (Cayenne). These specimens were dissected at Montpellier and Cayenne, and were subsequently stained with iodine in order to increase the contrast of head muscles and allow to µ-CT scan and digitally reconstruct their morphologies. Some of these specimens were subjected to serial slicing in order to produce histological sections of muscles and

mandibles. Histological procedures were performed at the Institut de Recherche en Cancérologie de Montpellier (IRCM).

Data analysis

All morphometric data were processed and analyzed using free statistical analyses software R (Team, 2013). Geometric morphometrics analytical procedures were implemented with the geomorph v.3.5.0 R package (Adams *et al.*, 2017) and the R code provided in Claude (2008). Most analyses implied the Procrustes superimposition (Rohlf & Slice, 1999) of the landmark data sets in order to scale them to centroid size and optimally translate and rotate the specimens using least-squares criterion. Specific R packages and functions are listed in each chapter.

Phylogenetic framework

Historical review

In 1742, the French doctor and naturalist Félix Vicq-d'Azyr published the second volume of his "Système anatomique: quadrupèdes" (Vicq-d'Azyr, 1742), as part of a book series named "Encyclopédie Méthodologique". In this book, Vicq-d'Azyr named a new clade of mammals that he designated as "édentés/*Edentati*". The diagnostic trait for this group was the lack of incisor teeth. It comprised four genera, including sloths (*Pigri*), armadillos (*Loricati*), anteaters and the aardvark (*Myrmecophagi*), and pangolins (*Squammei*) (Vicq-d'Azyr, 1742). The name Edentata was posteriorly adopted by naturalists, and its structure re-organized into five different groups: armadillos, anteaters, sloths, aardvarks, and pangolins (e.g., Cuvier, 1798). Edentata has been used to designate these taxa (Rose, 1892; Tims, 1908), on the basis of common morphological traits that were considered as synapomorphies of the group.

Huxley's (1872) diagnosis of the Edentata (or Bruta, which translates to brute, coarse, or beast) reflected some of the convergently evolved morphological traits related to myrmecophagy. These include tooth loss or reduction, tooth structure simplification, hypselodonty, monophyodonty (except in some armadillos) and forelimbs adapted for digging (Huxley, 1872). Huxley (1872) divided the Edentata into two groups based on their feeding on plants (sloths; *Phytophaga*) or insects (*Entomophaga*), the latter group including anteaters, pangolins, armadillos, and aardvarks. Each of these taxa were placed separately in their own taxa, but no tentative affinities were proposed. By the time Huxley published his work, a little more than a hundred years after the formalization of the Edentata, an increasingly amount of knowledge

on the anatomy and physiology of these mammals allowed researchers to question the pertinence of such a grouping. Huxley (1872) himself precedes his diagnose and description of the Edentata by stating the group was "ill-defined" and heterogeneous.

However, it would take until the early 1900's for the first formal division of the Edentata in three clearly different orders. Weber (1904, p. 412) argued that although it became usual to group these taxa in the same order, the morphological differences were too many for the classification to be coherent. In the same sequence, Weber referred to the reduced dentition and tooth structure simplification as a "multiple reduction and transformation" (translated from German) that could not be used as a grouping factor (see below). Weber (1904) considered the Edentata as an "inferior" group within the therian mammals, the Paratheria, leaving its relationships with the remaining mammals ill-described. Weber (1904) divided the edentates in two groups: i) the Nomarthra including two orders of species with normal vertebral articulation (pangolins and aardvarks); ii) the order Xenarthra showing abnormal accessory articulations in the last thoracic and lumbar vertebrae (anteaters, sloths, and armadillos). Additionally, Weber (1904) coined the term Pholidota, the order in which pangolins are still classified, thus replacing the previous Squamata designation that was in synonymy with the reptile clade. Within Xenarthra, he maintained the previously used divisions between anteaters (Myrmecophagidae), sloths (Bradypodidae), and armadillos (Dasypodidae).

Since the early 20th century, the name Edentata has been used to refer to Xenarthra, and the similarities between the latter with Pholidota and Tubulidentata have been attributed to convergent evolution toward myrmecophagy (e.g., Rose & Emry, 1993; McGhee, 2011). This classification became broadly accepted, even before the beginning of the molecular phylogenetic era, with Xenarthra being considered on its own separate clade within Eutheria, split into two orders Cingulata (armadillos) and Pilosa (sloths and anteaters) (McKenna, 1975). McKenna (1975) considered the Pholidota on their own *incertae sedis* clade, while the Tubulidentata were grouped with the ungulates with a similar rank to the artiodactyl, proboscidean, or sirenian orders. These proposals, however, were not corroborated by the more recent molecular phylogenetic analyses (see below).

Present state of the phylogeny of placental mammals

Since the 1980's-1990's onwards, molecular phylogenies provided increasing evidence confirming the polyphyly of the Edentata (De Jong *et al.*, 1985; Springer *et al.*, 1997; de Jong, 1998; Murphy *et al.*, 2001b). Pangolins are a sister group to carnivores and are nested within the Laurasiatheria (Sarich, 1993;

Murphy *et al.*, 2001b,a; Meredith *et al.*, 2011). Aardvarks form a sub-clade with tenrecs and elephant shrews, within the Afrotheria (Waddell, Okada, & Hasegawa, 1999; Asher, Bennett, & Lehmann, 2009; Meredith *et al.*, 2011). Xenarthrans are the group with the most undefined position in the placental tree (Nishihara, Maruyama, & Okada, 2009; Teeling & Hedges, 2013; Foley, Springer, & Teeling, 2016), with its relationships changing in each of the three proposed hypothesis: i) Atlantogenata-Boreoeutheria (Fig. 1); ii) Afrotheria-Exafroplacentalia; iii) Xenarthra-Epitheria.. To date, the root of the placental tree is still unresolved, with all three hypotheses being currently considered equally likely (Nishihara *et al.*, 2009; Teeling & Hedges, 2013). Nevertheless, all provide unequivocal evidence for the polyphyly of Cuvier's Edentata, asserting the high degree of morphological convergence resulting from directional selection towards a myrmecophagous dietary regime.

Dissertation's main goals

In this thesis, I combined comparative anatomy and geometric morphometrics of the myrmecophagous skull and mandible, using modern μCT techniques and large museum collection sampling in order to provide new insights into the convergent evolution of the head, skull, and muscles of ant- and termite eating placental mammals. The studies here presented focus on the skull of 15 myrmecophagous placental species, including anteaters, the giant armadillo, pangolins, the aardvarks, and the aardwolf, as well as their closely related species.

In the first chapter, I used a landmark-based approach to describe and quantify inter- and intraspecific skull shape variation, as well as allometric patterns of the World most heavily poached mammals, pangolins (Pholidota).

In the second chapter, I analyzed the internal anatomy of the mandible of all myrmecophagous placental clades and compare it to non-myrmecophagous taxa in order to re-interpret phenotypic convergence and discuss functional aspects of tooth regression. I additionally used collection specimens and contrast-enhanced μCT scanning to perform a comparative anatomical description of the masticatory, hyoid, lingual, and facial musculatures of the three anteater genera (Vermilingua).

Finally, I assessed and compared intra- and interspecific phenotypic covariation patterns between myrmecophagous placentals, using a geometric morphometric approach. I used exploratory and confirmatory methods to understand the impact of myrmecophagy-driven morphological adaptation in skull modularity and integration.

The main goal of this dissertation was to generate knowledge on the cranial morphological convergence based on comparative anatomy and geometric morphometrics approaches, and to contribute to an integrative project (ConvergeAnt) including other aspects of myrmecophagy-driven adaptation at the genomic and microbiome levels.

Chapter 1: Morphological evolution, classifications and phylogeny

1.1-Historical background

From early in the history of humankind, the description of biological diversity led naturalists to create divisions as a mean to classify life in a logical way. The formal classification of living beings have their roots in the works of Aristotle, Theophrastus, or Pliny the Elder (Lecointre & Le Guyader, 2006). Since Greco-Roman times, several classification methods were proposed in order to create a widespread and "correct" way to group biological entities. In 1758, Carl Linnaeus published the tenth edition of his most remarkable work, *Systema Naturae*, in which a hierarchical system based on morphological similarities was proposed. It is in this edition that Linnaeus generalized the use of a binomial nomenclature for species. This classification was based on the idea of a natural order dictated by in the act of the creation of life by God (Linnaeus, 1758). As the philosophers of Ancient Greece, 18th century naturalists thought that the identity and function of biological entities determined their classification (essentialism; Cartwright, 1968; Lecointre & Le Guyader, 2006). The notion of time and the concept of phylogenetic relationships, as we know them today, were not present in Linnaeus' work. Nevertheless, this classification is the foundation of the taxonomic system has been used to the present day.

The Linnean classification scheme proved useful in the classification of living beings, but the French Revolution, at the end of the 18th century, led to a change in how naturalists conceived nature. Despite many philosophers had expressed proto-transformist ideas since Ancient Greece, it was the accumulation of knowledge during the Enlightenment and the separation of the religious and intellectual realms during the transition of the 18th and 19th centuries that propelled the ideas that species were not immutable entities (Stott, 2012). De Maillet, Erasmus Darwin, or Lamarck are just some examples of the people who paved the way to Charles Darwin and Alfred R. Wallace (Stott, 2012). If the dogma of a natural hierarchy determined by God lost consensus within the scientific community, it took until 1859 for the formalization of a hypothesis that could explain the diversity of groups (or taxa) described. Charles Darwin's *On the Origin of Species* (1859) is the keystone of evolutionary biology, associating facts from different research fields such as paleontology, geology, and economics to propose a hypothesis that could explain the origin of biodiversity. But the most revolutionary aspect of this work was the interpretation of species as stages, in time and space, of a variation spectrum. The main reason for this, was the fact that Darwin shifted the scale of morphological description and comparison. While previous thinkers followed

a typical essentialist approach to classify living beings, Darwin defined species based on simple mathematical concepts such as average and variance (Lecointre and Le Guyader, 2001). Based on his observations and published works on agricultural plant varieties and livestock breeding, Darwin became aware of the potential for variation within a single species (Darwin, 1859). As such, the boundaries of previously created "boxes" in which taxa were organized became less clear. Darwin's main question went beyond the simple attribution of living entities to a species, aiming at understanding why species were relatively discrete entities (average) while exhibiting an enormous potential to vary (variance; Lecointre and Le Guyader, 2001). Since then, the classification of living beings evolved into a two-layered universe, in which the first layer consists of an observed pattern, and the deeper layer of the processes underlying such pattern. With Darwin, variation became a central focus in biology and naturalist work shifted from recognizing morphological patterns to understanding why a certain species is constrained to present a specific set of average traits. Furthermore, given that life can be interpreted as a variation continuum, new research fields focused on the causes of variation and the constraints limiting it.

In sum, Darwin's main conclusion was that all living and fossil species are related, to some degree, and that the sets of traits that characterize species (phenotypes) are, in part, the result of selective pressures acting during a number of generations. The potential variation range presented by a species is thus reduced and the observed patterns are the result of both genealogical (phylogenetic) and environmental constraints. Darwin (1859) was the first to introduce the principle of genealogy - hierarchical relationship between individuals of the same kin – to the interpretation of life. From 1859 onwards, the concept of phylogenetic tree would be used as a means to associate phenotypic resemblance with the idea of ancestry (time dimension). The view of descent with modification is behind the foundation of evolutionary biology as a research field, and the source for systematics, the study of the relationships between living and extinct taxa (Lecointre and Le Guyader, 2001). Although Darwin's book became the paramount work in evolutionary biology, Alfred Wallace also proposed evolutionary hypotheses. As a result, both signed the first document to ever propose natural selection as the mechanism behind speciation (Darwin and Wallace, 1958). Despite the importance of Darwin and Wallace's works, most keystone concepts in evolutionary biology were defined either before, or after their publication. The best example is probably the word *phylogeny*, which was not coined until 1866, when Ernst Haeckel tried to synthesize Lamarck's and Darwin-Wallace's hypothesis in his "Ontogeny recapitulates phylogeny" (or biogenetic fundamental law; Haeckel, 1866). While the idea that the embryonic stages of "higher" species represented the adult stages of "primitive" organisms has been refuted several times (e.g., Sánchez-Villagra, 2012), Haeckel produced

the first figure with a non-schematic phylogenetic tree, in which the main groups of animals, plants, and the paraphyletic unicellular eukaryotes (Protista) are represented. Although Haeckel's biogenetic fundamental law and tree topology were not confirmed by posterior scientific and technological developments, his tree is a landmark that preconized the future of biology. The interpretation of the trait variation in a phylogenetic context is today one of the richest fields in the life sciences.

From the late 1800's to the 1960's, the description and quantification of phenotypic variation constituted the main source of information used to deduce phylogenetic relationships (Mooi & Gill, 2010; Lee & Palci, 2015). Recently, molecular data became increasingly used to perform phylogenetic inference, as continual methodological developments and computational capacity allow to treat an increasing amount of data (genome scale) and generate well-supported, fully-resolved trees (Lee & Palci, 2015). Molecular phylogenetics has allowed new insights into the tree of life and an increasingly better understanding of the evolutionary history of living beings (Zuckerkandl & Pauling, 1965; Woese, Kandler, & Wheelis, 1990). The development of these techniques has even allowed scientists to perform phylogenetic inference based on DNA and proteins collected from fossil specimens (Yang, Golenberg, & Shoshani, 1996; Poinar *et al.*, 1998; Delsuc *et al.*, 2019; Presslee *et al.*, 2019). In some cases, the coupling of fossil-based molecular and morphological data has completely restructured the morphology-based phylogenetic relationships, as recently exemplified by the case of sloths (Delsuc *et al.*, 2019), or resolved the phylogeny and biogeography of emblematic species like the New Zealand moas (Cooper *et al.*, 2001; Haddrath & Baker, 2001). Molecular phylogenies are, therefore, invaluable tools to propose alternative scenarios for the evolutionary history of phenotypic traits, facilitating the interpretation of ontogenetic, functional, and ecological signals by establishing a solid basis for ancestral state estimation (Lee & Palci, 2015). On the other hand, the study of evolution in a deep time context will always remain dependent on morphological data (fossils). Fossils are the only way by which the accurate estimation resulting from modeling of macroevolutionary dynamics (e.g., extinction rates) can be obtained (Rabosky, 2010). As such, the very basis of the study of evolution, as well as the reliability of its interpretation, still relies on concepts arising from comparative anatomy studies. The most relevant of all these concepts is almost certainly that of homology/homoplasy, which has become the conundrum of morphology-based phylogenetic analyses and is, at the same time, the engine boosting the field of comparative anatomy.

1.2-Speciation and species delimitation

Until this point, I focused this section on the aspects that gravitate around the taxonomic unit, more specifically the species. In its most classical concept, a species can be discerned by phenotypic distinctiveness (Benton & Pearson, 2001). This morphological species concept was adopted by Darwin (1859) in order to articulate his hypothesis of the speciation process. In focusing on morphological variation and polymorphism, Darwin and Wallace (Darwin & Wallace, 1858) provided the first glimpse of the mechanisms behind it. Phenotypic variation arises by the mutation of the genome, and genetic assimilation of such variation (Waddington, 1942, 1953) plays a key role in speciation (Benton & Pearson, 2001). However, how can a species be defined if it displays extreme phenotypic variation (i.e., polymorphism; Mallet, 1995) or almost no variation at all (i.e., cryptic species; Bickford *et al.*, 2007)? The biological concept of species proposed the possibility of interbreeding as a solid criterion to identify a species (Dobzhansky, 1937; Mayr, 1942). This concept has limitations exemplified by the natural occurrence of fertile hybrids of different species of palm trees (Papadopulos *et al.*, 2019) or the hybridization of putatively distinct duck species in captivity (Mallet, 1995). Speciation is a complex process, involving multiple mechanisms such as natural selection (including sexual selection), genetic drift, or mutation. Given this complexity, other concepts of species were since then proposed and discussed (Mayden, 1997; De Queiroz, 1998, 2007). Speciation is today considered as isolation in one or several ways, may it be due to extrinsic (e.g., behavior, ecology; Stresemann, 1943; Thorpe, 1945) or intrinsic (e.g., egg-sperm incompatibility, low hybrid fitness) factors (Ptacek & Hankison, 2009). As a result, species delimitation is increasingly based on an integrative approach, including the assessment of morphological distinctiveness and gene flow interruption/reduction (Puillandre *et al.*, 2009).

The relationship between genetic and morphological differentiation is today frequently tested (Barlow, Jones, & Barratt, 1997; Amato & Montresor, 2008; Miranda *et al.*, 2018). The study of morphological distinctiveness typically occurs at the static level, but the ontogenetic realm has become especially relevant, as ontogenetic allometries can be useful in a phylogenetic context (Bardin, Rouget, & Cecca, 2016). Allometry, size-related shape changes (Klingenberg, 2016), is a main player in generating biological diversity (Esquerré, Sherratt, & Keogh, 2017). Heterochrony, developmental changes in timing of certain events, can contribute to phenotypic and evolutionary changes and lead to speciation (Mitteroecker, Gunz, & Bookstein, 2005; Gerber & Hopkins, 2011; Esquerré *et al.*, 2017). On the other hand, ontogenetic allometry convergence/divergence can reveal directional selection of shape during development. In sum, a multidimensional (shape, size, time, etc.) analysis of phenotypic data holds

potential to interpret speciation events and can provide evidence of ongoing or recent speciation (Hautier *et al.*, 2017; Miranda *et al.*, 2018). In the following article, I present and discuss results that deal with phenotypic differentiation, ontogenetic allometry, and identification of cryptic lineages. I try to stress the importance of such studies for interpreting morphological evolution in the context of phylogenetics and the potential implications of morphological data for species conservation.

Article 1

Skull shape variation in extant pangolins (Pholidota: Manidae): allometric patterns and systematic implications.

In press: *Zoological Journal of the Linnean Society*

Supplemental information for this article is available in Appendix 1.

Zoological Journal of the Linnean Society, 2020, **188**, 255–275. With 8 figures.

Skull shape variation in extant pangolins (Pholidota: Manidae): allometric patterns and systematic implications

SÉRGIO FERREIRA-CARDOSO[1,*], GUILLAUME BILLET[2,*], PHILIPPE GAUBERT[3,4], FRÉDÉRIC DELSUC[1] and LIONEL HAUTIER[1,5]

[1]*ISEM, Université de Montpellier, CNRS, IRD, EPHE, Montpellier, France*
[2]*Centre de Recherche en Paléontologie Paris (CR2P), UMR CNRS 7207, MNHN, CNRS, SU, Muséum National d'Histoire Naturelle, Paris, France*
[3]*Laboratoire Evolution et Diversité Biologique (EDB), Université Paul Sabatier, Toulouse, France*
[4]*CIIMAR / CIMAR, Centro Interdisciplinar de Investigação Marinha e Ambiental, Universidade do Porto, Porto, Portugal*
[5]*Mammal Section, Life Sciences, Vertebrate Division, The Natural History Museum, London, UK*

Received 22 February 2019; revised 17 July 2019; accepted for publication 13 August 2019

Pangolins are among the most endangered groups of mammals, comprising eight extant species delineated into three genera. Despite several studies dedicated to their skeletal anatomy, the potential taxonomic insight from cranial morphological variation in extant Pholidota is yet to be assessed with modern geometric morphometric methods. We present the first comprehensive study on the cranial morphology of extant pangolins and discuss its implications for the taxonomy and evolution of the group. We performed landmark-based morphometric analyses on 241 museum specimens to describe the variation in skull shape in seven of the eight extant species. Our analyses revealed genus- and species-level morphological discrimination, with Asian species (*Manis* spp.) being grouped together, whereas African pangolins present distinct skull shapes between small (*Phataginus* spp.) and large (*Smutsia* spp.) species. Analyses of allometry also identified a set of traits whose allometric trajectories distinguish Asian from African specimens. Finally, we uncovered intraspecific variation in skull shape in white-bellied pangolins (*Phataginus tricuspis*) that partly corroborates recent DNA-based differentiation among biogeographically distinct populations. Overall, our results shed light on the morphological diversity of the skull of these enigmatic myrmecophagous mammals and confirm the genus-level classification and cryptic diversity within the white-bellied pangolin revealed by molecular phylogenetics.

ADDITIONAL KEYWORDS: allometry – conservation – cryptic lineages – ontogeny – systematic.

INTRODUCTION

Extant pangolins [Pholidota (Weber, 1904) Manidae (Gray, 1821)] are currently the most heavily poached mammals in the world (Challender *et al.*, 2014; Zhou *et al.*, 2014). The increasing demand for pangolin scales in Chinese traditional medicine is driving this entire group to the brink of extinction. In that context, detailed morphological and genetic studies constitute a prerequisite to trace the geographical origin of seized specimens and may prove fruitful to delimitate new and more effective conservation management units (von Helversen *et al.*, 2001; Hebert *et al.*, 2004; Bickford *et al.*, 2007; Moraes-Barros *et al.*, 2007; Galatius *et al.*, 2012; Hautier *et al.*, 2014; Sveegaard *et al.*, 2015; Gaubert *et al.*, 2016). The eight extant pangolin species are restricted to tropical and intertropical regions of sub-Saharan Africa and Southeast Asia (Gaubert, 2011; Gaudin *et al.*, 2019). They are classified in a single family (Manidae) within the order Pholidota, which is most closely related to carnivores within placental mammals (Murphy et al., 2001a, b). Pangolins have evolved a set of highly distinctive morphological traits, such as toothless jaws and an

*Corresponding author. E-mail: sergio.ferreira-cardoso@umontpellier.fr

elongated rostrum, linked to their highly specialized diet of ants and termites (Ferreira-Cardoso *et al.*, 2019; Gaudin *et al.*, 2019). Despite this unique evolutionary history and their current protection status, pangolins are among the least studied placental mammals, with some aspects of their phenotypic variation (i.e. cranial shape) still being completely unexplored (Gaubert *et al.*, 2018).

The taxonomy of extant pangolins has been relatively unstable, varying from a single genus (*Manis* Linnaeus, 1758; Jentink, 1882; Emry, 1970) to six genera (Pocock, 1924). Based on both morphological and molecular phylogenetic studies, the four African species have been split into two genera (*Phataginus* Rafinesque, 1821 and *Smutsia* Gray, 1865), whereas the four Asian species remained in a single genus (*Manis*) (Gaudin *et al.*, 2009; Gaubert *et al.*, 2018). A recent molecular phylogeographical study also identified six cryptic lineages within the widely distributed white-belied pangolin (*Phataginus tricuspis* Rafinesque, 1821), showing an unexpected intraspecific molecular divergence (Gaubert *et al.*, 2016). Likewise, several genetic clusters have been identified in the range of the Sunda pangolin (*Manis javanica* Desmarest, 1822), although their geographical delineation remains unclear (Zhang *et al.*, 2015; Nash *et al.*, 2018). Many aspects of inter- and intraspecific diversity of pangolins are still unexplored, and this newly described cryptic diversity has great potential to influence regional conservation policies and to identify the geographical origin of illegally trafficked specimens.

Geometric morphometrics has proved to be an efficient way to define the patterns of shape variation associated with species delimitation (interspecific taxonomy; e.g. Cardini & O'Higgins, 2004; Villemant *et al.*, 2007) and to unveil hidden morphological variation (intraspecific taxonomy; e.g. Hautier et al., 2014, 2017; Miranda *et al.*, 2018). Such methods also enable us to understand the role of interactions between size and shape, with the variation in shape correlated with size (allometry) being one of the main factors contributing to the integrated evolution of cranial shape (Cardini & Polly, 2013; Klingenberg, 2013; Cardini, 2019). In mammals, ontogenetic and evolutionary allometry is mainly associated with elongation of the rostrum (Cardini & Polly, 2013; Cardini *et al.*, 2015). However, the variation in shape and size of the pangolin skull has never been described in detail or quantified formally, although the elongated, toothless snout constitutes one of the main characteristics of their skull. A precise characterization of the changes in shape associated with growth in pangolins should enable us to understand the extent to which allometry has contributed to the evolution of the skull.

Here, we applied geometric morphometric methods to study the variation in shape of the skull within and among the eight extant pangolin species, with the aim of assessing their current taxonomy and the recently identified molecular lineages. First, we examined the patterns of ontogenetic allometry in extant Pholidota using regression and trajectory analyses. Second, we explored the variation in cranial morphological among and within the three extant genera by performing regression, ordination and discriminant analyses. Finally, we investigated the variation in the shape of the skull in two wide-ranging species (*P. tricuspis* and *M. javanica*) in order to assess whether molecular-based cryptic lineages (Gaubert *et al.*, 2018; Nash *et al.*, 2018) differ in skull shape.

MATERIAL AND METHODS

Biological sampling and data collection

The material used in this study belongs to the collections of the Natural History Museum (BMNH) in London (UK), the Museum für Naturkunde (MfN) in Berlin (Germany), the Muséum National d'Histoire Naturelle (MNHN) in Paris (France), the Royal Museum for Central Africa (KMMA/RMAC) in Tervuren (Belgium), the American Museum of Natural History (AMNH) in New York (NY, USA) and the National Museum of Natural History (USNM) in Washington (DC, USA).

Our dataset is the result of the landmarking of 243 specimens from the eight extant species of pangolins (Fig. 1): *P. tricuspis* (Fig. 2; white-bellied pangolin, $N = 97$), *Phataginus tetradactyla* (Linnaeus, 1766) (black-bellied pangolin, $N = 23$), *Smutsia gigantea* (Illinger, 1815) (giant ground pangolin, $N = 16$), *Smutsia temminckii* (Smuts, 1832) (Cape pangolin, $N = 21$), *Manis crassicaudata* Geoffroy, 1803 (Indian pangolin, $N = 10$), *M. javanica* (Sunda pangolin, $N = 38$), *Manis pentadactyla* Linnaeus, 1758 (Chinese pangolin, $N = 36$) and *Manis culionensis* (de Elera, 1915) (Palawan pangolin, $N = 2$; Supporting Information, Appendix S1). The skull shape of the Palawan pangolin could not be assessed quantitatively owing to the low number of specimens available and the relatively large number of missing landmarks [a principal components analysis (PCA) including this species is provided in the Supporting Information, Fig. S1]. Taxa were identified based on a list of morphological criteria identified in the present study and in previously published works (Supporting Information, Appendix S2; Hatt *et al.*, 1934; Gaudin et al., 2009, 2019). Different sizes of skulls were included to account for the change in shape during ontogeny. Given the absence of teeth in pangolins, the determination of age is not straightforward. For each species, juveniles were defined arbitrarily as those for which size (estimated by the centroid size; see below) fell

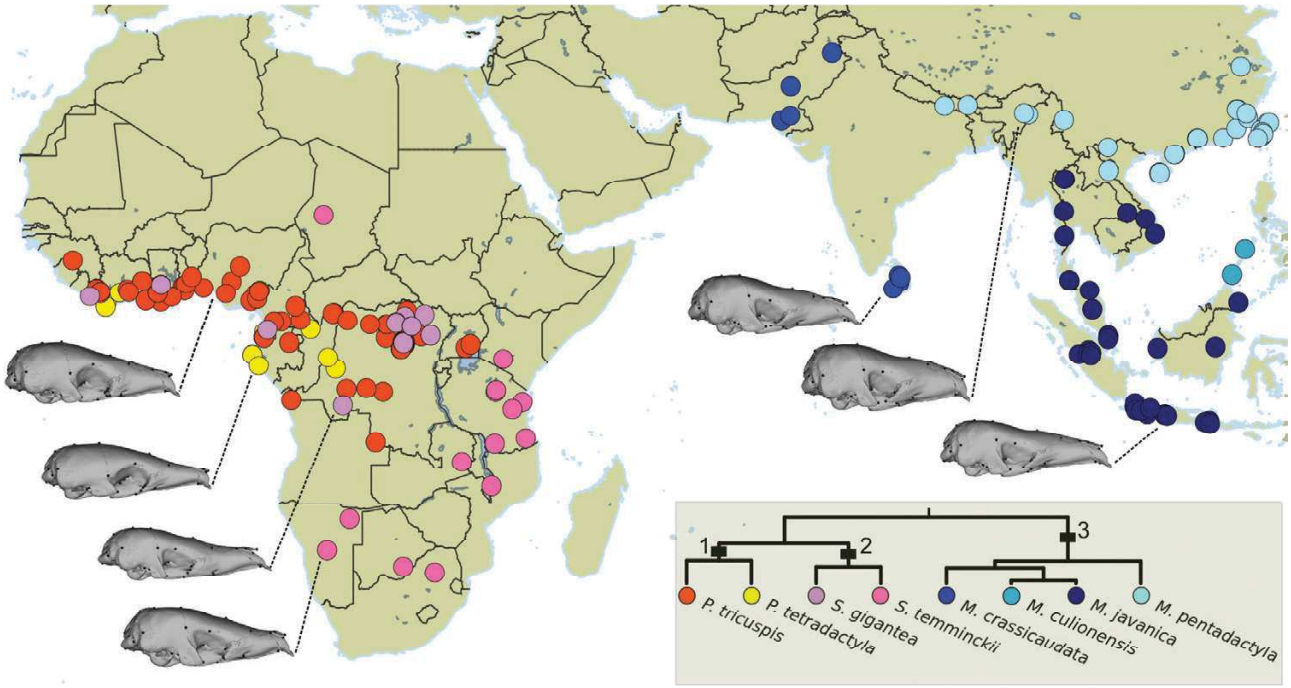

Figure 1. Geographical distribution of the sampled specimens (N = 243) belonging to eight species of pangolins. Mean shapes are illustrated for each species, except for *Manis culionensis*. The phylogenetic relationships used the branch lengths from Gaubert *et al.* (2018). 1, Phatagininae; 2, Smutsiinae; 3, Maninae.

below the first quartile value (25% smallest specimens) for each species.

We placed 75 three-dimensional landmarks on pangolin skulls using a Revware MicroScribe M 3D digitizer (Fig. 3; Supporting Information, Table S1). Our selection of landmarks was based on previous works focused on mammalian taxa (e.g. Goswami, 2006; Hautier *et al.*, 2017). In a significant number of specimens, the premaxillae were absent, loosely attached or broken and could not be landmarked. In pangolins, the jugal bone is often absent. However, some *M. pentadactyla* specimens presented a complete zygomatic arch (see also Emry, 2004). In such cases, the landmarks 58/72 (zygomatic process of the maxillae) were hard to define accurately. They were therefore considered as missing and estimated a posteriori.

Thin plate spline interpolations (Gunz *et al.*, 2009) were computed to estimate missing landmarks for each group (e.g. species, cryptic lineages). This approach was implemented in the software package 'geomorph' v.3.5.0 (Adams *et al.*, 2017) in R (R Development Core Team, 2013). A generalized Procrustes analysis (Rohlf & Slice, 1999) was performed on all sets of landmarks. All specimens were scaled to centroid size, optimally translated and rotated using a least-squares criterion. The coordinates retrieved by the generalized Procrustes analysis represented the shape of the skull of each specimen. An ANOVA was performed on a subset of our data for which sex determination was available (N = 120), in order to assess sexual dimorphism in skull shape.

Allometry in extant pangolins

The study of allometry can focus on three different levels (Cheverud, 1982; Klingenberg, 2016). Morphological changes can be associated with phylogenetic differences in size (evolutionary allometry), variation in size within a single ontogenetic stage (static allometry) or variation in size attributable to individual growth within a single species (ontogenetic allometry; e.g. Foth *et al.*, 2016; Esquerré *et al.*, 2017; Gray *et al.*, 2019). Here, we quantified evolutionary allometry and considered three traits of ontogenetic allometric trajectories: direction (slope), magnitude (length) and intercept. These aspects were controlled/investigated with three different analyses.

First, a phylogenetic multivariate regression of the mean shape of adult specimens (N = 173) against log-centroid size was performed to assess evolutionary allometry. This analysis was performed with *procD.pgls* from 'geomorph' using a consensus phylogeny from Gaubert *et al.*, (2018). Then, we focused on ontogenetic allometry using interspecific (N = 241) and intraspecific datasets. The cryptic lineages dataset including *P. tricuspis* included only

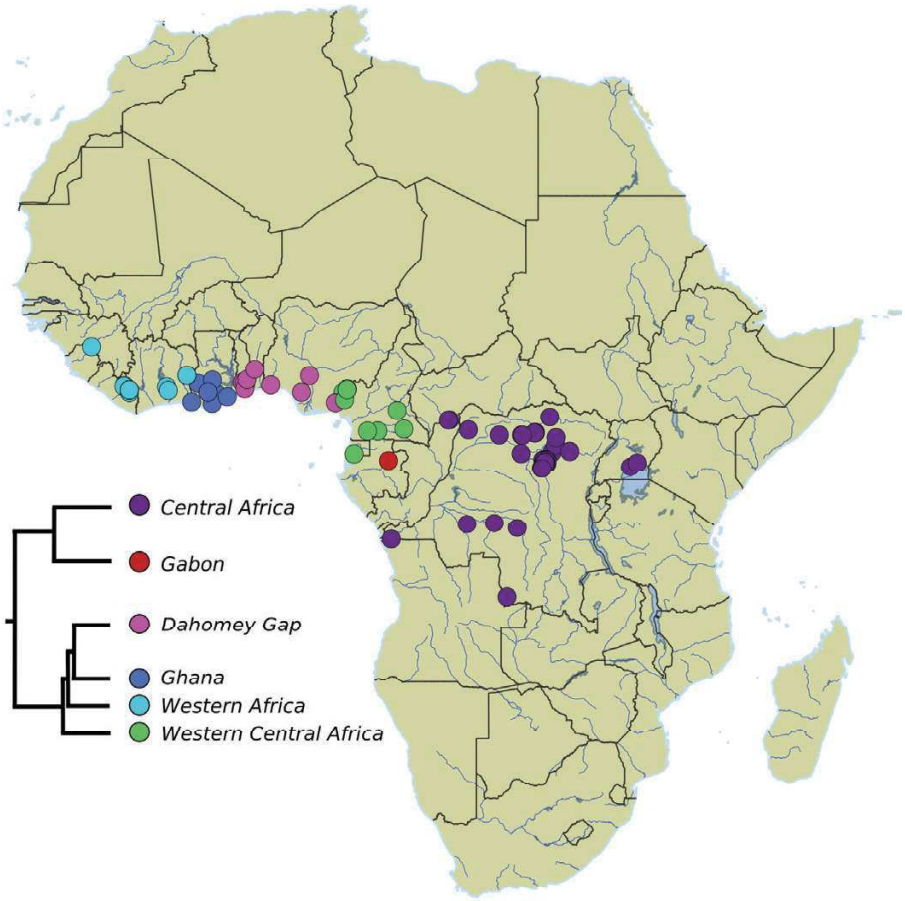

Figure 2. Map of Africa, with the locations of the sampled *Phataginus tricuspis* (N = 96) coloured according to the cryptic lineage (Gaubert *et al.*, 2016) to which they were attributed (right). The tree topology of the intraspecific affinities is based on Gaubert *et al.* (2018).

96 specimens (Fig. 2; KMMA 30808 was discarded owing to imprecise information on location). Details about the analysis of the *M. javanica* dataset can be found in the Supporting Information (Appendix S3). First, a multivariate regression was performed to assess covariation patterns between the logarithm of the centroid size and Procrustes-aligned coordinates (raw shapes) using *procD.lm* from 'geomorph'. The hypothesis of parallel group slopes was assessed with a homogeneity of slopes (HOS) test. This test consists of an analysis of covariance (ANCOVA) to assess the influence of size, groups and the interaction of size and groups on skull shape. The HOS test includes pairwise comparisons between groups (species/cryptic lineages) to assess significant differences of both the direction (angles) and magnitude (amount of change in shape with size) of allometric trajectories. Significance was assessed with a residual randomization permutation procedure with 10 000 iterations. The HOS tests were performed with *advanced.procD.lm* from the package 'geomorph'. The HOS tests were complemented by graphical representations of allometric trajectories and skull shape deformations (Adams & Nistri, 2010; Esquerré *et al.*, 2017). We plotted the first principal component (PC1) of the predicted values of multivariate regression of shape on log-centroid size vs. log-centroid size regressions for each species. We then assessed the significance of differences between the intercepts using a Tukey means comparison, to test for changes in shape explained by species differences in the resulting morphospace. Thin plate splines were generated using the function *tps3D* from the R package 'Morpho' v.2.5.1 (Schlager, 2017) in order to characterize differences in shape between the smallest and the largest specimens for each species (ontogenetic allometry). We then visualized landmark displacement during ontogeny using the function *deformGrid3d* from the same package. A phenotypic trajectory analysis (PTA) was also performed as a complementary analysis to the HOS test (see Supporting Information, Appendix S3; Adams & Collyer, 2009; Collyer & Adams, 2013).

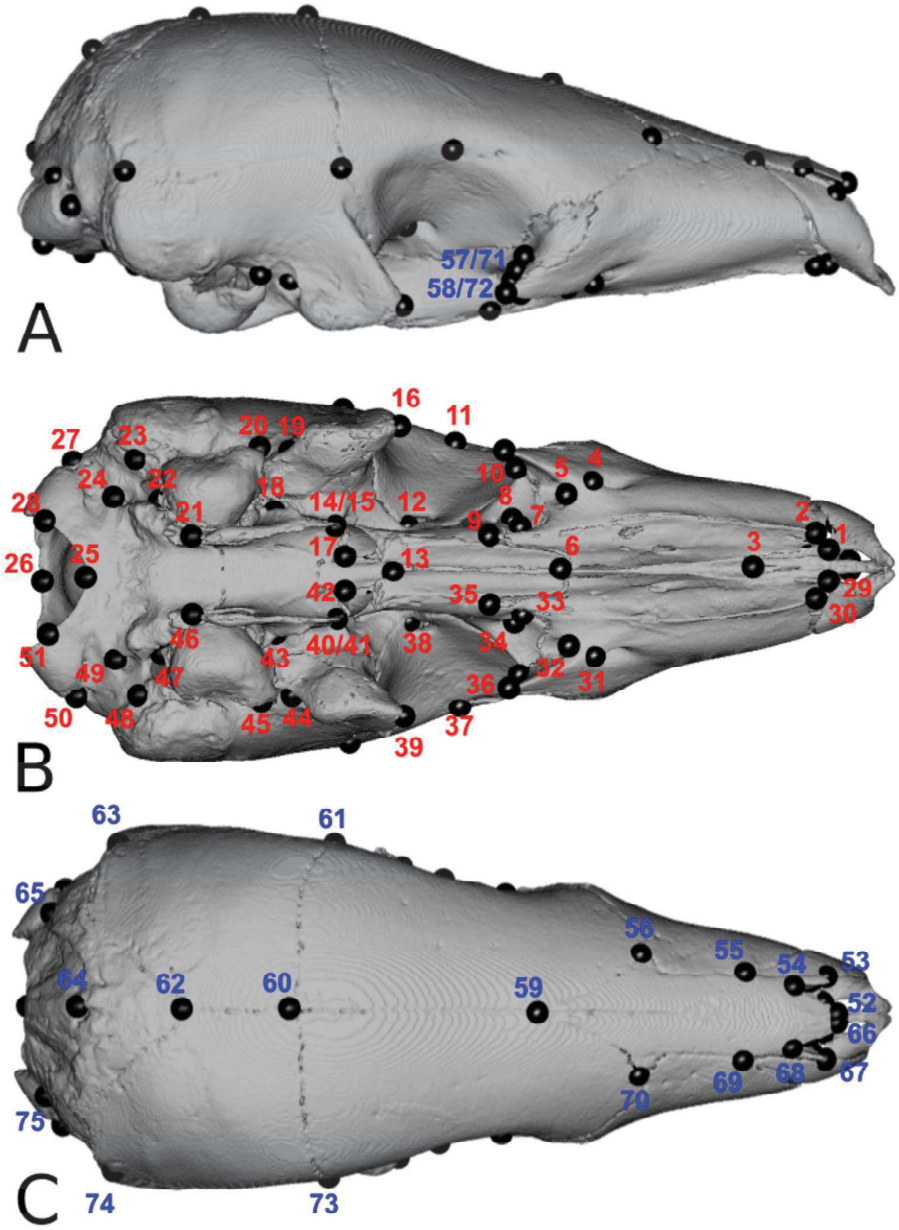

Figure 3. Landmarks digitized on the skull of *Phataginus tricuspis* (BMNH 34.6.2.92) in lateral (A), ventral (B) and dorsal (C) views. Red and blue numbers represent landmarks placed ventrally and dorsally, respectively.

Second, when the HOS test revealed parallel trajectories, we performed an additional analysis (overlap test) on multivariate shape data to test for overlap in ontogenetic allometric trajectories by comparing their differences with a set of 10 000 permutations (Piras *et al.*, 2011; Esquerré *et al.*, 2017). Intercepts were tested at $x = 5.125$, because we lacked fetuses and neonates of small size (close to $x = 0$), which could result in an incorrect estimate of minimum size ($x = 0$). The overlap test was performed only on the interspecific dataset.

Finally, if slopes were overlapping between species, a third analysis was performed to identify peramorphosis/paedomorphosis. This 'heterochrony test' enables the characterization of differences in skull shape at maximum size (Piras *et al.*, 2011; Esquerré *et al.*, 2017). Significance was assessed by comparing these differences with a set of 10 000

permutations. This test was performed only on the interspecific dataset.

Visualization of shape variation and statistical analysis

The variation of skull shapes was visualized using a PCA (Dryden & Mardia, 1993). Data were analysed without allometric correction in order to allow for a comparison of the results with morphological discrete characters used in phylogenetic analyses. Analyses with the allometry-corrected shapes for the interspecific and *P. tricuspis* datasets can be found in the Supporting Information (Appendix S3). Allometry-corrected shapes were obtained as the residuals of pooled within-group regressions. This method is used to obtain a common estimate for the allometry when comparing several groups (Sidlauskas *et al.*, 2011; Benítez *et al.*, 2013; Klingenberg, 2016). Pooled within-group regressions were performed in MorphoJ v1.06d (Klingenberg, 2011). For simplicity, when PCAs were performed on allometry-corrected shapes, axes were designated as PCres.

Interspecific variation in extant pangolins

A PCA was performed excluding specimens considered as juveniles (N = 173). A second PCA was performed on a dataset including juveniles and two specimens of *M. culionensis* (N = 243). We used a .ply surface of a micro-computed tomography-scanned *P. tricuspis* skull (BMNH 34.6.2.92), the species most closely resembling the mean shape. The surface was then deformed to the mean skull shape of Pholidota and used to visualize the variation in skull shape along the first three principal components (PCs). Triangular mesh warping via thin plate spline was performed with the package 'Morpho'.

A multivariate ANOVA was performed to assess whether skull shape differed between taxonomic groups. Pairwise comparisons between least-squares means were performed using *advanced.procD.lm*. If taxonomy had a significant effect on skull shape, a leave-one-out cross-validated linear discriminant analysis (LDA) was performed on a set of PCs explaining 90% of variance. The leave-one-out procedure allows evaluation of the accuracy with which unknown specimens can be identified (e.g. Evin *et al.*, 2013). Linear discriminant analyses and post hoc classification methods were performed with the 'MASS' package (Venables & Ripley, 2002) in R.

Intraspecific variation in P. tricuspis and M. javanica

A second subset including only adult *P. tricuspis* specimens was analysed separately in order to describe the intraspecific variation in skull shape (N = 71). We used the cryptic genetic lineages defined by Gaubert *et al.* (2016) to test the variation in skull shape linked to geographical distribution within *P. tricuspis*. Specimens were sorted according to six regions (Fig. 2): Western Africa (WAF), Ghana (GHA), Dahomey Gap (DHG), Western Central Africa (WCA), Central Africa (CAF) and Gabon (GAB). Skull shape difference tests and cross-validated LDA described in the previous paragraph were repeated on this dataset. If a posteriori attribution errors were consistently detected between two regions, these were merged, and the protocol was repeated with the new specimen sorting in order to test for its potential in assigning specimens with unknown geographical origin.

An equivalent protocol was applied to assess intraspecific variation in the skull of *M. javanica*. The geographical delimitation of cryptic lineages within this species is still uncertain (Zhang *et al.*, 2015; Nash *et al.*, 2018). These preliminary analyses can be found in the Supporting Information (Appendix S3).

The original landmark coordinates used in this study are provided in the Supporting Information (Appendix S1).

RESULTS

Allometry in extant pangolins

A multivariate regression (Table 1) performed on raw shape variables revealed significant effects of log-transformed centroid size ($F_{1,227}$ = 103.59, P < 0.001, R^2 = 0.16), species grouping ($F_{6,227}$ = 49.63, P < 0.001) and of an interaction between centroid size and species grouping ($F_{6,227}$ = 1.35, P < 0.001) on shape. When we accounted for phylogeny, the effect of size was marginally non-significant (P = 0.09), with evolutionary allometry explaining roughly one-third of skull shape variance (R^2 = 0.27; Supporting Information, Table S2). The non-significant P-value was probably attributable to the low number of species (N = 7). The HOS test

Table 1. ANOVA of shape (Procrustes coordinates) ~ log(centroid size)*species

	d.f.	R^2	F	P-value
Log(centroid size)	1	0.16	103.59	< 0.001*
Species	6	0.47	49.63	< 0.001*
Log(centroid size):species	6	0.01	1.35	< 0.001*
Residuals	227	0.37	–	–
Total	240	–	–	–

The randomized residual permutation procedure used 10 000 permutations.
*Significant P-value.

pairwise comparisons of ontogenetic allometric trajectories revealed small, significant differences (low z-values) between the slopes of *S. gigantea* compared with both *M. javanica* and *M. pentadactyla* (Supporting Information, Table S3). The remaining species did not present significantly different slope angles, which implied that allometric trajectories were parallel within each genus. The results for the PTA are presented in the Supporting Information (Appendix S3; Fig. S2; Tables S4 and S5).

The ontogenetic allometric trajectories overlapped in most species presenting parallel slopes except for *P. tricuspis* (Supporting Information, Table S6). The trajectory for *P. tetradactyla* overlapped with all the others except those of *M. javanica* and *P. tricuspis*. When comparison of the intercepts was performed considering shape predictions for $x = 0$, the ontogenetic allometric trajectories overlapped in all species (Supporting Information, Table S7). The heterochrony test showed that all species with overlapping trajectories presented heterochronic shifts with respect to each other (Supporting Information, Table S8).

The intercepts of the regressions of predicted values of shape against size (Fig. 4) were relatively distinct within *Phataginus* and *Manis*, whereas both *Smutsia* species presented overlapping trajectories, as revealed by the Tukey comparisons (Supporting Information, Table S9). Considering the predicted shapes for minimum and maximum size resulting from the multivariate regression, the main size-related intraspecific morphological change was the increase in length of the rostrum (Figs 4, 5). Landmarks in the anterior part of the nasal and maxilla tended to be more anterodorsally positioned, and the nasal projected more posteriorly (e.g. Fig. 4, 5). The braincase was relatively lower in the adult, across all species, with the dorsal landmarks on the midline of the skull being more ventral when compared with their position in the juveniles (Fig. 5). Additionally, the landmarks placed on the zygomatic process of the maxilla and associated structures (Fig. 3; landmarks 10, 57 and 58) showed a tendency to project more posteriorly in larger specimens (Fig. 5A–D). In contrast, *S. temminckii* showed no allometric growth of the posterior projection of the zygomatic processes (Fig. 5E). In contrast, this species presented the most significant change in the anterior projection of the zygomatic process of the squamosal, with this structure being noticeably less projected in smaller specimens (Fig. 5E).

Interspecific variation of the skull shape in extant pangolins

A Procrustes ANOVA revealed that both sex ($F_{1,105} = 1.80$, $P = 0.085$; $F_{1,106} = 2.03$, $P = 0.057$) and

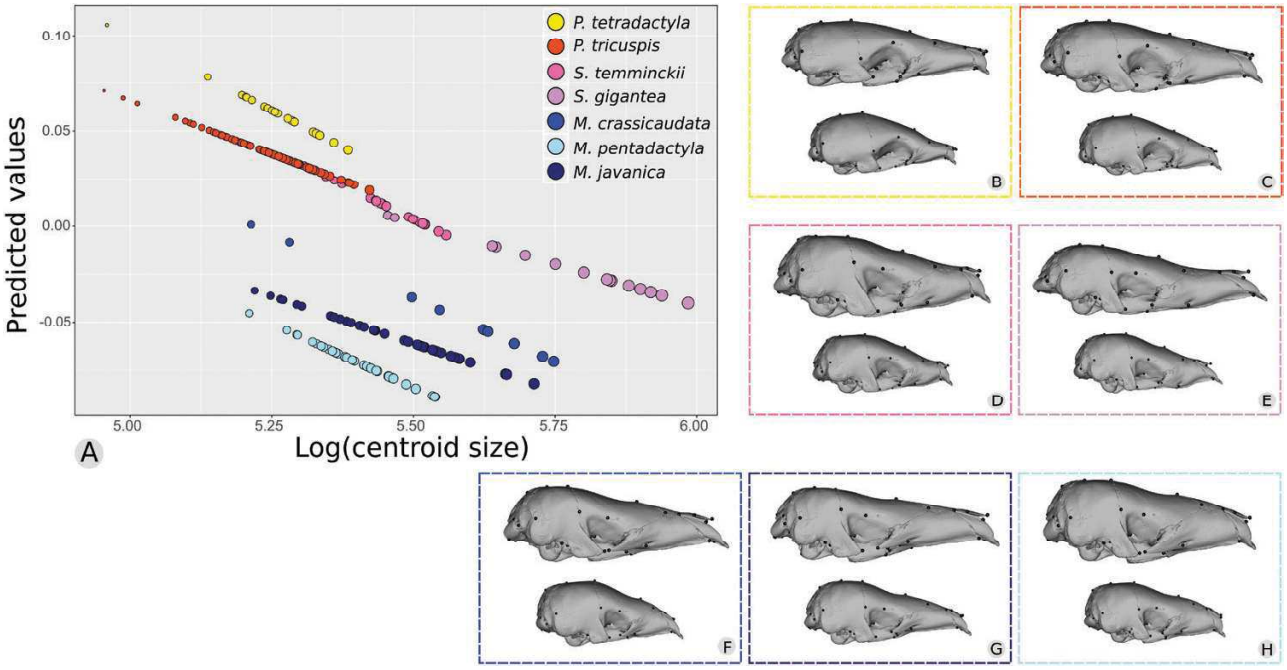

Figure 4. Allometric trajectories among seven pangolin species ($N = 241$). A, the x-axis values are the log-transformed centroid sizes for each specimen; the y-axis values are the principal component 1 of the predicted values of a multivariate regression of shape on size. B–H, deformed meshes for the maximum (top) and minimum (bottom) shapes predicted from a multivariate Procrustes regression for each species are presented.

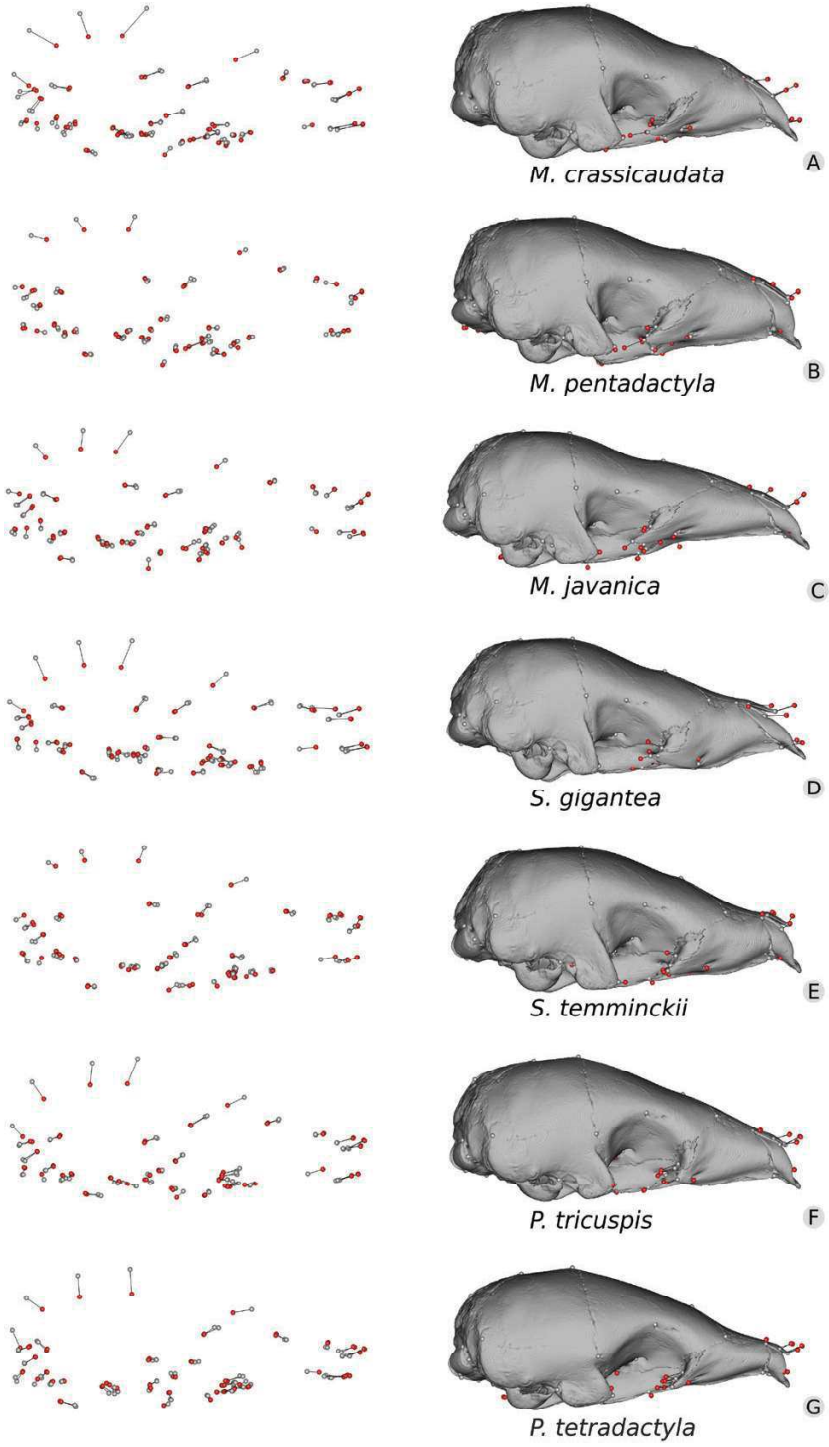

Figure 5. Mapping of ontogenetic variation in shape in seven pangolin species. A, *Manis crassicaudata*. B, *Manis pentadactyla*. C, *Manis javanica*. D, *Smutsia gigantea*. E, *Smutsia temminckii*. F, *Phataginus tricuspis*. G, *Phataginus tetradactyla*. Grey dots represent relative Procrustes coordinates positions in the juvenile (minimum-sized specimen), and red dots represent coordinates for the adult (maximum-sized specimen). Deformed meshes corresponding to juveniles were superimposed with the three-dimensional Procrustes coordinates.

the interaction between sex and species grouping ($F_{6,105}$ = 0.89, P = 0.656; $F_{6,106}$ = 1.07, P = 0.332) did not significantly influence shape, with and without considering size as a covariate in the model, respectively (N = 120; Supporting Information, Table S10). The Procrustes ANOVA performed with the adult dataset revealed a significant effect of species on skull shape ($F_{6,166}$ = 45.02, P < 0.001; Table 2). Pairwise comparisons showed that all species presented significantly different skull shapes (Supporting Information, Table S11). The variation in skull shape was visualized using a PCA performed on the raw shape variables of the seven pangolin species (Fig. 6). The results of a PCA including juveniles and *M. culionensis* (Supporting Information, Fig. S1) and a full analysis of allometry-corrected skull shape are presented in the Supporting Information (Appendix S3; Fig. S3; Tables S12, S13). Despite the non-parallel slopes, the variance explained by the interaction between size and species was relatively low (Table 1), allowing us to use the residuals of a multivariate regression of shape on size as allometry-corrected shapes.

Linear regressions performed on the first 30 PCs (90%) showed that size was significantly correlated with PCs 1–4 and PC7 (Supporting Information, Table S14). Size-related morphological changes captured by PC1 appeared to be associated mainly with evolutionary allometry, whereas change in shape along PC2 recovered differences related to ontogenetic allometry. The first two PCs explained 49.59% of the total variance (33.95 and 15.64%, respectively).

Principal component 1 was positively correlated with a high and wide rostrum, a nasofrontal inflation associated with an orbital constriction, posteriorly projected zygomatic processes of the maxillary and a high and wide braincase, with dorsal squamosal-parietal-frontal junctions. African specimens tended to display mostly negative PC1 scores, whereas the Asian clade exhibited positive PC1 scores (Fig. 6A, B). The sole exception was the African *S. gigantea*, which presented positive PC1 values and grouped with Asian specimens (Fig. 6). Principal component 1 also separated the two African genera (*Phataginus* presented the most negative scores). Juvenile specimens of Asian species were characterized by less positive PC1 values, plotting closer to African pangolins (see 'Results: allometry within extant pangolins'; Supporting Information, Fig. S1).

Principal component 2 was positively correlated with a long rostrum, a long posterior projection of the premaxilla on the midline, an anterolaterally projecting zygomatic process of the squamosal and a braincase with a pseudorectangular shape in dorsal view (Fig. 6). Principal component 2 separated the three species of *Manis* and the two *Smutsia*. *Smutsia temminckii* and *M. pentadactyla* scored the lowest PC2 average values, whereas *M. javanica* scored the highest. *Phataginus* spp., *S. gigantea* and *M. crassicaudata* presented PC2 scores ranging in between the two groups.

Principal component 3 scores were positively correlated with the anterior projection of the anterior flanges of the frontal, a wide and long palatine, a long infraorbital canal, an anteroposteriorly elongated dorsal edge of the zygomatic processes of the squamosal and posteriorly projected pterygoid hamuli (Fig. 6B). This axis separated species within *Phataginus* and *Smutsia*. *Phataginus tetradactyla* scored extremely positive PC3 values, whereas *S. gigantea* scored the most negative PC3. The three *Manis* species and *S. temminckii* presented values slightly above zero, on average, and *P. tricuspis* showed mostly negative values, but not as negative as *S. gigantea* (Fig. 6B).

An LDA was performed to take 90% of the variance into account (first 30 PCs). Linear discriminant analysis group a posteriori probabilities retrieved 100% accuracy for species attribution (Supplemental Information, Appendix S4). Specimens were grouped by species and were well discriminated on linear discriminants 1 and 2 (LD1, 54.0%; LD2, 15.6%; Fig. 6C, D). Asian pangolin skulls presented negative LD1 values, whereas African pangolins scored both negative (*Smutsia*) and extremely positive values (*Phataginus*; Fig. 6C, D). The three species of Maninae Gray, 1821 resembled each other the most, being discriminated only by LD2. Within the African clade, LD2 discriminated the two *Phataginus* species (*P. tetradactyla* showed the highest

Table 2. ANOVA of shape ~ taxa/geographical groups of adult specimens of the interspecific and *Phataginus tricuspis* datasets

Datasets	*N* taxa/geo	*N*	d.f.	R^2	*F*	*P*-value
Interspecific	7	173	166	0.62	45.02	< 0.001*
P. tricuspis (Gaubert *et al.*, 2016)	6	70	65	0.16	3.12	< 0.001*
P. tricuspis (geographical groups)	3	70	67	0.11	4.23	< 0.001*

The randomized residual permutation procedure used 10 000 permutations. Significant *P*-values indicate differences between skull shapes of taxa/geographical groups.
Abbreviation: *N* taxa/geo, number of taxa or geographical groups used as factors.
*Significant *P*-value.

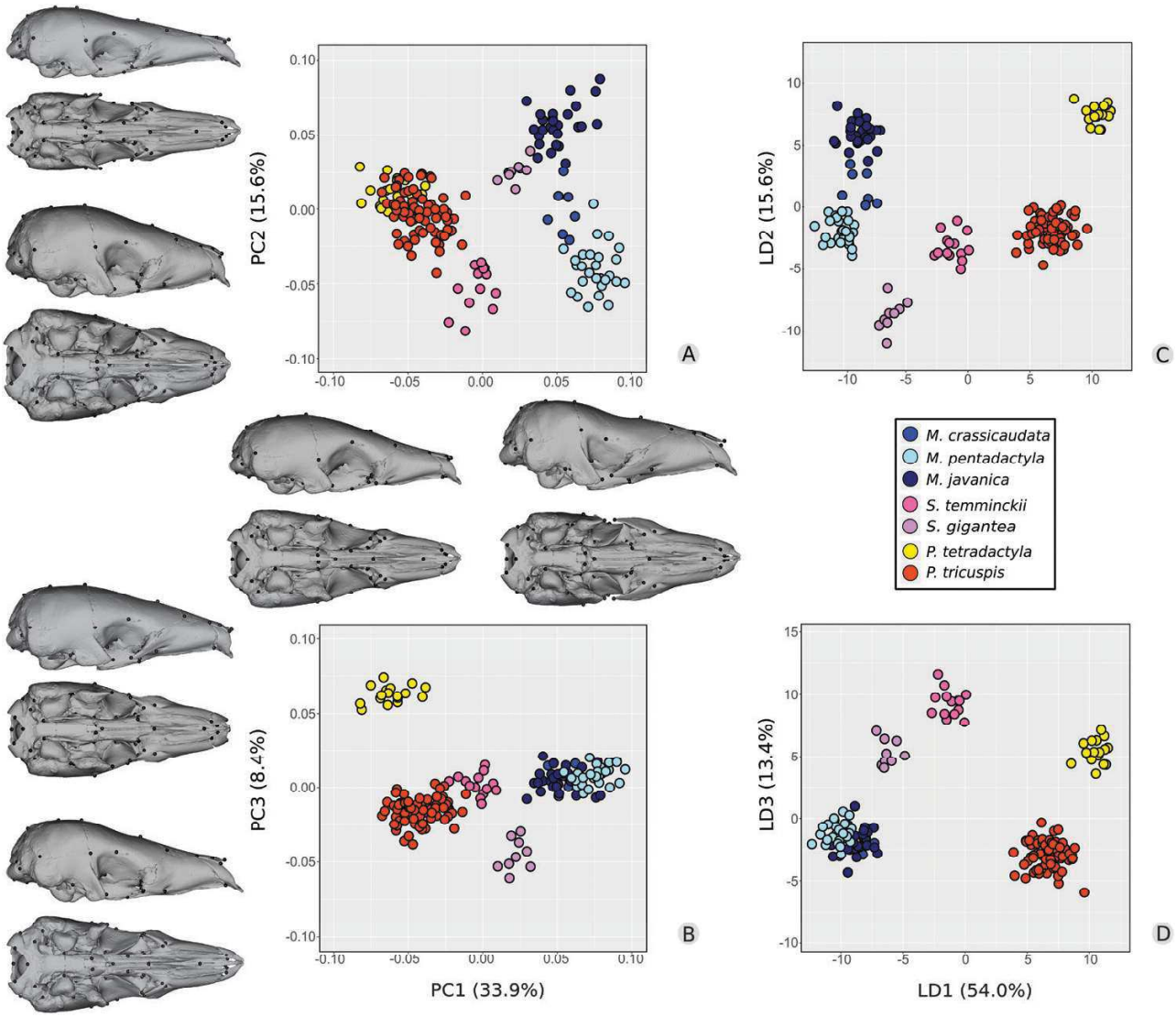

Figure 6. Principal components (A, PC1 vs. PC2; B, PC1 vs. PC3) and linear discriminant analyses (C, LD1 vs. LD2; D, LD1 vs. LD3) with associated variation in shape for crania of seven pangolin species (N = 173).

LD2 values). *Smutsia temminckii* and *S. gigantea* were well discriminated by LD1. *Smutsia* spp. showed the highest LD3 values.

The analyses on the allometry-corrected shapes revealed some differences that are discussed in detail in the Supporting information (Fig. S3; Tables S12 and S13).

Intraspecific variation of the skull shape in extant pangolins

Intraspecific variation in P. tricuspis

A multivariate regression revealed that log-transformed centroid size ($F_{1,84}$ = 11.56, P < 0.001) and geographical distribution (cryptic lineages; $F_{4,84}$ = 3.71, P < 0.001) had a highly significant effect on the cranial shape (Table 3). It also retrieved a significant effect of the interaction between size and geographical distribution ($F_{4,84}$ = 1.11, P = 0.001). However, the pairwise matrix effect sizes were relatively small, and corresponding P-values were not significant. Therefore, all cryptic lineages presented parallel allometric trajectories (Supporting Information, Fig. S4; Table S15). A Procrustes ANOVA revealed that cryptic lineages presented different skull shapes ($F_{4,65}$ = 3,12, P < 0.001; Table 2). Pairwise comparisons showed that all tested cryptic lineages presented significantly different skull shapes except for Ghana and Western Africa (Supporting Information, Table S16) Gabon was not tested owing to lack of replicates.

Table 3. ANOVA of shape (Procrustes coordinates) ~ log(centroid size)**Phataginus tricuspis* cryptic lineages ($N = 96$)

	d.f.	R^2	F	P-value
Log(centroid size)	1	0.10	11.56	< 0.001*
Cryptic lineages	5	0.15	3.71	< 0.001*
Log(centroid size):cryptic lineages	4	0.04	1.11	0.001*
Residuals	85	0.71	–	–
Total	95	–	–	–

The randomized residual permutation procedure used 10 000 permutations.
*Significant P-value.

Principal component 1 explained 12.8% of the variance of cranial shape within *P. tricuspis* and was positively correlated with a larger skull height and width, an anteroposteriorly short orbit, large tympanic bullae and a relatively round occipital region. Specimens from Central Africa mostly scored negative PC1 values (Fig. 7A, B). On average, specimens from WAF and GHA presented the most positive PC1 scores. The Western Central African cluster also presented mostly positive PC1 scores, whereas specimens from the Dahomey Gap presented a wide range of PC1 scores, varying from negative to positive values. The only specimen from Gabon scored negative PC1 values, plotting near the CAF morphospace.

Principal component 2 explained 9.7% of the variance and was positively correlated with a shorter palate with short maxillary projections, anteriorly projecting squamosal roots and shorter tympanic bullae well separated from the postglenoid foramina. Although specimens from CAF had a wide distribution along PC2, WCA, WAF and GHA presented a much narrower range of PC2 scores in the middle of the distribution. On average, DHG presented the most negative PC2 values.

Principal component 3 explained 6.4% of the variance (Fig. 7B) and did not segregate specimens according to geographical origin.

The LDA performed on the first 34 PCs (90% variance) discriminated WAF–GHA, DHG and CAF–WCA cryptic lineages, along LD1 (59.1%) (Fig. 7C). Western Africa–Ghana presented the most positive LD1 values, whereas CAF–WCA specimens presented mostly negative LD1 values (Fig. 7C, D). Specimens from DHG presented intermediate positive LD1 values. LD2 (23.7%) discriminated DHG skulls (negative values) from all other cryptic lineage specimens (Fig. 7C). LD3 (13.0%) discriminated the WCA specimens (most positive values) from the remaining lineages (Fig. 7D). Group a posteriori probabilities retrieved a 75.4% attribution accuracy (see Supporting Information, Appendix S4). The vast majority of incorrect attributions were found in the major divisions WAF–GHA and CAF–WCA. Based on this result, we performed an additional LDA with a priori attributions of WAF–GHA specimens to a western group (WES) and CAF–WCA specimens to an eastern group (CEN), while keeping DHG as a separate group (Fig. 8). Group a posteriori probabilities of the LDA of the three groups shows an attribution accuracy of 95.7% (see Supporting Information, Appendix S4).

The additional LDA discriminated CEN from WES and DHG groups along LD1 (73.3%). LD2 (26.7%) discriminated CEN and WES from DHG groups. We tested the statistical significance of the intraspecific variation in the three groups identified above. A Procrustes ANOVA revealed a significant effect of the division of *P. tricuspis* into three morphological groups, WES, DHG and CEN ($F_{2,67} = 4.23$, $P < 0.001$; Table 2). Pairwise comparisons showed that all groups presented significantly different skull shapes (Supporting Information, Table S17). We calculated the mean shapes for each group (Supporting Information, Fig. S5). The WES skulls presented the shortest and widest rostrum, a relatively elongated infraorbital canal and the longest zygomatic process of the maxillary. The DHG skulls presented the widest nasals posteriorly, the most posterior projections of the maxilla into the palatine and the most posterior ventral margin of the foramen magnum. Skulls from the CEN region were characterized by the narrowest rostra, the smallest tympanic bullae and the most anterior petrosal–squamosal–exoccipital intersection.

The analyses on the allometry-corrected shapes revealed similar results (Supporting Information, Appendix S3; Fig. S6; Tables S12, S18, and S19).

Intraspecific variation in M. javanica

The analyses on the *M. javanica* dataset showed that differences in shape were solely explained by differences in size (Supporting Information, Figs S7, S8; Tables S12 and S20).

DISCUSSION

Size influences skull shape in extant pangolins

Size explained a significant part of the total variation in skull shape among species within the Pholidota (evolutionary allometry; Table 1; Fig. 4; Supporting Information, Fig. S2; Table S2). The HOS and PTA tests showed that the directions of ontogenetic trajectories were conserved among pangolins, with only *M. javanica* and *M. pentadactyla* differing significantly from *S. gigantea* (HOS) and

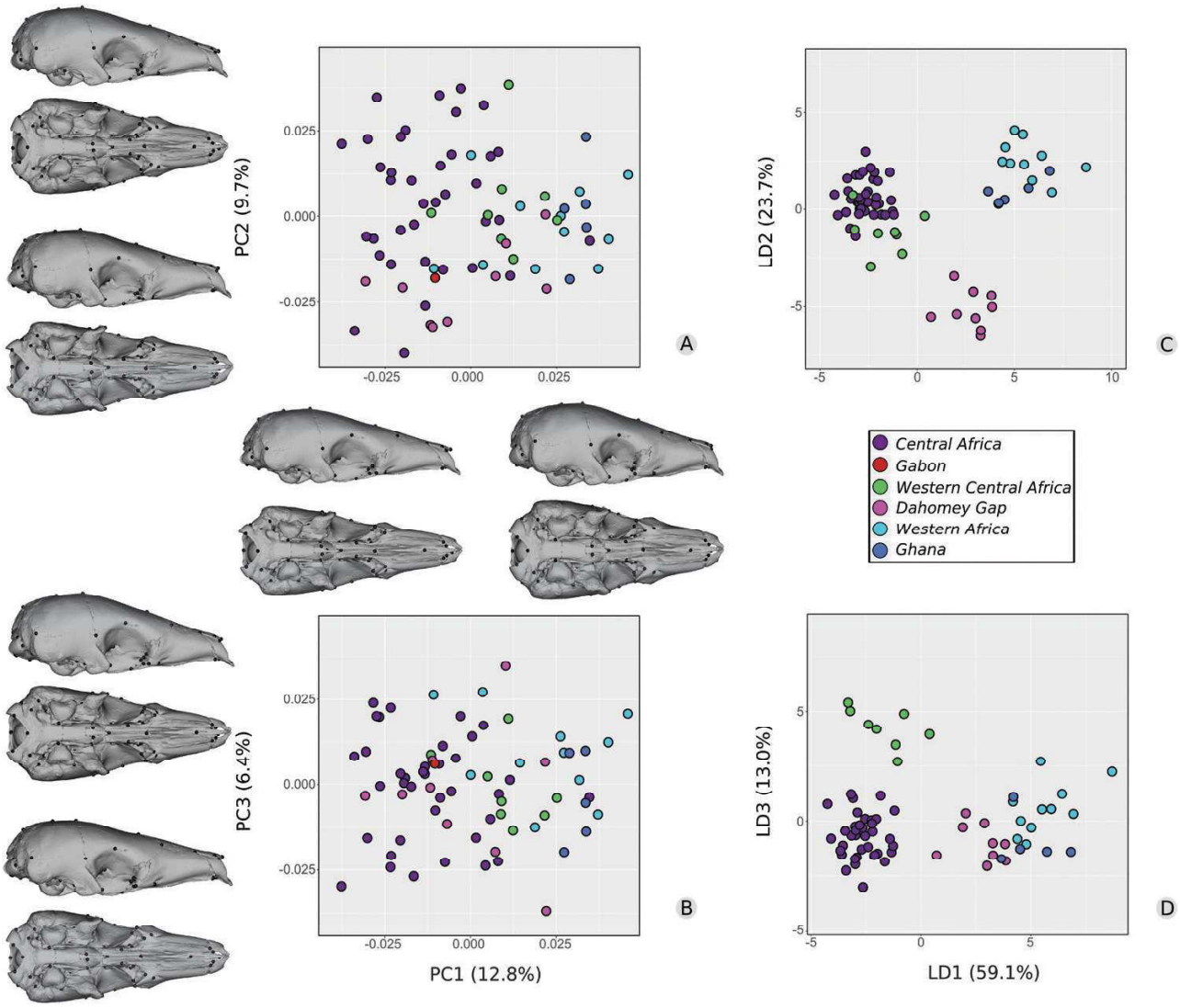

Figure 7. Principal components (A, PC1 vs. PC2; B, PC1 vs. PC3) and linear discriminant analyses (C, LD1 vs. LD2; D, LD1 vs. LD3) with associated variation in shape for crania of six cryptic lineages of *Phataginus tricuspis* (N = 71; Gaubert *et al.*, 2016).

P. tricuspis (PTA; Supporting Information, Tables S4 and S5). Ontogenetic trajectory angles did not differ within clades, which is consistent with observations that intraspecific (ontogenetic and/or static) allometric trajectories tend to differ as species divergence time increases (Voje *et al.*, 2014; Esquerré *et al.*, 2017).

Significant differences between the intercepts of multivariate regressions (overlap test) were found only between *P. tricuspis* and all other species and between *P. tetradactyla* and *M. javanica*. With the exception of the difference in intercept between the two *Phataginus* species, significant P-values were relatively close to 0.05 (i.e. same order of magnitude). This indicates that allometric trajectories are still relatively preserved across the Pholidota and suggests that cranial morphology is similar in early developmental stages. The heterochrony test showed that more than half of the pairwise comparisons performed (12 out of 19) revealed heterochronic changes. In fact, when the overlap test was performed taking size = 0 as reference, heterochrony was detected for all 19 comparisons (Supporting Information, Tables S6 and S7). This could suggest a major pattern of heterochrony driving the differentiation between the Asian and African clades, the first being putatively peramorphic by presenting longer rostra and longer zygomatic processes of the maxilla (traits associated with the PC1 of the predicted values; Figs 4, 5). However, given the absence of fetuses in our analyses, predictions of shape at minimum size (x = 0)

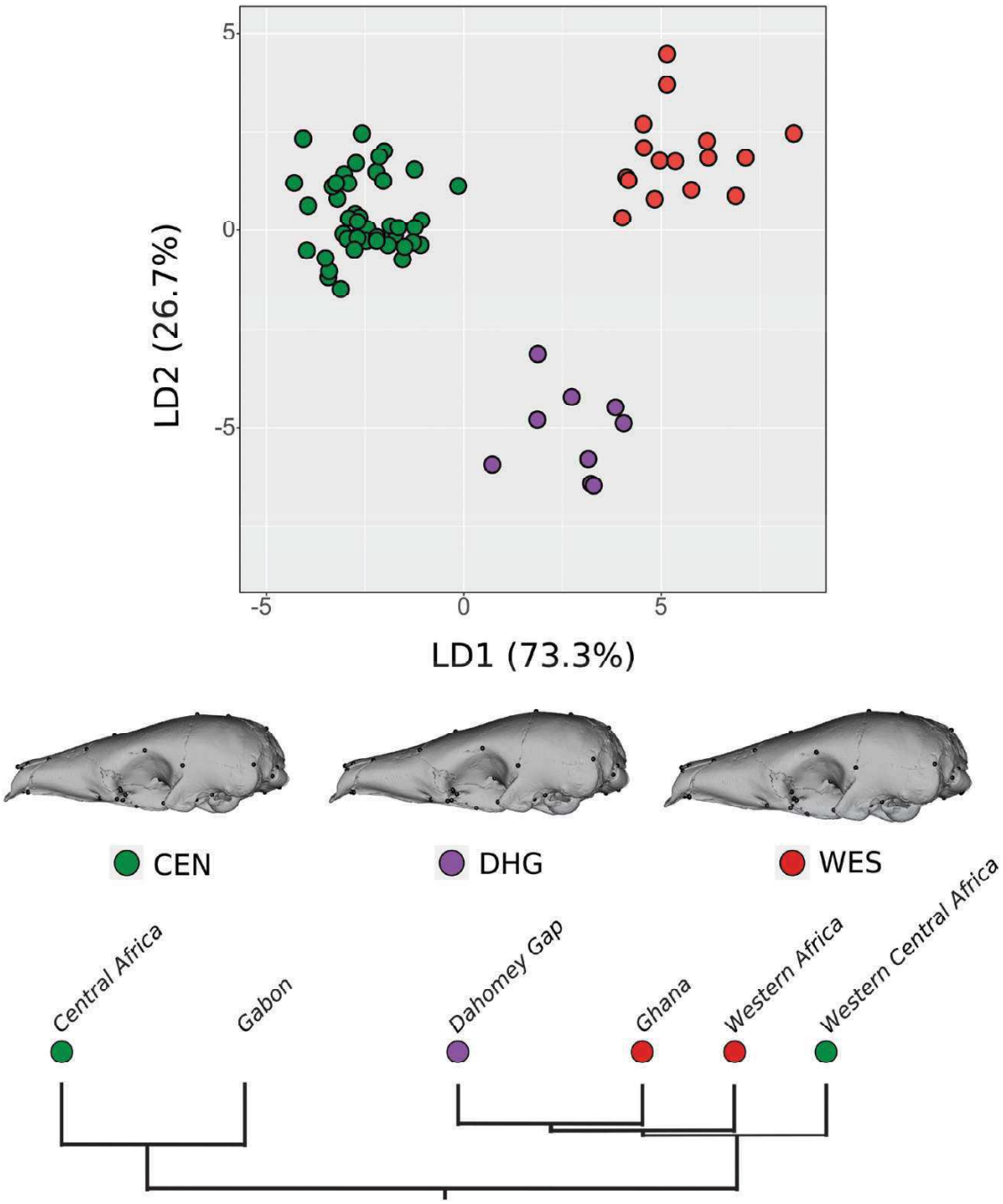

Figure 8. Linear discriminant analysis of the *Phataginus tricuspis* sample (N = 70) divided into three management units. Consensus shapes (mean shapes) of the proposed management units in lateral view. A, Central African region (CEN). B, Dahomey Gap region (DHG). C, western African region. Black dots are landmark positions.

should be considered with caution. Additionally, the heterogeneity of sampling between species might have influenced the significance of the overlap test, given that the largest differences between intercepts were not necessarily significant (Supporting Information, Table S6). The generally low P-values from the overlap test ($P < 0.23$) might reflect substantial differences in the intercepts, despite the non-significance yielded (Amrhein *et al.*, 2019).

Moreover, African and Asian clades clearly presented non-overlapping ontogenetic allometric trajectories for traits correlated with PC1 of the predicted values of multivariate regression of shape on size (Fig. 4), with African species sharing a higher intercept relative

to Asian ones. We interpret this size–shape space as a good representation of the evolutionary allometry. Considering that parameters of modelled growth trajectories can be used efficiently as continuous characters in phylogenies (Bardin *et al.*, 2017), these different intercept values could theoretically constitute a valuable character to distinguish members of the Asian and African clades. In fact, they corroborate previous morphology- and DNA-based results (Gaubert *et al.*, 2018) that described a split of the extant Manidae into two continental clades. The differences in the ontogenetic allometric patterns between the two size–shape spaces (multivariate vs. PC1 of the predicted values) might also suggest strong cranial modularity (i.e. rostrum module; Goswami, 2006). Cranial modules evolve semi-independently, and allometric patterns detected for highly integrated modules might differ from the overall pattern (Gerber & Hopkins, 2011). Further analyses are needed to confirm this hypothesis but would be beyond the scope of the present study.

Heterochronic changes are better illustrated by the ontogenetic allometric trajectories of the two *Smutsia* species (Fig. 4; Supporting Information, Tables S6–S8), as they overlap in both size–shape and shape spaces (Supporting Information, Fig. S1; Mitteroecker *et al.*, 2005; Esquerré *et al.*, 2017). Both PC1 of the predicted values and multivariate regressions suggest that *S. temminckii* is paedomorphic, because it tends to resemble juvenile *S. gigantea* (peramorphic). Nevertheless, heterochrony is not always associated with close phylogenetic affinities. Differing ontogenetic allometric trajectories between closely related species were reported previously in hominids (Mitteroecker *et al.*, 2004). Despite being sister taxa, humans and chimpanzees differ in skull shape from early ontogenetic stages. The allometric trajectories of the two *Phataginus* species exhibit a similar pattern (Fig. 4; Supporting Information, Table S6). Both species show rather distinct intercepts (distinct shapes from early stages).

Overall, our results suggest that complex allometric changes played an important role in the morphological evolution of the pangolin skull. All pangolins follow a similar ontogenetic trend characterized by the elongation of the rostrum and a posterior projection of the zygomatic process of the maxilla (Figs 4, 5). As a consequence, the braincase is relatively smaller in larger species. These ontogenetic patterns are in line with described patterns of evolutionary allometry in which large-sized mammals evolve longer rostra (Cardini & Polly, 2013; Cardini *et al.*, 2015; Cardini, 2019). Our allometric and phenotypic trajectories (Fig. 4; Supporting Information, Fig. S2), associated with the thin plate spline deformations, enable us to suggest that the ontogenetic drift of *S. gigantea* towards the Maninae (Asian pangolins) morphospace is attributable, in part, to the elongation of the skull associated with size (Fig. 5). Larger species with more elongated rostra (*Smutsia gigantea* and *Manis*) additionally present deep nasal notches (Supporting Information, Fig. S9).

Evolutionary patterns of ontogenetic allometry should therefore be taken into account in morphology-based studies. For instance, when looking at cranial character states in the morphology-based phylogeny from Gaudin *et al.* (2009), the depth of the nasal notch (character 306; Gaudin *et al.*, 2009) appears to be associated with size. The small-sized *Phataginus* species are the only ones presenting shallow nasal notches (Supporting Information, Fig. S9). The relative length of the parietal–squamosal suture (character 385; Gaudin *et al.*, 2009) also appears to be influenced by allometry (Figs 4, 5). The parietal–squamosal suture is relatively longer in skulls with shorter snouts, which is the case in *Phataginus* species (the smallest pangolins) that show a relatively long parietal–squamosal suture. This is to be expected, because skull length is influenced mostly by elongation of the rostrum in larger species (Figs 4, 5). According to Gaudin *et al.* (2009), *S. temminckii* is the only species presenting a multistate for this character [< 25% greatest skull length (0) or > 25% (1)], which is congruent with its short snout and intermediate average size between that of *Phataginus* spp. and that of *Manis* spp. and *S. gigantea* (Fig. 4). These results therefore call for a revision of some characters included in morphological matrices used to reconstruct extant and extinct pangolin phylogenetic relationships.

Patterns of skull shape variation support the classification of extant pangolins in three distinct genera

Based on morphological features, pangolins have been classified from a single genus (*Manis*) to a maximum of six different genera. In 1882, Jentink published a monograph on the comparative anatomy of extant pangolins, except for *M. culionensis*, in which he briefly referred to the remarkable differences between the skulls of the seven recognized species (Jentink, 1882). Nevertheless, he ascribed all pangolin species to the same genus, postponing a thorough investigation of skull morphology. A division of pangolins into six different genera was later proposed by Pocock (1924), with the African *Smutsia* (*S. temminckii* and *S. gigantea*), *P. tricuspis*, *Uromanis longicaudata* (Linnaeus, 1766) (*P. tetradactyla*) and the Asian *M. pentadactyla*, *Paramanis javanica* and *Phatages crassicaudata*. This classification was based on external/soft tissue characters only, but neglected cranial osteology.

Although the African–Asian split has been widely accepted, and the Asian genera have generally been merged into the single genus *Manis*, genus-level classifications have varied within the African clade. The four species have been ascribed either to a single genus, *Phataginus* (Patterson, 1978; Corbet & Hill, 1991), or kept separate in three distinct genera, as proposed by Pocock (1924; McKenna & Bell, 1997). Recent phylogenies based on morphological traits (Gaudin *et al.*, 2009) and molecular data (Gaubert *et al.*, 2018) have supported the view of an Asian–African split, with the Asian genus, *Manis* (Maninae), as the sister clade to the African pangolins composed of the two genera *Phataginus* (Phatagininae Gaubert, 2018) and *Smutsia* (Smutsiinae Gray, 1873).

Our results support the distinction of three extant pangolin genera, as recognized in previous works (Gaudin & Wible, 1999; Koenigswald, 1999; Gaudin *et al.*, 2009; Gaubert *et al.*, 2018). The PCAs and LDAs (Fig. 6A, B) largely reflect the division of extant Pholidota in Maninae (Asian; mostly positive PC1 values) and Smutsiinae + Phatagininae. The African clade was weakly supported in the most recent phylogeny based on anatomical characters (Gaudin *et al.*, 2009). In all analyses excluding fossil taxa, *Smutsia* spp. are recovered as a sister group to Maninae (Gaudin *et al.*, 2009). This might be explained, in part, by the detected allometric effect (see 'Discussion: Size influences skull shape in extant pangolins'; Fig. 4; Supporting Information, Fig. S2). Nevertheless, both the PCA (Fig. 6B) and LDA (Fig. 6C, D) reveal the grouping of all *Manis* species to the exclusion of *Smutsia* and *Phataginus*. These analyses also show a clear separation between *Smutsia* and *Phataginus*, with the small pangolins showing lower values of PC1 and higher values of LD1.

We also show some degree of variation in skull shape at the intrageneric level that confirms species-level delineation of extant pholidotans (Fig. 6). Despite the split between *S. gigantea* and *S. temminckii* being slightly more recent than in other genera (5.6–13.2 Mya for *Smutsia*, 10.3–15.6 Mya for *Manis* and 9.3–16.5 Mya for *Phataginus*; Gaubert *et al.*, 2018), their skulls appear comparatively more distinct. Some of the differences between *S. temminckii* and *S. gigantea* are related to size (see above; Fig. 4). The most extensive morphological phylogenetic work performed to date found that *Smutsia* was the least-supported modern genus, with only three unique unambiguous synapomorphies, none of which involve the cranium (Gaudin *et al.*, 2009). Our results on variation in skull shape are congruent with the low support for the *Smutsia* node. As discussed above, elongation of the rostrum largely influences this intrageneric difference in shape. This allometric pattern is present at both ontogenetic and evolutionary levels and explains some of the differences in skull shape between *S. gigantea* and *S. temminckii*. Although the shape of the skull of *S. gigantea* is more similar to that of Asian pangolins, *S. temminckii* is closer to *Phataginus* (Fig. 6). In addition to these substantial differences in skull shape within *Smutsia*, previous molecular analyses reported a relatively large mitogenomic distance within the genus (11.9%; Gaubert *et al.*, 2018), although lower than those reported within *Phataginus* (see below).

The two *Phataginus* species present the largest intrageneric mitogenomic distance (14.3%; Gaubert *et al.*, 2017). This distance is patent in PC3 and LD2 scores, which clearly separate *P. tetradactyla* from *P. tricuspis* (Fig. 6B, C). However, the cranial shape is more similar between the two *Phataginus* species than between the two *Smutsia* species (Supporting Information, Table S11). *Phataginus tetradactyla* was previously ascribed to the genus *Uromanis* (Pocock, 1924), but recent cladistic analyses based on osteological characters yielded a strong support for placement in the genus *Phataginus*, the best supported among all genera (Gaudin *et al.*, 2009). Of the seven unambiguous synapomorphies corresponding to cranial traits, the orientation and size of the zygomatic process of the squamosal (character 355; Gaudin *et al.*, 2009) is coded as ventrally directed and short dorsoventrally for both species of tree pangolin. We confirmed this character state (Fig. 6A; PC1), but additionally found that the shape of this process in the horizontal direction constitutes one of the main differences between the two species, with *P. tetradactyla* presenting the longest among all pholidotans (Fig. 6B; PC3).

Although three genera have been proposed in Maninae, recent studies have suggested that the three species should be grouped into the single genus, *Manis* (Gaudin *et al.*, 2009; Gaubert *et al.*, 2018). On average, *Manis* is the genus with the lowest (but still high) mitogenomic distance among species (mean = 9.3%), with *M. javanica–M. culionensis* showing the lowest value (3.1%) and *M. pentadactyla–M. javanica*/*M. culionensis*/*M. crassicaudata* showing the highest (12.2%; Gaubert *et al.*, 2017). The three species of Maninae show some overlap in morphospace, but are well segregated by PC2 (Fig. 6A). In contrast, *M. culionensis* overlaps with *M. javanica* in morphospace (Supporting Information, Fig. S1), which is congruent with the low mitogenomic distance and the recent divergence time estimated between these two species (0.4–2.5 Mya). However, our data are clearly insufficient to assess the morphological discrimination between *M. javanica* and *M. culionensis* (Supporting Information, Fig. S1).

Despite the strength of the Maninae node, infrageneric relationships have been greatly debated. Molecular-based analyses show a well-supported node (Bayesian posterior probability = 1), including

M. javanica/M. culionensis and *M. crassicaudata,* with *M. pentadactyla* as the sister taxon (Gaubert *et al.*, 2018). The *M. crassicaudata–M. javanica/M. culionensis* clade remains moderately supported in the Bayesian inference excluding mitogenomes (nuclear DNA only). In contrast, a moderately supported sister-group relationship between *M. pentadactyla* and *M. crassicaudata* is retrieved by morphology-based phylogenetic analyses (bootstrap value = 76; Gaudin *et al.*, 2009). The list of synapomorphies from Gaudin *et al.* (2009) for the node gathering *M. crassicaudata* and *M. pentadactyla* featured only three cranial traits. Among these, only the position of the foramen ovale at the level of the anterior edge of the ectotympanic is an unambiguous synapomorphy [character 379(1)]. Landmarks 18/43 and 20/45 describe this synapomorphy and contribute to segregate *M. crassicaudata* and *M. pentadactyla* from *M. javanica* along with other traits correlated with PC2 (Fig. 6A). Further anatomical investigation (i.e. internal characters) remains necessary to explore the morphological support for both hypotheses more thoroughly.

Skull shape variation corroborates cryptic phylogeographical lineages in *P. tricuspis*

Cranial osteological data are extremely useful to unveil patterns of cryptic speciation (Sukumaran & Knowles, 2017). Our results confirm, at least in part, the existence of several geographical groupings within *P. tricuspis* (Gaubert et al., 2016, 2018; Figs 2, 7; Supporting Information, Fig. S5). The PCA showed some degree of overlap between the different lineages in morphospace (Fig. 7A, B), although we were able to find significant differences among the skulls of four lineages or lineage groups (Western Africa + Ghana, Dahomey Gap, Western Central Africa and Central Africa). Homogeneity in skull shape might be explained by recent divergence times between these lineages (0.8–4.6 Mya for the most recent common ancestor of Western and Central African lineages; Gaubert et al., 2016, 2018). Nevertheless, we showed that two lineages (WAF and GHA) from a molecularly identified western lineage (DHG–GHA–WAF; Gaubert *et al.*, 2016) present a distinct cranial morphology (Figs 7C, D, 8). Furthermore, the Dahomey Gap lineage presents a distinct skull shape. Although the identification of group membership was not particularly high among cryptic lineages (75.4%), we showed that WAF–GHA, DHG and CAF–WCA form three morphologically distinct groups separated along a longitudinal gradient, with a high rate of a posteriori attributions (95.7%; Fig. 8).

Our results recover only partial evidence of the three nuclear groups found by Gaubert *et al.* (2016) that delineated Western Africa (WAF, GHA and DHG), Western Central Africa (WCA) and Central Africa (CA). Although the grouping of WAF–GHA is congruent with the molecular phylogeny, the Dahomey Gap group is morphologically divergent in this clade. In addition, the similarity between Central Africa and Western Central Africa groups could suggest that they both retained a plesiomorphic cranial shape. However, testing the congruence between molecular and morphological data would require further scrutiny.

In contrast, we posit that different environmental conditions might also explain some parts of the cranial variation among pangolin lineages. The Dahomey Gap corresponds to a savannah-like corridor that divides western and central lowland rain forests (Dupont & Weinelt, 1996), with a longitudinal gradient ranging from dry (Dahomey Gap) to more humid rainforest conditions (western and central rainforest). The adaptation to a drier climate resulting from tropical forest fragmentation (Salzmann & Hoelzmann, 2005) could explain the differentiation of a Dahomey Gap lineage. Concurrently, genetic drift resulting from an isolation-induced reduction of gene flow (Renaud & Millien, 2001) might also have played a role in the Dahomey Gap skull shape differentiation, following a vanishing refuge model of diversification (Vanzolini & Williams, 1981; Damasceno *et al.*, 2014; Gaubert *et al.*, 2016). At least three other endemic mammal species/subspecies have recently been described or confirmed on a genetic basis in the Dahomey Gap (Colyn *et al.*, 2010; Nicolas *et al.*, 2010; Houngbédji *et al.*, 2012). Further analyses are needed to assess the potential interaction between variation in skull shape and environmental conditions in pangolins.

Intraspecific variation in *M. javanica*

In contrast to *P. tricuspis*, we did not find solid evidence of skull shape discrimination between molecularly identified lineages within *M. javanica*, because differences in shape appear to be associated solely with size (Supporting Information, Appendix S3; Figs S7, S8). The lack of differences in skull shape might be explained by introgressions between lineages or by more recent divergence times (Nash *et al.*, 2018) than among *P. tricuspis* lineages. Additionally, the cryptic lineages within *M. javanica* might currently lack a well-defined geographical delimitation, attributable, in part, to the lack of precise geographical information for the wild specimens sampled (Nash *et al.*, 2018). Human-induced specimen translocation by the introduction of pangolin seizures of unknown origin might also have resulted in the mixing of different lineages (Pantel & Chin, 2009).

Conclusion

Our results are congruent with the currently accepted genus- and species-level classification of extant

pangolins. We found that heterochronic changes explain, in part, the morphological differentiation of the skull at an intrageneric level. However, some species appear to present different allometric trajectories resulting from changes in skull shape during early developmental stages. Asian and African clades can be discriminated on the basis of the allometric trajectories of traits related to PC1. Namely, we identified elongation of the rostrum to be related to ontogenetic allometry, and we hypothesized that this might be also present at the evolutionary level. This might explain the detected differences in rostral proportions between species of different sizes and the apparent morphological convergence between *S. gigantea* and *Manis* species. Our results underline the importance of accounting for allometry when performing phylogenetic analyses based on morphological characters.

Our results also show that skull shape differs between cryptic lineages within *P. tricuspis*, and that these can be circumscribed into three geographical groups from western Africa (WAF–GHA), the Dahomey Gap (DHG) and Central Africa (CAF–WCA). We show that skull shape is potentially useful to determine pangolin species identity and, at a finer scale, the geographical origin of specimens of white-bellied pangolins seized in illegal trade hubs or markets. Such information could help to determine differential poaching pressures, delimitate management units, and thus refine threat status at a regional level.

ACKNOWLEDGEMENTS

We thank Steffen Bock, Frieder Mayer, Detlef Willborn (MfN), Roberto Portela Miguez, Louise Tomsett (BMNH), Géraldine Veron (MNHN), Chris Conroy (MVZ), Darrin Lunde, Paula Bohaska, John Ososky (USNM) and Eleanor Hoeger (AMNH) for access to collections. We acknowledge Farah Ahmed, Amin Garbout (BMNH) and Renaud Lebrun (ISEM) for assistance with micro-computed tomography scanning. We also thank Pierre-Henri Fabre, Quentin Martinez, and Julien Claude (ISEM) for fruitful discussions. Finally, we thank two anonymous reviewers for helpful comments on the manuscript. S.F.-C., L.H. and F.D. were supported by a European Research Council (ERC) consolidator grant (ConvergeAnt #683257). L.H. and F.D. were supported by Centre National de la Recherche Scientifique (CNRS). This research received support from the Synthesys Project, https://www.synthesys.info/, financed by the European Community Research Infrastructure Action under the FP7 (GB-TAF-5606 and BE-TAF-5661). This work was supported by PANGO-GO (ANR-17-CE02-0001) and by 'Investissements d'Avenir' grants managed by Agence Nationale de la Recherche Labex CEMEB (ANR-10-LABX-0004), Labex NUMEV (ANR-10-LABX-0020). This is contribution ISEM 2019-150 of the Institut des Sciences de l'Évolution de Montpellier.

REFERENCES

Adams DC, **Collyer ML. 2009.** A general framework for the analysis of phenotypic trajectories in evolutionary studies. *Evolution* **63:** 1143–1154.

Adams D, **Collyer M**, **Kaliontzopoulou A**, **Sherratt E. 2017.** Geomorph: software for geometric morphometric analyses. R package, Version 3.0.5. Available at: https://cran.r-project.org/package=geomorph.

Adams DC, **Nistri A. 2010.** Ontogenetic convergence and evolution of foot morphology in European cave salamanders (Family: Plethodontidae). *BMC Evolutionary Biology* **10:** 216.

Amrhein V, **Greenland S**, **McShane B. 2019.** Scientists rise up against statistical significance. *Nature* **567:** 305–307.

Bardin J, **Rouget I**, **Cecca F. 2017.** Ontogenetic data analyzed as such in phylogenies. *Systematic Biology* **66:** 23–37.

Benítez HA, **Bravi R**, **Parra LE**, **Sanzana MJ**, **Sepúlveda-Zúñiga E. 2013.** Allometric and non-allometric patterns in sexual dimorphism discrimination of wing shape in *Ophion intricatus*: might two male morphotypes coexist? *Journal of Insect Science (Online)* **13:** 143.

Bickford D, **Lohman DJ**, **Sodhi NS**, **Ng PK**, **Meier R**, **Winker K**, **Ingram KK**, **Das I. 2007.** Cryptic species as a window on diversity and conservation. *Trends in Ecology & Evolution* **22:** 148–155.

Cardini A. 2019. Craniofacial allometry is a rule in evolutionary radiations of placentals. *Evolutionary Biology* **46:** 239–248.

Cardini A, **O'Higgins P. 2004.** Patterns of morphological evolution in *Marmota* (Rodentia, Sciuridae): geometric morphometrics of the cranium in the context of marmot phylogeny, ecology and conservation. *Biological Journal of the Linnean Society* **82:** 385–407.

Cardini A, **Polly PD. 2013.** Larger mammals have longer faces because of size-related constraints on skull form. *Nature Communications* **4:** 2458.

Cardini A, **Polly D**, **Dawson R**, **Milne N. 2015.** Why the long face? Kangaroos and wallabies follow the same 'rule' of cranial evolutionary allometry (CREA) as placentals. *Evolutionary Biology* **42:** 169–176.

Challender DWS, **Waterman C**, **Baillie JEM. 2014.** *Scaling up pangolin conservation. IUCN SSC Pangolin Specialist Group Conservation Action Plan.* London: Zoological Society of London.

Cheverud JM. 1982. Relationships among ontogenetic, static, and evolutionary allometry. *American Journal of Physical Anthropology* **59:** 139–149.

Collyer ML, **Adams DC. 2013.** Phenotypic trajectory analysis: comparison of shape change patterns in evolution and ecology. *Hystrix* **24:** 75–83.

Colyn M, **De Rennes U**, **Hulselmans J**, **Oude P. 2010.** Discovery of a new duiker species (Bovidae: Cephalophinae) from the Dahomey Gap, West Africa. *Zootaxa* **2637:** 1–30.

Corbet GB, Hill JE. 1991. *A world list of mammalian species*. London: Natural History Museum Publishing and Oxford University Press.

Damasceno R, Strangas ML, Carnaval AC, Rodrigues MT, Moritz C. 2014. Revisiting the vanishing refuge model of diversification. *Frontiers in Genetics* **5:** 353.

Dryden IL, Mardia KV. 1993. Multivariate shape analysis. *Sankhyā: The Indian Journal of Statistics, Series A* **55:** 460–480.

Dupont LM, Weinelt M. 1996. Vegetation history of the savanna corridor between the Guinean and the Congolian rain forest during the last 150,000 years. *Vegetation History and Archaeobotany* **5:** 273–292.

Emry RJ. 1970. A North American Oligocene pangolin and other additions to the Pholidota. *Bulletin of the American Museum of Natural History* **142:** 455–510.

Emry RJ. 2004. The edentulous skull of the North American pangolin, *Patriomanis americanus*. *Bulletin of the American Museum of Natural History* **285:** 130–138.

Esquerré D, Sherratt E, Keogh JS. 2017. Evolution of extreme ontogenetic allometric diversity and heterochrony in pythons, a clade of giant and dwarf snakes. *Evolution* **71:** 2829–2844.

Evin A, Cucchi T, Cardini A, Strand Vidarsdottir U, Larson G, Dobney K. 2013. The long and winding road: identifying pig domestication through molar size and shape. *Journal of Archaeological Science* **40:** 735–743.

Ferreira-Cardoso S, Delsuc F, Hautier L. 2019. Evolutionary tinkering of the mandibular canal linked to convergent regression of teeth in placental mammals. *Current Biology* **29:** 468–475.e3.

Foth C, Hedrick BP, Ezcurra MD. 2016. Cranial ontogenetic variation in early saurischians and the role of heterochrony in the diversification of predatory dinosaurs. *PeerJ* **4:** e1589.

Galatius A, Kinze CC, Teilmann J. 2012. Population structure of harbour porpoises in the Baltic region: evidence of separation based on geometric morphometric comparisons. *Journal of the Marine Biological Association of the United Kingdom* **92:** 1669–1676.

Gaubert P. 2011. Family Manidae. In: Wilson D, Mittermeier R, eds. *Handbook of the mammals of the world. Vol. 2. Hoofed mammals*. Barcelona: Lynx Edicions, **82–**103.

Gaubert P, Antunes A, Meng H, Miao L, Peigné S, Justy F, Njiokou F, Dufour S, Danquah E, Alahakoon J, Verheyen E, Stanley WT, O'Brien SJ, Johnson WE, Luo SJ. 2018. The complete phylogeny of pangolins: scaling up resources for the molecular tracing of the most trafficked mammals on earth. *The Journal of Heredity* **109:** 347–359.

Gaubert P, Njiokou F, Ngua G, Afiademanyo K, Dufour S, Malekani J, Bi SG, Tougard C, Olayemi A, Danquah E, Djagoun CA, Kaleme P, Mololo CN, Stanley W, Luo SJ, Antunes A. 2016. Phylogeography of the heavily poached African common pangolin (Pholidota, *Manis tricuspis*) reveals six cryptic lineages as traceable signatures of Pleistocene diversification. *Molecular Ecology* **25:** 5975–5993.

Gaudin TJ, Emry RJ, Wible JR. 2009. The phylogeny of living and extinct pangolins (Mammalia, Pholidota) and associated taxa: a morphology based analysis. *Journal of Mammalian Evolution* **16:** 235–305.

Gaudin TJ, Gaubert P, Billet G, Hautier L, Ferreira-Cardoso S, Wible JR. 2019. Evolution & morphology. In: Challender DWS, Nash H, Waterman C, eds. *Pangolins: science, society and conservation*. Cambridge: Academic Press.

Gaudin TJ, Wible JR. 1999. The entotympanic of pangolins and the phylogeny of the Pholidota (Mammalia). *Journal of Mammalian Evolution* **6:** 39–65.

Gerber S, Hopkins MJ. 2011. Mosaic heterochrony and evolutionary modularity: the trilobite genus *Zacanthopsis* as a case study. *Evolution* **65:** 3241–3252.

Goswami A. 2006. Cranial modularity shifts during mammalian evolution. *The American Naturalist* **168:** 270–280.

Gray JA, Sherratt E, Hutchinson MN, Jones MEH. 2019. Changes in ontogenetic patterns facilitate diversification in skull shape of Australian agamid lizards. *BMC Evolutionary Biology* **19:** 7.

Gunz P, Mitteroecker P, Neubauer S, Weber GW, Bookstein FL. 2009. Principles for the virtual reconstruction of hominin crania. *Journal of Human Evolution* **57:** 48–62.

Hatt RT, Lang H, Chapin JP. 1934. The pangolins and aardvarks collected by the American Museum Congo Expedition. *Bulletin of the American Museum of Natural History* **66:** 643–672.

Hautier L, Billet G, Eastwood B, Lane J. 2014. Patterns of morphological variation of extant sloth skulls and their implication for future conservation efforts. *The Anatomical Record* **297:** 979–1008.

Hautier L, Billet G, de Thoisy B, Delsuc F. 2017. Beyond the carapace: skull shape variation and morphological systematics of long-nosed armadillos (genus *Dasypus*). *PeerJ* **5:** e3650.

Hebert PDN, Penton EH, Burns JM, Janzen DH, Hallwachs W. 2004. Species realities and numbers in sexual vertebrates: perspectives from an asexually transmitted genome. *Proceedings of the National Academy of Sciences of the United States of America* **96:** 992–995.

von Helversen O, Heller KG, Mayer F, Nemeth A, Volleth M, Gombkötö P. 2001. Cryptic mammalian species: a new species of whiskered bat (*Myotis alcathoe* n. sp.) in Europe. *Die Naturwissenschaften* **88:** 217–223.

Houngbédji MG, Djossa BA, Adomou AC, Dakpogan SC, Sinsin B, Mensah GA. 2012. Conservation status of the red-bellied guenon (*Cercopithecus erythrogaster erythrogaster*) in the western Dahomey Gap in southwestern Benin and the adjacent Togodo Forest Reserve, south Togo. *African Primates* **7:** 184–192.

Jentink FA. 1882. Revision of the Manidae in the Leyden Museum. *Notes from the Leyden Museum* **4:** 193–209.

Klingenberg CP. 2011. MorphoJ: an integrated software package for geometric morphometrics. *Molecular Ecology Resources* **11:** 353–357.

Klingenberg CP. 2013. Cranial integration and modularity: insights into evolution and development from morphometric data. *Hystrix* **24:** 43–58.

Klingenberg CP. 2016. Size, shape, and form: concepts of allometry in geometric morphometrics. *Development Genes and Evolution* **226:** 113–137.

McKenna MC, **Bell SK. 1997.** *Classification of mammals above the species level.* New York: Columbia University Press.

Miranda FR, **Casali DM**, **Perini FA**, **Machado FA**, **Santos FR. 2018.** Taxonomic review of the genus *Cyclopes* Gray, 1821 (Xenarthra: Pilosa), with the revalidation and description of new species. *Zoological Journal of the Linnean Society* **183:** 687–721.

Mitteroecker P, **Gunz P**, **Bernhard M**, **Schaefer K**, **Bookstein FL. 2004.** Comparison of cranial ontogenetic trajectories among great apes and humans. *Journal of Human Evolution* **46:** 679–697.

Mitteroecker P, **Gunz P**, **Bookstein FL. 2005.** Heterochrony and geometric morphometrics: a comparison of cranial growth in *Pan paniscus* versus *Pan troglodytes*. *Evolution & Development* **7:** 244–258.

Moraes-Barros N, **Miyaki CY**, **Morgante JS. 2007.** Identifying management units in non-endangered species: the example of the sloth *Bradypus variegatus* Schinz, 1825. *Brazilian Journal of Biology* **64:** 829–837.

Murphy W, **Eizirik E**, **Johnson W**, **Zhang Y. 2001a.** Molecular phylogenetics and the origins of placental mammals. *Nature* **409:** 614–618.

Murphy W, **Eizirik E**, **O'Brien S**, **Madsen O**, **Scally M**, **Douady C**, **Teeling E**, **Ryder O**, **Stanhope M**, **De Jong W**, **Springer M. 2001b.** Resolution of the early placental mammal radiation using Bayesian phylogenetics. *Science* **294:** 2348–2351.

Nash HC, **Low GW**, **Choo SW**, **Chong JL**, **Semiadi G**, **Hari R**, **Sulaiman MH**, **Turvey TS**, **Evans TA**, **Rheindt FE. 2018.** Conservation genomics reveals possible illegal trade routes and admixture across pangolin lineages in Southeast Asia. *Conservation Genetics* **19:** 1083–1095.

Nicolas V, **Olayemi A**, **Wendelen W**, **Colyn M. 2010.** Mitochondrial DNA and morphometrical identification of a new species of *Hylomyscus* (Rodentia: Muridae) from West Africa. *Zootaxa* **2579:** 30–44.

Pantel S, **Chin SY. 2009.** *Proceedings of the workshop on trade and conservation of pangolins native to South and Southeast Asia*. Singapore: TRAFFIC Southeast Asia.

Patterson B. 1978. Pholidota and Tubulidentata. In: Maglio VJ, Cooke HBS, eds. *Evolution of African Mammals*. Cambridge: Harvard University Press, 268–278.

Piras P, **Salvi D**, **Ferrara G**, **Maiorino L**, **Delfino M**, **Pedde L**, **Kotsakis T. 2011.** The role of post-natal ontogeny in the evolution of phenotypic diversity in *Podarcis* lizards. *Journal of Evolutionary Biology* **24:** 2705–2720.

Pocock RI. 1924. The external characters of the pangolins (Manidae). *Proceedings of the Zoological Society of London* **94:** 707–723.

R Development Core Team. **2013.** *R: a language and environment for statistical computing*.

Renaud S, **Millien V. 2001.** Intra- and interspecific morphological variation in the field mouse species *Apodemus argenteus* and *A. speciosus* in the Japanese archipelago: the role of insular isolation and biogeographic gradients. *Biological Journal of the Linnean Society* **74:** 557–569.

Rohlf F, **Slice D. 1999.** Extensions of the Procrustes method for the optimal superimposition of landmarks. *Systematic Biology* **39:** 40–59.

Salzmann U, **Hoelzmann P. 2005.** The Dahomey Gap: an abrupt climatically induced rain forest fragmentation in West Africa during the late Holocene. *The Holocene* **15:** 190–199.

Schlager S. 2017. Morpho and Rvcg – shape analysis in R. In: Zheng G, Li S, Székely G, eds. *Statistical shape and deformation analysis*. London: Academic Press, 217–256.

Sidlauskas B, **Mol J**, **Vari R. 2011.** Dealing with allometry in linear and geometric morphometrics: a taxonomic case study in the *Leporinus cylindriformis* group (Characiformes: Anostomidae) with description of a new species from Suriname. *Zoological Journal of the Linnean Society* **162:** 103–130.

Sukumaran J, **Knowles LL. 2017.** Multispecies coalescent delimits structure, not species. *Proceedings of the National Academy of Sciences of the United States of America* **114:** 1607–1612.

Sveegaard S, **Galatius A**, **Dietz R**, **Kyhn L**, **Koblitz JC**, **Amundin M**, **Nabe-Nielsen J**, **Sinding MHS**, **Andersen LW**, **Teilmann J. 2015.** Defining management units for cetaceans by combining genetics, morphology, acoustics and satellite tracking. *Global Ecology and Conservation* **3:** 839–850.

Vanzolini P, **Williams E. 1981.** The vanishing refuge: a mechanism for ecogeographic speciation. *Papéis Avulsos de Zoologia* **34:** 251–255.

Venables WN, **Ripley BD. 2002.** *Modern applied statistics with S*. New York: Springer.

Villemant C, **Simbolotti G**, **Kenis M. 2007.** Discrimination of *Eubazus* (Hymenoptera, Braconidae) sibling species using geometric morphometrics analysis of wing venation. *Systematic Entomology* **32:** 625–634.

Voje KL, **Hansen TF**, **Egset CK**, **Bolstad GH**, **Pélabon C. 2014.** Allometric constraints and the evolution of allometry. *Evolution* **68:** 866–885.

Von Koenigswald W. 1999. Order Pholidota. In: Rössner G, Heissig K, eds. *The Miocene land mammals of Europe*. Munich: Dr Friedrich Pfeil, 75–80.

Zhang H, **Miller M**, **Yang F**, **Chan HK**, **Gaubert P**, **Ades G**, **Fischer GA. 2015.** Molecular tracing of confiscated pangolin scales for conservation and illegal trade monitoring in Southeast Asia. *Global Ecology and Conservation* **4:** 414–422.

Zhou ZM, **Zhou Y**, **Newman C**, **Macdonald DW. 2014.** Scaling up pangolin protection in China. *Frontiers in Ecology and the Environment* **12:** 97–98.

SUPPORTING INFORMATION

Additional supporting information may be found in the online version of this article at the publisher's web-site:

Appendix S1. Specimen list and landmark coordinates.

Appendix S2. Discrete traits.
Appendix S3. Additional analyses.
Appendix S4. LDA a posteriori attribution tables.
Table S1. Definitions of the 75 cranial landmarks used.
Table S2. Phylogenetic ANOVA of shape (Procrustes coordinates) ~ log(centroid size). *Significant *P*-value. The randomized residual permutation procedure used 10 000 permutations.
Table S3. Pairwise comparisons of the allometric trajectory angles for skull shape. *P*-values (10.000 iterations) are in the upper triangle and angles between slopes (in degrees) in the lower triangle. Significant results are written in bold.
Table S4. Pairwise comparisons of the phenotypic trajectory angles. *P*-values (10 000 iterations) are in the upper triangle and angles between path distances in the lower triangle. Significant results are written in bold.
Table S5. Pairwise comparisons of the phenotypic trajectory lengths. *P*-values (10 000 iterations) are in the upper triangle and absolute differences between path distances in the lower triangle. Significant results are written in bold.
Table S6. Pairwise comparison of the intercept (x = 5.125) of the multivariate Procrustes allometric regressions (overlap test). *P*-values (Hochberg corrected) of the difference between the intercepts computed with 10 000 iterations are in the upper triangle and observed differences in the lower triangle. Taxa with significantly non-parallel trajectories were not included in the test. Significant results are written in bold.
Table S7. Pairwise comparison of the intercept (x = 0) of the multivariate Procrustes allometric regressions (overlap test). *P*-values of the difference between the intercepts computed with 10 000 iterations are in the upper triangle and observed differences in the lower triangle. Taxa with significantly non-parallel trajectories were not included in the test. Significant results are written in bold.
Table S8. Pairwise comparisons of the predicted head shape (predicted Procrustes residuals) differences at maximum centroid size (heterochrony test). *P*-values (Hochberg corrected; in black for x = 5.125 and in blue for x = 0) of the difference between them computed with 10 000 iterations are in the upper triangle and observed differences in the lower triangle. Taxa with significantly non-parallel trajectories were not included in the test. Significant results are written in bold.
Table S9. Pairwise comparison of the principal component 1 (PC1) allometric trajectory intercepts for skull shape. *P*-values of a multiple comparison of means (Tukey's test) are in the upper triangle and the *t*-statistics values in the lower triangle. The same intercept in all species is the null hypothesis. The *P*-values are indicated for species that show the same intercept; *all other pairwise comparisons retrieved a *P*-value < 0.001. Only species with parallel slopes are included. Significant results are written in bold.
Table S10. ANOVA of shape (Procrustes coordinates) ~ sex*species and shape (Procrustes coordinates) ~ size + sex*species. *Significant *P*-value. The randomized residual permutation procedure used 10 000 permutations.
Table S11. Pairwise comparison of the Procrustes distances between least-squares (LS) means for species. *P*-values of the difference between the LS means computed with 10 000 iterations are in the upper triangle and observed distances in the lower triangle. Significant results are written in bold.
Table S12. ANOVA of shape ~ taxa/geographical groups of adult specimens of the interspecific, *Phataginus tricuspis* and *Manis javanica* datasets. Significant *P*-values indicate differences between skull shapes of taxa/geographical groups; *n groups* is the number of taxa or geographical groups used as factors. *Significant *P*-value. The randomized residual permutation procedure used 10 000 permutations.
Table S13. Pairwise comparison of the allometry-corrected Procrustes distances between least-squares (LS) means for species. *P*-values of the difference between the LS means computed with 10 000 iterations are in the upper triangle and observed distances in the lower triangle. Significant results are written in bold.
Table S14. Significant *t*-tests of principal components vs. log-transformed centroid size.
Table S15. Pairwise comparisons of the allometric trajectory angles for skull shape in *Phataginus tricuspis* cryptic lineages [homogeneity of slopes (HOS)]. *P*-values (10 000 iterations) are in the upper triangle and angles between slopes (in degrees) in the lower triangle. Significant results are written in bold.
Table S16. Pairwise comparison of the Procrustes distances between least-squares (LS) means for cryptic lineages (Gaubert *et al.*, 2016). *P*-values of the difference between the LS means computed with 10 000 iterations are in the upper triangle and observed distances in the lower triangle. Significant results are written in bold.
Table S17. Pairwise comparison of the Procrustes distances between least-squares (LS) means for three geographical groups. *P*-values of the difference between the LS means computed with 10 000 iterations are in the upper triangle and observed distances in the lower triangle. Significant results are written in bold.
Table S18. Pairwise comparison of the allometry-corrected Procrustes distances between least-squares (LS) means for cryptic lineages (Gaubert *et al.*, 2016). *P*-values of the difference between the LS means computed with

10 000 iterations are in the upper triangle and observed distances in the lower triangle. Significant results are written in bold.

Table S19. Pairwise comparison of the allometry-corrected Procrustes distances between least-squares (LS) means for three geographical groups. *P*-values of the difference between the LS means computed with 10 000 iterations are in the upper triangle and observed distances in the lower triangle. Significant results are written in bold.

Table S20. ANOVA of shape (Procrustes coordinates) ~ log(centroid size)*cryptic lineages (N = 35) in *M. javanica*. *Significant *P*-value.

Figure S1. Principal components analysis on the dataset including juveniles and two specimens of *Manis culionensis* (N = 243).

Figure S2. Phenotypic trajectory analysis among seven pangolin species. The morphospace delimited by principal component (PC)1 and PC2 explaining the variance between adults and juveniles within each species (N = 125) is shown. For each species, a trajectory representing the change in shape between the shape estimates for juveniles (light grey circles) and adults (dark grey circles) is represented. Deformed meshes represent the maximum and minimum shapes of PC1 and PC2.

Figure S3. Principal component (A, PC1 vs. PC2; B, PC1 vs. PC3) and linear discriminant analyses (C, LD1 vs. LD2; D, LD1 vs. LD3), with associated allometry-corrected variation in shape, for crania of seven pangolin species (N = 173). Shapes are the residuals of a pooled within-group multivariate regression of shape on log-transformed centroid size.

Figure S4. Allometric trajectories of the cryptic lineages (Gaubert *et al.*, 2016) of *Phataginus tricuspis* (N = 95). The x-axis values are the log-transformed centroid sizes for each specimen; the y-axis values are the principal component 1 of the predicted values of multivariate regression of shape ratios on size. The size of the dots indicates the size of the specimens. Abbreviation: CAF, Central Africa; DHG, Dahomey Gap; GHA, Ghana; WAF, Western Africa; WCA, Western Central Africa. GAB (Gabon) was excluded because our dataset included only one skull.

Figure S5. Mean shapes of proposed management units for the *Phataginus tricuspis* sample (N = 70) in lateral (left), ventral (middle) and dorsal (right) views. A, Central African region. B, Dahomey Gap region. C, Western African region. Black dots are landmark positions.

Figure S6. Principal components (A, PCres1 vs. PCres2; B, PCresC1 vs. PCres3) and linear discriminant analyses (C, LD1 vs. LD2; D, LD1 vs. LD3) with associated allometry-corrected variation in shape for crania of six cryptic lineages of *Phataginus tricuspis* (N = 71; Gaubert *et al.*, 2016). Shapes are the residuals of a pooled within-group multivariate regression of shape on log-transformed centroid size.

Figure S7. Allometric trajectories of the lineages (Nash *et al.*, 2018) of *Manis javanica* (N = 35). The x-axis values are the log-transformed centroid sizes for each specimen; y-axis values are the principal component 1 of the predicted values of multivariate regression of shape ratios on size. The size of the dots indicates the size of the specimens. Abbreviations: BOR, Borneo; JAV, Java; SUM/SIN, Sumatra/Singapore.

Figure S8. Principal components (A, PC1 vs. PC2; B, PC1 vs. PC3) with associated variation in shape for crania of *Manis javanica* lineages (N = 25; Nash *et al.*, 2018).

Figure S9. Minimum (left) and maximum (right) shape prediction from a multivariate regression on log-transformed centroid size for two species of small (A, B) and two species of large (C, D) pangolins in dorsal view. A, *Phataginus tricuspis*. B, *Phataginus tetradactyla*. C, *Smutsia gigantea*. D, *Manis javanica*. Grey and red dots mark landmark positions at minimum and maximum sizes, respectively. Black dots are landmark positions for maximum size predictions.

Chapter 2: Morphological evolution and convergence

In the previous chapter, I summarized several important concepts to understand the evolutionary history of morphology. An observed morphological pattern gives clues about function and, if thoroughly investigated, about the phylogenetic affinities of a group. However, it is the process by which phenotypes are generated that can ultimately serve to disentangle the evolutionary history of morphological traits. By process, I mean both evolutionary and developmental components of the phenotype that are ultimately interconnected by the information coded in DNA. Nevertheless, the evolutionary/hereditary, developmental, and functional components of the phenotype have not always been well separated during the long documented story of the study of biodiversity, dating back to Ancient Greece.

2.1-Homology and convergence

Under a Darwinian logic, *homology* has been defined as similarity due to common descent (Rieppel, 1994). Nevertheless, the definition of this term has been the subject of discussion for many generations (see Hall, 1994). The first formalized definition of homology can be attributed to Richard Owen (Idealistic homology; Wagner, 1989). Owen's definition of homology did not consider the phylogenetic history between taxa and was based on a "law of nature" (archetype) that established the anatomy of animals and plants (Wagner, 1989). Nevertheless, the use of this concept of homology can be traced back to Aristotle, the first relevant work on this matter consisting on the comparison of the skeleton of a bird and a human, by Belon in the 16th century (Rieppel, 1994). Belon illustrated both skeletons identifying each corresponding bone with the same letter, ignoring their shape and functional context within the skeleton. The identification of each structure was based on topology. Yet, a clear description of homology in the context of natural history only came in the early 19th century. Étienne Geoffroy Saint-Hilaire was probably one of the first anatomists of the Enlightenment to get a global view of the diversity of vertebrates, much aided by the access to specimens brought to Paris during the Napoleonic Wars (Ceriaco & Bour, 2012). As Belon, Saint-Hilaire defined homology based on topology. According to the latter, homologous structures could be identified in morphologically distinct taxa based on their connections to adjacent structures (Geoffroy Saint-Hilaire, 1822). Saint-Hilaire's "essential similarity" (homology) principle is based on accepting the existence of a shared structural plan (*Bauplan*), that can be exemplified by the presence of paired-appendages in animals as different as fish, amphibians, birds, or mammals (Rieppel, 1994). Belon and Saint-Hilaire's homology can thus be defined as a topological homology that is based

on connectivity and results from an atomist approach, which requires the decomposition of biological systems in separate organic structures, so that comparisons can be made in terms of connectivity within that system (Rieppel, 1986, 1994). This did not prevent Saint-Hilaire from accepting the importance of functional constraints in anatomy, but allowed him to propose a connection between taxa and reject Cuvier's idea that beings were created to fit perfectly their environment and ecology (Rieppel, 1994).

Accepting the idea of a *Bauplan*, it is pertinent to think that topology only can be safely used to identify homologous traits. However, topology will fail to detect homologies between the supernumerary cervical vertebrae of three-toed sloths (8-9; *Bradypus* spp.) and those of two-toed sloths (5-7; *Choloepus* spp.), or those of the other mammals that present a seven-vertebrae conservative structure of the neck somites (Hautier *et al.*, 2010). Topology on its own cannot test for the hypothesis of homology (Rieppel, 1994). An alternative to the atomist definition of homology is the concept of epigenetics, in which no single element of a biological system is preformed, with different parts being formed by growth and tissue differentiation (Rieppel, 1994). During development, complex biological structures can suffer from a re-arrangement resulting in a change of the identity of their elements (ontogenetic repatterning; Wake & Roth, 1989). Several cartilage precursors may fuse into a single cartilage, with the resulting bone being generated from a single ossification center (Rieppel, 1993). The original cartilaginous precursors lose their individuality as a result of ontogenetic repatterning. Consider different cartilages ossifying independently as the ancestral state in a given phylogenetic framework. If the pattern observed in the living taxon *x* is one single bone, an atomist approach would consider that elements were fused, thus allowing to homologize the fused and unfused elements on the basis of topology. From this it would derive a Haeckelian interpretation by which the adult of a "descendent species" would have presented, during embryonic development, structures present in its ancestor adult form that would ultimately become fused (historical homology). Given that cartilaginous precursors lose their identity through ontogenetic repatterning, one cannot homologize the single ossification of the descendent adult with the multiple ossification of the ancestral adult. Rieppel (1994) used the example of the evolution of the reptilian tarsus and the contrasting ossification pattern when compared to the tetrapod plesiomorphic state presenting multiple elements corresponding to independent ossifications of unfused cartilages. Potential homology can be detected based on topology, but the hypothesis of true homology can only be confirmed through epigenetic reasoning. In the light of evolutionary biology, homology is not a transformation from an ancestral to a derived state. Following von Baer's (1928) view that development is the deviation and differentiation from an ontogenetic *Bauplan*, homology can be defined as shared developmentally

individualized parts of the phenotype (biological homology; Wagner, 1989). With this, Wagner means that homologous structures between two individuals or within the same individual "share a set of developmental constraints, caused by locally acting self-regulatory mechanisms of organ differentiation".

When defining homology, Owen (1843) also re-adapted the term *analogue*, which was previously used as a synonymous to *homologue* by Saint-Hilaire (Rieppel, 1994). The definition of an *analogue* derived from Owen's simplistic definition of its antonym, referring to different structures or organs that fulfill the same functions in two different animals (Owen, 1843). Following Wagner's concept of biological homology, one can re-define analogy as functionally similar parts of the phenotype subjected to a different set of developmental constraints. In a phylogenetic context, homologous traits that define a monophyletic taxon are called synapomorphies (McGhee, 2011). On the other hand, similarly shaped or functionally equivalent structures that were not inherited from a direct common ancestor are denominated homoplasies. The development of homoplastic traits can happen in three different ways (McGhee, 2011; Fig. 3). When a homoplastic trait arises from developmentally distinct mechanisms involving different ancestral states, it means that a process of convergent evolution generated an analogous structure (McGhee, 2011). DDT is a well-known pesticide to which many arthropods have become resistant (Davies *et al.*, 2007). This has often occurred through amino acid substitutions in the voltage gate Sodium channel (paralysis *locus* on the *Drosophila melanogaster* X chromosome), hindering the binding of the insecticide (Davies *et al.*, 2007). However, DDT resistance is also achieved by the increased expression of the detoxifying enzyme cythochrome P450 (CYP6G1 gene; Daborn *et al.*, 2002). This is a case of true convergence in the origin of DDT resistance. The second case of homoplasy is parallel evolution. Fresh water three-spine sticklebacks populations are characterized by the independent evolution of a low number of body plates, in contrast with the completely plated marine morph (Colosimo *et al.*, 2005). In most of the low-plated populations, this phenotype resulted from mutations on the *Eda* gene that led to amino acid changes in Ectodyplasin (Colosimo *et al.*, 2005). This example of parallel evolution shows how the same condition is evolved independently from the same ancestral state (Lecointre & Le Guyader, 2006; McGhee, 2011). The last type of process originating homoplastic traits is reverse evolution (Omland & Lanyon, 2000). In this case, trait similarity is not a result of a directly inherited condition but of a reversion of a derived state to the ancestral state. For instance, the evolution of plumage color in orioles (*Icterus* spp.) shows several cases of reversal (Omland & Lanyon, 2000).

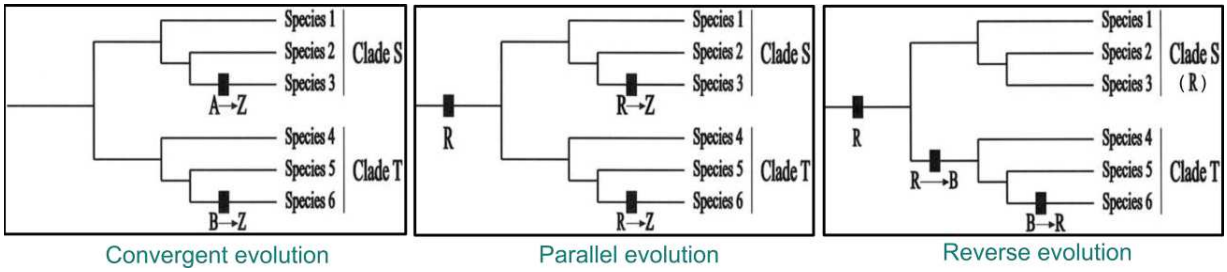

Figure 3 – Schemes of the three ways homoplasy arises (modified from McGhee, 2011). Left – convergent evolution of trait Z in species 3 and 6; middle – parallel evolution of trait Z in species 3 and 6; right – reverse evolution of trait R in species 6 within clade T.

2.2-Myrmecophagy, a definition

Perhaps one of the most curious cases is that of myrmecophagous mammals. Myrmecophagy or ant- and termite-eating, is a very specialized form of insectivory. Although several mammals include ants and/or termites in their diet, only a few present a stomach content consisting mostly of eusocial insects (>90%; Redford, 1987). Among mammals, myrmecophagy is known to have evolved at least seven times independently (McGhee, 2011). While one may think that ants and termites represent an omnipresent resource and therefore a preferential source of proteins to be exploited by mammals, feeding on eusocial insects requires both compromise and very specialized adaptations (Redford & Dorea, 1984; Redford, 1987). Indeed, the ubiquity of ants and termites must have been a critical factor for the evolution of specialized myrmecophagous mammals, mainly in tropical habitats in which ants appear to occupy the top position in biomass composition in the forest canopy (Erwin, 1983; Adis, Lubin, & Montgomery, 1984). Such an availability of food items was not only exploited by mammals, but also by reptiles such as the thorny devil (*Moloch horridus*) and the desert horned (*Phrynosoma platyrhinos*) lizards, and possibly by Cretaceous theropod dinosaurs like *Shuvuuia deserti* (Chiappe *et al.*, 1998; Longrich & Currie, 2009). On the other hand, preying on ants and termites has several drawbacks. First, ants and termites, with the exception of alate forms and larvae, are not a highly nutritious food source (Redford & Dorea, 1984). Second, their small size obliges myrmecophagous species to ingest huge amounts of individuals to fulfill their nutritive requirements. While eusociality may be an advantage, as ant nests and termitaria provide a concentrated food source, these insects evolved highly complex defensive mechanisms, such as alarm pheromones, chemical defenses, especially built nests, and a cast system with soldier elements that are responsible for attacking organisms threatening the colony (Redford & Dorea, 1984). Therefore, myrmecophagous species need to be quick both in opening nests and in the ingestion process. Observations show that attacks to ant or termite colonies are often quick strikes, with predators looking

for areas where the soldier concentration is lower (Redford, 1987). Another downside related to the small size of prey item in ant- and termite-eating specialists is the imprecision of the foraging process, with large amounts of inorganic material (i.e., dirt) being ingested (Redford & Dorea, 1984). In addition to low nutrition, small size, and developed defensive strategies, ants and termites, as other insects, present exoskeletons made of chitin, requiring the secretion of large amounts of chitinase enzymes in order to digest these animals (Redford & Dorea, 1984; Emerling *et al.*, 2018).

Diet is a continuous trait and its quantification can be difficult as it can vary due to seasonality or even intraspecific preferences (e.g., Redford, 1987). Many mammal species are found to have ants or termites in their stomachs, even if this might be a result of the ingestion of vegetation or prey items on environments with a large presence of these insects, rather than intentional predation (Redford, 1987). On the other hand, most insects provide an important source of proteins (Verkerk *et al.*, 2007; Bogart & Pruetz, 2011). Redford (1987) provides an extensive list of mammals that feed on ants, as well as proxies for the relative importance of these insects in their diets. Rodents provide some least known examples of myrmecophagy like the Dollman's tree mouse (*Prionomys batesi*), African striped squirrels (*Funisciurus* spp.), and the shrew-faced squirrel (*Rhinosciurus laticaudatus*) (Davis, 1962; Petter, 1966; Emmons, 1980; Denys, Colyn, & Nicolas, 2006). Carnivores such as the bat-eared fox (*Otocyon megalotis*) and the sloth bear (*Melursus ursinus*) feed on ants and termites, although their diets comprise a wider range of items such as other insects, carrion, honey or fruit (Kuntzsch & Nel, 1992; Nowak, 1999; Sreekumar & Balakrishnan, 2002; Stuart, Stuart, & Pereboom, 2003; Ramesh, Sankar, & Qureshi, 2009). We here define a myrmecophagous species based on the following criteria: i) ant and/or termites account for 90% or more of the diet based on the volume of stomach content (see Redford (1987), Table I); ii) support for myrmecophagy is based on several references/observations. Additionally, myrmecophagous species present one or more of the following derived features: i) extensible sticky tongues; ii) large salivary glands; iii) elongated snouts and jaws; iv) tooth loss or reduction in number or structural complexity; v) modified pyloric stomachs (gizzard-like), sometimes with keratinized "pyloric teeth" (Krause & Leeson, 1974) vi) strong claws and forelimbs adapted to dig. Strict/specialized myrmecophagy has independently evolved seven times during the evolution of mammals, one in Monotremata, one in Marsupialia, and five times in Placentalia.

Within Monotremata, the short-beaked echidna (*Tachyglossus aculeatus*) is an example of strict myrmecophagy (Nowak, 1999; Phillips, Bennett, & Lee, 2009). They present a toothless elongated rostrum, a long and sticky tongue, and powerful digging abilities. The second example of myrmecophagy

is a marsupial dasyuromorph, the numbat or banded anteater (*Myrmecobius fasciatus*; Nowak, 1999). This monospecific taxon has a diet composed of termites (and occasionally ants) and presents some traits associated to myrmecophagy such as a long tongue and a posteriorly projecting palate (Nowak, 1999). Although numbats present a high number of teeth (up to 52) they are small and simplified, varying in size, and being implanted separate from one another (Nowak, 1999).

The most remarkable case of convergent evolution of morphological traits towards myrmecophagy is found within the placental mammals. Adaptation to a myrmecophagous diet evolved in the hyaenid Carnivora (aardwolf; *Proteles cristatus*), the Pholidota (pangolins), the Tubulidentata (aardvark; *Orycteropus afer*), the Cingulata (giant armadillo; *Priodontes maximus*), and the Vermilingua (anteaters) (Redford, 1987; Nowak, 1999). All these species present tooth reduction, either in number of complexity (see below), or complete tooth loss (e.g., Davit-Béal *et al.*, 2009). Additionally, to the exclusion of the aardwolf, these taxa share a series of other convergently evolved traits such as elongated rostra and lower jaws, the presence of elongated protractile sticky tongues, powerful forelimbs with strong claws and modified pyloric stomachs that act like a gizzard during food digestion (Vizcaíno & Loughry, 2008; Davit-Béal *et al.*, 2009). These and other convergent traits have led to some confusion in the very first descriptions of pangolins, aardvarks, armadillos and anteaters (see above) and continue to be an issue for modern morphology-based phylogenetic analyses (O'Leary *et al.*, 2013; Springer *et al.*, 2013).

2.3-Morphological convergence in myrmecophagous placentals

Before proceeding further into the next article, it is important to make a brief note about the use of terms such as "evolutionary replicate" and "convergence". First, I use the term "replicate" in its *sensu lato*. Losos (2017) provided an extensive revision of examples of experimental designs that allow to dissect convergent evolution. Along with the many examples presented, the author provided an elegant discussion on the definition of an "evolutionary replicate", a natural or experimental occurrence of repeated evolution at the genetic, morphological, or ecological levels. Losos (2017) discussion accentuates the relevance of scale for the identification of convergent evolution. Secondly, I want to emphasize that the term "convergence" is used here with a broad sense, referring only to the observed phenotypic pattern while ignoring the underlying process.

McGhee (2011) used the myrmecophagous placentals as an example of the role of ecological niche in producing morphologically convergent phenotypes. The selective pressures involved in the adaptation

towards myrmecophagy have been so strong that doubts on how to classify ant- and termite-eating placentals remained present for more than 200 years (see "Phylogenetic framework"). Springer *et al.* (2013) argued that morphological traits often provide less well-supported phylogenetic reconstructions of higher-level relationships, when compared to molecular data. They justify this with the fact that the several habitats occupied by mammals all over the planet present similar conditions. In other words, geographically distant locations may present very similar conditions and their colonization may thus provide "evolutionary replicates". In the morphological tree recovered by O'Leary *et al.* (2013; Fig. S2), pangolins, aardvarks, and anteaters form a well-supported clade. This is despite the massive number of morphological traits (4541) coded in the supermatrix. These results are a good representation of the degree of morphological convergence in myrmecophagous placentals (Fig. 4).

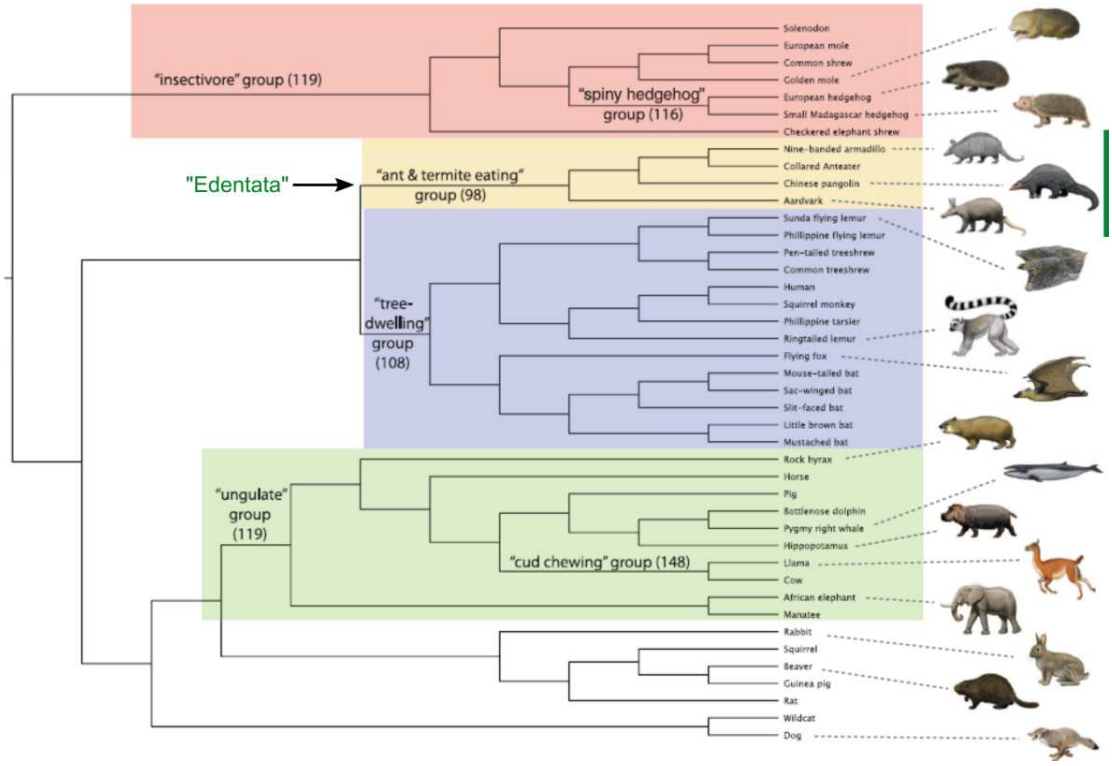

Figure 4 – Ecomorphology groups highlighted on the phenetic tree of extant mammals recovered by O'Leary et al. (2013; Fig S2), adapted from Springer *et al.* (2013). Green bar indicates the polyphyletic "Edentata".

2.4-Tooth loss

As stressed in the previous sections, the reduction of the dentition is a major feature of myrmecophagous placentals. When Georges Cuvier famously said "*Montrez-moi vos dents et je vous dirai qui vous êtes*" ("Show me your teeth and I will tell you who you are") he was definitely not thinking of anteaters and pangolins. In such cases, the study of teeth becomes a developmental, rather than a morphological subject. From the developmental question "How did you lose your teeth?" directly derives an evolutionary perspective: "When, during your evolutionary history, and why?". In this section I provide a brief review of the evolution of teeth in mammals, how they develop, and of our current knowledge about development and morphology in myrmecophagous placentals.

Part of the successful resource exploitation and niche occupation that occurred during the radiation of mammals is due to the mammal chewing system (Hemae, 1967; Weijs, 1994; Ungar, 2010). Teeth are typically divided in a dorsal crown and ventral roots (one or more). Both parts are composed of dentine, with the crown covered by an enamel layer and the root(s) sheathed with cementum. A hollow chamber in the crown (pulp cavity) is filled with nerves and blood vessels that pass through root canals (Ungar, 2010). These soft tissues make up the pulp branch from the mandibular canal (Ferreira-Cardoso *et al.*, 2019b). Mammals are thecodont, a condition in which teeth are firmly implanted in alveoli. Despite this common structure, variation in shape, size, and number of teeth allowed mammals to improve digestive efficiency and range from dietary specialists to capable generalists. Yet, some mammals lost the ability to form functional teeth, often losing molar occlusion and the ability to crush and grind food items (chewing). Inefficient or inexistent food processing reduces the assimilation of energy stored in food items (e.g., Morris *et al.*, 1977; Ungar, 2010). Absence of food processing is therefore a major energetic constraint, and the main reason why myrmecophagous placentals either evolved from lineages with low basal metabolic rates or were subjected to selective pressures in this direction (McNab, 1985; Richardson, 1987).

The tooth development process (odontogenesis) is probably conserved across vertebrates and likely represents the plesiomorphic condition of the group (Holland *et al.*, 1994; Hu & Marcucio, 2009; Rücklin *et al.*, 2012). Depending on the type of tooth (incisor, canine, premolar, molar), this process may show some variations, such as the presence of secondary enamel organs (e.g., multicusped teeth; Jernvall & Thesleff, 2012; Renvoisé & Michon, 2014). However, the evolutionary history of mammals shows several exceptional cases of tooth shape simplification (homodonty), enamel loss, reduction of tooth number or complete loss of teeth (Davit-Béal *et al.*, 2009; Meredith *et al.*, 2009). In the case of

myrmecophagous placentals, the process of tooth development was either: i) truncated in early stages (e.g., as in anteaters and pangolins), ii) stopped posterior to eruption (e.g., absence of replacement teeth for the anterior dentition of aardvarks), or iii) missed some part of the described traditional steps (e.g., armadillos and sloths). Additionally, the derived hypselodont dentition present in some animals (e.g., xenarthrans and aardvarks) results from a modification in odontogenesis, as at least one cervical loop remains active, with its stem cells differentiating into odontoblasts during the entire lifespan of the animal (Renvoisé & Michon, 2014).

Anteaters and pangolins appear to present early stages of tooth development (Gervais, 1867; Rose, 1892; Röse, 1892; Tims, 1908), despite the lack of unequivocal evidence for vestigial teeth. Aardvarks present deciduous teeth that are never replaced (Anthony, 1934b). All xenarthrans and the aardvark present enamel-less teeth (Davit-Béal *et al.*, 2009; Vizcaíno *et al.*, 2009; Meredith *et al.*, 2009). In the following article, osteological correlates of tooth innervation are investigated in order to understand how tooth sensorial function evolved following tooth loss.

Article 2

Evolutionary tinkering of the mandibular canal linked to convergent regression of teeth in placental mammals.

Published in: *Current Biology*

Supplemental information for this article is available in Appendix 2.

Report

Current Biology

Evolutionary Tinkering of the Mandibular Canal Linked to Convergent Regression of Teeth in Placental Mammals

Graphical Abstract

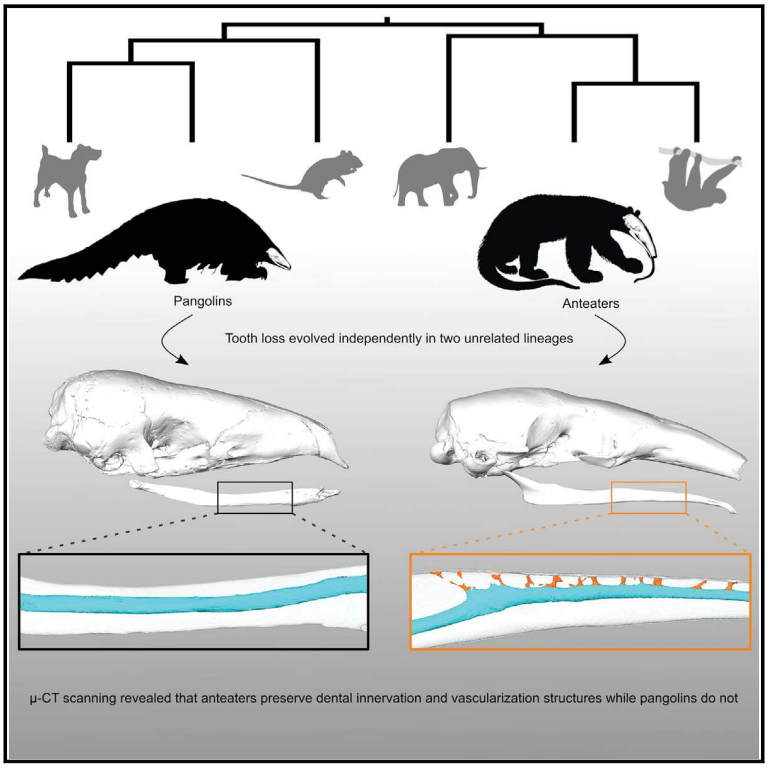

Authors

Sérgio Ferreira-Cardoso, Frédéric Delsuc, Lionel Hautier

Correspondence

sergio.ferreira-cardoso@umontpellier.fr (S.F.-C.), lionel.hautier@umontpellier.fr (L.H.)

In Brief

Tooth loss in anteaters and pangolins represents a textbook example of convergent evolution. Ferreira-Cardoso et al. show that anteaters still present tooth neurovascular systems (dorsal canaliculi) while pangolins do not. As in baleen whales, osseous and neurovascular structures of the anteater mandible were rewired following the loss of teeth.

Highlights

- Anteaters have preserved dental innervation structures despite tooth loss
- Pangolins lost both teeth and all traces of dental innervation
- The mandibular canal morphology in anteaters resembles that of baleen whales
- A striking example of evolutionary tinkering linked to the regression of teeth

Ferreira-Cardoso et al., 2019, Current Biology *29*, 468–475
February 4, 2019
https://doi.org/10.1016/j.cub.2018.12.023

CellPress

CellPress

Current Biology
Report

Evolutionary Tinkering of the Mandibular Canal Linked to Convergent Regression of Teeth in Placental Mammals

Sérgio Ferreira-Cardoso,[1,*] Frédéric Delsuc,[1,3] and Lionel Hautier[1,2,*]
[1]Institut des Sciences de l'Evolution de Montpellier (ISEM), CNRS, IRD, EPHE, Université de Montpellier, Montpellier, France
[2]Mammal Section, Life Sciences, Vertebrate Division, The Natural History Museum, London, UK
[3]Lead Contact
*Correspondence: sergio.ferreira-cardoso@umontpellier.fr (S.F.-C.), lionel.hautier@umontpellier.fr (L.H.)
https://doi.org/10.1016/j.cub.2018.12.023

SUMMARY

Loss or reduction of teeth has occurred independently in all major clades of mammals [1]. This process is associated with specialized diets, such as myrmecophagy and filter feeding [2, 3], and led to an extensive rearrangement of the mandibular anatomy. The mandibular canal enables lower jaw innervation through the passage of the inferior alveolar nerve (IAN) [4, 5]. In order to innervate teeth, the IAN projects ascending branches directly through tooth roots [5, 6], bone trabeculae [6], or bone canaliculi (i.e., dorsal canaliculi) [7]. Here, we used micro-computed tomography (μ-CT) scans of mandibles, from eight myrmecophagous species with reduced dentition and 21 non-myrmecophages, to investigate the evolutionary fate of dental innervation structures following convergent tooth regression in mammals. Our observations provide strong evidence for a link between the presence of tooth loci and the development of dorsal canaliculi. Interestingly, toothless anteaters present dorsal canaliculi and preserve intact tooth innervation, while equally toothless pangolins do not. We show that the internal mandibular morphology of anteaters has a closer resemblance to that of baleen whales [7] than to pangolins. This is despite masticatory apparatus resemblances that have made anteaters and pangolins a textbook example of convergent evolution. Our results suggest that early tooth loci innervation [8] is required for maintaining the dorsal innervation of the mandible and underlines the dorsal canaliculi sensorial role in the context of mediolateral mandibular movements. This study presents a unique example of convergent redeployment of the tooth developmental pathway to a strictly sensorial function following tooth regression in anteaters and baleen whales.

RESULTS

Evolution of Dorsal Canaliculi after Tooth Regression

Three-dimensional (3D) models of the mandibles, teeth, and mandibular canals of 26 species were investigated (Figures 1, S1, and S2). Detailed anatomical descriptions of the mandibular canal in each myrmecophagous species and sister taxa are provided as Supplemental Information (Figures S1, Data S1). A summary description of additional species used to reconstruct the ancestral condition of placental mammals is also provided as Supplemental Information (Figure S2, Data S1). For cetacean comparisons, we used a dataset that was recently published by Peredo et al. [7]. All toothed mammals get teeth innervated and vascularized, but this innervation and vascularization only occasionally happens through dorsal canaliculi. These canaliculi correspond to narrow tubular channels that connect the mandibular canal to tooth alveoli (Figures 2E and 2F). The teeth of the giant otter shrew (*Potamogale velox*), the aardwolf (*Proteles cristatus*), and the dog (*Canis lupus*) are rooted in close contact with the mandibular canal, with alveoli often surrounded by trabecular bone (Figures 1, S1I, S1J, and S1N). The investigated additional species revealed similar patterns with either deeply rooted teeth or trabeculae surrounding the alveoli (or both; Data S1; Figure S2). These species all lack dorsal canaliculi even for dorsally implanted teeth (e.g., aardwolf molars) (Figure S1I). Dorsal canaliculi were present in three (Pilosa, Cingulata, and Tubulidentata) of the 18 mammals orders sampled (including one marsupial). Ancestral reconstruction unambiguously showed that the absence of dorsal canaliculi likely represents the ancestral condition in placental mammals (Data S1) where alveolar branches (IAN and inferior alveolar artery, IAA) pass through the trabecular structures of the bone or directly through tooth roots. In contrast, armadillos (*Dasypus novemcinctus*, *D. pilosus*, and *Priodontes maximus*), sloths (*Bradypus tridactylus* and *Choloepus hoffmanni*), and the aardvark (*Orycteropus afer*) present dorsal canaliculi (Figures 1, 2E, 2F, 3C, 3D, S1, and S4), the so-called "dorsal branches" as previously described in baleen whales [7], whose dorsoventral length increases as the tooth is implanted further from the mandibular canal (Figures 2E and 2F). Most of these dorsal canaliculi are located in the anterior part of the mandible, where teeth are reduced or simply missing. In the nine-banded armadillo, we observed one anterior dorsal canaliculus that divides to open in four dorsal foramina (Figures 1 and S1F), while in the hairy long-nosed armadillo, we observed a dorsal canaliculus that divides in a plexus of three branches (Figures 1 and S1G). In the aardvark, three free dorsal canaliculi split and open in six dorsal foramina (Figures 1 and S1M). Intraspecific variation was detected and described (Figure S4; Data S1), but the presence and pattern

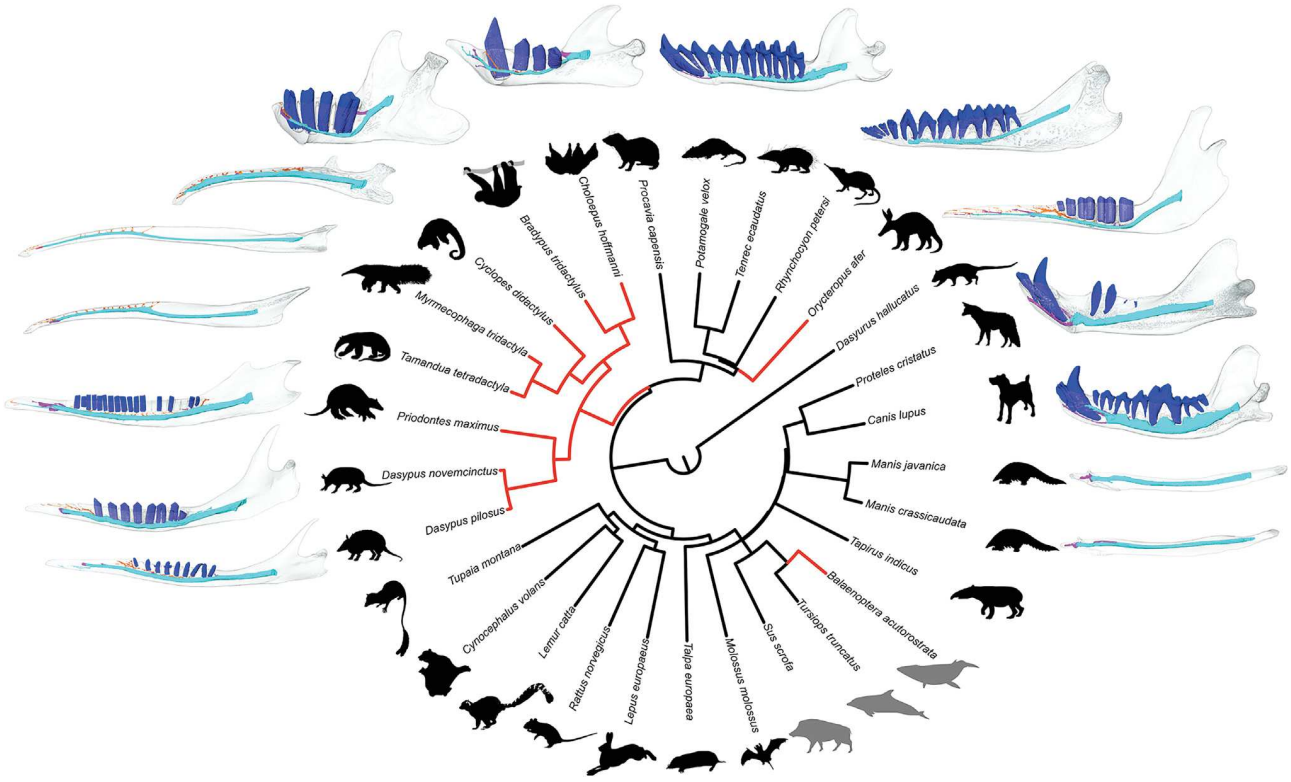

Figure 1. Evolution of Dorsal Canaliculi Linked to Tooth Regression in 28 Placentals and 1 Marsupial

Circular timetree (according to Kumar et al. [9]) with corresponding 3D reconstructions of the internal mandibular morphology with dorsal canaliculi (orange), mandibular canal (cyan), mental branches (purple), and teeth (dark blue). Tree branches are colored in orange (presence of dorsal canaliculi) and black (absence of dorsal canaliculi). Animal silhouettes are colored in black (sampled species) and gray (species from [7]).
See also Figures S1, S2, S4, and Data S1.

of dorsal canaliculi is always consistent among specimens. Ontogenetic variation was studied in two species of sloths in which fetuses display dorsal canaliculi associated with vestigial tooth loci (Figures 3A and 3B). These dorsal canaliculi are still present in adults of both species despite the resorption of vestigial teeth (Figures 3C and 3D).

Surprisingly, toothless species (anteaters and pangolins) display contrasted mandibular canal morphologies (Figures 1 and 2). All three investigated anteater species present dorsal canaliculi that open in small foramina (Figures 2A–2C and S1A–S1C). These foramina are placed along the anterior flattened dorsal margin of the mandible, which defines the dental pad, with only limited intraspecific and bilateral variations among specimens of the three species (Figure S4). Ontogenetic variation is equally limited, with similar patterns of dorsal canaliculi being observed in both adults and juvenile giant anteaters (*M. tridactyla*, Figure S4L–S4N) and nine-banded armadillos (*D. novemcinctus*, Figures S4A–S4F). Conversely, pangolins lack dorsal canaliculi (Figure 2D), with only several minute canaliculi that are parallel to the mandibular canal, both dorsally and ventrally, but rarely connected to it (Figures S1D and S1E). Foramina associated to these parallel canaliculi are scarce, invisible to the naked eye, and only occasionally open dorsally to the mandibular canal.

Histological Evidence for the Passage of Nerves and Blood Vessels in Dorsal Canaliculi

3D analyses were complemented by histological series, which enabled to identify internal soft structures associated to the dorsal canaliculi. The LFB (see Method Details) stained histological slices of the collared anteater (*T. tetradactyla*) mandible enabled us to describe the soft tissues encapsulated in the mandibular canal (Figure 4). We observed dorsal canaliculi that allow for the passage of an ascending branch of the inferior alveolar nerve (IANab; Figures 4C and 4C'), of the inferior alveolar artery (IAAab; Figure 4C), and of the inferior alveolar vein (IAVab; Figure 4B'). In *T. tetradactyla*, a keratinous dental pad (pa) covers the dorsal part of the mandible (Figure 4C). Ventrally, the epidermis (ep) consists of a small layer (Figure 4C), which lies dorsally to a thick dermis layer (de; Figure 4C). In addition to connective tissue, this dermis layer presents small blood vessels and nerve branches. Histological slices of bowhead whale [10] (Figure S3A) show a similar structuration of soft tissues, with accessory branches of the large IAN and IAA that most likely connect the mandibular canal to the vestigial tooth alveoli through dorsal canaliculi. The histological section [10] suggests a pronounced anterior projection of the dorsal canaliculi, similar to the pattern for the IAN ascending branches in odontocetes [4].

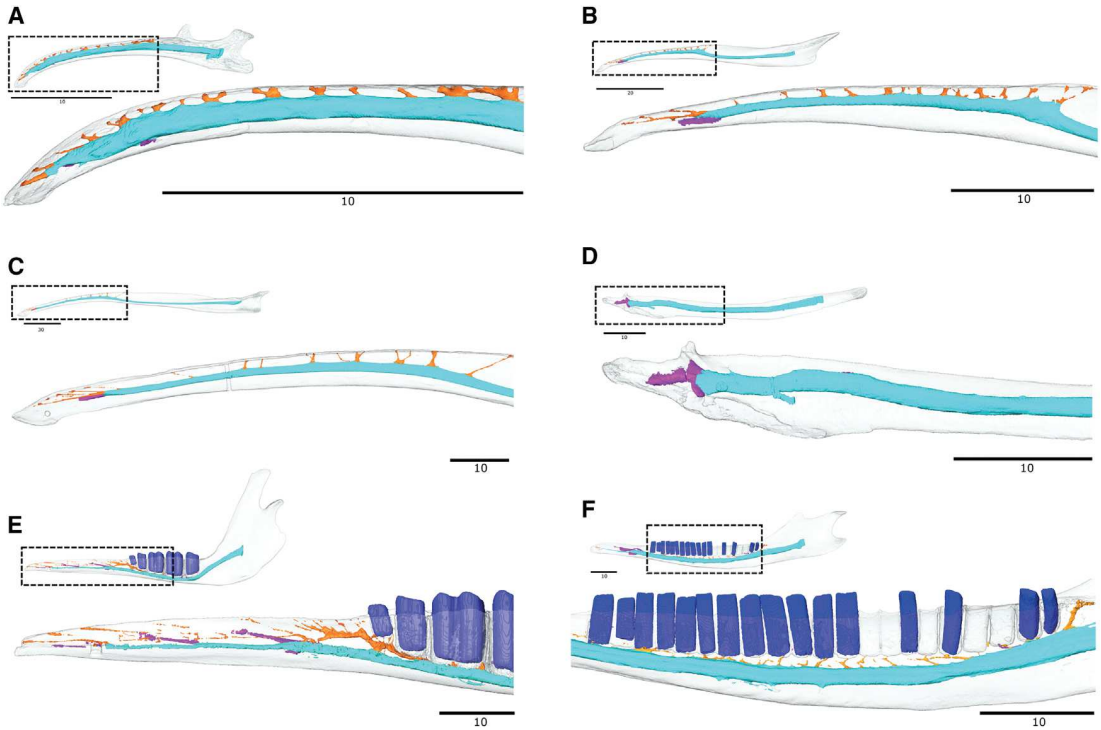

Figure 2. Evolution of Dorsal Canaliculi after Tooth Regression

(A–F) (A) *Cyclopes didactylus*; (B) *Tamandua tetradactyla*; (C) *Myrmecophaga tridactyla*; (D) *Manis javanica*; (E) *Orycteropus afer*; (F) *Priodontes maximus*. Bone is transparent. Dorsal canaliculi, orange; mental branches, purple; mandibular canal, cyan; teeth, dark blue. Scale in mm.
See also Figure S4 and Data S1.

DISCUSSION

Shadows of Regressed Tooth Buds in Dorsal Canaliculi

Enamelless sloths, armadillos, and aardvarks all present dorsal canaliculi that are associated with either tooth alveoli or vestigial tooth loci in the anterior part of the mandible. The corresponding nervous and vascular ascending branches should then be considered homologous to alveolar branches. If the number and shape of alveolar branches can vary [6, 11], especially in terminal bifurcations, each main alveolar branch usually corresponds to a single tooth root [6]. Establishing the direct homology between ascending and alveolar branches in anteaters is hindered by the absence of teeth. However, their closest relatives, sloths and armadillos, as well as the aardvark, also display some anterior dorsal canaliculi with no apparent connection to tooth alveoli (Figures 1, 2, and S1). Long-nosed armadillos present dorsal canaliculi in the anterior part of the mandible and the anterior most alveoli, while sloths present minute dorsal canaliculi in cheek teeth. This suggests that dorsal canaliculi likely evolved concomitantly with tooth simplification in cingulatans and pilosans. All these species have been shown to display vestigial tooth buds in the anterior part of the mandible during pre-natal development [12–14]. The observed pattern of anterior dorsal canaliculi in long-nosed armadillos (*Dasypus*) and the aardvark roughly matches the distribution of previously described vestigial teeth [13, 15–17]. In nine-banded armadillos, we found dorsal canaliculi that consistently split into three to six distinct dorsal foramina in the anterior part of the mandibles (Figure 1, S1F, and S4A–S4F), while Martin [13] identified five to six vestigial incisors. This difference is not surprising given the frequent dental formula variation observed in nine-banded armadillos [18]. The observed variation in dorsal canaliculi count of anteaters and nine-banded armadillos (Figure S4) was to be expected as the number and shape of alveolar branches vary in humans [6, 11], both at the intraspecific and bilateral levels. This variation also matches the variation observed in tooth count of placentals showing a reduced dentition such as the aardvark [14], long-nosed armadillos [18] and the giant armadillo [19]. Such bilateral variation in tooth number might result from the lack of stabilizing selection due to an absence of strict occlusion, as hypothesized for mysticetes [10]. In the aardvark [16], the lower milk dentition is normally composed of eight to ten teeth, with the second generation of teeth varying from five to eight in number depending on the presence of vestigial anterior premolars and canines [16, 17]. We found dorsal canaliculi that could correspond to two-four anterior premolars, one canine, and three incisors (Figure S1M). This number coincides with the deciduous dental formula of the aardvark [14]. Our observations therefore provide convincing evidence for a link between the presence of teeth, vestigial or not, and the development of dorsal canaliculi.

This developmental link was corroborated by the study of ontogenetic series of both extant sloth genera. Comparisons between sloth pre- and post-natal stages allowed us to directly

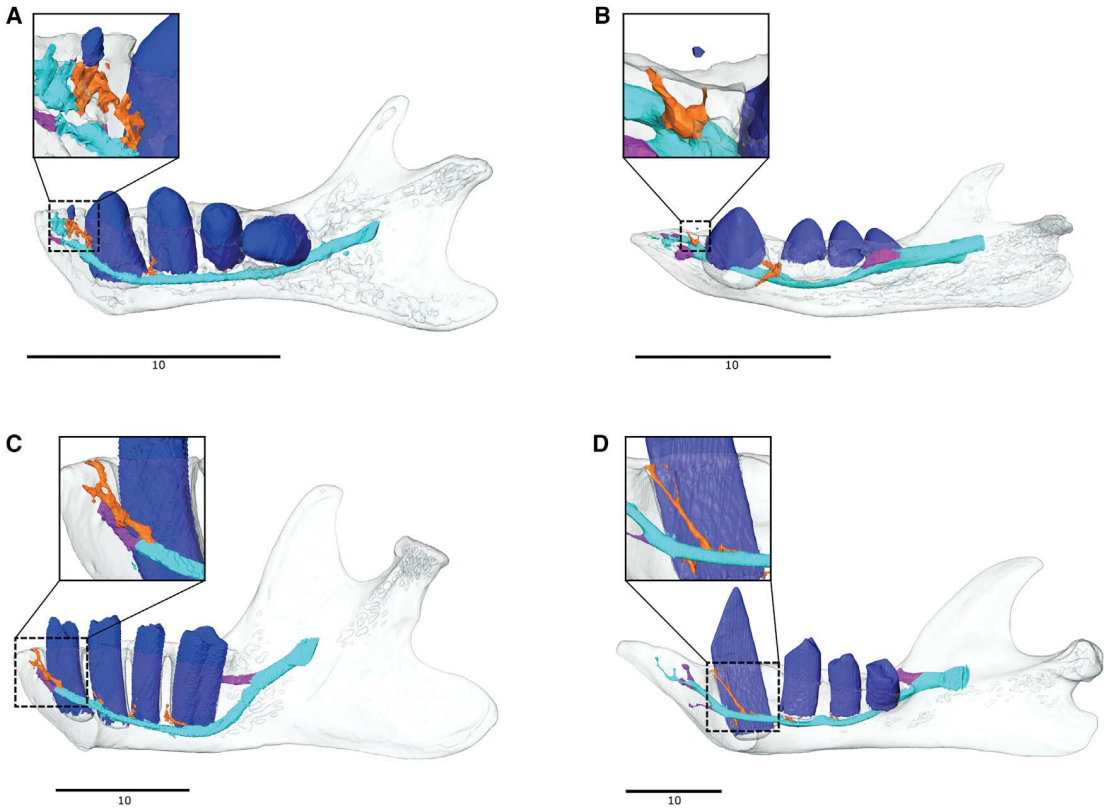

Figure 3. Ontogenetic Evidence of the Association of Dorsal Canaliculi to Vestigial Tooth Alveoli

(A–D) 3D models of the mandibles of sloth fetuses (A) *Bradypus tridactylus* and (B) *Choloepus didactylus*) and adults (C) *B. tridactylus* and (D) *Choloepus hoffmanni* in medial (A, C and D) and lateral (B) views. Bone is transparent. B is a mirrored lateral view for a better perspective of the dorsal canaliculus. Dorsal canaliculi – orange; mental branches – purple; mandibular canal – cyan; teeth – dark blue. Zoomed details of the dorsal canaliculi associated with the vestigial teeth are shown. Scale in mm. See also Data S1.

associate one long anterior dorsal canaliculus to a vestigial tooth locus (Figure 3), which is resorbed during development and is absent in adults. Based on histological sections (Figure 4), we showed that ascending branches of the IAN and IAA pass through dorsal canaliculi in the collared anteater (*T. tetradactyla*). Teeth innervation was likely retained after tooth resorption in all pilosans, and this could extend to all xenarthrans if we consider the anterior dorsal canaliculi of armadillos as representatives of vestigial tooth loci. Wadu et al. [6] showed that human tooth nerve bundles can also be retained—although slightly reduced—after tooth loss induced by senescence. Our observations of histological sections of toothless whale fetuses (see [10] and Data S1, Figure S3) suggest that vestigial tooth loci are associated to IAN and IAA ascending branches during development, a situation that mirrors the condition observed in toothed cetaceans [4, 5]. Ridgway et al. [4] described an elongation of the ascending branches of the inferior alveolar nerve in dolphins, while an anterodorsal inclination was also reported for the dorsal canaliculi of mysticetes [7]. However, the homology between alveolar branches and ascending branches carried by dorsal canaliculi was recently challenged for whales [7]. Instead, Peredo et al. [7] proposed that dorsal canaliculi and associated foramina constitute a derived character of crown Mysticeti since no internal evidence of such a structure was visible in other edentulous taxa [7]. Our results clearly contradict this assertion, as we showed that anteaters display both foramina and dorsal canaliculi. In our view, the ascending branches of IAN and IAA should be considered as homologous to alveolar branches since they include identical structures and are linked to the development of teeth. This implies that dorsal canaliculi evolved convergently in xenarthrans, aardvarks, and baleen whales following tooth reduction.

Unlike the other toothless species investigated, pangolins do not present dorsal canaliculi in their mandibles. The small parallel canaliculi (Figures S1D and S1E) present a distinct shape and topology hindering a hypothetical homology with the dorsal canaliculi. Tims [20] reported the presence of 13–14 tooth rudiments in the mandible of *M. javanica*, which he also compared to hair follicles. However, the observed number of up to four tooth vestiges per coronal slice [20] seems inconsistent with the position of the teeth along an anteroposterior axis. Unless *M. javanica* presents four tooth generations, no more than two tooth buds should be expected for each coronal slice [10, 21]. In this context, the 13–14 teeth reported by Tims [20] should be considered with caution and might correspond to distinct structures. The lack of tooth buds [22] might therefore explain the absence of dorsal canaliculi. Although an early dental lamina

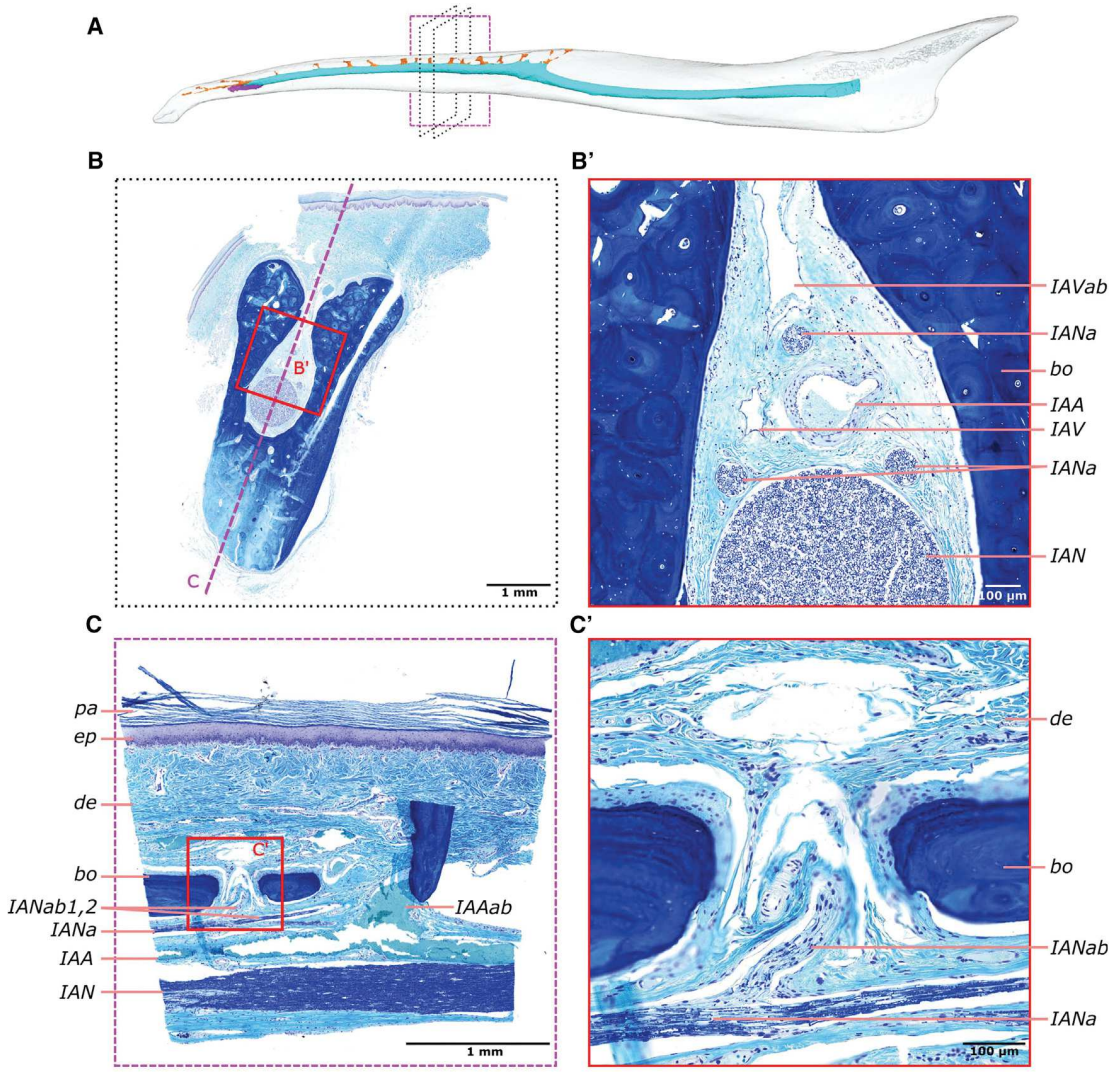

Figure 4. Histological Evidence for the Passage of Blood Vessels and Nerves in Dorsal Canaliculi

(A) 3D-model of a mandible with a purple dashed rectangle indicating where the sagittal cut was performed; black dashed rectangles indicate the limits of the coronal cut.

(B) Coronal cut showing the mandibular canal and a dorsal canaliculus; soft tissues are present dorsally to the mandibular canal, the dorsal canaliculus and the external dorsal, and dorso-lateral surfaces of the mandible; the red square represents the area of interest to be zoomed in (B'); the purple dashed line represents the sagittal section performed on the cut portion of the mandible (A).

(C) Sagittal section showing the mandibular canal, two dorsal canaliculi and associated soft tissues; soft tissues on the dorsal surface of the mandible are identified; the red square delimits the area zoomed in (C'). (C') An ascending branch of the IAN is present in the dorsal canaliculus. Abbreviations: *bo* bone; *de* dermis; *ep* epidermis; *IAA* inferior alveolar artery; *IAAab* inferior alveolar artery ascending branch; *IAN* inferior alveolar nerve; *IANa* inferior alveolar nerve accessory branch; *IANab* inferior alveolar nerve ascending branch; *IAV* inferior alveolar vein; *IAVab* inferior alveolar vein ascending branch; *pa* keratinous dentary pad. See also Figure S3 and Data S1.

may be present in pangolin embryos [15, 20], its development appears to be drastically reduced when compared to anteaters [22]. On the other hand, the lack of these structures in pangolins could be explained by phylogenetic constraints. Since dorsal canaliculi are also absent in carnivorans (Figures 1, S1I, and S1J), their absence might represent the ancestral state for Ferae (Pholidota + Carnivora). Additionally, complete tooth loss probably happened much earlier in pangolins than in anteaters, since the almost certainly toothed most recent common ancestor (MRCA) of Pilosa (~58 Mya [23]) is much more recent than the MRCA of Ferae (~80 Mya [24]). With the oldest fossil pangolin (~45 Mya [25]) being already toothless, the absence of dorsal canaliculi in pangolins might simply reflect a more ancient tooth loss. Importantly, our study shows that the external resemblances of the mandibles in anteaters and pangolins, which made them a textbook example of convergent evolution, have overshadowed the complex evolution of their internal morphology.

Functional Role of Dorsal Canaliculi in Toothless Species

Previous studies proposed that mammalian teeth might play a sensorial role in detecting a wide array of external stimuli including pressure, proprioception, and percussion [26] in addition to their role for food intake. Our results suggest that the development of dorsal canaliculi might be linked to the presence of tooth loci/vestigial teeth in both anteaters and baleen whales. One puzzling fact however is that the development of vestigial teeth remained preserved for so long during the evolutionary history of these taxa. In sloths, Hautier et al. [12] showed that the mineralization and resorption of the vestigial teeth is an integral part of prenatal dental development. Given the conservatism of sloth dental formula in the fossil record [27], they proposed that these vestiges were kept for at least 30 million years [23, 27], which implies that there is still a strong selective pressure for developing these structures. Such a complex and energetically costly developmental pathway might be the consequence of a strong developmental constraint in preserving the associated innervation and vascularization of the mandible. A similar developmental constraint was proposed for the initial development of a normal eye in blind cavefish [28]. These fish present normal eye development before showing sign of later degeneration. Given that there is no separation between cells giving rise to the retina and to the forebrain at the early stage of the nervous system (neural plate stage), the development of a viable embryo with a well-formed forebrain implies the early development of the eyes [28]. Tooth innervation develops synchronously with tooth development, being controlled by local molecular signals [8]. We therefore argue that tooth development, even in initiation stages, might be required for maintaining the dorsal innervation of the mandible. As a matter of fact, embryos of pygmy anteaters present early tooth development (dental lamina-tooth buds) [22, 29].

Histological slices allowed revealing the presence of dorsal projections of the IAN and IAA passing through the dorsal canaliculi in a mandible of the collared anteater. We propose that these structures respectively innervate and vascularize the mandibular keratinous pad that covers most of the dorsal margin of the horizontal ramus (Figure 4C). The oral sensory receptors that project via the IAN (a branch of the trigeminal nerve) may confer a somatosensory role to the mandibular keratinous pad. In fact, the pattern of innervation of this keratinous pad resembles that of bird beak [30]. Both structures display a superficial keratinous layer followed dorsally by epidermis and a large dermis with blood vessels and free nerve endings [30] (Figure 4). Early tooth development (bud stage) was previously reported in anteaters [22]. In birds, the keratinous ramphoteca was proposed to be responsible for the early interruption of odontogenesis at the lamina stage [31]. An early keratinization might be the triggering event for subsequent odontogenesis disruption during the development of both anteater keratinous pad and bird beak. Interestingly, toothless whales also present keratinous structures (baleens) that develop after odontogenesis interruption [10]. Thewissen et al. [10] argued that tooth development is a *sine qua non* condition to the development of baleens. This is in line with both fossil and molecular evidence suggesting a stepwise transition between teeth and baleen in mysticetes [2]. Ekdale et al. [32] also recently suggested that foramina for baleen vascularization in the upper jaw of toothless whales are likely homologous to tooth alveoli. Similarly, odontogenesis and associated dorsal canaliculi might be a prerequisite for mandibular keratinization in anteaters. Accordingly, the lack of keratinous pad and vestigial teeth might explain the absence of dorsal canaliculi in pangolins.

In rorqual whales, the peculiar distribution of dorsal canaliculi along the mandible was proposed to be related to movement coordination of lower jaws and alignment with the baleen plates during filter feeding [7]. Pyenson et al. [33] argued that nerves passing through the most anterior canaliculus connected the brain to a symphyseal organ/vibrissae system responsible for mandibular motor coordination and prey detection, respectively. Given the absence of external vibrissae in anteaters and the fact that they mainly use olfaction to detect their prey [34], dorsal canaliculi and respective extensions of the IAN are unlikely related to prey detection. However, several studies [34 and references therein] described the synchronization between tongue protrusion and mandible closing during feeding in anteaters (i.e., *Myrmecophaga* and *Tamandua*) as well as in ant-eating echidnas. In these groups, the mandibles rotate medio-laterally, with the oral cavity widening when the tongue is retracted and narrowing when it is protruded, forming a tube-like mouth to serve as physical support [35, 36]. This type of integrated movement would require a tactile feedback originating from the dorsal margin of the mandible, which is in contact with the protruding tongue and the upper jaw. A similar hypothesis has been proposed in whales [7] for the coordination between mandibles and baleens during gulping. Tooth pulp stimulation was shown to trigger a response of the digastric muscle in cats [37]. Dong et al. [38] also showed that cat teeth stimulation results in discharge signatures for different textures (e.g., rough or smooth). Furthermore, teeth are known to respond to non-painful stimuli in humans [39]. We propose that the ascending branches of the IAN might be part of the somatosensory system involved in mechanoreception, which could explain the convergent evolution of dorsal canaliculi in the toothless mandibles of baleen whales and anteaters. In contrast, no medio-lateral rotation of the mandibles was reported in pangolins [36], while the presence of a fused symphysis likely helps maintaining the tube-like shape of the oral cavity while feeding [40]. Compared to anteaters and baleen whales, such a relatively reduced mandibular mobility could potentially explain the absence of dorsal canaliculi in pangolins.

Our results support the hypothesis of convergent exaptation of the dorsal canaliculi in anteaters and baleen whales following tooth regression. We unequivocally showed that the IAN as well as blood vessels branch through the dorsal canaliculi and argue that keratinous structures and vestigial teeth have a crucial role in mandibular innervation, maintaining the sensorial function associated to the presence of teeth while strong selective pressures induced their loss. Despite the superficial resemblance of the masticatory apparatus between anteaters and pangolins, convergent tooth loss resulted in divergent structures in the internal morphology of their mandible. We propose that these differences likely reflect divergent phylogenetic histories and/or divergent functional constraints. Rewiring of the mandibular canal in anteaters and baleen whales provides a striking example of evolutionary tinkering linked to the regression of teeth.

STAR★METHODS

Detailed methods are provided in the online version of this paper and include the following:

- KEY RESOURCES TABLE
- CONTACT FOR REAGENT AND RESOURCE SHARING
- EXPERIMENTAL MODEL AND SUBJECT DETAILS
  - Institutional abbreviations
- METHOD DETAILS
  - Comparative anatomy
  - Acquisition of data
  - Histology

SUPPLEMENTAL INFORMATION

Supplemental Information includes four figures, one table, and one data file and can be found with this article online at https://doi.org/10.1016/j.cub.2018.12.023.

ACKNOWLEDGMENTS

We thank Steffen Bock, Peter Giere, Frieder Mayer, and Detlef Willborn (MfN); Roberto Portela Miguez, Louise Tomsett, Farah Ahmed, Amin Garbout, and Brett Clark (BMNH); Renaud Lebrun (ISEM/MRI platform), François Catzeflis, Pierre-Henri Fabre, and Quentin Martinez (ISEM); Guillaume Billet (MNHN); and Chris Conroy (MVZ) for access to collections and assistance with μ-CT scanning. We also thank Pierre-Henri Fabre, Chris Emerling, and two anonymous reviewers for helpful comments on the manuscript and Quentin Martinez, Mélanie Debiais-Thibaud, and Helder Gomes Rodrigues for fruitful discussions. We acknowledge J.G.M. Thewissen and the North Slope Borough Department of Wildlife Management for Figure S3A. We thank Nelly Pirot, Florence Bernex, and Marion Olive (INSERM) for assistance with histology. Finally, we thank Sarah Jones who helped to improve the English of the manuscript. S.F.-C., L.H. and F.D. were supported by a European Research Council (ERC) consolidator grant (ConvergeAnt #683257). S.F.C. benefitted from the SYNTHESYS Project (Project 312253) founded by the European Community Research Infrastructure Action under the FP7 Integrating Activities Programme. L.H. and F.D. were supported by Centre National de la Recherche Scientifique (CNRS). This work has been supported by "Investissements d'Avenir" grants managed by Agence Nationale de la Recherche Labex CEBA (ANR-10-LABX-25-01), Labex CEMEB (ANR-10-LABX-0004), and Labex NUMEV (ANR-10-LABX-0020). This is contribution ISEM 2018-275 of the Institut des Sciences de l'Evolution de Montpellier.

AUTHOR CONTRIBUTIONS

S.F.-C., L.H., and F.D. collected the data, conceived the study, and designed the study. S.F.-C., L.H., and F.D. contributed to discussion and drafted and edited the manuscript. L.H. and F.D. coordinated the study. All authors gave final approval for publication.

DECLARATION OF INTERESTS

The authors declare no competing interest.

Received: August 28, 2018
Revised: November 7, 2018
Accepted: December 13, 2018
Published: January 17, 2019

REFERENCES

1. Meredith, R.W., Gatesy, J., Murphy, W.J., Ryder, O.A., and Springer, M.S. (2009). Molecular decay of the tooth gene Enamelin (ENAM) mirrors the loss of enamel in the fossil record of placental mammals. PLoS Genet. *5*, e1000634.
2. Deméré, T.A., McGowen, M.R., Berta, A., and Gatesy, J. (2008). Morphological and molecular evidence for a stepwise evolutionary transition from teeth to baleen in mysticete whales. Syst. Biol. *57*, 15–37.
3. Meredith, R.W., Gatesy, J., and Springer, M.S. (2013). Molecular decay of enamel matrix protein genes in turtles and other edentulous amniotes. BMC Evol. Biol. *13*, 20.
4. Ridgway, S.H., Green, R.F., and Sweeney, J.C. (1975). Mandibular anesthesia and tooth extraction in the bottlenosed dolphin. J. Wildl. Dis. *11*, 415–418.
5. Gray, H. (1995). Anatomy, descriptive and surgical (Bristol: Parragon Book Service Ltd.).
6. Wadu, S.G., Penhall, B., and Townsend, G.C. (1997). Morphological variability of the human inferior alveolar nerve. Clin. Anat. *10*, 82–87.
7. Peredo, C.M., Pyenson, N.D., Uhen, M.D., and Marshall, C.D. (2017). Alveoli, teeth, and tooth loss: Understanding the homology of internal mandibular structures in mysticete cetaceans. PLoS ONE *12*, e0178243.
8. Fried, K., Lillesaar, C., Sime, W., Kaukua, N., and Patarroyo, M. (2007). Target finding of pain nerve fibers: neural growth mechanisms in the tooth pulp. Physiol. Behav. *92*, 40–45.
9. Kumar, S., Stecher, G., Suleski, M., and Hedges, S.B. (2017). TimeTree: a resource for timelines, timetrees, and divergence times. Mol. Biol. Evol. *34*, 1812–1819.
10. Thewissen, J.G.M., Hieronymus, T.L., George, J.C., Suydam, R., Stimmelmayr, R., and McBurney, D. (2017). Evolutionary aspects of the development of teeth and baleen in the bowhead whale. J. Anat. *230*, 549–566.
11. Kieser, J., Kieser, D., and Hauman, T. (2005). The course and distribution of the inferior alveolar nerve in the edentulous mandible. J. Craniofac. Surg. *16*, 6–9.
12. Hautier, L., Gomes Rodrigues, H., Billet, G., and Asher, R.J. (2016). The hidden teeth of sloths: evolutionary vestiges and the development of a simplified dentition. Sci. Rep. *6*, 27763.
13. Martin, B. (1916). Tooth development in *Dasypus novemcinctus*. J. Morphol. *27*, 647–961.
14. Anthony, R. (1934). La dentition de l'oryctérope. Morphologie, développement, structure, interprétation. Ann. Sci. Nat. Zool. *17*, 289–322.
15. Spurgin, A.M. (1904). Enamel in the teeth of an embryo edentate (*Dasypus novemcinctus* linn). Am. J. Anat. *3*, 75–84.
16. Thomas, O. (1889). A milk dentition in Orcyteropus. Proc. R. Soc. Lond. *47*, 246–248.
17. Lönnberg, E. (1906). On a new Orycteropus from Northern Congo and some remarks on the dentition of the Tubulidentata. Ark. Zool. *3*, 31–66.
18. Ciancio, M.R., Castro, M.C., Galliari, F.C., Carlini, A.A., and Asher, R.J. (2012). Evolutionary implications of dental eruption in *Dasypus* (Xenarthra). J. Mamm. Evol. *19*, 1–8.
19. Vizcaíno, S.F., Paleobiology, S., Summer, N., and Vizcaino, S.F. (2009). Paleontological Society The Teeth of the " Toothless. Novelties and Key Innovations in the Evolution of Xenarthrans. *35*, 343–366.
20. Tims, H.W. (1908). Tooth-vestiges and associated mouth parts in the Manidae. J Anat Physiol *42*, 375–387.
21. Ishikawa, H., and Amasaki, H. (1995). Development and physiological degradation of tooth buds and development of rudiment of baleen plate in southern minke whale, Balaenoptera acutorostrata. J. Vet. Med. Sci. *57*, 665–670.
22. Rose, C. (1892). Beitrage zur Zahnentwicklung der Edentaten. Anat. Anz. *7*, 495–512.
23. Gibb, G.C., Condamine, F.L., Kuch, M., Enk, J., Moraes-Barros, N., Superina, M., Poinar, H.N., and Delsuc, F. (2016). Shotgun mitogenomics provides a reference phylogenetic framework and timescale for living xenarthrans. Mol. Biol. Evol. *33*, 621–642.

24. Meredith, R., Janečka, J., Gatesy, J., Ryder, O., Fisher, C.F., Teeling, E.C., Goodbla, A., Eizirik, E., Simão, T.L.L., and Stadler, T. (2011). Impacts of the Cretaceous terrestrial revolution and KPg extinction on mammal diversification. Science (80-.) *334*, 521, 24.
25. Gaudin, T.J., Emry, R.J., and Wible, J.R. (2009). The phylogeny of living and extinct pangolins (Mammalia, Pholidota) and associated taxa: a morphology based analysis. J. Mamm. Evol. *16*, 235–305.
26. Nweeia, M.T., Eichmiller, F.C., Hauschka, P.V., Donahue, G.A., Orr, J.R., Ferguson, S.H., Watt, C.A., Mead, J.G., Potter, C.W., Dietz, R., et al. (2014). Sensory ability in the narwhal tooth organ system. Anat. Rec. (Hoboken) *297*, 599–617.
27. Gaudin, T.J. (2004). Phylogenetic relationships among sloths (Mammalia, Xenarthra, Tardigrada): the craniodental evidence. Zool. J. Linn. Soc. *140*, 255–305.
28. Rétaux, S., and Casane, D. (2013). Evolution of eye development in the darkness of caves: adaptation, drift, or both? Evodevo *4*, 26.
29. Gervais, P. (1867). In Zoologie et paléontologie générales: nouvelles recherches sur les animaux vertébrés vivants et fossiles, A. Bertrand, ed. (Paris: La Societé de Géographie).
30. Kuenzel, W.J. (2007). Neurobiological basis of sensory perception: welfare implications of beak trimming. Poult. Sci. *86*, 1273–1282.
31. Louchart, A., and Viriot, L. (2011). From snout to beak: the loss of teeth in birds. Trends Ecol. Evol. *26*, 663–673.
32. Ekdale, E.G., Deméré, T.A., and Berta, A. (2015). Vascularization of the gray whale palate (Cetacea, Mysticeti, *Eschrichtius robustus*): soft tissue evidence for an alveolar source of blood to baleen. Anat. Rec. (Hoboken) *298*, 691–702.
33. Pyenson, N.D., Goldbogen, J.A., Vogl, A.W., Szathmary, G., Drake, R.L., and Shadwick, R.E. (2012). Discovery of a sensory organ that coordinates lunge feeding in rorqual whales. Nature *485*, 498–501.
34. Lubin, Y., and Montgomery, G. (1981). Defenses of *Nasutitermes* termites (Isoptera, Termitidae) against *Tamandua* anteaters (Edentata, Myrmecophagidae). Biotropica *13*, 66–76.
35. Naples, V. (1999). Morphology, evolution and function of feeding in the giant anteater (Myrmecophaga tridactyla). J. Zool. (Lond.) *249*, 19–41.
36. Endo, H., Ito, K., Watabe, H., Nguyen, S., and Koyabu, D. (2017). Macroscopic and CT examinations of the mastication mechanism in the southern tamandua. Mammal Study *42*, 89–97.
37. Boissonade, F.M., and Matthews, B. (1993). Responses of trigeminal brain stem neurons and the digastric muscle to tooth-pulp stimulation in awake cats. J. Neurophysiol. *69*, 174–186.
38. Dong, W.K., Chudler, E.H., and Martin, R.F. (1985). Physiological properties of intradental mechanoreceptors. Brain Res. *334*, 389–395.
39. Chatrian, G.E., Fernandes de Lima, V.M., Lettich, E., Canfield, R.C., Miller, R.C., and Soso, M.J. (1982). Electrical stimulation of tooth pulp in humans. II. Qualities of sensations. Pain *14*, 233–246.
40. Endo, H., Nishiumi, I., Kurohmaru, M., Nabhitabhata, J., Chan-Ard, T., Nadee, N., Agungpriyono, S., and Yamada, J. (1998). The functional anatomy of the masticatory muscles of the Malayan pangolin, Manis javanica. Mammal Study *23*, 1–8.

STAR★METHODS

KEY RESOURCES TABLE

RESOURCE	SOURCE	IDENTIFIER
Biological Samples		
Proteles cristatus	This paper	BMNH 34.11.1.5
Canis lupus	https://www.morphosource.org/Detail/SpecimenDetail/Show/specimen_id/2716	LACM 23010 (MorphoSource: M7773)
Manis crassicaudata	This paper	BMNH 67.4.12.298
Manis javanica	This paper	BMNH 9.1.5.858
Orycteropus afer	This paper	BMNH 27.2.11.113
Potamogale velox	This paper	ZMB 71587
Tenrec ecaudatus	This paper	Martinez pers. coll.
Rhynchocyon petrsi	This paper	BMNH 55.149
Procavia capensis	https://www.morphosource.org/Detail/SpecimenDetail/Show/specimen_id/5258	UMZC H4980K (MorphoSource: M13296)
Cyclopes didactylus	This paper	MNHN 1986-1115
Cyclopes didactylus	This paper	BMNH 24.12.4.68
Tamandua tetradactyla	This paper	BMNH 34.9.2.196
Tamandua tetradactyla	This paper	ISEM 788N
Tamandua tetradactyla	This paper	MVZ 153482
Myrmecophaga tridactyla	This paper	ISEM 071 N
Myrmecophaga tridactyla	This paper	ISEM 065 V
Myrmecophaga tridactyla	This paper	MVZ 185238
Bradypus tridactylus	This paper	ZMB 18834
Bradypus tridactylus	This paper	MNHN 1999-1065
Choloepus didactylus	This paper	ZMB 4949
Choloepus hoffmanni	This paper	Hautier pers. coll.
Dasypus pilosus	This paper	ZMB 19240
Dasypus novemcinctus	This paper	USNM 033867
Dasypus novemcinctus	This paper	LSUMZ 8538
Dasypus novemcinctus	This paper	LSUMZ 29160
Dasypus novemcinctus	This paper	BMNH 11.10.27.3
Dasypus novemcinctus	This paper	ZMB 84-357
Dasypus novemcinctus	This paper	USNM 020920
Priodontes maximus	This paper	ZMB 47528
Tapirus indicus	http://dmm.pri.kyoto-u.ac.jp/dmm/WebGallery/dicom/dicomProperty.html?id=506	KUPRI: 506
Molossus molossus	https://www.morphosource.org/Detail/MediaDetail/Show/media_id/19283	AMNH 234923 (MorphoSource: M19283)
Talpa europaea	This paper	Martinez pers. coll.
Cynocephalus volans	https://www.morphosource.org/Detail/MediaDetail/Show/media_id/18020	FMNH 56521 (MorphoSource: M18020)
Lemur catta	https://www.morphosource.org/Detail/MediaDetail/Show/media_id/647	DPC-O92 (MorphoSource: M647)
Tupaia montana	https://www.morphosource.org/Detail/MediaDetail/Show/media_id/13025	FMNH 108831 (MorphoSource: M13025)
Lepus europaeus	https://www.morphosource.org/Detail/MediaDetail/Show/media_id/23932	DMET-LE1 (MorphoSource: M23932)

(*Continued on next page*)

Continued		
RESOURCE	SOURCE	IDENTIFIER
Rattus norvegicus	https://www.morphosource.org/Detail/MediaDetail/Show/media_id/28785	HACB-RN1 (MorphoSource: M28785)
Dasyurus hallucatus	http://digimorph.org/specimens/Dasyurus_hallucatus/	TMM M-6921
Reagents		
Acetic acid	Merck	537020
Distilled water	Aguettant	3293
Luxol Fast Blue	Georges T. GURR	B2580
Lithium carbonate	Diapath	M00188
Cresyl violet	Merck	5235
Software and Algorithms		
Avizo 9.4.0	FEI	https://www.fei.com/software/amira-avizo/
Other		
Voxel size used for 3D model segmentation	This paper	Table S1

CONTACT FOR REAGENT AND RESOURCE SHARING

Further information and requests for resources should be directed to and will be fulfilled by the Lead author Frédéric Delsuc (frederic.delsuc@umontpellier.fr).

EXPERIMENTAL MODEL AND SUBJECT DETAILS

The anatomical descriptions (Data S1) correspond to *Cyclopes didactylus* (MNHN 1986-1115), *Tamandua tetradactyla* (BMNH 34.9.2.196), *Myrmecophaga tridactyla* (ISEM – 065 V), *Manis crassicaudata* (BMNH 67.4.12.298), *Manis javanica* (BMNH 9.1.5.858), *Dasypus novemcinctus* (USNM 033867), *Dasypus pilosus* (ZMB 19240), *Priodontes maximus* (ZMB 47528), *Proteles cristatus* (BMNH 34.11.1.5), *Canis lupus* (LAMC 23010), *Bradypus tridactylus* (MNHN 1999-1065), and *Choloepus hoffmanni* (Hautier pers. Coll.), *Orycteropus afer* (BMNH 27.2.11.113), and *Potamogale velox* (ZMB 71587). Additional comparative observations include *Dasyurus hallucatus* (TMM M-6921), *Lemur catta* (DPC-O92), *Cynocephalus volans* (FMNH 56521), *Procavia capensis* (UMZC H4980K), *Tapirus indicus* (KUPRI 506), *Tenrec ecaudatus* (Martinez pers. coll.), *Lepus europaeus* (DMET-RN1), *Talpa europaea* (Martinez pers. coll.), *Tupaia montana* (FMNH 108831), *Rhynchocyon petersi* (BMNH 55149), *Rattus norvegicus* (HACB-RN1), *Molossus molossus* (AMNH 234923), *Dasypus novemcinctus* (USNM 033867, BMNH 11.10.27.3, LSUMZ 8538, LSUMZ 29160, ZMB 84-357, USNM 020920), *Cyclopes didactylus* (MNHN 1986-1115, BMNH 24.12.4.68), *Tamandua tetradactyla* (BMNH 34.9.2.196, MVZ 153482, ISEM 778N), and *Myrmecophaga tridactyla* (ISEM 065V, MVZ 185238, ISEM 071N).

Institutional abbreviations

MNHN, Muséum national d'Histoire naturelle; BMNH British Museum of Natural History; ISEM, Institut des Sciences de l'Evolution; USNM, Smithsonian National Museum of Natural History; ZMB, Museum für Naturkunde; LAMC, Natural History Museum of Los Angeles County; TMM, Texas Memorial Museum; DPC, Duke Lemur Center Division of Fossil Primates; FMNH, The Field Museum of Natural History; UMZC, University Museum of Zoology (Cambridge); KUPRI, Kyoto University Primate Reasearch Center; DMET, University of Hull; HACB, University of Liverpool; AMNH, American Museum of Natural History; LSUMZ, Louisianna State University Museum of Natural Science.

METHOD DETAILS

Comparative anatomy

We present an anatomical description of the mandibles and mandibular canals of 26 species (Figure 1) representing the following taxa: Vermilingua (anteaters) – *Cyclopes didactylus*, *Tamandua tetradactyla*, *Myrmecophaga tridactyla* (juvenile + adult); Cingulata (armadillos) – *Dasypus novemcinctus*, *Dasypus pilosus*, *Priodontes maximus*; Folivora (sloths) – *Bradypus tridactylus* (fetus + adult); *Choloepus* spp. (fetus + adult); Tubulidentata (aardvarks) – *Orycteropus afer*; Afrosoricida (tenrecs) – *Potamogale velox*, *Tenrec ecaudatus*; Macroscelidea (elephant shrews) – *Rhynchocyon petersi*; Hyracoidea (hyraxes) – *Procavia capensis*; Pholidota (pangolins) – *Manis crassicaudata*, *Manis javanica*; Carnivora (carnivores) – *Proteles cristatus*, *Canis lupus*; Perissodactyla (odd-toed ungulates) – *Tapirus indicus*; Chiroptera (bats) – *Molossus molossus*; Eulipotyphla (moles and shrews) – *Talpa europaea*; Lagomorpha (hares and rabbits) – *Lepus europaeus*; Rodentia (rodents) – *Rattus norvegicus*; Primates (primates) – *Lemur catta*; Dermoptera (colugos) – *Cynocephalus volans*; Scandentia (tree shrews) – *Tupaia montana*; *Dasyuromorphia* (carnivorous

marsupials) – *Dasyurus hallucatus*. Using this dataset, we were able to compare the morphology of the mandibular canal and dorsal canaliculi of closely related toothed and toothless taxa, as well as a wide range of species belonging to 18 mammalian orders. We additionally compared our results to the previously published research on cetaceans and even-toed ungulates (Cetartiodactyla) by Peredo et al. [7]. We segmented a total of five *D. novemcinctus*, three *M. tridactyla* (two adults + one juvenile), three *T. tetradactyla*, and two *Cy. didactylus* in order to account for intraspecific variation (Data S1, Figure S4). We also segmented left and right hemi-mandibles of the anteater specimens to assess the level of bilateral variation in dorsal canaliculi count (Data S1). Both fetus and adult specimens of *B. tridactylus* and *Choloepus* spp. were studied (Figure 3) in order to seek the presence of a dorsal canaliculus linked to the development of vestigial teeth [12] and to confirm that there was no major variation in the number of dorsal canaliculi through ontogeny. Mandibles were chosen to study dental innervation patterns because they are composed by a single bone (dentary) enclosing the IAN and the IAA. The mandibular canal soft tissues enter in a continuous canal posterior to the tooth row and project anteriorly to its anterior end. Compared to the cranium, all branching patterns of the mandibular canal are therefore more easily traceable. The mandible is, therefore, a simpler model to study innervation patterns with the techniques used for this manuscript.

Acquisition of data

The studied specimens belong to the following collections: Natural History Museum, London (BMNH); Muséum National d'Histoire Naturelle, Paris (MNHN); Museum für Naturkunde, Berlin (ZMB); University Museum of Zoology, Cambridge (UMZ); Institut des Sciences de l'Evolution, Montpellier (ISEM); Museum of Vertebrate Zoology, Berkeley (MVZ); Louisianna State University Museum of Zoology (LSUMZ); United States National Museum (USNM); L.H. personal collection. High-resolution microtomography (μCT) was performed at Montpellier Rio Imaging (MRI; Microtomograph RX EasyTom 150, X-ray source 40-150 kV) platform, Imaging Analysis Center (BMNH; Nikon Metrology HMX ST 225, X-ray source 225 kV), and the Helmholtz Zentrum Berlin (HZB, Hamamatsu L8121-3, X-ray source 40-150 kV). The scan resolution differed according to the size of specimens (Table S1). Eight specimens were obtained from MorphoSource (https://www.morphosource.org), one from Digimorph (www.digimorph.org), and one from the Digital Morphology Museum (http://dmm4.pri.kyoto-u.ac.jp/dmm/WebGallery/index.html). The left hemi-mandibles (the right one was used if the left one was missing or broken) were reconstructed, with respective mandibular canals and teeth. Avizo 9.4.0 (Visualization Sciences Group) was used to perform the 3D reconstructions. When teeth were absent, the mental branches were distinguished from the dorsal canaliculi by their larger diameter and their lateral projection to the mental foramina on the lateral aspect of the mandible [5, 7]. Dorsal canaliculi were defined as dorsal projections of the mandibular canal opening on the dorsal surface of the mandible.

Histology

We also dissected the head of an adult specimen of *T. tetradactyla* (ISEM 778N) fixed in formalin. The right mandible was extracted and its associated musculature removed. The mandible was then subjected to decalcification during forty five days, following standard protocols. A portion of the mandible was then cut (as shown in Figure 4*A*) with the use of a scalpel, and fixed in paraffin. Serial slicing was performed to produce 3μm thick coronal and sagittal sections of the mandible. Luxol Fast Blue (LFB) was used to stain the slices in order to allow for the blue staining of the myeline sheaths insulating nerve cell axons. The LFB staining protocol was composed of several phases (1-11) in which acetic acid (10%), Luxol Fast Blue (0.1%), lithium carbonate (0.05%), and cresyl violet (0.1%) were used. (1) Histological sections were placed in a sealed container with the Luxol Fast Blue solution and were left overnight inside an oven at 58°C; (2) Sections were rinsed with ethanol (96%); (3) Sections were rinsed with distilled water; (4) Sections were differentiated in a lithium carbonate solution during 30 s; (5) Sections were placed in a rack with ethanol (70%) and were then stirred manually twice during periods of 15 s; (6) Sections were placed in a rack with distilled water and were then stirred manually during 1 min; (7) A counterstain was performed by placing the sections in a cresyl violet solution during 10 min; (8) Samples were quickly rinsed twice with ethanol (96%); (9) Sections were placed on ethanol (100%) for two periods of 2 min each; (10) Sections were placed on xylene (dimethylbenzene) for the same duration as in step (9); (11) Sections were mounted with a resinous medium (Pertex). A histological slice of a coronal section of the mandible of *Balaena mysticetus* (provided by J.G.M. Thewissen [10]) was used for anatomical comparisons (Figure S3A).

2.5-Morphological adaptation of the head musculature

Ecological convergence is often coupled with both behavioral and morphological convergence (e.g., Stuart-Fox & Moussali, 2007; McGhee, 2011). In an evolutionary context, a replicate is therefore expected to show a correlation between behavior, ecology, and morphology (Johnson, Revell, & Losos, 2009; Losos, 2017). Function overlaps with behavioral, ecological, and morphological realms of evolution. The exploitation of an ecological niche is associated to the evolution of specific morphologies that correlate to function, which is often associated to behavior. For instance, the morphological evolution of the skull of durophagous bats of the genus *Chiroderma* is associated with the exploitation of a specific ecological niche (grain eating) within the phylogeny of fruit bats (Nogueira *et al.*, 2005). On the other hand, morphology can be a correlate of function. Nogueira *et al.* (2009) showed that bite force was relatively weak in long-snouted nectarivorous bats when compared to their insectivorous sister taxa. The authors showed that low bite forces were associated with morphological traits such as elongated rostra and narrow zygomatic arches. Hautier *et al.* (2012) showed differences in the skull and mandibles of hystricognathous rodents associated to dietary strategies, which they associated to the origin and insertion of masticatory muscles (function). The authors also show a morphological convergence associated to habitat (niche exploitation). These are just a few examples of shape-function interactions during processes of adaptive evolution toward an ecological niche. The literature presents numerous studies addressing convergent evolution of shape and function (e.g. Herrel *et al.*, 2004; Stayton, 2006; Wroe & Milne, 2007; Tseng, 2013; Tseng *et al.*, 2016).

In the majority of these studies, the concept of "constraint" is omnipresent. Often, function or functional proxies (e.g., muscle volume) are less correlated with shape than hypothetically assumed (Figueirido *et al.*, 2011; Fabre *et al.*, 2018). Adaptation can be overlain by phylogenetic constraints (Stayton, 2005; Hautier *et al.*, 2012). In other cases, morphology and function appear to be decoupled from behavior (Smith & Redford, 1990). Given the complexity of morphological traits, one is confronted with the need to study convergent adaptive evolution as a continuous trait (e.g., magnitude of convergence; Stayton, 2006; Martinez *et al.*, 2018; Arbour & Zanno, 2019) and to consider convergence as a plastic concept that is susceptible to scale and level of analysis (Losos, 2017). In such scenario, are there true evolutionary replicates? The answer to this question is dependent on another one: "is adaptation perfect?" Travis and Reznick (2009) answered this question by splitting traits between adaptive and non-adaptive ones. The latter are normally referred to as "constraints". Phenotypic traits may tend to an optimum, as groups of adaptive traits are acted on by natural selection, but organismal integration (inter-trait

covariation/correlation) caused by the common pathways between adaptive and non-adaptive traits will restrict that optimum (Travis & Reznick, 2009). Therefore, evolutionary replicates may present variable degrees of convergence. As a result, the dissection of cases of evolutionary convergence may result in one conclusion: each level (ecological, morphological, and functional) depends on the extent of phenotypic evolvability allowed by the adaptive/non-adaptive trait correlation specific to each clade, as well as to the ability to detect and quantify variation. Aspects related to phenotypic integration are developed in chapter 3.

Muscles are responsible for motion of skeletal elements and soft tissues in animals (Rizzo, 2015). Therefore, functional adaptation is often assessed or described on the basis of muscular anatomy (Naples, 1985, 1986, 1999b; Endo *et al.*, 1998, 2002; Marshall, 2009), biomechanical models (Weijs, 1980; Gueldre & Vree, 1990; Fabre *et al.*, 2017), and muscle performance (Herrel *et al.*, 1999; Santana, Dumont, & Davis, 2010; Ginot *et al.*, 2018). The mammalian skull is a highly modular system in which developmental and functional constraints interact to limit or promote the evolution of certain axes of variation (e.g., Hallgrímsson *et al.*, 2004; Goswami, 2006; Porto *et al.*, 2009; see 'Morphological evolution, integration and modularity' section). One of the main epigenetic factors generating covariance during the ontogeny of complex skeletal structures is muscle-bone interactions (Cheverud, 1982a; Hallgrímsson *et al.*, 2007; Zelditch *et al.*, 2008). Muscular activity during the embryonic development of the skull applies mechanical forces on both bones and cartilages (Hall & Herring, 1990; Herring, 1993). Those forces, or mechanical loading, act on the embryonic solid surfaces influencing the direction, and amount of growth or compression (Herring, 1993). The absence of muscular contraction during embryonic development results in skeletal anomalies including the loss and reduction of certain bones and cartilages (Hall & Herring, 1990; Rot-Nikcevic *et al.*, 2006; Anthwal, Peters, & Tucker, 2015). Muscular activity has been detected in development as early as during the differentiation of myoblasts in muscle precursors (Natsuyama, 1991). This shows that the generation of covariance on the skull through muscle-bone interactions happens much earlier than functional movements like sucking or chewing.

Evidence of the role of muscular contraction in bone morphology is exemplified by the case-studies presented by Anthwal *et al.* (2015) and Herring (1993). Anthwal *et al.* (2015) used a knockout experiment to show that the initiation of coronoid growth in the mouse mandible is dependent on the expression of the transcription factor *Pax9*. However, the subsequent growth of the coronoid process is also dependent on the activation of *Sox9* expression by the application of mechanical loading. The expression of some growth-related genes is activated by mechanical loading (Hatton *et al.*, 2003). In

mutants with a reduced *temporalis* (the muscle attaching on the coronoid process), the coronoid was vestigial and eventually lost in later ontogenetic stages (Aggarwal *et al.*, 2010). In the second example, Herring (1980) showed that the *masseter* of pigs, one of the muscles originating on the jugal, presents a posterodorsal extension on the zygomatic arch, when compared to their sister clade, the peccaries. This muscular projection is matched by posterior process of the jugal. Herring (1993) suggests that the posterior extension of the *masseter* induced the development of this jugal process. Such a process is similar to that studied by Anthwal and colleagues (2015). These two examples are illustrative of the importance of muscle development in skull evolution.

Despite its role in early development, mechanical loading is often considered an important motor of covariance generation during the postnatal life of mammals (Herring & Teng, 2000; Zelditch *et al.*, 2006; Hallgrímsson *et al.*, 2007). Shifts in covariance just posterior to weaning were partly associated to muscular activity in the cotton rat skull, although other factors may also play an important role (Zelditch & Carmichael, 1989). On the other hand, a transition from weaning to a hard food diet is probably responsible for a shift in direction of the ontogenetic trajectory of phenotypic covariance in mice (Mitteroecker & Bookstein, 2009). The magnitude and direction of mechanical loading is not constant during an animal's lifespan (Sun, Lee, & Herring, 2004). This likely contributes to the repatterning of covariation at different stages of postnatal development (Mitteroecker & Bookstein, 2009). When considering shifts of muscular strain (either magnitude or direction) in postnatal life, muscle-bone interactions in the skull can be interpreted as an environmental factor (at least partially; Herring, 1993). This is because functional movements are dependent on the type of diet (hard or soft). Mechanical loading is therefore a critical factor of skull shape from the first appearance of muscle anlagen in the embryo, and may change patterns of covariance during adult life.

Given the intimate association between musculature and skull shape, it is highly relevant to analyze these two systems in the context of adaptive evolution. In the case of convergent evolution towards myrmecophagy, qualitative and quantitative analyses of the muscles of the masticatory apparatus can shed light on the functional adaptation of ant- and termite-eating placentals (Endo *et al.*, 1998, 2007, 2017; Naples, 1999b; Reiss, 2001). Additionally, comparative anatomy of auxiliary mastication, tongue, and hyoid muscles can provide a better view over the similarities and differences in functional morphology across myrmecophagous placentals. Ultimately, this type of information constitutes an essential asset to test functional convergence in the skull of ant- and termite-eaters.

In the following article I describe the masticatory apparatus, the transverse mandibular musculature, and the muscles of the hyoid, thyroid, the sternum, and the face in anteaters. I additionally compare their muscular anatomy to descriptions of other myrmecophagous placentals available in the literature.

Article 3

Comparative anatomy of the facial, masticatory, intermandibular, and hyoid musculatures in anteaters (Vermilingua, Xenarthra) and its implications for the interpretation of morphological convergence in myrmecophagous placentals.

In preparation: to be submitted to *PeerJ*

Supplemental information for this article is available in Appendix 3.

Title: **Comparative anatomy of the facial, masticatory, intermandibular, and hyoid musculatures in anteaters (Vermilingua, Xenarthra) and its implications for the interpretation of morphological convergence in myrmecophagous placentals.**

Authors: **Ferreira-Cardoso**[1]**,** Sérgio**; Fabre**[1]**,** Pierre-Henri**; De Thoisy**[2,3]**,** Benoit; **Delsuc**[1]**,** Frédéric; **Hautier**[1,4]**,** Lionel

[1]Institut des Sciences de l'Evolution de Montpellier (ISEM), CNRS, IRD, EPHE, Université de Montpellier, Montpellier, France.

[2]Institut Pasteur de la Guyane, Cayenne, French Guiana, France

[3]Kwata NGO, Cayenne, French Guiana, France

[4]Mammal Section, Life Sciences, Vertebrate Division, The Natural History Museum, London, UK.

Introduction

The Cretaceous terrestrial revolution and the Cretaceous-Paleogene (K-Pg) mass extinction event are often viewed as milestones in placental mammal evolution (Meredith *et al.*, 2011). These events promoted the opening of terrestrial ecological niches available to placentals, contributing to their morphological diversification (Romer, 1974; Alroy, 1999). The adaptation of the placental masticatory apparatus likely contributed to this radiation, as mechanical processing of food items is essential to ensure a better energetic intake (Hiiemae, 2000).

Dietary specialization is often a main driver of cranial morphological specialization (Varrela, 1990; Barlow, Jones, & Barratt, 1997; Nogueira, Peracchi, & Monteiro, 2009; Hautier, Lebrun, & Cox, 2012; Klaczko, Sherratt, & Setz, 2016; Maestri *et al.*, 2016). The masticatory apparatus of placental mammals is composed by the temporal and pterygoid fossae, and the zygomatic arch of the skull, by the jaws, and by a series of mostly adductor muscles responsible for mandibular movements involved in the chewing process (Hiiemae, 2000; Hylander, 2006). This apparatus is composed by the temporal, the masseter, and pterygoid muscles (Turnbull, 1970). These powerful muscles are derived from the plesiomorphic "adductor mandibulae" plate of sarcopterygians (Edgeworth, 1935; Diogo, 2018). Although several other muscles contribute to mastication, the mandibular movement is mainly operated by the elevator forces of the temporal and masseter, the mandibular protrusion mainly involve the pterygoids and the masseter, and condylar stability is provided by the pterygoids and the zygomaticomandibularis (Turnbull, 1970; Naples, 1999; Hylander, 2006). The homogeneity in the composition of the masticatory apparatus contrasts with the broad morphofunctional disparity of the placental skull. This functional diversity is mostly reflected by differences in muscle morphologies and proportions. These are often associated with phylogenetic constraints and ecological specialization (Parsons & G., 1896; Druzinsky, Doherty, & De Vree, 2011; Hautier *et al.*, 2012; Fabre *et al.*, 2017; Ginot, Claude, & Hautier, 2018).

The evolution of myrmecophagy (ant- and termite-eating) in mammals is a textbook example of morphological convergence driven by diet (McGhee, 2011) leading to modified skulls with tooth reduction, extreme snout elongation, and long extensible tongues (Rose & Emry, 1993; Davit-Béal *et al.*, 2009; Ferreira-Cardoso *et al.*, 2019; Gaudin *et al.*, 2019). Morphological changes driven by the adaptation to myrmecophagy even led some myrmecophagous placentals, as anteaters, pangolins, or giant armadillos, to lose the ability to chew (Naples, 1999; Davit-Béal *et al.*, 2009; Vizcaíno *et al.*, 2009). Aardvarks, on the other side, are still able to chew (Patterson, 1975). Anteaters (Vermilingua, Xenarthra) consist of up

to ten extant species included in two molecularly divergent families that diverge more than 37 million years ago (Mya; Gibb *et al.*, 2016), the Cyclopedidae (seven *Cyclopes* spp.) and the Myrmecophagidae (two *Tamandua* spp. and *M. tridactyla*) (Gaudin & Branham, 1998; Gibb *et al.*, 2016; Miranda *et al.*, 2018). All species display a unique combination of morphological traits such as a complete tooth loss, an unfused mandibular symphysis, an extremely reduced mandibular coronoid process, and an elongated tongue. These features and concomitant loss of mastication have been the target of several studies dedicated to the anatomy and function of their cephalic musculature (Owen, 1856; Macalister, 1875; Redford, 1987; Reiss, 1997, 2001; Naples, 1999; Endo *et al.*, 2007, 2017).

The degree of variation in shape, size, and architecture of masticatory, hyoid, and thyroid musculature across the three anteater genera has not been fully addressed, despite the morphological divergence of skull and mandible shape between *Cyclopes* and myrmecophagids. The extreme elongation of the myrmecophagid rostrum and the loss of the jugal bone in *Cyclopes* are illustrative examples of the contrasts between taxa with similar diets and food ingestion strategies (Montgomery, 1983, 1985). A comprehensive comparative description of the masticatory apparatus of the Vermilingua is a prerequisite to shed light on the diversity of functional morphology among myrmecophagous placentals. Here, we describe the masticatory muscles in the three anteater genera *Cyclopes*¸ *Tamandua*, and *Myrmecophaga* (Gaudin & Branham, 1998). We used a combination of traditional and virtual dissections to accurately measure muscular mass and volumes, while reconstructing 3D surfaces based on iodine-enhanced µCT-scanning (e.g., Gignac & Kley, 2014; Ginot *et al.*, 2018). Our study aims to provide the first thorough description of the anteater masticatory apparatus and to compare it to those of other myrmecophagous placentals (pangolins and aardvarks). We further hope to contribute to an accurate baseline for future biomechanical studies.

Materials and methods

Biological sampling

We dissected specimens from the three extant anteater genera: *Cyclopes didactylus* (n = 2); *Tamandua tetradactyla* (n = 3); *Myrmecophaga tridactyla* (n = 1). *C. didactylus* and *T. tetradactyla* specimens were roadkill while *M. tridactyla* was a zoo specimen. All wild specimens were collected in French Guiana and were stored in the collections of the Institut Pasteur de la Guyane (IPG; JAGUARS collection, Cayenne,

France) and the Institut des Sciences de l'Evolution (ISEM; Montpellier, France). *C. didactylus* and one specimen of *T. tetradactyla* (UM-778-N) were collected and immediately fixed in a 10% formaldehyde solution. *M. tridactyla* and another specimen of *T. tetradactyla* (M-3074) were collected and frozen. M-3075 (*T. tetradactyla*) was collected and immediately dissected. All heads were extracted, as well as the complete sternum and the tongue musculature that were also detached when possible (M-1525, M-3075). Frozen and fresh heads were then fixed in a 10% formaldehyde solution. All specimens were stored in 70% ethanol.

Dissections

For each specimen, only one side was dissected. The areas of insertion and origin were described and each muscle was then stored separately in a 70% ethanol solution. All muscles were weighted with a Sartorius A 120 S precision weighing scale (precision = 0.01mg). Measurements for all specimens are given on Table S1.

Iodine-enhanced CT-scanning

The most complete and well-preserved specimen from each species was selected to be stained. The three specimens were µCT-scanned prior to staining, so that the bone tissue could be easily reconstructed. A second scan was performed after specimens were stained (see below). High-resolution microtomography (µCT) was performed at Montpellier Rio Imaging (MRI; Microtomograph RX EasyTom 150, X-ray source 40-150 kV) platform. Scan resolutions are provided in Table 2.

The contrast enhancement protocol was adapted from (Cox & Jeffery, 2011). All specimens were placed in a solution of iodine (5% I_2KI) for a period of two to eight weeks, depending on size. This concentration represents a trade-off between observed staining efficiency and the soft-tissue shrinkage associated with iodone staining, even if incubation period seems to have a limited effect in soft-tissue shrinkage, after the first two days (Vickerton, Jarvis, & Jeffery, 2013). In *T. tetradactyla* and *M. tridactyla*, small volumes of I_2KI solution were injected directly in the muscles, as the large size of the specimens hinders an efficient passive diffusion of the contrast agent.

The contrast-enhanced scans were imported to Fiji (Schindelin *et al.*, 2012) and 2-fold binning was performed in order to allow for a better handling of the three-dimensional (3D) volumes. The reconstruction of the 3D volumes was performed using Avizo 9.7.0. The volumes were extracted for each muscle. Contrast-enhanced μCT-scans results in an increase of density of the soft tissues and thus the contrast between muscles and bone is lost (Cox & Jeffery, 2011). Therefore, the skull volume was reconstructed from a CTscan prior to staining. We generated surfaces for the skull and muscles separately and then used the function "register" in Avizo 9.7.0 to align these reconstructions. Most tendons and aponeuroses were not stained by the iodine solution, and were therefore not reconstructed. Some muscles may thus appear detached from the skull (e.g., *masseter superficialis* in myrmecophagids).

We tried to reconstruct the maximum muscles related to the masticatory, facial, hyoid/thyroid and sternum musculature in each species. This was highly dependent on specimen condition at the time of skinning and on the staining results. In *M. tridactyla*, only the suprahyoid musculature was reconstructed and described.

Nomenclature

We follow the muscular nomenclature for the masticatory apparatus of xenarthrans defined by Naples (1985) based on the dissection of the two extant sloth species (*Choloepus hoffmanni* and *Bradypus variegatus*). This terminology adapted previously existing nomenclature for other mammals (Rinker, 1954; Turnbull, 1970). The most recent thorough description of the cranial and tongue musculature of the giant anteater (Naples, 1999) followed the same terminology used in Naples (1985). More recent descriptions of the masticatory apparatus of *M. tridactyla* and *T. tetradactyla* adopted the English version of the same terminology (Endo *et al.*, 2007, 2017). We also follow Naples (1999) nomenclature for the muscles associated to the tongue, the hyoid apparatus (suprahyoid and infrahyoid muscles), and the facial-masticatory muscles. We here modified the designation of the facial *nasolabialis* into *maxillolabialis*. All muscle names are fully written in Latin.

Abbreviations

Masticatory muscles: MP – *masseter profundus*; MS – *masseter superficialis*; pa-MS – *masseter superficialis pars anterior*; pp-MS – *masseter superficialis pars posterior*; TS – temporalis superficialis; ps-PE – *pterygoideus externus pars superior*; pi-PE – *pterygoideus externus pars inferior*; PM – *pterygoideus medius*; pa-PM – *pterygoideus medius pars anterior*; pp-PM – *pterygoideus medius pars posterior*; pz-TS – *temporalis superficialis pars zygomatica*; pm-TP – *temporalis profundus pars medialis*; pl-TP – *temporalis profundus pars lateralis*.

Facial-masticatory muscles: pe-B – *buccinatorius pars externa*; pi-B – *buccinatorius pars interna*; MA – *mandibuloauricularis*.

Facial musculature: DN – *dilator nasi*; pi-MLs – *maxillolabialis superficialis pars inferior*; ps-MLs – *maxillolabialis superficialis pars superior*; pa-MLp – *maxillolabialis profundus pars anterior*; pi-MLp – *maxillolabislis profundus pars inferior*; pm-MLp – *maxillolabialis profundus pars media*; ps-MLp – *maxillolabialis profundus pars superior*.

Intermandibular musculature: IA – *intermandibularis*; pa-Mh – *mylohyoideus pars anterior*; pp-Mh – *mylohyoideus pars posterior*.

Hyoid, thyroid, and cricoid musculature: CaL – *cricoarytenoideus lateralis*; CaP – *cricoarytenoideus posterior*; CeH – *ceratohyoideus*; po-CTh – *cricothyroideus pars obliqua*; pr-CTh – *cricothyroideus pars recta*; Gh – *geniohyoideus*; Ish – *interstylohyoideus*; Mst – *mastostyloideus*; pl-ThA – *thyroarytenoideus pars lateralis*; pm-ThA – *thyroarytenoideus pars medialis*; ThH – *thyrohyoideus*.

Pharynx musculature: CP – *constrictores pharyngeus*; Sph – *stylopharyngeus*; l-VP – *levator veli palatini*; m-VP – *medialis veli palatini*; t-VP – *tensor veli palatini*.

Sternum musculature: Sg – *sternoglossus*; Sm – *sternomandibularis*; SM – *sternomastoideus*; Sth – *sternothyroideus*.

Table 1 – Masticatory muscle volumes (up; mm³) and percentages (down) obtained from the 3D models of the contrast-enhanced specimens segmentation. TS – *temporalis superficialis*; pz-TS – *temporalis superficialis pars zygomatica*; pm-TP – *temporalis profundus pars medialis*; pl-TP – *temporalis profundus pars lateralis*; MP – *masseter profundus*; MS – *masseter superficialis*; ps-PE – *pterygoideus externus pars superior*; pi-PE – *pterygoideus externus pars inferior*; pa-PM – *pterygoideus medius pars anterior*; pp-PM – *pterygoideus medius pars posterior*.

		Muscle volume in cm³									
Species	Total	TS	pz-TS	pm-TP	pl-TP	MP	MS	ps-PE	pi-PE	pa-PM	pp-PM
C. didactylus	332.3	139.8	8.0	19.5	33.6	-	60.4	9.4	14.0	46.50	
T. tetradactyla	2757.8	575.2	153.9	120.2	128.0	307.1	806.1	135.3	59.0	227.9	245.1
M. tridactyla	12762.2	1718.1	1198.0	510.2	594.1	1592.6	3951.6	1013.6	489.5	851.8	842.8
		Masticatory muscle volume (%)									
Species		TS	pz-TS	pm-TP	pl-TP	MP	MS	ps-PE	pi-PE	pa-PM	pp-PM
C. didactylus		42,2	2,4	5,9	10,1	-	18.2	2,8	4,2	14.0	
T. tetradactyla		20,9	5,6	4,4	4,6	11,1	29,2	4,9	2,1	8,3	8,9
M. tridactyla		13,5	9,4	4,0	4,7	12,5	31,0	7,9	3,8	6,7	6,6

Table 2 – Facial-masticatory muscle volumes (left; mm³) and percentages (right) obtained from the 3D models of the segmentation of the contrast-enhanced specimens. pe-B – *buccinatorius pars externa*; pi-B – *buccinatorius pars interna*; MA – *mandibuloauricularis*.

		Facial-masticatory muscle volume (mm³)			Facial-masticatory muscle proportion (%)		
Species	Total	pe-B	pi-B	MA	pe-B	pi-B	MA
C. didactylus	69.7	17.9	49.9	1.94	25.6	71.6	2.8
T. tetradactyla	1356.7	371.9	911.1	73.7	27.4	67.2	5.4
M. tridactyla	6579.8	990.4	5589.4	NA	15.1	85.0	NA

Results

Measurements of the muscles involved in mastication are summarized in Tables 1 and 2. Volume measurements were performed on the segmented muscles of the contrast-enhanced specimens. Mass measurements of all dissected specimens are provided in Tables S1 and S2. Below, we provide an anatomical description of the musculature of each of the three species in our study. The description is followed by a comparative anatomy section in which muscle shape, size (Tables 1 and 2), and architecture are compared among anteaters. Anatomical structures of the skull, mandible, hyoid-thyroid, and sternum that are relevant to the description are depicted on figures 1, 2, and 3.

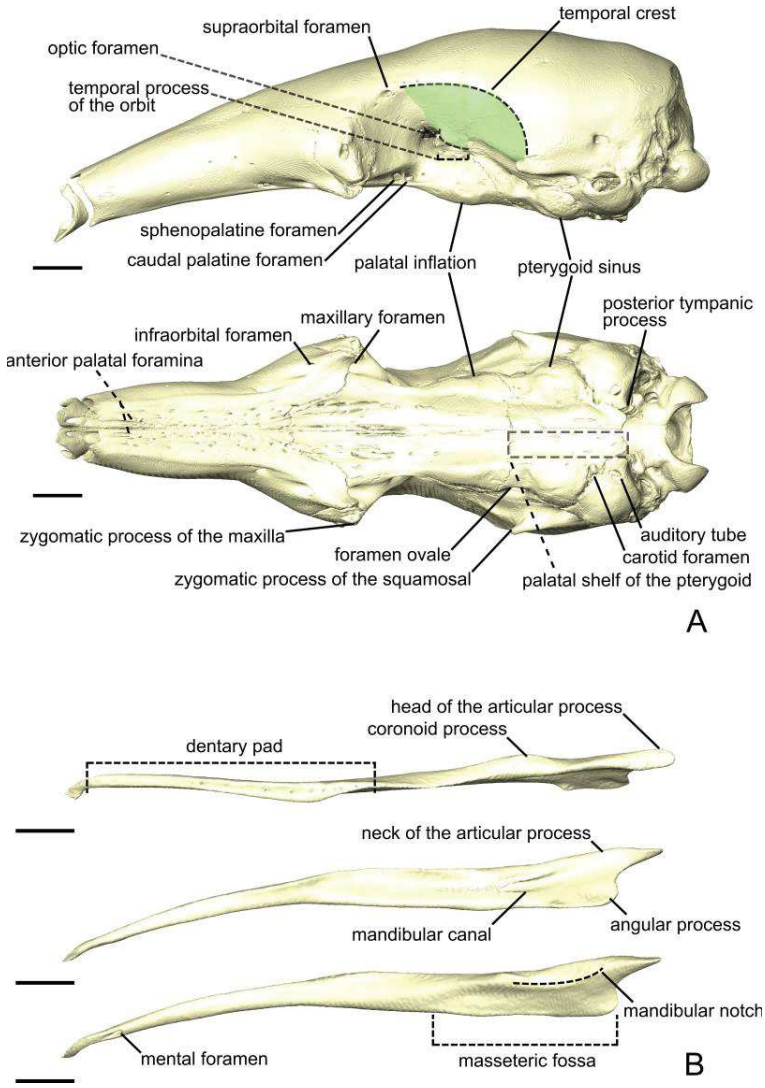

Figure 1 – The skull (A) and mandible (B) of *Tamandua tetradactyla*. The skull is shown in lateral (up) and ventral (down) views. The area in green delimitates the temporal fossa. The mandible is shown in dorsal (up), medial (middle), and lateral (down) views. Anterior is to the left. Scale bar 10 mm.

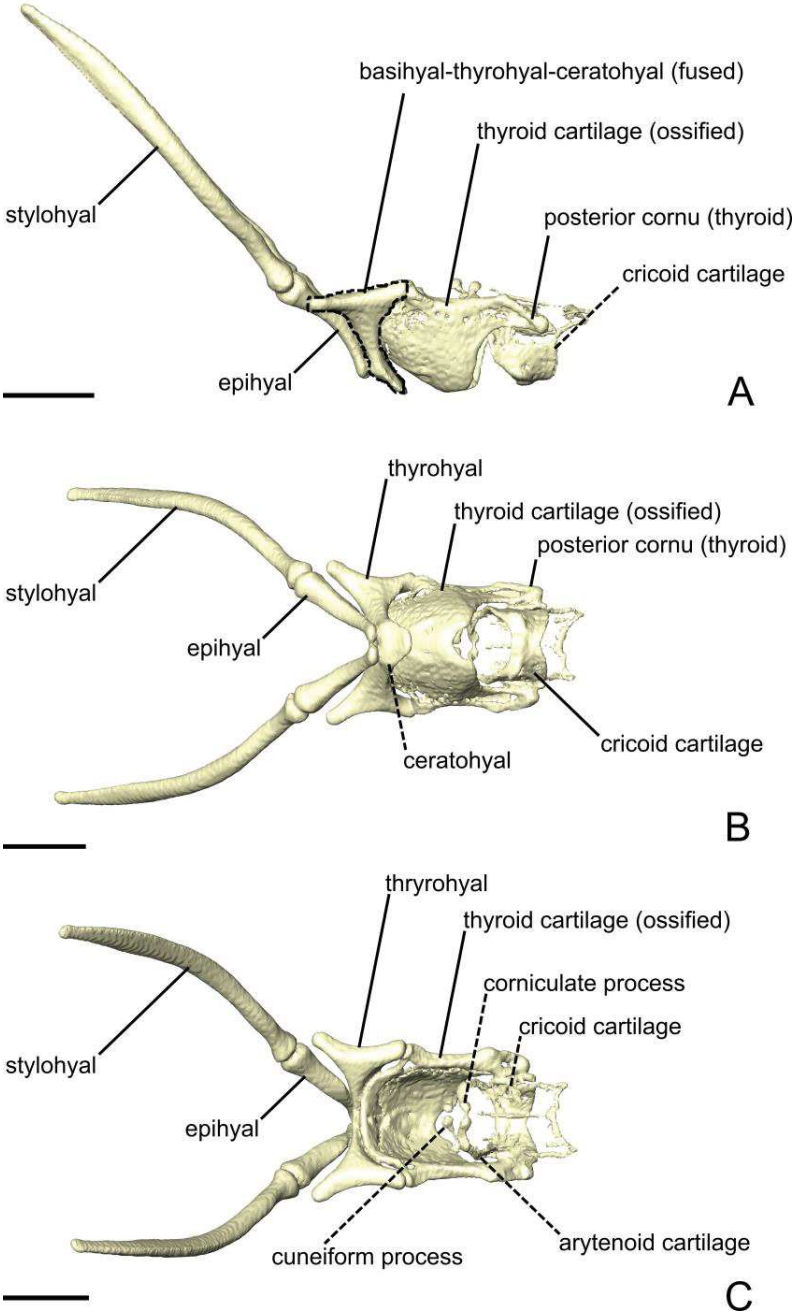

Figure 2 – The hyoid apparatus of *Tamandua tetradactyla* in lateral (A), ventral (B), and dorsal (C) views. Anterior to the left. Scale bar 10 mm.

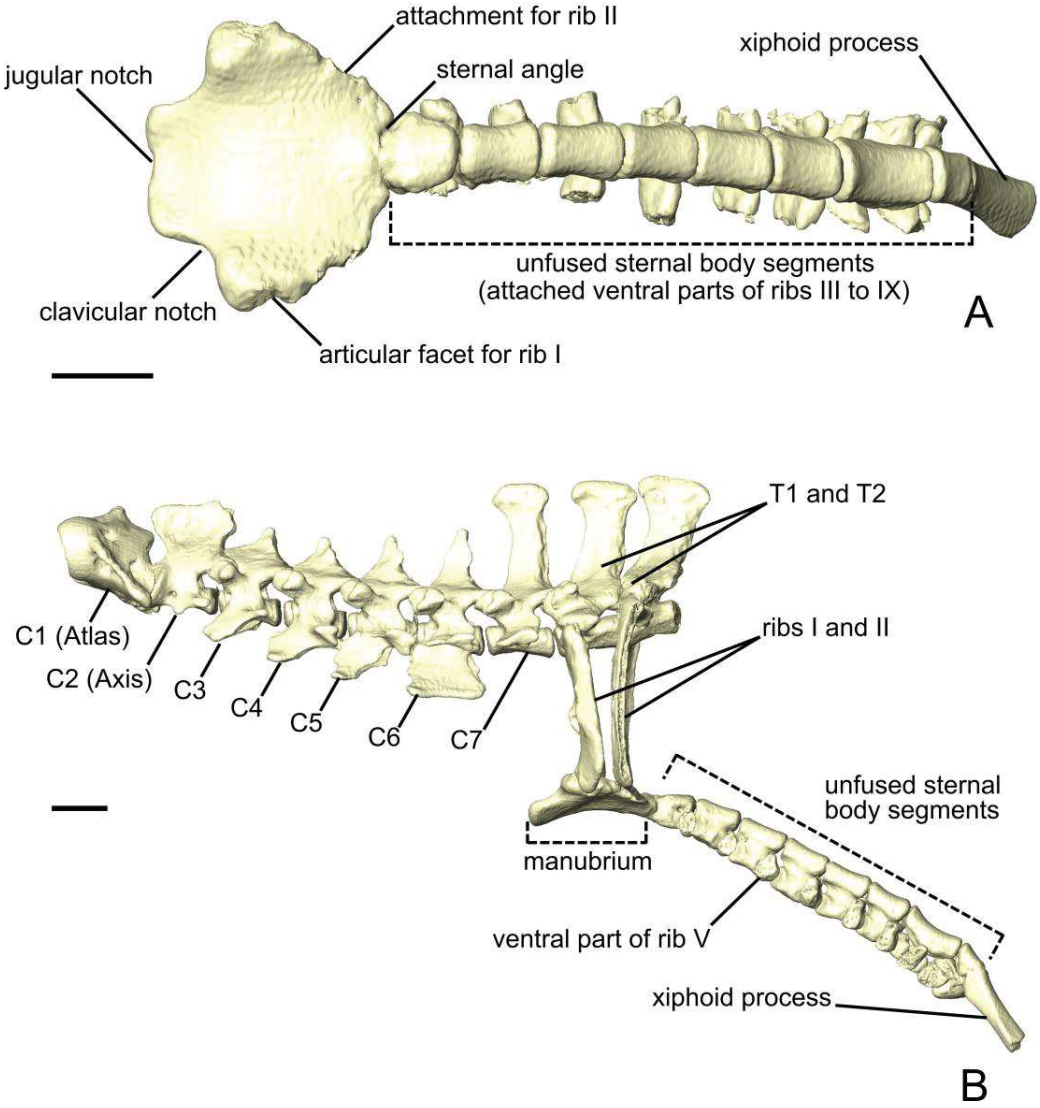

Figure 3 – The sternum of *Tamandua tetradactyla* in dorsal (A), lateral (B) views. C – cervical vertebrae; T – thoracic vertebrae. Anterior to the left. Scale bar 10 mm.

Anatomical description

Cyclopes didactylus

Masticatory apparatus

Masseter superficialis

The *masseter superficialis* (MS; Fig. 4) is the only muscle of the masseter muscle complex present in *C. didactylus*. The MS is anteroposteriorly elongated and originates from the lateral surface of the zygomatic

process of the maxilla. Its origin consists of a long and strong posteroventrally projecting tendon that covers the most anterior half of the muscular part. The muscular part of the MS can be divided in two parts (Fig. 4; Fig. S1A). The *pars anterior* of the MS (pa-MS), which is covered by the tendon laterally, inserts laterally from the posterior part of the dentary pad (Fig. 1B) to the anterior margin of the condyle. The pa-MS presents a *pars reflexa* inserting on the ventral margin of the ascending ramus of the mandible extending anteroposteriorly from the anterior margin of the coronoid process to the level of the mandibular canal. The *pars posterior* of the MS (pp-MS) covers the pa-MS posteriorly to the coronoid process and inserts on the angular process of the mandible (Fig. 4). Its *pars reflexa* is continuous with the *pars reflexa* of the pa-MS and almost reaches the most posterior point of the angular process. The fibers of the MS have an anteroposterior orientation, being more gradually oblique anteriorly close to the tendon.

Temporalis superficialis

The *temporalis superficialis* (TS; Fig. 4) is the largest of the four muscles of the temporal complex. It is a fan-shaped muscle that originates from a scar along the dorsal edge of the temporal fossa. The temporal crest runs from the posterior end of the orbital ridge to the anterior surface of the root of the zygomatic process of the squamosal. A thick tendinous layer streches from the origin of the TS and covers the posterodorsal part of the muscle. The TS is thinner at its origin and thicker at its insertion. The insertion is muscular on the dorsal tip and the dorsal part of the posterior margin of the coronoid process. An aponeurosis runs dorsoventrally along the anterior surface of the TS and completely covers the lateral and anterior surfaces of the coronoid process. The fibers of the TS are organized in a bipennate structure (Fig. S1B). Deep fibers are dorsomedially oriented while superficial ones are dorsolaterally oriented. In cross section, the insertion angle of medial fibers with the axis of pennation is about 26°, while lateral fibers present and angle of around 12°.

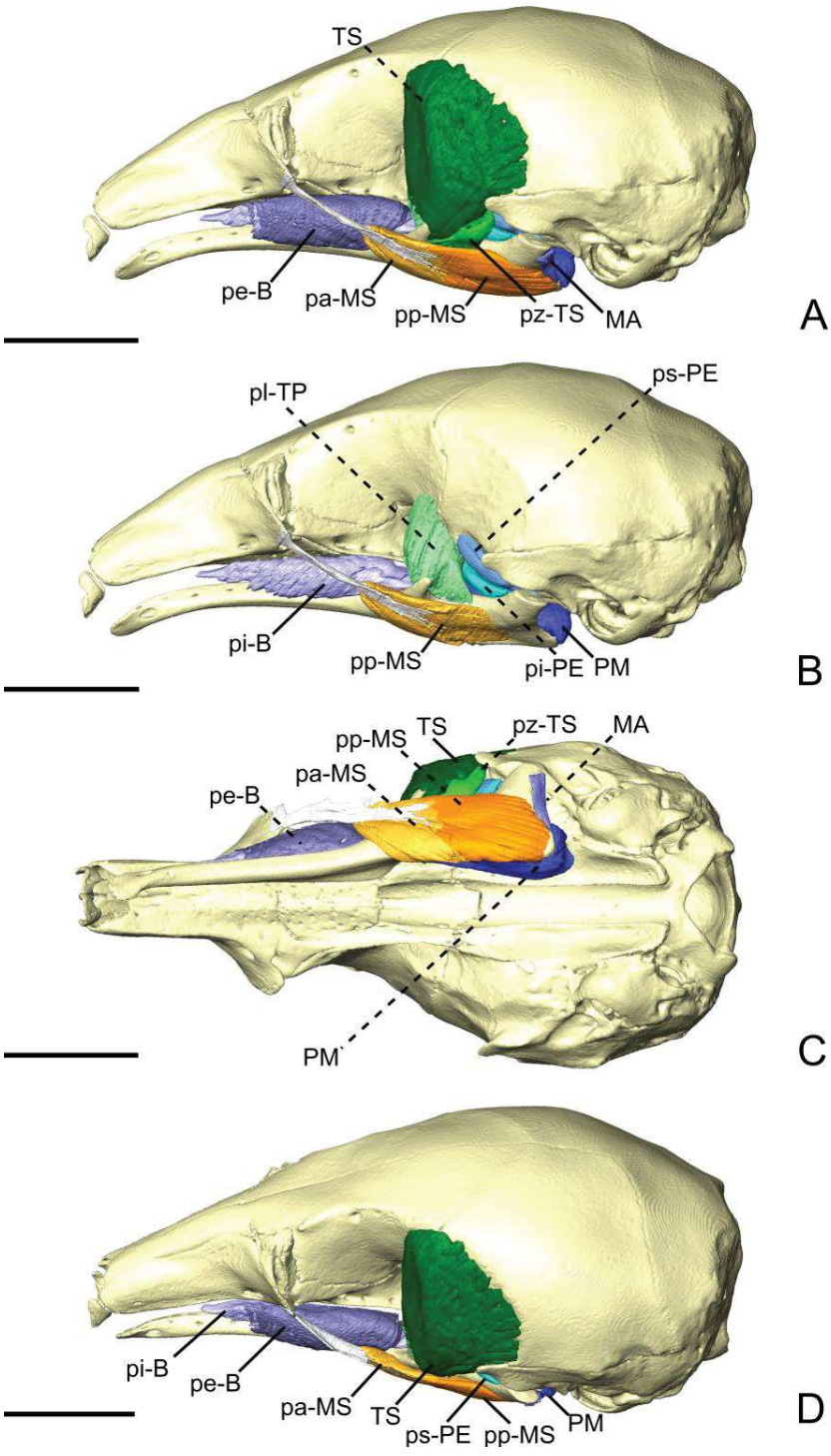

Figure 4 – The masticatory and facial-masticatory musculature of *Cyclopes didactylus* in lateral (A, B), ventral (C), and dorsolateral (D) views. Scale bar 10 mm. The more superficial muscles were removed in B.

Temporalis profundus pars lateralis

The temporal complex includes a deep component divided in two parts, the *temporalis profundus pars lateralis* (pl-TP; Fig. 5A) being the largest. The pl-TP takes its origin on a pseudoelliptical area that extends from the posteroventral part of the orbital contribution of the frontal to the anteroventral part of the temporal fossa. The insertion of the pl-TP covers most of the posterolateral surface of the coronoid process, and narrows posteriorly stretching along the dorsal depression located between the coronoid process and the condyle. Contrary to the TS, the pl-TP does not present a pennate structure, with fibers roughly vertically oriented.

Temporalis profundus pars medialis

The *temporalis profundus pars medialis* (pm-TP; Fig. 5A) consists on the inner part of the TP that takes its origin from the orbit, between the ventral edge of the temporal fossa and the orbital/rotundum foramina. The anterior portion of the pm-TP is anastomosed with the pl-TP. However, the separation between both parts is clear posteriorly on the insertion, with the posterior tip of the pm-TP occupying a more ventromedial position at the level of the mandibular foramen. Fiber orientation and shape of the pi-TP is similar to that of pe-TP, but the former's volume is about two thirds that of the latter.

Temporalis superficialis pars zygomatica

The *temporalis superficialis pars zygomatica* (pz-TS; Fig. 4A, C) is a relatively small muscle, which is well separated from the TS. It originates from the ventromedial part of the zygomatic process of the squamosal and broadens ventrally to end on an anteroposteriorly elongated muscular insertion. The insertion occupies the lateral part of the mandibular notch. The pz-TS is wider dorsally and thinner ventrally, with fibers presenting an oblique orientation.

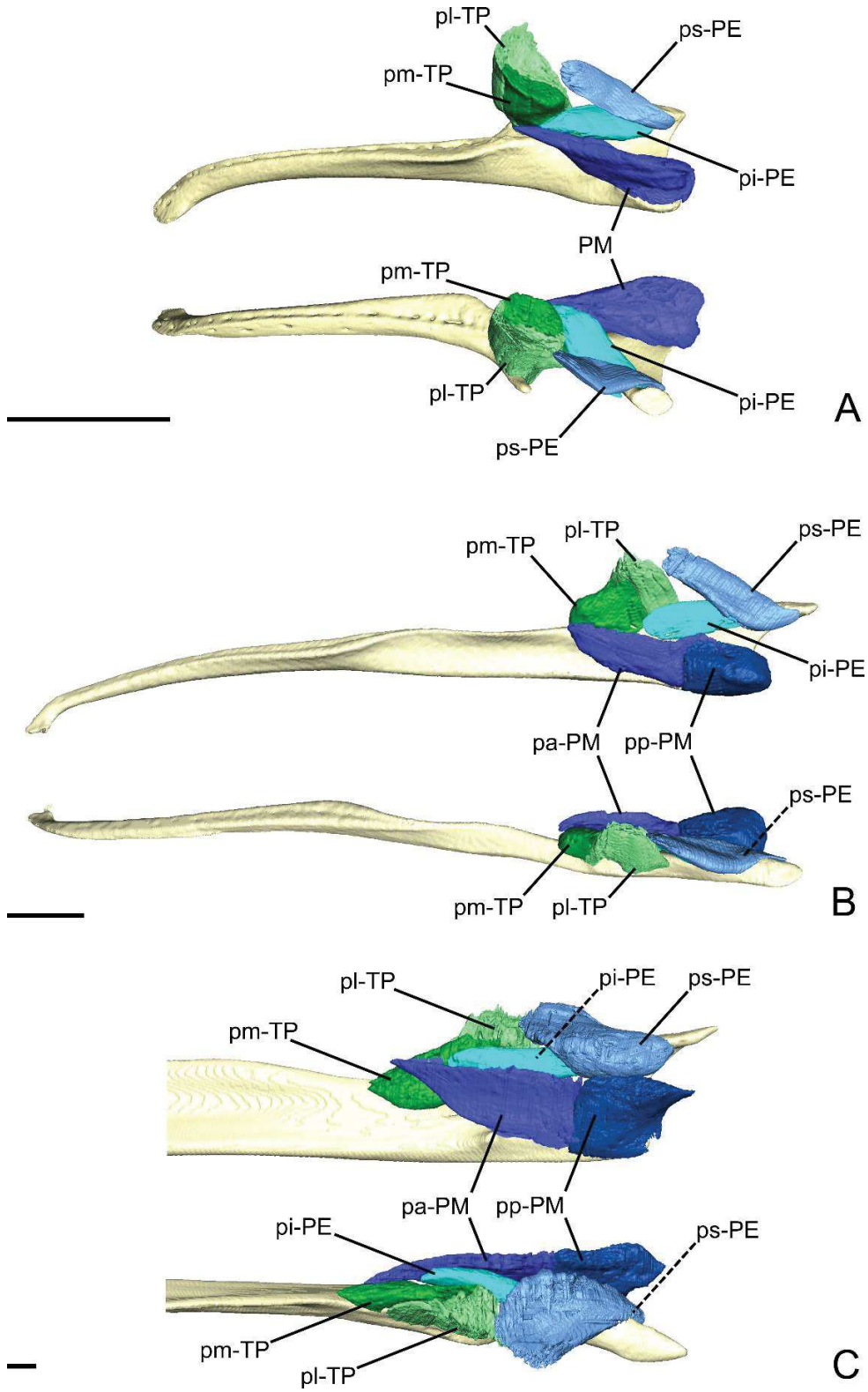

Figure 5 – The pterygoideus and *temporalis profunfus* muscle complexes of *C. didactylus* (A), *T.* tetradactyla (B), and *M. tridactyla* in lateral (up) and dorsal (down). C is zoomed on the ascending ramus. Scale bar 10 mm.

Pterygoid externus pars superior

The *pterygoid externus pars superior* (ps-PE; Fig. 4B and 5A) is a small anteroposteriorly elongated muscle. The ps-PE arises from a fossa that extends from the ventral part of the parietal, at the lower limit of the temporal fossa, into the glenoid fossa. It is the only part of the pterygoid muscle complex that takes its origin outside the pterygoid fossa. The muscle is mediolaterally compressed and obliquely oriented. Its posterior part presents a small torsion anterior to its ventrolateral projection towards the mandible. The insertion of the ps-PE consists of a small concavity just medioventrally to the head of the articular condyle.

Pterygoideus externus pars inferior

The *pars inferior* of the PE (pi-PE; Figs. 4B and 5A) is similar in shape with the ps-PE. The pi-PE originates from a small area in the sphenoid, laterally to the foramen rotundum, and dorsally adjacent to the origin of the *pterygoideus medius*. The muscle is mediolaterally wide and presents a more horizontal orientation than the ps-PE. The muscle projects posterolaterally to insert on the anterior margin of the articular condyle, at mid-height. The medial part of the pi-PE projects posteriorly, inserting below the insertion area of the ps-PE, reaching the mid-length of the head of the condyle.

Pterygoideus medius

The *pterygoid medius* (PM; Figs. 4 and 5) arises from the pterygoid fossa and consists of a fleshy block that originates from the posterolateral part of the palatine to the level of the anterior margin of the ectotympanic. Its fibers run anteroposteriorly with an oblique orientation and insert medially on the angular process of the mandible, from the level of the anterior margin of the head of the articular condyle to its posterior margin. In the most posterior part of their insertion, the fibers assume a more posteroventral direction and form a small *pars reflexa* that wraps the posteriormost tip of the angular process. A dense connective tissue lies dorsally to the insertion of the *pterygoideus medius*, posterior to the opening of the mandibular canal.

Facial-masticatory musculature

Buccinatorius pars externa

The *buccinatorius pars externa* (pe-B; Fig. 4A, C, D) is distinguishable from the internal part of this muscle. It is a sheet-like muscle that envelopes the external surface of the *buccinatorius pars interna*. Its origin stretches along the ventral edge of the maxilla and the palatine, from anteriorly to the inferior orbital foramen until the anterior part of the insertion of the *pterygoideus medius*. The ventral part of the pe-B wraps the ventral portion of the *buccinatorius pars interna* and attaches on a broad insertion area on the lateral surface of the mandible. The fibers have a dorsoventral direction.

Buccinatorius pars interna

The *pars interna* of the *buccinatorius* muscle (pi-B; Fig. 4B) is more voluminous when compared to the *pars interna*. The pi-B originates from a thin fiber bundle posterior to the buccal commissure and is covered by the pe-B just posteriorly. It is a long muscle that reaches as far posteriorly as the level of the coronoid process. The pi-B is characterized by a triangular-shaped buccal projection that sits between the upper and the lowers jaws. The lateral part of the pi-B contacts the pe-B and does not attach to any bone surface. Posteriorly, the pi-B inserts on the dorsomedial surface of the mandible, along the fossa located between the posterior part of the dentary pad and the coronoid process. Its insertion ends posteriorly to the coronoid process where it contacts the *temporalis profundus pars medialis* and the anterior part of the *pterygoid medius*. The fibers of the pi-B are anteroposteriorly oriented.

Facial musculature

Dilator nasi

The *dilator nasi* (DN, Fig. 6E, F) is sheet-like, becoming thinner and narrower anteriorly. It takes its origin on the posterodorsal part of the maxilla, anterior to the lacrimal bone. The insertion of the muscle is tendinous and was not preserved in the specimens. The fibers are anterodorsally directed and horizontally oriented.

Maxillolabialis superficialis pars superior

The *maxillolabialis pars superior* (ps-MLs; Fig. 6E) originates more posterodorsally than the DN, with some fibers arising from the lacrimal and the frontal bone. However, most of the area of origin is on the maxilla. The muscle becomes narrower anteriorly and its anterior portion is linked to a tendon that inserts anteriorly in the lip region. The tendon, unfortunately, is invisible in the iodine-stained specimen. This muscle covers the origin of the *dilator nasi*, and the *maxillolabialis profundus pars superior*. It overlies most of the anterodorsal part of the *maxilolabialis profundus pars inferior*.

Maxillolabialis profundus pars inferior

The *maxillolabialis profundus pars inferior* (pi-MLp; Fig. 6E, F) is the longest labial muscles. It takes its origin on the posterodorsal margin of the cranium, stretching from the ventralmost point of the maxilla-lacrimal suture to about two third of the height of the lacrimal. The muscle is flat posteriorly and becomes narrower and triangular in cross-section, anteriorly. The pi-MLp narrows anteriorly with slightly oblique fibers attached to a tendon, close to the buccal commissure. This muscle is overlain by the *pars superior* of the MLp and a small ventral part of the posterior part of the *maxillolabialis pars pars profunda*.

Maxillolabialis profundus pars superior

The *maxillolabialis pars profunda* is the smallest part of the labial muscle complex (ps-MLp; Fig. 6F). It is a tape like muscle with the origin just dorsal to the origin of the *maxillolabialis pars inferior*, being slightly overlain by the latter. The tendon for the insertion of the ps-MLp is not preserved in this specimen. Nevertheless, given the position of the muscle, the anteroposteriorly directed fibers were probably horizontally oriented.

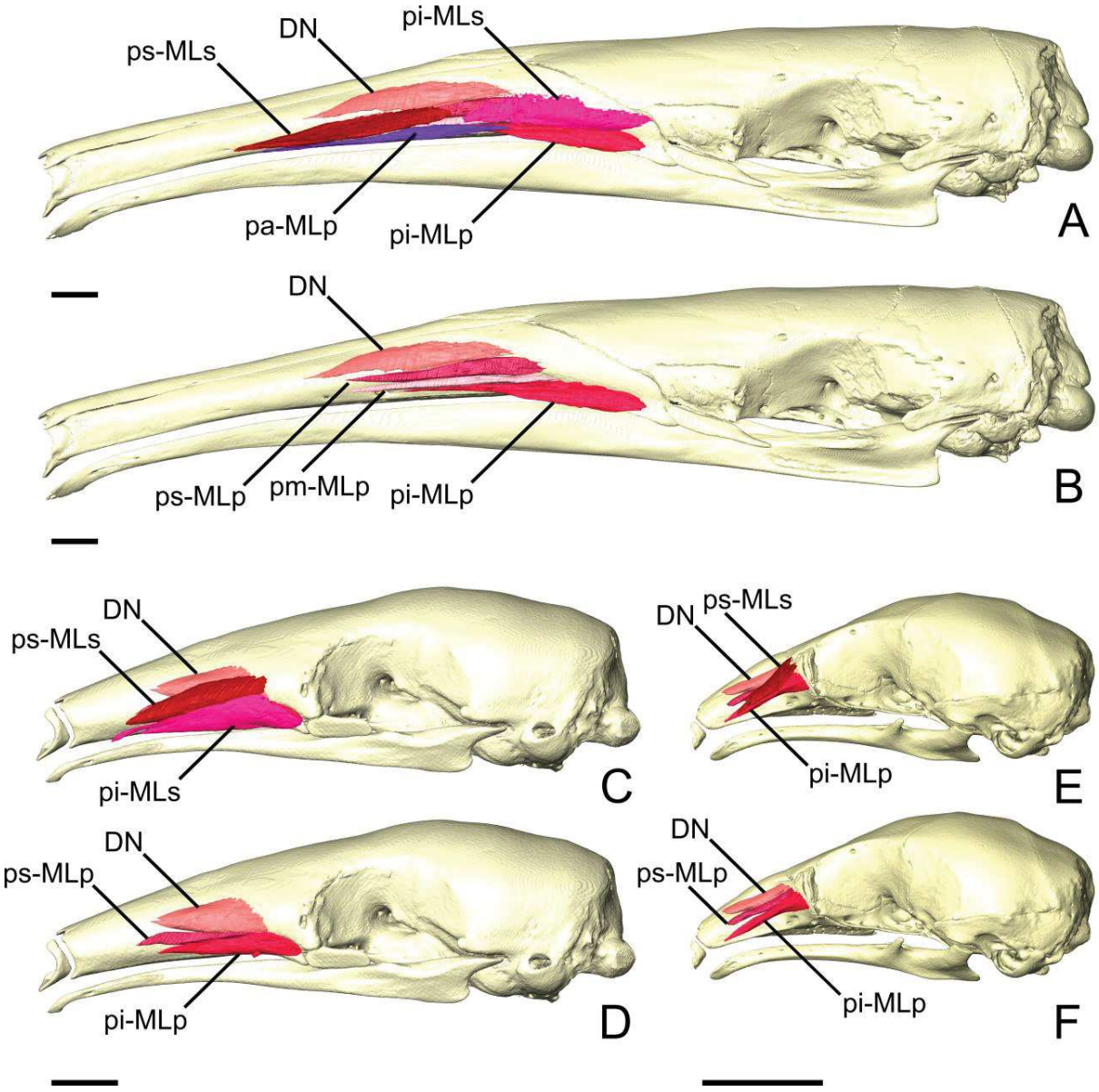

Figure 6 – The facial musculature of *M. tridactyla* (A, B), *T. tetradactyla* (C, D), and *C. didactylus* (E, F) in lateral view. A, C, and E show more superficial muscles; B, D, and F show deeper muscles. Scale bar 10 mm.

Intermandibular musculature

Intermandibularis anterior

The *transversus mandibularis* (IA; Fig. 7) is a thin, dorsolaterally wide, and elongated muscle. Naples (1999a) described this muscle as the anterior part of the *mylohyoideus pars anterior*. The IA takes its origin on the cartilage of the unfused mandibular symphysis. The muscle has two insertions on the

ventrolateral margin of both hemimandibles, wrapping around their ventral edges. In ventral view (Fig. 7B), it covers the anterior part of the base of the tongue and the anterior part of the *geniohyoideus* (see 'Hyoid, thyroid, and cricoid musculature'). The IA extends posteriorly for about half the length of the mandible, its posterior end being clearly separated from the anterior margin of the *mylohyoideus pars anterior* (see 'Intermandibular musculature'). Its fibers are transversely oriented and are continuous between mandibles, with this muscle consisting of one single element.

Mylohyoideus pars anterior

The *mylohyoideus pars anterior* (pa-Mh; Fig. 7) consists of a fibrous sheet that originates ventrally to the dentary pad, on the medial surface of the mandible. This muscle is homologous to the *pars medius* of the *mylohyoideus* described by Naples (1999a). The origin area stretches from the widest point of the dentary pad to its posteriormost point. Posteriorly, its origin shifts from the mandible to the ventromedial surface of the *pterygoideus medius* (PM). At the posterior end of the PM the origin changes again, creating a dorsolateral gap separating the anterior and the posterior fibers. We consider this to be the posterior limit of the pa-Mh, with the posterior part being considered the *mylohyoideus pars posterior*. The fibers are transversely oriented ventrally and insert along a fibrous midline raphe that connects the left and right pa-Mhs (Fig. S1C).

Mylohyoideus pars posterior

The *mylohyoideus pars posterior* (pp-Mh; Fig. 7) is continuous with the pa-Mh. The division between the two parts is set by the difference of the origin. The pp-Mh *mylohyoideus* takes its origin on the ventromedial surface of the tympanic bulla, parallel to the auditory tube. The fibers display the same orientation as in the *pars anterior* and insert on a fibrous midline raphe. However, near the posterior end of the hard palate, the left and right muscles appear to anastomose in the midline, with the intertonguing contact becoming less spaced. As the *interstylohyoideus* and the posterior part of the *mylohyoideus pars posterior* were not preserved in our specimens of *C. didactylus*, the attachment of the pp-Mh to the hyoid system is not visible.

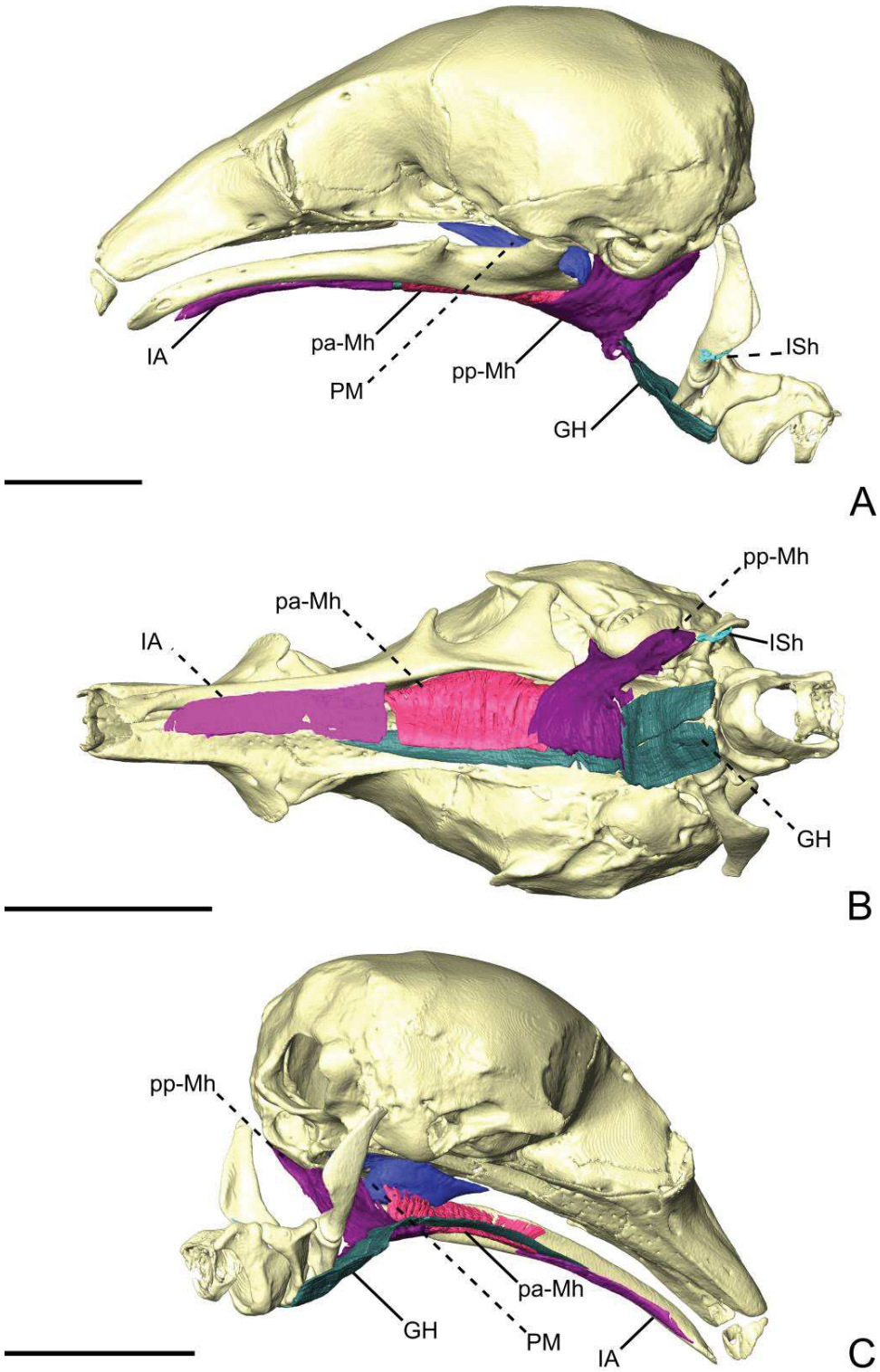

Figure 7 – The intermandibular musculature, *geniohyoideus*, and *pterygoideus medius* of *C. didactylus* in lateral (A), ventral (B), and posteromedial (C) view. A small vestige of the *interstylohyoideus* is also depicted. Scale bar 10 mm.

Hyoid, thyroid, and cricoid musculature

Geniohyoideus

The *geniohyoideus* (GH; Figs. 7 and 8) has a tendinous origin and arises from the mandibular symphysis cartilage. The GH is a very long and dorsoventrally compressed muscle that rests ventral to the base of the tongue and dorsal to the *transversus mandibularis* (anteriorly) and the *mylohyoideus* (posteriorly). The tendon is about half the length of the mandible, with the horizontally oriented muscular fibers originating at the level of the caudal palatine foramen. In ventral view, the anterior part of the GH is pointy, widening posteriorly until it anastomoses with its symmetric counterpart. The right and left bellies are anatomosed from the posterior part of the palatine to the basisphenoid-presphenoid suture. Posteriorly, the two muscles present a fibrous connection, but the bilateral elements are clearly separated (Fig. 7). The GH passes just ventrally to the ventral part of the epihyal and the ceratohyal and inserts along the posterolateral surface of the basihyal. The most lateral part of the muscle has a small insertion on the most ventral part of the thyrohyal. The fibers of the GH are horizontally oriented throughout its entire length.

Ceratohyoideus

The *ceratohyoideus* (CeH; Fig 8A, B, D, E) is a small hyoid muscle with a subtriangular shape in lateral view. It takes its origin on the depression of the lateral surface of the thyrohyal bone, ventral to its anterodorsal process. Its obliquely oriented fibers are anteroposteriorly short and project anteroventrally to insert on a fossa on the posterior surface of the epihyal. This muscle has no clear homologous in other mammals (Greene, 1935; Naples, 1999). It might be homologous to the *stylohyoideus* of cetaceans (Reidenberg & Laitman, 1994).

Thyrohyoideus

The *thyrohyoideus* (ThH; Fig. 8A, B, D, E) covers most part of the lateral surface of the thyroid cartilage. It originates on a dorsoventral scar along the posterior part of the thyroid and its obliquely oriented fibers insert on the concave ventral edge of the thyrohyal.

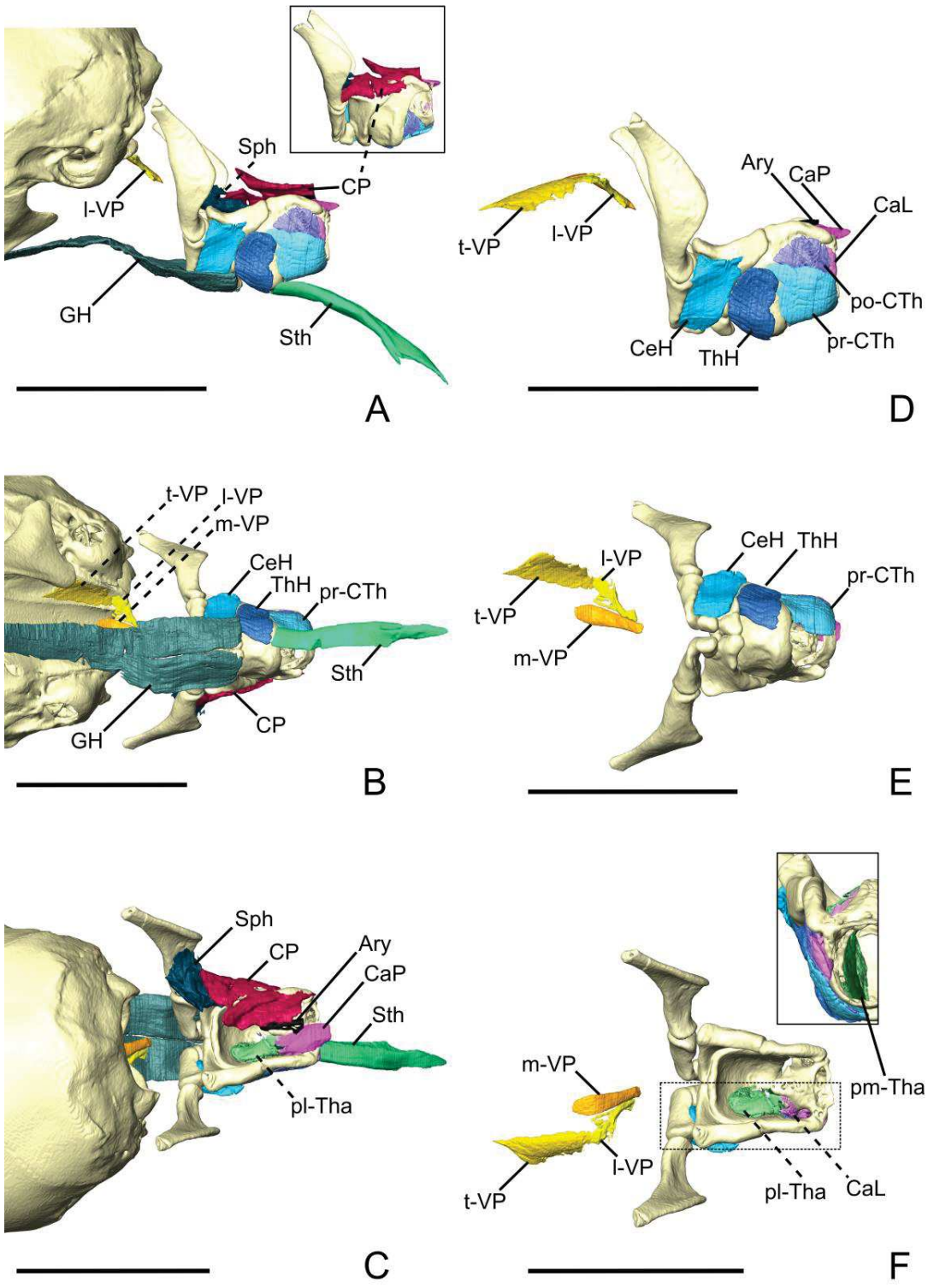

Figure 8 – The hyoid, thyroid, and pharyngial musculatures of *C. didactylus* in lateral (A, D), ventral (B, E), and posteromedial (C, F) view. Rectangle in E shows a zoomed posterior view of the thyroid-cricoid system. Scale bar 10 mm.

Cricothyroideus pars recta

The *pars recta* of the *cricothyroideus* (pr-CTh; Fig. 8B, D, E) is a sheet like muscle with its origin at the posterior margin of the cricoid cartilage, stretching from its most ventral point to its mid-height. The pr-CTh is composed of horizontally oriented fiber bundles that insert on the posterolateral surface of the thyroid cartilage, posterior to the origin of the ThH. The insertion area is most posterior ventrally and extends anterodorsally, being slightly overlain by the dorsal part of the ThH.

Cricothyroideus pars obliqua

The *cricothyroideus pars obliqua* (po-CTh; Fig. 8A, D) corresponds to the medial part of the pr-CTh. The two parts anastomose at their origin. The po-CTh consists of an extremely thin inner sheet that extends anterodorsally. Its insertion is located dorsally on the thyroid cartilage and accompanies the shape of its dorsal border. Only the dorsal part of the po-CTh is exposed laterally, giving it a fan-like aspect anteriorly. The remaining dorsal portion of the muscle is overlain by pr-CTh. As for the *pars recta*, the name of the po-CTh derives from the orientation of its fibers.

Cricoarytenoideus posterior

The arytenoid cartilage is the insertion area of a few small muscles that originate posteriorly on the cricoid cartilage (Fig. 2). The *cricoarytenoideus posterior* is the most dorsal muscle (CaP; Fig. 8C, F, D). This muscle is small and pseudorectangular in dorsal view. This thick sheet of muscular fibers originates on the posterodorsal surface of the cricoid cartilage and its fibers run posteroanteriorly to reach the arytenoid cartilage, anteroventrally. The anterior part of the CaP becomes thinner and hard to distinguish from the remaining muscles that attach to the arytenoid cartilage.

Cricoarytenoideus lateralis

The muscle attaches the arytenoid cartilage from the lateral surface of the cricoid cartilage (CaL; Fig. 8D, F) and takes its origin dorsally to that of the *cricothyroideus* complex. In lateral view, the CaL is covered by both the latter and the posterior process of the thyroid cartilage. The fibers of this small fleshy muscle

are obliquely oriented and insert ventrally to the CaP. The anterior part is not clear on the iodine stained μCT scan, which suggests that the tendinous insertion occurs roughly at the level of the anterior part of the CaP.

Thyroarytenoideus pars lateralis

The *thyroarytenoideus pars lateralis* (pl-Tha; Fig. 8C, F) is the largest muscle attaching to the arytenoid cartilage in *C. didactylus*. It occupies approximately one third of the volume inside the thyroid cartilage and covers most of its concave medial wall. In lateral view, the muscle is semicircular in shape. The pl-Tha fibers are dorsoventrally oriented, the anterior ones bending anteriorly at the midlength. The origin of the pl-Tha consists of a shallow and short anteroposteriorly elongated scar at the base of the thyroid cartilage. Ventrally, the pl-Tha inserts laterally on the arytenoid cartilage.

Thyroarytenoideus pars medialis

The *thyroarytenoideus pars medialis* (pm-Tha; Fig. 8F) corresponds to a small and extremely thin part with a fiber arrangement similar to that of the pl-Tha. It originates posteriorly and is parallel to the posterior fiber of the *pars anterior.* The pm-Tha shares a similar origin with that of the pl-Tha, between the latter and the trachea. However, both parts are separated by a sheet of conjunctive tissue from the origin to the insertion. Anterodorsally, the fibers appear to insert on a ventral projection of the arytenoid cartilage.

Pharynx musculature

Tensor veli palatini

The *tensor veli palatine* (t-VP; Fig. 8B, D, E, F) is a very thin ribbon-like muscle posteriorly adjacent to the *levator veli palatin*i. Its fibers run obliquely from the lateral to the medial edges of the pterygoid bone shelf, dorsal to the auditory tube. Anteroposteriorly, the t-VP stretches from the level of the anterior margin of the external auditory meatus to the opening of the auditory tube. Anteriorly, the t-VP is adjacent

to the posterior part of the origin of the *pterygoideus medius* (PM) while posteriorly it is connected to the origin of the *levator veli palatini*.

Levator veli palatini

The *levator veli palatini* (l-VP; Fig. 8) originates on the ventral surface of the posterior part of the pterygoid process. At the origin, the l-VP is flat and resembles the shape of the t-VP. Anteriorly the l-VP is thin and strap-like, while posteriorly it forms a fleshier bundle. The fibers run medially from a small origin area to insert on the soft palate just a few millimeters posteroventrally. The l-VP meets the anterior part of the *medialis veli palatini*. Its fibers slightly bend posteriorly and become parallel to the *medialis veli palatini* (Fig. 8F).

Medialis veli palatini

In *C. didactylus*, the *medialis veli palatini* (m-VP; 8B, E, F) is a strap of longitudinally running fibers. The muscle is flat at its origin on the soft palate and becomes fleshier and narrower posteriorly. The m-VP is about the same length as the l-VP (≈ 5mm) and makes up the central axis of the oropharynx. Most of the muscles and tissues surrounding the m-VP were too damaged to be described.

Stylopharyngeus

The *stylopharyngeus* was badly damaged during the dissection. The muscle is illustrated (Sph; Figs. 8C and 9A) but a formal description cannot be given.

Constrictores pharyngeus

The *constrictores pharyngeus* were badly damaged during the dissection. The muscle is illustrated (CP; Figs. 8C and 9A) but a formal description cannot be given.

Sternum musculature

Sternomandibularis

The origin of the *sternomandibularis* (Sm; Fig. 9) is located anterodorsally on anterodorsal surface of the manubrium. The fibers of this elongated muscle are anteroventrally directed and form a tape-like element. The Sm is mediolaterally wide and has a tendinous insertion on the ventral margin of the mandibular ramus, with a small portion wrapping around to attach on the lateral surface. The posterior part and origin of the Sm were not preserved in the stained specimen.

Sternoglossus

The *sternoglossus* (Sg; Fig. 9) is the longest of all the muscles in *C. didactylus*. It originates on the cartilaginous xiphisternum (not visible on the stained specimen). The posterior half of the Sg is strap-like and follows a parallel direction to the trachea. It flanks the hyoid apparatus, to which it is attached, at the level of the thyrohyoid, by some muscular fibers that connect the enveloping conjunctive tissue. Anterior to the hyoid apparatus, the Sg cross-section becomes elliptical and enters the base of the tongue anterior to the epihyal. As it enters the mouth, the sternoglossus cross-section becomes cylindrical in shape. Its diameter reduces as it projects anteriorly, with the anteroposteriorly oriented fibers progressively unwrapping from the muscular bundle to cover the epidermal wall of the tongue. At the level of the orbital foramen, the Sg loses its shape original, which gives a whip-like aspect to its buccal portion.

Sternothyroideus

The *sternothyroideus* (Sth; Figs. 8 and 9) arises from the sternum at the level of the second and third ribs. It fuses to its bilateral counterpart just anteriorly to the second rib. The Sth is anteroposteriorly elongated as the Sm and the Sg. In contrast, the Sth is less strap-like, with its cross-section being pseudo-rectangular. The obliquely oriented fibers end anteriorly on a tendinous insertion of the posteroventral part of the base of the thyroid cartilage.

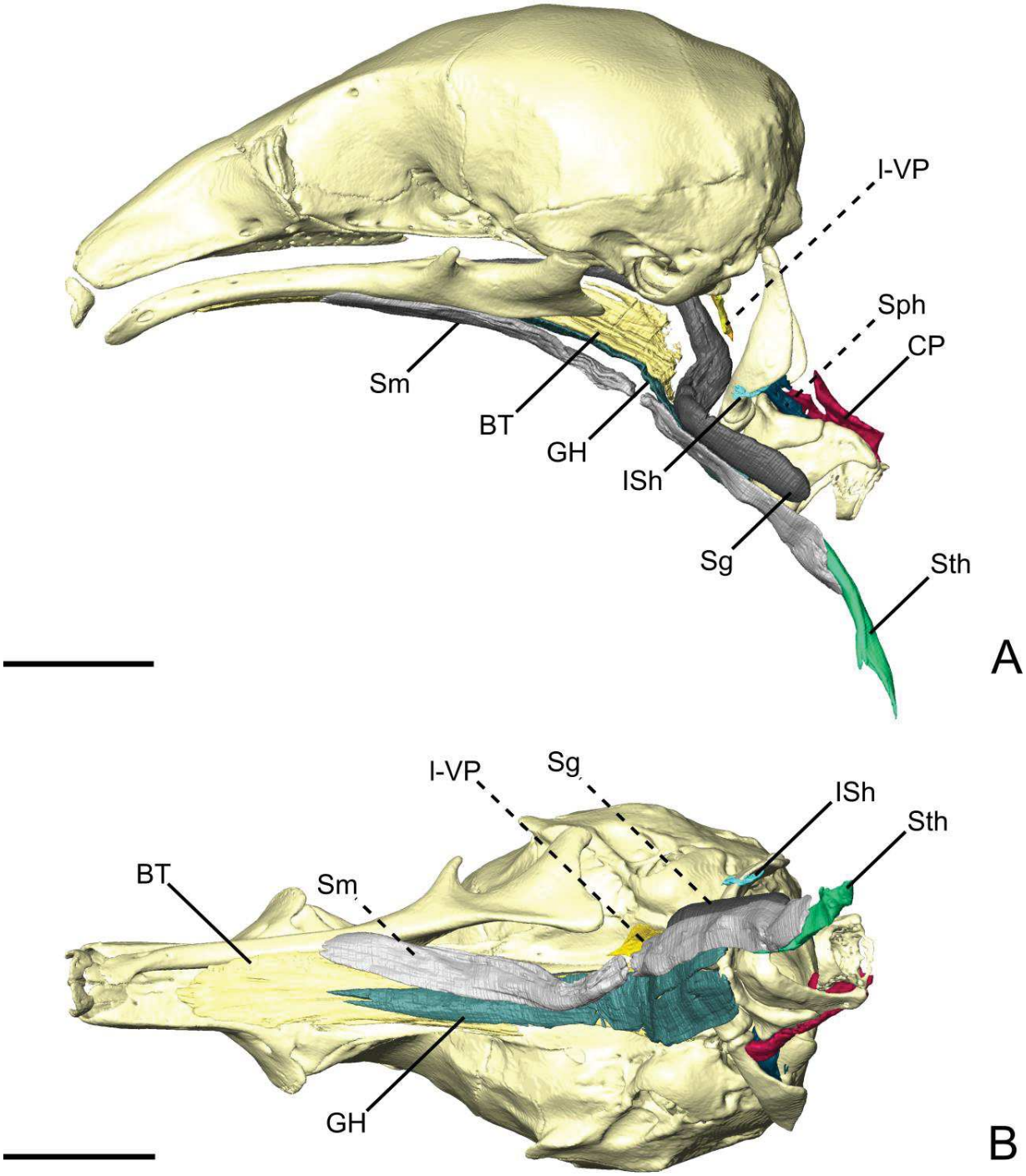

Figure 9 – The sternum and pharyngeal musculatures, and the *geniohyoideus* of *C. didactylus* in lateral (A) and ventral (B) views. Scale bar 10 mm.

Tamandua tetradactyla

Masticatory apparatus

Masseter superficialis

The *masseter superficialis* (MS; Fig. 10) is a fleshy anteroposteriorly long muscle; it is pseudorectangular in shape in lateral view. The fibers of the MS are slightly oblique and take their origin on the lateral surface of the zygomatic process of the maxilla through a strong tendon. The MS inserts on the shallow masseteric fossa of the mandible. It covers most of the lateral surface of the ascending ramus, including most of the more anterior *masseter profundus* (see below). The MS is thicker posteriorly, and thins down anteriorly as it overlies the *masseter profundus*. The tendon of the MS was not visible in the contrast-enhanced specimen. The MS presents a *pars reflexa* that runs from the level of the posterior part of the jugal to the posterior tip of the angular process of the mandible. The *pars reflexa* attaches to the ventral surface of the *masseter profundus* anteriorly. Anteriorly, the MS presents a small projection towards the zygomatic process of the mandible.

Masseter profundus

The *masseter profundus* (MP; Figs. 5B and 10) is smaller than its superficial counterpart (MS). It takes its origin on the anterior part of the ventromedial surface of the jugal bone. Anteriorly, its origin area includes the most posteroventral surface of the zygomatic process of the maxilla. The fibers of the MP run obliquely to insert posteroventrally on the lateral surface of the mandible. The fibers are more vertical than those of the MS. The muscle presents a lateral and a slight anterior component to their orientation. The insertion area on the mandible stretches from the coronoid process to the level of the sphenopalatine foramen. Contrary to the MS, the MP is thicker at its origin than at its insertion.

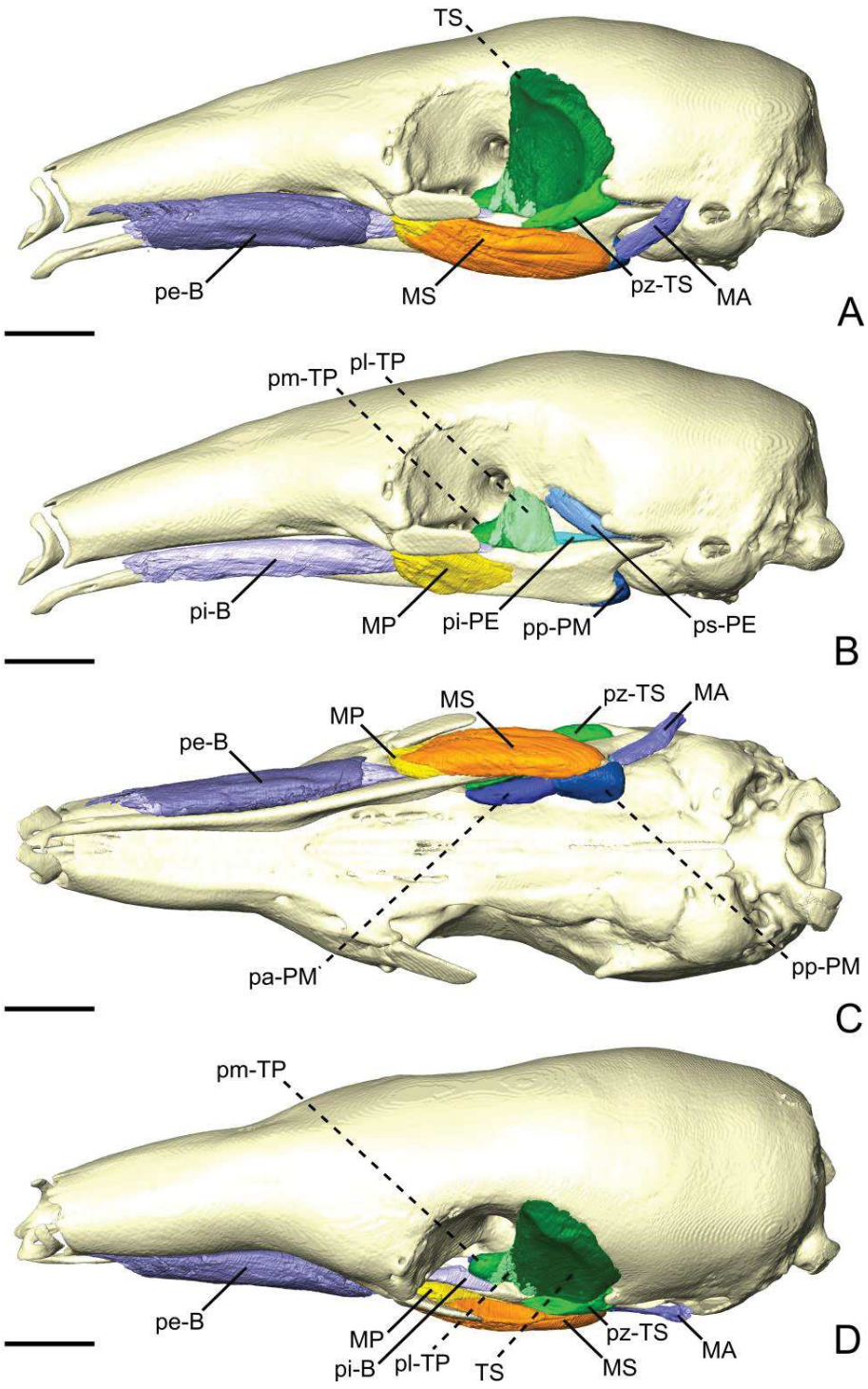

Figure 10 – The masticatory and facial-masticatory musculature of *T. tetradactyla* in lateral (A, B), ventral (C), and dorsolateral (D) views. Scale bar 10 mm. The more superficial muscles were removed in B.

Temporalis superficialis

The *temporalis superficialis* (TS; Fig. 10) is one of the three muscles that forms the temporal complex. It is also the largest, arising from a relatively large surface between the dorsal edge of the temporal fossa and the origin of the *pterygoideus externus pars superior* (Fig. 10). It is wide and broad in lateral view, and transversely compressed. It presents a fan-like shape, the fibers converging ventrally towards a small and flat coronoid process. The TS is medial to a large lacrimal gland, which fills most of the temporal fossa. The lateral surface of the TS is covered by a thin tendinous layer. Ventrally, the TS inserts on the dorsomedial surface of the coronoid process via a large aponeurosis. The TS muscle fibers are oriented vertically in the anterior part of the muscle, and are more oblique posteriorly.

Temporalis superficialis pars zygomatica

The *pars zygomatica* of the TS (pz-TS; Fig. 10) is a small fleshy strip on the ventral margin of the TS. Unlike the TS, the pz-TS originates on a small area limited to the ventral surface of the zygomatic process of the squamosal (Fig. 10). Its obliquely oriented fibers insert on the dorsolateral surface of the mandibular notch. While the insertion area and orientation of the fibers are distinct from the anterior part of the TS, both muscles become harder to separate posteriorly, almost anastomosing at mid-lenght.

Temporalis profundus pars lateralis

The *temporalis profundus* (TP; Fig. 5B and 10) is divided into two distinct parts. The *pars lateralis* (pl-TP) is a small fleshy block deep to the larger TS. The pl-TP takes its origin from the crest/orbital process formed between the anteroventral border of the temporal fossa and the groove for the ophthalmic vein and the oculomotor nerve (III). The pl-TP transversely widens from its origin to its insertion. Fiber orientation is similar to that of the anterior part of the TS, although they are slightly more oblique in coronal view. The insertion of the pl-TP is short and extends from the mid-lenght of the mandibular notch to the anterior limit of the coronoid process. It covers most of the dorsal surface of the mandible in width. While the insertion is mostly muscular, the pl-TP shares the aponeurosis with the TS, anteriorly.

Temporalis profundus pars medialis

The *temporalis profundus pars medialis* (pm-TP; Fig. 5B and 10) is the smallest part of the temporal muscle complex. It has no insertion, as it anastomoses with the pl-TP posterolaterally, but both parts could be easily separated during dissection. The fibers of the pm-TP are vertically oriented. Their insertion is medial to that of the pl-TP and extends from the level of the anterior tip of the *pterygoideus externus pars inferior* to the anterior margin of the optic foramen. The medialmost part of the pi-TP wraps the mandible medially, inserts on its dorsomadial surface and contacts the dorsal part of the *mylohyoideus pars anterior* (see 'Intermandibular musculature').

Pterygoid externus pars superior

The *pars superior* of the *pterygoideus externus* (ps-PE; Fig. 5b and 10B) is a strap-like muscle that arises from an elongated fossa along the ventral limit of the temporal fossa. Its obliquely oriented fibers run posteriorly to wrap around the head of the articular condyle of the mandible, medially (Fig. 5B). The insertion extends from the anterior limit to the posterior tip of the blunt articular condyle. The ps-PE overlies the insertion of the *pterygoideus externus pars inferior* (see below).

Pterygoid externus pars inferior

Similarly to the ps-PE, the *pterygoideus externus pars inferior* (pi-PE; Fig. 5B) has a strap-like shape. In contrast with its upper counterpart, the pi-PE takes its origin on the pterygoid fossa. Specifically, the origin of the pi-PE is a small flattened area on the lateral surface of the palatal inflation. Its fibers are obliquely oriented and insert dorsally on the neck of the condylar process of the mandible.

Pterygoideus medius pars anterior

The *pterygoideus medius* (PM) is divided into two distinct parts that were easily separated during the classical dissection. The *pars anterior* (pa-PM; Fig. 5B and 10C) takes its origin on the lateral and ventrolateral surfaces of the palatine inflation. The origin is muscular and spans from the caudal palatine foramen to an area just posterior to the origin of the pi-PE, near the posterior limit of the palatine inflation.

The fibers are more oblique anteriorly than posteriorly, and insert on the dorsal part of the pterygoid fossa of the mandibular ascending ramus. The posterior part of the pa-PM is thinner than its anterior part. The thick portion of the pa-PM serves as an attachment area for a small anterior projection of the *pars posterior* of the *mylohyoideus* (see 'Intermandibular musculature').

Pterygoideus medius pars posterior

The *pars posterior* of the *pterygoideus medius* (pp-PM; Fig. 5B and 10B, C) consists of a fleshy block that takes its origin on an area located between the posterior part of the palatine inflation and the small fossa anterior to the pterygoid sinus. A coronal section shows that the fibers are obliquely oriented (Fig. S1D). The pp-PM presents a very small *pars reflexa* that extends from the anterior- to the posteriormost part of the pterygoid fossa of the ascending ramus, wrapping around the margin of the small angular process (Fig. 5B).

Facial-masticatory musculature

Buccinatorius pars externa

The *pars externa* of the *buccinatorius* muscle (pe-B; Fig. 10) is a thin sheet of obliquely oriented muscle fibers that envelops the *pars interna* of the *buccinatorius*. The muscle takes its narrow and anteroposteriorly elongated origin on the maxilla. Its posterior limit attaches just posteroventral to the zygomatic process of the maxilla. Its anterior part consists of a thin strap on the lateral surface of the maxilla, close to the lateral limit of the nasal cavity. The muscle wraps around the *buccinatorius pars interna* and reflects medially to insert along the dorsal part of the lateral surface of the mandible. Its insertion is shorter than its origin, extending from the level of the infraorbital foramen for the posterior two thirds of the length of the horizontal ramus.

Buccinatorius pars interna

The *buccinatorius pars interna* (pi-B; Fig. 10B) is an elongated and fleshy muscle that takes its origin just anteriorly to the coronoid process of the mandible. Posteriorly, the origin is laterally adjacent to that of

the *temporalis profundus pars medialis*, at level of the optic foramen. It extends anteriorly to reach the level of the maxillary foramen. The orbital part of the pi-B is flattened due to the presence of the large lacrimal gland, dorsally. Laterally, it is limited by the presence of the *temporalis superficialis pars anterior*. The muscle slightly broadens anteriorly with a thin projection of its dorsal part wrapping around the lateral border of the dentary pad, to project into the space between the upper and lowers jaws. The pi-B is enveloped by the pe-B, laterally. The muscle fibers are horizontally oriented and extend until the level of the caudal nasal foramina. Anteriorly, the pi-B inserts on the ventral part of the lateral surface of the maxilla.

Mandibuloauricularis

The *mandibuloauricularis* (MA; Fig. 10) is a small fleshy muscle with a pseudocylindrical shape. It takes its origin on the anteroventral part of the auricular cartilage. The MA narrows ventrally towards its insertion on a small area of the posterodorsal margin of the angular process of the mandible, between the insertions of the *masseter superficialis* and the *pterygoideus medius*. The MA presents dorsoventrally directed fibers with a slight medial component.

Facial musculature

Dilator nasi

The *dilator nasi* (DN; Fig. 6C, D) is one of the five strap-like facial muscles in *T. tetradactyla.* The DN is thin and subtriangular in shape. It originates on the lateral surface of the maxilla with its ventralmost part reaching the level of the dorsal margin of the infraorbital foramen. The posterior margin of the DN is anteriorly inclined. The muscle narrows down anteriorly. The muscular part of the DN ends at about half the length of the rostrum and its fibers are horizontally oriented. The anterior end of the DN bifurcates. A long tendon inserts on the dorsal part of the nasal cartilage, anterior margin of the nasal bones. These tendons, as the remaining tendons of the facial muscles, were not visible in the contrast-enhanced scan.

Maxilolabialis superficialis pars superior

Similar to the DN, the *maxilolabialis superficialis pars superior* (ps-MLs; Fig. 6C) is a thin strap-like muscle. It is thinnest at the origin, which is slightly posterior to the origin of the DN. It is dorsoventrally short, stretching between the dorsal and the ventral lacrimal foramina. Therefore, the ps-MLs is narrower than most of the other facial muscles, with the exception of the *maxilolabialis profundus pars superior* (see below). Yet, it covers much of the ventral part of the DN. The muscular part of the ps-MLs narrows anteriorly from around a third of the rostrum length and reaches the tendinous part just posterior to the level of the foramina for the caudal nasal nerves (Evans & De Lahunta, 2013). The long tendon attaches slightly obliquely oriented fibers of the ps-MLs to their insertion point on the upper lip, just dorsally to the labial commissure.

Maxilolabialis profundus pars inferior

The *pars inferior* of the *maxilolabialis profundus* (pi-MLp; Fig. 6D) is narrower than, but about the same length, as its superior counterpart. It takes its origin along the anteroventral part of the suture between the maxilla and the lacrimal (Fig. 6D). Posteriorly, it reaches the level of the lacrimal foramen, just anterior to the attachment of the jugal bone. Its fibers run horizontally, the muscular body stretching anteriorly from the origin. The tendinous part of the pi-MLp arises slightly anterior to the mid-lenght of the rostrum and inserts on the lower lip, ventrally to the labial commissure.

Maxilolabialis profundus pars superior

The *maxilolabialis profundus pars superior* (ps-MLp; Fig. 6D) is almost completely covered by the ps-MLs and the pi-MLp. The latter overlies its posteroventral part, while the former covers it anterodorsally. The ps-MLp is the narrowest of the anterior facial muscles. Its small origin area is located ventrally to that of the DN, and posteriorly reaches the ventral margin of the infraorbital foramen (Fig. 6D). The tape-like muscle thickens from its origin area to the posterior half of its length. It becomes thinner and narrower anteriorly, with its horizontally oriented fibers inserting on a tendon connecting the nasal cartilage (Fig. 6D). The tendon is almost as long as its muscular counterpart.

Maxilolabialis superficialis pars inferior

The *maxilolabialis superficialis pars inferior* (pi-MLs; Fig. 6C) is the longest of the facial muscles. It has a triangular shape and overlies almost completely the pi-ML. The upper margin of the pi-MLs is adjacent to the ps-MLs, and is therefore equally slanted ventrally. Ventrally, the pi-MLs fibers cover the origin of the *buccinatorius internus* (see 'Facial-masticatory muscles'). Anteriorly, the muscular body of the pi-MLs bifurcates, with the dorsal and ventral branches attaching to tendons with slightly different orientations. These tendons were not completely preserved on the specimen, but appear to insert ventrally on the lower lip.

Intermandibular musculature

Intermandibularis anterior

The *intermandibularis anterior* (IA; Fig. 11; *mylohyoideus pars anterior sensu* Naples (1999b)) is a sheet-like muscle that arises from the symphysial cartilage. As the name indicates, the fibers are transversely oriented. They insert on both hemimandibles, covering the base of the tongue and the tendon of the *geniohyoideus* (see 'Intermandibular musculature') in ventral view. The IA is, therefore, a non-bilaterally symmetric muscle (Fig. S1E). It wraps around the ventral margin of the mandible to insert just dorsally to it, on the lateral surface. The IA extends posteriorly for slightly more than half the length of the horizontal ramus of the mandible. Posteriorly, it is adjacent with the anterior margin of the *mylohyoideus pars anterior*.

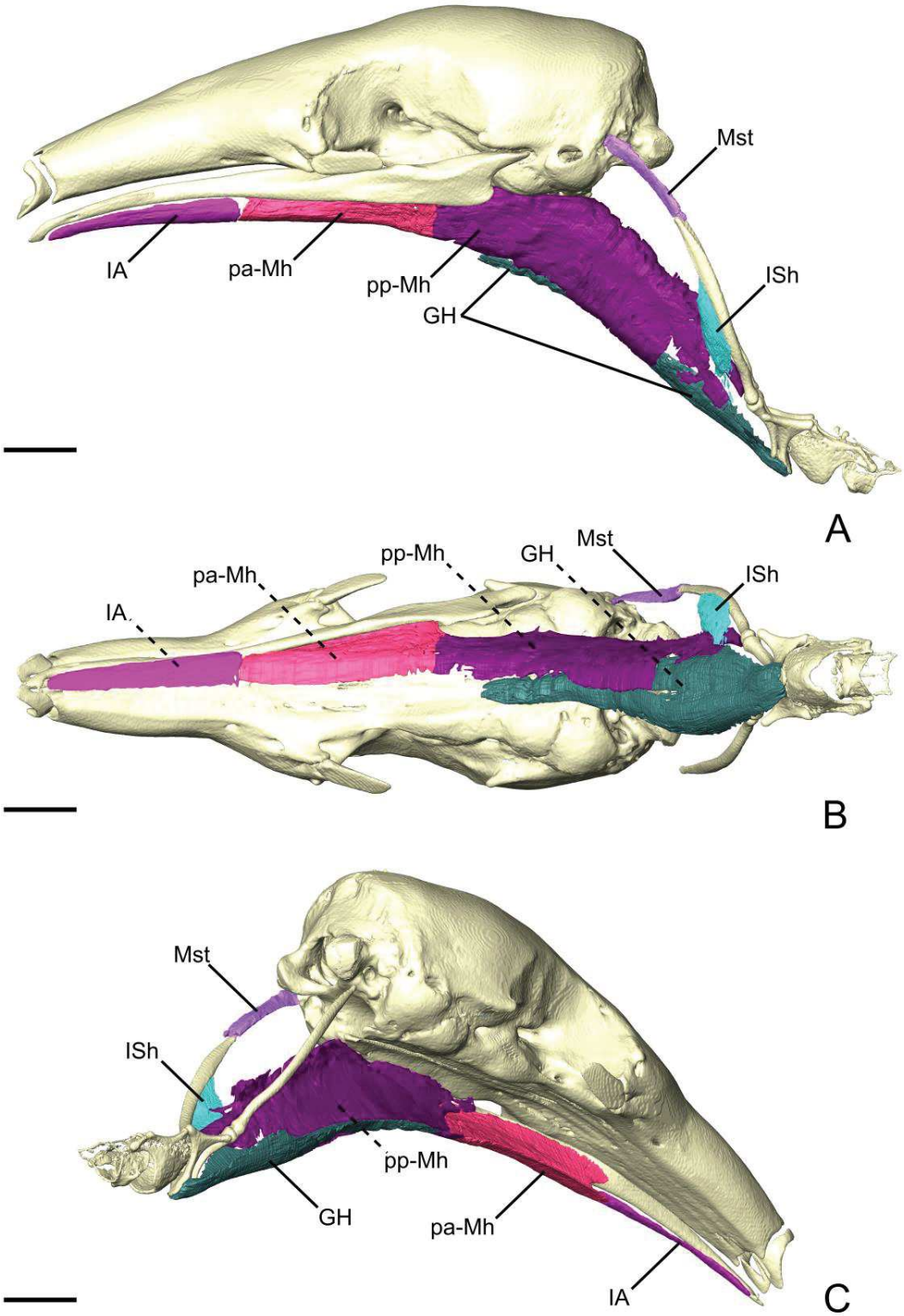

Figure 11 – The intermandibular musculature, *geniohyoideus*, and *interstylohyoideus*, and *sternomandibularis* of *T. tetradactyla* in lateral (A), ventral (B), and posteromedial (C) view. Scale bar 10 mm.

Mylohyoideus pars anterior

The *pars anterior* of the *mylohyoideus* (pa-Mh; Fig. 11) is a sheet-like muscle with transversely oriented, and covers the base of the tongue and the long tendon of the *geniohyoideus* (see below). Its morphological similarities with the *intermandibularis anterior* took previous studies to describe the latter as a distinct part of the *mylohyoideus* complex (Naples, 1999). In contrast to the *intermandibularis anterior*, the pa-Mh insertion takes its origin on ventral part of the medial surface of the mandible, between the widest point of the dentary pad and the pterygoid fossa posteriorly (Fig. 11). In addition to a different insertion, the pa-Mh is a bilaterally symmetric element, with both counterparts united medially by a small layer of conjunctive tissue. The pa-Mh is slightly thicker than the *intermandibularis anterior*. Posteriorly, the pa-Mh anastomoses with the *mylohyoideus pars posterior*, the two parts being continuous. In coronal view, the division between the two muscles is characterized by the passage of the sublingual artery (Evans & De Lahunta, 2013), ventral to the *pterygoideus medius pars anterior* (Fig. S1F).

Mylohyoideus pars posterior

The *pars posterior* of the *mylohyoideus* (pp-Mh; Fig. 11) is broader than pa-Mh. At the level of the orbital fissure, sublingual artery (Evans & De Lahunta, 2013) splits the insertions of the pa-Mh and the pp-Mh. While the pa-Mh inserts on the mandibular ramus, the insertion of the pp-Mh extends along the medial surface of the palatine inflation, then along the ventromedial surface of the pterygoid sinus to continue posteriorly until the rostral tympanic process of the petrosal (Fig. 11). Additionally, a thin muscular projection inserts on the medial surface of the *pterygoideus medius pars anterior*. Posterior to the hard palate, the pp-Mh inserts on the soft palate, keeping its shape until it reaches the anterior part of the *stylopharingeus*, where it bifurcates. A fleshy fiber extension projects posteriorly to attach on a small area of the anterior surface of the stylohyal, just dorsal to its suture with the epihyal. On the other hand, a ventral sheet-like projection attaches to the tendon of the *interstylohyoideus*. As in other cases, the tendon could not be segmented. Nevertheless, the presence of muscular fibers of the *interstylohyoideus* confirm the position of the insertion of the pp-Mh described in previous studies (Reiss, 1997).

Hyoid, thyroid, and cricoid musculature

Geniohyoideus

The *geniohyoideus* (Gh, Figs. 11 and 12) consists of a very long bilaterally symmetric element. Anteriorly, the Gh takes its origin on the ligament of the mandibular symphysis (Naples, 1999). Although the tendon is not visible in the contrast-enhanced scan, its origin can be traced by the empty gap, between the base of the tongue (dorsally) and the *transversus mandibularis*, pa-Mh, and pp-Mh (ventrally). This midline tendinous part of the Gh ends at the level of the zygomatic process of the squamosal, where the muscular fibers appear (Fig. 11). The fibers are horizontally oriented and grouped in two bilateral structures. Nevertheless, both bellies appear to anastomose in the anterior half of the muscle. The Gh is overlain by the pp-Mh until near the *interstyloideus* ligament. The Gh inserts on the ventral surface of the fused ceratohyal and basihyal.

Interstylohyoideus

This muscle (ISh; Fig. 11) consists of a very thin sheet of transversely oriented fibers that take their origin along the anteroventral margin of the stylohyal. Its origin is located on the middle section of the stylohyal, and extends for roughly a third of its length. Ventrally, the muscular part of the ISh converges to a narrow tendon that wraps around the Gh and connects both bilateral elements. This tendon is the most posteroventral origin of the pp-Mh.

Mastostyloideus

The *mastostyloideus* (Mst; Fig. 12A-C) is a strap-like element that arises from the ventral part of a tiny vertically oriented gutter, which originates posteriorly to the stylomastoid foramen. The horizontally oriented fibers form a relatively thick bundle that inserts on the anterior tip of the stylohyal. This muscle is overlain by the *sternomastoideus* and borders the *splenius capitis* medially.

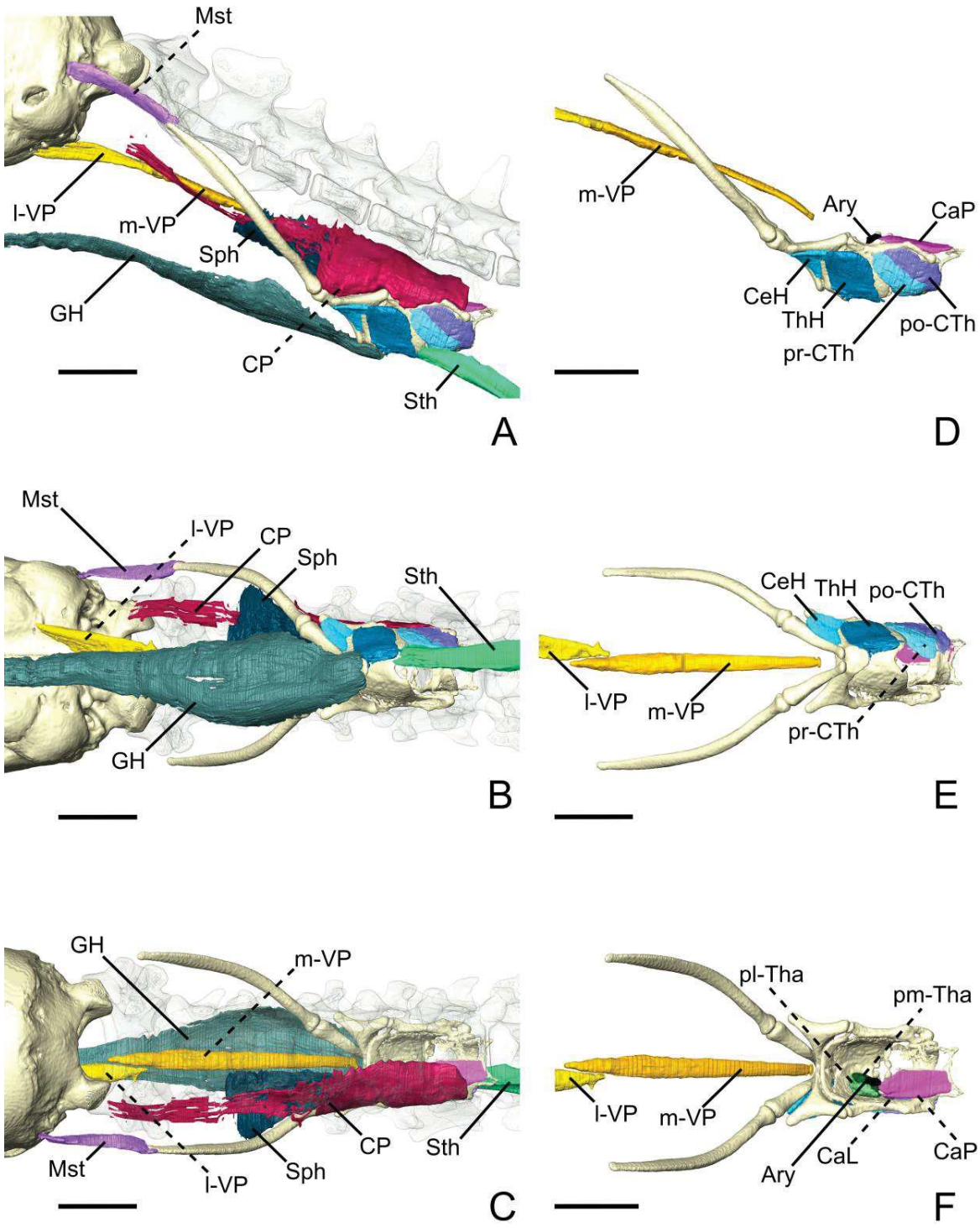

Figure 12 – The hyoid, thyroid, and pharyngial musculatures of *T. tetradactyla* in lateral (A, D), ventral (B, E), and posteromedial (C, F) view. Scale bar 10 mm.

Ceratohyoideus

The *ceratohyoideus* (CeH; Fig. 12D-F) is triangular in shape and its obliquely oriented fibers are organized in a sheet-like element that takes its origin on the lateral surface of the epihyal bone. The origin stretches along the middle section of the bone. The CeH attaches on the thyrohyal from the ventrolateral margin of the anterior process, and extends towards the posterior process without reaching it. Ventrally, the CeH inserts along the slightly concave anterolateral surface of the thyrohyal, ending just dorsally to the fused suture with the ceratohyal.

Thyrohyoideus

The *thyrohyoideus* (ThH; Fig. 12D, E) is sheet-like, as other muscles lateral to the thyroid cartilage. It is subquadrangular in shape and its origin is dorsoventrally elongated, extending from just ventrally to the anterior process of the thyroid cartilage to the most ventral part of its lateral surface. Its ventral part wraps around the lateral aspect of the thyroid, presenting a small *pars reflexa* (Fig. 12E). Posteroventrally, its origin is adjacent with the insertion of the *sternohyoideus* (see 'Sternum musculature'). The ThH insertion area is thin and as elongated as its origin one. It extends from just ventrally to the insertion of the CeH all the way ventrally to the posterior margin of the ceratohyal.

Cricothyroideus pars recta

The *cricothyroideus pars recta* (pr-CTh; Fig. 12D, E) is the most lateral parts of this muscle. It consists of a relatively thick muscle strap, which takes its origin from the most anterior part of the ventral and ventrolateral surfaces of the thyroid cartilage. Ventrally, the pr-CTh presents a *pars reflexa* that connects the anterior margin of the cricoid cartilage to the posterolateral surface of the thyroid. The posterior part of the *pars reflexa* wraps around the small protuberance on the lateral aspect of the cricoid; its muscles fibers insert anteriorly on the posterodorsal part of the lateral surface of the thyroid. If the contrast does not allow to characterize the orientation of the muscle fibers of the pr-CTh, they were obliquely oriented, despite its name.

Cricothyroideus pars obliqua

The *pars obliqua* of the *cricothyroideus* (po-CTh; Fig. 12D, E) is placed medially to the *pars recta*. It presents a similar size to its lateral counterpart, which covers a small part of its anteroventral surface. The po-CTh takes its origin on the posterolateral surface of the cricoid cartilage. Contrary to the pr-Cth, the medial component of the muscle presents a small *pars reflexa* posterior to the lateral protuberance of the cricoid. The obliquely oriented fibers attach the cricoid posterolateral surface to the posterior process of the thyroid. The insertion of the po-CTh is located just ventrally to the rounded dorsal edge of the thyroid, and extends from the ventral surface of the tubercle of the posterior process to the level of the arytenoid cartilage.

Cricoarytenoideus posterior

The *cricoarytenoideus posterior* (CaP; Fig. 12D, F) covers the dorsal part of the cricoid cartilage. This muscle is sheet-like, pseudorectangular in dorsal view, and elongated anteroposteriorly. Its horizontally oriented fibers (Diogo, 2018) take their origin on the posterior edge of the cricoid cartilage and insert on the ventrolateral surface of the arytenoid cartilage. The muscle thickens mediolaterally, presenting a round lateral edge for most of its length. This round edge is not present near the origin or insertion. At the anterior limit of the lateral edge, the CaP is briefly connected to the dorsal part of the *cricoarytenoideus lateralis* by connective tissue.

Cricoarytenoideus lateralis

The *cricoarytenoideus lateralis* (CaL; Fig. 12F) is the smallest muscle of the hyoid complex. It is a fleshy elongated muscle that originates on the cricoid cartilage. The muscle is wider dorsally and thins down ventrally, where it attaches to the medial surface of the pr-CTh by connective tissue. The insertion on the arytenoid cartilage is located slightly anterior to its cricoid origin. Its insertion is tendinous and is not visible on the 3D reconstruction. Laterally to its insertion on the arytenoid cartilage, the CaL is attached to the *thyroarytenoideus pars medialis*.

Thyroarytenoideus pars lateralis

The *thyroarytenoideus pars lateralis* (pl-ThA; Fig. 12F) is the largest part of the biggest muscle of the hyoid-related cartilaginous complex. In lateral view, this muscle is oval-shaped and takes its origin on a very shallow anteroposterior groove on the medial surface of the ventral part of the thyroid cartilage. Its origin is limited to the deepest part of the thyroid concavity, posteriorly. The fibers are vertically oriented. The muscle is thick anteriorly, and thinner posteriorly. Its cross-section is medially concave, following the shape the thyroid cartilage that constitutes its lateral border. Medially, the pl-ThA is tightly bound to the *pars medialis*. Dorsally, the fibers converge towards its insertion area on the most lateral part of the arytenoid cartilage. The small tendinous part of the insertion is not visible on the 3D reconstruction.

Thyroarytenoideus pars medialis

The *pars medialis* of the *thyroarytenoideus* (pm-ThA; Fig. 12F) is much less voluminous than the pl-ThA. Both parts anastomose ventrally and share a common origin. The pm-ThA and pl-ThA are similar in morphology. The CaL bounds to the posterodorsal margin of pm-ThA.

Pharynx musculature

Levator veli palatini

The *levator veli palatini* (l-VP; Fig. 12) is a small strap arising from the ventrolateral surface of the secondary hard palate formed by the medial pterygoid processes. The origin is narrow and extends from a medioventral point of the foramen of the auditory tube to the posteriormost margin of the pterygoid process. In cross-section, the most posterior part of the l-VP forms a separate flatter unit compared to the posterior fleshy block (Fig. S2A). The fibers of the posteromedial part of the l-VP were not well-stained, hindering the complete delineation of the two unit. They appear to eventually anastomose posteriorly. The fibers run posteroventrally, with a small medial angle, to insert on the soft palate. The posterior part of the l-VPs thins down and assumes a pointy shape. Bilaterally symmetric l-VPs flank the anterior tip of the *medialis veli palatini* (Fig. 12); they attach to the latter and to each other via a layer of connective tissue.

Medialis veli palatini

The medial element of the *veli palatini* (m-VP; Fig. 12) consists of the long fleshy and dorsoventrally compressed medial axis of the soft palate. Its anteroposteriorly oriented fibers arise from the soft palate, medial to the two l-VPs. The putative ligament connecting the muscle to the pterygoid shelves (Reiss, 1997) were not visible in the contrast-enhanced scan. The m-VP widens posteriorly to the origin and then gradually narrows down in the direction of the hyoid-thyroid complex (Fig. 12E, F). At its posterior end, the m-VP bifurcates into two thin straps that run medially to the *stylopharyngeus* and *contrictores pharyngeus* (see below), and then migrate dorsally to finally insert on the dorsal part of the pharynx (Fig. 13).

Stylopharyngeus

The *stylopharyngeus* (Sph; Fig 12A-C and 13) is a large muscle arising from the medioventral surface of the stylohyal. Its fibers are transversally oriented and arranged in a compact fashion laterally, conferring the Sph a sheet-like shape. Anteriorly, the Sph is in tight connection with the fibers of the *mylohyoideus pars posterior* (pp-Mh). Medially the muscle becomes thick as it inserts on the m-VP and the ventrolateral external surface of the nasopharynx. This description corresponds to the *pars pharyngea* of the Sph (*sensu* Reiss, 1997). Posteriorly, the fibers have a longitudinal orientation, and form a fleshy projection that is pseudo-sigmoidal in cross-section (Fig. S2B). According to Reiss (1997), this is the *pars thyroidea* of the Sph. As individual fibers were hard to delineate, the recognition of two parts in this muscle was not possible based on the contrast-enhanced scan. The posterior part of the Sph is flanked by the *constrictures pharyngeus.* Posteriorly, the Sph becomes mediolaterally thinner. It runs dorsolaterally along the wall of the oro-laryngopharyx. Part of the Sph posteriormost fibers present a small insertion on the posterior part of the dorsal surface. The remaining fibers attach to the medial wall of the inferior part of the *constrictures pharyngeus* (Fig. S2B).

Constrictores pharyngeus

The *constrictores pharyngeus* (CP; Fig. 12A-C and 13) is a complex of muscles composed by three different parts (e.g., Diogo & Abdala, 2010): *constrictor pharyngis superior* (anterior; CPa), *constrictor pharyngis medius* (median; CPm), and *constrictor pharyngis inferior* (posterior; CPp). Because the contrast-enhanced scan did not allow to recognize individual fibers (mainly in the median and posterior parts), these three parts could not be discretize. For simplicity sake, we refer to each part based on the external shape of the muscle, its origins/insertions, and its topology. The CPa is the longest part of the CP, it is easily identifiable by its tape-like shape (Fig. 13A-C and 13). It,takes its origin on the tuberosity medial to the auditory tube. Although the anteriormost part of the CPa was not visible in the contrast-enhanced scan, its attachment to the ventrolateral surface of the *splenius capitis* muscle suggests a similar relative position of both muscles' origins. The muscle runs posteriorly, being enclosed between the ventral surface of the *splenius capitis* and the dorsal margin of the *milohyoideus pars posterior* (pp-Mh). At the length of the epihyal-stylohyal suture, the CPa lies as a thin layer between the *splenius capitis* and the Sph. At this level, the muscle fibers shift from a longitudinal to a transverse orientation. The transversely oriented fibers of the CPm arise from the most apical part of the posterior margin of the epihyal and from the dorsal surface of the thyrohyal (Fig. 12A). The CPm merges medially with its bilateral counterpart. It overlies the posterior part of the Sph laterally and dorsally (Fig. 12A and S1B). The posterior part of the CP complex arises from the dorsal surface of the thyroid cartilage. In dorsal view, the CPp covers the anterior part of the *cricoarytenoideus posterior* (Fig. 12C). At the posterior end, a well distinguishable muscle arises from the dorsomedial edge of the cricoid cartilage (Fig. 12C). This represents the *pars cricopharingea* of the CPp (Saban, 1968; Diogo, 2018).

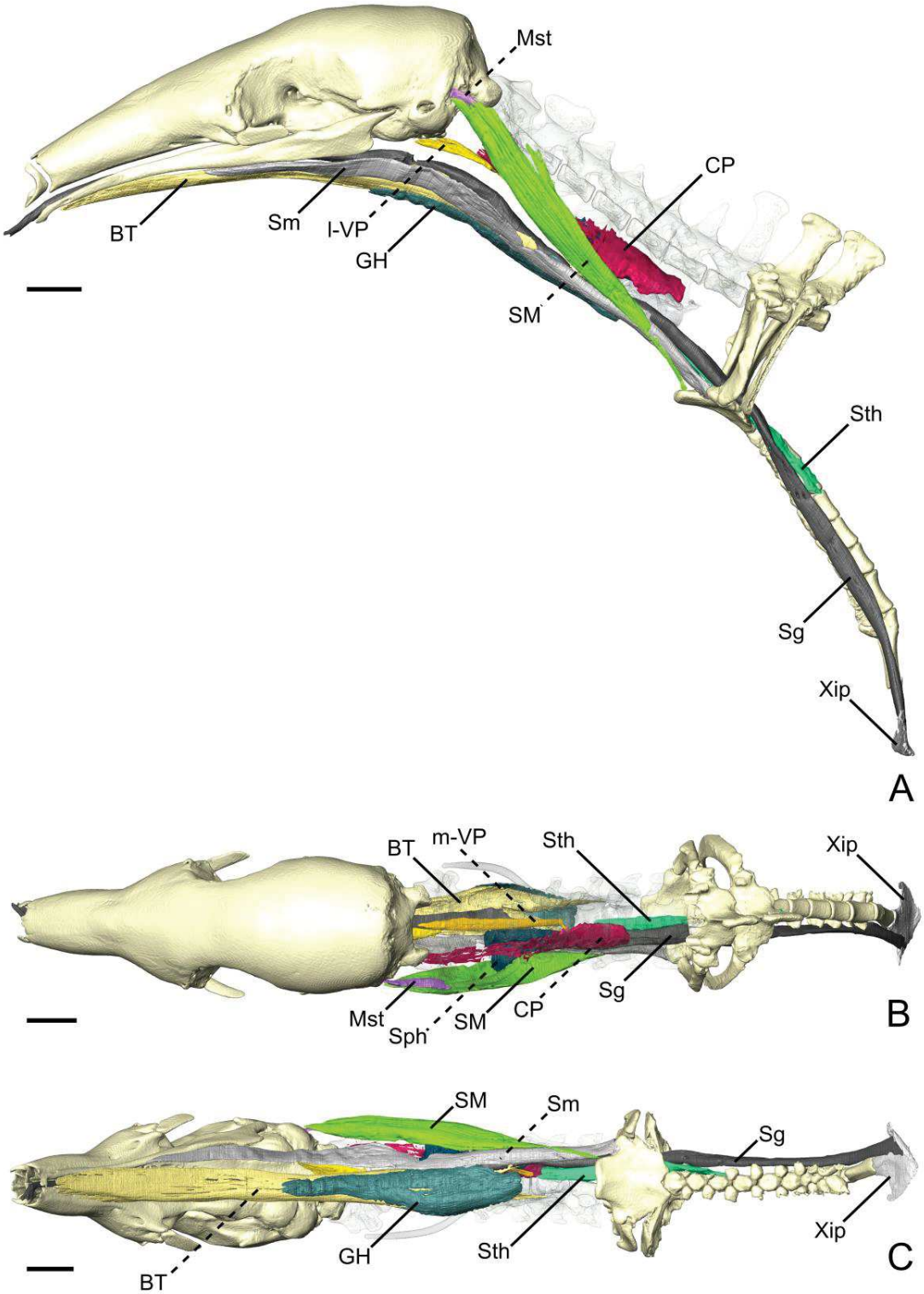

Figure 13 – The sternum and pharyngeal musculatures, *mastostyloideus*, and *sternomastoideus* of *T. tetradactyla* in lateral (A), dorsal (B), and ventral (C) views. Scale bar 10 mm.

Sternum musculature

Sternomandibularis

The *sternomandibularis* (Sm; Fig. 13A, C) is an anteroposterioly elongated muscle that takes its origin on the anterior surface of the lateral protuberance of the manubrium, just anterior to the articulation of the first rib. This muscle is tape-like in shape and passes ventrolaterally to the hyoid apparatus and pharynx. Its anterior half is thinner than the posterior one. Anterior to the atlas, the Sm becomes narrower. Its insertion on the ventral edge of the horizontal ramus is relatively long, extending from the level of the sphenopalatine foramen to the dorsal margin of the infraorbital foramen.

Sternoglossus

The *sternoglossus* (Sg; Fig. 13) is extremely long. This muscle takes its origin on the cartilaginous extension in the posteriormost part of the sternum (xiphisternum). Near the origin, the muscle has a tape-like shape. It is bound to the sternal body segments until it reaches the manubrium, passing just dorsally to it. Anterior to the manubrium, the Sg thickens slightly. It binds to the hyoid complex, medially, and to the Sm laterally, by thick layers of the connective tissue. Between the manubrium and the cricoid cartilage, a large artery is imbedded in the Sg and follows its trajectory anteriorly. From this point, the Sg presents a circular cross-section. Anterior to the hyoid complex, it shifts to a midline position, meets its bilateral counterpart and becomes attached to the base of the tongue (*genioglossus*). Both Gh and pp-Mh wrap around the tongue, ventrally (both) and laterally (pp-Mh). Anteriorly, both right and left Sg are enveloped by a dermal tissue. At the level of the occipital condyles, the two Sgs become detached from the base of the tongue. The base of the tongue (*genioglosssus*) extends anteriorly, almost until the mandibular symphysis, attaching to the medioventral surface of the anterior third of both mandibles. The Sgs narrow anteriorly until the most anterior tip of the tongue.

Sternothyroideus

The *sternothyroideus* (Sth; Fig 13) takes its origin on the sternum, at the level of the second and third ribs. This strap-like muscle remains attached to the sternum by connective tissue, projecting to the thyroid cartilage from the posterior margin of the manubrium. The Sth follows a parallel and adjacent trajectory

to that of the Sg, until it inserts posterolaterally on the ventral margin of the thyroid cartilage, just ventral to the insertion of the pr-CTh.

Sternomastoideus

The *sternomastoideus* (SM; Fig. 13) is an elongated muscle that takes its origin from the anterior part of the manubrium. The origin is tendinous, small, and is located on the angle of the anterior flap-like projection of the manubrium, lateral to the jugular notch and just medial to the clavicular notch (Fig. 13C). The muscular fibers are extremely long anteroposteriorly, and depart from the manubrium with an inclination of approximately 36°. The SM runs anterodorsally on the lateral side of the neck. With the exception of a few muscular fibers, the muscular part of the SM arises from its tendon anteriorly to the posterior cornu of the thyroid cartilage (Fig. 13A), around 20mm from the origin. The muscle broadens dorsoventrally giving the SM a strap-like shape. It also thickens mediolaterally, to a lesser extent. The SM becomes fleshy and runs in attachment with the lateral margin of the stylohyal bone. Anteriorly, it is tightly connected to the *stylomastoideus* muscle. The muscle fibers of the SM end near the tendinous insertion on a small groove just posterodorsally to the stylomastoid foramen.

Myrmecophaga tridactyla

Masticatory apparatus

Masseter superficialis

In *M. tridactyla*, the *masseter superficialis* (MS; Fig. 14) is a fleshy and anteroposteriorly elongated muscle. The MS originates from the ventrolateral margin of the zygomatic process of the maxilla. A strong tendon connects the origin to the almost horizontally oriented muscular fibers. The MS is thin at the origin, as it overlies the posterior part of the *masseter profundus*. It thickens posteriorly, as it extends anteriorly to the lacrimal foramen to the posterior limit of the masseteric fossa. The MS presents a *pars reflexa* throughout its full length. The *pars reflexa* wraps around the ventral edge of the mandible and becomes larger posteriorly, covering but the very posteroventral tip of the small angular process (Fig. 14A,C).

Masseter profundus

The *masseter profundus* (MP; Fig. 14B) takes its origin on the anterior part of the ventrolateral surface of the zygomatic arch. Its area of origin includes the small jugal bone and the posteroventral surface of the zygomatic process of the maxilla. The MP is in contact with the posterior part of the *buccinatorius internus*, medially (Fig. 14D). The MP is obliquely oriented; its inserts ventrally on the mandible and presents a small *pars reflexa*. The muscle is thick at its origin but thins down posteriorly, where it is overlain by the MS. The MP is half the length of the MS, with its insertion area stretching from the most posterior point of the lacrimal-maxilla suture to near the level of the coronoid process.

Temporalis superficialis

The *temporalis superficialis* (TS; Fig. 14) is a flat muscle covered almost entirely by the large lacrimal gland. It is a fan-like muscle arising from the temporal fossa extending from the level of the optic foramen to the root of the zygomatic process of the squamosal. The lateral surface of the TS is covered by a tendinous layer that thickens ventrally near the insertion of the muscle on the small coronoid process. While the ventrally converging fiber of the TS reach the coronoid process posteriorly, the anterior part of the muscle inserts on the mandible uniquely via its tendinous layer (Fig. 14). The TS is well-separated from the *pars zygomatica*, posteriorly, due to the very distinct orientation of the muscular fibers.

Temporalis superficialis pars zygomatica

The *pars zygomatica* of the TS (pz-TS; Fig. 14) is the thickest part of the TS complex. It arises from the medial and posteroventral surfaces of the zygomatic process of the squamosal and extends anteroventrally with an oblique orientation. The pz-TS displays a medial portion that extends along the anterior margin of the neck of the mandibular articular process and inserts on the posterior surface of the blunt coronoid process. The lateral part of the pz-TS is larger and extends along the surface lateral to the mandibular notch. The ventralmost part of the pz-TS is slightly overlain by the dorsal margin of the MS. The pz-TS is easily distinguishable from its larger counterpart due to the different orientation angle of its fibers.

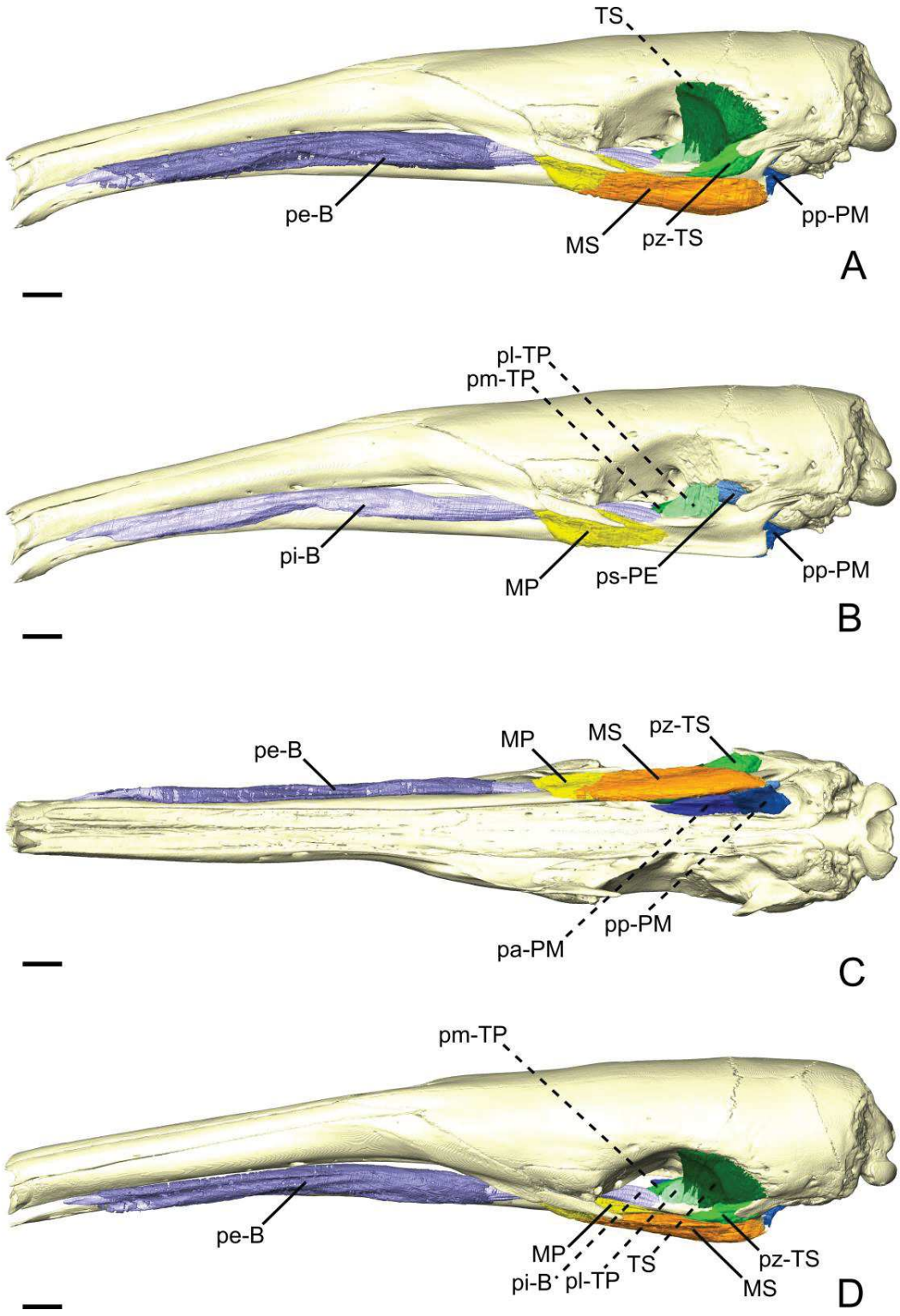

Figure 14 – The masticatory and facial-masticatory musculature of *M tridactyla* in lateral (A, B), ventral (C), and dorsolateral (D) views. Scale bar 10 mm. The more superficial muscles were removed in B.

Temporalis profundus pars lateralis

The *temporalis profundus* (TP; Figs. 5C and 14B, D) is divided into medial and lateral parts. The *pars lateralis* (pl-TP) is a blocky-shaped muscle arising from the ventral limit of the temporal fossa between the anterior tip of the orbital process and the insertion of the *pars superior* of the *pterygoideus externus*. The posterior part of the pl-TP presents a quadrangular shape in lateral view, with the anterior part tapering in near the *buccinatorius internus*. The muscular fibers are dorsoventrally oriented with an oblique transversal component. The pl-TP inserts on the dorsal surface of the ascending ramus deep to the insertion of the TS. While the TP is well separated from the TS during the classical dissection, the incomplete staining of the former makes it sometimes hard to delimit. Anteriorly, the insertion of the pl-TP extends until the level of the anterior margin of the optic foramen (Fig. 5C).

Temporalis profundus pars medialis

The *temporalis profundus pars medialis* (pm-TP; Figs. 5C and 14B, C) in *M. tridactyla* is a medioventrally extending projection of the pl-TP. Both parts are anastomosed posteriorly, sharing the medial part of the TP origin. The pm-TP arises from the ventral surface of the orbital process lateral to the orbital fissure and the foramen rotundum. Slightly anterior to its origin, the pm-TP extends ventrally on the lateral surface of the ascending ramus (Fig. 5C). Anterior to this point, the two parts of the TP are distinguished by different insertion areas, with pm-TP reflecting medially. The insertion of the pm-TP is broad and extends ventrally almost until the level of the mandibular canal. It is limited posteriorly by the mandibular canal. The pm-TP tapers anteriorly to its contact with the posterior part of the *buccinatorius internus* at the orbit midlength. Fiber orientation in the pm-TP is similar to that of the pl-TP.

Pterygoideus externus pars superior

The *pars superior* of the *pterygoideus externus* (ps-PE; Figs. 5C and 14B) is a broad and wide fleshy sheet muscle arising from the large fossa extending from the anteroventral part of the squamosal to the ventral part of the temporal fossa. Its fibers are obliquely oriented and extend posteroventrally to insert on the mandible just anteriorly to the jaw joint. The posteroventral part of the ps-PE is characterized by a large

pars reflexa that wraps around the medial edge of the articular process. The *pars reflexa* of the ps-PE overlays the posterior part of the *pars inferior* of the PE.

Pterygoideus externus pars inferior

The *pars inferior* of the *pterygoideus externus* (pi-PE; Fig. 5C) is a strap-shaped muscle that originates from the anterior part of the pterygoid fossa, at the level of the optic foramen. In contrast with the ps-PE, the pi-PE is narrow and elongated. Its origin is thin, and lies medially to the p*ars interna* of the *temporalis profundus* (pi-TP). The anterior part of the pi-PE is in tight contact with the *pars anterior* of the *pterygoideus medius*. The pi-PE slightly thickens up posteriorly, assuming a circular cross-section. The muscular fibers are horizontally oriented, with transversal oblique component as they insert posterolaterally on the anterior part of the neck of the articular process (Fig. 5C). The insertion of the pi-PE reaches about half the length of the neck and is overlain laterally by the *pars reflexa* of the ps-PE. The pi-PE merges with the *pars reflexa* of the ps-PE by a thick band of conjunctive tissue.

Pterygoideus medius pars anterior

The *pars anterior* (pa-PM; Figs. 5C and 14C) is the larger of the two parts of the *pterygoideus medius*. It takes its origin from the small crest formed by the lateral edge of the palatine. In lateral view, the pa-PM presents a pseudorectangular shape. Anteriorly the muscle narrows down (Fig. 5C). The most anterior fibers originate just anteriorly to the level of the ethmoid foramen. The fibers extend ventrally to insert on a lateral prominence of the mandibular ascending ramus, ventrally to the passage of the inferior alveolar nerve and artery. Posteriorly, the fibers are dorsoventrally oriented, with an oblique transverse component. Both origin and insertion of the pa-PM end roughly at the level of the palatine-pterygoid suture.

Pterygoideus medius pars posterior

The smallest component of the *pterygoideus medius* is a fleshy pseudorectangular band in lateral view (Fig. 5C). The origin of the *pars posterior* of the *pterygoideus medius* (pp-PM; Figs. 5C and 14C) is very thin and extends from near the palatine-pterygoid suture to the pterygoid sinus at the level of the posterior limit of the jaw joint. The pp-PM is the continuation of the pa-PM until the tip of the angular process,

where it reaches the insertion area of the *auriculomandibularis*. In lateral view, the fibers are vertically oriented, with a transversal component of about 21° relative to the sagittal axis of the skull. Posteriorly, the pa-PM becomes thicker but it tapers off abruptly at the level of the pterygoid sinus.

Facial-masticatory musculature

Buccinatorius pars externa

The *pars externa* of the *buccinatorius* (pe-B; Fig. 14) is an extremely sheet enveloping the much thicker *pars interna* (see below). The fibers of the pe-B have an oblique orientation, arising from the long and extremely narrow origin on the maxilla. The origin extends from the level of the most posterior mental foramen to the anterior edge of the zygomatic process of the maxilla. The pe-B extends ventrally, envelopes the *pars interna* and reflects medially. The muscle wraps around the ventromedial margin of the *pars interna* of the *buccinatorius* and projects dorsally to insert on the dorsolateral surface of the mandibular horizontal ramus. Its insertion and origin areas are similar in length, but the bad preservation of the soft tissues in the snout did not permit to clearly observe of the anterior tip of its origin.

Buccinatorius pars interna

The *pars interna* of the *buccinatorius* (pi-B; Fig. 14B) is extremely long anteroposteriorly, reflecting the elongation of the rostrum. The muscle takes its origin on the maxilla, adjacent to the labial commissure of the mouth. Its fibers go on to insert on the dorsal surface of the horizontal ramus of the mandible, ventrally to the eye and the lacrimal gland. The fibers have an almost horizontal orientation, leaning slightly ventrally. In cross section, the anterior part of the pi-B is dorsoventrally elongated, showing a small ventromedial projection. The most anterior part of the pi-B presents a medial flap-like projection that rests between both jaws (Figs. 14B and S2). At the length of the anterior most tip of the nasal, the pi-B drifts ventrally and narrows dorsoventrally (Fig. 14C). Posteriorly to the zygomatic process of the maxilla, the pi-B leans medially to a position between the jaws, deep to the *masseter superficialis* (MS). This marks the beginning of the insertion of the pi-B, which extends until the anterior part of the insertion of the *temporalis profundus* (TP), just anterior to the level of the optic foramen.

Mandibuloauricularis

The *mandibuloauricularis* (MA) consists of a small fiber bundle that takes its origin from the anterior part of the auricular cartilage. It inserts on the posterior tip of the angular process, between the *pars posterior* of both *masseter superficialis* (pp-MS) and *pterygoideus medius* (pp-PM). This muscle was damaged on the digitally dissected side of the skull and was described based on its right counterpart.

Facial musculature

Dilator nasi

The *dilator nasi* (DN; Fig. 6A,B) is an extremely thin sheet of horizontally oriented fibers. It is the most dorsal of the anterior facial muscles. It takes its origin on the dorsal part of the lateral surface of the maxilla, with the muscular fibers stretching anteriorly from the level of the most posterior point of the nasal to about mid-length of the rostrum The DN broadens slightly anteriorly to its origin and narrows down abruptly at its most anterior part, which attaches via a tendon. The length of the tendon more than doubles the length of the muscular portion of the DN. It runs for more than half of the rostrum length to insert on the nasal cartilage at the level of the nostrils.

Maxillolabialis superficialus pars superior

The *maxillolabialis superficialis pars superficialis* (ps-MLs; Fig. 6A) is the more anterior of the dorsal facial muscles. This thin and elongated muscle is broader at its posterior and median parts, thinning anteriorly. The ps-MLs is slightly thicker ventrally than dorsally. Its posterior and middle parts overlie the *maxillolabialis profundus pars media* and *pars superior* anteriorly. The ps-MLs and the DN are similar in length. A tendon, as long as its muscular counterpart, connects the ps-MLs to the upper lip.

Maxillolabialis superficialis pars inferior

The *pars inferior* of the *maxillolabialis superficialis* (pi-MLs; Fig. 6A) is the most posterior of the facial muscles described in this section. It arises from an area dorsal to the maxilla-frontal-lacrimal contact. Its anterior half covers the posterior parts of the *pars media* and *pars superior* of the *maxillolabialis*

profundus. The muscle fibers reach just posterior to the most anterior point of the fronto-nasal sutures. From this point, an extremely long tendon runs anteriorly to insert just posteroventrally to the buccal commissure. In *M. tridactyla*, the pi-MLs is dorsally placed when compared to the condition in *T. tetradactyla*.

Maxillolabialis profundus pars inferior

The *maxillolabialis profundus pars inferior* (pi-MLp; Fig. 6B) takes its origin on the anterodorsal surface of the zygomatic arch of the maxilla. Its origin overlies the anterior part of the tendon of the *masseter superficialis*. The height of the posterior part of the pi-MLp contrasts with its extremely thin anterior part. The anterior half of the muscle consists of an extremely thin bundle of a few horizontally oriented fibers. The muscular part of the pi-MLp runs for slightly more than a third of the rostrum length. This muscle appears to insert on the *pars anterior* of the MLp, as an individual tendon was hard to identify during the classical dissection.

Maxillolabialis profundus pars anterior

The *pars anterior* of the *maxillolabialis profundus* (pa-MLp; Fig. 6A) is extremely thin compared to its posterior counterpart (pi-MLp). The pa-MLp overlies the anterior half of the pi-MLp. This muscle might correspond to an anterior extension of the pi-MLp. The anterior part of the pa-MLp flanks the ventral margin of the ps-MLs. The insertion of the pa-MLp just posteriorly to the buccal commissure is done through a tendon almost equivalent in length to its fibers.

Maxillolabialis profundus pars media

This part of the *maxillolabialis profundus* (pm-MLp; Fig. 6B) is a thin fiber bundle between the *pars inferior* and the *pars superior* of the MLp. The pm-MLp is the most dorsoventrally compressed of the dorsal facial muscles, with a length similar to that of the DN. Its origin is anterodorsal to that of the *pars inferior* of the MLp. As previously described, the anterior part of this muscle is covered by the ps-MLs. The pm-MLp tendon appears to be fused with that of the pm-MLp and the pi-MLp, which is in line with previous observations (Naples, 1985a).

Maxillolabialis profundus pars superior

The *maxillolabialis profundus pars superior* (ps-MLp; Fig. 6B) is a more dorsal and broader replicate of the pm-MLp. The origin is just slightly anterior to that of the pm-MLp, and both muscles are similar in length. From classical dissection, this muscle appears to share a tendon with the ps-MLs, with both muscles sharing an insertion posterodorsally to the buccal commissure.

Intermandibular musculature

Intermandibularis anterior

The *transversus mandibularis* (IA; Fig. 15; *mylohyoideus pars anterior sensu* Naples, 1999a) is extremely elongated, extending for almost half the mandibular length (127.4 mm). This muscle is very thin and forms a sheet covering the tendon of the *genioglossus* as well as the tongue (not figured). Each fiber is attached to thin areas on the ventrolateral surfaces of both mandibles. The muscle wraps around the ventral margin of the mandible and the transversely oriented stretch to insert on the symmetric element. The fibers are continuous between mandibles.

Mylohyoideus pars anterior

The postcranial muscles in our specimen were not successfully stained by the iodine solution and, therefore, could not be illustrated and described (Fig. 15). The *pars anterior* of the *mylohyoideus* (pa-Mh; Fig. 15; *mylohyoideus pars media* sensu Naples, 1999a) is only partially stained and thus not completely represented in our 3D reconstructions. This muscle forms a thick sheet ventral to the tongue musculature and the hyoid apparatus. Its fibers are transversely oriented, connecting a midline of conjunctive tissue to the medial surface of the mandible (Fig. 15). Both symmetric counterparts of the pa-Mh unite in the midline, but could be easily distinguished both during the classical and digital dissections. The pa-Mh is clearly separated from the *pars posterior* by a shift in the insertion from the mandible to the skull. The posterior end and transition between the *pars anterior* and *posterior* of the *mylohyoideus* could not be segmented during the digital dissection.

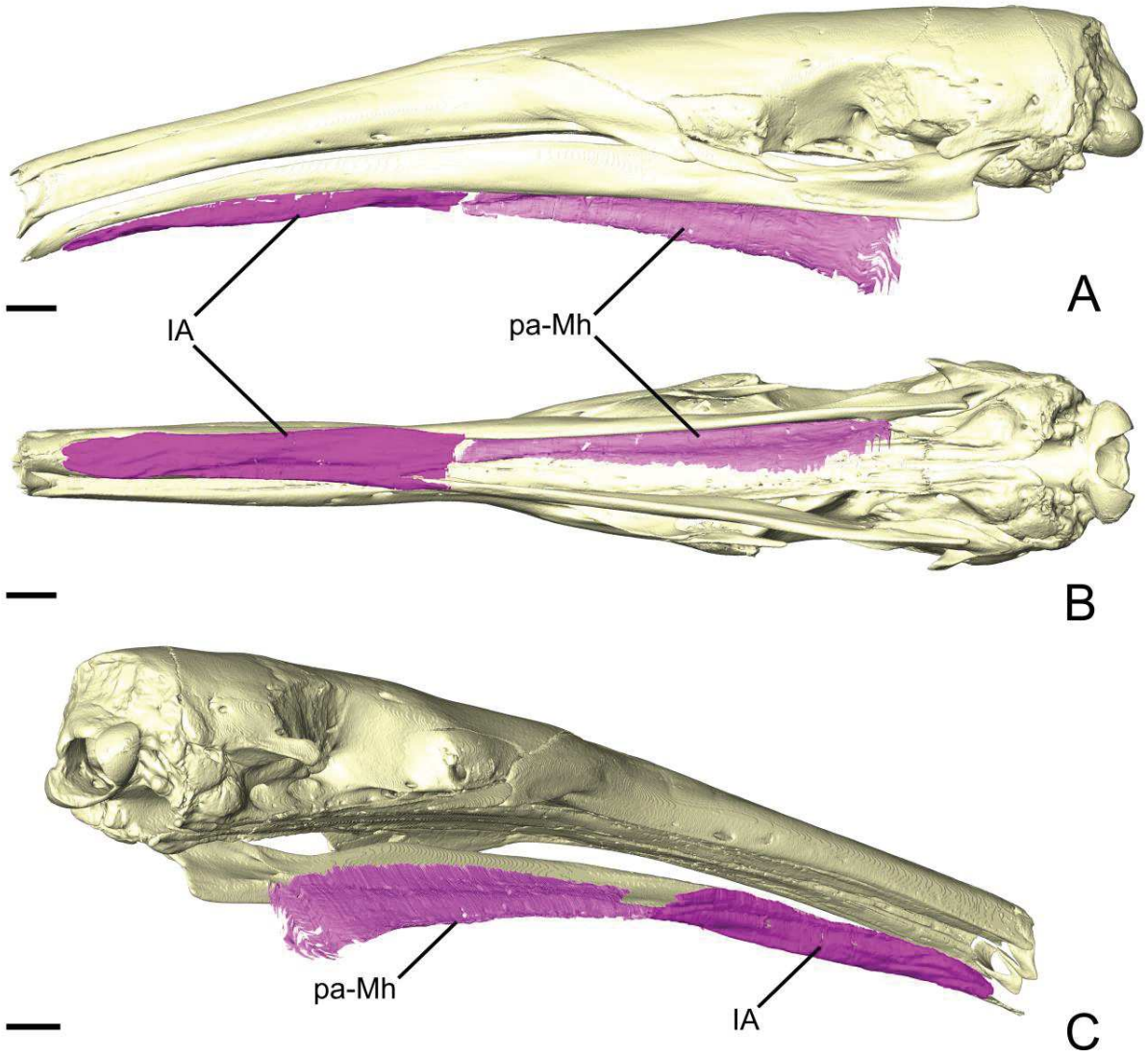

Figure 15 – The intermandibular musculature of *M. tridactyla* in lateral (A), ventral (B), and posteromedial (C) view. Scale bar 10 mm.

Comparison

Masticatory apparatus, auxiliary facial muscles, and intermandibular musculature

The anatomy of the masticatory apparatus is similar in the three studied species of anteater (Figs. 4, 10, 14). However, the *pterygoideus* and *masseter* complexes present different number of elements between the Cyclopedidae and the Myrmecophagidae. While in *M. tridactyla* and *T. tetradactyla* the *pterygoideus medius* (PM) is divided into anterior (pa-PM) and posterior (pp-PM) parts, *C. didactylus* shows one single

unit (Fig. 5) that could not be separated neither with digital or classical dissection. The PM of *C. didactylus* also differs from that of Myrmecophagidae in the more reduced anterior extension of its origin. In *M. tridactyla* and *T. tetradactyla*, the pa-PM origin on the palate extends anteriorly to the level of the optic foramen (Figs. 10C and 14C, while in *C. didactylus* it is slightly more posterior (Figs. 5 and 7A). *C. didactylus* also presents a very dense layer of connective tissue, which is located laterodorsally to the insertion of the PM on the mandible.

The mandibular musculature of *C. didactylus* can also be distinguished from that of the other anteaters by the presence of a dorsolaterally oriented *mandibuloauricularis* (MA). This is due to a more anterior position of the auricular cartilage in *C. didactylus* compared to myrmecophagids. The fossa for the external auditory meatus is anterodorsally elongated, with its anterior margin reaching the base of the zygomatic process of the squamosal (Fig. 4B). Another trait that distinguishes *C. didactylus* musculature is the absence of a *masseter profundus*. *C. didactylus* also lacks a jugal bone, which is the origin of the *masseter profundus* in myrmecophagids. The *masseter superficialis* muscle fibers are further posteroventrally from the upper jaw in *C. didactylus* compared to the myrmecophagids. Therefore, the *masseter superficialis* is attached to the upper jaw by a long tendon in *C. didactylus* (Fig. 4). Additionally to the lack of a *masseter profundus, C. didactylus* displays a bipartite *masseter superficialis* (Fig. 4), while it is composed by a single layer in myrmecophagids (Figs. 10 and 14). Volume wise, the *masseter superficialis* (MS) is much larger in *T. tetradactyla* and *M. tridactyla* (Table 1). These differences are reflected in the muscle shape, with the MS being thicker in the latter two than in *C. didactylus*.

The remaining differences between the masticatory apparatus of *C. didactylus* and myrmecophagids relates to muscle shape and proportions. The *temporalis* muscle complex is proportionally much larger in *C. didactylus* than in myrmecophagids (Table 1). The *temporalis superficialis* (TS) accounts for 42.2% of the total volume of the masticatory apparatus, while in *T. tetradactyla* this proportion is reduced by half (20.9%) and to 13.5% in *M. tridactyla* (Table 1). In myrmecophagids, the TS is flatter and compressed by the large lacrimal gland (Figs. 10, 14). Contrary to *M. tridactyla* and *C. didactylus*, the TS fibers are bipennated (Fig. S1B), their insertion on the coronoid process is muscular rather than aponeurotic. The *temporalis profundus* (TP) is relatively larger compared to its counterparts in *M. tridactyla* and *T. tetradactyla*. The *pars lateralis* (pl-TP) is twice as large in *C. didactylus* (Table 1) and shows a higher origin in the temporal fossa (Figs. 4B, 10B, and 14B). The *pars*

zygomatica of the *temporalis superficialis* (pz-TS) presents an inverse trend in volume percentage, being smaller in *C. didactylus* than in myrmecophagids (Table 1).

The volumes of the *pterygoideus* complex show a trend for an increase of the *pars superior* of the *pterygoideus externus* (ps-PE) with specimen size. Both *pterygoideus externus pars inferior* (pi-PE) and *pterygoideus medius* showed some differences in volume that do not appear to present any correlation with specimen size (Table 1).

Volume percentages in the facial-masticatory and transverse mandibular muscles show similar values in all three species. Anatomically, the muscles are very similar in all species, with the *buccinatorius* muscles (B) changing proportionately with rostrum elongation. This layer exhibits keratinous spicules with the apex oriented posteromedially.

The *intermandibularis anterior* is similar in all three species.

Hyoid, thyroid, and pharynx musculature

We report four main differences between *T. tetradactyla* and *C. didactylus*. First, we describe the presence of a *tensor veli palatini* (t-VP) in *C. didactylus* while this muscle is absent in *T. tetradactyla*. Secondly, the *levator veli palatine* (l-VP) presents a slightly individualized posterodorsal layer (Fig. S1) in *T. tetradactyla* while it forms a simple strap in *C. didactylus*. The *medialis veli palatini* (m-VP) is extremely elongated in *T. tetradactyla* compared to that of *C. didactylus* (Figs. 8 and 12). In the former, the posterior tip of the m-VP projects more posteriorly relative to the dorsal margin of the thyrohyal. Lastly, the *ceratohyoideus* (CeH) is relatively much larger in *C. didactylus* than in *T. tetradactyla* (Figs. 8 and 12).

The only noteworthy difference is the attachment of the posterior part of the *mylohyoideus pars anterior* (pa-Mh) to the posterior part of the PM in *C. didactylus*. In *T. tetradactyla* and *M. tridactyla*, this muscle detaches from the mandible to attach directly to the pterygoid bone, posteriorly.

Facial musculature

Differences in the facial musculature are related with the number of individual elements (Fig. 6). *C. didactylus* present the lowest number of muscles (*n* = 4) and *M. tridactyla* the largest number (*n* = 7), while *T. tetradactyla* is more intermediate (n = 5). The *dilator nasi* (DN) and the *maxillolabialis profundus pars inferior* (pi-MLp) are present in all species (Fig. 6). In *C. didactylus*, the pi-MLp originates dorsally on the maxilla, just dorsal to the tendinous insertion of the *masseter superficialis* (MS). In myrmecophagids, the origin of the pi-MLp is located more ventrally (Fig. 6). The *maxillolabialis profundus pars superior* (ps-MLp) is also present in all species, with a second similar but smaller element present between the former and the pi-MLp. We name it *maxillolabialis profundus pars media* (pm-MLp; see 'Results'). *M. tridactyla* presents a unique *maxillolabialis profundus pars anterior* (pa-MLp) that resembles an anterior extension of the pi-MLp (Fig. 6).

The superficial layer of the *maxillolabialis* complex is made up of one element in *C. didactylus* and two in *T. tetradactyla* and *M. tridactyla* (Fig. 6). The *maxillolabialis superficialis pars superior* (ps-MLs; Fig. 6) is topologically similar in *T. tetradactyla* and *C. didactylus*. It overlies, to some extent, the DN and the pi-MLp in both species, but also the pi-MLp in *C. didactylus*. Its origin is located over the maxilla-frontal-lacrimal intersection in *C. didactylus*, with the muscle fibers becoming more anterior in the largest species (Fig. 6). In *M. tridactyla*, the posterior fibers arise at the level of the anterior process of the frontal. The *maxillolabialis superficialis pars inferior* (pi-MLs) is only present in the myrmecophagids (Fig. 6). It forms a sheet that resembles the pi-MLp in *T. tetradactyla*, while its origin is more dorsal and only marginally overlies the pi-MLp in *M. tridactyla* (Fig. 6).

Discussion

Comparative myology in anteaters

The upper and lower jaws of anteaters represent a unique example of extreme skull elongation within mammals. Anteaters are completely toothless and have lost the ability to perform chewing movements (Naples, 1999). Despite this, as in most other mammals, their jaw mechanics is defined by a conserved number of homologous muscular elements (Greaves, 2012).

Our results mostly agree with previous descriptions of the muscular anatomy of anteaters (Owen, 1856; Windle & Parsons, 1899; Naples, 1985a, 1999; Reiss, 1997; Endo *et al.*, 2007, 2017), except for the recognition of the *intermandibularis anterior* muscle (IA). Naples (1999) considered this muscle as being a part of the *mylohyoideus* (ML). We showed that this muscle is attached to the ventrolateral margin of the anterior part of the lower jaws, which contrasts with the insertion area of the *mylohyoideus*. Furthermore, we confirmed that the IA is made of transversally continuous fibers. The *mylohyoideus pars posterior* (pp-Mh) and *pars anterior* (pa-Mh) comprise two bilaterally symmetric muscles that join along a midline axis (Fig. S1C). A similar condition is found in anteaters' sister taxon, sloths (Naples, 1986), as well as in other mammals like moonrats (Turnbull, 1970), nectarivorous bats (Wille, 1954), and humans (Gray, 1995). Turnbull (1970) uses two criteria to assign a *digastricus pars anterior* to the *mylohyoideus*: i) the presence of intertonguing connection at the midline, and ii) the contiguity of the attachment on the mandible. None of these conditions was found in the "*pars anterior* of the *mylohyoideus*" (*sensu* Naples, 1999). Therefore, we propose to consider this muscle as the *intermandibularis anterior* (Diogo *et al.*, 2008). The *mylohyoideus pars anterior* (*sensu* Naples, 1999), the *transversus mandibularis* of rats (Greene, 1935) and the *pars anterior* of the *mylohyoideus* of tree-shrews (Le Gros Clark, 1924) are developmentally distinct from the true *mylohyoideus*, the former being homologous with the sarcopterygian *intermandibularis anterior* while the latter is homologous to the *intermandibularis posterior* (Diogo *et al.*, 2008). This muscle acts as a stabilizer of the mandibular symphysis (Hautier & Saksiri, 2009). It is found mostly in mammals in which this structure is especially mobile (Hiiemae & Houston, 1971).

In agreement with previous works (Naples, 1999; Endo *et al.*, 2007, 2017), we showed that the complexity of the *masseter* is reduced compared to the condition observed in other mammals (Naples, 1985b). We follow Naples (1999) in considering that *C. didactylus* presents a single *masseter superficialis*, divided in two parts. *C. didactylus* presents one single large tendon that connects the *masseter* musculature to the zygomatic process of the maxilla, with both parts presenting a *pars reflexa*. This suggests that the *masseter* muscle of *C. didactylus* is reduced to a superficial element. On the other hand, Endo (2007, 2017) divided the *masseter* musculature of *T. tetradactyla* and *M. tridactyla* in deep and superficial separate muscles. This would imply that the *masseter profundus* was lost in the cyclopedid lineage. In other mammals, the *masseter profundus* arises from the zygomatic arch (Turnbull, 1970; Cox & Jeffery, 2011; Fabre *et al.*, 2017; Ginot *et al.*, 2018), which is absent in *C. didactylus.* Such a loss could be linked to the absence of a *masseter profundus,* given that cartilage-bone development is partly dependent on

embryonic muscular contractions (Hall & Herring, 1990; Atchley & Hall, 1991; Rot-Nikcevic *et al.*, 2006; Zelditch *et al.*, 2008). In contrast, jugal bones are present in *T. tetradactyla* and *M. tridactyla*, and associated with a separate *masseter profundus*, as observed in their sister taxon (i.e. sloths; Naples, 1985b). The presence of two *masseter* muscles therefore represents the plesiomorphic condition for anteaters. The complete loss of a functional zygomatic arch and *masseter profundus* in *C. didactylus* offers a striking example of developmental integration linked to muscle bone interaction, as well as an empirical evidence of modularity within the masticatory apparatus.

Despite the presence of a jugal bone in *Tamandua* and *Myrmecophaga*, all anteaters putatively lack a *zygomaticomandibularis* muscle (Edgeworth, 1923; Naples, 1999). However, we found a well-separated *pars zygomatica* of the *temporalis superficialis* in the three species of anteaters, especially in *C. didactylus*. Naples (1985b) proposed that the *temporalis superficialis* of *Choloepus* spp. (two-toed sloths) presented a *pars zygomatica*. Naples (1999) homologized the posterolateral part of the *temporalis superficialis* of *M. tridactyla* with the *pars zygomatica* of *Choloepus*. Contrary to the *temporalis superficialis pars zygomatica* in the two-toed sloths (Naples, 1999), we showed that the *pars zygomatica* does not insert on the anterior edge of the coronoid process, in anteaters. Instead, it inserts on along the medial part of the mandibular notch (Figs. 1B, 4, 10, 14). Edgeworth (1914) argues that the *zygomaticomandibularis* (*sensu* Turnbull, 1970) separates from the temporal during the development of *Dasyurus* spp. (quolls), which might be equally the case in other mammals (Druzinsky *et al.*, 2011). According to Druzinsky *et al.* (2011), the *zygomaticomandibularis* is not separable from either the *masseter* or the *temporalis* complexes in some carnivores, ungulates, bats, and marsupials. We argue that the *temporalis superficialis pars zygomatica* of anteaters is not homologous to that of *Choloepus* spp. (Naples, 1985b) and other xenarthrans (Edgeworth, 1923), but instead might be related to the "*zygomaticomandibularis posterior*" (Druzinsky *et al.*, 2011; Fabre *et al.*, 2017). This homology is retained here as a working hypothesis. We propose that the name of the *temporalis superficialis pars zygomatica* should not be changed until further evidence is collected from embryological data.

Functionally, we found evidence for a shift between *C. didactylus* and the myrmecophagid anteaters. The temporal musculature appears to play a much more relevant role in mandibular movements in *C. didactylus* (42.2%) than in larger anteaters (13.5-20.9%). On the other hand, both myrmecophagids present a *masseter* musculature accounting for about a third of the total volume, while it is three times smaller in *C. didactylus*. While this may relate directly with the loss of a true deep *masseter*, it also implies

a change in the position and orientation of the main vector of force contributing for mandibular elevation (Hylander, 2006; Greaves, 2012). The *masseter superficialis* generates anterodorsally directed forces (Barbenel, 1972; Baron & Debussy, 1979; Fabre *et al.*, 2017). On the other hand, the *temporalis* complex generates forces with vertical to posterodorsal directions (e.g., Barbenel, 1972; Baron & Debussy, 1979). This is due to its subdivisions (two to four) that contribute with differently oriented force vectors (e.g., Turnbull, 1970; Otten, 1988). Naples (1999) suggested that the *masseter* and *temporalis* musculature plays a role in depressing the medial and ventral edges of the mandible in *M. tridactyla*. The *temporalis* generates a medial rotation of the dorsal edge of the ascending ramus of the mandible, while the *masseter* contributes to the rotation of its ventral margin (Naples, 1999). As a result, the anteroventral part of the mandibular body depresses while the unfused mandibular symphysis cartilage stretches during tongue protrusion.

We showed that the masticatory apparatus of *T. tetradactyla* is very similar to that of *M. tridactyla* and therefore support Endo's (2017) view that mandibular movement is probably similar in both species. The musculature of the masticatory apparatus of *C. didactylus* differs not only in terms of proportions and number of *masseter* elements, but also at the level of the fiber architecture, with its *temporalis superficialis* exhibiting a bipennate arrangement of oblique fibers (Fig. S1B). Bipennate and multipennate muscles generate larger forces (increased physiological cross-section areas) than unipennate muscles or muscles with parallel fiber arrangement (Turnbull, 1970; Gans & de Vree, 1987; Hylander, 2006). This appears to correlate with the relatively more developed ascending ramus of the mandible, particularly the coronoid process. Although the initiation of the coronoid development is an intrinsic process to the mandibular ossification, its growth is dependent on muscle-bone interaction (Anthwal, Peters, & Tucker, 2015). As discussed previously, the absence of jugal bone is probably related the extremely reduced *masseter* musculature. A similar condition is found in the tailless tenrec (*Tenrec ecaudatus*; Oron & Crompton, 1985). As in *C. didactylus*, tailless tenrecs have lost the jugal bones and the *masseter profundus*, displaying a relatively small *masseter superficialis* with a tendinous insertion on the zygomatic process of the maxilla (Oron & Crompton, 1985). Their *temporalis* musculature, on the other side, makes up for most of the adductor muscles' volume (Oron & Crompton, 1985).

Despite the differences between *C. didactylus* and myrmecophagids, all anteaters present many similarities regarding their adaptations to ant- and termite-eating: an unfused mandibular symphysis, the presence of an *intermandibularis anterior*, a well-developed *mylohyoideus* muscle, an extremely long

sternoglossus, and the absence of a *digastricus* muscle. This suggests that mouth opening during tongue protrusion in *C. didactylus* might be similar to that of *T. tetradactyla* and *M. tridactyla.* The orientation of the ascending ramus and the coronoid process supports this view. Contrary to other mammals (e.g., Turnbull, 1970), *C. didactylus* presents laterally oriented coronoid processes (Figs. 4B, 5A). Then, the contraction of the *temporalis superficialis* pulls the coronoid process medially, causing the ventral margin of the mandibular body to rotate laterally. The larger forces generated by the *temporalis* complex and the shorter horizontal body of the mandible in *C. didactylus* compared to myrmecophagids, might result in very similar mandibular movements and global momentum to those in myrmecophagids, despite the reduction of the *temporalis* muscle in the latter. As in anteaters, the mandibular symphysis of the tailless tenrecs is highly mobile, allowing a high degree of movement around the longitudinal axis of the mandible (Mills, 1966; Oron & Crompton, 1985). Oron and Crompton (1985) suggested that the loss of the *masseter profundus* and the reduced complexity of molars facilitate the mediolateral rotation of the mandible during occlusion. The morphological similarities between *C. didactylus* and *T. ecaudatus* suggest that similar mediolateral rotation of the jaws is possible despite a shift in force distribution during the chewing cycle.

In addition to anteaters and tenrecs, mandibular mediolateral rotation plays a key role in mysticetes (Marshall, 2009; Pyenson *et al.*, 2012). The innervation patterns of the toothless dorsal margin of the mandible in anteaters and baleen whales, and its sensorial role in the coordination between mandibular movements and tongue protrusion/gulping (anteaters and baleen whales respectively) was previously discussed (Peredo *et al.*, 2017; Ferreira-Cardoso *et al.*, 2019). Assuming this link, the presence of similar patterns of dorsal canaliculi in *C. didactylus* and myrmecophagids is an additional evidence of similar mandibular movements. However, this will have to be demonstrated by applying biomechanical models to the masticatory apparatus of all three anteater genera.

Similar function in morphologically distinct masticatory apparatus makes extant anteaters an example of many-to-one-mapping of form to function (Wainwright *et al.*, 2005; Strobbe *et al.*, 2009). Extant anteaters lineages diverged during the late Eocene (≈37.8 Mya, Gibb *et al.*, 2016) with the earliest fossil dating back from the Late Oligocene to the Early Miocene (≈23.0 Mya; Carlini *et al.*, 1992). Currently, it is not known if their most recent common ancestor was toothless and myrmecophagous. Nevertheless, Meredith *et al.* (2009) showed that the enamelin gene (*ENAM*) was already non-functional (pseudogene) in the common ancestor of Pilosa (anteater and sloths). Furthermore, their ancestral state reconstruction indicated that the common ancestor to the Vermilingua was probably toothless. In this

scenario, strict myrmecophagy is plesiomorphic to this clade, with associated functional adaptation and changes to the masticatory apparatus occurring differently under in the two extant lineages (Cyclopedidae and Myrmecophagidae).

Endo (2017) described a vestigial "*digastricus posterior*" in *T. tetradactyla*, but probably referred to the *mandibuloauricularis*, as no connections were found with the hyoid apparatus. We did not find a *digastricus pars posterior* neither during the classical nor the virtual dissections, confirming observations by Naples (1999). Contrary to previous publications (Naples, 1985a; Reiss, 1997) we identified a *pars externa* of the *buccinatorius* in *C. didactylus*. Our observations of the *buccinatorius* (*pars interna* and *externa*) confirmed the importance of this muscle in the feeding apparatus of all extant anteaters. Naples (1999) highlighted the role of this muscle in contributing to the removal of attached ants during tongue protrusion.

Comparison with the myology of pangolins

Pangolins are often referred to as scaly-anteaters and are a well-known example of ecological and morphological convergence with anteaters (McGhee, 2001; Rose *et al.*, 2005). However, pangolins present several muscular differences with anteaters in their skull. First, the *masseter* muscle appears to be more complex than in anteaters, with three parts described in *Manis javanica* (Sunda pangolin; Endo *et al.*, 1998). In contrast, Windle and Parsons (1899) reported that the *masseter* is thin and "unilaminar" in *Manis* spp., taking its origin on a "fibrous zygoma". Three muscle bundles are visible in Endo *et al*. (1998; Fig. 7), the anterior two putatively originating on the zygomatic process of the maxilla, while the posterior one originates from the zygomatic arch. The areas of origin of the *masseter* are not illustrated and differences in fiber orientation are not provided (Endo *et al.*, 1998), although the most anterior bundle appears to be the most vertically oriented (Fig. 7; Endo *et al.*, 1998). This might suggest the existence of a *masseter superficialis* with two parts, as in *C. didactylus*, with a small *masseter profundus* anteriorly. However, the origins reported by Endo and colleagues (1998) do not correspond to such divisions (e.g., Turnbull, 1970). Edgeworth (1923) describes the *masseter* as arising from the "lower margin of the zygomatic portion of the superior maxilla", while a more oblique muscle arises from the medial surface of the zygomatic arch ("*zygomaticomandibularis*"). The figures associated to Edgeworth's (1923; Figs. 59 and 60) suggest that the author's *zygomaticomandibularis* could also be a *masseter profundus*. It is not possible, with the available information, to establish clear homologies with the *masseter* of anteaters.

However, previous reports suggested that the *masseter* of pangolins is multi-layered (*contra* Windle and Parsons, 1899), possibly composed of two separate parts as in *T. tetradactyla* and *M. tridactyla*. Furthermore, if pangolins have a "true" *zygomaticomandibularis*, this muscle is not homologous to the putative *zygomaticomandibularis* of anteaters as discussed above.

Second, the *pterygoideus* complex of pangolins is composed of a *pterygoideus externus*, and a *pterygotympanicus* (Edgeworth, 1923; Endo *et al.*, 1998). Edgeworth (1923) described a *pterygoideus medius* that is atrophied during development, with a medial *pterygo-hyoideus* connecting to the epihyal-stylohyal bones. Yeh (1984) and Endo *et al.* (1998) reported the absence of *pterygoideus medius.* An accurate description of the *pterygo-hyoideus* in the adult pangolin was not provided. As for the *pterygoideus externus*, Endo *et al.* (1998) suggested the presence of two muscles bundles, but did not consider this muscle to be divided in two parts, as in anteaters. It appears that the *pterygoideus externus* of pangolins corresponds to the *pars inferior* of the muscle in anteaters, as it arises from the pterygoid bone (Edgeworth, 1923). In anteaters the *pars superior* of the *pterygoideus externus* arises from the parietal bone, just ventrally to the temporal fossa. Lastly, pangolins present a muscle not found in anteaters: the *pterygotympanicus* (Edgeworth, 1923) that takes its origin on the ventral part of the alisphenoid bone and inserts on the tympanic bulla. A posteromedial projection of this muscle gives rise to the *tensor veli palatini*, a muscle that we found exclusively in *C. didactylus*.

Unlike anteaters, pangolins appear to present a *digastricus* (Endo *et al.*, 1998). It is, nevertheless, less developed than in other mammals (e.g., Turnbull, 1970). Endo *et al.* (1998) described two parts of the digastric, with the lateral part corresponding to what is commonly known as the "posterior belly". Windle and Parsons (1899) also described a *digastricus* in pangolins, although not dividing it into two distinct parts. Edgeworth (1923) homologized the *digastricus* of Windle and Parsons (1899) to the *mandibuloauricularis*.

In pangolins, the tongue musculature is composed of a *sternoglossus* (fusion of the *hyoglossus* with the *sternohyoideus*) reaching an extremely long xiphoid cartilage at the posterior end of the sternum (Macalister, 1875; Jentink, 1882; Edgeworth, 1923). This condition is similar to that found in anteaters, although the xiphoid cartilage is relatively much longer in pangolins (Doran & Allbrook, 1973). Unlike in anteaters, the *sternohyoideus* does not contribute to the posterior part of the *sternomandibularis*, and this muscle appears to be completely absent (Windle & Parsons, 1899; Edgeworth, 1923; Endo *et al.*,

1998). The *geniohyoideus* fuses with its bilateral counterpart into a medial band, then presenting two lateral bands posteriorly, as in anteaters.

Also, in pangolins, both *intermandibularis anterior* and *posterior* have been described (Edgeworth, 1923). However, both present a medial raphe, which suggests that these elements are homologous to the *mylohyoideus pars anterior* and *posterior* of anteaters. The attachment of the latter to the pterygoid bone is similar to the condition in *T. tetradactyla* (Fig. 11). Endo (1998) described a single *mylohyoideus* in *Manis javanica* (Sunda pangolin), but gave no details about the origin of the muscle's attachment to the skull. Previous description appeared to suggest the absence of a true *intermandibularis anterior* (*sensu* Diogo *et al.*, 2008) in pangolins. This is congruent with the presence of a fused symphysis. However, further dissections are needed to verify the presence of this muscle.

Edgeworth (1923) reported the early differentiation of the *thyrohyoideus* and the *sternothyroideus* from the *rectus cervicis*, describing the origin and insertions of these muscles, which are similar to those in anteaters. The author also described the presence of the larynx dilator *cricoarytenoideus posterior* ("*crico-arytenoideus posticus*"), the *arytenoideus*, and the *thyroarytenoideus*. As in anteaters, the *thyroarytenoideus* arises from the basal part of the thyroid cartilage and inserts on the arytenoid cartilage, and is divided in two parts that are designated as *superior* (*thyroarytenoideus pars lateralis*) and the smaller *inferior* (*thyroarytenoideus pars medialis;* Figs. 8 and 12). In *Manis* spp., the origin of the *thyrohyoideus pars medialis* is located on a median posterior process (Edgeworth, 1923), which is absent in the thyroid of anteaters. The *arytenoideus lateralis* is illustrated, as well as the *cricothyroideus*. Edgeworth (1923) did not report the division of the former in two parts, as is the case in anteaters. Both *stylopharyngeus* and the *constrictores pharingis* were also described, with no differences to report.

Despite several studies dedicated to the head musculature of pangolins (e.g., Macalister, 1875; Windle & Parsons, 1899; Edgeworth, 1923; Imai, 1978; Endo *et al.*, 1998), these articles present virtually no information concerning volume or mass ratios and references to the functional aspect are anecdotic. The different nomenclatures used by each author and the different level of detail, associated with poor illustration, call for a unifying description of the musculature of pangolins. Future research on the pangolin head musculature would greatly contribute to assess the putative morphological convergence of their masticatory apparatus with that of anteaters. Key questions, like the existence of an *intermandibularis anterior* (*sensu* Diogo, 2008), and the biomechanics of the pangolin masticatory apparatus would much benefit from a thorough review. In particular, the putative absence of an *intermandibularis anterior* in

pangolins suggests a decreased degree of symphysial mobility when compared to anteaters. Furthermore, pangolins lack dorsal canaliculi, structures hypothesized to be associated to the coordination of the mediolateral rotation of the mandibles in anteaters (Ferreira-Cardoso *et al.*, 2019). A quantitative assessment using modern techniques is key to associate these morphological traits to function.

Comparison with aardvark myology

The head muscles of the aardvark (*Orycteropus afer*), a myrmecophagous tubulidentate, ,have been the subject of several studies (Humphry, 1868; Galton, 1869; Windle & Parsons, 1899; Bender, 1909; Edgeworth, 1924; Sonntag, 1925). Although information on volume, mass, or rations is currently unavailable for head muscles, the masticatory, intermandibular, and hyoid musculature is relatively well-described and illustrated (Edgeworth, 1924; Sonntag, 1925). Similarly to other myrmecophagous species, the aardvark also possesses an elongated and specialized tongue (Goździewska-Harłajczuk, Klećkowska-Nawrot, & Barszcz, 2018), an elongated snout, and a regressed dentition lacking enamel. However, the aardvark presents a developed ascending ramus of the mandible, with prominent coronoid and condylar processes, and a broad masseteric fossa (e.g., Edgeworth, 1924; Ferreira-Cardoso *et al.*, 2019). The aardvark is also able to chew (Patterson, 1975).

The *masseter* of *O. afer* has been characterized as thin and flat (Sonntag, 1925), but it is fan-like (vertical to longitudinal fibers) and presents a *pars reflexa* posterodorsally (Edgeworth, 1924; Sonntag, 1925). In the absence of more details, it appears that the architecture of the *masseter* of *O. afer* is more complex than that of anteaters and pangolins. Unlike anteaters, *O. afer* presents a *zygomaticomandibularis* that inserts on the lateral surface of the mandible dorsally to the *masseter*. This muscle has vertically oriented fibers and originates along the jugal and the anterior part of the zygomatic process of the squamosal (Edgeworth, 1924; Sonntag, 1925). It is probably not related to the *masseter pars zygomatica* of anteaters, as its insertion on the mandible is much more anteroventral and its origin further apart from the temporal fossa (Edgeworth, 1924). The *temporalis* of *O. afer* also differs from that of anteaters as it extends dorsally and posteriorly into the cranial vault and covers both lateral and medial surfaces of the coronoid process, as well as its anterior and posterior margins (Edgeworth, 1924; Sonntag, 1925).

The *pterygoideus* complex in *O. afer* presents some differences when compared to that of anteaters (Edgeworth, 1924; Sonntag, 1925). Its *pterygoideus medius* presents three parts, while only two were

identified in *M. tridactyla* and *T. tetradactyla*, and a single in *C. didactylus.* The *pterygoideus externus* is composed of a single part arising from the alisphenoid bone which makes it probably homologous to the *pars inferior* of the same muscle in anteaters (Fig. 5). As in pangolins, the aardvark presents a *pterygotympanicus* that originates on the ectotympanic and displays a tendinous connection to the *tensor veli palatini*, on the palate (Edgeworth, 1924; Sonntag, 1925). The association of the *pterygotympanicus* with the *tensor veli palatini* suggests that both muscles might aid in the elevation of the soft palate by the *levator veli palatini* (Auer *et al.*, 1999; Kishimoto *et al.*, 2016). *T. tetradactyla* and *M. tridactyla* lack both the *pterygotympanicus* and a separate *tensor veli palatini*. *C. didactylus* lacks the former, but presents a *tensor veli palatine* in close association with the posterior fibers of the *pterygoideus medius* on the palate.

O. afer presents a longitudinal "*intermandibularis*" that takes its origin on the hyoid and sends two tendons that insert anteriorly on the ventrolateral surface of the mandibles (Edgeworth, 1924). Sonntag (1925) suggested that this muscle might correspond to the *mylohyoideus,* but the attachment to the mandible and the longitudinal orientation resemble more those of a *digastricus pars anterior* (Turnbull, 1970; Gray, 1995). Inversely, both Sonntag (1925) and Edgeworth (1924) suggested that the transversely oriented muscle attaching medially to the posterior half of the mandibles is a "*digastricus anterior*". This muscle presents a variable median raphe, such as the *mylohyoideus* musculature in anteaters and other mammals (Edgeworth, 1914; Saban, 1968; Turnbull, 1970), and it does not connect to the *digastricus pars posterior* (Edgeworth, 1924; Sonntag, 1925). Therefore, we propose that the "*digastricus anterior*" (*sensu* Sonntag, 1925; and Edgeworth, 1924) of the aardvark is a *mylohyoideus pars anterior*. We also propose that the "*intermandibularis*" of Edgeworth (1924) and Sonntag (1925) is homologous to the *geniohyoideus* of anteaters, as both are longitudinally oriented, present an anterior bifurcation of the muscular fibers, and take their origin on the ceratohyal and basihyal. While we cannot confirm the correct identity of these muscles in *O. afer*, it is clear that, as in pangolins, both *pars anterior* and *posterior* of the *digastricus* are present. Both of these muscles are absent in anteaters.

Despite being elongated, the tongue of the aardvark does not attach to the sternum like in anteaters (Windle & Parsons, 1899; Sonntag, 1925). Both the *genioglossus* (which forms the base of the tongue) and the *hyoglossus* attach to the hyoid system (Sonntag, 1925). Additionally, a separated *sternohyoideus* is present in the aardvark (Sonntag, 1925). In anteaters, *hyoglossus* and *sternohyoideus* merge to form the extremely long *sternoglossus* (Edgeworth, 1935; Naples, 1999). The tongue musculature of the aardvark

therefore presents a structure similar to other mammals, such as sloths or rats (Greene, 1935; Naples, 1986).

The hyoid-thyroid and thyroid-cricoid musculatures were described by Sonntag (1925). This author omitted any references to the *ceratohyoideus*, but this muscle was illustrated by Edgeworth (1924), under the "*branchio-hyoideus*" designation. This muscle serves both as a stabilizer of the hyoid apparatus, as well as a probable depressor of the pharynx (Reidenberg & Laitman, 1994). Sonntag (1925) also described the *crocothyroideus*, although no reference was made to the subdivision of this muscle. Apart from the absence of the *arytenoideus* in *O. afer*, the description of the remaining muscles is similar to those found in anteaters. Further comparison, mainly regarding the shape and size of these muscles, is not possible with the details available from the literature.

The aardvark facial muscles are also different from anteaters, as suggested by Sonntag, (1925) and include a *buccinatorius internus*, which consists of a thin sheet in the aardvark. The aardvark presents a fleshy "*levator nasi*" that arises from the zygomatic process of the maxilla and extends to the anterior part of the snout, where it contributes with muscular fibers to the *"levator labii superioris alaeque nasi*" (Sonntag, 1925). The "*levator nasi*" appears to be homologous to the *maxillolabialis* of anteaters. In *O. afer*, the *maxillolabialis* lacks long tendons anteriorly and assumes a dorsal position in the snout (Sonntag, 1925). Whereas in anteaters we identified six separate muscles associated to the upper lip and buccal commissure, the single muscle "*levator labii superioris alaeque nasi*" appears to be responsible for elevating and retracting the snout. This muscle is also associated to the large sheet-like "*levator naso-labialis*" that arises from the frontal bone and inserts on the anterior tip of the snout and upper lip (Sonntag, 1925). Again, this condition contrasts with the much smaller *dilator nasi* in anteaters (Fig. 6), both in size, origin, and length of muscular fibers.

Although myrmecophagous, the masticatory apparatus of aardvarks is functionally different from that of anteaters. The biomechanics of their masticatory apparatus has not yet been quantitatively assessed, but the muscular and bone anatomy already indicate that movements and forces involved will be highly divergent from those of anteaters. The large *temporalis* and *masseter* muscles, the presence of an ossified zygomatic arch, and the fused mandibular symphysis suggest significant functional differences. The presence of a vertically oriented *zygomaticomandibularis* also suggests a more important vertical component of force when compared to anteaters. The aardvark actively chews in order to eat cucumber-like plants from which they take their water (Patterson, 1975). The articular condyle is well dorsal to their

tooth row, which typically allows for an increase in the momentum of force applied to food item (Greaves, 2012). These are both functional and phylogenetic constraints that likely affect the tongue movement and speed of ant and termite intake.

Conclusion

Here we described and illustrated the masticatory apparatus, hyoid, thyroid, and sternum musculatures of the three genera of extant anteaters. While *T. tetradactyla* and *M. tridactyla* showed very similar morphologies, the masticatory apparatus of *C. didactylus* was shown to be more different than previously thought. However, we suggested that different morphologies, mainly those of the *temporalis* and *masseter* complexes, allow very similar functions. We further compared data from the literature and showed that the biomechanics of anteaters may well differ from that of pangolins, despite of the ecological convergence (McGhee, 2011). We also compared the head musculature of anteaters with that of the aardvark and show that they differ in some key aspects, mainly related to the tongue and masticatory musculature. Further studies will be needed to assess biomechanical differences, notably the magnitude of forces applied to the mediolateral rotation of the lower jaws (e.g., Oron & Crompton, 1985), and to characterize jaws movement in anteaters and pangolins.

References

Alroy J. 1999. The fossil record of North American mammals: evidence for a Paleocene evolutionary radiation (P Waddell, Ed.). *Systematic Biology* 48: 107–118.

Anthwal N, Peters H, Tucker AS. 2015. Species-specific modifications of mandible shape reveal independent mechanisms for growth and initiation of the coronoid. *EvoDevo* 6: 35.

Atchley W, Hall B. 1991. A model for development and evolution of complex morphological structures. *Biological Reviews* 66: 101–157.

Auer JA, Stick JA, Kūmmerle JM, Prange T. 1999. *Equine surgery*.

Barbenel JC. 1972. The biomechanics of the temporomandibular joint: a theoretical study. *Journal of Biomechanics* 5: 251–256.

Barlow KE, Jones G, Barratt EM. 1997. Can skull morphology be used to predict ecological relationships between bat species? A test using two cryptic species of pipistrelle. *Proceedings of the Royal Society of London. Series B: Biological Sciences* 264: 1695–1700.

Baron P, Debussy T. 1979. A biomechanical functional analysis of the masticatory muscles in man. *Archives of Oral Biology* 24: 547–553.

Bender O. 1909. Die Halsorgane von *Orycteropus afer= capensis* (Pallas) und *Tamandua tetradactyla* L. *Denkschriften Der Medicinisch-Naturwissenschaftlichen Gesellschaft zu Jena* 15: 373–400.

Carlini AA, Scillato-Yane GJ, Vizcaino SF, Dozo MT. 1992. Un singular Myrmecophagidae (Xenarthra, Vermilingua) de Edad Colhuehuapense (Oligoceno tardío-Mioceno temprano) de Patagonia, Argentina. *Ameghiniana* 29.

Cox PG, Jeffery N. 2011. Reviewing the morphology of the jaw-closing musculature in squirrels, rats, and guinea pigs with contrast-enhanced microCT. *The Anatomical Record* 294: 915–928.

Davit-Béal T, Tucker A, Sire J. 2009. Loss of teeth and enamel in tetrapods: fossil record, genetic data and morphological adaptations. *Journal of anatomy* 214: 477–501.

Diogo R. 2018. Head and neck muscle evolution from sarcopterygian fishes to tetrapods, with a special focus on mammals. In: Diogo R, Ziermann J, Molnar J, Siomava N, and Abdala V, eds. *Muscles of chordates: development, homologies, and evolution*. Boca Raton, Florida: CRC Press, .

Diogo R, Abdala V. 2010. Muscles of vertebrates: comparative anatomy, evolution, homologies and development.

Diogo R, Abdala V, Lonergan N, Wood BA. 2008. From fish to modern humans - comparative anatomy, homologies and evolution of the head and neck musculature. *Journal of Anatomy* 213: 391–424.

Doran GA, Allbrook DB. 1973. The tongue and associated structures in two species of African pangolins, *Manis gigantea* and *Manis tricuspis*. *Journal of Mammalogy* 54: 887–899.

Druzinsky RE, Doherty AH, De Vree FL. 2011. Mammalian masticatory muscles: homology, nomenclature, and diversification. *Integrative and Comparative Biology* 51: 224–234.

Edgeworth F. 1914. On the development and hyoid of the mandibular and hyoid muscles of mammals. *Quarterly Journal of Microscopical Science*.

Edgeworth FH. 1923. On the development of the cranial muscles of *Tatusia* and *Manis*. *Journal of anatomy* 57: 313–35.

Edgeworth FH. 1924. On the masticatory, intermandibular, and hyoid muscles of *Orycteropus capensis*. *Journal of anatomy* 58: 134–9.

Edgeworth F. 1935. *The cranial muscles of vertebrates.* Cambridge: Cambridge University Press.

Endo H, Ito K, Watabe H, Nguyen S, Koyabu D. 2017. Macroscopic and CT examinations of the mastication mechanism in the southern tamandua. *Mammal Study* 42: 89–96.

Endo H, Niizawa N, Komiya T, Kawada S, Kimura J. 2007. Three-dimensional CT examination of the mastication system in the giant anteater. *Zoological science* 24: 1005–11.

Endo H, Nishiumi I, Kurohmaru M, Nabhitabhata J, Chan-Ard T, Nadee N, Agungpriyono S, Yamada J. 1998. The functional anatomy of the masticatory muscles of the Malayan pangolin, *Manis javanica*. *Mammal Study* 23: 1–8.

Evans HE, De Lahunta A. 2013. *Miller's Anatomy of the Dog.* Elsevier Health Sciences.

Fabre PH, Herrel A, Fitriana Y, Meslin L, Hautier L. 2017. Masticatory muscle architecture in a water-rat from Australasia (Murinae, *Hydromys*) and its implication for the evolution of carnivory in rodents. *Journal of Anatomy* 231: 380–397.

Ferreira-Cardoso S, Delsuc F, Hautier L. 2019. Evolutionary tinkering of the mandibular canal linked to convergent regression of teeth in placental mammals. *Current Biology* 29: 468-475.e3.

Galton JC. 1869. XII. The myology of the upper and lower extremities of *Orycteropus capensis*. *Transactions of the Linnean Society of London* 26: 567–608.

Gans C, de Vree F. 1987. Functional bases of fiber length and angulation in muscle. *Journal of morphology* 192: 63–85.

Gaudin T, Branham D. 1998. The phylogeny of the Myrmecophagidae (Mammalia, Xenarthra, Vermilingua) and the relationship of Eurotamandua to the Vermilingua. *Journal of Mammalian Evolution*.

Gaudin TJ, Gaubert P, Billet G, Hautier L, Ferreira-Cardoso S, Wible JR. 2019. Evolution & morphology. In: Challender, D.W.S., Nash, H., Waterman C, ed. *Pangolins: Science, Society and Conservation*. Cambridge, MA: Academic Press, .

Gibb G, Condamine F, Kuch M, Enk J. 2016. Shotgun mitogenomics provides a reference phylogenetic framework and timescale for living xenarthrans. *Molecular Biology and Evolution* 33: 621–642.

Gignac PM, Kley NJ. 2014. Iodine-enhanced micro-CT imaging: methodological refinements for the study of the soft-tissue anatomy of post-embryonic vertebrates. *Journal of Experimental Zoology Part B: Molecular and Developmental Evolution* 322: 166–176.

Ginot S, Claude J, Hautier L. 2018. One skull to rule them all? Descriptive and comparative anatomy of the masticatory apparatus in five mouse species. *Journal of Morphology* 279: 1234–1255.

Goździewska-Harłajczuk K, Klećkowska-Nawrot J, Barszcz K. 2018. Macroscopic and microscopic study of the tongue of the aardvark (*Orycteropus afer*, Orycteropodidae). *Tissue and Cell* 54: 127–138.

Gray H. 1995. *Anatomy, descriptive and surgical*. Bristol: Parragon Book Service Ltd.

Greaves WS. 2012. *The mammalian jaw : a mechanical analysis*. Cambridge University Press.

Greene EC. 1935. *Anatomy of the rat*. New York: Hafner Publishing CO.

Le Gros Clark W. 1924. The myology of the tree-shrew (<i>Tupaia minor<i/>). *Proceedings of the Zoological Society of London*: 461–497.

Hall BK, Herring SW. 1990. Paralysis and growth of the musculoskeletal system in the embryonic chick.

Journal of Morphology 206: 45–56.

Hautier L, Lebrun R, Cox PG. 2012. Patterns of covariation in the masticatory apparatus of hystricognathous rodents: Implications for evolution and diversification. *Journal of Morphology* 273: 1319–1337.

Hautier L, Saksiri S. 2009. Masticatory muscle architecture in the Laotian rock rat *Laonastes aenigmamus* (Mammalia, Rodentia): new insights into the evolution of hystricognathy. *Journal of Anatomy* 215: 401–410.

Hiiemae K. 2000. *Feeding in mammals* (K Schwenk, Ed.). San Diego: Academic Press.

Hiiemae K, Houston W. 1971. The structure and function of the jaw muscles in the rat (*Rattus norvegicus* L.). *Zoological Journal of the Linnean Society* 50: 75–99.

Humphry G. 1868. On the myology of *Orycteropus capensis* and *Phoca communis*. *Journal of Anatomy and Physiology* 2.

Hylander W. 2006. Functional anatomy and biomechanics of the masticatory apparatus. *Temporomandibular Disorders: An Evidenced Based Approach to Diagnosis and Treatment*.3–34.

Imai M. 1978. The facial muscles of *Manis pentadactyla* Linne. *Okajimas Folia Anatomica Japonica* 55: 1–18.

Jentink FA. 1882. Revision of the Manidae in the Leyden Museum. *Notes from the Leyden Museum*: 193–209.

Kishimoto H, Yamada S, Kanahashi T, Yoneyama A, Imai H, Matsuda T, Takeda T, Kawai K, Suzuki S. 2016. Three-dimensional imaging of palatal muscles in the human embryo and fetus: development of levator veli palatini and clinical importance of the lesser palatine nerve. *Developmental Dynamics* 245: 123–131.

Klaczko J, Sherratt E, Setz EZF. 2016. Are diet preferences associated to skulls shape diversification in xenodontine snakes? (AR Evans, Ed.). *PLOS ONE* 11: e0148375.

Macalister A. 1875. Report on the anatomy of insectivorous Edentates. *The Transactions of the Irish Academy* 25: 491–508.

Maestri R, Patterson BD, Fornel R, Monteiro LR, de Freitas TRO. 2016. Diet, bite force and skull

morphology in the generalist rodent morphotype. *Journal of Evolutionary Biology* 29: 2191–2204.

Marshall CD. 2009. Feeding morphology. *Encyclopedia of Marine Mammals*. Academic Press, 406–414.

McGhee GR. 2001. Exploring the spectrum of existent, nonexistent and impossible biological form. *Trends in Ecology & Evolution* 16: 172–173.

McGhee GR. 2011. *Convergent evolution : limited forms most beautiful*. MIT Press.

Meredith RW, Gatesy J, Murphy WJ, Ryder OA, Springer MS. 2009. Molecular decay of the tooth gene enamelin (ENAM) mirrors the loss of enamel in the fossil record of placental mammals. *PLoS Genetics* 5.

Meredith R, Janečka J, Gatesy J, Ryder O, Fisher CF, Teeling EC, Goodbla A, Eizirik E, Simão TLL, Stadler T. 2011. Impacts of the Cretaceous terrestrial revolution and KPg extinction on mammal diversification. *Science* 334: 521–24.

Mills JRE. 1966. The functional occlusion of the teeth of Insectivora. *Journal of the Linnean Society of London, Zoology* 46: 1–25.

Miranda FR, Casali DM, Perini FA, Machado FA, Santos FR. 2018. Taxonomic review of the genus *Cyclopes* Gray, 1821 (Xenarthra: Pilosa), with the revalidation and description of new species. *Zoological Journal of the Linnean Society* 183: 687–721.

Montgomery G. 1983. *Cyclopes didactylus* (tapacara, serafin de platanar, silky anteater). *Costa Rican natural history*.461–463.

Montgomery G. 1985. Movements, foraging and food habits of the four extant species of Neotropical vermilinguas (Mammalia; Myrmecophagidae). In: Montgomery G, ed. *The evolution and ecology of armadillos, sloths and vermilinguas*. Washington, D.C.: Smithsonian Institution Press, 365–377.

Naples V. 1985a. The superficial facial musculature in sloths and vermilinguas (anteaters).

Naples VL. 1985b. Form and function of the masticatory musculature in the tree sloths, *Bradypus* and *Choloepus*. *Journal of Morphology* 183: 25–50.

Naples V. 1986. The morphology and function of the hyoid region in the tree sloths, *Bradypus* and *Choloepus*. *Journal of Mammalogy* 67: 712–724.

Naples V. 1999. Morphology, evolution and function of feeding in the giant anteater (Myrmecophaga tridactyla). *Journal of Zoology* 249: 19–41.

Nogueira MR, Peracchi AL, Monteiro LR. 2009. Morphological correlates of bite force and diet in the skull and mandible of phyllostomid bats. *Functional Ecology* 23: 715–723.

Oron U, Crompton AW. 1985. A cineradiographic and electromyographic study of mastication inTenrec ecaudatus. *Journal of Morphology* 185: 155–182.

Otten E. 1988. Concepts and models of functional architecture in skeletal muscle. *Exercise and Sport Sciences Reviews* 16: 89–138.

Owen R. 1856. On the anatomy of the great anteater (*Myrmaecophaga jubata*, Linn.). *The Transactions of the Zoological Society of London* 4: 117–140.

Parsons, G. F. 1896. Myology of rodents. Part II. An account of the myology of the myomorpha, together with a comparison of the muscles of the various suborders of rodents. *Proc. Zool. Soc. London* 20: 159–192.

Patterson B. 1975. The fossil aardvarks (Mammalia: Tubulidentata). *Bulletin of the Museum of Comparative Zoology at Harvard College* 147.

Peredo C, Pyenson N, Uhen M, Marshall C. 2017. Alveoli, teeth, and tooth loss: understanding the homology of internal mandibular structures in mysticete cetaceans. *PloS one* 12.

Pyenson N, Goldbogen J, Vogl A, Szathmary G. 2012. Discovery of a sensory organ that coordinates lunge feeding in rorqual whales. *Nature* 485: 498–501.

Redford K. 1987. Ants and termites as food. *Current mammalogy*.

Reidenberg JS, Laitman JT. 1994. Anatomy of the hyoid apparatus in Odontoceti (toothed whales): specializations of their skeleton and musculature compared with those of terrestrial mammals. *The Anatomical Record* 240: 598–624.

Reiss KZ. 1997. Myology of the feeding apparatus of myrmecophagid anteaters (Xenarthra: Myrmecophagidae). *Journal of Mammalian Evolution* 4: 87–117.

Reiss KZ. 2001. Using phylogenies to study convergence: the case of the ant-eating mammals. *American Zoologist* 41: 507–525.

Rinker G. 1954. The comparative myology of the mammalian genera *Sigmodon*, *Oryzomys*, *Neotoma*, and *Peromyscus* (Cricetidae).

Romer AS. 1974. *Vertebrate paleontology*. Chicago: Chicago University Press.

Rose KR, Emry RJ. 1993. Relationships of Xenarthra, Pholidota, and fossil 'Edentates': the morphological evidence. In: Szalay FS, Novacek MJ, and McKenna MC, eds. *Mammal phylogeny: placentals*. New York: Springer-Verlag, 81–102.

Rose K, Emry R, Gaudin T, Storch G. 2005. Xenarthra and Pholidota. In: Rose, Kenneth D.; Archibald JD, ed. *Placental mammals: origin, timing, and relationships of the major extant clades*. Baltimore, MD: Johns Hopkins University Press, 106–126.

Rot-Nikcevic I, Reddy T, Downing KJ, Belliveau AC, Hallgrímsson B, Hall BK, Kablar B. 2006. Myf5 −/− :MyoD −/− amyogenic fetuses reveal the importance of early contraction and static loading by striated muscle in mouse skeletogenesis. *Development Genes and Evolution* 216: 1–9.

Saban R. 1968. Musculature de la tête. In: Grassé P, ed. *Traité de Zoologie, XVI*. Paris: Masson et Cie, 229–472.

Schindelin J, Arganda-Carreras I, Frise E, Kaynig V. 2012. Fiji: an open-source platform for biological-image analysis. *Nature*.

Sonntag CF. 1925. A monograph of *Orycteropus afer*. - I. Anatomy except the nervous system, skin, and skeleton. *Proceedings of the Zoological Society of London* 95: 331–437.

Strobbe F, McPeek MA, De Block M, De Meester L, Stoks R. 2009. Survival selection on escape performance and its underlying phenotypic traits: a case of many-to-one mapping. *Journal of Evolutionary Biology* 22: 1172–1182.

Turnbull WD. 1970. Mammalian masticatory apparatus. *Fieldiana Geology* 18: 149–356.

Varrela J. 1990. Effects of attritive diet on craniofacial morphology: a cephalometric analysis of a Finnish skull sample. *The European Journal of Orthodontics* 12: 219–223.

Vickerton P, Jarvis J, Jeffery N. 2013. Concentration-dependent specimen shrinkage in iodine-enhanced microCT. *Journal of Anatomy* 223: 185–193.

Vizcaíno SF, Paleobiology S, Summer N, Vizcaino SF. 2009. The teeth of the " toothless ": novelties and

key innovations in the evolution of xenarthrans. *Paleobiology* 35: 343–366.

Wainwright PC, Alfaro ME, Bolnick DI, Hulsey CD. 2005. Many-to-one mapping of form to function: a general principle in organismal design? *Integrative and Comparative Biology* 45: 256–262.

Wille A. 1954. Muscular adaptation of the nectar-eating bats (Subfamily Glossophaginae). *Transactions of the Kansas Academy of Science* 57: 315.

Windle B, Parsons FG. 1899. On the myology of the Edentata. *Proceedings of the Zoological Society of London* 67: 314–339.

Yeh YC. 1984. Comparative studies on characteristic structures of sensory and motor mechanisms in the stomatognathic system of the pangolin, Manis aurita (Mammalia) Part 1. Masticatory muscle and their spindle supply in the pangolin. *The Journal of the Stomatological Society, Japan* 51: 674–688.

Zelditch ML, Wood AR, Bonett RM, Swiderski DL. 2008. Modularity of the rodent mandible: Integrating bones, muscles, and teeth. *Evolution & Development* 10: 756–768.

Chapter 3: Morphological evolution, integration and modularity

3.1-Variation and covariation

Regardless of the process by which homoplasy is produced, evolutionary convergence is extremely common in nature. The reason why convergence is that ubiquitous is that life on Earth occupies just a small fraction of the theoretical morphospace (McGhee, 1999). Shapes are limited by functional constraints, since mutations often produce life forms that are lethal. Additionally, morphology is limited by developmental constraints, which derives from the fact that organismal differentiation is conditioned to the original cell, the genetic coding, the interaction between cell tissues, and to all the geometric, physical, and chemical laws to which that mother cell is subjected to (McGhee, 2011). Constraints either prevent or shift the direction of evolutionary change, thus channeling evolution while restricting the evolvability of a biological system (Klingenberg, 2005). Evolvability is the degree to which an organism can respond to selection or evolve due to drift. The more evolvable a system, the more directions it can vary within the theoretical morphospace (Klingenberg, 2005). A constraint is considered to be "positive" when evolvability is channeled (canalization; see below) towards specific directions in the morphospace, and "negative" when evolvability is reduced in every directions (Klingenberg, 2005). Additionally, constraints can be separated in absolute and relative constraints. The first are rare, if not inexistent, in nature, as they assume that all variation is contained in a subspace, with null variation along the remaining morphospace axes (Klingenberg, 2005). Relative constraints result in differential variation between axes of the morphospace, causing some axes to have a greater propensity to suffer selection or drift, therefore increasing the evolvability of certain traits to the detriment of others (Klingenberg, 2005).

Evolution is thus a result of a trade-off between natural selection, functional constraints, and the developmental processes. As previously referred, with his "*loi de correlation des formes*", Georges Cuvier proposed that each species was perfectly adapted to its environment and that its body parts were correlated, so that one could predict the shape of one part in the presence of another. The correlated evolution of morphological traits would be formalized by Olson and Miller (1958) as morphological integration. However, as opposed to Cuvier's ideas, the correlation of morphological traits is not strictly due to adaptation to a functional optimum. Integration arises at both the intra-individual and the population levels (Cheverud, 1996). Intra-individual integration comprises both functional and developmental aspects, corresponding to the two sets of constraints that limit existing shape in the theoretical morphospace

(McGhee, 2011). Mandibular occlusion is a typical example of a process originating functional integration, as it depends on a coordinated variation of size and shape between the upper and lower jaws. Developmental integration occurs during the formation process of morphological structures. For instance, integration can be introduced due to high levels of growth hormone that promote structural growth (e.g., limb long bones) and thus increase covariation between associated morphological traits (Cheverud, 1996). Integration occurring at the population level can be divided in genetic and evolutionary components (Cheverud, 1996). Logically, both intra-individual and population levels are inter-related. Genetic integration occurs when integrated sets of morphological traits are inherited. The morphological expression of genetic integration is developmental integration. Cheverud (1996) sets the difference between both types of integration arguing that developmental integration is related to the physiological effects of genes occurring in each individual, while genetic integration involves the transfer of integration from one generation to another within a population. Genetic integration can be exemplified by the inheritance of proportionally large hind- and forelimbs (Leamy, 1977). Limb lengths covary due to genetic integration of two distinct developmental processes. Finally, evolutionary integration is a coordinated evolutionary trend of morphological elements, caused by both inherited integration and the effect of natural selection on a set of traits (Felsenstein, 1988).

If Cuvier described what can be called, in modern terms, functional integration, Étienne Geoffroy Saint-Hilaire and von Baer works orbit around the concept of developmental integration. If the first saw a common topology to all vertebrates, highlighting a common plan from which they derived to adapt to the most contrasting environments, the second observed structural differentiation and interaction, and somatic growth during ontogeny. However, none of them had the knowledge and tools to fully understand the implications of developmental integration and the full extent of its complexity. How important is the intrinsic tendency of biological systems to generate variation? If we consider the *Bauplan* or the 'archetype' of a given species as a cluster of individualized developmental processes, to which degree does it influence the evolution of its lineage?

Developmental constraints are the main factors introducing covariation between morphological traits (Hallgrímsson *et al.*, 2009), and given that certain sets of conditions are more likely to evolve than others, strong correlation between traits might constitute an evolutionary constraint (Klingenberg, 2005). As such, the levels to which integration occurs in organisms are inter-related and inter-dependent. Nevertheless, developmental integration appears to have a predominant role in maintaining the unity of an organism. When looking at the skeleton, the topology and connectivity of elements are extremely

similar in elephants and mice despite the obvious difference of functional constraints and selective pressures acting on animals with such different sizes and ecologies. Covariation of morphological traits arises from two different types of mechanisms (Klingenberg, 2005). The first type consists of direct interactions between developmental pathways (Fig. 5); a factor affects pathway "A", with a posterior interaction between pathways "A" and "B" causing trait covariation (Fig. 5). Variation by direct interaction can also be introduced when one factor affects one precursor pathway "Z" that posteriorly splits into pathways "C" and "D"; traits resulting from "C" and "D" covary due to a factor acting on "Z" (Fig. 5). The second interaction is designated parallel variation and occurs when variation is generated by the action of a factor over multiple pathways simultaneously (Fig. 5). This mechanism can be typically exemplified as a result of the action of environmental factors over a series of developmental processes (e.g., temperature differences; Klingenberg, 2005). In such cases, covariation between traits results from an external factor with no interaction between pathways. Both direct interaction and parallel variation can happen simultaneously, with covariation between traits being strengthened by both pathway interactions and the action of an external factor.

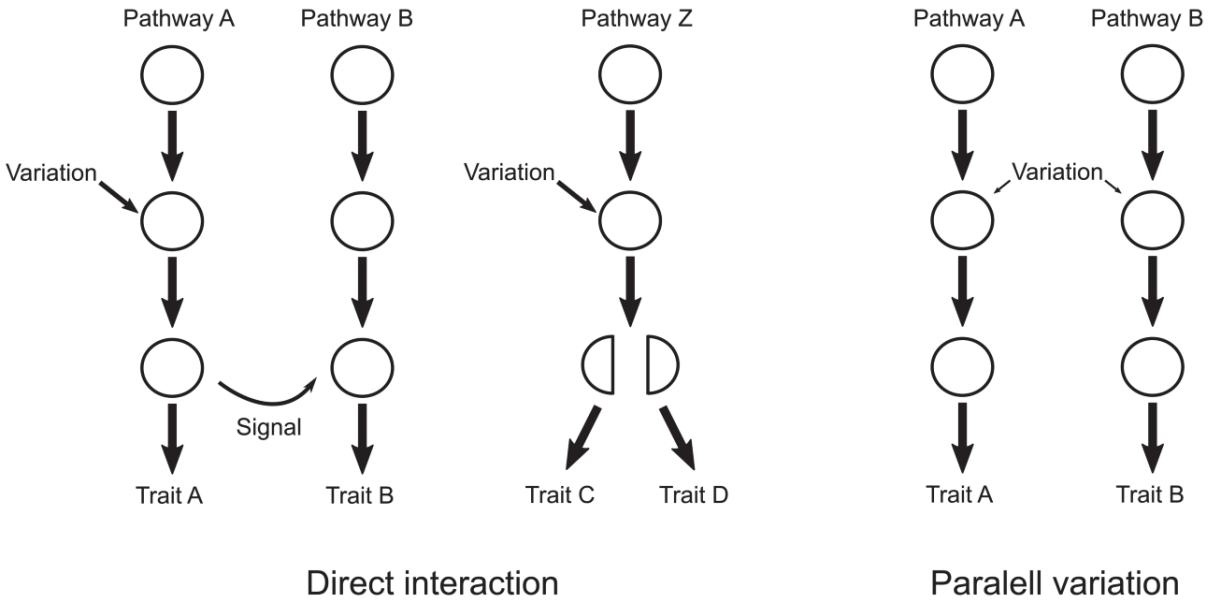

Figure 5 – Mechanisms responsible for generating trait covariation (adapted from Klingenberg, 2005).

Covariation of phenotypic traits arising due to interactions between several developmental pathways has an underlying genetic basis, as allelic differences are a source of variation in the genes

associated to such pathways (Klingenberg, 2005). Briefly, allelic variation at a given locus results in pleiotropy. Pleiotropy can be separated into two categories that correspond to the two types of developmental interactions described above (Klingenberg, 2005). Hadorn (1945) defined "primary" pleiotropy as the direct consequence of the constitution of cells that form traits (shared upstream genetic variation), which corresponds to the parallel variation of developmental pathways. On the other hand, "secondary" pleiotropy results from the transmission of variation generated in one cell population to another (genetic variation transmitted downstream), which corresponds to the direct interaction between developmental pathways. The categorization of pleiotropy, signaling interaction, and its consequences to developmental covariation is a complex subject on which thorough reviews and discussions have been provided elsewhere (Workman *et al.*, 2002; Klingenberg, 2004, 2005). Here we aimed to give a simple description of pleiotropic effects as a source of covariation, and thus the bases of integration produced by developmental processes.

3.2-Modularity

Regardless of the type of integration concerned, its magnitude is not constant within an organism. Groups of traits presenting strong and numerous interactions can be highly integrated internally (modules; Fig. 6). Each of these modules presents fewer and weaker interactions with other modules (Cheverud, 1996; Wagner, 1996). A phenotypic module can be defined as a unit with a strict functional role and strong pleiotropic effects of genetic variation (Raff, 1996; Wagner, 1996). Modularity can be considered either as an inherent property of organismal development, or as a byproduct of natural selection (Wagner, 1996). From the first perspective Wagner (1996) sees modularity as a result of the living being as a self-maintaining system (i.e., as a result of the chemistry that defines the structural organization of cells, tissues, organs, etc.). In this sense, modularity exists independently of function and could be compared as a modern concept for Saint-Hilaire's hypothesis of an intrinsic common organization to all beings. The second perspective on modularity is based on the formulation of morphological integration given by Olson and Miller (1951, 1958), which was then adopted and developed in several studies of modularity and integration (e.g., Cheverud, 1982; Goswami, 2006). It assumes that integration of functionally associated traits is selected, thus promoting modularity (Wagner, 1996). Modularity is conceptually hierarchical, with small and highly integrated modules being grouped in larger and less integrated ones (Klingenberg, 2005; Goswami, 2006). The mammalian skull is a classic example of modularity, with the skull being typically split between facial and neurocranial modules (Drake & Klingenberg, 2010). Within each module, the

skull is further divided into anatomical sub-regions representing smaller modules (Cheverud 1982; Goswami, 2006). Within the smaller cranial modules, it is theoretically possible to envision even smaller modules (e.g., individual bones) until reaching the molecule level. The hierarchical organization of modules is directly related to their dynamism through time (Raff, 1996). Developmental modules undergo temporal transformations, not necessarily associated to their relative timing of occurrence (heterochrony) but rather to their structural integrity from early to late stages of ontogeny (Raff, 1996). The totipotent cells from the ventral ectoderm of *Drosophila* are at the origin of its central nervous system (Raff, 1996). The expression of the *Notch* gene causes most of these cells to form neuroblasts that then contribute to the production of neurons (Doe & Goodman, 1985). The remaining cells incorporate the hypodermal layer of the skin, resulting in a different functional module. This example not only demonstrates the temporal transformations of the modular structure but highlights the hierarchical nature of modular systems as well as the process of duplication and differentiation underlying the formation of new modules (Muller & Wagner, 1991; Wagner & Altenberg, 1996; Winther, 2001).

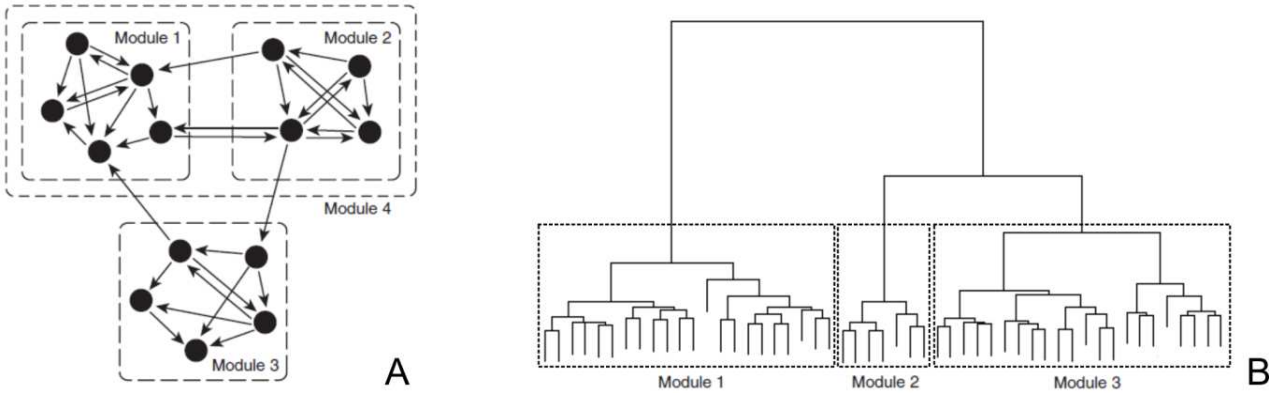

Figure 6 – Two representations of modular systems: network with interactions (arrows) between traits (circles) and dashed lines representing the hierarchical structure (A; modified from Klingenberg, 2005); hierarchical clustering of traits (tree tips) according to the degree of covariance (B).

Modularity, as a result of natural selection, arises through integration and parcellation (Wagner, 1996). If the ancestral state is the presence of poorly correlated morphological traits, modularity originates from integration that will evolve to prevent non-adaptive independent variation (Riedl, 1978); in other words, integration promotes variation of functionally coupled traits, increasing evolvability and reducing adaptively redundant variation (Wagner & Laubichler, 2004). If the ancestral state consists of a highly integrated system, modularity arises by reducing pleiotropic effects among traits belonging to different

functional complexes (parcellation). If we take as an example, once again, the process of occlusion between the upper and lower jaws, we would expect to observe an increase in covariation between these two blocks of traits due to a selective pressure favoring pleiotropy among them (Klingenberg, 2005). By a process of parcellation, pleiotropy is maximized among the traits involved in mastication, and reduced among these and other traits with different functional demands. From here is derived the concept of genetic module, a group of loci strongly integrated due to pleiotropic effects, affecting the developmental pathways of morphological traits sharing the same function (functional modules; Wagner and Altenberg, 1996). Modularity can be represented by a "phenotype-genotype map", a direct correspondence between gene variation and differences in phenotype (Wagner and Altenberg, 1996).

From the previous two paragraphs, one can deduce that the concept of modularity is able to include both Cuvier's functionalism and Saint-Hilaire's "essential similarity" (*Bauplan*). Although not explicitly, the two anatomists focused on two different aspects of phenotype evolution, which are important to define at this point. The first one is *variation*, which was already used here, and consists of measurable differences among or between individuals of a sample (Wagner and Altenberg, 1996). The second one is "variability", which is the propensity of a phenotypic trait to vary, and correspond to a trait response to environmental and genetic factors (Wagner & Altenberg, 1996). Phenotypic variation can be simply quantified by a measure of dispersion (e.g., phenotypic variance), while the quantification of variability is less straightforward, requiring more complex designs (Wagner & Altenberg, 1996). Nevertheless, phenotypic variation can be used as a rough proxy for variability, since if variation of a module within an organism is high, then one can assume that the variability is high too. Similarly, if a given module presents a weak variation, one can suspect the existence of constraints on variability (Alberch, 1983). Epistatic effects, the influence of one gene locus over the effects of other loci, control genetic variability and have an impact on the evolvability of phenotypic traits. Waddington (1942) first introduced the concept of *canalization*. According to Waddington (1942), canalization is the tendency of a developmental process to produce similar phenotypes independently of minor variations in environmental conditions. Developmental processes are usually canalized in organisms subjected to natural selection. Waddington (1942) used the genotype of *Drosophila* to demonstrate this, arguing that there is much less genetic variability in the wild type than in mutants. Canalization buffers the phenotype not only against environmental variations, but also allelic variation (Waddington, 1942). A strong stimulus (e.g., environmental; mutation) might cause this buffering mechanism to fail (de-canalization) and thus may allow for cryptic genetic variation to be expressed in the phenotype (Dworkin, 2005). The phenomenon

of canalization can be defined and quantified on the basis of the phenotypic variance observed between two populations exposed to two distinct environments (Dworkin, 2005; Fig. 8-2). The "canalized" population presents a non-significantly different variance around a mean measure (e.g., least-square means) between two environmental conditions, while the "de-canalized" population shows an increase in variance as a result of cryptic genetic variation released for selection (Dworkin, 2005). Hallgrímsson et al. (2009) used the scaled variances of eigenvalues to show that inbred mutant populations of mice showed not only a shift in means, but also an increased phenotypic variation when compared to the wild types of several species of muroid rodents (Jamniczky & Hallgrímsson, 2009). This is an empirical example of de-canalization due to a stimulus in developmental processes (i.e., induced mutations). Hallgrímsson et al. (2009) also showed that overall integration tended to increase in mutant populations, when compared to the wild types. Such discoveries show the complexity of the processes producing covariation, while highlighting that natural selection and canalization processes synergistically play a role in the integration of biological structures.

In addition to the increase of integration, Hallgrimsson et al. (2009) also showed that changes in variation among mutant lineages are not evenly distributed across all traits (Fig. 8d *in* Hallgrímsson et al., 2009). External stimuli affect some morphological modules, while having little or no effect in the remaining traits. This supports the previously presented consideration that modules allow for the evolution of complex phenotypes. Organisms are modular, showing discrete parts evolving differently while maintaining a common evolutionary trajectory that enables to preserve a common functionality. Raff (1996) arguably proposed that modularity is the most important facilitator of evolution. The author considers that this evolutionary relevance arises from three different processes occurring within a module: dissociation, duplication and divergence, and co-option (Raff, 1996). Dissociation can be temporal, spatial, or could occur in the interaction between modules. Temporal dissociation, or heterochrony, occurs when the relative timing of developmental processes changes during evolution. Spatial dissociations (heterotypy) refer to shifts in spatial relationships like changes of the cell type in which a gene is expressed, the production of repeated structures, or the modification of relative proportions of structures (Raff, 1996). Finally, dissociation of developmental modules occurs when related processes can occur independently. For instance, the development of the lens in amphibian eye can still occur if the retina is removed (Jacobson, 1966). This means that the two structures became two separate developmental modules. Another example can be found in gene duplication, in which function-changing mutations may occur in the copied gene. If these mutations are not deleterious, then natural selection starts to act on the

divergent trait condition, possibly creating a new functional module (through integration, parcellation, or both). For example, the bone morphogenetic proteins (BMP), responsible for bone growth, constitute a family of related proteins that have been experimentally shown to have distinct expression sites (Raff, 1996). In the first place duplication might have occurred, with each protein evolving distinct functions and thus originating a modular pattern. The third category of processes contributing for modular evolution is co-option. This consists of the adaptation of a structure to a different functional role than that ancestrally observed (*exaptation* following Gould & Vrba, 1982). The Paleozoic radiation of jawed vertebrates (Gnathostomata) resulted from an evolutionary advantage that is an illustrative example of a combination of spatial dissociation, duplication and divergence, and co-option (Raff, 1996). The lower jaw evolved from the most anterior of the seriously homologous gill arches, which was co-opted to grasp prey. A new function acted upon by a different selection pressure resulted in the evolution of an extremely specialized and ultimately diversified structure, without lethally disrupting the gill arches modules. If on one side spatial dissociation, duplication, and co-option promote evolvability of complex organisms, they are also the reason why modules are repeated and conserved within and across taxa, or across different hierarchical levels of organismal organization (e.g., molecular, cellular, tissue-level; Brandon, 2005). The development of completely unrelated new modules is theoretically rare, if not impossible, as the basic units of organismal construction are common across the Metazoa ("standard parts"; Raff, 1996; Winther, 2005). Modules are formed from the clustering of standard parts, with the highest levels being ubiquitous across tetrapods, vertebrates, or even the entire biological spectrum (Riedl, 1978). All in all, morphological innovation by the generation of a "new module" tends to occur by the differentiation of repeated elements (Simon, 1962; Akam, Dawson, & Tear, 1988; Muller & Wagner, 1991).

It becomes clear that modularity is an evolved property of biological organisms (Wagner & Altenberg, 1996). Consequently, modules can be seen as main drivers of organismal evolution, or evolutionary units. In sum, modules allow for the differential evolution of complex organisms as their semi-independence grants more degrees of liberty to certain developmental processes that become free from the constraints of a fully integrated structure (Riedl, 1978). If the coordinated variation of discrete parts of an organism in different directions of the morphospace appears to boost organismal evolvability, to what extend does that covariation limit or facilitate the evolvability within a module? The role of integration as either a constraint or a facilitator of evolution has been discussed in several works (Goswami & Polly, 2010; Parr *et al.*, 2016; Felice & Goswami, 2018; Felice *et al.*, 2019). Martin *et al.* (2005) used the DNA of a plant virus (Maize streak virus) to show that genes with highly complex interactions (highly

integrated networks) are less likely to maintain their function posterior to horizontal transfer. As a result, the contribution of gene recombination to evolvability is inversely proportional to integration of interaction networks. This supports the hypothesis that considers integration as an evolutionary constraint within a module. However, other studies found some evidence that integration may increase the evolutionary rate of a module. Goswami and Polly (2010) used a measure of morphological disparity to show that, in the skull of carnivores and primates, highly integrated modules tend to present lower disparity values, which was interpreted as a constraint to modular evolvability. However, they also showed that some highly integrated modules present high disparity, supporting the facilitation hypothesis. Parr *et al.* (2016) equally found evidence for the validity of both hypotheses within a sample. Goswami and Polly (2010) showed that integration and disparity are often simply uncorrelated.

3.3-The skull of placental mammals

In the previous section, I introduced the study of modularity of the placental skull. As in all vertebrates, the skull of placental mammals is a complex structure both developmentally and phylogenetically (Klaauw, 1952; Cheverud, 1982a; Gans, 1989; Hanken & Thorogood, 1993). The skull can be generally divided into three parts: neurocranium; viscerocranium; dermatocranium (Hanken & Thorogood, 1993). The neurocranium develops as a cartilage at the base of the brain and surrounds the sensory organs (inner ear, eye, olfactory organ; Friede, 1981; Hanken & Thorogood, 1993; Jin *et al.*, 2016). This cartilage is replaced by the skull in later stages. Ventral do the neurocranium, the walls of the primitive pharynx give origin to the cartilaginous (later ossified) viscerocranium or branchial arches, from which structures like the mandible, the middle ear ossicles, and the hyoid apparatus derived during the evolution of tetrapods (Hanken & Thorogood, 1993; Donoghue, Sansom, & Downs, 2006). This part of the skull normally counts seven arches in total (De Beer, 1937). Lastly, the dermatocranium consists of ossified plates that protect the brain dorsally and laterally and also includes mineralized tissues (e.g., dentine, enamel; Schilling & Thorogood, 2000).

The dermatocranium and viscerocranium differentiate from neural crest-derived mesenchyme, with cells from the dermatocranium migrating anteriorly to form the face (Noden, 1983; Osumi-Yamashita & Eto, 1990; Osumi-Yamashita *et al.*, 1994). On the other hand, the neurocranium, as the axial appendicular skeleton, is mostly derived from paraxial-mesoderm (Wilkinson, Bhatt, & Herrmann, 1990; Couly, Coltey, & Le Douarin, 1993). The three parts of the cranium can also be grouped according to their

ossification type (Schilling & Thorogood, 2000). The dermatocranium is a membrane bone, ossifying within the dermis, while the viscerocranium and neurocranium form as a cartilage which is secondarily ossified (e.g., Jollie, 1968).

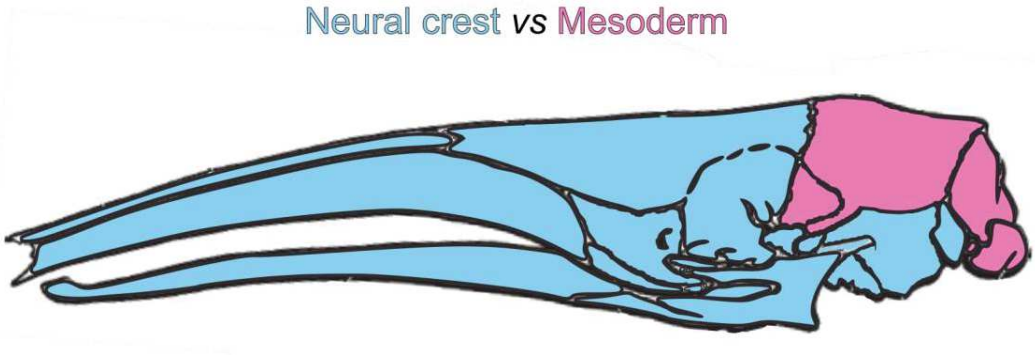

Figure 7 – Illustration of the skull of *Myrmecophaga tridactyla* (modified from Naples, 1999). Bones are colored according to the corresponding embryonic origin, neural crest (blue) and mesoderm (pink).

The embryonic origin of the skull is relatively conserved across vertebrates (Fig. 7; Piekarski *et al.*, 2014). In the mouse, neural crest-derived bones include the nasals, premaxillae, vomers, septomaxillae, maxillae, lacrimals, frontals, jugals, sphenoid complex, palatines, pterygoids, squamosals, and medial elements of the interparietals (Chai *et al.*, 2000; Jiang *et al.*, 2002; Koyabu, Maier, & Sánchez-Villagra, 2012). Dentaries and teeth are also derived from the neural crest. Mesoderm-derived ossifications includes parietals, lateral elements of the interparietals (tabulars; Koyabu *et al.*, 2012), supraoccipitals, exoccipitals, and basioccipital. In mammals, the skull has been traditionally divided into two developmentally separated parts (or modules) roughly based on their embryonic tissue origin: the face and the "neurocranium" (Drake & Klingenberg, 2010). The face consists of all neural crest-derived bones, with the exception of the squamosal, the alisphenoid, and the medial parts of the interparietal (postparietals; Koyabu *et al.*, 2012). The former two were integrated into the neurocranium, becoming an integral part of the lateral wall of the braincase to accommodate the growth of the cerebral hemispheres during the evolution of mammals (Goodrich, 1930; Morriss-Kay, 2001). The interparietal is included in the cranial vault, surrounded by mesoderm-derived elements. The tissue origin, type of ossification, unit topology have been used as the basis for studies of modularity and development in mammalian skull (Hallgrímsson *et al.*, 2004; Goswami, 2006; Porto *et al.*, 2009; Drake & Klingenberg, 2010; Evin *et al.*, 2017).

This brief introduction to the developmental origins of the mammalian skull is intended to present the complex character of this structure, but also its evolutionary conservatism across clades. In 1951, Everett Olson and Robert Miller introduced the principle of intercorrelation between linear measurements of the skull, which they would later call morphological integration (Olson & Miller, 1951). They hypothesized that the biological meaning of correlations between cranial distances could be related to either function (e.g., mastication), or development (Olson & Miller, 1951). Cheverud (1982) showed that the face of the rhesus macaque could be split in functional parts related to vision (orbital), olfaction (nasal), food taking/biting/sensing (oral), and food grinding (masticatory). The oral and masticatory functional components of the skull integrate the feeding apparatus, a part of the skull linked to food resources exploitation and intimately connected to radiations occurring during mammalian evolution (Schwenk, 2000). These radiations were possible due to the plasticity of the feeding apparatus (bone and interacting muscle tissue) despite a common *Bauplan*. Such adaptability has been evidenced from the intra-individual to the evolutionary level. The simple diet hardness reduction has been shown to decrease bone volume in rats (Moore, 1965). This hypothetically resulted from the reduction of the contraction force applied by the masticatory muscles.

The feeding apparatus holds a significant number of adaptive traits, which makes it particularly susceptible to produce homoplasy in a comparative phylogenetic context. Many examples have been reported, whether we consider tooth shape (Lazzari *et al.*, 2008), jaw shape (McCurry *et al.*, 2017; Page & Cooper, 2017), or tooth loss (Charles *et al.*, 2013). The morphological expression of genetic, developmental, and functional modules has been shown in a wide range of taxa and morphological structures (Cheverud, 1982a; Klingenberg *et al.*, 2001; Goswami, Weisbecker, & Sánchez-Villagra, 2009; Suzuki, 2013; Parr *et al.*, 2016; Goswami & Finarelli, 2016; Randau & Goswami, 2017; Felice & Goswami, 2018; Heck *et al.*, 2018; Churchill *et al.*, 2019; Randau, Sanfelice, & Goswami, 2019; Bardua *et al.*, 2019). However, the vertebrate skull has been the focus of most researches on morphological modularity, mostly due to the highly diversified shapes that resulted from the radiation of Gnathostomes in the Paleozoic (Raff, 1996). Cheverud (1982, 1995) produced the first studies that aimed at measuring the correlation between functional, genetic, and phenotypic modules in the mammalian skull. The functional multiplicity of the skull offers the possibility to test hypotheses of modularity within a well-known genetic and developmental framework (Cheverud, 1982a). Using inter-landmark distances and hierarchical clustering analyses, Cheverud (1982) found that the skull of the rhesus macaque was divided in eight phenotypic clusters, consisting of seven modules: frontal, parietal, occipital, orbital, small nasal,

oral (including two clusters), and masticatory (molar). Using an approach based on Cheverud (1982), Goswami (2006) showed that, as a general rule, the mammalian skull was divided in six morphological modules. These modules consisted of an oral-nasal region, a molar-palate region, the orbit, a zygomatic-pterygoid complex, the cranial vault, and the basicranium. More recent research on the integration and modularity in mammals retrieved similar results, with the mammalian skull being typically found to present either two (Drake & Klingenberg, 2010; Santana & Lofgren, 2013; Randau *et al.*, 2019), six (Goswami & Finarelli, 2016; Heck *et al.*, 2018; Churchill *et al.*, 2019; Randau *et al.*, 2019). Traits often present different magnitude of correlation (integration) within each of the cranial modules (Goswami, 2006). With the implementation of new methods to test the hypothesis of modularity (Claude, 2008; Klingenberg, 2009; Suzuki, 2013; Adams, 2016; Goswami & Finarelli, 2016) and the increasing accessibility of μCT (micro-computed tomography) scan data and geometric morphometrics hardware and software, research on patterns of integration and modularity have recently blossomed, especially concerning the vertebrate skull (Porto *et al.*, 2009; Goswami & Finarelli, 2016; Simon & Marroig, 2017; Felice & Goswami, 2018; Heck *et al.*, 2018; Hendrick *et al.*, 2019; Churchill *et al.*, 2019; Felice *et al.*, 2019; Randau *et al.*, 2019; Bardua *et al.*, 2019).

Despite the amount of studies focusing on cranial modularity showing some congruence regarding functional and developmental modules, there are still inconsistent results and alternative hypotheses regarding the patterns of morphological modularity across vertebrates. In the context of mammalian cranial modularity, an alternative hypothesis to the six functional/developmental modules (Cheverud, 1982a; Marroig & Cheverud, 2001; Goswami, 2006) is the "Palimpsest model" (Hallgrímsson *et al.*, 2009). Hallgrimsson et al. (2009) put together a set of conceptual and empirical arguments to argue that there is no basis for the partition of the mammalian skull in subsets directly referable to developmental modules. An important difference lies on the definition of integration itself. Hallgrimsson et al. (2009) define integration as "the tendency of a developmental system to produce covariation". They argue that the use of observed correlations as a measure of integration (Goswami, 2006; Porto *et al.*, 2009; Klingenberg, 2009; Goswami & Polly, 2010; Goswami & Finarelli, 2016) is not appropriate. Instead of following the conceptualization of Olson and Miller (1958), they propose a different definition that makes integration independent of the presence of variation, being a property of developmental systems. In Hallgrimsson et al.'s (2009) conception, integration is a process instead of a pattern (of covariation), consisting of the developmental interactions between sets of traits that confer the potential to induce covariation. As such, covariation structure can be altered without any modification of the developmental

interactions (integration; Hallgrimsson *et al.*, 2007). Hallgrimsson et al. (2009) used geometric morphometric methods to test five hypothesis of modularity based on developmental processes such as the two-module tissue origin hypothesis or a three-module muscle-bone interaction hypothesis. While not finding support for any of the hypothesis tested, Hallgrimsson et al. (2009) proposes that the developmental processes involved in the skull development are too complex to be represented by morphological covariation patterns. In sum, the skull covariation patterns should be considered as a mosaic of variation-generating processes whose imprints overlap in space (sometimes in time) and whose resulting structure is not easily predictable.

In the following article, I explore the patterns of intraspecific and interspecific modularity and integration of the skull of myrmecophagous placentals. I show that the modular architecture in these species is similar to that of other placental mammals, despite the some extreme cases of tooth loss and rostrum elongation. We discuss the implications of our results on the convergent evolution the myrmecophagous cranial phenotype.

Article 4

Patterns of cranial modularity in convergent lineages of ant-eating placentals.

In preparation: to be submitted to *BMC Evolutionary Biology*

Supplemental information for this article is available in Appendix 4.

Title: **Patterns of cranial modularity in convergent lineages of ant-eating placentals**

Ferreira-Cardoso[1] *et al*.

[1] Institut des Sciences de l'Evolution de Montpellier (ISEM), CNRS, IRD, EPHE, Université de Montpellier, Montpellier, France.

Introduction

Modularity is probably the most ubiquitous characteristic of biological systems (Winther, 2001; Klingenberg, 2005). Developmental modules are organizational units of traits with underlying high density of pleiotropic interactions (Wagner, 1996; Klingenberg, 2005). Phenotypic modules are sets of traits that share putative functional roles and common developmental processes (Olson & Miller, 1958; Cheverud, 1982). Such constraints limit the axes along which the phenotype can vary within each module, and are potential generators of coordinated phenotypic variation (Hallgrímsson *et al.*, 2007, 2009). Therefore, traits tend to be integrated within each module, varying semi-independently in relation to the whole system. Trait integration and modular organismal parcellation (the process of division in modules) are suggested to play a crucial role in the evolution of complex structures by reducing adaptive redundancy (Riedl, 1977, 1978; Wagner & Laubichler, 2004). In other words, modularity allows functionally integrated traits to covary within a module, while limiting the effects of mutations or the action of directional selection on uncorrelated characters occurring in other modules. This trade-off between intrinsic organismal variation properties and specific adaptive landscapes might promote the evolvability of certain functional units (Riedl, 1978; Wagner, 1996; Wagner & Laubichler, 2004; Wagner, Pavlicev, & Cheverud, 2007). As a result, testing of the modularity hypothesis and defining modular organisation has been the target of several studies in a wide range of organisms and body parts such as insect wings (Klingenberg *et al.*, 2001; Klingenberg, 2009b; Suzuki, 2013), mammalian mandibles (Klingenberg, Leamy, & Cheverud, 2004; Zelditch *et al.*, 2008), limbs (Goswami, Weisbecker, & Sánchez-Villagra, 2009), and vertebrae (Randau & Goswami, 2017).

The correlations among traits of the cranium have been intensively studied in the vertebrate skull and explained in terms of functional and ontogenetic constraints. Investigations on the skull modularity and integration patterns have been conducted in birds (Klingenberg & Marugán-Lobón, 2013; Felice & Goswami, 2018), amphibians (Simon & Marroig, 2017; Bardua *et al.*, 2019), reptiles (Piras *et al.*, 2014) and mammals (Hallgrímsson *et al.*, 2004; Porto *et al.*, 2009). The mammalian skull presents a modular pattern with a major separation between the face and neurocranium (Drake & Klingenberg, 2010), as well as between the rostrum, vault, and basicranium (del Castillo *et al.*, 2017). Further regionalization of its modular architectures has been proposed (Cheverud, 1982; Marroig & Cheverud, 2001; Goswami, 2006) with the recognition of six modules corresponding to the oro-nasal, molar-palate, orbit, zygomatic arch-pterygoid, vault, and basicranium regions. These phenotypic modules have been suggested to correspond

to both developmental and functional constraints, some specifically related to food detection and capture (oro-nasal), food processing (molar-palate), and origin for adductor muscles (zygomatic-pterygoid).

Shifts in diet are known to influence skull shape and produce distinct phenotypes across a wide range of vertebrates such as turtles (Claude *et al.*, 2004), frogs (Emerson, 1985), bats (Nogueira, Peracchi, & Monteiro, 2009), and carnivorous placentals and marsupials (Wroe & Milne, 2007). The morphological diversification of the feeding apparatus has played a major role in tetrapod radiations, varying from strong jaws with bone-crushing teeth to the edentulous and elongated jaws of ant- and termite-eating (i.e. myrmecophagous) mammals (Schwenk, 2000). The loss or reduction of teeth has occurred in all major mammalian clades (Meredith *et al.*, 2009; Ferreira-Cardoso, Delsuc, & Hautier, 2019b) and is often associated to a specialized myrmecophagous diet (Davit-Béal, Tucker, & Sire, 2009; Meredith, Gatesy, & Springer, 2013). Myrmecophagy evolved independently in divergent placental lineages such as anteaters, giant armadillos, pangolins, aardwolves, and aardvarks. The evolution of these taxa towards this specialized diet led to an extensive rearrangement of the skull morphology (Patterson, 1975; Redford, 1986; Rose & Emry, 1993; Vizcaino, 1994; Vizcaíno *et al.*, 2009). These morphological changes occurred in the context of developmental conservatism of the mammalian skull.

Compared to toothed placentals, we predict that myrmecophagous mammals might present three main differences in covariance-generating processes. First, tooth reduction or absence should decrease variance generated by tooth development and eruption (e.g., Cheverud, 1996; Zelditch *et al.*, 2008). Second, the loss of masticatory function, mastication associated structures (e.g., zygomatic arch), and reduction of mastication muscles volume (Edgeworth, 1923; Yeh, 1984; Naples, 1999) should alter the covariance patterns at their origin in the skull. In chicken and mice, bone formation appears to be dependent on functional muscles that perform embryonic muscle contraction (Hall & Herring, 1990; Rot-Nikcevic *et al.*, 2006). Third, the extreme snout elongation of myrmecophagous placentals, particularly anteaters, should add increasing amounts of variance in this part of the skull (Olson & Miller, 1958; Cardini & Polly, 2013; Cardini, 2019a), somatic growth of bone tissues being one of the main processes contributing to structural covariation on the mammalian skull (Hallgrímsson *et al.*, 2007, 2009, 2019; Gonzalez *et al.*, 2013).

Here, we used exploratory and confirmatory methods to describe the previously unexplored modular architecture of 15 myrmecophagous placentals. We compared modularity and integration patterns between species in order to understand if the evolution towards myrmecophagy is reflected in a convergent change in cranial covariation/correlation patterns. We additionally performed a comparative analysis by

adding 21 non-myrmecophagous sister taxa to compare cranial morphologies and to test if morphological adaptation towards myrmecophagy translated into similar rates of evolution among ant- and termite-eating placentals.

Materials and methods

Biological sampling

Skull digitization included specimens from the collections of the Natural History Museum (BMNH) in London (United Kingdom), the Museum für Naturkunde (MfN) in Berlin (Germany), the Muséum National d'Histoire Naturelle (MNHN) in Paris (France), the Institut des Sciences de l'Evolution in Montpellier (France), the Royal Museum for Central Africa (KMMA/RMAC) in Tervuren (Belgium), the American Museum of Natural History (AMNH) in New York (United States of America), the National Museum of Natural History (USNM) in Washington DC (United States of America), and the Museum of Vertebrate Zoology (MVZ) in Berkeley (United States of America). Our dataset is composed of cranial landmarks of 480 specimens from 15 extant species of myrmecophagous placentals and 21 specimens from non-myrmecophagous sister taxa. The myrmecophagous species include four anteater species (n = 215), seven pangolin species (n = 178), the aardvark (*Orycteropus afer*; n = 40), the aardwolf (*Proteles cristatus,* n = 25), the giant armadillo (*Priodontes maximus*; n = 14), and the bat-eared fox (*Otocyon megalotis*; n = 8).

We placed 54 three-dimensional landmarks on skulls using a Revware MicroScribe M 3D digitizer (Fig. 1; Table S1). We selected homologous anatomical landmarks for our morphologically diversified sample based on previous works (Goswami, 2006; Hautier *et al.*, 2014, 2017; Ferreira-Cardoso *et al.*, 2019a). Given that modularity analyses are based on the covariation/correlation structure of the data, we opted out the placement of semilandmarks to avoid autocorrelation issues (Cardini, 2019b). In a significant number of pangolin and anteater specimens (82% of our myrmecophagous sample) premaxillae were either absent, loosely attached, or broken, and were therefore not landmarked. Missing landmarks were estimated via thin plate spline interpolations (Claude, 2008), for each species, using the 'estimate.missing' function in *geomorph* v.3.5.0 (Adams *et al.*, 2017) in R (Team, 2013). Landmark sets were symmetrized (left side) and then subjected to species-specific Generalized Procrustes Analysis (GPA; Gower, 1975; Rohlf & Slice, 1999) prior to modularity analyses. A single GPA was performed on the dataset for interspecific comparisons. The GPA scales to centroid size, optimally translates and rotates the specimens using least-squares criterion.

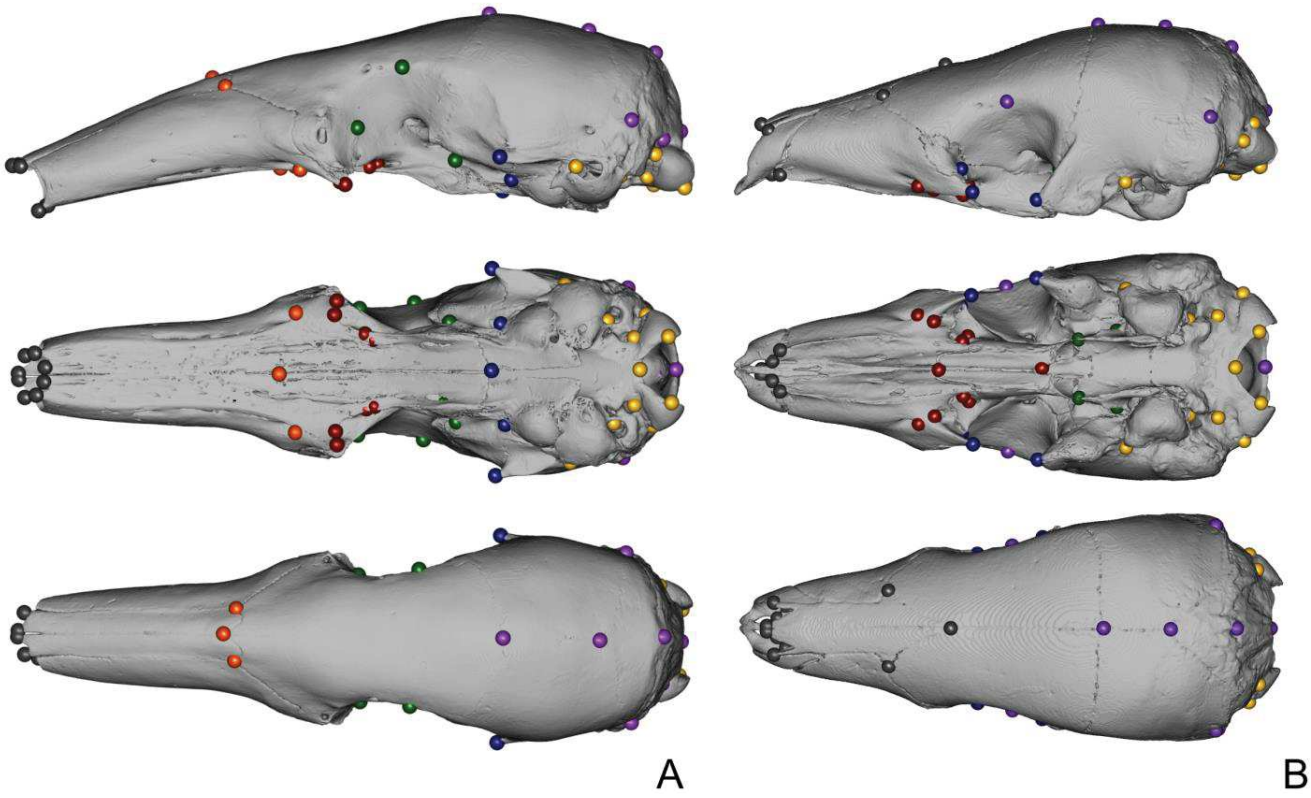

Figure 1 – The two most frequently recovered modular structures with EMMLi. Landmarks are placed on skulls of *Tamandua mexicana* (A) and *Phataginus tricuspis* (B). Each color corresponds to a module of the seven-module EDMA-derived hypothesis (A) and the MCN-derived pattern for *P. tricuspis* (B).

Modularity

Intraspecific modularity

We used four different methods to assess patterns of modularity within each of the studied species (15). First, we used two exploratory methods without *a priori* hypotheses (Euclidean Distance Matrix Analysis on non-superimposed landmark configurations – EDMA; Morphological Correlation Network – MCN) to visualize the structure of the data and their raw patterns of covariation and correlation. Secondly, we used two widely used methods to test for *a priori* hypotheses of modularity (maximum likelihood approach – EMMLi; Covariance Ration – CR).

We used pairwise interlandmark distances to perform EDMA (Lele & Richtsmeier, 1991), in order to detect modular structures while avoiding the potentially undesirable effects of Procrustes superimposition (Cardini, 2019b). EDMA consisted of four steps: (1) reconstruction of the mean shape coordinates obtained from the average form matrix using the 'mEDMA2' function from Claude (2008);

(2) extraction of a covariance matrix based on all configurations; (3) extraction of the eigenvectors with corresponding positive eigenvalues resulting from the covariance matrix; (4) scaling the eigenvectors by using the eigenvalues; (5) calculation of the inter-trait Euclidean distances matrix from the scaled eigenvectors; (6) identification of trait clusters using Ward's clustering method. For the last step, we used the Gap statistic (Tibshirani, Walther, & Hastie, 2001) as implemented in the function 'clusGap' of *cluster* v.2.0.8 R package. For each species, we tested the splitting of the tree in 2 to 10 clusters. The preferred number of clusters was selected and, we then determined cluster composition with bootstrap resampling using the 'clusterboot' function in *fpc* R package (Hennig, 2007, 2008). Whenever clusters were biologically meaningless (e.g., formed by two bilaterally symmetric landmarks) their number was reduced until they became integrated in larger ones, in order to avoid overfitting the data.

The second exploratory analysis performed (MCN) consisted of the association of three methods: the RV coefficient (Escoufier, 1973); the Reichardt and Bornholdt community detection method based on the spin-glass model (Reichardt & Bornholdt, 2006); the consensus clustering in complex networks (Lancichinetti & Fortunato, 2012). Landmark configurations were subjected to a Generalized Procrustes Analysis (Gower, 1975; Rohlf & Slice, 1999) implemented in *geomorph* R package v.3.0.7 (Adams *et al.*, 2017). All specimens were scaled to centroid size, optimally translated and rotated using least-squares criterion. We then used a similar approach to the one proposed by Suzuki (2013), in which a pairwise RV coefficient matrix (RV_{ij} Procrustes aligned coordinates) is converted into a weighted adjacency matrix, for each studied species. The Reichardt and Bornholdt community detection method was then used to recover a modular architecture corresponding the minimum energy state (Suzuki, 2013). Because the spin glass model includes several energy states near the minimum level, a total of 300 trials were run to find the modular architecture of each network. Increasing the number of trials did not improve the results and made the analyses extremely long. Given the multitude of slightly different solutions (module number and module composition), a consensus matrix C_{ij} was built, with each case containing the probability of *i* and *j* to be clustered in the same module (Lancichinetti & Fortunato, 2012). The consensus matrix was then used to generate a new weighted adjacency matrix that was submitted to another set of 300 trials to recover modular architectures. In total, the spin glass – consensus matrix sequence was repeated three times for each species. The MCN was implemented with a custom code integrating the 'cluster_spinglass' function from the *igraph* v1.2.2 package (Csardi & Nepusz, 2006) in R (Team, 2013).

In order to test *a priori* hypotheses of modular partitioning of the skull, a matrix of trait correlations (congruent coefficient) was constructed for each species using the 'doctorr' function of the *paleomorph*

v0.1.4 R package (Lucas & Goswami, 2017). Multiple modular architectures were tested using the 'EMMLi' function in the *EMMLi* v0.0.3 R package (Goswami & Finarelli, 2016). This approach selects the best model based on maximum likelihood, comparing models with different number of modules with different variations within the same model related to inter- and intra-modular correlation pattern heterogeneity (Goswami & Finarelli, 2016). *EMMLi* was performed twice for each species, with option *abs* set to FALSE in the second analysis in order to allow negative inter-modular correlations to be retrieved (Simon & Marroig, 2017). We tested 10 different modular architectures varying from a fully integrated skull (one single module) to the therian mammal six-module architecture (Goswami, 2006). Our *a priori* architectures additionally included a variant of Goswami (2006)'s therian six-module architecture with the zygomatic process landmarks added to the zygomatic-pterygoid module, analogues of those previously tested by Hallgrímsson *et al.* (2004; three and six modules), and a variant of the therian six-module architecture with the oro-nasal module coded as unintegrated (Churchill *et al.*, 2019). To this set of hypotheses, we added a classical division of the skull in two modules (face-neurocranium), as well as two architectures derived from the network analysis with the *P. tricuspis* and *T. tetradactyla* datasets, and two seven-module architectures (Hallgrímsson, 2004; Goswami, 2006) modified according to EDMA. The models tested are hereafter referred to in roman numerals (Models I-X) as presented in Table 1.

In addition to the correlation matrices calculated from the Procrustes aligned coordinates, modular architecture was tested on static allometry-corrected residuals extracted from a Procrustes ANOVA (shape ~ logarithm transformed centroid size) performed with the 'procD.lm' function in *geomorph* R package. Modularity was not tested in species with non-significant allometric effect.

We additionally used the covariance ratio (CR; Adams, 2016) to test for *a priori* hypotheses of modular architecture using the 'modularity.test' function in *geomorph* R package. For each species, we submitted the most likely modular architecture to the CR test.

In order to remove correlation among modules that would result from pure architectural constraints and from the Procrustes analysis considering the skull as a whole, between- and within-modules correlations were tested using the MCN-derived architectures to divide the skull in individually Procrustes aligned modules. Pairwise partial least-squares analyses (PLS) were performed between all separately-aligned modules, to assess the significance and degree of covariation of the two blocks. PLS were performed with the 'pls2B' function of the *Morpho* v2.6 R package (Schlager, 2017). This procedure was not repeated for the allometry-corrected shapes. Additionally, we used correlation matrices in order to calculate the average correlation within modules in order to compare the magnitude of integration between

datasets with common and separated Procrustes superimpositions. Given that these tests aimed at providing an empirical example of the covariation introduced by Procrustes superimposition, they were performed for the two best sampled species only (*P. tricuspis* and *T. tetradactyla*).

Table 1 – Modular architectures evaluated with a maximum likelihood method (*EMMLi*). Architectures are ordered by number of modules.

Architecture	Number of modules	Other designations
I	2	Face-neurocranium 2
II	3	Hallgrimsson 3
III	4	Network tetradactyla 4
IV	5	Rostrum unintegrated
V	6	Therian 6
VI	6	Therian 6 zyg-zygpte
VII	6	Network P. tricuspis
VIII	6	Hallgrimsson 7(6)
IX	7	Therian 6 EDMA
X	7	Hallgrimsson EDMA

Evolutionary modularity

In order to understand the interaction between snout elongation and modularity, we calculated mean shapes for each of our focal species and built a dataset (n = 36) integrating non-myrmecophagous sister taxa. Firstly, we visualized the skull shape variation on a principal component analysis (Dryden & Mardia, 1993). We then performed a Procrustes ANOVA with the 'procD.lm' function in *geomorph* to assess the effect of log-transformed centroid size on shape, and extracted the residuals from this analysis (allometry-corrected shapes). We visualized the allometry-corrected data on a principal component space in order to describe changes associated to the first two principal components (PCs) explaining most variance. Secondly, we divided the skull shapes in rostrum and neurocranium (Model I) and used the 'compare.evol.rates' function in *geomorph* to obtain species evolutionary rates for the two modules (Drake & Klingenberg, 2010), using 10.000 iterations. We divided the skull in these two modules in order to understand if myrmecophagous species presented a higher evolutionary rate associated to changes in the rostrum. The phylogeny was generated from timetree.org (Kumar *et al.*, 2017) and imported into *Mesquite* v.3.6 (Maddison & Maddison, 2018) to add additional species and adjust node ages based on molecular phylogenies from Gibb *et al.* (2016) and Gaubert *et al.* (2017). We then applied the maximum-likelihood modular architecture selection described in the previous section on the interspecific dataset. We used the most likely architecture and calculated species evolutionary rates for each module. The evolutionary rates were plotted on a phylogeny using the 'plotBranchbyTrait' function of the *phytools* R package (Revell, 2012). Finally, we divided the dataset using dietary (myrmecophagous *vs* non-myrmecophagous) and

taxonomic (myrmecophagous *vs* non-myrmecophagous within Atlantogenata and Laurasiatheria), in order to assess differences in evolutionary rates. We also compared these rates with a Marsupial outgroup and a Primate (outgroup to pangolins+carnivores). Significance levels were assessed via permutation tests (Adams & Collyer, 2018).

Comparison of covariance matrices

In addition to the modularity analyses, we used principal coordinate analysis (PCoA) in order to compare the covariance matrices of each species in the morphospace. First, we performed a common Procrustes superimposition of the entire dataset (n = 480). We performed a PCA on the aligned coordinates and extracted the first seven axes explaining 90% of the variance. We then computed 15 species-specific covariance matrices based on those seven principal components. Euclidean distances were calculated for all pairs of covariance matrices and compiled on a distance matrix. Finally, we performed a PCoA of the distance matrix.

We conducted a second set of analyses to assess the change in skull covariance patterns during ontogeny. We selected the two best-sampled species (*T. tetradactyla* and *P. tricuspis*), for which we had a wide range of sizes. In these two species, the absence of teeth hinders age determination based on tooth eruption. We thus used size as a proxy for age (Ferreira-Cardoso *et al.*, 2019a). For each species, four categories were created corresponding to the first to fourth quantiles of the centroid size (stages 1-4). Specimens in stage 1 presented skull traits associated to juveniles, such as unfused or loose basicranial and occipital sutures, or the presence of spongious bones. The remaining stages presented mainly differences in size and shape. We considered stage 1 as juveniles, stage 4 as mature adults, while stages 2 and 3 represent intermediate ages. For each species, we computed covariance matrices for each stage and then followed a similar procedure to the one described in the previous paragraph. The final PCoAs can be considered as an approximation of correspond to species ontogenetic trajectories of covariance (Mitteroecker & Bookstein, 2009).

Computation of covariance and squared distance matrices were respectively performed with the ‘cov.group’ and ‘mat.sq.dist’ functions of the *vcvComp* v1.0.1 R package (Le Maitre & Mitteroecker, 2019).

Results

Exploratory analyses of modularity - MCN

The network analysis (MCN) retrieved a modular organization of the skull that varied between three to ten modules (Table S2). The most frequent architectures for each species varied from three to six modules, with a three-module architectures being the most frequent in five species, four modules in three species, five modules in two species, and a six-module architecture in four species (Table S2). When the number of modules was the same, they varied in composition between species. However, in most cases, the resulting modules either grouped functionally unrelated landmarks or showed gross modular partition (e.g., see Fig. S1). We frequently found clusters of landmarks belonging to the basicranium (e.g., landmarks from the foramen magnum and occipital condyles) and structures from the anterior tip of the rostrum (e.g., *P. tricuspis*). Nevertheless, the modular architecture retrieved for the best sampled species could be associated to functional/developmental modules defined in previous studies (Goswami, 2006). For brevity, we here describe in detail the architecture for the two best sampled species only. We recovered a six-module architecture for *P. tricuspis*, with landmarks corresponding to the basicranium, the vault, the orbit (limited to the alisphenoid), the molar-palate region, the zygomatic arch, and the oro-nasal/rostrum region (Figs. 2A). Similar to other species, *P. tricuspis* presented landmarks from the occipital condyles grouped with the rostrum cluster. In *Tamandua tetradactyla*, the six-module architecture was the most frequently found in the network analysis (Fig. 2), but only four of these clusters corresponded to morpho-functional regions, i.e. the basicranium, orbit, vault, and oro-nasal/rostrum. Contrary to *P. tricuspis*, the landmarks from palatine/molar cranial and anterior zygomatic regions were grouped with the oro-nasal/rostrum module. The most anterodorsal projection of the zygomatic process of the squamosal was grouped with landmarks from the orbital region. The landmarks placed on the infraorbital foramina (#3/23) formed a two-landmark cluster. The sphenopalatine and caudal palatine foramina (#6/25 and #7/26) formed a separated cluster from the rostrum (Fig. 2), but still strongly connected to it, so these two groups were subsequently treated as a single module.

We ran the MCN procedure on a randomly selected subset of *P. tricuspis* specimens (n = 36) to test the sensitivity of this method to reduced sample sizes. We obtained a different configuration consisting of four models (Fig. 2a) with landmarks from different modules grouping together instead of presenting a similar structure to the full dataset analysis. These clusters consisted of groupings including merged landmarks from the anterior zygomatic, molar-palate, and oro-nasal modules (face/rostrum) and three

other groups that roughly represented skull regions like the cranial vault, the basicranium, and a grouping of landmarks from the occipital and rostrum regions.

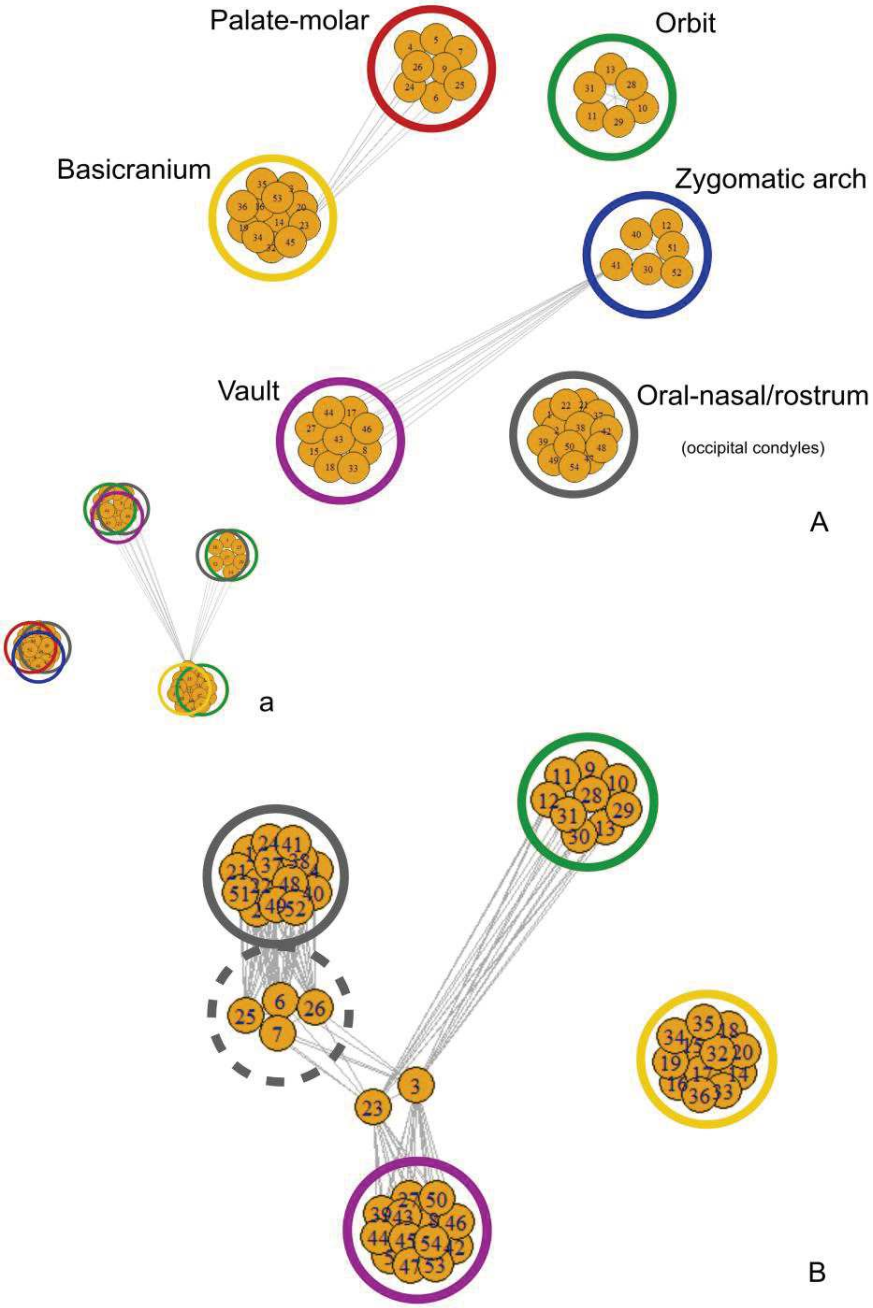

Figure 2 – Networks of skull landmarks of *Phataginus tricuspis* (A; *n* = 72) and *Tamandua tetradactyla* (B; *n* = 74). (a) Modular architecture of *P. tricuspis* showing the effects of sample reduction by half (*n* = 36). Dashed circles represent separated landmarks that are strongly integrated with the module of the corresponding color. Grey links show strong correlations between landmarks in distinct modules.

Exploratory analyses of modularity - EDMA

Manis crassicaudata (*n* = 7) and *Otocyon megalotis* (*n* =8) were the least sampled species in this study. The modular structures resulting from EDMA were not well-defined in these two species, with clusters including landmarks distributed heterogeneously in the skull. The Gap test revealed that the skull was optimally divided between 3 and 9 clusters, with the exception of *Smutsia gigantea* and *Orycteropus afer*, which were considered to optimally consist of one single cluster. In these cases, we arbitrarily divided the skull in five modules. A high number of clusters was often associated to grouping of two bilaterally symmetric landmarks, and in some cases bilaterally symmetric clusters (e.g., the molar/zygomatic regions of *Proteles cristatus*). For each species, we reduced the number of clusters to the point to which no cluster was formed by single or bilaterally symmetric landmarks only. Concerning the division of the skull, the oro-nasal and the basicranium regions were well-preserved across all taxa. The oro-nasal was composed by the landmarks at the anterior parts of the maxilla and nasal in all species. The basicranium included the landmarks of the occipital region (basioccipital, exoccipital, and the supraoccipital). In *Tamandua* spp. and *Cyclopes didactylus* (Fig. S2), the most posterior cluster was restricted to the occipital region. However, the basicranium was in the same module as the landmarks of the midline of the cranial vault and the anterior margin of the tympanic ring in pangolins (Fig. S2). In *P. tricuspus*, the intersection between interfrontal and interparietal sutures is excluded from the basicranium/tympanic ring cluster. In *S. gigantea*, *P. tetradactyla*, and *M. pentadactyla* this cluster also included the zygomatic processes of the squamosal (Fig. S3). *O. afer* showed a cluster including the occipital region associated to the posteriormost point of the interparietal suture. *Priodontes maximus* showed a similar cluster to that of *O. afer*, with the anterior margin of the tympanic bulla (Fig. S3).

The other parts of the skull were, however, much less conserved across the species (Fig. S2-3). The middle part of the skull presented two main clusters, one including the pterygoid region (#12/30, #13/31, #14/32) and landmarks from the vault (#43 and sometimes #44), and another consisting of the molar-palate regions. The landmarks of the orbit region were often split between the pterygoid and the molar-palate modules, with a few exceptions in which it formed an independent cluster (e.g., *T. mexicana* and *S. gigantea*).

The naso-frontal/maxilla-palatine interaction region presented different partitions among myrmecophagous placentals. These differences were related to the landmarks at the posterior part of the nasals (#39/50, #42) and the infraorbital foramen (#3/23). In most species these landmarks clustered together with points located more posteriorly, as the maxillary foramen (#4/24), the palatine foramina

(#6/25, #7/26), the point between the interpalatine-intermaxilla sutures (#5), and the zygomatic processes of the maxilla (#41/52). However, in *T. tetradactyla*, *T. mexicana*, and *O. afer*, the landmarks at the nasal-frontal interaction and those at the level of the maxilla-palatine suture clustered separately from the others (Fig. S2-3). In *P. maximus* and *M. tridactyla*, the intermaxilla-interpalatine point or the infraorbital foramen were excluded from this naso-palatine cluster, respectively. Additionally, in *P. tetradactyla*, the landmarks on the posterior part of the nasal formed a small cluster.

A priori modular architecture hypothesis testing

The results of the modular architecture selection by maximum-likelihood (EMMLi) including all *a priori* hypotheses and those modified based on EDMA and obtained from MCN analyses (Tables 1-3). In the MCN-architectures obtained for *P. tricuspis* (VII), the occipital condyles landmarks were re-allocated to the basicranium. Before correcting data for static allometry, EMMLi retrieved a seven-module architecture (eight of which, architecture IX) for nine species. Five species (*P. tricuspis*, *S. gigantea*, *S. temminckii, M. pentadactyla,* and *P. cristatus*) showed a six-module architecture, and one species (*M. crassicaudata*) was found to present a three-module architecture. In the case of *M. crassicaudata* and *P. maximus*, the most likely architecture presented a posterior probability below 50%. In *O. megalotis*, the most likely architecture presented a posterior probability of 80%, but three other architectures showed at least 5% (Table S3). Static allometry was detected for all species, except *P. maximus*, *M. crassicaudata*, *P. cristatus*, and *O. megalotis*. Apart from these species, results reported herein relate to the allometry-corrected data (Table 3). Static allometry did not affect the number of retrieved modules except in *M javanica*, which presented a four-module architecture (III) after allometry correction (Table 3). Allometric-correction also changed the modular architecture of *O. afer*, *P. tetradactyla*, and *S. temminckii*, but without changing the number of modules. Landmark changes occurred in the zygomatic-pterygoid and nasal-frontal regions (*S. temminckii*; Table 3). Of the eleven species for which static allometry was a significant component of skull shape, allometry-corrected skulls presented a seven-module architecture in six species. Four species presented a six-module architecture and only one presented a four-module architecture.

All anteaters, *P. tetradactyla*, *P. maximus*, and *O. megalotis* presented architecture IX (Table 3). This consists of the six functional modules (Goswami, 2006) with an additional naso-palatine module derived from the EDMA analyses. In *P. tetradactyla*, the posterior probability for architecture IX was just 42%, with III, V, VI, and VII showing probabilities between 10-20% (Table S4). *O. afer*, presented the

other seven-module architecture tested (X). In comparison with architecture IX, the landmarks from the maxillary foramen (#4/24) are included in the oro-nasal module. Additionally, the posterior limit of the interpalatine suture (#9) is included in the molar-palate module, while the zygomatic process of the maxilla (#41/52) is integrated with the zygomatic-pterygoid region along with the zygomatic process of the squamosal (#12/30) and the foramen ovale (#13/31). EMMLi retrieved architecture VII, recovered from the MCN analyses of *P. tricuspis,* for *M. pentadactyla*, *S. gigantea*, *S. temminckii, P. tricuspis*, and *P. cristatus* (Table 3). These species present a rostral module with landmarks from the oro-nasal region associated to the more posterior landmarks along the naso-frontal sutures (Fig. 1B). They also show a module corresponding to the anterior and posterior parts of the zygomatic arch, and a module that groups the optic foramen (#10/28) and the foramen rotundum (#11/29) with the foramen ovale (#13/31). *S. temminckii* showed a low posterior probability for this architecture (27%), with architectures III and IV being almost as likely (21% and 25%). *M. javanica*, the only species for which the number of modules changed after allometric correction, presented the four-module architecture derived from the MCN of *T. tetradactyla* (III; Table 3). In architecture III, the oro-nasal and molar-palate modules are integrated in a single module. In addition, this architecture differs from the six-module functional hypothesis (V; Goswami, 2006) in having landmarks located along the naso-frontal sutures (#39/50 and #42) grouped with the vault module and in the three most anterior landmarks from the molar-palate region (#3/23 and #5) unintegrated. Architecture III lacks an orbit module, with the landmarks from the optic foramina (#10/28) being clustered with the zygomatic-pterygoid (Fig. S4B). *M. crassicaudata* presented the least modular skull structure, with only three modules (II; Hallgrimsson, 2004). In *M. crassicaudata*, the landmarks from the oro-nasal, molar-palate, and anterior part of the orbit grouped in a rostrum module. The foramen rotundum (#11/29) and the most anterodorsal point of the zygomatic process of the squamosal (#12/30) correlate with those associated to the vault region. The third module is the basicranium, including the foramen ovale and the most posterior point of the interpalatal suture (#9). EMMLi retrieved a low posterior probability for the skull partition of *M. crassicaudata* in three modules (21%). Other possibilities found were a different distribution of integration on the same three-module architecture (17%), the two-module face-neurocranium hypothesis (I) with two different distributions of integration between modules (18% and 16%), and the six-module functional hypothesis (16%).

Regarding the integration level (Fig. 3), EMMLi retrieved models for which both *M. crassicaudata* and *P. maximus* presented a constant integration level across all modules ($\rho = 0.32$ and $\rho = 0.26$, respectively; Table 3). For all other species, the module with the strongest average integration was that

corresponding to the oro-nasal region (Tables 2 and 3; Fig. 3A). Anteaters presented the highest integration values for this module ($0.44 < \rho < 0.65$). *P. tetradactyla* ($\rho = 0.49$) showed the highest value among pangolins. *S. gigantea*, which presented a rostrum module including the oro-nasal and naso-frontal regions, also exhibited a relatively high integration ($\rho = 0.37$). *O. megalotis* also showed an oro-nasal module as integrated as that of *M. tridactyla* ($\rho = 0.61$). *S. temminckii* showed the least integrated oro-nasal region ($\rho = 0.21$).

Table 2 – Modular architectures of 15 myrmecophagous species. Number of specimens (*N*), most likely modular architectures recovered with EMMLi (*MLi*), covariance ratio (*CR*), within-module absolute correlations (ρ), and correlation between oro-nasal and molar-palate modules assuming a therian six-module (V) architecture (ρ *abs*). (1) Oro-nasal/rostrum, (2) molar-palate, (3) orbit, (4) zygomatic-pterygoid, (5) vault, (6) basicranium, (7) naso-palatine. All CR values were significant.

	N	*MLi*	*CR*	ρ *1*	ρ *7*	ρ *2*	ρ *3*	ρ *4*	ρ *5*	ρ *6*	ρ *abs 1-2*	Mean ρ
T. tetradactyla	74	IX (7)	**0.54**	0.59	0.16	0.48	0.35	0.32	0.12	0.45	-0.43	0.35
T. mexicana	43	IX (7)	**0.64**	0.45	0.19	0.43	0.23	0.30	0.20	0.28	-0.32	0.30
M. tridactyla	38	IX (7)	**0.86**	0.66	0.33	0.59	0.53	0.25	0.40	0.58	-0.54	0.48
C. didactylus	60	IX (7)	**0.67**	0.65	0.15	0.41	0.20	0.37	0.17	0.17	-0.25	0.30
P. maximus	14	IX (7)	**0.78**	0.26	0.26	0.26	0.26	0.26	0.26	0.26	-0.19	0.26
O. afer	40	IX (7)*	**0.71**	0.36	0.15	0.23	0.34	0.19	0.21	0.33	-0.15	0.26
M. crassicaudata	7	II (3)*	**0.90**	0.32	-	-	-	-	0.32	0.32	-0.07	0.32
M. javanica	28	IX (7)	**0.68**	0.43	0.26	0.35	0.32	0.24	0.21	0.24	-0.29	0.29
M. pentadactyla	27	VII (6)	**0.68**	0.31	-	0.24	0.42	0.25	0.21	0.19	-0.13	0.27
S. temminckii	15	V (6)	**0.88**	0.48	-	0.22	0.29	0.25	0.28	0.18	-0.14	0.28
S. gigantea	12	VII (6)	**0.80**	0.49	-	0.54	0.48	0.40	0.30	0.26	-0.36	0.41
P. tricuspis	72	VII (6)	**0.60**	0.24	-	0.22	0.40	0.28	0.17	0.16	-0.16	0.26
P. tetradactyla	17	X (7)	**0.81**	0.49	0.24	0.33	0.22	0.26	0.22	0.20	-0.31	0.28
P. cristatus	25	VII (6)	**0.70**	0.26	-	0.22	0.39	0.23	0.14	0.23	-0.13	0.25
O. megalotis	8	IX (7)*	**0.80**	0.61	0.50	0.37	0.32	0.22	0.23	0.49	-0.11	0.39

S. gigantea presented the highest integration for the molar-palate module ($\rho = 0.53$; Table 3), above the average for the remaining species (Table 3; Fig. 3B). Species that showed a seven-module architecture presented a relatively high correlation for this module, as it is composed of only three bilaterally symmetric landmarks. *P. cristatus* presented the lowest integration level for the molar-palate module ($\rho = 0.21$).

The orbit module was generally less integrated than the modules from the rostrum. *S. gigantea*, *S. temminckii*, *P. tricuspis*, *M. pentadactyla*, and *P. cristatus* were the exceptions in consistently presenting a relatively well integrated orbit (Tables 2 and 3; Fig. 3C). These species all showed the modular pattern

VII, in which landmarks for the orbit module are restricted to the orbitosphenoid/alisphenoid complex. *C. didactylus* showed the least integrated orbit (ρ = 0.21; Table 3).

Table 3 – Static allometry-corrected modular architectures of 15 myrmecophagous mammals. Number of specimens (*N*), most likely modular architectures recovered with EMMLi (*MLi*), covariance ratio (*CR*), within-module absolute correlations (*ρ*), and correlation between oro-nasal and molar-palate modules assuming a therian six-module (V) architecture (*ρ abs*). (1) Oro-nasal/rostrum, (2) molar-palate, (3) orbit, (4) zygomatic-pterygoid, (5) vault, (6) basicranium, (7) naso-palatine. All CR values were significant.

	N	*MLi*	*CR*	*ρ 1*	*ρ 7*	*ρ 2*	*ρ 3*	*ρ 4*	*ρ 5*	*ρ 6*	*ρ abs 1-2*	Mean *ρ*
T. tetradactyla	74	IX (7)	**0.54**	0.58	0.16	0.48	0.34	0.34	0.12	0.46	-0.43	0.35
T. mexicana	43	IX (7)	**0.64**	0.44	0.19	0.45	0.24	0.31	0.20	0.27	-0.33	0.30
M. tridactyla	38	IX (7)	**0.61**	0.61	0.32	0.41	0.30	0.21	0.25	0.46	-0.31	0.37
C. didactylus	60	IX (7)	**0.68**	0.65	0.15	0.42	0.21	0.38	0.18	0.18	-0.25	0.31
P. maximus	14	-	**-**	-		-	-	-	-	-	-	-
O. afer	40	X (7)	**0.64**	0.29	0.14	0.40	0.28	0.21	0.17	0.31	-0.17	0.26
M. crassicaudata	7	-	**-**	-		-	-	-	-	-	-	-
M. javanica	28	III (4)	**0.69**	0.31	-	-	-	0.28	0.15	0.23	-0.27	0.24
P. pentadactyla	27	VII (6)	**0.69**	0.31	-	0.24	0.42	0.25	0.20	0.19	-0.15	0.27
S. temminckii	15	VII* (6)	**0.85**	0.21	-	0.25	0.44	0.27	0.23	0.17	-0.17	0.26
S. gigantea	12	VII (6)	**0.82**	0.37	-	0.53	0.41	0.46	0.32	0.23	-0.29	0.39
P. tricuspis	72	VII (6)	**0.61**	0.23	-	0.23	0.40	0.27	0.17	0.16	-0.15	0.24
P. tetradactyla	17	IX* (7)	**0.81**	0.45	0.27	0.33	0.21	0.32	0.21	0.20	-0.28	0.28
P. cristatus	25	-	**-**	-		-	-	-	-	-	-	-
O. megalotis	8	-	**-**	-		-	-	-	-	-	-	-

The zygomatic-pterygoid module is poorly integrated, with *C. didactylus*, and *S. gigantea* revealing higher than average levels of integration for this module (Table 3; Fig. 3D). *O. afer* and *M. tridactyla* were the species with the lowest integration magnitude (ρ = 0.20) for this module.

The vault was the least integrated module, overall (Tables 2 and 3; Fig. 3E). *S. gigantea* showed an averagely integrated vault (ρ = 0.32). The species with the least integrated cranial vault was *T. tetradactyla* (ρ = 0.12).

The basicranium was strongly integrated in *T. tetradactyla*, *M. tridactyla*, and *O. megalotis* (Tables 2 and 3; Fig. 3F). Pangolins revealed relatively low integration values of the basicranium, with *P. tricuspis* presenting the lowest values (ρ = 0.16). *C. didactylus* also showed a very weakly integrated basicranium (ρ = 0.18). *O. afer* presented a moderately integrated basicranium.

In species presenting a naso-palatine module, this region was weakly integrated in four of them (*Tamandua* spp., *C. didactylus*, and *O. afer*), moderately integrated in *M. tridactyla* and *P. tetradactyla*, and well-integrated in *O. megalotis*. In all species with different between-module correlations, the naso-palatine module was more strongly correlated with the oro-nasal than with the molar-palate module (Table

4; correlation level was similar in *O. megalotis* and *P. maximus*). This was more pronounced in *Tamandua* spp. and *M. tridactyla*. In *Tamandua* spp., *C. didactylus*, and *O. afer*, the naso-palatine module was more strongly integrated with the oro-nasal than within itself (Table 4).

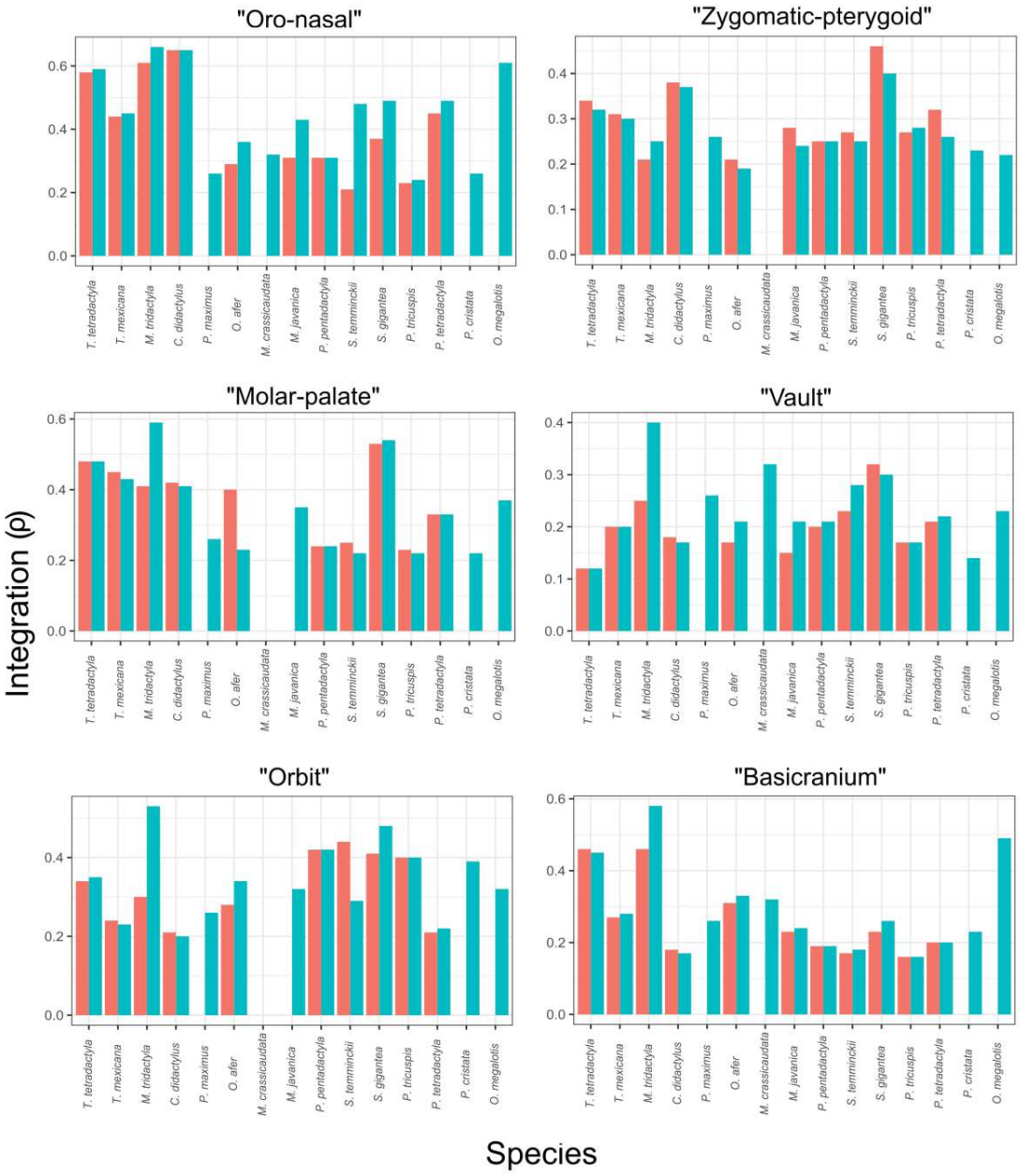

Figure 3 – Histogram of the within- and between-module correlations (ρ) for the main six modules of the placental skull (Cheverud, 1982; Goswami, 2006) for all 15 species. Blue bars represent raw correlations and pink bars represent allometry-corrected correlations (Tables 2 and 3). Null values indicate either the absence of a module in the respective species or the inexistence of allometry in the sample.

When the absolute correlations between the oro-nasal and molar/palatine regions were considered, they were more negative in specimens with a longer rostrum (Tables 2 and 3). *P. cristatus, O. megalotis,* and *M. crassicaudata* presented the less negative correlations ($\rho < -0.13$), while *S. gigantea*, *Tamandua* spp., and *M. tridactyla* showed more negative values ($-0.31 \geq \rho \geq 0.45$). Non-corrected values showed a similar pattern, but this analysis showed that these negative correlations were partially a result of static allometry in *M. tridactyla* and *S. gigantea* (Table 3).

Table 4 – Static allometry-corrected (when detected) integration magnitudes of the oro-nasal (1), naso-palatine (7), and molar-palate (2) modules in myrmecophagous mammals with a 7 module architecture. Values for the interspecific data set are also shown. Number of specimens (*N*), most likely modular architectures (*EMMLi*), within-module absolute correlations (ρ), and correlation between oro-nasal, and molar-palate modules with the naso-palatine (ρ *1-7*, ρ *2-7*).

	N	*EMMM*	ρ *1*	ρ *7*	ρ *2*	ρ *1-7*	ρ *2-7*
T. tetradactyla	74	IX (7)	0.58	0.16	0.48	0.26	0.11
T. mexicana	43	IX (7)	0.44	0.19	0.45	0.23	0.13
M. tridactyla	38	IX (7)	0.61	0.32	0.41	0.28	0.16
C. didactylus	60	IX (7)	0.65	0.15	0.42	0.17	0.14
P. maximus	14	IX (7)	0.26	0.26	0.26	-	-
O. afer	40	X (7)	0.29	0.14	0.40	0.16	0.13
P. tetradactyla	17	IX* (7)	0.45	0.27	0.33	0.19	0.14
O. megalotis	8	IX* (7)	0.61	0.50	0.37	-	-
Interspecific	36	X	0.68	0.28	0.76	0.33	0.41

The PLS analyses between independently aligned modules of the two most sampled species revealed that covariation was not significant between all modules (Tables S5 and S6). In *P. tricuspis*, less than half of the inter-module correlations were significant after adjusting the *p*-values for multiple comparisons. The oro-nasal/dorsal rostrum region showed a marginally non-significant correlation with the molar-palate module ($p = 0.06$). The molar-palate module was significantly correlated with the small orbit, the zygomatic-pterygoid, and the basicranium. The orbit significantly correlated with the zygomatic-pterygoid and the vault, while the latter presented a significant correlation with the vault. In *T. tetradactyla* none of the four modules recovered with the MCN analysis significantly correlated with each other, after adjusting for multiple comparisons. Before the adjustment of the *p*–values, the correlation between the rostrum and the zygomatic pterygoid was marginally significant. In both species, PLS performed between modules from a common Procrustes superimposition showed an increase in the number of significant correlations (Tables S5 and S6). In *P. tricuspis*, all but one correlation were highly significant (oro-nasal+molar-palate was marginally significant; $p = 0.4$), while *T. tetradactyla* presented a non-significant

zygomatic-pterygoid+vault ($p = 0.10$) and a marginally significant oro-nasal+vault ($p = 0.04$) correlations. Both *P. tricuspis* and *T. tetradactyla* modular integration changed substantially when separate Procrustes superimpositions were performed per module (Table S5 and S6). In *P. tricuspis,* the integrations of the oro-nasal, orbit/alisphenoid slightly decreased, those of the molar-palate, zygomatic-pterygoid, and vault increased, while that of the basicranium remained unchanged (Table S5). In *T. tetradactyla*, only the vault became more integrated when aligned separately. The remaining modules presented decreased integrations, when compared to those measured from a single Procrustes superimposition (Table S6). The integration of the rostrum and the basicranium decreased by more than 50%.

Evolutionary modularity

The Procrustes ANOVA reveals a weak ($R^2 = 0.07$) but marginally significant effect of size on skull shape ($F_{1,34} = 2.37$; $p = 0.04$). The principal component analyses on the residuals of this regression showed that, despite the phylogenetic affinities, the different skull morphologies clearly separated anteaters from their sister taxa armadillos and sloths, as well as pangolins from carnivores. Most of the skull shape variation (90%) is explained by the first seven principal components (PCs). PC1 explains 39.64% of the variance and mainly explained the degree of anterior projection of the nasal bones relative to both frontal bone and the anterior most part of the maxillae, the distance between the maxillary and squamosal zygomatic processes, and the width of the rostrum (Fig. 4). Ferae species (Carnivora + Pholidota) present mostly negative or low positive PC1 values, while anteaters (to the exception of *Cyclopes didactylus*), armadillos, and the aardvark score positive values. The sloths present low PC1 values, due to their short snout. PC2 explains 22.53% of the variance and explained the projection of the anterior margin of the maxilla, the posterior projection of the palatine, the position of the zygomatic processes of the maxilla and squamosal in respect to each other, and the length of the interparietal suture associated with a differential contribution of the supraoccipital to the skull roof (Fig. 4). Toothless anteaters and pangolins show positive PC2 values while toothed species mostly present negative PC2 scores. *Orycteropus afer* and *Tenrec ecaudatus* also presented positive PC2 values closer to anteaters and pangolins. The toothless species with the lowest PC2 scores is *Cyclopes didactylus* (Fig 4).

EMMLi recovered the seven-module naso-palatine (X; derived from Hallgrimsson et al., 2004) architecture to be the most likely architecture for our interspecific dataset, both when using correlations matrices derived from raw shape coordinates and allometry-corrected shapes (Table 5). The oro-nasal/rostrum module was strongly integrated ($\rho = 0.66/0.68$) and showed the highest inter-modular

correlation with the palate/molar module (ρ = 0.53/0.54). The oro-nasal/rostrum was also well correlated with the orbit (ρ = 0.47/0.48). The molar-palate was the most integrated of all modules (ρ = 0.78/0.78), with the orbit (ρ = 0.41), the zygomatic (ρ = 0.21/0.22), and the vault (ρ = 0.27/0.28) showing the lowest values (Table 5). The basicranium was also strongly integrated (ρ = 0.48/0.52), although less than the two modules of the rostrum. The CR test found the modular architecture X to be significant for both raw shape coordinates (CR = 0.85; p = 0.001) and allometry-corrected shapes (CR = 0.84; p = 0.001) datasets.

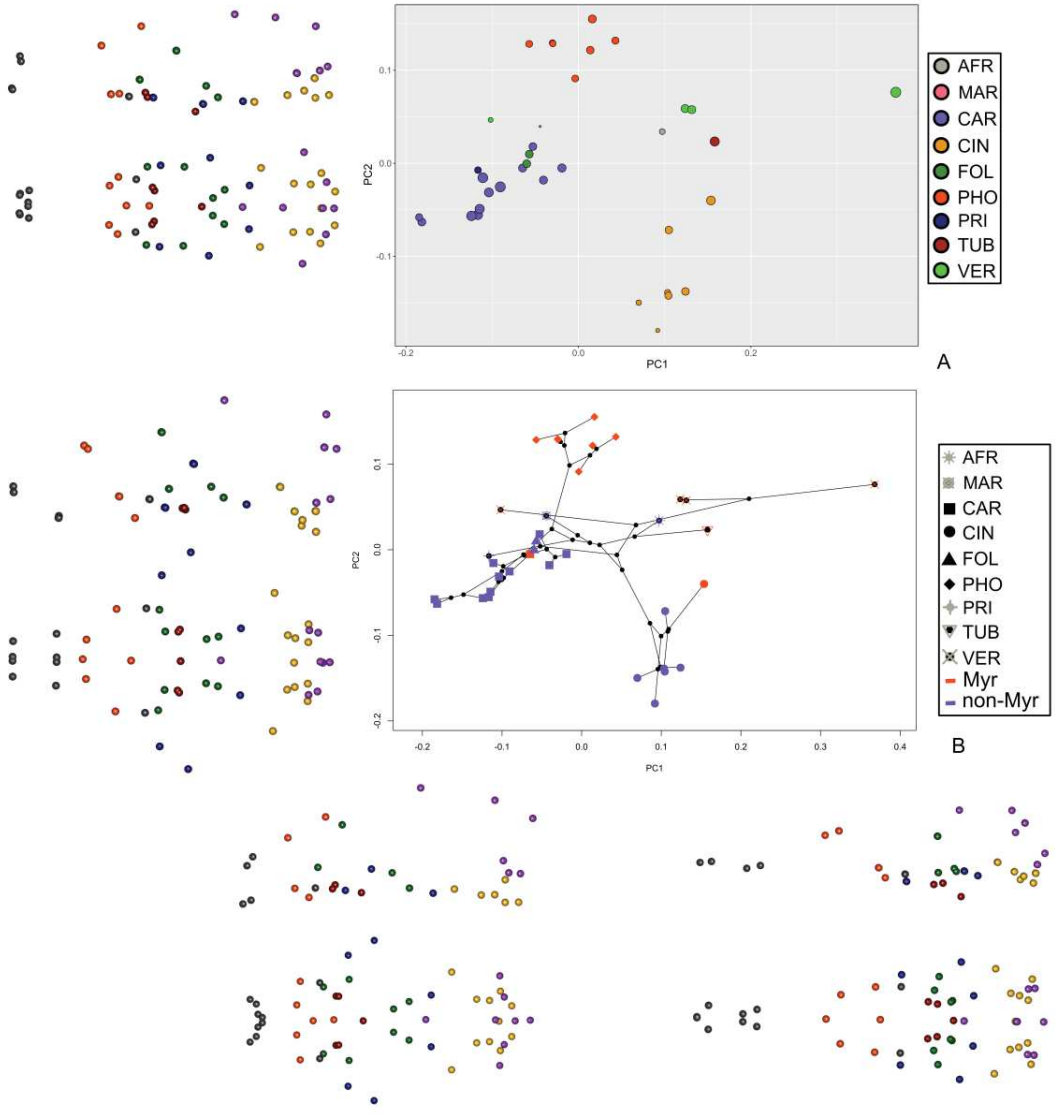

Figure 4 – Principal component morphospace of the interspecific dataset (n = 36). Morphospace formed by PC1 and 2 with points representing the average shape per species. (A) Points are colored by clade and scaled to centroid size; maximum and minimum shapes are presented for each axis with landmarks colored according to the seven-module architecture X identified for the interspecific dataset. (B) Phylogenetic relationships plotted on the morphospace; colors indicate diet and shapes indicate clades. Shape coordinates are allometry-corrected.

Table 5 – Within- and between-modules correlations from the most likely (Hallgrimsson 7) modular architecture for 15 myrmecophagous and 21 non-myrmecophagous species. (1) Oro-nasal/rostrum, (2) molar-palate, (3) orbit, (4) pterygoid, (5) vault, (6) basicranium, (7) naso-palatine. Respective within-module correlations (ρ) for raw shape coordinates and allometry-corrected shapes are in bold. Between-module correlations output from EMMLi in the upper (allometry-corrected coordinates) and lower (raw shape coordinates) triangles.

	1	2	3	4	5	6	7
1	**0.66/0.68**	0.54	0.48	0.27	0.39	0.33	0.33
2	0.53	**0.78/0.78**	0.36	0.18	0.37	0.35	0.41
3	0.47	0.37	**0.41/0.41**	0.24	0.30	0.34	0.20
4	0.26	0.19	0.24	**0.21/0.22**	0.19	0.21	0.24
5	0.36	0.35	0.29	0.18	**0.27/0.28**	0.36	0.24
6	0.31	0.33	0.32	0.21	0.35	**0.48/0.52**	0.24
7	0.32	0.41	0.20	0.15	0.23	0.25	**0.29/0.28**

Table 6 – Evolutionary rates and significance of pairwise comparisons of the face (upper triangle) and neurocranium (lower triangle) modules for allometry-corrected shape data. R face – evolutionary rate for the face; R neuro; evolutionary rate for the neurocranium; Myr – myrmecophagous; non-Myr – non-myrmecophagous; Ver – Vermilingua; Pho – Pholidota; Car – Carnivora; Atl – Atlantogenata. Values for the first two columns correspond to morphological evolutionary rates; remaining values correspond to *p*-values of pairwise comparisons. Significant *p*-values are in bold. *significant at α=0.10

	R face	R neuro	Myr	non-Myr	Ver	Pho	Car	Atl	Mar	Eua
Myr	$5.41x10^{-6}$	$2.27x10^{-6}$	-	0.24	-	-	-	-	-	
non-Myr	$2.91x10^{-6}$	$1.20x10^{-6}$	0.73	-	-	-	-	-	-	
Ver	$1.28x10^{-5}$	$3.71x10^{-6}$	-	-	-	**<0.01**	**0.01**	0.07*	**<0.01**	0.06*
Pho	$2.10x10^{-6}$	$1.62x10^{-6}$	-	-	0.06*	-	0.68	0.47	0.11	0.94
Car	$2.76x10^{-6}$	$1.89x10^{-6}$	-	-	0.11	0.71	-	0.77	0.06*	0.67
Atl	$3.48x10^{-6}$	$2.25x10^{-6}$	-	-	0.23	0.39	0.64	-	**0.04**	0.43
Mar	$5.10x10^{-7}$	$4.40x10^{-7}$	-	-	**0.01**	0.09*	0.07*	**0.04**	-	0.12
Eua	$2.00x10^{-6}$	$1.92x10^{-6}$	-	-	0.29	0.76	0.97	0.75	0.10	-

Evolutionary rates were assessed for allometry-corrected skull shapes only. The measurement of skull shape evolutionary rates for the face-neurocranium two-module architecture revealed that the rostrum/face tend to faster than the neurocranium (Table 6). Anteaters were the clade that showed the highest evolutionary rates for the rostrum/face, while pangolins showed one of the lowest (the lowest if we exclude single-membered groups as Marsupials and Euarchantoglires; Fig. 5A, Table 6). Within anteaters, *M. tridactyla* and *C. didactylus* showed the faster rates, while these decrease in the genus *Tamandua*, when compared to the sister taxon within the Myrmecophagidae. In pangolins, the branches leading to *Phataginus* spp., *M. pentadactyla*, and *M. crassicaudata* exhibit the slowest morphological evolutionary rates, alongside *U. arctos*. Rostrum/face shape increases in the branches leading to *Smutsia* spp., particularly the large bodied *S. gigantea.* Within the genus *Manis*¸ the branch leading to *M. javanica*

shows a slightly faster evolutionary rate. Xenarthrans showed relatively fast evolving rostra/faces when compared to those of other clades (Fig. 5A). Within Xenarthra, *Tamandua* showed slowly changing neurocrania/basicrania (Fig. 5B). The comparison of the evolutionary rates between myrmecophagous and non-myrmecophagous mammals did not yield a significant difference, both when comparing the rostrum/face, or the neurocranium/basicranium (Tables 6).

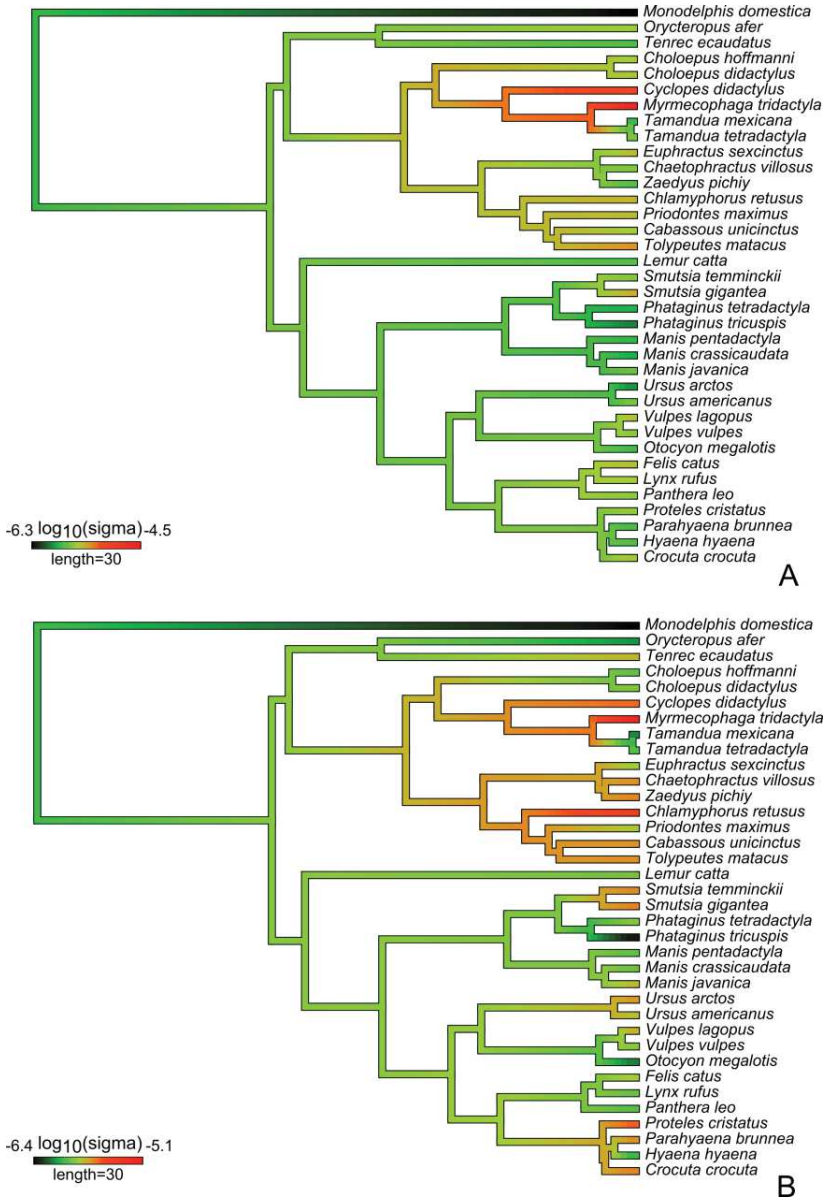

Figure 5 – Morphological evolutionary rates (σ) of the face (A) and neurocranium (B) modules plotted on a phylogeny. Black color indicates slow evolutionary rates and red indicates fast evolutionary rates. σ values are $\log_{10}$-transformed.

When toothless species and respective sister taxa were split into separate groups (Pholidota *vs* Carnivora; Vermilingua *vs* Atlantogenata), the pairwise comparisons showed that the rostrum/face of anteaters showed a significantly faster evolutionary rate than that of pangolins and carnivores (Table 5). The same test revealed a close to significance ($p = 0.07$) difference between the evolutionary rate of the anteater rostrum compared to that of the remaining Atlantogenata. Concerning the neurocranium/basicranium, the shape in anteaters evolved marginally faster than that of pangolins (Table 6). Comparisons with Carnivora and the sister-taxa within Atlantogenata did not yield significant rate differences. Evolutionary rates for the individual rostrum modules presented similar patterns to those obtained for the full rostrum module. Therefore, in order to avoid a redundant comparison, we present the results in a graphical way only (Fig. S5). The module naso-palatine module was not represented, as its validation as an independent module is uncertain (see 'Discussion').

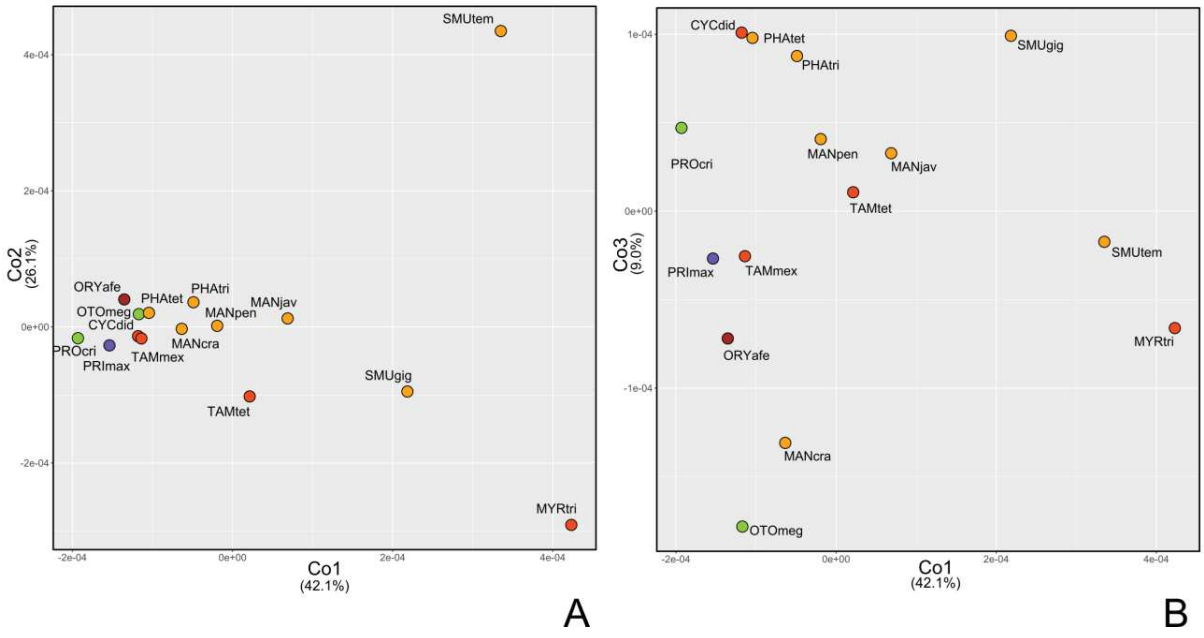

Figure 6 – Principal coordinates ordination of the covariance matrices of the 15 analysed myrmecophagous species. Each point represents a species. Points are coloured by Order: Vermilingua (orange), Cingulata (purple), Pholidota (dark yellow), Tubulidentata (brown), and Carnivora (Green).

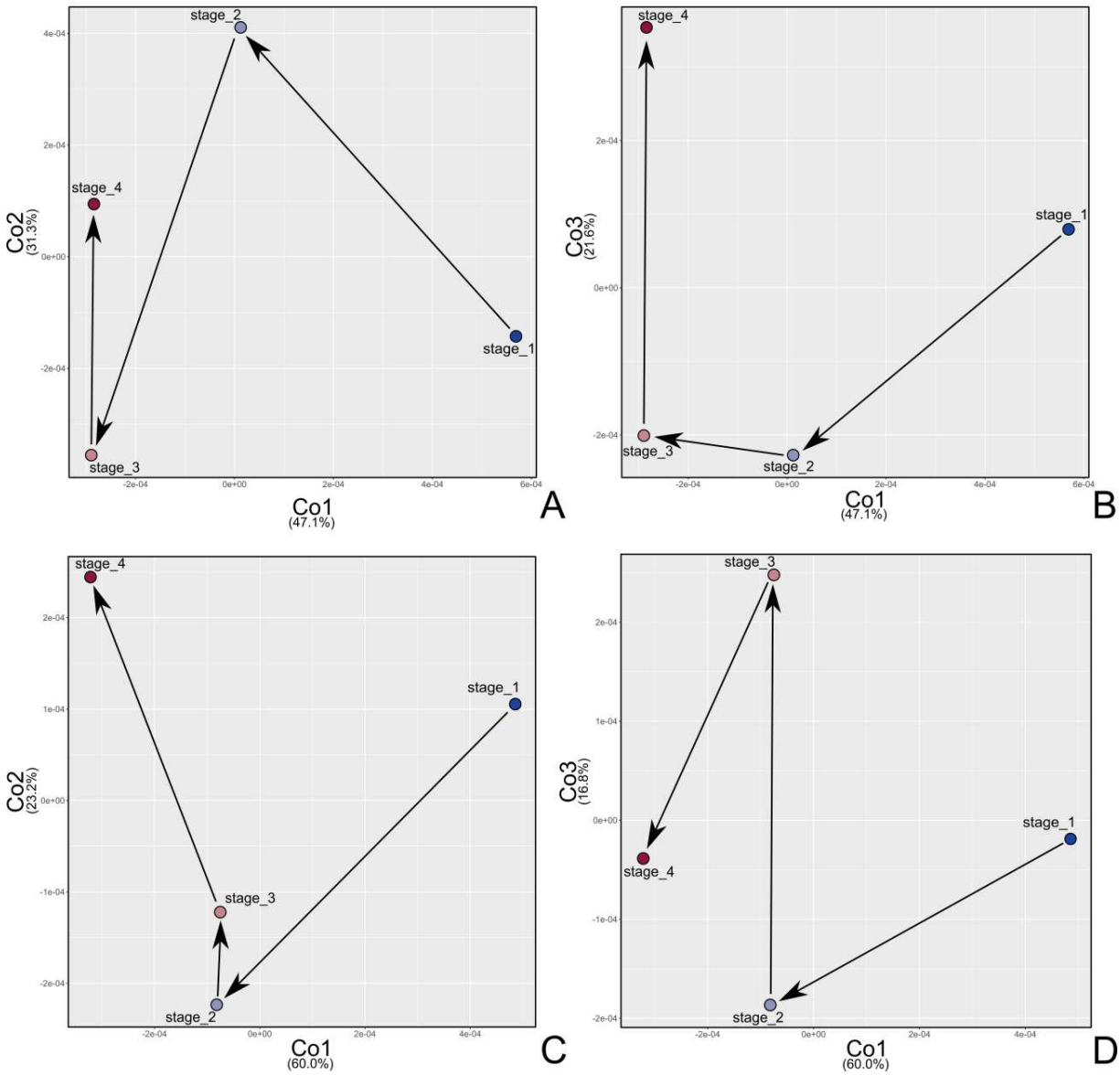

Figure 7 – Principal coordinates ordination of the covariance matrices of the interspecific dataset of *P. tricuspis* (A, B) and *T. tetradactyla* (C, D). Each point represents the covariance matrix of one of the four ontogenetic stages (juvenile to adult). The black arrows represent the ontogenetic trajectory of the covariance matrix for each species.

Comparison of covariance matrices

The PCA performed on the Procrustes aligned coordinates of the full dataset revealed that 90% of the variance was explained by the first seven PCs. These axes were retained for all posterior analyses. The PCoA performed on the 15-species Euclidean distance matrix showed that 90% of the variance was explained by the first five coordinates (Cos) of the multidimensional space. Co1 (42.1%; Fig. 6A) shows

a trend from toothed (negative values) to toothless and long-snouted (positive values) species. *P. cristatus* presents the lowest Co1 value, while *M. tridactyla* presents the highest. Co2 (26.1%; Fig. 6A) mostly segregates *S. temminckii* (outlier with high positive values), *T. tetradactyla*, *S. gigantea*, and *M. tridactyla* from all the remaining species. *M. tridactyla* presents the most negative Co2 value, followed by *T. tetradactyla* and *S. gigantea* with values relatively closer to the cluster including most of the species on the middle-left side of the morphospace (Fig. 6). Cos 3 (9.0%; Fig. 6B) and 4 (7.0%) do not appear to show an identifiable biological signal associated to the covariation patterns.

The PCA performed on the Procrustes aligned coordinates of *P. tricuspis* (including juveniles) revealed that 90% of the variance in skull shape was distributed in the first 25 axes of the morphospace. The PCoA performed on the resultant distance matrix including four age/size groups revealed that the relationship between phenotypic covariance and size is not linear during the ontogeny in *P. tricuspis* (Fig. 7A, B). The analysis performed on the distance matrix for the *T. tetradactyla* dataset (24 PCs) revealed a similar result, although the trajectory was different (Fig. 7C, D). In both cases, stage 1 is separated from the remaining ones by Co1, with later stages being separated by Co2.

Discussion

Exploratory analysis of modularity

Exploratory methods are a good complement to *a priori* hypothesis testing, as they may reveal patterns that are not predicted in *a priori* developmental, functional, or even physiological hypotheses (Zelditch *et al.*, 2008). We applied, for the first time, the morphological correlation networks methodology (MCN, Suzuki, 2013) to assess the modular patterns of the mammalian skull. Our results show that, for most species, the clusters recovered from the network analyses did not deliver a fine grouping of functional modules (Goswami, 2006).

Some of the illogical and gross clusters found might result from methodological biases. Typically, landmarks from the oro-nasal region were often found to cluster with basicranial structures (Fig. 2A). This particular case might be related to covariance introduced by the Procrustes superimposition (see 'Procrustes superimposition in integration and modularity').

Nevertheless, the networks resulting from our most sampled species *P. tricuspis* (n=72) and *T. tetradactyla* (n = 74) retrieved modular patterns resembling those found in previous studies (Cheverud, 1982; Goswami, 2006). While this could be related to a strong modular structure of the skull for these two species, MCN might also be sensitive to the number of sampled individuals (Fig. 2a). Anatomically, the

modular pattern retrieved from the MCN performed on *P. tricuspis* and *T. tetradactyla* showed a clear differentiation between these two species, mainly at the level of the division of the rostrum and palate and the structures of the orbit and zygomatic-pterygoid.

Goswami (2006), Cheverud (1982), and Parr *et al.* (2016) found an individualized orbit module that includes the anterodorsal part of the orbit and the border region between the nasal and frontal bones. In the MCN-derived *P. tricuspis* architecture, the orbit module is much smaller and consists of the ali- and orbitosphenoid. As for the dog (Parr *et al.*, 2016), the zygomatic and pterygoid regions are not included in the same module in *P. tricuspis*. In both cases, a zygomatic arch module was recovered. The MCN-derived modular architecture for *P. tricuspis* also revealed a change in the covariation patterns within the rostrum (Fig. 1B). While the posteroventral part of the rostrum follows a similar pattern to that of other mammals, landmarks from the oro-nasal and the fronto-nasal regions are included in a single module, which contrasts with the condition seen in dogs (Parr *et al.*, 2016), rhesus macaques (Cheverud, 1982), and the therian six-module pattern (Goswami, 2006).

Contrary to *P. tricuspis*, *T. tetradactyla* showed a four-module architecture. The absence of an orbit module *sensu* Goswami (2006) in *T. tetradactyla* is similar to the condition in *P. tricuspis*. However, *T. tetradactyla* exhibited integrated oro-nasal and molar regions, while these were grouped independently in *P. tricuspis*. Contrary to *P. tricuspis*, the naso-frontal region of *T. tetradactyla* is integrated with the landmarks of the vault module. This might be explained by a more pronounced projection of the anterior flanges of the frontal bone, associated with the facial process outgrowth (Hallgrímsson *et al.*, 2007, 2009). The zygomatic-pterygoid module of *T. tetradactyla* corresponds to the one defined by Goswami (2006) plus the ali- and orbitosphenoid orbit foramina. It is restricted to the posterior part of the skull, as neither the zygomatic process of the maxilla nor the highest point of the maxilla-palatine suture are included in this module (opposite to *P. tricuspis*). Landmarks corresponding to the midline of the palatines-maxillae suture and the infraorbital foramen were separated from all other clusters. This might represent a shift associated to either rostrum elongation or tooth loss, resulting in a dissociation from the molar-palate.

Contrary to MCN, the EDMA procedure does not require landmarks to be aligned with Procrustes superimposition. This avoids the issues related to estimations of variability of the landmarks that are placed further from the centroid of shape (Lele & Richtsmeier, 2001). Although the number of clusters is not straightforward to determine (Jung *et al.*, 2003; Salvador & Chan, 2004; Kassambara, 2017), hierarchical clustering is useful in detecting potential modules when the general organization of a structure is unknown (Cheverud, 1982; Lele & Richtsmeier, 1991; Goswami, 2006). The visual comparison of

modular patterns recovered from our species allowed us to notice that the landmarks from the naso-palatine region tended to cluster apart from our *a priori* defined molar-palate module. This was particularly evident in *T. tetradactyla*, in which these landmarks clustered separately from the rest of the skull (Fig. S2A). In *T. mexicana, M. tridactyla* and *O. afer* the naso-frontal and maxilla-palatine landmarks were also separated from the orbit and molar-palate regions, respectively. These landmarks appear to represent a decoupling of naso-palatine landmarks that could be related to skull elongation or to the release from constraints associated to tooth eruption in anteaters (Mitteroecker & Bookstein, 2009; Klingenberg & Navarro, 2012). However, this decoupling was not as evident in other myrmecophagous species, such as pangolins or the aardwolf. This result could indicate structural constraints associated to phylogenetic relatedness, given that both groups are sister taxa (Murphy *et al.*, 2001a). It could also suggest the relaxation of phylogenetic constraints in anteaters and aardvarks.

Procrustes superimposition in integration and modularity

Recently, Cardini (2019b) alerted for the risk of spurious results in analyses of integration and modularity using a single Procrustes analysis to superimpose landmark coordinate datasets. The author demonstrated that undesirable covariation is introduced during the process of alignment, rotation, and scaling. The covariation introduced by the Procrustes superimposition may create modular structures in non-modular datasets (Cardini, 2019b). In the same time, performing separate Procrustes superimpositions per module may also remove a biologically relevant part of the covariance, especially the one relative to size and orientation of the modules (Klingenberg, 2009b; Cardini, 2019b). Given that somatic growth and resulting allometric signal are the dominant promoters of integration (Hallgrímsson *et al.*, 2007; Porto *et al.*, 2009), this can be problematic in the case of myrmecophagous mammals, in which rostrum growth is an important variance generator.

Our results are in line with those of Cardini (2019b), showing that some correlations between modules are created by Procrustes superimposition (Tables S5 and S6). For instance, our partial least-squares (PLS) analyses between separately superimposed modules in *P. tricuspis* showed that the oro-nasal and basicranium regions (associated in the MCN) do not significantly covary (Table S5 and S6). Procrustes superimposition also appears to have an important effect in the magnitude of integration, as shown by our comparisons between single and separated Procrustes superimposition. In general, intramodule correlations present more similar values when Procrustes superimpositions are performed by module than when a single Procrustes is performed for the whole skull.

The modular partition of the skull obtained from EDMA also showed that landmarks from the anterior and posterior parts of the skull never cluster together. On the other hand, the modules obtained from this method roughly correspond to those recovered with methods relying on Procrustes superimposition (e.g., oro-nasal, basicranium, zygomatic-pterygoid; Fig. S2-3). Our results indicate that, despite the introduction of correlations with no biological meaning, the modular partition of the skull obtained after superimposing landmarks configurations provides comparable results to those of methods avoiding it. Nevertheless, further studies are needed in order to accurately assess the amount of noise introduced by Procrustes superimposition.

Analysis of *a priori* modular architectures in myrmecophagous mammals

Some of the first works that addressed the modular patterns of the skull of mammals used exploratory methods (Cheverud, 1982; Goswami, 2006). However, hypothesis testing methods have become increasingly used, assessing if sets of traits exhibit modular structures when compared to a random organization (Klingenberg, Mebus, & Auffray, 2003; Claude, 2008; Klingenberg, 2009a; Adams, 2016).

Using a recently proposed maximum-likelihood approach (EMMLi; Goswami & Finarelli, 2016), we showed that the modular organization of the skull in ant- and termite-eating placental mammals varies between three to seven modules. The species presenting the lowest number of modules (Model II) was also the least sampled (*Manis crassicaudata*; $n = 7$). Its modularity pattern probably represents a gross pattern of modularity, as suggested by the inconsistent modular patterning obtained from the hierarchical clustering based on EDMA analyses. The three-module architecture in *M. crassicaudata* shows a very low posterior probability (0.21), with four other architectures showing values above the 0.05 threshold taken as reference by Goswami and Finarelli (2016). A similar result was obtained for *Otocyon megalotis* ($n = 8$), which precludes any further interpretation of the results for these two species.

Most of the species presented a six- (VII) and seven-module (IX and one species with X) architectures. MCN results showed that the basicranium and posterior part of the vault have similar landmark composition of in both *P. tricuspis* and *T. tetradactyla*. The structure of these parts of the skull is quite conserved and correspond to those in previously proposed architectures (Cheverud, 1982; Hallgrímsson *et al.*, 2004; Goswami, 2006). These regions originate from the mesoderm in the very early stages of skull development (e.g., Piekarski *et al.*, 2014; Hallgrímsson *et al.*, 2019). In addition to their common tissue origin, covariance-generating processes such as muscle-bone interaction, tooth eruption,

or occlusion (Hallgrímsson *et al.*, 2007, 2009, 2019; Bookstein & Mitteroecker, 2014) mostly occur anterior to the temporal fossa.

In contrast, we showed that the anterior half of the skull shows more parcellation, as previously suggested in mammals (Cheverud, 1982; Goswami, 2006; Porto *et al.*, 2009; Makedonska, Wright, & Strait, 2012; Parr *et al.*, 2016). Nevertheless, we found relatively conserved modular patterns among myrmecophagous species. Most presented the same seven-module architecture derived from Goswami (2006) functional hypothesis with the addition of a naso-palatine module as suggested by the EDMA hierarchical clusters. However, this result largely contrasts with the MCN result for *Tamandua tetradactyla*. One possible explanation could be that EMMLi favours architectures with larger numbers of modules compared to models with fewer partitions (e.g., Felice & Goswami, 2018; Bardua *et al.*, 2019). When the seven-module architectures were removed from the EMMLi tests, both *Tamandua* spp. presented the model corresponding to that obtained from the MCN of *T. tetradactyla* (III; Table S7). A look at the correlations between modules shows that the naso-palatine module is more strongly correlated with the oro-nasal module than within itself (Table 4). Theoretically, a phenotypic module should share stronger interactions within it than with the surrounding elements of the system (Klingenberg, 2005). Therefore, oro-nasal and naso-palatine could potentially represent a single module in *Tamandua* spp (Table 4). MCN and EMMLi results do not, however, invalidate each other. As revealed by EMMLi, the oro-nasal and the molar-palate are well-integrated in *T. tetradactyla* ($\rho = 0.43$), which is in line with the single rostrum module retrieved by the MCN. On the other hand, the landmarks of the nasal-frontal suture might simply be more correlated with the anterior part of the cranial vault (frontal bone) than with the oro-nasal, which would justify its coupling with the cranial vault in the MCN.

Overall, modular architectures in *Tamandua* spp./*M. tridactyla* (both MCN- and EDMA-derived), and most pangolins (MCN-derived) appear to suggest a trend for rostrum integration, which might translate the preservation of covariance generated early in ontogeny (orofacial region; Zelditch & Carmichael, 1989), with a reduction of parcellation associated to tooth eruption and functional muscle-bone interaction normally linked to later developmental stages (Herring, 1993; Hallgrímsson *et al.*, 2007; Mitteroecker & Bookstein, 2009).

Modularity and the evolution of myrmecophagy

Despite some differences detected among myrmecophagous placentals, the modularity patterns were comparable to those found in previous studies including mammals (Cheverud, 1982; Goswami,

2006; Parr *et al.*, 2016; Heck *et al.*, 2018; Churchill *et al.*, 2019; Randau, Sanfelice, & Goswami, 2019). Given that the skull and the masticatory apparatus perform virtually the same functions across tetrapods (Schwenk, 2000), especially in mammals (Hiiemae, 2000), the maintenance of a functional partition of the skull across all mammals is beneficial in promoting the evolvability of functionally related structures (Riedl, 1978; Wagner & Altenberg, 1996).

Anteaters are a good example of modular conservatism, with the giant (*M. tridactyla*) and the pigmy (*C. didactylus*) anteaters showing completely different skull shapes (Fig. 4), but a similar seven-module cranial architecture (IX). In fact, considerable shape change can occur while phenotypic modularity patterns are maintained, as a result of extreme directional selection acting on conserved partitions (Parsons *et al.*, 2018). Our projection of the covariance matrices of our 15 myrmecophagous species showed that most species present quite conserved patterns of phenotypic covariation (Fig. 6). With the exception of *T. tetradactyla*, *M. javanica*, *S. temminckii*, *S. gigantea*, and *M. tridactyla*, most species cluster in a relatively small phenotypic covariation morphospace. These results are in line with EMMLi output in which the majority of the architectures fall within the expected variation reported among mammals (e.g., Goswami, 2006; Porto *et al.*, 2009). Curiously, the two closely related (Gibb *et al.*, 2016) and morphologically similar (Wetzel, 1975) *T. tetradactyla* and *T. mexicana* were apart in the phenotypic covariation morphospace. This might reflect the more pronounced intramodular integration in the oro-nasal, orbit, and basicranium region displayed by *T. tetradactyla* (Tables 2 and 3).

Nevertheless, our results suggest that extreme rostrum elongation and tooth loss might have affected covariance patterns in *Tamandua* and *Myrmecophaga*. The naso-palatine landmarks are more correlated to the oro-nasal than to the molar or orbit landmarks, in both genera. On the contrary, the naso-palatine module is more correlated with the molar-palate module, in the interspecific dataset. In *O. afer*, *P. maximus*, or *C. didactylus* the correlations between nasal-palatine and the other rostrum modules are not substantially different (Table 4).

Concerning the modular organization of the zygomatic-pterygoid region, we found a conserved zygomatic arch module in *P. cristatus*, *O. afer*, as well as in the maximum-likelihood model selection performed with the interspecific dataset. This is congruent with the role of this structure as the origin for part of the mandibular adductor musculature. Despite being myrmecophagous, *P. cristatus* and *O. afer* retain active mastication and biting functions (Patterson, 1975; Anderson, Richardson, & Woodall, 1992). However, the connection between modularity and function is not straightforward, exemplified by the presence of a zygomatic arch module in four pangolins (*P. tricuspis, Smutsia* spp. and *M. pentadactyla*).

All pangolins are toothless and unable to chew (Endo *et al.*, 1998). The presence of a zygomatic module is better explained by the strong ontogenetic allometric trend towards the growth of the zygomatic process of the maxilla reported in pangolins (Ferreira-Cardoso *et al.*, 2019a). Porto *et al.* (2013) found the zygomatic module to be absent in several mammalian groups with chewing and biting ability, which suggests a decoupling between masticatory function and the presence of a zygomatic arch module.

In the two species for which we had juvenile specimens (*P. tricuspis* and *T. tetradactyla*) we showed that, although missing the early stages of post-natal development, the covariance structure of the skull is changing throughout ontogeny (Fig 7). On the light of the 'Palimpsest model', modules derive from developmental processes with the potential to generate coordinated variation during skull ontogeny (Hallgrímsson *et al.*, 2007, 2009). These processes, such as neural crest migration (embryonic variation) or brain growth, all introduce variation at a certain stage, with the static phenotypic covariance patterns being a result of the overlap of several determinants of covariation (Hallgrímsson *et al.*, 2007, 2009). Specific determinants of covariation (e.g., masticatory function) might therefore be hard to infer from static modularity patterns (Fischer-Rousseau, Cloutier, & Zelditch, 2009).

Overall, the modular architectures recovered for the myrmecophagous species appeared to reflect a slight change in covariation patterns in the anterior half of the skull. In some species, tooth loss and snout elongation may have contributed for a less modular rostrum. Additionally, the masseter musculature and the structure of the zygomatic arch appear to be reflected in a quite inconstant composition of the zygomatic-pterygoid module. Namely, there appears to be a tendency for species without a functional zygomatic arch to maintain only the posterior part of this module preserved, but this is hardly related to function. The variability of modular structures in anteating mammals is particularly evident when comparing the phenotypic covariance matrices (PCoA), with toothed species occupying a much less dispersed in the morphospace. We also showed that significant differences on shape (e.g., *C. didactylus* vs *M. tridactyla*) do not necessarily translate into different modularity patterns, as an increase in variance on a few axes might reflect in very distinct morphologies due to pleiotropic effects.

Morphological integration and allometry

Previous studies showed that both within-modules and total integration vary across taxa (Goswami, 2006; Porto *et al.*, 2009; Goswami & Polly, 2010; Randau *et al.*, 2019). As in other mammal clades (e.g., Goswami, 2006; Porto *et al.*, 2009), the oro-nasal module of myrmecophagous species is more integrated than the remaining ones, with some taxa showing a moderately integrated basicranium.

The stronger integration of the oro-nasal module is explained by ontogenetic allometry and represents a pattern common to all mammals (Cardini & Polly, 2013; Cardini, 2019a). In the context of myrmecophagy, extreme rostrum elongation was reflected by the negative correlation between the oro-nasal and the molar-palate modules (*sensu* Goswami, 2006). These correlations were more negative in *M. tridactyla* and the two *Tamandua* compared to all the remaining species. On the opposite pole, *P. cristatus* and *O. megalotis* presented the less negative correlations. A negative correlation suggests a strong ontogenetic allometric effect on the rostrum region, reflecting the opposite directions of variation in its anterior and posterior parts (e.g., Ferreira-Cardoso *et al.*, 2019a). The best examples of this trend are *M. tridactyla*, *Tamandua* spp., and *S. gigantea*. Additionally, in the largest anteater and pangolin species (*M. tridactyla* and *S. gigantea*) a significant part of these negative correlations is associated with static allometry (Tables 2 and 3).

Our results also show that overall integration increases with size. *M. tridactyla* and *S. gigantea* are the largest species within anteaters and pangolins, respectively. Overall, all their modules are much more integrated than in their sister species (Tables 2 and 3). This can be explained by the covariation generated by the overall size increase of the skull and thus influencing all traits in the sample (Nijhout, 2011). Nevertheless, in *M. tridactyla* and *S. gigantea*, static allometry appears to be responsible for a good part of the integration, given that in general its values dropped after allometric correction (particularly those of the oro-nasal ragion). On the other hand, in *Tamandua* spp. show similar integration values after accounting for static allometry, which could indicate that most of the covariance was generated before adulthood (Table 3). For example, judging from the elongated shape of the rostra of anteaters fetuses (Fig. 1C; Hautier *et al.*, 2011), it is likely that a significant part of the somatic growth behind the increase in the integration of the rostrum regions (mainly oro-nasal) occurs during pre-natal development (Zelditch & Carmichael, 1989). Nevertheless, our phenotypic covariance trajectories (Fig. 7) show that changes may still occur in covariance/correlation matrices during post-natal development (Fig. 7).

We confirm that size variation is an important factor influencing integration magnitude in the mammal skull. While this was previously shown to be an evolutionary trend among placentals (Cardini & Polly, 2013; Porto *et al.*, 2013; Cardini, 2019a), our intraspecific analysis shows how canalized cranial variation is in placentals. In this case, selective pressures associated to myrmecophagy triggered a phenotypic response along axes of variation that are very conserved at the evolutionary level. This response might have been facilitated by complete tooth loss. Although early stages of tooth development occur in anteaters (Gervais, 1867; Rose, 1892), osteogenesis associated to that process (e.g., trabecular

bone) is much reduced (Ferreira-Cardoso *et al.*, 2019b). Therefore, the reduction of covariance introduced by tooth development might have released the naso-palatine module to co-vary more with the oro-nasal region (e.g., anteaters). This might explain why covariance matrices are more conserved within toothed myrmecophagous placentals when compared to the toothless ones (Fig. 6). Although the long-snouted *S. gigantea* appears to have a conserved molar-palate module, the inclusion of the naso-frontal landmarks in the oro-nasal module might also have a similar explanation.

Rates of morphological evolution

We showed that myrmecophagous mammals present a morphological convergence in the morphospace (Fig. 4). Our results also show that this convergence did not result from the convergence of the rates of morphological evolution. Instead, we found that the evolution of the morphology of the anteater rostrum is a result of high morphological evolutionary rates compared not only to its sister taxa but also to the remaining species included in the analyses (Fig. 5; Table 6). Surprisingly, the equally toothless pangolins showed a completely opposed scenario, showing very low rates of morphological evolution. While the high rates of morphological evolution could explain the average high integration of the rostrum and oro-nasal regions compared to the other modules within anteaters, it does not explain the shift of pangolins in the morphospace, when compared to their carnivoran sister taxa (Murphy *et al.*, 2001b,a). The relatively low evolutionary rates might be explained by the absence of recently diverged sister taxa to pangolins, and probably reflects a sampling/methodology bias. The addition of a toothed sister taxon to pangolins, like the palaeanodonts (Emry, 1970; Gaudin, Emry, & Wible, 2009) could help in the better estimating the shape of the pangolin ancestor, therefore enabling a better estimation of the evolutionary history of skull morphology in this group. On the other hand, the morphospace occupied by anteaters extends much more than that occupied by pangolins, as well as the distance from their sister group, the sloths (Fig. 4). Although a larger sampling at the placental scale would be needed and different models of evolution (e.g., Ornstein-Uhlenbeck, Early Burst; Harmon *et al.*, 2008; Alfaro *et al.*, 2009), our results suggest that the ecological convergence towards myrmecophagy did not involve the same degree of evolutionary rates of the rostra modules in anteaters, pangolins, and the remaining ant-eating placentals.

Conclusion

We showed that morphological changes in ant- and termite-eating lineages did not radically change the modular patterns in myrmecophagous placentals. Considering phenotypic correlations and covariances as

proxies for modularity and integration, we propose the following set of complementary possibilities to explain our results: 1) The genetic and developmental basis of the placental skull are extremely conserved, hindering drastic changes in modularity patterns even under strong selective pressures or eventual minor mutations (canalization); 2) Under a canalization scenario, limited axes of variation are available for the phenotype; these axes, under specific selective pressures, may generate extreme trait covariation/correlation (i.e., integration) of functionally related traits, while preserving phenotypic organizational modules (Cardini & Polly, 2013; Parsons *et al.*, 2018; Felice *et al.*, 2019); 3) Anteaters represent an exception, showing a putative a new module with differing variance direction (e.g., naso-palatine module in myrmecophagid anteaters). We interpret the anteater example as decanalization (Waddington, 1953; Stern, 1958) resulting from strong selective pressures and extreme ecological specialization.

Under the complementary paths 1) and 2), we would assume that myrmecophagy could have driven to changes of correlation in the functional modules of the rostrum. In this case, our data fails to detect a convergent shift among myrmecophagous placentals. However, changes in the morphospace and adaptation to functionally demanding ecologies (e.g., fossoriality) do not mandatorily impact structural integration (Sansalone *et al.*, 2019).

Under scenario 3), we can consider that the interaction between the nasal-frontal and maxillary-palatine condensations might represent a sub-module that has shifted from being correlated to the molar-palate module in placentals, to a sub-module of the oro-nasal. In the case of most pangolins and *P. cristatus*, only the naso-frontal region shows this shift. Our results might indicate that long-snouted myrmecophagous placentals tend to preserve modularity patterns associated to developmental processes occurring early in ontogeny (orofacial growth; Zelditch, 1988; Zelditch & Carmichael, 1989) both due to reduced covariance generated by occlusion and to the pronounced variation generated by the allometric growth of the rostrum.

References

Adams DC. 2016. Evaluating modularity in morphometric data: challenges with the RV coefficient and a new test measure (P Peres-Neto, Ed.). *Methods in Ecology and Evolution* 7: 565–572.

Adams DC, Collyer ML. 2018. Multivariate Phylogenetic Comparative Methods: Evaluations, Comparisons, and Recommendations. *Systematic Biology* 67: 14–31.

Adams D, Collyer M, Kaliontzopoulou A, Sherratt E. 2017. Geomorph: software for geometric morphometric analyses. R package version 3.0.5.

Alfaro ME, Santini F, Brock C, Alamillo H, Dornburg A, Rabosky DL, Carnevale G, Harmon LJ. 2009. Nine exceptional radiations plus high turnover explain species diversity in jawed vertebrates. *Proceedings of the National Academy of Sciences of the United States of America* 106: 13410–4.

Anderson MD, Richardson PRK, Woodall PF. 1992. Functional analysis of the feeding apparatus and digestive tract anatomy of the aardwolf *Proteles cristatus*. *Journal of Zoology* 228: 423–434.

Bardua C, Wilkinson M, Gower DJ, Sherratt E, Goswami A. 2019. Morphological evolution and modularity of the caecilian skull. *BMC Evolutionary Biology* 19: 30.

Bookstein FL, Mitteroecker P. 2014. Comparing covariance matrices by relative eigenanalysis, with applications to organismal biology. *Evolutionary Biology* 41: 336–350.

Cardini A. 2019a. Craniofacial allometry is a rule in evolutionary radiations of placentals. *Evolutionary Biology* 46: 239–248.

Cardini A. 2019b. Integration and modularity in Procrustes shape data: is there a risk of spurious results? *Evolutionary Biology* 46: 90–105.

Cardini A, Polly PD. 2013. Larger mammals have longer faces because of size-related constraints on skull form. *Nature Communications* 4: 2458.

del Castillo DL, Viglino M, Flores DA, Cappozzo HL. 2017. Skull ontogeny and modularity in two species of *Lagenorhynchus* : Morphological and ecological implications. *Journal of Morphology* 278: 203–214.

Cheverud JM. 1982. Phenotypic, genetic, and environmental morphological integration in the cranium. *Evolution* 36: 499–516.

Cheverud JM. 1996. Developmental integration and the evolution of pleiotropy. *American Zoologist* 36: 44–50.

Churchill M, Miguel J, Beatty BL, Goswami A, Geisler JH. 2019. Asymmetry drives modularity of the skull in the common dolphin (*Delphinus delphis*). *Biological Journal of the Linnean Society* 126: 225–239.

Claude J. 2008. *Morphometrics with R*. New York: Springer.

Claude J, Pritchard PCH, Tong H, Paradis E, Auffray JC. 2004. Ecological correlates and evolutionary divergence in the skull of turtles: a geometric morphometric assessment (J Kim, Ed.). *Systematic Biology* 53: 933–948.

Csardi G, Nepusz T. 2006. The igraph software package for complex network research. *InterJournal* Complex Sy: 1695.

Davit-Béal T, Tucker A, Sire J. 2009. Loss of teeth and enamel in tetrapods: fossil record, genetic data and morphological adaptations. *Journal of anatomy* 214: 477–501.

Drake AG, Klingenberg CP. 2010. Large-scale diversification of skull shape in domestic dogs: disparity and modularity. *The American naturalist* 175: 289–301.

Dryden IL, Mardia K V. 1993. Multivariate shape analysis. *Sankhyā: The Indian Journal of Statistics, Series A (1961-2002)* 55: 460–480.

Edgeworth FH. 1923. On the development of the cranial muscles of *Tatusia* and *Manis*. *Journal of anatomy* 57: 313–35.

Emerson SB. 1985. Skull shape in frogs: correlations with diet. *Herpetologica* 41: 177–188.

Emry RJ. 1970. A North American Oligocene pangolin and other additions to the Pholidota. *Bulletin of the American Museum of Natural History* 142.

Endo H, Nishiumi I, Kurohmaru M, Nabhitabhata J, Chan-Ard T, Nadee N, Agungpriyono S, Yamada J. 1998. The functional anatomy of the masticatory muscles of the Malayan pangolin, *Manis javanica*. *Mammal Study* 23: 1–8.

Escoufier Y. 1973. Le traitement des variables vectorielles. *Biometrics* 29: 751–760.

Felice RN, Goswami A. 2018. Developmental origins of mosaic evolution in the avian cranium. *Proceedings of the National Academy of Sciences of the United States of America* 115: 555–560.

Felice RN, Tobias JA, Pigot AL, Goswami A. 2019. Dietary niche and the evolution of cranial morphology in birds. *Proceedings of the Royal Society B: Biological Sciences* 286: 20182677.

Ferreira-Cardoso S, Billet G, Gaubert P, Delsuc F, Hautier L. 2019a. Skull shape variation in extant pangolins (Manidae, Pholidota): allometric patterns and systematic implications. *Zoological Journal of the Linnean Society*.

Ferreira-Cardoso S, Delsuc F, Hautier L. 2019b. Evolutionary tinkering of the mandibular canal linked to convergent regression of teeth in placental mammals. *Current Biology* 29: 468-475.e3.

Fischer-Rousseau L, Cloutier R, Zelditch ML. 2009. Morphological integration and developmental

progress during fish ontogeny in two contrasting habitats. *Evolution & Development* 11: 740–753.

Gaubert P, Antunes A, Meng H, Miao L, Peigné S, Justy F, Njiokou F, Dufour S, Danquah E, Alahakoon J, Verheyen E, Stanley W, O'Brien S, Johnson W, Luo S. 2018. The complete phylogeny of pangolins: scaling up resources for the molecular tracing of the most trafficked mammals on Earth. *Journal of Heredity* 109: 347–359.

Gaudin TJ, Emry RJ, Wible JR. 2009. The phylogeny of living and extinct pangolins (Mammalia, Pholidota) and associated taxa: a morphology based analysis. *Journal of Mammalian Evolution* 16: 235–305.

Gervais P. 1867. *Zoologie et paléontologie générales: nouvelles recherches sur les animaux vertébrés vivants et fossiles* (A Bertrand, Ed.). Paris: La Societé de Géographie.

Gibb G, Condamine F, Kuch M, Enk J. 2016. Shotgun mitogenomics provides a reference phylogenetic framework and timescale for living xenarthrans. *Molecular Biology and Evolution* 33: 621–642.

Gonzalez PN, Kristensen E, Morck DW, Boyd S, Hallgrímsson B. 2013. Effects of growth hormone on the ontogenetic allometry of craniofacial bones.

Goswami A. 2006. Cranial modularity shifts during mammalian evolution. *The American Naturalist* 168: 270–280.

Goswami A, Finarelli JA. 2016. EMMLi: A maximum likelihood approach to the analysis of modularity. *Evolution* 70: 1622–1637.

Goswami A, Polly PD. 2010. The influence of modularity on cranial morphological disparity in Carnivora and Primates (Mammalia) (AW Shingleton, Ed.). *PLoS ONE* 5: e9517.

Goswami A, Weisbecker V, Sánchez-Villagra MR. 2009. Developmental modularity and the marsupial-placental dichotomy. *Journal of Experimental Zoology Part B: Molecular and Developmental Evolution* 312B: 186–195.

Gower JC. 1975. Generalized procrustes analysis. *Psychometrika* 40: 33–51.

Hall BK, Herring SW. 1990. Paralysis and growth of the musculoskeletal system in the embryonic chick. *Journal of Morphology* 206: 45–56.

Hallgrímsson B, Jamniczky H, Young NM, Rolian C, Parsons TE, Boughner JC, Marcucio RS. 2009. Deciphering the palimpsest: studying the relationship between morphological integration and phenotypic covariation. *Evolutionary Biology* 36: 355–376.

Hallgrímsson B, Katz D, Aponte JD, Larson JE, Devine J, Gonzalez P, Young NM, Roseman CC, Marcucio RS. 2019. Integration and the developmental genetics of allometry. *Integrative and*

Comparative Biology.

Hallgrímsson B, Lieberman D, Young N, Parsons T, Wat S. 2007. Evolution of covariance in the mammalian skull. *Novartis Foundation Symposium* 184: 164–185.

Hallgrímsson B, Willmore K, Dorval C, Cooper DML. 2004. Craniofacial variability and modularity in macaques and mice. *Journal of Experimental Zoology Part B: Molecular and Developmental Evolution* 302B: 207–225.

Harmon LJ, Weir JT, Brock CD, Glor RE, Challenger W. 2008. GEIGER: investigating evolutionary radiations. *Bioinformatics* 24: 129–131.

Hautier L, Billet G, Eastwood B, Lane J. 2014. Patterns of morphological variation of extant sloth skulls and their implication for future conservation efforts. *The Anatomical Record* 297: 979–1008.

Hautier L, Billet G, Thoisy B De, Delsuc F. 2017. Beyond the carapace: skull shape variation and morphological systematics of long-nosed armadillos (genus Dasypus). *PeerJ* 5: e3650.

Hautier L, Weisbecker V, Goswami A, Knight F, Kardjilov N, Asher RJ. 2011. Skeletal ossification and sequence heterochrony in xenarthran evolution. *Evolution & Development* 13: 460–476.

Heck L, Wilson LAB, Evin A, Stange M, Sánchez-Villagra MR. 2018. Shape variation and modularity of skull and teeth in domesticated horses and wild equids. *Frontiers in Zoology* 15: 14.

Hennig C. 2007. Cluster-wise assessment of cluster stability. *Computational Statistics & Data Analysis* 52: 258–271.

Hennig C. 2008. Dissolution point and isolation robustness: Robustness criteria for general cluster analysis methods. *Journal of Multivariate Analysis* 99: 1154–1176.

Herring S. 1993. Formation of the Vertebrate Face Epigenetic and Functional Influences. *American Zoologist* 33: 472–483.

Hiiemae K. 2000. *Feeding in mammals* (K Schwenk, Ed.). San Diego: Academic Press.

Jung Y, Park H, Du DZ, Drake BL. 2003. A decision criterion for the optimal number of clusters in hierarchical clustering. *Journal of Global Optimization* 25: 91–111.

Kassambara A. 2017. *Practical guide to cluster analysis in R : unsupervised machine learning*. Statistical Tools for High-throughput Data Analysis.

Klingenberg CP. 2005. Developmental constraints, modules, and evolvability. In: Hallgrímsson B, Hall BK, eds. *Variation*. Elsevier Academic Press, 219–247.

Klingenberg CP. 2009a. Morphometric integration and modularity in configurations of landmarks: tools for evaluating a priori hypotheses. *Evolution & Development* 11: 405–421.

Klingenberg CP. 2009b. Morphometric integration and modularity in configurations of landmarks: tools for evaluating a priori hypotheses. *Evolution & Development* 11: 405–421.
Klingenberg CP, Badyaev A V, Sowry SM, Beckwith NJ. 2001. Inferring developmental modularity from morphological integration: analysis of individual variation and asymmetry in bumblebee wings. *The American naturalist* 157: 11–23.
Klingenberg CP, Leamy LJ, Cheverud JM. 2004. Integration and modularity of quantitative trait locus effects on geometric shape in the mouse mandible. *Genetics* 166: 1909–21.
Klingenberg CP, Marugán-Lobón J. 2013. Evolutionary Covariation in Geometric Morphometric Data: Analyzing Integration, Modularity, and Allometry in a Phylogenetic Context. *Systematic Biology* 62: 591–610.
Klingenberg CP, Mebus K, Auffray JC. 2003. Developmental integration in a complex morphological structure: how distinct are the modules in the mouse mandible? *Evolution and Development* 5: 522–531.
Klingenberg C, Navarro N. 2012. Development of the mouse mandible: a model system for complex morphological structures. In: Macholan M, Baird S, Munclinger P, and Pialek J, eds. *Evolution of the house mouse*. Cambridge: Cambridge University Press, .
Kumar S, Stecher G, Suleski M, Hedges SB. 2017. TimeTree: a resource for timelines, timetrees, and divergence times. *Molecular Biology and Evolution* 34: 1812–19.
Lancichinetti A, Fortunato S. 2012. Consensus clustering in complex networks. *Scientific Reports* 2: 336.
Lele S, Richtsmeier JT. 1991. Euclidean distance matrix analysis: A coordinate-free approach for comparing biological shapes using landmark data. *American Journal of Physical Anthropology* 86: 415–427.
Lele S, Richtsmeier J. 2001. *An invariant approach to statistical analysis of shapes*. CRC Press.
Lucas T, Goswami A. 2017. paleomorph: Geometric Morphometric Tools for Paleobiology. R package version 0.1.4.
Maddison WP, Maddison DR. 2018. Mesquite: a modular system for evolutionary analysis.
Le Maitre A, Mitteroecker P. 2019. Multivariate comparison of variance in R. *Methods in Ecology and Evolution*.
Makedonska J, Wright BW, Strait DS. 2012. The effect of dietary adaption on cranial morphological integration in capuchins (Order Primates, Genus Cebus) (S Gursky-Doyen, Ed.). *PLoS ONE* 7: e40398.
Marroig G, Cheverud JM. 2001. A comparison of phenotypic variation and covariation patterns and the role of phylogeny, ecology, and ontogeny during cranial evolution of New World monkeys. *Evolution* 55:

2576–2600.
Meredith RW, Gatesy J, Murphy WJ, Ryder OA, Springer MS. 2009. Molecular decay of the tooth gene enamelin (ENAM) mirrors the loss of enamel in the fossil record of placental mammals. *PLoS Genetics* 5.
Meredith RW, Gatesy J, Springer MS. 2013. Molecular decay of enamel matrix protein genes in turtles and other edentulous amniotes. *BMC Evolutionary Biology* 13: 20.
Mitteroecker P, Bookstein F. 2009. The ontogenetic trajectory of the phenotypic covariance matrix, with examples from craniofacial shape in rats and humans. *Evolution* 63: 727–737.
Murphy W, Eizirik E, Johnson W, Zhang Y. 2001a. Molecular phylogenetics and the origins of placental mammals. *Nature* 409: 614–618.
Murphy W, Eizirik E, O'brien S, Madsen O, Scally M, Douady C, Teeling E, Ryder O, Stanhope M, de Jong W, Springer M. 2001b. Resolution of the early placental mammal radiation using Bayesian phylogenetics. *Science* 294: 2348–2351.
Naples V. 1999. Morphology, evolution and function of feeding in the giant anteater (Myrmecophaga tridactyla). *Journal of Zoology* 249: 19–41.
Nijhout HF. 2011. Dependence of morphometric allometries on the growth kinetics of body parts. *Journal of Theoretical Biology* 288: 35–43.
Nogueira MR, Peracchi AL, Monteiro LR. 2009. Morphological correlates of bite force and diet in the skull and mandible of phyllostomid bats. *Functional Ecology* 23: 715–723.
Olson EC, Miller RL. 1958. *Morphological integration*. University of Chicago Press.
Parr WCH, Wilson LAB, Wroe S, Colman NJ, Crowther MS, Letnic M. 2016. Cranial shape and the modularity of hybridization in dingoes and dogs; hybridization does not spell the end for native morphology. *Evolutionary Biology* 43: 171–187.
Parsons KJ, Son YH, Crespel A, Thambithurai D, Killen S, Harris MP, Albertson RC. 2018. Conserved but flexible modularity in the zebrafish skull: implications for craniofacial evolvability. *Proceedings of the Royal Society B: Biological Sciences* 285: 20172671.
Patterson B. 1975. The fossil aardvarks (Mammalia: Tubulidentata). *Bulletin of the Museum of Comparative Zoology at Harvard College* 147.
Piekarski N, Gross JB, Hanken J. 2014. Evolutionary innovation and conservation in the embryonic derivation of the vertebrate skull. *Nature Communications* 5: 5661.
Piras P, Buscalioni AD, Teresi L, Raia P, Sansalone G, Kotsakis T, Cubo J. 2014. Morphological

integration and functional modularity in the crocodilian skull. *Integrative Zoology* 9: 498–516.

Porto A, de Oliveira FB, Shirai LT, De Conto V, Marroig G. 2009. The evolution of modularity in the mammalian skull I: morphological integration patterns and magnitudes. *Evolutionary Biology* 36: 118–135.

Porto A, Shirai LT, de Oliveira FB, Marroig G. 2013. Size variation, growth strategies, and the evolution of modularity in the mammalian skull. *Evolution* 67: 3305–3322.

Randau M, Goswami A. 2017. Morphological modularity in the vertebral column of Felidae (Mammalia, Carnivora). *BMC Evolutionary Biology* 17: 133.

Randau M, Sanfelice D, Goswami A. 2019. Shifts in cranial integration associated with ecological specialization in pinnipeds (Mammalia, Carnivora). *Royal Society Open Science* 6: 190201.

Redford K. 1986. Dietary specialization and variation in two mammalian myrmecophages (variation in mammalian myrmecophagy). *Revista Chilena de Historia Natural*.

Reichardt J, Bornholdt S. 2006. Statistical mechanics of community detection. *Physical Review E* 74: 016110.

Revell LJ. 2012. phytools: an R package for phylogenetic comparative biology (and other things). *Methods in Ecology and Evolution* 3: 217–223.

Riedl R. 1977. A systems-analytical approach to macro-evolutionary phenomena. *The Quarterly Review of Biology* 52: 351–370.

Riedl R. 1978. *Order in living organisms: a sustems analysis of evolution.* New York: Wiley.

Rohlf F, Slice D. 1999. Extensions of the Procrustes method for the optimal superimposition of landmarks. *Systematic Biology* 39: 40–59.

Rose C. 1892. Beitrage zur Zahnentwicklung der Edentaten. *Anatomischer Anzeiger* 7: 495–512.

Rose KR, Emry RJ. 1993. Relationships of Xenarthra, Pholidota, and fossil ‘Edentates’: the morphological evidence. In: Szalay FS, Novacek MJ, and McKenna MC, eds. *Mammal phylogeny: placentals*. New York: Springer-Verlag, 81–102.

Rot-Nikcevic I, Reddy T, Downing KJ, Belliveau AC, Hallgrímsson B, Hall BK, Kablar B. 2006. Myf5 −/− :MyoD −/− amyogenic fetuses reveal the importance of early contraction and static loading by striated muscle in mouse skeletogenesis. *Development Genes and Evolution* 216: 1–9.

Salvador S, Chan P. 2004. Determining the number of clusters/segments in hierarchical clustering/segmentation algorithms. *16th IEEE International Conference on Tools with Artificial Intelligence*. Boca Raton, Florida: IEEE Comput. Soc, 576–584.

Sansalone G, Colangelo P, Loy A, Raia P, Wroe S, Piras P. 2019. Impact of transition to a subterranean lifestyle on morphological disparity and integration in talpid moles (Mammalia, Talpidae). *BMC Evolutionary Biology* 19: 179.

Schlager S. 2017. Morpho and Rvcg – Shape Analysis in R: R-Packages for Geometric Morphometrics, Shape Analysis and Surface Manipulations. *Statistical Shape and Deformation Analysis*: 217–256.

Schwenk K. 2000. *Feeding : form, function, and evolution in tetrapod vertebrates*. Academic Press.

Simon MN, Marroig G. 2017. Evolution of a complex phenotype with biphasic ontogeny: contribution of development versus function and climatic variation to skull modularity in toads. *Ecology and Evolution* 7: 10752–10769.

Stern C. 1958. Selection for subthreshold differences and the origin of pseudoexogenous adaptations. *The American Naturalist* 92: 313–316.

Suzuki TK. 2013. Modularity of a leaf moth-wing pattern and a versatile characteristic of the wing-pattern ground plan. *BMC Evolutionary Biology* 13: 158.

Team RC. 2013. R: A language and environment for statistical computing.

Tibshirani R, Walther G, Hastie T. 2001. Estimating the number of clusters in a data set via the gap statistic. *Journal of the Royal Statistical Society: Series B (Statistical Methodology)* 63: 411–423.

Vizcaino S. 1994. Mecanica masticatoria de *Stegotherium tessellatum* Ameghino (Mammalia, Xenarthra) del Mioceno de Santa Cruz (Argentina). *Ameghiniana* 31: 283–290.

Vizcaíno SF, Paleobiology S, Summer N, Vizcaino SF. 2009. The teeth of the " toothless ": novelties and key innovations in the evolution of xenarthrans. *Paleobiology* 35: 343–366.

Waddington CH. 1953. Genetic assimilation of an acquired character. *Evolution* 7: 118–126.

Wagner G. 1996. Homologues, natural kinds and the evolution of modularity. *American Zoologist* 36: 36–43.

Wagner GP, Altenberg L. 1996. Perspective: complex adaptations and the evolution of evolvability. *Evolution* 50: 967–976.

Wagner GP, Laubichler MD. 2004. Rupert Riedl and the re-synthesis of evolutionary and developmental biology: Body plans and evolvability. *Journal of Experimental Zoology* 302B: 92–102.

Wagner GP, Pavlicev M, Cheverud JM. 2007. The road to modularity. *Nature Reviews Genetics* 8: 921–931.

Wetzel R. 1975. The species of *Tamandua* Gray (Edentata, Myrmecophagidae). *Proceedings of the Biological Society of Washington* 11: 95–112.

Winther RG. 2001. Varieties of modules: kinds, levels, origins, and behaviors. *Journal of Experimental Zoology* 291: 116–129.

Wroe S, Milne N. 2007. Convergence and remarkably consistent constraint in the evolution of carnivore skull shape. *Evolution* 61: 1251–1260.

Yeh YC. 1984. Comparative studies on characteristic structures of sensory and motor mechanisms in the stomatognathic system of the pangolin, Manis aurita (Mammalia) Part 1. Masticatory muscle and their spindle supply in the pangolin. *The Journal of the Stomatological Society, Japan* 51: 674–688.

Zelditch ML. 1988. Ontogenetic variation in patterns of phenotypic integration in the laboratory rat. *Evolution* 42: 28–41.

Zelditch ML, Carmichael C. 1989. Ontogenetic variation in patterns of developmental and functional integration in skulls of *Sigmodon fulviventer*. *Evolution* 43: 814–824.

Zelditch ML, Wood AR, Bonett RM, Swiderski DL. 2008. Modularity of the rodent mandible: Integrating bones, muscles, and teeth. *Evolution & Development* 10: 756–768.

4-Conclusion and perspectives

The background for this thesis was carved in the early 19th century by Étienne Geoffroy Saint-Hilaire and Georges Cuvier. The concepts of structural and topological constraint, associated to the correlation of forms with the environment have since been given many definitions, and several manners to quantify it have been developed. Today, in the light of Darwin and Wallace's theory (Darwin & Wallace, 1858; Darwin, 1859) and a rather stable phylogenetic context, the goal of this work was to explore convergent evolution, in the context of strong dietary selective pressures applied to a complex system, the placental skull. Along the way, I tried to understand the multiple factors behind skull shape variation both at a broad phylogenetic scale (myrmecophagous mammals) and in a more evolutionary constrained context (pangolins).

In the first chapter of this thesis, I went on to answer to explore skull shape variation among pangolins species, the most heavily poached mammal on Earth. Using geometric morphometrics, I was able to show that seven of the eight extant species of pangolins display very distinct skull shapes. If classifications based on morphology (Gaudin, Emry, & Wible, 2009) and genetics (Gaubert *et al.*, 2018) are mostly congruent, the major generator of skull shape variance among mammals (allometry) can introduce noise and flawed conclusions based on phenetics. In particular, I showed how heterochrony within a single genus has the ability to play a strong role in cranial shape differentiation, and how such differentiation is mostly ruled by different allometric patterns between well-defined face/rostrum and the neurocranium modules (Drake & Klingenberg, 2010). The second aspect of the first chapter consisted in exploiting the concept of cryptic species (Bickford *et al.*, 2007) by assessing the potential of skull shape to delimitate molecularly divergent lineages (Gaubert *et al.*, 2016). This chapter evokes several aspects of morphological variation and exemplifies the role played by ontogenetic allometry in skeletal shape. It also took a glimpse on the morphological differentiation during speciation, and presents an example of a decoupling between genetic and morphological divergence in a recent cladogenesis event (Bickford *et al.*, 2007).

In the second chapter of this thesis, convergent evolution was dissected, literally (Article 3) and conceptually, on the basis of comparative anatomy. The convergent evolution of myrmecophagy allowed for testing the strict evolutionary repeatability in the case of phylogenetically distant organisms. Ant- and termite-eating can be considered a "natural experiment" in which genetically and morphologically different populations were exposed, during millions of years, to similar conditions. In the first part of the

chapter, the comparison of the internal anatomy of the mandible at the scale of placentals showed that external convergence (i.e., tooth loss) was not corresponded by convergent internal features (i.e., maintenance of tooth innervation/irrigation) in anteaters and pangolins. This suggests that the anteater-pangolin example is indeed a case of true convergence (McGhee, 2011), as toothlessness evolved through different processes in the two clades. In other words, differences in mandibular innervation/irrigation patterns might have resulted from distinct timings/mechanisms of odontogenesis interruption. This example is in line with the existence of multiple pathways of evolution in response to one specific selective pressure (Bock, 1959). In reverse, my study suggests that odontogenesis is rather conserved across mammals, assuming a correlation between similar the phenotypes in anteaters and toothless whales and their development. Conway Morris' view that evolution would happen the same way, were it to be repeated again and again, is based on the idea that there is a restricted number of solutions available to life. The anteater-mysticete example is congruent with this view, and conforms to the idea that life is limited to a theoretical morphospace (McGhee, 1999). The explanation behind these apparently contradicting examples might be explained by slightly different functions performed by the mandibles of pangolins, anteaters, and mysticetes, which could demand a more developed sensorial system in the latter two groups.

In the second parts of the chapter 2, the comparison between head musculatures of the three living anteater genera showed how hypothetically similar functional systems may present distinct morphologies. This is the very concept of many-to-one-mapping as defined by Wainwright *et al.* (2005). Adaptive evolution may respond differently to identical selective pressures, ultimately resulting in a multitude of equally optimal responses (Bock, 1959). While this research is limited by its qualitative nature, it paves the way to future studies on the biomechanics on the feeding apparatus of ant- and termite-eating placentals, as it stresses the need for performance testing. In line with the first article of the chapter 2, the comparison of the head musculature in anteaters with previous descriptions of those of pangolins and aardvarks allowed to trace the limits of convergence, as some key differences are observed between these three distantly related clades.

Lastly, the third chapter of this thesis focused on the patterns of phenotypic covariance in the skull of myrmecophagous species. The results showed that despite the morphological differences characterizing these species, the modular patterns were conserved. I failed to associate loss of function (i.e., mastication) with the covariance patterns of the skull. The genetic and developmental basis of the placental skull are extremely conserved, hindering drastic changes in modularity patterns even under strong selective

pressures (canalization). Under this scenario, limited axes of variation are available for the phenotype, with morphological changes happening through changes in integration within conserved phenotypic organizational modules (Cardini & Polly, 2013; Parsons et al., 2018; Felice et al., 2019). This study points instead to an apparent conservation patterns associated to early ontogeny (i.e., facial growth) that could be associated to both the absence of tooth eruption and to the pronounced allometric growth of the rostrum (e.g., myrmecophagid anteaters).

This thesis tried to provide an integrative approach to cranial morphological variation, including a set of different geometric morphometrics and comparative anatomy techniques, while taking advantage of the increasing availability of μ-CT scanning and its combination with contrast-enhanced methods for reconstruction of soft-tissues. I tried to use these methods to give new insights on the systematics, allometric patterns, tooth loss, muscular anatomy, and phenotypic covariance patterns among the convergently evolved myrmecophagous placentals. There are, however, several subjects that remain to be studied.

As in the first chapter, similar approaches should be used to explore the phenotypic variation and allometric patterns among anteaters, especially the genus *Tamandua*. Variation between populations of *Tamandua tetradactyla* and differences between this species and its sister taxon, *T. mexicana*, would benefit from a re-evaluation with modern geometric morphometric methods in comparison to molecular datasets. This would allow to revive the interest on geographical phenotypic variation in these species and add up to previous works covering systematics (Reeve, 1941; Wetzel, 1975) and allometric patterns (Reeve, 1940) of the Vermilingua. Most importantly, it could provide essential knowledge with direct application in conservation, such as the identification of potential management units (Palsbøll, Bérubé, & Allendorf, 2007; Hautier *et al.*, 2014; Ferreira-Cardoso *et al.*, 2019a).

The investigation of patterns of mandibular innervation in myrmecophagous placentals opened several questions related the mechanism behind the ondontogenesis interruption in toothless mammals. The methodology used in the Article 2 could be applied to a particular case of myrmecophagous placentals, the aardvark. Tooth eruption and tooth number variation are well-reported for this species (Lönnberg, 1906; Le Gros Clark & Sonntag, 1926; Anthony, 1934b). An intraspecific study of the internal anatomy of adult aardvarks coupled with a developmental series could shed light on the homology of tooth loci in this toothless mammal. Additionally, this could help to understand the history of tooth loss in aardvarks, particularly to establish homologies between vestigial tooth loci and teeth present in fossil species (e.g., the “canine”; de Bonis & Koufos, 1994; Lehmann, 2006, 2007). A second topic of interest

comes from the discovery of a dentary pad, covered by orthokeratin, stretching along the putative tooth row locus in anteaters. This raises the question of the relationship between teeth and the evolution of keratinous structures on the mammalian jaws. An ongoing and very lively debate over the origin of keratinous structures (baleen) in mysticetes has drawn the attention of several recent studies (Ekdale, Deméré, & Berta, 2015; Peredo & Pyenson, 2017; Peredo *et al.*, 2017, 2018; Thewissen *et al.*, 2017; Lanzetti, 2019). Sirenians are an interesting group in this regard, because all extant and recently extinct sirenians present a keratinized oral pad in the anterior part of the jaws, innervated by alveolar nerves (Reep *et al.*, 1998; Marshall *et al.*, 2003; Csorba, Buzás, & Farkas, 2004). This clade presents a relatively well-known fossil record (e.g., Domning *et al.*, 2017) with species showing a complete dentition while others are completely toothless (i.e., Steller's sea cow). An ongoing project aims at μ-CT scanning most of the extant and fossil diversity of sirenian skull and mandibles, in order to understand the connection between teeth and the oral pad, through the use of dorsal canaliculi as an osteological proxy to vestigial tooth loci. Additionally, this project aims to understand how tooth innervation evolved along with the horizontal tooth replacement pattern presented by manatees (Domning & Hayek, 1984; Rodrigues *et al.*, 2011).

Lastly, our study on the phenotypic covariance patterns in myrmecophagous mammals left one main axis of research open: the study of ontogenetic phenotypic trajectories. Tooth eruption is a main factor influencing covariation in the mammals skull (Mitteroecker & Bookstein, 2009). The use of developmental series of skulls is necessary to better understand the influence of tooth development in the functional repatterning of the mammalian skull. This could be achieved by collecting μ-CT scans of fetus from the most abundant myrmecophagous species (*P. tricuspis* and *T. tetradactyla*) in natural history collections. Comparing the ontogenetic phenotypic covariance trajectories of pangolins, anteaters, and two toothed sister taxa would reveal how precisely covariance patterns differ between toothless and toothed species, and between evolutionary replicates.

As a general conclusion, the approaches used in this thesis show that the combination of geometric morphometrics, μ-CT scanning, histology, and soft tissue staining provide the ability to dissect convergence through morphology. These techniques allowed to dive deeper into the complexity that underlies macroscopic adaptive evolution. Developmental constraints are ubiquitous across mammals, and any form of life (McGhee, 2001), and so is convergence (McGhee, 2011). By acting on developmentally integrated systems, selection drives change on morphological subunits in directions that are more likely to produce more adapted phenotypes (Riedl, 1978). This thesis allowed to understand that this theoretical assumption does not always translate into exactly identical morphologies in convergently evolved

organisms. The phylogenetic context also constraints the intraspecific theoretical morphospace. The exposure to a certain environmental stimulus will therefore translate into the best compromise available (Bock, 1959). “Life finds a way”, as a popular fictional chaotician once said, and I showed that multiple ways were found during the evolution of myrmecophagy.

5-References

(article references are not included)

Adams DC. 2016. Evaluating modularity in morphometric data: challenges with the RV coefficient and a new test measure (P Peres-Neto, Ed.). *Methods in Ecology and Evolution* 7: 565–572.

Adams D, Collyer M, Kaliontzopoulou A, Sherratt E. 2017. Geomorph: software for geometric morphometric analyses. R package version 3.0.5.

Adis J, Lubin YD, Montgomery GG. 1984. Arthropods from the canopy of inundated and terra firme forests near Manaus, Brazil, with critical considerations on the pyrethrum-fogging technique. *Studies on Neotropical Fauna and Environment* 19: 223–236.

Aggarwal VS, Carpenter C, Freyer L, Liao J, Petti M, Morrow BE. 2010. Mesodermal Tbx1 is required for patterning the proximal mandible in mice. *Developmental Biology* 344: 669–681.

Akam M, Dawson I, Tear G. 1988. Homeotic genes and the control of segment diversity. *Development* 104: 123–133.

Alberch P. 1983. Morphological Variation in the Neotropical Salamander Genus Bolitoglossa. *Evolution* 37: 906.

Amato A, Montresor M. 2008. Morphology, phylogeny, and sexual cycle of *Pseudo-nitzschia mannii* sp. nov. (Bacillariophyceae): a pseudo-cryptic species within the *P. pseudodelicatissima* complex. *Phycologia* 47: 487–497.

Anthony R. 1934a. Données nouvelles sur l'évolution de la morphologie dentaire et crânienne des Tubulidentata (oryctéropes). *Bull Soc Zool Fr*.

Anthony R. 1934b. La dentition de l'oryctérope. Morphologie, développement, structure, interprétation. *Annales de Sciences Naturelles Zoologie* 17: 289–322.

Anthwal N, Peters H, Tucker AS. 2015. Species-specific modifications of mandible shape reveal independent mechanisms for growth and initiation of the coronoid. *EvoDevo* 6: 35.

Arbour VM, Zanno LE. 2019. Tail weaponry in ankylosaurs and glyptodonts: an example of a rare but strongly convergent phenotype. *The Anatomical Record*.

Asher RJ, Bennett N, Lehmann T. 2009. The new framework for understanding placental mammal evolution. *BioEssays* 31: 853–864.

Bardin J, Rouget I, Cecca F. 2016. Ontogenetic Data Analyzed As Such in Phylogenies. *Systematic Biology* 66: 23–37.

Bardua C, Wilkinson M, Gower DJ, Sherratt E, Goswami A. 2019. Morphological evolution and modularity of the caecilian skull. *BMC Evolutionary Biology* 19: 30.

Barlow KE, Jones G, Barratt EM. 1997. Can skull morphology be used to predict ecological relationships between bat species? A test using two cryptic species of pipistrelle. *Proceedings of the Royal Society of London. Series B: Biological Sciences* 264: 1695–1700.

De Beer G. 1937. *The development of the vertebrate skull*. Oxford: Oxford University Press.

Benton MJ, Pearson PN. 2001. Speciation in the fossil record. *Trends in Ecology & Evolution* 16: 405–411.

Bickford D, Lohman DJ, Sodhi NS, Ng PKL, Meier R, Winker K, Ingram KK, Das I. 2007. Cryptic species as a window on diversity and conservation. *Trends in Ecology & Evolution* 22: 148–155.

Bock WJ. 1959. Preadaptation and multiple evolutionary pathways. *Evolution* 13: 194–211.

Bogart SL, Pruetz JD. 2011. Insectivory of savanna chimpanzees (Pan troglodytes verus) at Fongoli, Senegal. *American Journal of Physical Anthropology* 145: 11–20.

de Bonis L, Koufos G. 1994. The first aardvarks (Mammalia) from the late Miocene of Macedonia, Greece. *Neues Jahrbuch für Geologie und Paläontologie* 194: 343–360.

Brandon R. 2005. Evolutionary modules: conceptual analyses and empirical hypotheses. In: Callebaut W, and Rasskin-Gutman D, eds. *Modularity: understanding the development and evolution of natural complex systems*. Cambridge, MA: MIT Press, 51–60.

Cartwright R. 1968. Some remarks on essentialism. *The Journal of Philosophy* 65: 615–626.

Casali DM, Martins-Santos E, Santos ALQ, Miranda FR, Mahecha GAB, Perini FA. 2017. Morphology of the tongue of Vermilingua (Xenarthra: Pilosa) and evolutionary considerations. *Journal of Morphology* 278: 1380–1399.

Ceriaco LMP, Bour R. 2012. Schweigger's (1812) chelonian types from the extinct eighteenth century Portuguese "Royal cabinet of natural history of Ajuda": some contributions for their identification and nomenclatural implications. *Zootaxa* 3395: 18.

Chai Y, Jiang X, Ito Y, Bringas P, Han J, Rowitch DH, Soriano P, McMahon AP, Sucov HM. 2000. Fate of the mammalian cranial neural crest during tooth and mandibular morphogenesis. *Development* 127.

Charles C, Solé F, Rodrigues HG, Viriot L. 2013. Under pressure? dental adaptations to termitophagy and vermivory among mammals. *Evolution* 67: 1792–1804.

Cheverud JM. 1982a. Phenotypic, genetic, and environmental morphological integration in the cranium. *Evolution* 36: 499–516.

Cheverud JM. 1982b. Relationships among ontogenetic, static, and evolutionary allometry. *American Journal of Physical Anthropology* 59: 139–149.

Cheverud JM. 1995. Morphological integration in the saddle-back tamarin (*Saguinus fuscicollis*) cranium. *The American Naturalist* 145: 63–89.

Cheverud JM. 1996. Developmental integration and the evolution of pleiotropy. *American Zoologist* 36: 44–50.

Chiappe LM, Norell MA, Clark JM. 1998. The skull of a relative of the stem-group bird Mononykus. *Nature* 392: 275–278.

Churchill M, Miguel J, Beatty BL, Goswami A, Geisler JH. 2019. Asymmetry drives modularity of the skull in the common dolphin (*Delphinus delphis*). *Biological Journal of the Linnean Society* 126: 225–239.

Claude J. 2008. *Morphometrics with R*. New York: Springer.

Colosimo PF, Hosemann KE, Balabhadra S, Villarreal G, Dickson M, Grimwood J, Schmutz J, Myers RM, Schluter D, Kingsley DM. 2005. Widespread parallel evolution in sticklebacks by repeated fixation of Ectodysplasin alleles. *Science (New York, N.Y.)* 307: 1928–33.

Cooper A, Lalueza-Fox C, Anderson S, Rambaut A, Austin J, Ward R. 2001. Complete mitochondrial genome sequences of two extinct moas clarify ratite evolution. *Nature* 409: 704–707.

Couly GF, Coltey PM, Le Douarin NM. 1993. The triple origin of skull in higher vertebrates: a study in quail-chick chimeras. *Development* 117: 409–429.

Csorba G, Buzás B, Farkas B. 2004. A previously undescribed skull of Steller's sea cow, *Hydrodamalis gigas* (Mammalia: Sirenia: Dugongidae) in the Hungarian Natural History Museum. 96: 317–320.

Cuvier G. 1798. *Tableau élémentaire de l'histoire naturelle des animaux*. Paris: Baudouin.

Daborn PJ, Yen JL, Bogwitz MR, Le Goff G, Feil E, Jeffers S, Tijet N, Perry T, Heckel D, Batterham P, Feyereisen R, Wilson TG, ffrench-Constant RH. 2002. A single p450 allele associated with insecticide resistance in Drosophila. *Science (New York, N.Y.)* 297: 2253–6.

Darwin C. 1859. *On the origin of species by means of natural selection or the preservation of favoured races in the struggle for life.* London: John Murray.

Darwin C, Wallace A. 1858. On the tendency of species to form varieties; and on the perpetuation of varieties and species by natural means of selection. *Journal of the Proceedings of the Linnean Society of London. Zoology* 3: 45–62.

Davies TGE, Field LM, Usherwood PNR, Williamson MS. 2007. DDT, pyrethrins, pyrethroids and insect sodium channels. *IUBMB Life* 59: 151–162.

Davis D. 1962. Mammals of the lowland rain-forest of north Borneo. *Bulletin of the Singapore National Museum* 31: 3–128.

Davit-Béal T, Tucker A, Sire J. 2009. Loss of teeth and enamel in tetrapods: fossil record, genetic data and morphological adaptations. *Journal of anatomy* 214: 477–501.

Delsuc F, Kuch M, Gibb GC, Karpinski E, Hackenberger D, Szpak P, Martínez JG, Mead JI, McDonald HG, MacPhee RDE, Billet G, Hautier L, Poinar HN. 2019. Ancient mitogenomes reveal the evolutionary history and biogeography of sloths. *Current Biology* 29: 2031-2042.e6.

Delsuc F, Metcalf JL, Wegener Parfrey L, Song SJ, González A, Knight R. 2014. Convergence of gut microbiomes in myrmecophagous mammals. *Molecular Ecology* 23: 1301–1317.

Denys C, Colyn M, Nicolas V. 2006. First record of the Dollman's tree mouse (*Prionomys batesi*; Mammalia: Nesomyidae) in the Republic of Congo and additional description of this rare Central African rodent. *Zootaxa*: 59–68.

Dobzhansky T. 1937. *Genetics and the Origin of Species*. New York: Columbia University Press.

Doe CQ, Goodman CS. 1985. Early events in insect neurogenesis: I. Development and segmental differences in the pattern of neuronal precursor cells. *Developmental Biology* 111: 193–205.

Domning DP, Hayek LAC. 1984. Horizontal tooth replacement in the Amazonian manatee (*Trichechus inunguis*). *Mammalia* 48: 105–128.

Domning DP, Heal GJ, Sorbi S. 2017. *Libysiren sickenbergi* , gen. et sp. nov.: a new sirenian (Mammalia, Protosirenidae) from the middle Eocene of Libya. *Journal of Vertebrate Paleontology* 37: e1299158.

Donoghue PCJ, Sansom IJ, Downs JP. 2006. Early evolution of vertebrate skeletal tissues and cellular interactions, and the canalization of skeletal development. *Journal of Experimental Zoology Part B: Molecular and Developmental Evolution* 306B: 278–294.

Drake AG, Klingenberg CP. 2010. Large-scale diversification of skull shape in domestic dogs: disparity and modularity. *The American naturalist* 175: 289–301.

Dworkin I. 2005. Canalization, cryptic variation, and developmental buffering: a critical examination and analytical perspective. In: Hallgrímsson B, and Hall BK, eds. *Variation*. Elsevier Academic Press, 131–158.

Ekdale EG, Deméré TA, Berta A. 2015. Vascularization of the gray whale palate (Cetacea, Mysticeti, *Eschrichtius robustus*): soft tissue evidence for an alveolar source of blood to baleen. *The Anatomical Record* 298: 691–702.

Emerling C, Delsuc F. 2018. Enamel loss in placental mammals. *Science Advances* 4.

Emmons LH. 1980. Ecology and resource partitioning among nine species of African rain forest squirrels. *Ecological Monographs* 50: 31–54.

Endo H, Aoki R, Taru H, Kimura J, Sasaki M, Yamamoto M, Arishima K, Hayashi Y. 2002. Comparative functional morphology of the masticatory apparatus in the long-snouted crocodiles. *Anatomia, Histologia, Embryologia: Journal of Veterinary Medicine Series C* 31: 206–213.

Endo H, Ito K, Watabe H, Nguyen S, Koyabu D. 2017. Macroscopic and CT examinations of the mastication mechanism in the southern tamandua. *Mammal Study* 42: 89–96.

Endo H, Niizawa N, Komiya T, Kawada S, Kimura J. 2007. Three-dimensional CT examination of the mastication system in the giant anteater. *Zoological science* 24: 1005–11.

Endo H, Nishiumi I, Kurohmaru M, Nabhitabhata J, Chan-Ard T, Nadee N, Agungpriyono S, Yamada J. 1998. The functional anatomy of the masticatory muscles of the Malayan pangolin, *Manis javanica*. *Mammal Study* 23: 1–8.

Erwin TL. 1983. Tropical forest canopies: the last biotic frontier. *Bulletin of the Entomological Society of America* 29: 14–20.

Esquerré D, Sherratt E, Keogh JS. 2017. Evolution of extreme ontogenetic allometric diversity and heterochrony in pythons, a clade of giant and dwarf snakes. *Evolution* 71: 2829–2844.

Evin A, Owen J, Larson G, Debiais-Thibaud M, Cucchi T, Vidarsdottir US, Dobney K. 2017. A test for paedomorphism in domestic pig cranial morphology. *Biology Letters* 13: 20170321.

Fabre PH, Herrel A, Fitriana Y, Meslin L, Hautier L. 2017. Masticatory muscle architecture in a water-rat from Australasia (Murinae, *Hydromys*) and its implication for the evolution of carnivory in rodents. *Journal of Anatomy* 231: 380–397.

Fabre AC, Perry JMG, Hartstone-Rose A, Lowie A, Boens A, Dumont M. 2018. Do muscles constrain skull shape evolution in strepsirrhines? *The Anatomical Record* 301: 291–310.

Felice RN, Goswami A. 2018. Developmental origins of mosaic evolution in the avian cranium. *Proceedings of the National Academy of Sciences of the United States of America* 115: 555–560.

Felice RN, Tobias JA, Pigot AL, Goswami A. 2019. Dietary niche and the evolution of cranial morphology in birds. *Proceedings of the Royal Society B: Biological Sciences* 286: 20182677.

Felsenstein J. 1988. Phylogenies and quantitative characters. *Annual Review of Ecology and Systematics* 19: 445–471.

Ferreira-Cardoso S, Araújo R, Martins NE, Martins GG, Walsh S, Martins RMS, Kardjilov N, Manke I, Hilger A, Castanhinha R. 2017. Floccular fossa size is not a reliable proxy of ecology and behaviour in vertebrates. *Scientific Reports* 7: 2005.

Ferreira-Cardoso S, Billet G, Gaubert P, Delsuc F, Hautier L. 2019a. Skull shape variation in extant pangolins (Manidae, Pholidota): allometric patterns and systematic implications. *Zoological Journal of the Linnean Society*.

Ferreira-Cardoso S, Delsuc F, Hautier L. 2019b. Evolutionary tinkering of the mandibular canal linked to convergent regression of teeth in placental mammals. *Current Biology* 29: 468-475.e3.

Figueirido B, MacLeod N, Krieger J, De Renzi M, Pérez-Claros JA, Palmqvist P. 2011. Constraint and adaptation in the evolution of carnivoran skull shape. *Paleobiology* 37: 490–518.

Foley NM, Springer MS, Teeling EC. 2016. Mammal madness: is the mammal tree of life not yet resolved?

Philosophical Transactions of the Royal Society B: Biological Sciences 371: 20150140.

Friede H. 1981. Normal development and growth of the Human neurocranium and cranial Base. *Scandinavian Journal of Plastic and Reconstructive Surgery* 15: 163–169.

Gans C. 1989. Stages in the origin of vertebrates: analysis by means of scenarios. *Biological Reviews* 64: 221–268.

Gaubert P, Antunes A, Meng H, Miao L, Peigné S, Justy F, Njiokou F, Dufour S, Danquah E, Alahakoon J, Verheyen E, Stanley W, O'Brien S, Johnson W, Luo S. 2018. The complete phylogeny of pangolins: scaling up resources for the molecular tracing of the most trafficked mammals on Earth. *Journal of Heredity* 109: 347–359.

Gaubert P, Njiokou F, Ngua G, Afiademanyo K, Dufour S, Malekani J, Bi SG, Tougard C, Olayemi A, Danquah E, Djagoun CAMS, Kaleme P, Mololo CN, Stanley W, Luo SJ, Antunes A. 2016. Phylogeography of the heavily poached African common pangolin (Pholidota, *Manis tricuspis*) reveals six cryptic lineages as traceable signatures of Pleistocene diversification. *Molecular Ecology* 25: 5975–5993.

Gaudin T, Branham D. 1998. The phylogeny of the Myrmecophagidae (Mammalia, Xenarthra, Vermilingua) and the relationship of Eurotamandua to the Vermilingua. *Journal of Mammalian Evolution*.

Gaudin TJ, Emry RJ, Wible JR. 2009. The phylogeny of living and extinct pangolins (Mammalia, Pholidota) and associated taxa: a morphology based analysis. *Journal of Mammalian Evolution* 16: 235–305.

Gaudin TJ, Wible JR, Hopson JA, Turnbull WD. 1996. Reexamination of the morphological evidence for the cohort Epitheria (Mammalia, Eutheria). *Journal of Mammalian Evolution* 3: 31–79.

Geoffroy Saint-Hilaire E. 1822. *Philosophie anatomique*. Paris: l'Imprimerie de Rignoux.

Gerber S, Hopkins MJ. 2011. Mosaic heterochrony and evolutionary modularity: the trilobite genus *Zacanthopsis* as a case study. *Evolution* 65: 3241–3252.

Gervais P. 1867. *Zoologie et paléontologie générales: nouvelles recherches sur les animaux vertébrés vivants et fossiles* (A Bertrand, Ed.). Paris: La Societé de Géographie.

Gibb G, Condamine F, Kuch M, Enk J. 2016. Shotgun mitogenomics provides a reference phylogenetic framework and timescale for living xenarthrans. *Molecular Biology and Evolution* 33: 621–642.

Ginot S, Herrel A, Claude J, Hautier L. 2018. Skull size and biomechanics are good estimators of *in Vivo* bite force in murid rodents. *The Anatomical Record* 301: 256–266.

Goodrich E. 1930. *Studies of the structure and development of vertebrates*. New York and London: MacMillan and Co.

Goswami A. 2006. Cranial modularity shifts during mammalian evolution. *The American Naturalist* 168: 270–280.

Goswami A, Finarelli JA. 2016. EMMLi: A maximum likelihood approach to the analysis of modularity. *Evolution* 70: 1622–1637.

Goswami A, Polly PD. 2010. The influence of modularity on cranial morphological disparity in Carnivora and Primates (Mammalia) (AW Shingleton, Ed.). *PLoS ONE* 5: e9517.

Goswami A, Weisbecker V, Sánchez-Villagra MR. 2009. Developmental modularity and the marsupial-placental dichotomy. *Journal of Experimental Zoology Part B: Molecular and Developmental Evolution* 312B: 186–195.

Gould SJ, Vrba ES. 1982. Exaptation - a aissing term in the science of form. *Paleobiology* 8: 4–15.

Goździewska-Harłajczuk K, Klećkowska-Nawrot J, Barszcz K. 2018. Macroscopic and microscopic study of the tongue of the aardvark (*Orycteropus afer*, Orycteropodidae). *Tissue and Cell* 54: 127–138.

Le Gros Clark W, Sonntag C. 1926. A monograph of *Orycteropus afer* III, the skull, the skeleton of the trunk, and limbs. *Proceedings of the Zoological Society of London* 96: 445–485.

Gueldre G, Vree F. 1990. Biomechanics of the masticatory apparatus of *Pteropus giganteus* (Megachiroptera). *Journal of Zoology* 220: 311–332.

Haddrath O, Baker AJ. 2001. Complete mitochondrial DNA geonome sequences of extinct birds: ratite phylogenetics and the vicariance biogeography hypothesis. *Proceedings of the Royal Society of London. Series B: Biological Sciences* 268: 939–945.

Hadorn E. 1945. Zur Pleiotropie der Genwirkung. *Archiv. der Julius Klaus-Stift. für Verebungsforsch* 20: 82–95.

Haeckel E. 1866. Generelle Morphologie der Organismen. Allgemeine Grundzüge der organischen Formen-Wissenschaft, mechanisch begründet durch die von C. Darwin.

Hall BK (Brian K. 1994. *Homology : the hierarchical basis of comparative biology*. Academic Press.

Hall BK, Herring SW. 1990. Paralysis and growth of the musculoskeletal system in the embryonic chick. *Journal of Morphology* 206: 45–56.

Hallgrímsson B, Jamniczky H, Young NM, Rolian C, Parsons TE, Boughner JC, Marcucio RS. 2009. Deciphering the palimpsest: studying the relationship between morphological integration and phenotypic covariation. *Evolutionary Biology* 36: 355–376.

Hallgrímsson B, Lieberman D, Young N, Parsons T, Wat S. 2007. Evolution of covariance in the mammalian skull. *Novartis Foundation Symposium* 184: 164–185.

Hallgrímsson B, Willmore K, Dorval C, Cooper DML. 2004. Craniofacial variability and modularity in macaques and mice. *Journal of Experimental Zoology Part B: Molecular and Developmental Evolution* 302B: 207–225.

Hanken J, Thorogood P. 1993. Evolution and development of the vertebrate skull: the role of pattern formation. *Trends in Ecology & Evolution* 8: 9–15.

Hansen TF, Houle D. 2008. Measuring and comparing evolvability and constraint in multivariate characters. *Journal of Evolutionary Biology* 21: 1201–1219.

Hatton JP, Pooran M, Li CF, Luzzio C, Hughes-Fulford M. 2003. A short pulse of mechanical force induces gene expression and growth in MC3T3-E1 osteoblasts via an ERK 1/2 pathway. *Journal of Bone and Mineral Research* 18: 58–66.

Hautier L, Billet G, Eastwood B, Lane J. 2014. Patterns of morphological variation of extant sloth skulls and their implication for future conservation efforts. *The Anatomical Record* 297: 979–1008.

Hautier L, Billet G, Thoisy B De, Delsuc F. 2017. Beyond the carapace: skull shape variation and morphological systematics of long-nosed armadillos (genus Dasypus). *PeerJ* 5: e3650.

Hautier L, Lebrun R, Cox PG. 2012. Patterns of covariation in the masticatory apparatus of hystricognathous rodents: Implications for evolution and diversification. *Journal of Morphology* 273: 1319–1337.

Hautier L, Weisbecker V, Sánchez-Villagra MR, Goswami A, Asher RJ. 2010. Skeletal development in sloths and the evolution of mammalian vertebral patterning. *Proceedings of the National Academy of Sciences of the United States of America* 107: 18903–8.

Heck L, Wilson LAB, Evin A, Stange M, Sánchez-Villagra MR. 2018. Shape variation and modularity of skull and teeth in domesticated horses and wild equids. *Frontiers in Zoology* 15: 14.

Hemae KM. 1967. Masticatory Function in the Mammals. *Journal of Dental Research* 46: 883–893.

Hendrick B, Mutumi G, Munteanu D, Sadier A, Davies KTJ, Rossiter SJ, Sears KE, Dávalos LM, Dumont E. 2019. Morphological diversification under high integration in a hyper diverse mammal clade. *Journal of Mammalian Evolution*: 1–13.

Herrel A, Spithoven L, Van Damme R, DE Vree F. 1999. Sexual dimorphism of head size in *Gallotia galloti* : testing the niche divergence hypothesis by functional analyses. *Functional Ecology* 13: 289–297.

Herrel A, Vanhooydonck B, Van Damme R. 2004. Omnivory in lacertid lizards: adaptive evolution or constraint? *Journal of Evolutionary Biology* 17: 974–984.

Herring S. 1980. Functional design of cranial muscles comparative and physiological studies in pigs. *American Zoologist* 20: 283–293.

Herring S. 1993. Formation of the Vertebrate Face Epigenetic and Functional Influences. *American Zoologist* 33: 472–483.

Herring SW, Teng S. 2000. Strain in the braincase and its sutures during function. *American journal of physical anthropology* 112: 575–93.

Hiiemae K. 2000. *Feeding in mammals* (K Schwenk, Ed.). San Diego: Academic Press.

Holland PWH, Garcia-Fernàndez J, Williams NA, Sidow A. 1994. Gene duplications and the origins of vertebrate development. *Development* 1994: 125–133.

Hu D, Marcucio RS. 2009. Unique organization of the frontonasal ectodermal zone in birds and mammals. *Developmental Biology* 325: 200–210.

Huxley TH. 1872. *A manual of the anatomy of vertebrated animals*. New York: D. Appleton and Co.

Jacobson A. 1966. Inductive processes in embryonic development. *Science* 152: 25–34.

Jamniczky HA, Hallgrímsson B. 2009. A comparison of covariance structure in wild and laboratory muroid crania. *Evolution* 63: 1540–1556.

Jernvall J, Thesleff I. 2012. Tooth shape formation and tooth renewal: evolving with the same signals. *Development (Cambridge, England)* 139: 3487–97.

Jiang X, Iseki S, Maxson RE, Sucov HM, Morriss-Kay GM. 2002. Tissue Origins and Interactions in the Mammalian Skull Vault. *Developmental Biology* 241: 106–116.

Jin SW, Sim KB, Kim SD. 2016. Development and Growth of the Normal Cranial Vault : An Embryologic Review. *Journal of Korean Neurosurgical Society* 59: 192–6.

Johnson MA, Revell LJ, Losos JB. 2009. Behavioral convergence and adaptive radiation: effects of habitat use on territorial behavior in *Anolis* lizards. *Evolution* 64: 1151–1159.

Jollie M. 1968. The head skeleton of a new-born *Manis javanica* with comments on the ontogeny and phylogeny of the mammal head skeleton. *Acta Zoologica* 49: 227–305.

de Jong WW. 1998. Molecules remodel the mammalian tree. *Trends in Ecology & Evolution* 13: 270–275.

De Jong WW, Zweers A, Joysey KA, Gleaves TJ, Boulter D. 1985. Protein sequence analysis applied to xenarthran and pholidote phylogeny. *The evolution and ecology of armadillos, sloths and vermilinguas*.65–76.

Klaauw V Der. 1952. Size and position of the functional components of the skull. A contribution to the knowledge of the architecture of the skull, based on data in the literature. *Archives Néerlandaises de Zoologie* 9.

Klingenberg C. 2004. Integration, modules, and development: molecules to morphology to evolution. In: Pigliucci

M, and Preston K, eds. *Phenotypic Integration: Studying the Ecology and Evolution of Complex Phenotypes*. New York: Oxford University Press, 213–230.

Klingenberg CP. 2005. Developmental constraints, modules, and evolvability. In: Hallgrímsson B, and Hall BK, eds. *Variation*. Elsevier Academic Press, 219–247.

Klingenberg CP. 2009. Morphometric integration and modularity in configurations of landmarks: tools for evaluating a priori hypotheses. *Evolution & Development* 11: 405–421.

Klingenberg CP. 2016. Size, shape, and form: concepts of allometry in geometric morphometrics. *Development Genes and Evolution* 226: 113–137.

Klingenberg CP, Badyaev A V, Sowry SM, Beckwith NJ. 2001. Inferring developmental modularity from morphological integration: analysis of individual variation and asymmetry in bumblebee wings. *The American naturalist* 157: 11–23.

Koyabu D, Maier W, Sánchez-Villagra MR. 2012. Paleontological and developmental evidence resolve the homology and dual embryonic origin of a mammalian skull bone, the interparietal. *Proceedings of the National Academy of Sciences of the United States of America* 109: 14075–80.

Krause WJ, Leeson CR. 1974. The stomach of the pangolin (*Manis pentadactyla*) with emphasis on the pyloric teeth. *Acta Anatomica* 88: 1–10.

Kumar S, Stecher G, Suleski M, Hedges SB. 2017. TimeTree: a resource for timelines, timetrees, and divergence times. *Molecular Biology and Evolution* 34: 1812–19.

Kuntzsch V, Nel JAJ. 1992. Diet of bat-eared foxes *Otocyon megalotis* in the Karoo. *Koedoe* 35: 37–48.

Lanzetti A. 2019. Prenatal developmental sequence of the skull of minke whales and its implications for the evolution of mysticetes and the teeth-to-baleen transition. *Journal of Anatomy* 235: 725–748.

Lazzari V, Charles C, Tafforeau P, Vianey-Liaud M, Aguilar JP, Jaeger JJ, Michaux J, Viriot L. 2008. Mosaic Convergence of Rodent Dentitions (JE Stajich, Ed.). *PLoS ONE* 3: e3607.

Leamy L. 1977. Genetic and environmental correlations of morphometric traits in randombred house mice. *Evolution* 31: 357–369.

Lebrun R. 2018. MorphoDig.

Lecointre G, Le Guyader H. 2006. *The tree of life : a phylogenetic classification*. Belknap Press of Harvard University Press.

Lee MSY, Palci A. 2015. Morphological phylogenetics in the genomic age. *Current Biology* 25: 922–929.

Lehmann T. 2006. The biodiversity of the Tubulidentata over Geological time. *Afrotherian Conservation* 4: 6–11.

Lehmann T. 2007. Amended taxonomy of the order Tubulidentata (Mammalia, Eutheria). *Annals of the Transvaal Museum* 44: 179–196.

Linnaeus C. 1758. Systema naturae, Vol. 1. *Systema naturae, Vol. 1*.

Longrich NR, Currie PJ. 2009. Albertonykus borealis, a new alvarezsaur (Dinosauria: Theropoda) from the Early Maastrichtian of Alberta, Canada: implications for the systematics and ecology of the Alvarezsauridae. *Cretaceous Research* 30: 239–252.

Lönnberg E. 1906. On a new Orycteropus from Northern Congo and some remarks on the dentition of the Tubulidentata. *Arkiv för Zoologi* 3: 31–66.

Losos JB. 2017. *Improbable destinies: fate, chance, and the future of evolution.* New York: Riverhead Books.

Mallet J. 1995. A species definition for the modern synthesis. *Trends in Ecology & Evolution* 10: 294–299.

Marroig G, Cheverud JM. 2001. A comparison of phenotypic variation and covariation patterns and the role of phylogeny, ecology, and ontogeny during cranial evolution of New World monkeys. *Evolution* 55: 2576–2600.

Marroig G, Shirai LT, Porto A, de Oliveira FB, De Conto V. 2009. The evolution of modularity in the mammalian skull II: evolutionary consequences. *Evolutionary Biology* 36: 136–148.

Marshall CD. 2009. Feeding morphology. *Encyclopedia of Marine Mammals*. Academic Press, 406–414.

Marshall CD, Maeda H, Iwata M, Furuta M, Asano S, Rosas F, Reep RL. 2003. Orofacial morphology and feeding behaviour of the dugong, Amazonian, West African and Antillean manatees (Mammalia: Sirenia): functional morphology of the muscular vibrissal complex. *Journal of Zoology* 259: 245–260.

Martin B. 1916. Tooth development in *Dasypus novemcinctus*. *Journal of Morphology* 27: 647–961.

Martin DP, van der Walt E, Posada D, Rybicki EP. 2005. The Evolutionary Value of Recombination Is Constrained by Genome Modularity. *PLoS Genetics* 1: e51.

Martinez Q, Lebrun R, Achmadi AS, Esselstyn JA, Evans AR, Heaney LR, Miguez RP, Rowe KC, Fabre PH. 2018. Convergent evolution of an extreme dietary specialisation, the olfactory system of worm-eating rodents. *Scientific Reports* 8: 17806.

Mayden RL. 1997. A hierarchy of species concepts: the denouement in the saga of the species problem. In: Claridge M, Dawah H, and Wilson M, eds. *Species: The units of diversity*. Chapman & Hall, 381–423.

Mayr E. 1942. *Systematics and the Origin of Species*. Columbia University Press.

McCurry MR, Evans AR, Fitzgerald EMG, Adams JW, Clausen PD, McHenry CR. 2017. The remarkable convergence of skull shape in crocodilians and toothed whales. *Proceedings of the Royal Society B: Biological Sciences* 284: 20162348.

McGhee G. 1999. *Theoretical morphology: the concept and its applications*. New York: Columbia University Press.

McGhee GR. 2001. Exploring the spectrum of existent, nonexistent and impossible biological form. *Trends in Ecology & Evolution* 16: 172–173.

McGhee G. 2006. *The geometry of evolution: adaptive landscapes and theoretical morphospaces*. Cambridge: Cambridge University Press.

McGhee GR. 2011. *Convergent evolution : limited forms most beautiful*. MIT Press.

McKenna MC. 1975. Toward a phylogenetic classification of the Mammalia. *Phylogeny of the Primates*. Boston, MA: Springer US, 21–46.

McNab B. 1985. Energetics, population biology, and distribution of xenarthrans, living and extinct. In: Montgomery G, ed. *The evolution and ecology of armadillos, sloths and vermilinguas*. Washington, D.C.: Smithsonian Institution Press, 219–232.

Meredith RW, Gatesy J, Murphy WJ, Ryder OA, Springer MS. 2009. Molecular decay of the tooth gene enamelin (ENAM) mirrors the loss of enamel in the fossil record of placental mammals (HS Malik, Ed.). *PLoS Genetics* 5.

Meredith R, Janečka J, Gatesy J, Ryder O, Fisher CF, Teeling EC, Goodbla A, Eizirik E, Simão TLL, Stadler T. 2011. Impacts of the Cretaceous terrestrial revolution and KPg extinction on mammal diversification. *Science* 334: 521–24.

Miranda FR, Casali DM, Perini FA, Machado FA, Santos FR. 2018. Taxonomic review of the genus *Cyclopes* Gray, 1821 (Xenarthra: Pilosa), with the revalidation and description of new species. *Zoological Journal of the Linnean Society* 183: 687–721.

Mitteroecker P, Bookstein F. 2009. The ontogenetic trajectory of the phenotypic covariance matrix, with examples from craniofacial shape in rats and humans. *Evolution* 63: 727–737.

Mitteroecker P, Gunz P, Bookstein FL. 2005. Heterochrony and geometric morphometrics: a comparison of cranial growth in *Pan paniscus* versus *Pan troglodytes*. *Evolution & Development* 7: 244–258.

Mooi RD, Gill AC. 2010. Phylogenies without synapomorphies—a crisis in fish systematics: time to show some character. *Zootaxa* 2450: 26.

Moore WJ. 1965. Masticatory function and skull growth. *Proceedings of the Zoological Society of London* 146: 123–131.

Morris JG, Trudell J, Pencovic T. 1977. Carbohydrate digestion by the domestic cat (*Felis catus*). *British Journal of Nutrition* 37: 365–373.

Morriss-Kay G. 2001. Derivation of the mammalian skull vault. *Journal of Anatomy* 199: 143–151.

Muller GB, Wagner GP. 1991. Novelty in evolution: restructuring the concept. *Annual Review of Ecology and Systematics* 22: 229–256.

Murphy W, Eizirik E, Johnson W, Zhang Y. 2001a. Molecular phylogenetics and the origins of placental mammals. *Nature* 409: 614–618.

Murphy W, Eizirik E, O'brien S, Madsen O, Scally M, Douady C, Teeling E, Ryder O, Stanhope M, de Jong W, Springer M. 2001b. Resolution of the early placental mammal radiation using Bayesian phylogenetics. *Science* 294: 2348–2351.

Naples VL. 1985. Form and function of the masticatory musculature in the tree sloths, *Bradypus* and *Choloepus*. *Journal of Morphology* 183: 25–50.

Naples V. 1986. The morphology and function of the hyoid region in the tree sloths, *Bradypus* and *Choloepus*. *Journal of Mammalogy* 67: 712–724.

Naples V. 1999a. Morphology, evolution and function of feeding in the giant anteater (Myrmecophaga tridactyla). *Journal of Zoology*.

Naples V. 1999b. Morphology, evolution and function of feeding in the giant anteater (Myrmecophaga tridactyla). *Journal of Zoology* 249: 19–41.

Natsuyama E. 1991. In utero behavior of human embryos at the spinal-cord stage of development. *Neonatology* 60: 11–29.

Nishihara H, Maruyama S, Okada N. 2009. Retroposon analysis and recent geological data suggest near-simultaneous divergence of the three superorders of mammals. *Proceedings of the National Academy of Sciences* 106: 5235–5240.

Noden DM. 1983. The role of the neural crest in patterning of avian cranial skeletal, connective, and muscle tissues. *Developmental Biology* 96: 144–165.

Nogueira MR, Monteiro LR, Peracchi AL, de Araújo AFB. 2005. Ecomorphological analysis of the masticatory apparatus in the seed-eating bats, genus Chiroderma (Chiroptera: Phyllostomidae). *Journal of Zoology* 266: 355–364.

Nogueira MR, Peracchi AL, Monteiro LR. 2009. Morphological correlates of bite force and diet in the skull and mandible of phyllostomid bats. *Functional Ecology* 23: 715–723.

Nowak R. 1999. *Walker's Mammal's of the World Volume I* (R Nowak, Ed.). Baltimore and London: Johns Hopkins University Press.

O'Leary M, Bloch J, Flynn J, Gaudin T. 2013. The placental mammal ancestor and the post–K-Pg radiation of placentals. *Science* 339: 662–667.

Olson EC, Miller RL. 1951. A mathematical model applied to a study of the evolution of species. *Evolution* 5: 325.

Olson EC, Miller RL. 1958. *Morphological integration*. University of Chicago Press.

Omland KE, Lanyon SM. 2000. Reconstructing plumage evolution in orioles (*Icterus*): repeated convergence and reversal in patterns. *Evolution* 54: 2119–2133.

Osumi-Yamashita N, Eto K. 1990. Mammalian Cranial Neural Crest Cells and Facial Development. (cranial neural crest cells/facial development/mammal/retinoic acid receptor/gene expression). *Development, Growth and Differentiation* 32: 451–459.

Osumi-Yamashita N, Ninomiya Y, Eto K, Doi H. 1994. The contribution of both forebrain and midbrain crest cells to the mesenchyme in the frontonasal mass of mouse embryos. *Developmental Biology* 164: 409–419.

Owen R. 1843. *Lectures on the comparative anatomy and physiology of the invertebrate animals, delivered at the Royal College of Surgeons*. London: Longman, Brown, Green, and Longmans.

Owen R. 1856. On the anatomy of the great anteater (*Myrmaecophaga jubata*, Linn.). *The Transactions of the Zoological Society of London* 4: 117–140.

Page CE, Cooper N. 2017. Morphological convergence in 'river dolphin' skulls. *PeerJ* 5: e4090.

Palci A, Lee MSY. 2018. Geometric morphometrics, homology and cladistics: review and recommendations. *Cladistics*.

Palsbøll PJ, Bérubé M, Allendorf FW. 2007. Identification of management units using population genetic data. *Trends in Ecology & Evolution* 22: 11–16.

Papadopulos AST, Igea J, Smith TP, Hutton I, Baker WJ, Butlin RK, Savolainen V. 2019. Ecological speciation in sympatric palms: 4. Demographic analyses support speciation of Howea in the face of high gene flow. *Evolution* 73: 1996–2002.

Parr WCH, Wilson LAB, Wroe S, Colman NJ, Crowther MS, Letnic M. 2016. Cranial shape and the modularity of hybridization in dingoes and dogs; hybridization does not spell the end for native morphology. *Evolutionary Biology* 43: 171–187.

Peredo C, Pyenson N. 2017. Decoupling tooth loss from the evolution of baleen in whales. *Frontiers in Marine*.

Peredo CM, Pyenson ND, Marshall CD, Uhen MD. 2018. Tooth loss precedes the origin of baleen in whales. *Current Biology* 28: 3992-4000.e2.

Peredo C, Pyenson N, Uhen M, Marshall C. 2017. Alveoli, teeth, and tooth loss: understanding the homology of internal mandibular structures in mysticete cetaceans. *PloS one* 12.

Petter F. 1966. *Dendroprionomys rousseloti* gen. nov., sp. nov., rongeur nouveau du Congo (Cricetidae, Dendromurinae). *Mammalia*.

Phillips MJ, Bennett TH, Lee MSY. 2009. Molecules, morphology, and ecology indicate a recent, amphibious ancestry for echidnas. *Proceedings of the National Academy of Sciences of the United States of America* 106:

17089–94.

Piekarski N, Gross JB, Hanken J. 2014. Evolutionary innovation and conservation in the embryonic derivation of the vertebrate skull. *Nature Communications* 5: 5661.

Poinar H, Hofreiter M, Spaulding W, Martin P, Stankiewicz B, Bland H, Evershed R, Possnert G, Paabo S. 1998. Molecular coproscopy: dung and diet of the extinct ground sloth Nothrotheriops shastensis. *Science* 281: 402–406.

Porto A, de Oliveira FB, Shirai LT, De Conto V, Marroig G. 2009. The evolution of modularity in the mammalian skull I: morphological integration patterns and magnitudes. *Evolutionary Biology* 36: 118–135.

Presslee S, Slater GJ, Pujos F, Forasiepi AM, Fischer R, Molloy K, Mackie M, Olsen J V., Kramarz A, Taglioretti M, Scaglia F, Lezcano M, Lanata JL, Southon J, Feranec R, Bloch J, Hajduk A, Martin FM, Salas Gismondi R, Reguero M, de Muizon C, Greenwood A, Chait BT, Penkman K, Collins M, MacPhee RDE. 2019. Palaeoproteomics resolves sloth relationships. *Nature Ecology & Evolution* 3: 1121–1130.

Ptacek M, Hankison S. 2009. The pattern and process of speciation. In: Ruse M,, In: Travis J, eds. *Evolution: the first four billion years*. Cambridge, MA: The Belknap Press of Harvard University Press, 177–207.

Puillandre N, Baylac M, Boisselier MC, Cruaud C, Samadi S. 2009. An integrative approach to species delimitation in Benthomangelia (Mollusca: Conoidea). *Biological Journal of the Linnean Society* 96: 696–708.

De Queiroz K. 1998. The general lineage concept of species, species criteria, and the process of speciation. In: Howard D, and Berlocher S, eds. *Endless forms: species and speciation*. New York and Oxford: Oxford University Press, 57–75.

De Queiroz K. 2007. Species Concepts and Species Delimitation. *Systematic Biology* 56: 879–886.

Rabosky DL. 2010. Extinction rates should not be estimated from molecular phylogenies. *Evolution* 64: 1816–1824.

Raff RA. 1996. *The shape of life: genes, development, and the evolution of animal form.* Chicago and London: The University of Chicago Press.

Ramesh T, Sankar K, Qureshi Q. 2009. Additional notes on the diet of sloth bear *Melursus ursinus* in Mudumalai tiger reserve as shown by scat analysis. *Journal of the Bombay Natural History Society* 106.

Randau M, Goswami A. 2017. Morphological modularity in the vertebral column of Felidae (Mammalia, Carnivora). *BMC Evolutionary Biology* 17: 133.

Randau M, Sanfelice D, Goswami A. 2019. Shifts in cranial integration associated with ecological specialization in pinnipeds (Mammalia, Carnivora). *Royal Society Open Science* 6: 190201.

Redford K. 1981. Quick-snacking anteater avoids attack. *Sci. News* 120.

Redford K. 1987. Ants and termites as food. *Current mammalogy*.

Redford KH, Dorea JG. 1984. The nutritional value of invertebrates with emphasis on ants and termites as food for mammals. *Journal of Zoology* 203: 385–395.

Reep RL, Marshall CD, Stoll ML, Whitaker DM. 1998. Distribution and innervation of facial bristles and hairs in the Florida manatee (*Trichechus manatus latirostris*). *Marine Mammal Science* 14: 257–273.

Reeve ECR. 1940. Relative growth in the snout of anteaters. A study in the application of quantitative methods to systematica. *Proceedings of the Zoological Society of London* A110: 47–80.

Reeve ECR. 1941. A statistical analysis of taxonomic differences within the genus *Tamandua* Gray (Xenarthra). *Proceedings of the Zoological Society of London* A111: 279–302.

Reiss KZ. 1997. Myology of the feeding apparatus of myrmecophagid anteaters (Xenarthra: Myrmecophagidae). *Journal of Mammalian Evolution* 4: 87–117.

Reiss KZ. 2001. Using phylogenies to study convergence: the case of the ant-eating mammals. *American Zoologist* 41: 507–525.

Renvoisé E, Michon F. 2014. An Evo-Devo perspective on ever-growing teeth in mammals and dental stem cell maintenance. *Frontiers in physiology* 5: 324.

Richardson P. 1987. Food consumption and seasonal variation in the diet of the aardwolf *Proteles cristatus* in southern Africa. *Zeitschrift für Säugetierkunde* 52: 307–325.

Riedl R. 1978. *Order in living organisms: a sustems analysis of evolution.* New York: Wiley.

Rieppel O. 1986. Atomism, epigenesis, preformation and pre-existence: a clarification of terms and consequences. *Biological Journal of the Linnean Society* 28: 331–341.

Rieppel O. 1993. Studies on skeleton formation in reptiles. v. Patterns of ossification in the skeleton of *Alligator mississippiensis* Daudin (Reptilia, Crocodylia). *Zoological Journal of the Linnean Society* 109: 301–325.

Rieppel O. 1994. Homology, topology, and typology: the history of modern debates. In: Hall B, ed. *Homology: the hierarchical basis of comparative biology*. San Diego: Academic Press, 64–95.

Rizzo D. 2015. *Fundamentals of anatomy and physiology* (D Rizzo, Ed.). Boston, MA: Cengage Learning.

Rodrigues HG, Marangoni P, Šumbera R, Tafforeau P, Wendelen W, Viriot L. 2011. Continuous dental replacement in a hyper-chisel tooth digging rodent. *Proceedings of the National Academy of Sciences of the United States of America* 108: 17355–9.

Rohlf F, Slice D. 1999. Extensions of the Procrustes method for the optimal superimposition of landmarks. *Systematic Biology* 39: 40–59.

Rose C. 1892. Beitrage zur Zahnentwicklung der Edentaten. *Anatomischer Anzeiger* 7: 495–512.

Röse C. 1892. Uber rudinmentare Zahnanlagen der Gattung Manis. *Anat. Anzeiger* Ed. vii.: 618–622.

Rose KR, Emry RJ. 1993. Relationships of Xenarthra, Pholidota, and fossil 'Edentates': the morphological evidence. In: Szalay FS, Novacek MJ, and McKenna MC, eds. *Mammal phylogeny: placentals*. New York: Springer-Verlag, 81–102.

Rot-Nikcevic I, Reddy T, Downing KJ, Belliveau AC, Hallgrímsson B, Hall BK, Kablar B. 2006. Myf5 −/− :MyoD −/− amyogenic fetuses reveal the importance of early contraction and static loading by striated muscle in mouse skeletogenesis. *Development Genes and Evolution* 216: 1–9.

Rücklin M, Donoghue PCJ, Johanson Z, Trinajstic K, Marone F, Stampanoni M. 2012. Development of teeth and jaws in the earliest jawed vertebrates. *Nature* 491: 748–751.

Sánchez-Villagra M. 2012. *Embryos in deep time: the rock record of biological development*. Berkeley, Los Angeles, and London: University of California Press.

Santana SE, Dumont ER, Davis JL. 2010. Mechanics of bite force production and its relationship to diet in bats. *Functional Ecology* 24: 776–784.

Santana SE, Lofgren SE. 2013. Does nasal echolocation influence the modularity of the mammal skull? *Journal of Evolutionary Biology* 26: 2520–2526.

Sarich VM. 1993. Mammalian systematics: twenty-five years among their albumins and transferrins. In: Szalay FS, Novacek MJ, and McKenna MC, eds. *Mammal Phylogeny*. New York: Springer-Verlag, 103–113.

Schilling T, Thorogood P. 2000. Development, growth, and evolution : implications for the study of the hominid skeleton. In: O'Higgins P, and Cohen M, eds. *Development, growth, and evolution : implications for the study of the hominid skeleton*. Academic Press, 57–78.

Schindelin J, Arganda-Carreras I, Frise E, Kaynig V. 2012. Fiji: an open-source platform for biological-image analysis. *Nature*.

Schwenk K. 2000. *Feeding : form, function, and evolution in tetrapod vertebrates*. Academic Press.

Simon HA. 1962. The Architecture of Complexity. *Facets of Systems Science*. Boston, MA: Springer US, 457–476.

Simon MN, Marroig G. 2017. Evolution of a complex phenotype with biphasic ontogeny: Contribution of development versus function and climatic variation to skull modularity in toads. *Ecology and Evolution* 7: 10752–10769.

Smith K, Redford KH. 1990. The anatomy and function of the feeding apparatus in two armadillos (Dasypoda): anatomy is not destiny. *Journal of Zoology* 222: 27–47.

Springer MS, Cleven GC, Madsen O, de Jong WW, Waddell VG, Amrine HM, Stanhope MJ. 1997. Endemic African mammals shake the phylogenetic tree. *Nature* 388: 61–64.

Springer MS, Meredith RW, Teeling EC, Murphy WJ. 2013. Technical comment on "The placental mammal ancestor and the post–K-Pg radiation of placentals". *Science* 341.

Sreekumar PG, Balakrishnan M. 2002. Seed dispersal by the sloth bear (*Melursus ursinus*) in South India. *Biotropica* 34: 474–477.

Stayton CT. 2005. Morphological evolution of the lizard skull: a geometric morphometrics survey. *Journal of Morphology* 263: 47–59.

Stayton CT. 2006. Testing hypotheses of convergence with multivariate data: morphological and functional convergence among herbivorous lizards. *Evolution* 60: 824–841.

Stott R. 2012. *Darwin's ghosts: the secret history of evolution*. New York: Spiegel & Grau.

Stresemann E. 1943. Oekologische Sippen-, Rassen- und Artunterschiede bei Vögeln. *Journal für Ornithologie* 91: 305–324.

Stuart-Fox D, Moussali A. 2007. Sex-specific ecomorphological variation and the evolution of sexual dimorphism in dwarf chameleons (*Bradypodion* spp.). *Journal of Evolutionary Biology* 20: 1073–1081.

Stuart C, Stuart C, Pereboom V. 2003. *Diet of the bat-eared fox (*Otocyon megalotis*), based on scat analysis, on the Western Escarpment, South Africa*.

Sun Z, Lee E, Herring SW. 2004. Cranial sutures and bones: growth and fusion in relation to masticatory strain. *The Anatomical Record* 276A: 150–161.

Suzuki TK. 2013. Modularity of a leaf moth-wing pattern and a versatile characteristic of the wing-pattern ground plan. *BMC Evolutionary Biology* 13: 158.

Team RC. 2013. R: A language and environment for statistical computing.

Teeling EC, Hedges SB. 2013. Making the impossible possible: rooting the tree of placental mammals. *Molecular Biology and Evolution* 30: 1999–2000.

Thewissen JGM, Hieronymus TL, George JC, Suydam R, Stimmelmayr R, McBurney D. 2017. Evolutionary aspects of the development of teeth and baleen in the bowhead whale. *Journal of Anatomy* 230: 549–566.

Thorpe W. 1945. The evolutionary significance of habitat selection. *Journal of Animal Ecology* 14: 67–70.

Tims HW. 1908. Tooth-vestiges and associated mouth parts in the Manidae. *Journal of anatomy and physiology* 42: 375–87.

Travis J, Reznick D. 2009. Adaptation. In: Ruse M, and Travis J, eds. *Evolution: the first four billion years*. Cambridge, MA: The Belknap Press of Harvard University Press, 105–131.

Tseng ZJ. 2013. Testing adaptive hypotheses of convergence with functional landscapes: a case study of bone-cracking hypercarnivores (AA Farke, Ed.). *PLoS ONE* 8: e65305.

Tseng ZJJ, Grohé C, Flynn JJJJ. 2016. A unique feeding strategy of the extinct marine mammal Kolponomos: convergence on sabretooths and sea otters. *Proceedings of the Royal Society B* 283: 20160044.

Ungar PS. 2010. *Mammal teeth : origin, evolution, and diversity*. Johns Hopkins University Press.

Verkerk MC, Tramper J, van Trijp JCM, Martens DE. 2007. Insect cells for human food. *Biotechnology Advances* 25: 198–202.

Vicq-d'Azyr MF. 1742. Systême anatomique des quadrupèdes. *Encyclopédie méthodique*: 632.

Vizcaíno S, Loughry W. 2008. Xenarthran biology: past, present, and future. In: Vizcaíno S, and Loughry W, eds. *The biology of the Xenarthra*. Gainsville: University Press Florida, 1–7.

Vizcaíno SF, Paleobiology S, Summer N, Vizcaino SF. 2009. The teeth of the " toothless ": novelties and key innovations in the evolution of xenarthrans. *Paleobiology* 35: 343–366.

Waddell PJ, Okada N, Hasegawa M. 1999. Towards Resolving the Interordinal Relationships of Placental Mammals. *Systematic Biology* 48: 1–5.

Waddington C. 1942. Canalization of development and the inheritance of acquired characters. *Nature*.

Waddington CH. 1953. Genetic assimilation of an acquired character. *Evolution* 7: 118–126.

Wagner GP. 1989. The Biological Homology Concept. *Annual Review of Ecology and Systematics* 20: 51–69.

Wagner G. 1996. Homologues, natural kinds and the evolution of modularity. *American Zoologist* 36: 36–43.

Wagner GP, Altenberg L. 1996. Perspective: complex adaptations and the evolution of evolvability. *Evolution* 50: 967–976.

Wagner GP, Laubichler MD. 2004. Rupert Riedl and the re-synthesis of evolutionary and developmental biology: Body plans and evolvability. *Journal of Experimental Zoology* 302B: 92–102.

Wainwright PC, Alfaro ME, Bolnick DI, Hulsey CD. 2005. Many-to-one mapping of form to function: a general principle in organismal design? *Integrative and Comparative Biology* 45: 256–262.

Wake D, Roth G. 1989. The linkage between ontogeny and phylogeny in the evolution of complex systems. *Complex organismal functions: Integration and evolution in vertebrates*. John Wiley and Sons, 361–377.

Weber M. 1904. *Die Säugetiere. Einführung in die Anatomie und Systematik der recenten und fossilen Mammalia* (G Fischer, Ed.). Jena, Germany.

Weijs W. 1980. Biomechanical models and the analysis of form: a study of the mammalian masticatory apparatus. *American Zoologist* 20: 707–719.

Weijs WA. 1994. Evolutionary approach of masticatory motor patterns in mammals. Springer, Berlin, Heidelberg, 281–320.

Wetzel R. 1975. The species of *Tamandua* Gray (Edentata, Myrmecophagidae). *Proceedings of the Biological Society of Washington* 11: 95–112.

Wilkinson DG, Bhatt S, Herrmann BG. 1990. Expression pattern of the mouse T gene and its role in mesoderm formation. *Nature* 343: 657–659.

Winther RG. 2001. Varieties of modules: kinds, levels, origins, and behaviors. *Journal of Experimental Zoology* 291: 116–129.

Winther R. 2005. Evolutionary developmental biology meets levels of selection: modular integration or competition, or both.61–97.

Woese CR, Kandler O, Wheelis ML. 1990. Towards a natural system of organisms: proposal for the domains Archaea, Bacteria, and Eucarya. *Proceedings of the National Academy of Sciences of the United States of America* 87: 4576–9.

Workman MS, Leamy LJ, Routman EJ, Cheverud JM. 2002. Analysis of quantitative trait locus effects on the size and shape of mandibular molars in mice. *Genetics* 160.

Wroe S, Milne N. 2007. Convergence and remarkably consistent constraint in the evolution of carnivore skull shape. *Evolution* 61: 1251–1260.

Yang H, Golenberg EM, Shoshani J. 1996. Phylogenetic resolution within the Elephantidae using fossil DNA sequence from the American mastodon (Mammut americanum) as an outgroup. *Proceedings of the National Academy of Sciences of the United States of America* 93: 1190–4.

Zelditch ML, Carmichael C. 1989. Ontogenetic variation in patterns of developmental and functional integration in skulls of *Sigmodon fulviventer*. *Evolution* 43: 814–824.

Zelditch ML, Mezey J, Sheets HD, Lundrigan BL, Garland T. 2006. Developmental regulation of skull morphology II: ontogenetic dynamics of covariance. *Evolution and Development* 8: 46–60.

Zelditch ML, Wood AR, Bonett RM, Swiderski DL. 2008. Modularity of the rodent mandible: Integrating bones, muscles, and teeth. *Evolution & Development* 10: 756–768.

Zuckerkandl E, Pauling L. 1965. Molecules as documents of evolutionary history. *Journal of Theoretical Biology* 8: 357–366.

6-Appendices

6.1-Appendix 1

Supplemental information to Article 1

Supplemental figures

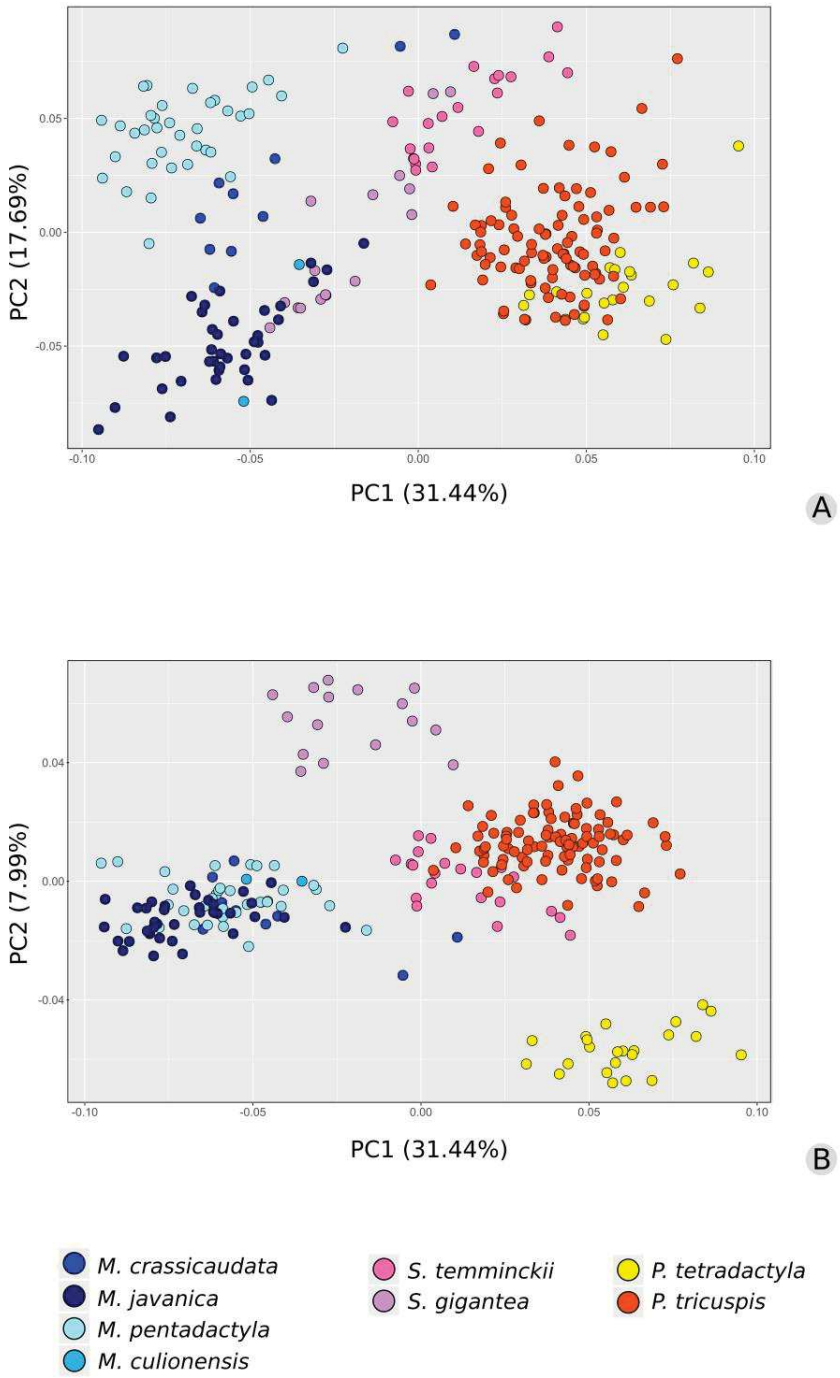

Fig. S1. Principal component analysis on data set including juveniles and two specimens of *Manis culionensis* (*n*=243; A, B).

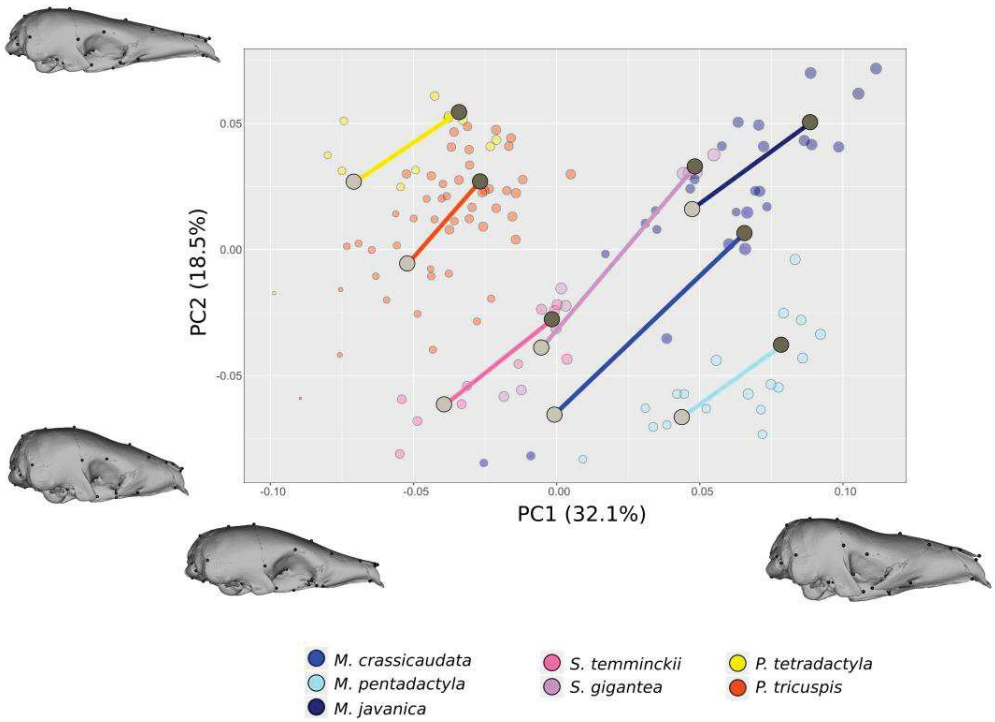

Fig. S2. Phenotypic trajectory analysis among seven pangolin species. The morphospace delimited by PC1 and PC2 explaining the variance between adults and juveniles within each species (n = 125). For each species, a trajectory representing the shape change between the shape estimates for juveniles (light gray circles) and adults (dark gray circles) is represented. Deformed meshes represent the maximum and minimum shapes of PC1 and PC2.

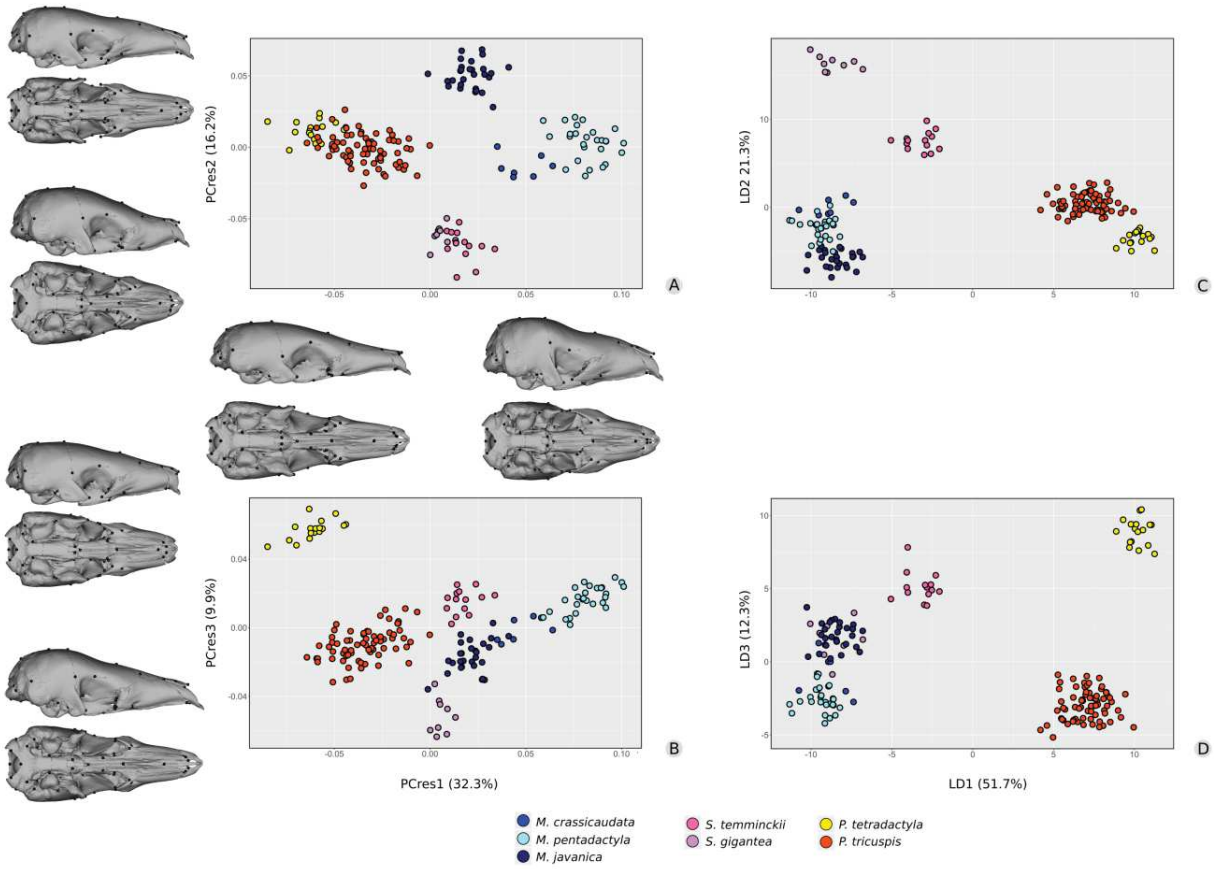

Fig. S3. Principal component (A: PC1 *vs* PC2; B: PC1 *vs* PC3) and linear discriminant analyses (C: LD1 *vs* LD2; D: LD1 *vs* LD3) with associated allometry-corrected shape variation for crania of seven pangolin species. Shapes are the residuals of a pooled within-group multivariate regression of shape on logarithm-transformed centroid size.

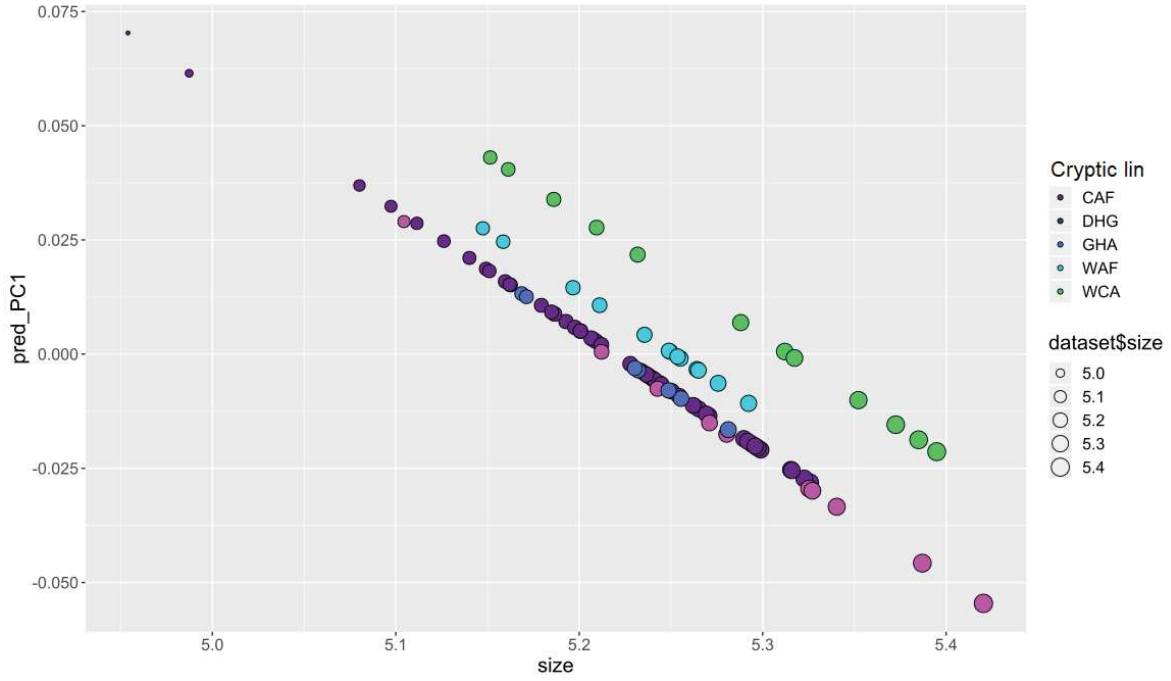

Fig. S4. Allometric trajectories of the cryptic lineages (Gaubert et al., 2016) of **P. tricuspis (n=95)**. X-axis values are the logarithm transformed centroid sizes for each specimen; Y-axis values are the PC1 of the predicted values of multivariate regression of shape ratios on size. The size of the dots indicates specimen size. CAF – Central Africa, DHG – Dahomey Gap, GHA – Ghana, WAF – Western Africa, WCA – Western Central Africa. GAB was excluded because our dataset counted with only one skull.

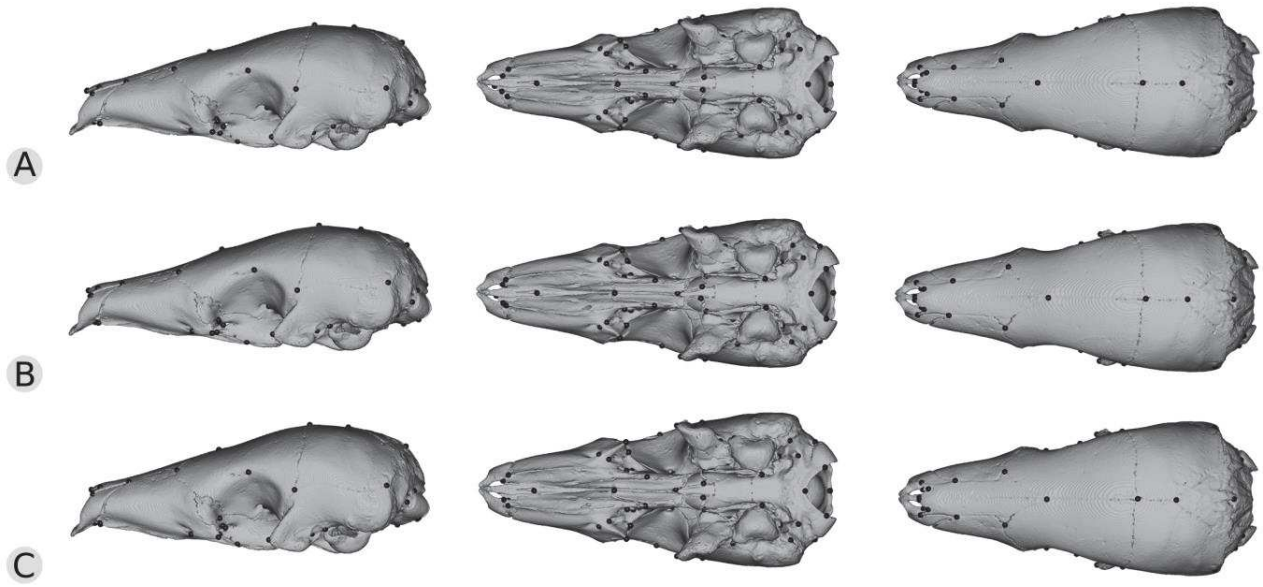

Fig. S5. Mean shapes of proposed management units for the *P. tricuspis* sample (*n* = 70) in lateral (left), ventral (middle), and dorsal (right) views. Central African region - CEN (A), Dahomey Gap region - DHG (B), and Western African region (C). Black dots are landmark positions. Tree topology of the intraspecific affinities based on Gaubert et al. (2018)

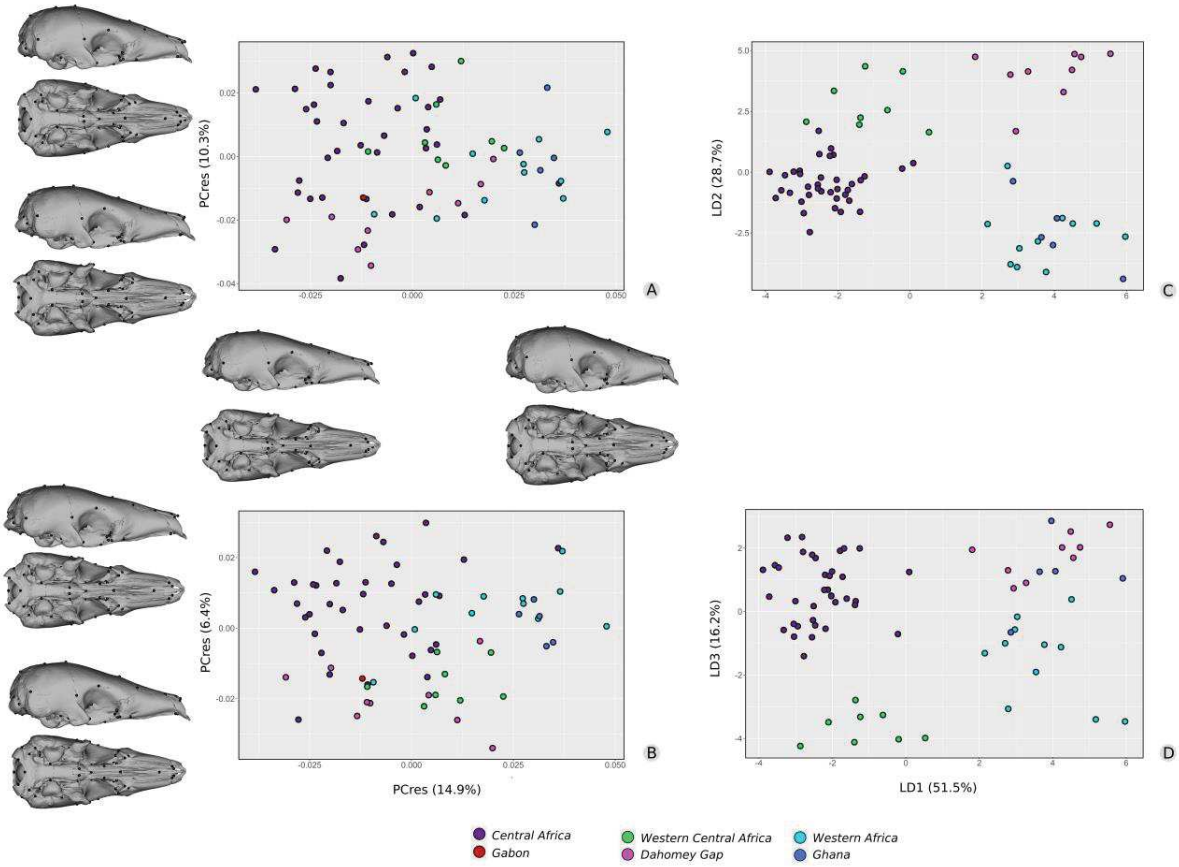

Fig. S6. Principal component (A: PCres1 *vs* PCres2; B: PCresC1 *vs* PCres3) and linear discriminant analyses (C: LD1 *vs* LD2; D: LD1 *vs* LD3) with associated allometry-corrected shape variation for crania of six cryptic lineages of *Phataginus tricuspis* (Gaubert *et al*. 2016). Shapes are the residuals of a pooled within-group multivariate regression of shape on logarithm-transformed centroid size.

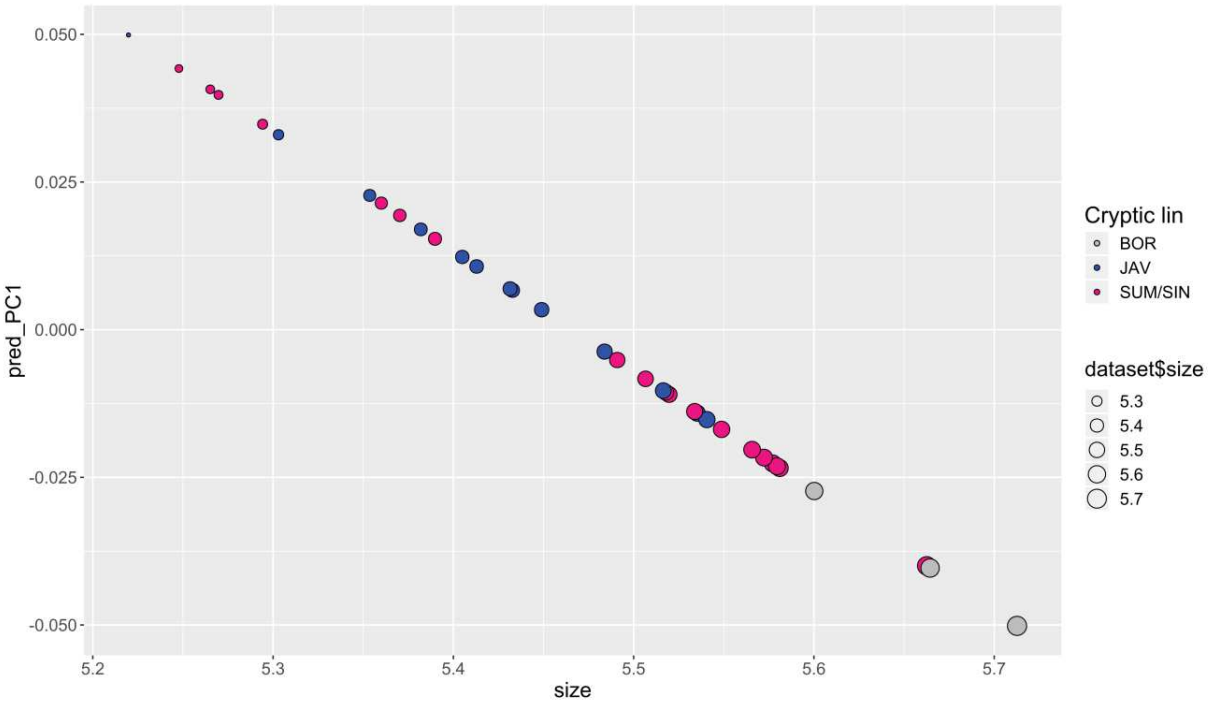

Fig. S7. Allometric trajectories of the lineages (Nash *et al.*, 2018) of *M. javanica* . X-axis values are the logarithm transformed centroid sizes for each specimen; Y-axis values are the PC1 of the predicted values of multivariate regression of shape ratios on size. The size of the dots indicates specimen size. BOR – Borneo, JAV – Javanica, SUM/SIN – Sumatra/Singapore.

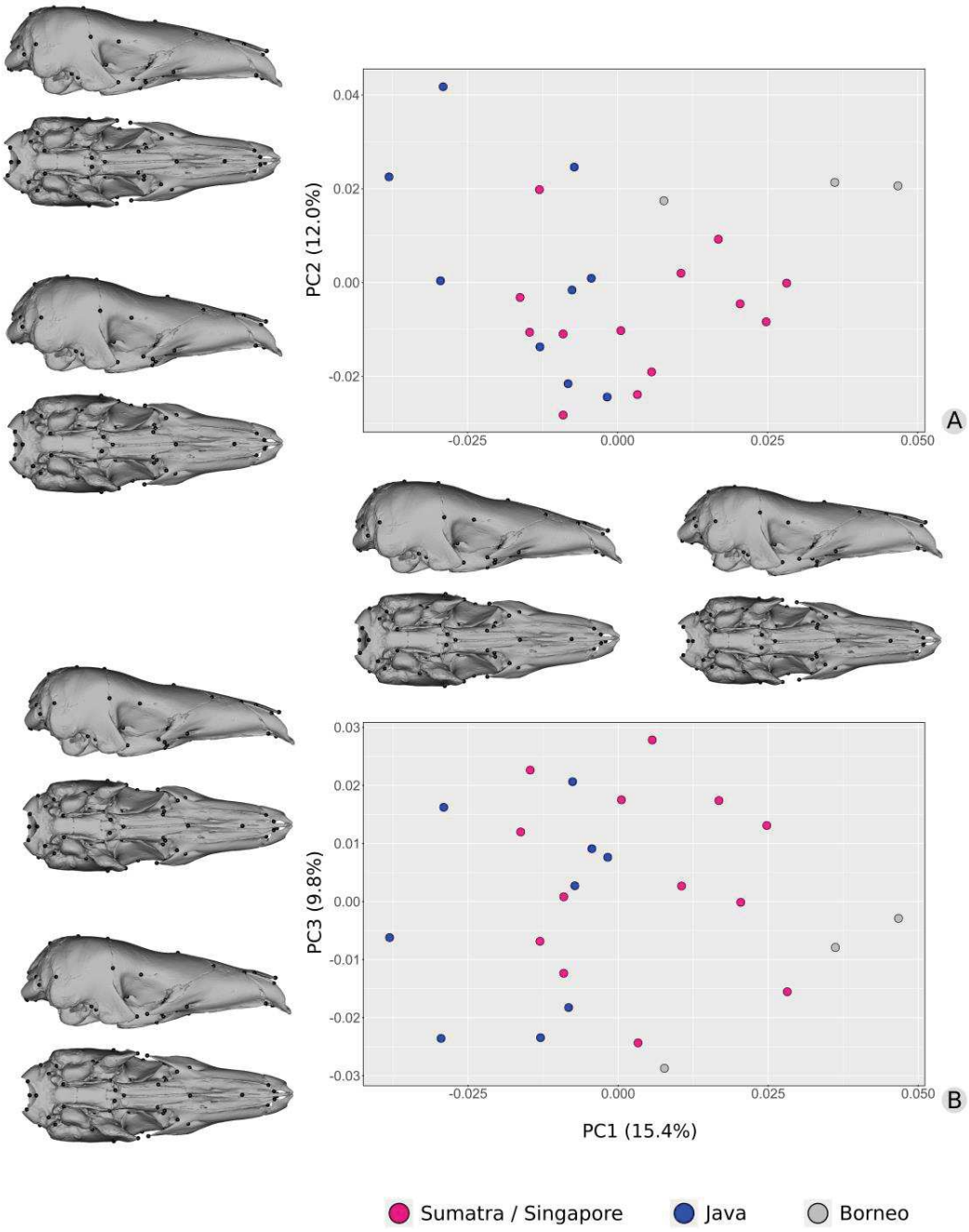

Fig. S8. Principal component (A: PC1 *vs* PC2; B: PC1 *vs* PC3) with associated shape variation for crania of *Manis javanica* lineages (Nash *et al*. 2018).

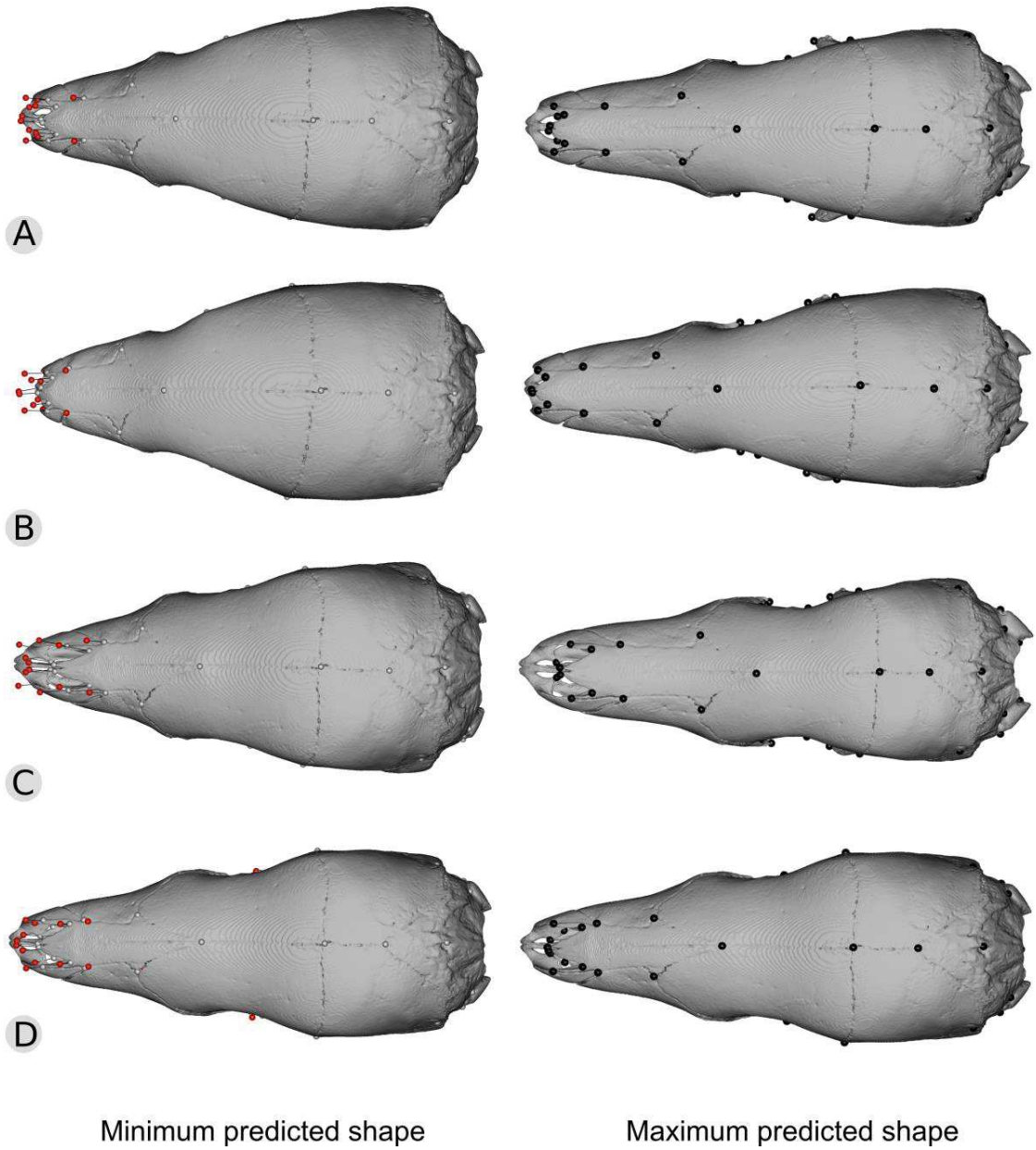

Fig. S9. Minimum (left) and maximum (right) shape prediction from a multivariate Procrustes regression on logarithm-transformed centroid size for two species of small (A, B) and two species of large sized pangolins (C, D) in dorsal view. *P. tricuspis* (A), *P. tetradactyla* (B), *S. gigantea* (C), and *M. javanica* (D). Grey and red dots mark landmark position at minimum and maximum sizes, respectively. Black dots are landmark positions for maximum size predictions.

Supplemental tables

Table S1. Definitions of the 75 cranial landmarks used.

Numbers	Definition
1 and 29	Most antero-ventral point of the maxilla
2 and 30	Most anterior point of the intersection between maxillary crest and the premaxillary
3	Most posterior point of the premaxillary on the midline
4 and 31	Ventral margin of the infraorbital foramen
5 and 32	Ventral margin of the maxillary foramen
6	Intersectionbetween maxilla and palatine sutures
7 and 33	Ventral margin of the sphenopalatine foramen
8 and 34	Posterior caudal palatine foramen
9 and 35	Most posterior tip of maxillary projection into the palatine
10 and 36	Most lateral point of the maxillary-palatine suture
11 and 37	Most dorsal point of orbital edge
12 and 38	Postero-Ventral margin of the ethmoid foramen
13	Most posterior point of the palatine sutures
14 and 39	Most postero-ventral point of the optic foramen
15 and 40	Most postero-ventral point of the sphenorbital fissure
16 and 41	Anteriormost part of the zygomatic process of the squamosal
17 and 42	Intersection presphenoid-basipsphenoid-palatine
18 and 43	Most posterior point of the foramen ovale
19 and 44	Most posterior point of the post-glenoid foramen
20 and 45	Concavity at contact with the tympanic bulla
21 and 46	Most posterior point of the pterygoid hamulus
22 and 47	Anteriormost point of the jugular foramen
23 and 48	Petrosal-exoccipital-squamosal triple joint
24 and 49	Posteriormost point of hypoglossus foramen
25	Most anterior point of the foramen magnum
26	Most postero-dorsal point of the foramen magnum
27 and 50	Most lateral point of the occipital condyle
28 and 51	Limit between the articular facet of the condyle and the foramen magnum
52 and 66	Anteriormost point of the nasal
53 and 67	Most antero-lateral point of the premaxilla-nasal suture
54 and 68	Nasal notch
55 and 69	Intersection pmx-mx-nasal

56 and 70	Intersection mx-nasal-frontal
57 and 71	Most dorsal max/palatine contact
58 and 72	Posteriormost point of the maxillary process of the zygomatic arch
59	Intersection between inter-nasal and inter-frontal sutures
60	Intersection between inter-parietal and inter-frontal sutures
61 and 73	Intersection between frontal-parietal-squamosal
62	Intersection between interparietal suture with supraoccipital
63 and 74	Intersection between squamosal-parietal-exoccipital
64	Posteriormost point of the skull roof portion of the supraoccipital
65 and 75	Concavity located above the condyle

Table S2. Phylogenetic ANOVA of shape (Procrustes coordinates) ~ log(centroid size). *Df* – degrees of freedom; *F* – value of *F*-statistics; *significant *p*-value. Randomized residual permutation procedure used 10,000 permutations.

	Df	***R^2***	***F***	***p*-value**
Log(centroid size)	1	0.27	1.84	0.093
Residuals	5		-	-
Total	6		-	-

Table S3. Pairwise comparisons of the allometric trajectory angles for skull shape. *P*-values (10.000 iterations) are on the upper triangle and angles between slopes (in degrees) are on the bottom triangle. Significant results are written in bold.

	M. cra	***M. jav***	***M. pen***	***S. gig***	***S. tem***	***P. tri***	***P. tet***
M. cra	-	0.403	0.437	0.074	0.469	0.647	0.900
M. jav	29.526	-	0.106	**<0.001**	0.439	0.062	0.865
M.pen	37.559	40.465	-	**0.016**	0.290	0.106	0.769
S. gig	33.734	39.406	45.444	-	0.095	0.352	0.589
S. tem	41.153	39.039	47.825	45.749	-	0.495	0.756
P. tri	29.121	32.515	41.959	27.244	39.522	-	0.957
P. tet	36.292	34.916	42.207	39.267	45.043	33.236	-

Table S4. Pairwise comparisons of the phenotypic trajectory angles. *P*-values (10,000 iterations) are on the upper triangle and angles between path distances are on the bottom triangle. Significant results are written in bold.

	M. cra	***M. jav***	***M. pen***	***S. gig***	***S. tem***	***P. tri***	***P. tet***
M. cra	-	0.832	0.764	0.972	0.809	0.836	0.600
M. jav	38.035	-	0.122	0.599	0.393	**0.029**	0.340
M. pen	40.329	41.102	-	0.590	0.157	**0.011**	0.131
S. gig	37.346	40.091	41.041	-	0.582	0.987	0.719
S. tem	42.100	40.297	46.455	44.608	-	0.125	0.345
P. tri	34.410	38.097	43.088	25.980	42.521	-	0.131
P. tet	46.155	40.240	46.331	41.228	45.175	40.729	-

Table S5. Pairwise comparisons of the phenotypic trajectory lengths. *P*-values (10,000 iterations) are on the upper triangle and absolute differences between path distances are on the bottom triangle. Significant results are written in bold.

	M. cra	*M. jav*	*M. pen*	*S. gig*	*S. tem*	*P. tri*	*P. tet*
M. cra	-	**0.004**	**0.002**	0.515	**0.010**	**<0.001**	**0.003**
M. jav	0.051	-	0.5243	**0.010**	0.694	0.192	0.826
M. pen	0.058	0.007	-	**0.002**	0.360	0.578	0.744
S. gig	0.011	0.040	0.047	-	**0.024**	**0.001**	**0.006**
S. tem	0.045	0.005	0.012	0.034	-	0.176	0.566
P. tri	0.064	0.013	0.006	0.052	0.018	-	0.431
P. tet	0.054	0.003	0.004	0.043	0.008	0.010	-

Table S6. Pairwise comparison of the intercept (x = 5.125) of the multivariate Procrustes allometric regressions (overlap test). *P*-values (Hochberg corrected) of the difference between the intercepts computed with 10,000 iterations (upper triangle) and observed differences (bottom triangle). Taxa with significantly non-parallel trajectories were not included in the test. Significant results are written in bold.

	M. cra	*M. jav*	*M. pen*	*S. gig*	*S. tem*	*P. tri*	*P. tet*
M. cra	-	0.064	0.156	0.226	0.226	**0.032**	0.152
M. jav	0.137	-	0.156	-	0.181	**0.017**	**0.042**
M.pen	0.105	0.113	-	-	0.188	**0.033**	0.064
S. gig	0.129	-	-	-	0.226	**0.020**	0.156
S. tem	0.110	0.160	0.134	0.124	-	**0.017**	0.156
P. tri	0.130	0.096	0.122	0.155	0.129	-	**0.002**
P. tet	0.154	0.129	0.163	0.192	0.143	0.089	-

Table S7. Pairwise comparison of the intercept (x = 0) of the multivariate Procrustes allometric regressions (overlap test). *P*-values of the difference between the intercepts computed with 10,000 iterations (upper triangle) and observed differences (bottom triangle). Taxa with significantly non-parallel trajectories were not included in the test. Significant results are written in bold.

	M. cra	*M. jav*	*M. pen*	*S. gig*	*S. tem*	*P. tri*	*P. tet*
M. cra	-	0.417	0.632	0.767	0.638	0.741	0.870
M. jav	0.845	-	0.506	-	0.517	0.407	0.749
M.pen	0.961	1.205	-	-	0.514	0.575	0.803
S. gig	0.879	-	-	-	0.432	0.699	0.748
S. tem	1.186	0.204	1.324	1.307	-	0.445	0.642
P. tri	0.730	0.737	0.955	0.700	1.137	-	0.849
P. tet	0.939	0.909	1.062	1.025	0.824	0.824	-

Table S8. Pairwise comparisons of the predicted head shape (predicted Procrustes residuals) differences at maximum centroid size (heterochrony test). *P*-values (Hochberg corrected; in black for x = 5.125, in blue for x = 0) of the difference between them computed with 10,000 iterations (upper triangle) and observed differences (bottom triangle). Taxa with significantly non-parallel trajectories were not included in the test. Significant results are written in bold.

	M. cra	*M. jav*	*M. pen*	*S. gig*	*S. tem*	*P. tri*	*P. tet*
M. cra	-	**0.002**	**0.001**	**0.002**	**0.001**	**0.001**	**0.001**
M. jav	0.085	-	**0.001**	-	**0.001**	**0.001**	**0.001**
M.pen	0.076	0.112	-	-	**0.001**	**0.001**	**0.001**
S. gig	0.103	-	-	-	**0.001**	**0.001**	**0.001**
S. tem	0.113	0.146	0.114	0.119	-	**0.001**	**0.001**
P. tri	0.111	0.118	0.129	0.094	0.097	-	**0.001**
P. tet	0.141	0.145	0.159	0.143	0.124	0.086	-

Table S9. Pairwise comparison of the PC1 allometric trajectory intercepts for skull shape. *P*-values of a multiple comparison of means (Tukey test) are on the upper triangle and the *t* statistics values are on the bottom triangle. The same intercept in all species is the null hypothesis. The *P*-values are indicated for species that show the same intercept; *all other pairwise comparisons retrieved a *P*-value <0.001. Only species with parallel slopes are included. Significant results are written in bold.

	M. cra	*M. jav*	*M. pen*	*S. gig*	*S. tem*	*P. tri*	*P. tet*
M. cra	-	*	*	*	*	*	*
M. jav	-5.385	-	*	*	*	*	*
M.pen	-10.390	-8.141	-	*	*	*	*
S. gig	9.722	-17.084	-20.792	-	0.966	1	*
S. tem	9.659	20.995	27.682	-0.910	-	0.765	*
P. tri	10.620	25.017	36.291	0.086	1.427	-	*
P. tet	14.371	27.015	35.402	4.311	7.256	-8.511	-

Table S10. ANOVA of shape (Procrustes coordinates) ~ sex*species and shape (Procrustes coordinates) ~ size+sex*species. *Df* – degrees of freedom; *F* – value of *F*-statistics; *significant *p*-value. Randomized residual permutation procedure used 10,000 permutations.

	Df	***F***	***p*-value**	***Df***	***F***	***p*-value**
Log(centroid size)	-	-	-	1	54.86	<0.001*
Sex	1	2.03	0.057	1	1.80	0.085
Species	6	26.67	<0.001*	6	25.33	<0.001*
Sex:species	6	1.07	0.332	6	0.89	0.656
Residuals	106	-	-	105	-	-
Total	119	-	-	119	-	-

Table S11. Pairwise comparison of the Procrustes distances between least-squares (LS) means for species. *P*-values of the difference between the LS means computed with 10,000 iterations (upper triangle) and observed distances (bottom triangle). Significant results are written in bold.

	M. cra	***M. jav***	***M. pen***	***S. gig***	***S. tem***	***P. tri***	***P. tet***
M. cra	-	**<0.001**	**0.002**	**<0.001**	**<0.001**	**<0.001**	**<0.001**
M. jav	0.078	-	**<0.001**	**<0.001**	**<0.001**	**<0.001**	**<0.001**
M.pen	0.073	0.104	-	**<0.001**	**<0.001**	**<0.001**	**<0.001**
S. gig	0.102	0.095	0.122	-	**<0.001**	**<0.001**	**<0.001**
S. tem	0.105	0.131	0.108	0.112	-	**<0.001**	**<0.001**
P. tri	0.111	0.114	0.126	0.103	0.091	-	**<0.001**
P. tet	0.140	0.137	0.159	0.145	0.119	0.086	-

Table S12. ANOVA of shape ~ taxa/geographical groups of adult specimens of the interspecific, *P. tricuspis* and *M. javanica* data sets. Significant *p*-values indicate differences between skull shapes of taxa/geographical groups. *n groups* – number of taxa or geographical groups used as factors; *N* – sample size; *Df* – degrees of freedom; R^2 – R-squared; *F* – value of *F*-statistics; *significant *p*-value. Randomized residual permutation procedure used 10,000 permutations.

Data sets	***n groups***	***N***	***Df***	R^2	***F***	***p*-value**
Interspecific allometry-corrected	7	173	166	0.65	50.35	<0.001*
P. tricuspis allometry-corrected (Gaubert et al., 2016)	6	70	65	0.19	3.77	<0.001*
P. tricuspis allometry-corrected Regions	3	70	67	0.13	5.01	<0.001*
M. javanica (Nash et al., 2018)	3	25	22	0.16	2.12	<0.001*
M. javanica allometry-corrected (Nash et al., 2018)	3	25	22	0.09	1.13	0.225

Table S13. Pairwise comparison of the allometry-corrected Procrustes distances between least-squares (LS) means for species. *P*-values of the difference between the LS means computed with 10,000 iterations (upper triangle) and observed distances (bottom triangle). Significant results are written in bold.

	M. cra	***M. jav***	***M. pen***	***S. gig***	***S. tem***	***P. tri***	***P. tet***
M. cra	-	**<0.001**	**<0.001**	**<0.001**	**<0.001**	**0.001**	**<0.001**
M. jav	0.089	-	**<0.001**	**<0.001**	**<0.001**	**<0.001**	**<0.001**
M.pen	0.076	0.096	-	**<0.001**	**<0.001**	**<0.001**	**<0.001**
S. gig	0.105	0.127	0.134	-	**<0.001**	**<0.001**	**<0.001**
S. tem	0.092	0.125	0.111	0.094	-	**<0.001**	**<0.001**
P. tri	0.102	0.087	0.120	0.104	0.100	-	**<0.001**
P. tet	0.136	0.119	0.154	0.150	0.127	0.084	-

Table S14. Significant *t*-tests of Principal components versus logarithm-transformed centroid size.

	R^2	***t*-test**	***p*-value**
PC1	0.39	10.64	<0.001
PC2	0.07	3.637	<0.001
PC3	0.02	-2.287	0.023
PC4	0.29	-8.433	<0.001
PC7	0.06	-3.519	<0.001

Table S15. Pairwise comparisons of the allometric trajectory angles for skull shape in *P. tricuspis* cryptic lineages (HOS). *P*-values (10.000 iterations) are on the upper triangle and angles between slopes (in degrees) are on the bottom triangle. Significant results written in bold.

	CAF	DHG	GAB	GHA	WAF	WCA
CAF	-	0.054	1	0.516	0.916	0.061
DHG	49.453	-	1	0.441	0.522	0.126
GAB	NA	NA	-	1	1	1
GHA	63.095	68.940	NA	-	0.911	0.122
WAF	44.734	59.582	NA	61.804	-	0.101
WCA	46.947	54.805	NA	77.977	69.995	-

Table S16. Pairwise comparison of the Procrustes distances between least-squares (LS) means for cryptic lineages (Gaubert et al., 2016). *P*-values of the difference between the LS means computed with 10,000 iterations (upper triangle) and observed distances (bottom triangle). Significant results are written in bold.

	CAF	DHG	GAB	GHA	WAF	WCA
CAF	-	**<0.001**	NA	**<0.001**	**<0.001**	**0.002**
DHG	0.041	-	NA	**0.001**	**<0.001**	**0.001**
GAB	NA	NA	-	NA	NA	NA
GHA	0.049	0.050	NA	-	0.181	**0.028**
WAF	0.040	0.047	NA	0.035	-	**0.012**
WCA	0.034	0.043	NA	0.043	0.036	-

Table S17. Pairwise comparison of the Procrustes distances between least-squares (LS) means for three geographical groups. *P*-values of the difference between the LS means computed with 10,000 iterations (upper triangle) and observed distances (bottom triangle). Significant results are written in bold.

	CEN	DHG	WES
CEN	-	**<0.001**	**<0.001**
DHG	0.040	-	**<0.001**
WES	0.037	0.045	-

Table S18. Pairwise comparison of the allometry-corrected Procrustes distances between least-squares (LS) means for cryptic lineages (Gaubert et al., 2016). *P*-values of the difference between the LS means computed with 10,000 iterations (upper triangle) and observed distances (bottom triangle). Significant results are written in bold.

	CAF	DHG	GAB	GHA	WAF	WCA
CAF	-	**<0.001**	NA	**<0.001**	**<0.001**	**<0.001**
DHG	0.040	-	NA	**<0.001**	**<0.001**	**0.002**
GAB	NA	NA	-	NA	NA	NA
GHA	0.048	0.050	NA	-	0.200	**0.002**
WAF	0.038	0.046	NA	0.032	-	**0.003**
WCA	0.035	0.042	NA	0.045	0.037	-

Table S19. Pairwise comparison of the allometry corrected Procrustes distances between least-squares (LS) means for three geographical groups. *P*-values of the difference between the LS means computed with 10,000 iterations (upper triangle) and observed distances (bottom triangle). Significant results are written in bold.

	CEN	**DHG**	**WES**
CEN	-	**<0.001**	**<0.001**
DHG	0.038	-	**<0.001**
WES	0.036	0.045	-

Table S20. ANOVA of shape (Procrustes coordinates) ~ log(centroid size)*cryptic lineages (*n* = 35) in *M. javanica*. *Df* – degrees of freedom; *F* – value of *F*-statistics; *significant *p*-value.

	Df	***R^2***	***F***	***p*-value**
Log(centroid size)	1	0.20	8.33	<0.001*
Cryptic lineages	2	0.07	1.41	0.001*
Log(centroid size):cryptic lineages	2	0.04	0.90	0.125
Residuals	29	0.69	-	-
Total	34		-	-

Appendix S1

Number	Institution	*Genus and species*	Country	Sex
12-12-3-1	BMNH	*Phataginus tricuspis*	DR Congo	-
12-12-3-3	BMNH	*Phataginus tricuspis*	DR Congo	-
34-11-18-9	BMNH	*Phataginus tricuspis*	DR Congo	Female
34-6-2-92	BMNH	*Phataginus tricuspis*	Uganda	Male
6-3-8-52	BMNH	*Phataginus tricuspis*	Uganda	-
7-7-8-260	BMNH	*Phataginus tricuspis*	DR Congo	Male
1967-980	MNHN	*Phataginus tricuspis*	Central African Republic	?
1967-981	MNHN	*Phataginus tricuspis*	Central African Republic	?
19624	RMCA	*Phataginus tricuspis*	DR Congo	?
20206	RMCA	*Phataginus tricuspis*	DR Congo	?
90.042-M-0131	RMCA	*Phataginus tricuspis*	DR Congo	?
83.006-M-0575	RMCA	*Phataginus tricuspis*	DR Congo	?
83.006-M-0585	RMCA	*Phataginus tricuspis*	DR Congo	?
83.006-M-0588	RMCA	*Phataginus tricuspis*	DR Congo	?
90.042-M-0129	RMCA	*Phataginus tricuspis*	DR Congo	?
90.042-M-0132	RMCA	*Phataginus tricuspis*	DR Congo	?
90.042-M-0136	RMCA	*Phataginus tricuspis*	DR Congo	?
90.042-M-0139	RMCA	*Phataginus tricuspis*	DR Congo	?
90.042-M-0142	RMCA	*Phataginus tricuspis*	DR Congo	?
90.042-M-0143	RMCA	*Phataginus tricuspis*	DR Congo	?
90.042-M-0146	RMCA	*Phataginus tricuspis*	DR Congo	?
90.042-M-0157	RMCA	*Phataginus tricuspis*	DR Congo	?
90.042-M-0158	RMCA	*Phataginus tricuspis*	DR Congo	?
90.042-M-0162	RMCA	*Phataginus tricuspis*	DR Congo	?
83.006-M-0580	RMCA	*Phataginus tricuspis*	DR Congo	?
90.042-M-0145	RMCA	*Phataginus tricuspis*	DR Congo	?
11490	RMCA	*Phataginus tricuspis*	DR Congo	Female
12331	RMCA	*Phataginus tricuspis*	DR Congo	Female
12332	RMCA	*Phataginus tricuspis*	DR Congo	Male
12543	RMCA	*Phataginus tricuspis*	DR Congo	?
12544	RMCA	*Phataginus tricuspis*	DR Congo	?
15907	RMCA	*Phataginus tricuspis*	DR Congo	?
21668	RMCA	*Phataginus tricuspis*	DR Congo	?
28686	RMCA	*Phataginus tricuspis*	DR Congo	?
30808	RMCA	*Phataginus tricuspis*	DR Congo	?
634 c	RMCA	*Phataginus tricuspis*	DR Congo	?
6993	RMCA	*Phataginus tricuspis*	DR Congo	?
83.006-M-0576	RMCA	*Phataginus tricuspis*	DR Congo	?
83.006-M-0577	RMCA	*Phataginus tricuspis*	DR Congo	?
83.006-M-0579	RMCA	*Phataginus tricuspis*	DR Congo	?
83.006-M-0582	RMCA	*Phataginus tricuspis*	DR Congo	?
83.006-M-0583	RMCA	*Phataginus tricuspis*	DR Congo	?
90.042-M-0133	RMCA	*Phataginus tricuspis*	DR Congo	?
90.042-M-0135	RMCA	*Phataginus tricuspis*	DR Congo	?
90.042-M-0148	RMCA	*Phataginus tricuspis*	DR Congo	?
90.042-M-0150	RMCA	*Phataginus tricuspis*	DR Congo	?
90.042-M-0152	RMCA	*Phataginus tricuspis*	DR Congo	?
90.042-M-0154	RMCA	*Phataginus tricuspis*	DR Congo	?
90.042-M-0156	RMCA	*Phataginus tricuspis*	DR Congo	?
90.042-M-0159	RMCA	*Phataginus tricuspis*	DR Congo	?
90.042-M-0161	RMCA	*Phataginus tricuspis*	DR Congo	?
90.042-M-0162	RMCA	*Phataginus tricuspis*	DR Congo	?
56-61	BMNH	*Phataginus tricuspis*	Sierra Leone	Male
1962-2118	MNHN	*Phataginus tricuspis*	Ivory Coast	?
38506	RMCA	*Phataginus tricuspis*	Liberia	?
239440	AMNH	*Phataginus tricuspis*	Liberia	Female
450073	USNM	*Phataginus tricuspis*	Ivory Coast	Male
465920	USNM	*Phataginus tricuspis*	Ivory Coast	Female
465924	USNM	*Phataginus tricuspis*	Ivory Coast	Male
465923	USNM	*Phataginus tricuspis*	Ivory Coast	Female
465926	USNM	*Phataginus tricuspis*	Ivory Coast	Female
481811	USNM	*Phataginus tricuspis*	Liberia	Female
481813	USNM	*Phataginus tricuspis*	Liberia	Female
481812	USNM	*Phataginus tricuspis*	Liberia	Male
38504	RMCA	*Phataginus tricuspis*	Liberia	?
48-1320	BMNH	*Phataginus tricuspis*	Cameroon	Male

48-1325	BMNH	*Phataginus tricuspis*	Cameroon	Female
48-1329	BMNH	*Phataginus tricuspis*	Cameroon	Male
48-133	BMNH	*Phataginus tricuspis*	Cameroon	Female
48-1332	BMNH	*Phataginus tricuspis*	Cameroon	Female
77.032-M-0078	RMCA	*Phataginus tricuspis*	Cameroon	?
19138	MfN	*Phataginus tricuspis*	Cameroon	?
37810	MfN	*Phataginus tricuspis*	Cameroon	?
37813	MfN	*Phataginus tricuspis*	Cameroon	?
38099	MfN	*Phataginus tricuspis*	Cameroon	?
75076	MfN	*Phataginus tricuspis*	Equatorial Guinea	Male
241130	AMNH	*Phataginus tricuspis*	Cameroon (East)	Male
12-10-28-58	BMNH	*Phataginus tricuspis*	Nigeria	Male
1999-115	BMNH	*Phataginus tricuspis*	Nigeria	?
20-3-18-42	BMNH	*Phataginus tricuspis*	Nigeria	Female
9075	MfN	*Phataginus tricuspis*	Togo	?
1956-725	MNHN	*Phataginus tricuspis*	Togo	Female
1956-724	MNHN	*Phataginus tricuspis*	Togo	Male
1956-728	MNHN	*Phataginus tricuspis*	Togo	Male
1956-729	MNHN	*Phataginus tricuspis*	Togo	Female
439127	USNM	*Phataginus tricuspis*	Benin	Female
379617	USNM	*Phataginus tricuspis*	Nigeria	Male
35-10-22-155	BMNH	*Phataginus tricuspis*	Ghana	Female
35-10-22-157	BMNH	*Phataginus tricuspis*	Ghana	Female
46-500	BMNH	*Phataginus tricuspis*	Ghana	Female
70-7-16-1	BMNH	*Phataginus tricuspis*	Ghana	Female
412726	USNM	*Phataginus tricuspis*	Ghana	Male
465927	USNM	*Phataginus tricuspis*	Ghana	Female
465928	USNM	*Phataginus tricuspis*	Ghana	Female
1990-48	MNHN	*Phataginus tricuspis*	Gabon	Female
537784	USNM	*Phataginus tricuspis*	DR Congo	Female
537785	USNM	*Phataginus tricuspis*	DR Congo	Male
1-11-21-35	BMNH	*Phataginus tetradactyla*	Equatorial Guinea	?
35-10-22-156	BMNH	*Phataginus tetradactyla*	Ghana	Female
64-12-1-10	BMNH	*Phataginus tetradactyla*	?	?
48-1327	BMNH	*Phataginus tetradactyla*	Cameroon	Male
1942-189	MNHN	*Phataginus tetradactyla*	Ivory Coast	?
1958-194	MNHN	*Phataginus tetradactyla*	Gabon	Female
1962-1174	MNHN	*Phataginus tetradactyla*	Ivory Coast	Male
14620	RMCA	*Phataginus tetradactyla*	DR Congo	Female
37804	MfN	*Phataginus tetradactyla*	Cameroon	?
37968	MfN	*Phataginus tetradactyla*	Equatorial Guinea	?
1958-193	MNHN	*Phataginus tetradactyla*	Gabon	Male
1985-101	MNHN	*Phataginus tetradactyla*	Central African Republic	Female
150409	AMNH	*Phataginus tetradactyla*	?	?
53868	AMNH	*Phataginus tetradactyla*	DR Congo	Female
53869	AMNH	*Phataginus tetradactyla*	DR Congo	Female
53866	AMNH	*Phataginus tetradactyla*	DR Congo	Female
53870	AMNH	*Phataginus tetradactyla*	DR Congo	Male
53872	AMNH	*Phataginus tetradactyla*	DR Congo	
86840	AMNH	*Phataginus tetradactyla*	DR Congo	Male
89399	AMNH	*Phataginus tetradactyla*	Ivory Coast	?
220402	USNM	*Phataginus tetradactyla*	Gabon	Male
481806	USNM	*Phataginus tetradactyla*	Liberia	Male
481805	USNM	*Phataginus tetradactyla*	Liberia	Male
2954	RMCA	*Smutsia gigantea*	DR Congo	Male
12946	RMCA	*Smutsia gigantea*	DR Congo	?
15320	RMCA	*Smutsia gigantea*	DR Congo	?
19113	RMCA	*Smutsia gigantea*	DR Congo	?
25479	RMCA	*Smutsia gigantea*	DR Congo	Female
27982	RMCA	*Smutsia gigantea*	DR Congo	Male
83.006-M-0591	RMCA	*Smutsia gigantea*	DR Congo	?
83.006-M-0592	RMCA	*Smutsia gigantea*	DR Congo	?
35717	RMCA	*Smutsia gigantea*	?	Female
38194	RMCA	*Smutsia gigantea*	Liberia	?
29-5-29-38	BMNH	*Smutsia gigantea*	Ghana	?
1913-113	MNHN	*Smutsia gigantea*	?	?
53850	AMNH	*Smutsia gigantea*	DR Congo	Male
53846	AMNH	*Smutsia gigantea*	DR Congo	?

53849	AMNH	*Smutsia gigantea*	DR Congo	Female
598576	USNM	*Smutsia gigantea*	Equatorial Guinea	Female
1937-9-1-847	BMNH	*Smutsia temminckii*	Namibia	Male
93-7-9-18	BMNH	*Smutsia temminckii*	Malawi	?
22-12-17-248	BMNH	*Smutsia temminckii*	?	Male
1-5-3-4	BMNH	*Smutsia temminckii*	Zambia	?
34-7-4-1	BMNH	*Smutsia temminckii*	Chad	?
76-137	BMNH	*Smutsia temminckii*	?	?
20334/335	MfN	*Smutsia temminckii*	Tanzania	?
37969	MfN	*Smutsia temminckii*	Tanzania	?
75060	MfN	*Smutsia temminckii*	Tanzania	?
20337	MfN	*Smutsia temminckii*	Kenya	?
105445	MfN	*Smutsia temminckii*	?	?
29304	MfN	*Smutsia temminckii*	Tanzania	?
75124	MfN	*Smutsia temminckii*	Tanzania	?
75066	MfN	*Smutsia temminckii*	Namibia	?
(Kisher, 1.X.04)	MfN	*Smutsia temminckii*	?	?
75120	MfN	*Smutsia temminckii*	Tanzania	?
75122	MfN	*Smutsia temminckii*	Tanzania	?
83609	AMNH	*Smutsia temminckii*	South Africa	?
244696	AMNH	*Smutsia temminckii*	?	?
168954	AMNH	*Smutsia temminckii*	Botswana	Female
314972	USNM	*Smutsia temminckii*	Zoo	Female
35750	RMCA	*Manis crassicaudata*	Pakistan	Male
50-29	BMNH	*Manis crassicaudata*	Sri Lanka	Male
77-3-14-8	BMNH	*Manis crassicaudata*	Sri Lanka	?
67-1114	BMNH	*Manis crassicaudata*	Pakistan	Female
76-151	BMNH	*Manis crassicaudata*	?	?
*****	MfN	*Manis crassicaudata*	?	?
34255	AMNH	*Manis crassicaudata*	Sri Lanka	Female
150067	AMNH	*Manis crassicaudata*	Sri Lanka	Male
244407	AMNH	*Manis crassicaudata*	Pakistan	Female
244406	AMNH	*Manis crassicaudata*	Pakistan	Female
9-1-5-860	BMNH	*Manis javanica*	Java	Male
9-1-5-857	BMNH	*Manis javanica*	Java	?
98-8-3-6	BMNH	*Manis javanica*	Thailand	?
98-10-5-48	BMNH	*Manis javanica*	Thailand	Female
26-10-4-199	BMNH	*Manis javanica*	Vietnam	Male
73-158	BMNH	*Manis javanica*	?	?
3-2-6-81	BMNH	*Manis javanica*	Malaysian Peninsula	Male
37805	MfN	*Manis javanica*	Malaysia (Borneo)	?
49377	MfN	*Manis javanica*	Indonesia (Sumatra)	?
75152	MfN	*Manis javanica*	Indonesia (Java)	?
2720	MfN	*Manis javanica*	Indonesia (Java)	Female
4621	MfN	*Manis javanica*	Singapore	?
60539	MfN	*Manis javanica*	Indonesia (Java)	?
75151	MfN	*Manis javanica*	Indonesia (Java)	?
36071	MfN	*Manis javanica*	Indonesia (Java)	?
34906	MfN	*Manis javanica*	Indonesia (Bali)	?
60537	MfN	*Manis javanica*	Indonesia (Sumatra)	?
60538	MfN	*Manis javanica*	Indonesia (Sumatra)	?
44131	MfN	*Manis javanica*	Indonesia (Sumatra)	?
75153	MfN	*Manis javanica*	Myanmar	?
75104	MfN	*Manis javanica*	Indonesia (Java)	?
1932	MfN	*Manis javanica*	Indonesia (Sumatra)	?
60540	MfN	*Manis javanica*	Indonesia (Java)	?
1962-2119	MNHN	*Manis javanica*	Vietnam	?
167959	AMNH	*Manis javanica*	Thailand	Male
167960	AMNH	*Manis javanica*	Thailand	?
102148	AMNH	*Manis javanica*	Indonesia (Bali)	Female
87624	AMNH	*Manis javanica*	Laos	Male
107600	AMNH	*Manis javanica*	Indonesia (Bali)	Female
102041	AMNH	*Manis javanica*	Indonesia (Java)	Male
142460	USNM	*Manis javanica*	Indonesia (Borneo)	Male
083250	USNM	*Manis javanica*	Thailand	Female
083513	USNM	*Manis javanica*	Thailand	Male
257682	USNM	*Manis javanica*	Thailand	Male
A49936	USNM	*Manis Javanica*	Indonesia (Sumatra)	Male

198852	USNM	*Manis javanica*	Indonesia (Borneo)	Male
300025	USNM	*Manis javanica*	Zoo	Male
395132	USNM	*Manis javanica*	Zoo	Female
1938-9-7-57	BMNH	*Manis pentadactyla*	China	Male
33-4-1-508	BMNH	*Manis pentadactyla*	?	Female
33-4-1-506	BMNH	*Manis pentadactyla*	Vietnam	Male
38-9-7-58	BMNH	*Manis pentadactyla*	China	Male
72.11.13.10 728o	BMNH	*Manis pentadactyla*	China	?
728c	BMNH	*Manis pentadactyla*	India	?
7-7-3-25	BMNH	*Manis pentadactyla*	China	Male
21-8-2-27	BMNH	*Manis pentadactyla*	India	Female
47-326	BMNH	*Manis pentadactyla*	India	?
43340	MfN	*Manis pentadactyla*	China	Male
17520	MfN	*Manis pentadactyla*	China	?
43339	MfN	*Manis pentadactyla*	China	Male
18639	MfN	*Manis pentadactyla*	Taiwan	?
75095	MfN	*Manis pentadactyla*	China	?
18640	MfN	*Manis pentadactyla*	Taiwan	?
47852	AMNH	*Manis pentadactyla*	China	Female
57059	AMNH	*Manis pentadactyla*	China	Male
47851	AMNH	*Manis pentadactyla*	China	Male
47854	AMNH	*Manis pentadactyla*	China	?
60020	AMNH	*Manis pentadactyla*	China	Male
45563	AMNH	*Manis pentadactyla*	China	?
60004	AMNH	*Manis pentadactyla*	China	Male
183148	AMNH	*Manis pentadactyla*	Taiwan	?
173637	AMNH	*Manis pentadactyla*	Taiwan	Male
294178	USNM	*Manis pentadactyla*	Taiwan	Female
308865	USNM	*Manis pentadactyla*	Taiwan	Female
332898	USNM	*Manis pentadactyla*	Taiwan	Male
238735	USNM	*Manis pentadactyla*	China	Female
308864	USNM	*Manis pentadactyla*	Taiwan	Female
311292	USNM	*Manis pentadactyla*	Taiwan	?
308733	USNM	*Manis pentadactyla*	?	Female
240168	USNM	*Manis pentadactyla*	China	Female
582702	USNM	*Manis pentadactyla*	?	Male
332899	USNM	*Manis pentadactyla*	Taiwan	Female
307385	USNM	*Manis pentadactyla*	Zoo	Male
314135	USNM	*Manis pentadactyla*	Zoo	Female
29245	AMNH	*Manis culionensis*	Philipines	?
841822	MNHN	*Manis culionensis*	Philipines	?

Appendix S2

Common traits of the African pangolins:

- The vomer protrudes through the inter-maxillary suture and is visible in the palate (in *M. crassicaudata* this also happens)
- Anteroposteriorly elongated opening of the ectotympanic
- Posteriorly projecting maxillary process of the maxillae into the palatine

Common traits of the genus *Phataginus*:

- Small nasal notches (relative to *Smutsia*)
- Much smaller size than *Smutsia*
- Unfused/present lacrimal bone

Common traits of the genus *Smutsia*:

- Lateral opening of the mandibular canal
- Large size
- Fused/absent lacrimal bone

Distinctive traits within the genus *Phataginus*:

Phataginus tricuspis

- Broader snout (Hatt, 1934)
- Reduced inflation of the epitympanic sinus (Hatt, 1934)
- Zygomatic process of the squamosal is large and projects laterally (Hatt, 1934)
- Sphenopalatine foramen open ventrally (Hatt, 1934)
- Foramen ovale is always posterior to post-glenoid foramen
- Lacrimal tends to be larger than in *P. tetradactyla*

Phataginus tetradactyla

- Antorbital constriction resulting in narrow snout (Hatt, 1934)
- Rather inflated epitympanic sinus (Hatt, 1934)
- Zygomatic process of the squamosal is small, projects anteriorly and displays a root-like shape (Hatt, 1934)
- Sphenopalatine foramen opens posteriorly (Hatt, 1934)
- Foramen ovale is always anterior to post-glenoid foramen
- Lacrimal tends to be smaller than in *P. tricuspis*

Distinctive traits within the genus *Smutsia*

Smutsia gigantea

- In ventral view, the most anterior part of the maxillary ridge (LM2) is slightly more anterior than the most anterior point of the maxilla on the midline (LM1).
- Larger and with longer rostrum, when compared to *S. temminckii*
- Maxillary foramen is v-shaped in ventral view
- Fronto-nasal suture is short
- Bilateral maxilla-nasal-frontal intersection points are close (narrow nasals)

Smutsia temminckii

- In ventral view, the most anterior part of the maxillary ridge (LM2) is more posterior than the most anterior point of the maxilla on the midline (LM1).
- Smaller and with shorter rostrum than *S. gigantea*.
- Maxillary foramen is circular in ventral view
- Fronto-nasal suture is long
- Bilateral maxilla-nasal-frontal intersection points are distant (wide nasals)

Common traits of the Asian pangolins:

- The vomer does not protrude through the inter-maxillary suture and is not visible in the palate (except in *M. crassicaudata*)
- Crescent shape opening of the ectotympanic
- Short maxillary processes of the maxillae into the palatine

Distinctive traits within the genus Manis:

Manis javanica

- Anterior extension of the palatines into the maxillae is much more pronounced than in other Asian species
- Post-glenoid foramen is placed posterior to the zygomatic process of the squamosal

Manis pentadactyla

- Presence of a small fossa just posteriorly to the maxillary foramen, between the palatine and the maxilla
- Post-glenoid foramen is more lateral than in *M. javanica*
- Significant contribution of the palatine to the zygomatic processes of the maxillae
- Slightly inflated posterior margins of the palatine

Manis crassicaudata

- Post-glenoid foramen is more lateral than in *M. javanica*
- Vomer protrudes through the maxillae and is visible in ventral view

Appendix S3

PTA analysis

Materials and methods

We performed a phenotypic trajectory analysis (PTA) to compare the direction and length of the trajectories between juveniles and adults of all species in the morphospace (Adams and Collyer 2009; Collyer and Adams 2013). Adults and juveniles were defined as the specimens presenting a centroid size above the third quartile and below the first quartile, respectively. Specimens with intermediate centroid size values were excluded to prevent errors in the attribution of age categories. Significance of phenotypic trajectory lengths and angles was assessed with a pairwise comparison between groups. The PTA was only performed on the interspecific dataset.

Results

The PTA (50.06% explained variance; Fig S2) retrieves a significant effect of species ($F_{6,111} = 28.34$, $p < 0.001$), age (derived from centroid size; $F_{1,111} = 27.03$, $p < 0.001$), and the interaction between the two factors ($F_{6,111} = 1.51$, $p < 0.001$) on shape. Pairwise comparisons between the angles of the trajectories do not significantly differ between most species, with the exception of *Phataginus tricuspis* that presents a significantly different trajectory angle compared to *Manis pentadactyla* and *Manis javanica* (Table S4). *Manis crassicaudata* and *Smutsia gigantea* show a significantly longer trajectory than all other species (Table S4). These two species are the largest species, in average, implying an increase of either growth rate or a growth time (Fig. S2). Given that some species are relatively rare in museum collections (e.g., *M. crassicaudata*), trajectory length must be interpreted with caution, as sampling is not homogeneous across all developmental stages.

Allometry-corrected analysis of the interspecific dataset

Results

A Procrustes ANOVA performed on the allometry-corrected shapes reveals that species present different skull shapes ($F_{6,166} = 50.35$, $p < 0.001$; Table S12). Pairwise comparisons showed that all species presented significantly different skull shapes (Table S13). The first axis of the PCA explains 32.3% and the split between African and Asian species is less evident when compared to the PCA on raw Procrustes coordinates (Fig. 6A), with *Smutsia* spp and *M. javanica* presenting overlapping values (Fig. S3A). Asian species are characterized by positive PCres1 values, while the African species present either negative (*Phataginus* spp.) or positive (*Smutsia* spp.) values. Morphologically, specimens with positive values present a wider and more robust skull, with the zygomatic processes of the maxillae projecting posteriorly until half length of the orbit. *M. pentadactyla* is by far the species scoring higher values, followed by *M. crassicaudata* and *M. javanica*. The latter presents PCres1 values similar to those of *Smutsia* species. *P. tetradactyla* presents the lowest PCres1 values, while *P. tricuspis* presents a wide range of negative values (Fig. S3). PCres2 (16.2%) separates specimens with a long rostrum (positive values) from those with a relatively small rostrum (negative values). Thus, *M. javanica* shows the highest values PCres2 values, while *S. temminckii* presents the lowest (Fig. S3). *S. gigantea* scores PCres2 values overlapping those of *S. temminckii*, while all other species occupy a morphospace

in between. PCres3 shows a similar pattern to the one observed in Fig. 6B, showing a relatively low effect of size on the traits explained by this axis (Table S14).

The allometric-correction did not influence the *a posteriori* attribution rates of the LDA performed on the PCress explaining 90% of the variance, when compared to the results using the raw Procrustes data (Data S3).

Discussion

When compared to the analysis with the raw Procrustes coordinates, the main change in the morphospace relates to the first and second axes. The morphospace and the Procrustes distances between the LS means showed that, when allometry is accounted for, *S. gigantea* occupies a radically different morphospace, compared to the Asian pangolins (Fig. S3), in particular to *M. javanica*, to which it resembled when size was not taken into account (Fig. 6). When the data was corrected for allometry, *S. gigantea* occupies a morphospace that is much closer to its sister taxon, *S. temminckii*. We showed that allometry adds noise when considering the intrageneric relationships within *Smutsia*.

Allometry-corrected analysis of the *P. tricuspis* dataset

Results

A Procrustes ANOVA performed on the allometry-corrected shapes reveals that cryptic lineages present different skull shapes ($F_{4,65} = 3.77$, $p < 0.001$; Table 12). Pairwise comparisons showed that all tested cryptic lineages presented significantly different skull shapes except for Ghana (GHA) and Western Africa (WAF; Table S18). Gabon (GAB) was not tested due to lack of replicates. Globally, the morphospace did not change significantly when compared to the PCA performed on the raw Procrustes coordinates (Fig. 5). PCres1 (14.9%) roughly segregates CAF (negative values) from WAF-GHA (positive values), with both DHG and WCA skulls scoring values in between (Fig. S6). DHG specimens present a wide range of PCres1 values, ranging from the most negative to positive values close to WAF and GHA. PCres2 (10.3%) range of values are also similar to the PCA on raw Procrustes data, except for the WCA skulls, which score slightly higher values, on average (Fig. S6A). PCres3 (6.0%) values are higher for WAF-GHA skull when allometry is taken into account. Nevertheless, this difference is slight and this axis does not efficiently segregate between cryptic species. The specimen from Gabon occupies a similar morphospace as described for the raw Procrustes coordinates (see 'Results: Intraspecific variation within *P. tricuspis*').

The allometric-correction had a noticeable influence on the *a posteriori* attribution rates of the LDA performed on the PCress explaining 90% of the variance, when compared to the analysis on the raw Procrustes data (Data S3). Allometric correction increased the *a posteriori* attribution rates from 75.4% to 82.9%. However, the incorrect attributions occurred mostly between CAF-WCA and WAF-GHA as described in the analysis of the raw Procrustes coordinates (Data S3). Therefore, a cross-validated LDA was performed with the same three regional groups.

A Procrustes ANOVA revealed a significant effect of the division of *P. tricuspis* in three morphological groups, WES, DHG and CEN ($F_{2,67} = 5.01$, $p < 0.001$; Table S12). Pairwise comparisons showed that all groups presented significantly different skull shapes (Table S19). This shows that size did not influence the segregations of the skull of the three groups based on skull shape. While

***Manis javanica* cryptic lineages**

Methods

Intraspecific variation within Manis javanica: A third subset including adult *M. javanica* specimens with known locations (n=25) was used and we applied the same procedure as for *P. tricuspis* (see 'Materials and methods') in order to investigate intraspecific geographical variations in skull shape. The genetic clusters from Nash *et al*. (2018) were used: Sumatra / Singapore (Sumatra, Thailand and Burma), Java (Java and Bali), and Borneo.

Given that the genetic clusters in *M. javanica* present very similar slopes (Fig. S7), allometry-corrected residuals were obtained from a multiple regression of shape coordinates against size (i.e., shape~log(size)).

Results

Using the main groups identified by Nash *et al*. (2018) as categories, an ANOVA yields a significant effect of logarithm transformed centroid size ($F_{1,29} = 8.33$, $p < 0.001$) and geographical distribution ($F_{2,29} = 1.41$, $p < 0.001$; Table S20). The effect of the interaction between both variables ($F_{2,29} = 0.90$, $p = 0.125$) is not significant, indicating that the slopes for the three groups (Sumatra / Singapore, Java, and Borneo) are parallel (Fig. S9). Procrustes ANOVAs revealed that skull shape significantly differ between cryptic lineages ($F_{2,22} = 2.12$, $p < 0.001$; Table S12). However, this difference was not significant when allometry was taken into account ($F_{2,22} = 1.13$, $p = 0.225$). Therefore, we describe only the PCA performed on the raw Procrustes coordinates. PC1 (15.4%) positively correlates with rostrum length, palatine width, a short posterior projections of the maxillae on the palatines, and a relatively small braincase with a dorsal basioccipital compared to the palate (Fig. S8). Skulls from Java score negative values, while specimens from Sumatra/Singapore show a range of negative and positive values, on average higher. The only three skulls from Borneo score, on average, the highest PC1 scores. PC2 (12.0%) and PC3 (9.8%) appear to explain shape changes associated to ontogenetic allometry (see 'Results: Allometry within extant pangolins'), and do not segregate between cryptic lineages. We interpret the small range of PC2-3 values of the Borneo lineage as a result of the low sampling.

Discussion

Our results on skull shape variation in *M. javanica* are not conclusive regarding the recognition of cryptic lineages, as we did not retrieve significant differences among the potential groups defined by Nash *et al*. (2018). Differences between groups are appear to separate Sumatra/Singapore from Java (Fig. S8). However, differences between genetic clusters are non-significant when allometry-corrected shapes are considered. The existence of at least two divergent mitochondrial lineages within *M. javanica* was recently described by Zhang *et al*. (2015). If our sample size is clearly insufficient, the lack of evidence for the differentiation of skull morphologies between the three *M. javanica* lineages may be a result of introgressions, exemplified by sample from Java showing evidence of introgression from Singapore/Sumatra and Borneo (Nash *et al.*, 2018). Additionally, the divergence time for cryptic lineages within *M. javanica* (0.4 – 2.5 Mya; TMRCA of *M. javanica*-*M. culionensis*) is likely more recent compared to the split between Western and Central African lineages within *P. tricuspis* (0.8 - 4.6 Mya; Gaubert *et al.*, 2017). Additional sampling effort on the Sunda and Philippine pangolins is key to unveil a putative morphological disparity within South-East Asian pangolins.

6.2-Appendix 2

Supplemental information to Article 2

Current Biology, Volume *29*

Supplemental Information

Evolutionary Tinkering of the Mandibular Canal Linked to Convergent Regression of Teeth in Placental Mammals

Sérgio Ferreira-Cardoso, Frédéric Delsuc, and Lionel Hautier

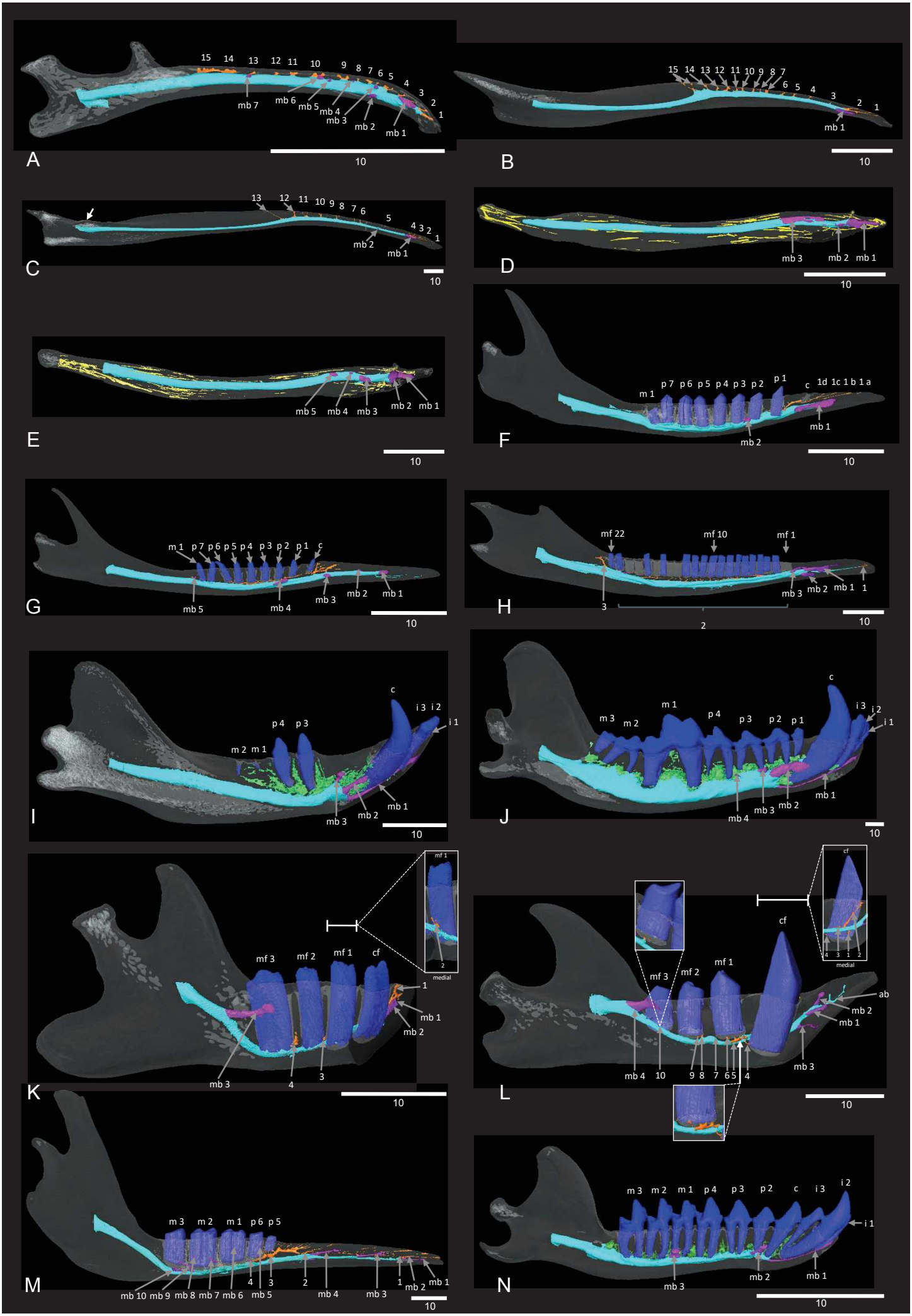
A
15 14 13 12 11 10 9 8 7 6 5 4 3 2 1
mb 7 mb 6 mb 5 mb 4 mb 3 mb 2 mb 1
10
B
15 14 13 12 11 10 9 8 7 6 5 4 3 2 1
mb 1
10
C
13 12 11 10 9 8 7 6 5 4 3 2 1
mb 2 mb 1
10
D
mb 3 mb 2 mb 1
10
E
mb 5 mb 4 mb 3 mb 2 mb 1
10
F
m 1 p 7 p 6 p 5 p 4 p 3 p 2 p 1 c 1d 1c 1b 1a
mb 2 mb 1
10
G
m 1 p 7 p 6 p 5 p 4 p 3 p 2 p 1 c
mb 5 mb 4 mb 3 mb 2 mb 1
10
H
mf 22 mf 10 mf 1
3 2
mb 3 mb 2 mb 1 1
10
I
c
i 3 i 2 i 1
p 4 p 3
m 2 m 1
mb 3 mb 2 mb 1
10
J
c
m 3 m 2 m 1 p 4 p 3 p 2 p 1
i 3 i 2 i 1
mb 4 mb 3 mb 2 mb 1
10
K
mf 1
2
medial
mf 3 mf 2 mf 1 cf
1
mb 1 mb 2
mb 3 4 3
10
L
cf
4 3 1 2
medial
mf 3 mf 2 mf 1
ab mb 2 mb 1
mb 4 10 9 8 7 6 5 4 mb 3
10
M
m 3 m 2 m 1 p 6 p 5
mb 10 mb 9 mb 8 mb 7 mb 6 mb 5 4 3 2 mb 4 mb 3 1 mb 2 mb 1
10
N
m 3 m 2 m 1 p 4 p 3 p 2 c i 3 i 2 i 1
mb 3 mb 2 mb 1
10

Figure S1. 3D models of fourteen mandibles (five toothless and nine toothed) in lateral view. Related to Figure 1. (A) *Cyclopes didactylus* (MNHN 1986-1115); (B) *Tamandua tetradactyla* (BMNH 34.9.2.196); (C) *Myrmecophaga tridactyla* (ISEM – 065 V); (D) *Manis crassicaudata* (BMNH_67.4.12.298); (E) *Manis javanica* (BMNH 9.1.5.858); (F) *Dasypus novemcinctus* (USNM 033867); (G) *Dasypus pilosus* (ZMB 19240); (H) *Priodontes maximus* (ZMB 47528); (I) *Proteles cristatus* (BMNH 34.11.1.5); (J) *Canis lupus* (LAMC 23010); (K) *Bradypus tridactylus* (MNHN 1999-1065); (L) *Choloepus hoffmanni* (Hautier pers. Coll.); (M) *Orycteropus afer* (BMNH 27.2.11.113); (N) *Potamogale velox* (ZMB 71587). Bone is transparent. Dorsal canaliculi (numbered) – orange; mental branches (mb) – purple; mandibular canal – cyan; parallel canaliculi – yellow. Scale in mm.

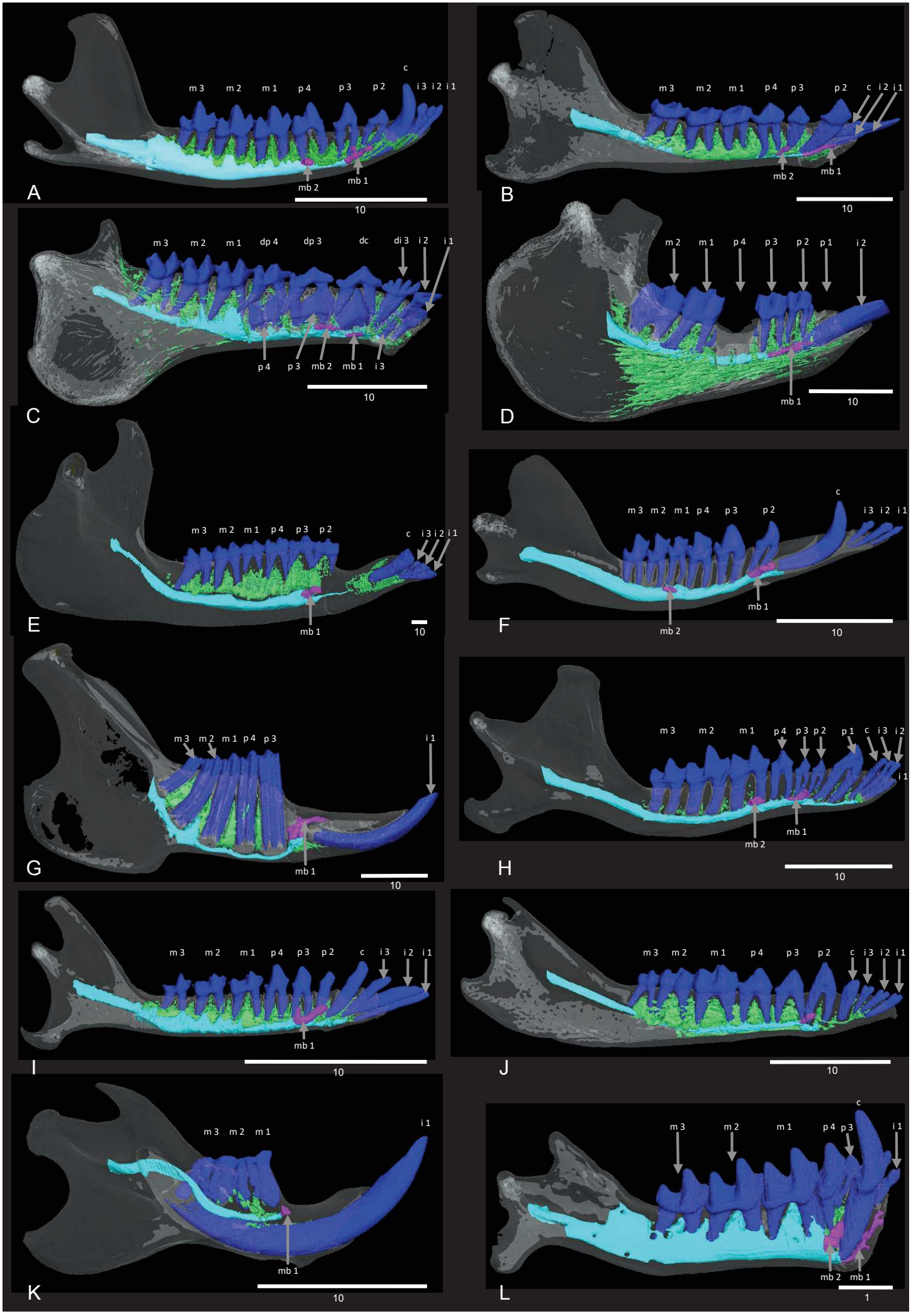
A
m 3 m 2 m 1 p 4 p 3 p 2 c i 3 i 2 i 1
mb 2
mb 1
10
B
m 3 m 2 m 1 p 4 p 3 p 2 c i 2 i 1
mb 2
mb 1
10
C
m 3 m 2 m 1 dp 4 dp 3 dc di 3 i 2 i 1
p 4 p 3 mb 2 mb 1 i 3
10
D
m 2 m 1 p 4 p 3 p 2 p 1 i 2
mb 1
10
E
m 3 m 2 m 1 p 4 p 3 p 2 c i 3 i 2 i 1
mb 1
10
F
m 3 m 2 m 1 p 4 p 3 p 2 c i 3 i 2 i 1
mb 1
mb 2
10
G
m 3 m 2 m 1 p 4 p 3 i 1
mb 1
10
H
m 3 m 2 m 1 p 4 p 3 p 2 p 1 c i 3 i 2 i 1
mb 1
mb 2
10
I
m 3 m 2 m 1 p 4 p 3 p 2 c i 3 i 2 i 1
mb 1
10
J
m 3 m 2 m 1 p 4 p 3 p 2 c i 3 i 2 i 1
10
K
m 3 m 2 m 1 i 1
mb 1
10
L
m 3 m 2 m 1 p 4 p 3 c i 1
mb 2 mb 1
1

Figure S2. 3D models of 12 toothed mandibles in lateral view. Related to Figure 1. (A) *Dasyurus hallucatus* (TMM M-6921); (B) *Lemur catta* (DPC-O92); (C) *Cynocephalus volans* (FMNH 56521); (D) *Procavia capensis* (UMZC H4980K); (E) *Tapirus indicus* (KUPRI 506); (F) *Tenrec ecaudatus* (Martinez pers. coll.); (G) *Lepus europaeus* (DMET-RN1); (H) *Talpa europaea* (Martinez pers. coll.); (I) *Tupaia montana* (FMNH 108831); (J) *Rhynchocyon petersi* (BMNH 55149); (K) *Rattus norvegicus* (HACB-RN1); (L) *Molossus molossus* (AMNH 234923). Bone is transparent. Mental branches (mb) – purple; mandibular canal – cyan; teeth – dark blue; trabeculae – green. Scale in mm.

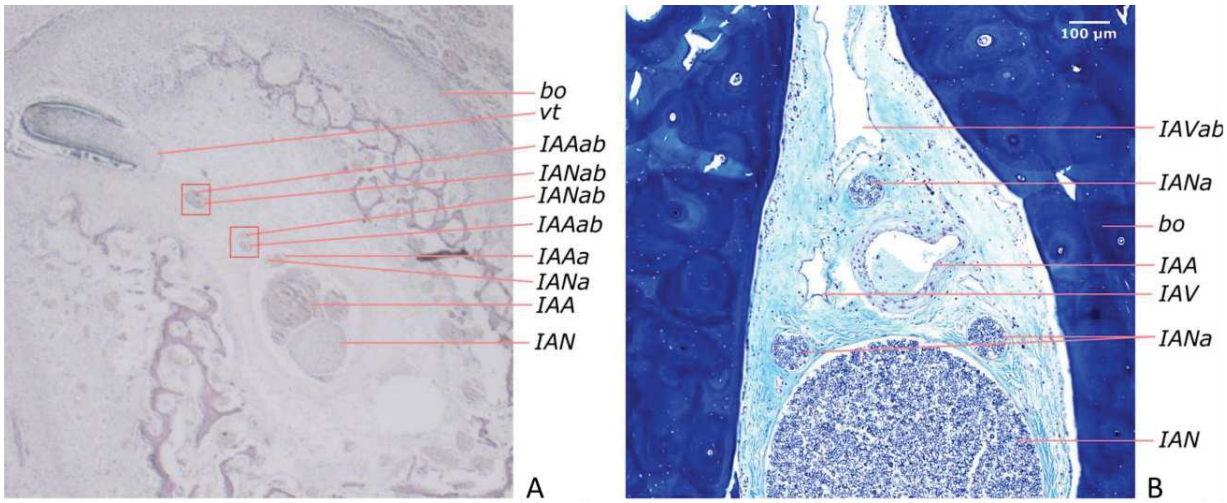

Figure S3. Histological slice of coronal sections of the mandibles of a bowhead whale and a collared anteater. Related to Figure 4. Coronal sections of the mandibles of (A) *Balaena mysticetus* [S1] and (B) a formalin preserved *Tamandua tetradactyla* (ISEM 778N; LFB stained). For B bone tissue is colored in dark blue and soft tissues stained in different tones of blue and purple. The dark blue colored myelin layers can be observed. Coronal cuts showing the mandibular canal and dorsal canaliculi; soft tissues are present on mandibular canals and dorsal canaliculi. *bo* bone; *IAA* inferior alveolar artery; *IAAa* inferior alveolar artery accessory branch; *IAAab* inferior alveolar artery ascending branch; *IAN* inferior alveolar nerve; *IANa* inferior alveolar nerve accessory branch; *IANab* inferior alveolar nerve ascending branch; *IAV* inferior alveolar vein; *IAVab* inferior alveolar vein ascending branch; *vt* vestigial tooth (1st generation).

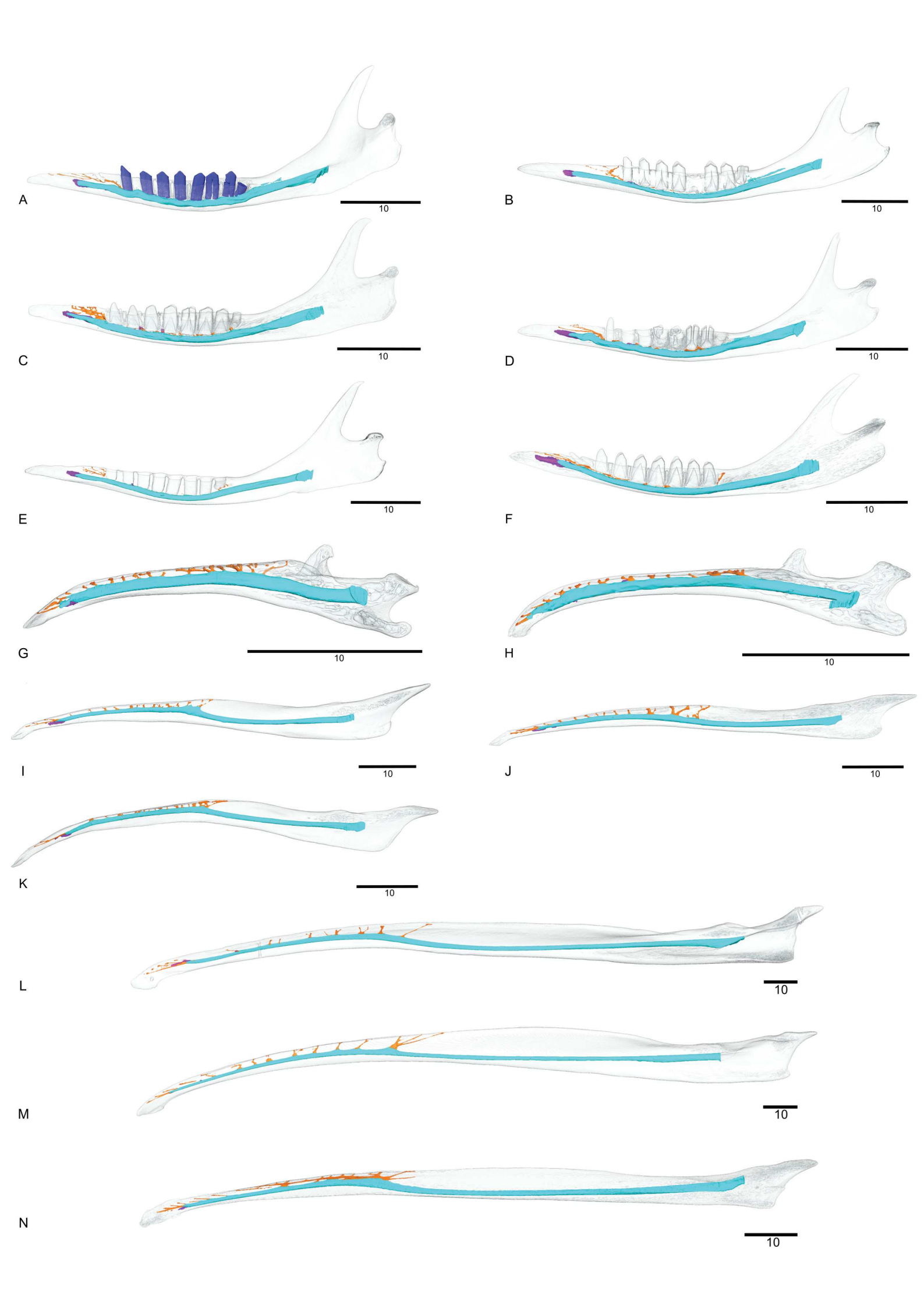
A
10
B
10
C
10
D
10
E
10
F
10
G
10
H
10
I
10
J
10
K
10
L
10
M
10
N
10

Figure S4. 3D models showing intraspecific variation of dorsal canaliculi. Related to Figures 1 and 2. (A-F) *Dasypus novemcinctus* (USNM 033867, BMNH 11.10.27.3, LSUMZ 8538, LSUMZ 29160, ZMB 84-357, USNM 020920); (G-H) *Cyclopes didactylus* (MNHN 1986-1115, BMNH 24.12.4.68); (I-K) *Tamandua tetradactyla* (BMNH 34.9.2.196, MVZ 153482, ISEM 778N); (L-N) *Myrmecophaga tridactyla* (ISEM 065V, MVZ 185238, ISEM 071N). Teeth are segmented in (A) only. Bone is transparent. Dorsal canaliculi – orange; mental branches – purple; mandibular canal – cyan; teeth – dark blue. Scale in mm.

Species	Specimen	Voxel size (µm)	Scanning platform
Proteles cristatus	BMNH 34.11.1.5	73.6	BMNH
Canis lupus	LACM 23010	600.0	-
Manis crassicaudata	BMNH 67.4.12.298	59.2	BMNH
Manis javanica	BMNH 9.1.5.858	49.6	BMNH
Orycteropus afer	BMNH 27.2.11.113	116.5	BMNH
Potamogale velox	ZMB 71587	72.0	HZB
Tenrec ecaudatus	Martinez pers. coll.	69.4	RIO
Rhynchocyon petrsi	BMNH 55149	94.0	BMNH
Procavia capensis	UMZC H4980K	86.0	-
Cyclopes didactylus	MNHN 1986-1115	36.0	RIO
Cyclopes didactylus	BMNH 24.12.4.68	32.2	BMNH
Tamandua tetradactyla	BMNH 34.9.2.196	79.8	NMNH
Tamandua tetradactyla	ISEM 788N	57.1	RIO
Tamandua tetradactyla	MVZ 153482	45.1	RIO
Myrmecophaga tridactyla	ISEM 071 N	79.0	RIO
Myrmecophaga tridactyla	ISEM 065 V	74.3	RIO
Myrmecophaga tridactyla	MVZ 185238	63.7	RIO
Bradypus tridactylus	ZMB 18834	41.7	HZB
Bradypus tridactylus	MNHN 1999-1065	113.2	RIO
Choloepus didactylus	ZMB 4949	83.8	HZB
Choloepus hoffmanni	Hautier pers. coll.	83.9	RIO
Dasypus pilosus	ZMB 19240	72	HZB

Dasypus novemcinctus	USNM 033867	36.0	RIO
Dasypus novemcinctus	LSUMZ 8538	36.0	RIO
Dasypus novemcinctus	LSUMZ 29160	36.0	RIO
Dasypus novemcinctus	BMNH 11.10.27.3	58.3	RIO
Dasypus novemcinctus	ZMB 84-357	58.3	HZB
Dasypus novemcinctus	USNM 020920	36.0	RIO
Priodontes maximus	ZMB 47528	72.0	RIO
Tapirus indicus	KUPRI 506	625.0(x,y)x300.0(z)	KUPRI
Molossus molossus	AMNH 234923	20.0	-
Talpa europaea	Martinez pers. coll.	89.0	RIO
Cynocephalus volans	FMNH 56521	65.0	-
Lemur catta	DPC-O92	100.0	-
Tupaia Montana	FMNH 108831	40.0	-
Lepus europaeus	DMET-LE1	137.4	-
Rattus norvegicus	HACB-RN1	54.0	-
Dasyurus hallucatus	TMM M-6921	35(x,y)x78(z)	-

Table S1. Resolution of the performed µ-CT scans and scanning platform information. Related to STAR methods.

Supplemental references

S1 Thewissen, J.G.M., Hieronymus, T.L., George, J.C., Suydam, R., Stimmelmayr, R., and McBurney, D. (2017). Evolutionary aspects of the development of teeth and baleen in the bowhead whale. J. Anat. *230*, 549–566.

S2. Ulm, C., Kneissel, M., Hahns, M., and Solar, P. (1997). Characteristics of the cancellous bone of edentulous mandibles. Clin. oral Implant. *8*, 125–130.

S3. Kieser, J., Kieser, D., and Hauman, T. (2005). The course and distribution of the inferior alveolar nerve in the edentulous mandible. J. Craniofac. Surg. *16*, 6–9.

S4. Martin, B. (1916). Tooth development in *Dasypus novemcinctus*. J. Morphol. *27*, 647–961.

S5. Ciancio, M.R., Castro, M.C., Galliari, F.C., Carlini, A.A., and Asher, R.J. (2012). Evolutionary implications of dental eruption in *Dasypus* (Xenarthra). J. Mamm. Evol. *19*, 1–8.

S6. Hautier, L., Gomes Rodrigues, H., Billet, G., and Asher, R.J. (2016). The hidden teeth of sloths: evolutionary vestiges and the development of a simplified dentition. Sci. Rep. *6*, 27763.

S7 Anthony, R. (1934). La dentition de l'oryctérope. Morphologie, développement, structure, interprétation. Ann. Sci. Nat. Zool. 17, 289–322.

S8. Pyenson, N., Goldbogen, J., Vogl, A., and Szathmary, G. (2012). Discovery of a sensory organ that coordinates lunge feeding in rorqual whales. Nature *485*, 498–501.

S9. Peredo, C., Pyenson, N., Uhen, M., and Marshall, C. (2017). Alveoli, teeth, and tooth loss: understanding the homology of internal mandibular structures in mysticete cetaceans. PLoS One *12*.

S10. Greene, E.C. (1955). Anatomy of the rat Second Edi. (New York: Hafner Publishing CO.).

S11. Gray, H. (1995). Anatomy, descriptive and surgical (Bristol: Parragon Book Service Ltd.).

S12. Hirschfeld, S. (1976). A New Fossil Anteater (Edentata, Mammalia) from Colombia, S . A . and Evolution of the Vermilingua. 419–432.

S13. Davit-Béal, T., Tucker, A., and Sire, J. (2009). Loss of teeth and enamel in tetrapods: fossil record, genetic data and morphological adaptations. J. Anat. *214*, 477–501.

S14. Yang, Z., Kumar, S., and Nei, M. (1995). A new method of inference of ancestral nucleotide and amino acid sequences. Genetics *141*, 1641–1650.

S15. Kumar, S., Stecher, G., Suleski, M., and Hedges, S.B. (2017). TimeTree: a resource for timelines, timetrees, and divergence times. Mol. Biol. Evol. *34*, 1812–19.

S16 Revell, L.J. (2012). phytools: an R package for phylogenetic comparative biology (and other things). Methods Ecol. Evol. 3, 217–223.

S17 Team, R.C. (2013). R: A language and environment for statistical computing.

Data S1

1. Anatomical descriptions of myrmecophagous mammals and sister taxa

Pygmy anteater (*Cyclopes didactylus*)

The mandible of *Cyclopes didactylus* is low and slender. In lateral view, the horizontal ramus is thin, elongated and is highly curved with a ventral concavity, which makes it distinctive from all other anteaters. The ascending ramus is extremely inclined laterally, with the hook-like coronoid process projecting laterally. The mandible presents seven mental foramina (Figure S1*A*). We here designate the flattened part of the horizontal ramus of the mandible as the dentary pad. This dentary pad extends from the most anterior tip of the mandible to the posterior end of the coronoid process. This pad displays several dorsal foramina with foramina for dorsal canaliculi 9 to 15 forming a continuous groove. Nineteen foramina are present on the left dentary pad, 20 on the right mandible.

The mandibular canal displays a straight trajectory until it reaches the dentary pad, from where it curves ventrally, accompanying the shape of the mandible. The mandible has an elliptic-like section, and the major axis rotates, in anterior direction, from an almost transversal plane parallel position to a coronal one. The mandibular canal is positioned dorsally. The size of the mandibular canal remains constant along the horizontal plane, and decreases towards the symphysis. The mandibular canal presents several dorsal canaliculi (dc), which connect dorsomedially with the opening foramina. In total, there are fifteen dorsal (eighteen on the right mandible) and seven mental branches. Some of the dorsal canaliculi bifurcate and vary in diameter, with dc14 and dc15 being the largest (Figure S1*A*). The first four dorsal canaliculi (dc1 to dc4) are

anterodorsally oriented, as well as dc12, dc13 and the anterior projections of the bifurcating canaliculi. The mental branches also vary in diameter, with the most anterior one (mb1) being, by far, the largest, but no specific trend observed.

Collared anteater (*Tamandua tetradactyla*)

In *Tamandua tetradactyla* the edentulous horizontal ramus is long, slightly curved ventrally, and gets gradually shallower postero-anteriorly. The dentary pad is more anterior, narrower in its most posterior part, and not as medially inclined as in *C. didactylus* (Figure S1*B*); it is perforated by 17 foramina (Figure S1*B*, dc 1-15); a small and shallow groove connects the most posterior ones. Only one anterior mental foramen is present (Figure S1*B*, mb1). The ascending ramus is rather shallow and presents incipient coronoid and angular processes; the condyloid process is posteriorly projected.

The mandibular foramen (mb1, Figure S1*B*) is parallel to the mandibular canal. The mandibular canal opens on the medial surface of the ascending ramus and projects anteriorly with a slight ventral inclination. It projects dorsally from the posterior edge of the dentary pad, as is typical of toothed mammals after tooth loss [S2,S3]. Similarly to *C. didactylus*, dorsal canaliculi are present. Each quadrant presents 15 dorsal canaliculi; only dc1 and dc15 are bifurcated (Figure S1*B*). The canals of the dorsal canaliculi are relatively narrower than those observed in *C. didactylus*. Although the most anterior canals (dc1 to dc6) are slightly anteriorly oriented, this trend is not present on the most posterior ones (dc7 to dc14), which display a more random inclination. The most posterior canaliculus (dc15) is posteriorly inclined. Dorsal canaliculi dc1 and dc2 are spatially and morphologically distinct from the remaining (Figure S1*B*), and highly anteriorly inclined. Dc1 is extremely elongated and splits into two parts anteriorly.

Giant anteater (*Myrmecophaga tridactyla*)

The mandible of the adult *Myrmecophaga tridactyla* is, in many ways, similar to that of *T. tetradactyla*. It is larger in size but presents the same general morphology, with the body being elongated, transversely compressed and lacking teeth, and the ascending ramus being extremely simplified when compared to toothed xenarthrans. As in *T. tetradactyla*, the anterior part of the mandible is slightly curved, with the anterior tip tapering ventrally. A dentary pad occupies more than half of the total length of the jaw (Figure S1*C*), which is narrow posteriorly. Sixteen foramina are present on the dentary pad, and correspond to the dorsal opening of the dorsal canaliculi. Two mental foramina are present in the anterior part of the mandible, with the most anterior one (mb1, Figure S1*C*) opening laterally at the level of dc4 and the second one (mb2, Figure S1*C*), much smaller, opening at the level of dc5.

The mandibular canal opens in the medial surface of the ascending ramus, just dorsally to the position of the coronoid process, with an aperture with a long antero-posterior axis. A groove runs anteriorly along the canal. The latter gradually descends along the lengthy horizontal ramus, until it reaches the level of the posterior margin of the dentary pad (Figure S1*C*). It then projects dorsally to reach the level of dc5, from where it maintains its position in the mandible until it opens to the mental foramen (mb1), anteriorly. Along this path, thirteen main dorsal canaliculi open dorsally in the dentary pad. Dc13, the longest and most posterior dorsal canaliculus projects postero-dorsally. Dc12 to dc6 project dorsally, with some dorsal canaliculi displaying a simple column shaped, while others bifurcate dorsally. Dc5 is anteriorly inclined and has a much reduced diameter. Close to the symphysis, the first five dorsal canaliculi (dc1-5) form a distinct complex of long and anteriorly inclined canaliculi, similar to *T. tetradactyla*. In summary, the morphology of the mandibular canal of *M. tridactyla* is similar to *T.*

tetradactyla, except for the dorsoposteriorly oriented dorsal canaliculus (i.e. 13), and for the larger number of dorsal canaliculi on the anterior complex.

A juvenile specimen (ISEM - 071 N) was also analysed to check on the number of dorsal canaliculi. There are 16 dorsal canaliculi on the left side and 18 dorsal canaliculi on the right hemi-mandible. The posterior part of the mandibular canal is not well ossified and the division between branches is less clear. The posteriormost dorsal canaliculus is long and posteriorly projecting and does not reach the top of the mandible.

Indian pangolin (*Manis crassicaudata*)

The mandible of *Manis crassicaudata* is greatly compressed transversely and shallow. The ascending branch lack a true coronoid process as consists of a slightly dorsally inclined posterior knob-like projection. Three mental foramina (Figure S1*D*, mb1-3) are present on the anterior part of the horizontal ramus.

The mandibular foramen is antero-posteriorly elongated and has an anterior position in the ascending ramus. The mandibular canal projects anteriorly in a straight trajectory, near the dorsal margin of the mandible. From about the middle of the horizontal ramus the mandibular canal trajectory accompanies the dorsal edge mandible. This contrasts with anteaters, in which the mandibular canal position is ventral until it drifts dorsally at the posterior part of the dentary pad. The transversal section of the canal varies between a circular and an oval shape. From its most posterior part, the canal displays several small canaliculi that depart from the main mandibular canal, parallel to it. These parallel canaliculi are present around the mandibular canal, along its entire length, both dorsally and ventrally. Their density is higher on the anterior half of the horizontal ramus and the posterior part of the ascending ramus. On the anterior part of the mandible, the dorso-laterally projecting pseudo-tooth displays a small foramen for a parallel canaliculus and the very anterior tip of the horizontal ramus presents two of

these canaliculi. Most parallel canaliculi show no connection to the mandibular canal and only a few open in microscopic foramina (Figure S1*D*). The most posterior mental branch (Mb3) is short and opens in an elongated foramen just before it bifurcates. The remaining two mental foramina (associated to mb2 and mb3) open laterally close to the sharp anterior tip of the mandible. The small mb2 splits posteriorly to the pseudo-tooth while the large and elongated mb1 drifts laterally at the level of this prong.

Malayan pangolin (*Manis javanica*)

The mandible in *Manis javanica* is shallower than in *M. crassicaudata*. It presents five anterior mental foramina (Figure S1*E*, mb1-5), with the second most anterior (mb2) being clearly larger than the remaining ones. Between the posterior end of the symphysis and the pseudo-tooth, two small circular foramina open medially (Figure S1*E*).

The mandibular foramen in *M. javanica* differs from *M. crassicaudata*; it displays an elliptical shape with an extremely elongated antero-posterior axis. The dorsal and ventral margins of the foramen fade posteriorly and its internal surface becomes continuous with the medial surface of the ascending ramus.

Similar to its sister taxon, *M. javanica* displays a mandibular canal that presents a rather homogeneous shape and position along its path. Posteriorly, it slightly descends accompanying the inclination of the mandibular foramen and follows the general shape of the dorsal margin of the horizontal ramus until it reaches the mental foramina. The transversal section of the mandibular canal becomes slightly dorso-ventrally compressed at mid-length, but immediately assumes its former shape anteriorly. As described for *M. crassicaudata*, several parallel canals are present along the entire length of the mandible. The density of these small canals is particularly high in the anterior portion of the mandible as well as in the posterior part, at the level of the mandibular foramen.

Their morphology is in all aspects similar to the structures observed in *M. crassicaudata*, including the presence of a couple of vertical canaliculi that project dorsally and open through two small foramina in the pseudo-tooth, as well as the presence of a couple of canaliculi that reach the mandible surface in all directions. The mandible presents five mental branches: the three more posterior ones (Figure S1*E*, mb3-5) are short and small, and open laterally in small elliptical foramina posterior to the pseudo-tooth; the largest mental branch (Figure S1*E*, mb2) drifts antero-laterally to form a short branch at the level of the prong, opening in a large diamond shaped foramen; the most anterior mental branch (Figure S1*E*, mb1) represents the last remaining part of the main mandibular canal that projects anteriorly and opens just ahead of mb2 in an low and antero-posteriorly elongated foramen anterior to the pseudo-tooth.

Nine-banded armadillo (*Dasypus novemcinctus*)

Dasypus novemcinctus displays a thin, low and elongated horizontal ramus and a slightly broader ascending ramus characterized by its high and slender coronoid process. Anteriorly, the mandible is extremely low and transversely compressed, and displays a short symphysis. It is higher posteriorly and becomes transversely wider at the level of the tooth row. The dental formula is c 1, p 7, m 1. The anterior quarter of the mandible is completely toothless but an alveolus for a canine [S4,S5] is visible at the level of the first mandibular foramen (Figure S1*F*, mb1), and is separated from the rest of the tooth row by a small diastema. The molar is not erupted. This specimen displays two mental foramina: the most posterior one (mb2) is located between the second and the third premolars while the anterior one (mb1) opens anteriorly to p 1.

Below the anterior edge of the coronoid process, a slightly elongated mandibular foramen opens on the medial surface of the ascending ramus, at roughly the same height of the alveoli. It projects ventrally with an inclination of around 14° until the

posterior end of the tooth row. The canal describes a shallow dorsal facing concavity contouring the alveoli ventrally and accompanying the curvature of the ventral edge of the horizontal ramus. Immediately anteriorly to the third premolar, a slightly antero-dorsally inclined posterior mental foramen is present on the medial side of the mandible. Anteriorly to the first molar, the main branch of the mandibular canal opens laterally in an antero-posteriorly elongated mental foramen. This foramen is particularly large and elongated. Anteriorly to the first molar, a dorsal canaliculus with a rather large diameter is also oriented antero-dorsally in the direction of the alveolus for the canine. The canaliculus opens in the alveolus and continues anteriorly – with less than half the diameter – to split into two ramifications. The most posterior ramification bifurcates just dorsally to mental foramen 1 and opens into two small foramina (Figure S1*F*, dc 1c,d) on the dorsal margin of the mandible. The anterior ramification (dc 1a,b) describes a long trajectory antero-ventrally to dc 1c,d, and bifurcates near the anterior tip of the mandible. All bifurcation of the dorsal canaliculus (dc 1a,b,c,d) open into tiny foramina on the dorsal side of the mandible.

In a juvenile specimen (USNM 020920), the canal does not open directly into the first five premolars and the canine. Therefore, the juvenile mandible displays longer dorsal canaliculi for the premolar dentition than the adults. A large dorsal canaliculus is associated to the first molar, which is absent. Anterior to the canine, a dorsal canaliculus projects anterodorsally, splitting in a plexus of three smaller canaliculi that open dorsally in three individual foramina. The dorsal canaliculi pattern is similar to the one observed in adults.

Hairy long-nosed armadillo (*Dasypus pilosus*)

The anterior part of the slender mandible is sharp and its height slightly increases at mid-length of the horizontal ramus. A row of rather spaced peg-like teeth occupies the

second third of the mandible. *D. pilosus* presents a c 1, p 7, m 1 lower dental formula. The c1 and m1 present a basic peg-like shape. The anterior four mental foramina are positioned between the p 3 and the margin of the most anterior and largest mental foramen (Figure S1*G*, mb1), at the level of the fused symphysis. The most posterior and smallest of the five mental foramina is located posterior to the m 1 alveolus.

The symphysis is elongated, reaching the level of the anterior margin of mb1. The mandibular canal is ventrally positioned at the level of the alveolar portion of the mandible. The canal opens posteriorly in a high mandibular foramen and extends ventrally towards the centre of the tooth row at the level of the fourth premolar. From this point it projects slightly dorsally, accompanying the shape of the mandible, until the level of mental foramen 3. Anterior to mb3, the mandibular canal presents a straight trajectory. Immediately dorsal to the mandibular canal, the horizontal ramus displays a small canal that originates in the p 6 alveolus and passes through all alveoli until p 2. From this point it projects antero-dorsally, as a dorsal canaliculus, to reach the p 1 alveolus. From this alveolus it projects further antero-dorsally to the c 1 alveolus and extends in the same direction until the level of third mental foramen. This dorsal canaliculus presents a bifurcation anterior to c 1 (Figure S1*G*). A second dorsal canaliculus arises at the level of mental foramen 3, bifurcating and ending just anteriorly. Neither of these canaliculi reaches the dorsal margin of the mandible. No foramina open in the anterior part of the mandible, close to the symphysis.

Giant armadillo (*Priodontes maximus*)

The mandible is long and displays a long tooth row extending for about half its total length. Similarly to *D. novemcinctus* and *D. pilosus,* the mandible is narrow, transversely compressed, although it is slightly more robust. As in anteaters, this mandible presents a medio-lateral rotation anteriorly. The left tooth row is composed of 22 hypselodont teeth,

23 on its right counterpart. In lateral view, three mental foramina (Figure S1*H*, mb 1-3) can be observed just anterior the tooth row. A fourth small one is present in the same area, but appears to be an extra branching of mental foramen (mb1) with no symmetrical branch on the right hemi-mandible.

The transversely compressed mandibular canal of *P. maximus* exhibits some differences compared to the other genus of armadillo here studied. The mandibular foramen is dorsoventrally elongated as in *Dasypus* but its position is more dorsal in the ramus when compared to the alveolar plane. The canal extends ventrally with a weak inclination (~12.2°). Posterior to mf 22, a large dorsal canaliculus (Figure S1*H*, dc3), slightly inclined posteriorly, projects dorsally and opens into several small foramina. Anteriorly, although alveoli for mf 1 and mf 2 are almost adjacent to the canal, small dorsal canaliculi are visible. As the canal projects ventrally towards alveolus for mf16, the dorsal canaliculi become longer. Their morphology varies, being anteriorly oriented and sometimes bifurcated. These canaliculi vary in diameter and can bifurcate (e.g., below alveolus for mf 17 and mf 18, Figure S1*H*), with a branch projecting dorsally and the other anteriorly, to merge with the immediately anterior dorsal canaliculus. Anteriorly to alveolus of mf 16 the mandibular canal displays a parallel trajectory to the alveoli row until alveolus for mf 9. From this point, it projects dorsally until mental foramen 1, being positioned immediately ventral to the nine most anterior alveoli. Along its path to the symphyseal portion of the mandible, the mandibular canal displays several minor mental branches before it splits into three larger mental canals (Figure S1*H*, mb 1-3) anterior to the first alveolus. The most posterior and smaller mental branch splits from the main canal right anteriorly to alveolus for mf 1, projecting anterodorsally and then drifting laterally. A second larger mental branch (mb2) splits anteriorly, departing from the dorsolateral part of the mandibular canal and opening in an antero-posteriorly elongated foramen. The most anterior and largest mental branch (mb1) also opens into an antero-

posteriorly elongated foramen. A more anterior small branch is visible on the lateral side of the mandible, but corresponds to a small ramification of the largest mental branch (mb1). Another canaliculus of the mandibular canal, which splits from the posterior part of the mb1, continues anteriorly toward the antero-dorsal end of the mandible. This small canaliculus (dc1) divides into three smaller ramifications, which open on the medial side of the anterior tip of the mandible.

Aardwolf (*Proteles cristatus*)

Proteles cristatus displays a mandible with a relatively high horizontal ramus displaying an anteriorly projected anterior margin. The specimen displays the following dental formula: i 3, c 1, p 2, m 2. This mandible displays three mental foramina (Figure S1*I*, mb1-3), with the first and second mental foramina displaying oval apertures of similar size. The first mental foramen is located on the anterior margin of the mandible and the second one is anterior to the canine, below the anterior end of the diastema. The third mental foramen is located below the diastema, half way through the height of the mandible.

The mandibular foramen is oval shaped, located in the middle of the ascending ramus, antero-ventral to the dorsal tip of the coronoid process. The mandibular canal has an oval section, being noticeably dorso-ventrally elongated from the anterior end of the coronoid process to the level of the m 1. The mandibular canal projects slightly ventrally until the posterior limit of the diastema. None of the four check teeth alveoli is adjacent to the mandibular canal. The first and second molars are dorsally placed relative to the canal; no dorsal canaliculus reaches their alveoli. The inferior alveolar nerve and artery branches reach the teeth through the many hollow cavities of the alveolar portion of the mandible. The trabecular nature of the molar area is particularly evident anteriorly (Figure S1*I*), dorsally and posteriorly to the premolar alveoli, almost

reaching the dorsal edge of the mandible. Posteriorly, fused trabeculae form a sort of posteriorly projecting canals, which reach the dorsally placed m 1 and m 2 alveoli. Anterior to the c, below the diastema, three mental branches (Figure S1*I*, mb1-3) split and project antero-dorsally. Mb3 projects dorsally and opens laterally right ventrally to the midpoint of the diastema. Mb2 projects antero-dorsally and is laterally inclined, opening latero-ventrally to the canine. Mb1 is long and projects antero-dorsally, passing through the middle of i 2 and i 3 and opens in the anterior margin of the mandible.

Dog (*Canis lupus*)

Canis lupus presents a mandible with a high ascending ramus, with a relatively broad coronoid process. The mandible presents 11 tooth loci (i 3, c 1, p 3, m 3) and contrasts with *P. cristata* in its complete tooth row (no diastema), its shorter symphysis and rather vertical anterior margin. Four mental foramina are present (Figure S1*J*, mb1-4). The first mental foramen opens anteriorly, ventral to i 2. The second and largest mental foramen opens laterally between p 1 and c 1. The third mental foramen opens at the level of the anterior root of p 3 and the fourth mental consists of a rather small lateral aperture located between the ventral tips of the anterior and posterior roots of p 4 and p 3, respectively.

The mandibular foramen resembles *P. cristata*, yet the canal projects slightly more ventrally. Just posteriorly to the anterior edge of the coronoid process, the mandibular canal becomes more extended anterodorsally (Figure S1*J*), displaying a pseudo elliptical cross section. This is a main characteristic of the mandibular canal of the dog. With the exception of m 3, teeth are rooted deeply enough to be in close contact with the dorsal edge of the mandibular canal. The trajectory of the mandibular canal follows the shape of the ventral margin of the mandible from the level of the posterior root of m 1 until p 2, where it branches (Figure S1*J*). The large m 1 is so deeply

rooted that both its roots protrude ventrally into the mandibular canal. Along its trajectory, the mandibular canal is topped by a complex of trabeculae that surrounds the tooth roots. From about the second m 1 cusp, the mandibular canal gradually decreases in height anteriorly. All but the small fourth mental branch project anterolaterally. Mb4 is a very thin branch that projects posterolaterally below the posterior edge of p 3. Mb3 is comparatively larger and splits from the mandibular canal just ventrally the anterior root of p 3. Mb2 is large in diameter and projects anterolaterally ventrally to p 2 to open in an oval-shaped foramen between p1 and c (Figure S1*J*). Mb1 is a rather thin and extremely long ramification of the mandibular canal that projects anteriorly to pass dorsally to the c and i 1-3 roots and open in the anterior margin of the horizontal ramus. In its trajectory, mb1 opens to the alveolus of i 3. Dorsally to the branching point of mb1, a relatively large accessory branch of the mandibular canal projects anterodorsally. This branch is medially oriented and almost reaches the symphysis, posterior to which it divides into several trabeculae.

Pale-throated three-fingered sloth (*Bradypus tridactylus*)

In the adult *Bradypus tridactylus*, the mandible is characterized by a short but robust horizontal ramus, bearing one caniform (Cf) and three molariform teeth (mf 1-3), and a high ascending ramus. The tooth row almost occupies the entire length of the body of the mandible, with teeth inclination becoming more medial along the antero-posterior axis. All four teeth are tall, lack roots and are deeply rooted in the mandible. The mandible presents two mental foramina with one at the anterior tip of the mandible (Figure S1*K*, mb 1) and a larger one at the level of the mf 4 (Figure S1*K*, mb2).

The morphology of the mandibular canal is very distinct from that observed in anteaters and armadillos. The mandibular foramen is elliptical in shape, with the major axis oriented anteroposteriorly with a similar inclination to the condylar process. The

canal projects antero-ventrally from the mandibular foramen until it reaches its lowest position in the mandible, at the level of the mf 3 At the same level, but higher in the body of the mandible, the largest and most posterior mental branch opens on the lateral side of the mandible, after branching midway between the mandibular foramen and the lowest mandibular canal position. The mandibular canal then runs anteriorly and gradually projects dorsally in the mandible until it reaches mental foramen 1. There is one small dorsal canaliculus (dc 1-3) for each of mf 1, mf 2 and mf 3. Dc4 is originates ventrally to mf3 but extends anterodorsally to reach the alveolus on its anterior margin. The mandibular canal runs medial to the first tooth and divides into dorsal and mental branches. The mental branches follow the same direction and inclination as the main branch and eventually reach the anterior tip of the mandible, lateral to the symphysis. The dorsal canaliculus assumes a steep trajectory (roughly parallel to the anterior margin of the mandible) and exits the mandible dorsally. This dorsal canaliculus likely corresponds to a remnant of the innervation/vascularization of an additional tooth locus identified in a previous work [S6] and opens anteriorly to alveolus for Cf. The juvenile specimen (ZMB 18834) displays a vestigial tooth in the same position; its mandibular canal of the foetus presents a similar general morphology, differing in number of mental and medial branches. The foetal mandible presents four foramina for accessory branches that open in the medial side of the mandible and four mental foramina. This mandible is much less ossified, compared to the adult.

Two fingered sloth (*Choloepus hoffmanni*)

The mandible of *Choloepus hoffmanni* presents shallower horizontal and ascending rami compared to *B. tridactylus*. The anterior tip of the horizontal ramus is shovel-shaped and elongated. The mandible bears three molariform teeth (mf 1-3) and one anterior caniniform tooth (cf). In total, the *C. hoffmanni* mandible presents four mental foramina,

a large one at the level of the root of the coronoid process and three small ones anterior to the caniniform tooth.

Due to the differences in mandible shape, the morphology of the mandibular canal is also different between the two sloth genera. Here again, the dorsal canaliculi of the mandibular canal are present when the tooth alveoli are more dorsal. The canal starts at the level of the dorsal edge of the horizontal ramus and runs anteriorly until it reaches the level of the posterior margin of the tooth row. At this level, the mandibular canal bifurcates, with a mental branch (Figure S1*L*, mb4) projecting antero-laterally to open in a large mental foramen, just anteroventrally to the root of the coronoid process. The main branch projects medially from the mandibular foramen, passing marginally ventrolaterally to mf 3. A small dorsal canaliculus of the mandibular canal (Figure S1*L*, dc 10) projects medially and allows for the innervation and vascularization of mf 3, which is medially oriented. As the mandibular canal runs anteriorly, its position gradually changes to a more medial one. This contrasts with the morphology of the mandible of the adult *B. tridactylus*, in which the mandibular canal is medially positioned along the entire length of the tooth row. Two dorsal canaliculi of the mandibular canal (df8-9) are ventral to the anterior half of mf2. Three dorsal canaliculi (dc5-7) reach the alveolus for mf 1. Dc5 is a small canal that splits at mid-lenght of the alveolus and joins the main canal just anteriorly to it (Figure S1*L*). From this canal, three small dorsal projections reach the alveolus. Two smaller additional innervation/vascularization canaliculi are present posteriorly (Figure S1*L*, dc 6-7). Close to the symphysis, the mandibular canal steadily projects dorsally. The main branch passes medially to the cf and, as in *B. tridactylus*, its position is dorsal to the base of the alveolus. In fact, dorsal canaliculi reach the alveolus of the cf. The more posterior canaliculus (Figure S1*L*, dc4) bifurcates from the mandibular canal antero-ventrally just anterior to the alveolus for the cf. Anteriorly, a small canaliculus (dc3) splits from the mandibular canal and projects

laterally into the same alveolus. The third canaliculus that connects to the alveolus of the cf (dc1) is located just anterior to the mandibular canal steep antero-dorsal projection in the direction of the anterior tip of the mandible. A long dorsal canaliculus (Figure S3*B*, dc2) splits from the mandibular canal in the direction of the rudimentary alveolus of the vestigial tooth that is observed on earlier ontogenetic stages. The vestigial alveolus, located just antero-medially to the anterior edge of cf, is also innervated/vascularized, with the dorsal canaliculus further splitting in two ventrally to its dorsal opening. Three small mental branches (Figure S1*L*, mb1-3) are present in the anterior part of the mandible: the most posterior (mb3) departs from the mandibular canal to open laterally at the level of mb2; mb2 projects dorsolaterally near the dorsal margin of the mandible; mb1 splits at about the same length as mb2, but projects anterolaterally. Anteriorly to the level of the foramen for mb1, a small branch (Figure S1*L*, ab) reaches the mandible shovel-shape projection and further divides into two small canals that open dorso-medially. These canals are not present in *B. tridactylus*.

The mandible of the foetus of *Ch. didactylus* (ZMB 4949) presents a lower level of ossification and allometric shape differences. Nevertheless, the mandibular canal of the foetus presents the same branch pattern as observed in the adult.

Aardvark (*Orycteropus afer*)

This mandible consists of a transversely compressed long and shallow horizontal ramus and a comparatively very high ascending ramus. The anterior half of the horizontal ramus is edentulous, while its posterior half presents three molars and two premolars (i 0, c 0, p 2, m 3; Figure S1*M*). The molars are large and deeply rooted and display an oblanceolate shape in dorsal view; the premolars are much smaller, transversely compressed, and are rooted more dorsally. The mandible of *Orycteropus afer* displays four major mental foramina (Figure S1*M*, mb1-4), with six small mental branches

laterally positioned compared to the tooth row (Figure S1*M*, mb5-10). A total of seven foramina for dorsal canaliculi are present. The anteriormost four foramina are aligned just anteriorly to p 5 (*sensu* [S7]; dc3). Another small foramen is present anteriorly, at the level of the third mental foramen (dc2). Two slightly larger and longer foramina open between mental foramina 1 and 2 (dc2). The most anterior foramen (dc 1) opens anteriorly in the middle of the anterior apical portion of the mandible. The dc1 foramen resembles the reticular alveolar foramen of whales [S8,S9].

The mandibular foramen is narrow and located well above the tooth row level, from where the canal projects ventrally. Between m 3 and m 1, the trajectory of the mandibular canal changes as it gradually projects dorsally, accompanying the height decrease of the horizontal ramus. The mandibular canal is adjacent to alveoli of m 1-3 and dorsal canaliculi are absent. From m 3 to p 5, only mental branches bifurcate from the mandibular canal (mb 5-10). The p5 and p6 alveoli are placed more dorsally in the mandible and are connected to the mandibular canal by two dorsal canaliculi, which project antero-dorsally. The two canaliculi dorsal to p 5 and p 6 (dc3 and dc4) are connected by a small canal parallel to the mandibular canal. Anterior to p 5, the main dorsal canaliculus (dc3) steadily extends dorsally, and then divides into four small canals linked to foramina dorsally. At the level of mb4, dc3 projects ventrally to merge with the mandibular canal, and a new dorsal canaliculus (dc2, Figure S1*M*) projects antero-dorsally. Dc 2 is long and presents a small diameter. It bifurcates three times: just anteriorly to its origin, a small ramification projects antero-dorsally to open at the level of mb4; the dorsal canaliculus continues anteriorly and bifurcates again between mb1 and mb2, with one branch projecting antero-dorsally but never opening dorsally; a thin branch of dc2 continues until it splits in several smaller canals near the third mental foramen, with one of them opening dorsally at the level of the second mental foramen. Mb2 and dc1 split near the anterior end of the mandibular canal. Dc1 bifurcates – with

one branch projecting antero-dorsally and the other anteriorly – before it opens in two foramina. The most posterior branch of dc1 opens at the level of the second mental foramen. The most anterior canaliculus reaches the anterior tip of the mandible, ending in a foramen similar in position to the reticular alveolar foramen found in rorquals [S8,S9].

Giant otter-shrew (*Potamogale velox*)

The mandible of *Potamogale velox* presents a relatively low horizontal ramus with a rather long and anteriorly inclined symphysis. The ascending ramus of is high due to the presence of a broad sub-triangular coronoid process. The tooth row is composed of ten teeth (i 3, c 1, p 3, m 3). Three mental foramina are present in the mandible (Figure S1*N*, mb1-3). The first mental foramen is small and opens on the anterior margin of the mandible. The second and third mental foramina are relatively larger and open laterally at the level of p1 and the posterior root of m1, respectively.

The mandibular foramen has a pseudo circular shape. Posteriorly, the mandibular canal presents a slightly descending trajectory until it reaches the m 2. The trajectory is then practically horizontal until the canine. Small complexes of trabeculae are present dorsally to the mandibular canal. The trabeculae surround the tooth roots, which are deeply implanted in the mandible. With the exception of the c and i 1-3, all alveoli enter in contact of the mandibular canal. The most posterior mental branch (Figure S1*N*, mb3) is the largest in diameter and projects laterally at the level of the tip of m 1 posterior root and opens slight dorsally in an elliptical shaped foramen. At the level of p 2, the trajectory of the canal drifts slightly dorsally, accompanying the small ventral concavity of the ventral edge of the horizontal ramus. Two branches split from the mandibular canal, dorsal to p 1, and project laterally. These branches merge into one larger mental branch, opening laterally in a single foramen (Figure S1*N*, mb2). Mb1

consists of a rather long branch, small in diameter, which projects anteriorly (Fig S1*N*, mb1). This branch passes ventrally to c alveolus and gradually projects dorsally to open anteriorly, between i 2 and i 1. Two accessory branches of the mandibular canal split at the level of p 1 and c. The posterior one projects anterodorsally until it divides into a trabeculae complex at the level of i 3 and i 2 alveoli. The anterior one also projects anterodorsally but it meets the trabeculae briefly anteriorly to its branching point. This trabeculae complex is located medially in the mandible and is associated with the i 2 alveolus and the symphysis.

Anatomical description of additional taxa

A total of 12 species were segmented in order to reconstruct the phylogenetic history of the absence/presence of dorsal canaliculi (Figure 1). One Afrosoricida (*Tenrec eucaudatus*) and one Macroscelidea (*Rhynchocyon petersi*) were additionally segmented to increase the number of species with relatively close phylogenetic affinities to *Orycteropus afer* (Figure 1). Neither of the 12 species described in this section presents dorsal canaliculi. With the exception of the brown rat (*Rattus norvegicus*) and the velvet free-tailed bat (*Molossus molossus*), all the species present mandibular canals very similar in shape (Figure S2*A*-*I*). The mandibular foramen displays a descending trajectory anteriorly until the third molar (m 3). It projects anteriorly, ventrally to the tooth row, with its dorsal margin that usually opens directly to adjacent post-canine tooth alveoli (Figure S2). In some species (e.g., *Dasyurus hallucatus*, *Lemur catta*, *Cynocephalus volans*, or *Procavia capensis*; Figure S4*A*-D) a large amount of trabecular tissue is visible around the teeth, and connects the mandibular canal to the alveoli, only when both structures are not adjacent to each other. The Malayan tapir (*Tapirus indicus*, Figure S2*E*) constitutes the most remarkable case of innervation/vascularization via trabeculae, with a mandible characterized by non-adjacent tooth alveoli and mandibular

canal. In almost all species, an incisor branch projects anteriorly at the level of the most anterior mental branch, and usually splits into several trabeculae that wrap both canine and incisor teeth. In the rock hyrax (*Procavia capensis*), however, the incisor branch opens directly into the corresponding alveolus. The tailless tenrec (*Tenrec ecaudatus*, Figure S2*F*) also presents a slightly different morphology of the incisor branch, with the mandibular canal opening directly into the alveolus of the canine, with the latter being connected to the following alveolus. In the brown rat (*Rattus norvegicus*, Figure S2*K*) the incisor branch is absent, with the alveolus of the incisor tooth extending back into the ascending ramus of the mandible. The innervation/vascularization of the incisor tooth arrives ventral to the coronoid process, as the mandibular canal partially merges with the alveolus. Although the Malayan tapir exhibits a classical incisor branching of the mandibular canal, the latter differs in from other species by its extremely reduced diameter (Figure S2*E*). The overall shape of the mandibular canal of the brown rat is peculiar due to the extreme posterodorsal projection of the incisor alveolus (Figure S2*K*). The mandibular canal merges with the incisor alveolus medially, just anteriorly to the mandibular foramen. It projects anteriorly at the level of the m 3 and its trajectory follows the shape of the dorsal margin of the incisor alveolus. The mandibular canal opens directly to the m 3 and m 2. In the most anterior portion of the alveolar part of the mandible, which corresponds to the alveolus of the m 1, the mandibular canal presents a relatively ventral position relative to the first molar alveolus, the tooth being likely innervated/vascularized via trabecular bone. The mandibular canal opens dorsolaterally in a single mental foramen, just anteriorly to the m 1. The velvet free-tailed bat also presents a distinct mandibular canal morphology (Figure S2*L*). Compared to other species, the mandibular canal is unusually high. Here again, all pre-canine tooth alveoli are adjacent to the mandibular canal. However, the mandibular canal seems to extend dorsally, in between tooth roots (Figure S2). This might be a result of the scan resolution

compared to the reduced size of the specimen, for in other segmented placental mammals, those spaces are normally filled with trabeculae (Figure S2). Apart from this abnormal height, the mandibular canal of the velvet free-tailed bat resembles those of other toothed species; it is positioned ventrally to the tooth row and bifurcates anteriorly, with a mental branch that projects laterally while the other branch of the canal opens into a trabecular system wrapping the canine and the incisors. An anterodorsally projecting mental branch is also present and opens ventrally to the incisors, similar to the condition observed in carnivores (Figure S1*I*, *J*).

2. Homology of dorsal canaliculi between anteaters and baleen whales

The trigeminal nerve originates in the pons and has two different roots, a sensory and a motor root [S10]. The mandibular branch of the trigeminal is composed of both sensory and motor roots and is designated by inferior alveolar nerve (IAN) [S10]. The nerve enters the medial side of the mandible through the mandibular foramen, and is accompanied by the inferior alveolar artery [S11]. Typically, the inferior alveolar nerve separates into four types of branches [S10,S11]: the mylohyoid branch supplies the hyoid musculature; the dental/inferior dental branches supply molars and premolars, each nerve branch innervating one tooth; the incisor branch supplies canine and incisors. The mental branch supplies the lip integument (the number of mental branches may vary between taxa). Here, we will group dental and incisor branches to follow the nomenclature of previous references for edentulous placentals [S9].

In *Tamandua tetradactyla*, the large inferior alveolar nerve (Figure 4*B'*, IAN) is placed dorsally in the mandibular canal. Two accessory branches of the IAN (Figure 4*B'*, IANa) are present dorsolaterally to the IAN. The inferior alveolar artery (Figure 4*B'*, IAA) lies dorsally to the IAN. An irregularly shaped branch of the inferior alveolar vein (Figure

4*B'*, IAV) is placed laterally to the IAA. A third branch of the IAN (Figure 4*B'* and S3*B*, IANa) is visible dorsally to the IAA. Dorsally to it, the ascending branch of the IAV (Figure 3*B'* and S3*B*, IAVab) is present in the dorsal canaliculus of the mandibular canal. A keratinous dental pad covers the dorsal part of the mandible (Figure 4*C*, pa). Ventrally, the epidermis consists of a small layer (Figure 4*C*, ep) and, which lies dorsally to the thick dermis layer (Figure 4*C*, de). In addition to connective tissue, the dermis presents several blood vessels and small nerve branches. The most posterior dorsal canaliculus allows for the passage of an ascending branch of the IAN (Figure 4*C*,*C'*, IANab1); the anterior dorsal canaliculus displays a large ascending branch of the IAA (Figure 4C, IAAab) and likely features a second ascending branch of the IAN (Figure 4*C*, IANab2) that projects anterodorsally.

A histological section (coronal plane) of the mandible of a bowhead whale (*Balaena mysticetus*) showing the 15th vestigial tooth [S1] shows the mandibular canal and associated soft tissues (inferior alveolar nerve, blood vessels) with two small canals (Figure S3*A*, red squares) dorsally. The most dorsal small canal is most likely associated to the vestigial teeth observed in the figure, while the most ventral one is associated to the 14th vestigial tooth. Its position between the mandibular canal and the tooth row, plus the presence of branches of the inferior alveolar artery and the inferior alveolar nerve inside these small canals, highly suggest that these are homologous to the dorsal canaliculi observed in the collared anteater (*T. tetradactyla*). Dorsal canaliculi are anteriorly inclined in whales [S9], thus histological slices produce circular section for each canaliculus.

3. Intraspecific and bilateral variation of dorsal canaliculi

Dorsal canaliculi were present in all segmented anteater (n=8) and long-nosed armadillo (n=6) mandibles (Figure S4). All six long-nosed armadillos displayed an anterior dorsal canaliculi plexus splitting in three to six dorsal foramina (Figure S4*A*-*F*), including the juvenile (Figure S4*F*). A canine, as well as its corresponding dorsal canaliculus, was present in two specimens (Figure S4*A*, *F*). The mandibular canal morphology was similar in the six specimens. The two pygmy anteater (*C. didactylus*, n=2) mandibles presented bilateral variation and showed between 15 and 17 dorsal canaliculi (MNHN 1986-1115, 15L/17R; BMNH 24.12.4.68, 17L/15R; Figure S4*G*, *H*). Bilateral variation was observed in two collared anteaters (*T. tetradactyla*, n=3) and two giant anteaters (*M. tridactyla*, n=3). The collared anteaters (*T. tetradactyla*) showed between 14 (MVZ 153482, 14L/14R) to 17 (ISEM – 788N, 17L/16R) dorsal canaliculi (Figure S4*I*-*K*). The two adult giant anteaters presented 14 (ISEM – 065 V) and 13/14 (MVZ – 185238) dorsal canaliculi, while the juvenile presented slightly more canaliculi with a slightly larger bilateral variation (16L/18R; Figure S4*L*-*N*). Nevertheless, the observed pattern of dorsal canaliculi morphology and distribution along the mandible is similar.

4. Insights into the ancestral number of teeth in anteaters

All known anteater fossil skulls are toothless [S12,S13]. However, our data confirmed that the earliest representatives of the group were toothed, assuming the homology between dorsal canaliculi and alveolar vestiges. There are, however, several limitations in using the number of dorsal canaliculi to estimate tooth number: 1) it is not clear weather bifurcating dorsal canaliculi would correspond to one or more alveoli– although bifurcating dorsal canaliculi mostly appear to correspond to only one tooth in *P. maximus*

– which can lead to an overestimation of the number teeth with the present method; 2) a high mandibular canal merges the lower part of the dorsal canaliculi from the posterior part of the mandibular canal of the juvenile *M. tridactyla* makes it difficult to discriminate dorsal canaliculi; 3) intraspecific variation may partly explained the observed number of dorsal canaliculi, especially when comparing the bilateral variation to the interspecific variation observed in other clades within Xenarthra (Cingulata). If we were to reconstruct the dental formula based on the number of dorsal canaliculi regardless of the abovementioned arguments, we would propose that each mandibular quadrant of earliest Vermilinguans comprised between thirteen and seventeen teeth.

5. Ancestral state estimation of the tree internal nodes

Based on our dataset composed of extant species, we reconstructed the ancestral condition of placental mammals concerning the presence of dorsal canaliculi (figure available at https://i.imgur.com/j8ko4hi.png). We used the re-rooting method of Yang et al. [S14] to perform an ancestral state reconstruction under a continuous time Markov chain. The posterior probabilities for the presence of dorsal canaliculi are presented for each node (figure available at https://i.imgur.com/j8ko4hi.png). We used the same tree as presented in Figure 1, obtained from www.timetree.org [S15]. This tree includes 29 species and 28 internal nodes. Due to the absence of fossil taxa in the analysis, all nodes presented posterior probabilities close to zero or one. The probability of the presence of dorsal canaliculi was high in all nodes within Xenarthra. Excluding this clade, the highest probability for the evolution of dorsal canaliculi was found in the most recent common ancestor (MRCA) of cetaceans (node 12), with 4.86%. We found a 0.37% probability for the evolution of dorsal canaliculi in the MRCA of all placentals

(node 2). This suggests that the absence of dorsal canaliculi (0) likely corresponds to the ancestral condition of placentals. The ancestral state reconstruction was performed with the phytools package [S16] in R [S17].

6.2-Appendix 3

Supplemental information to Article 3

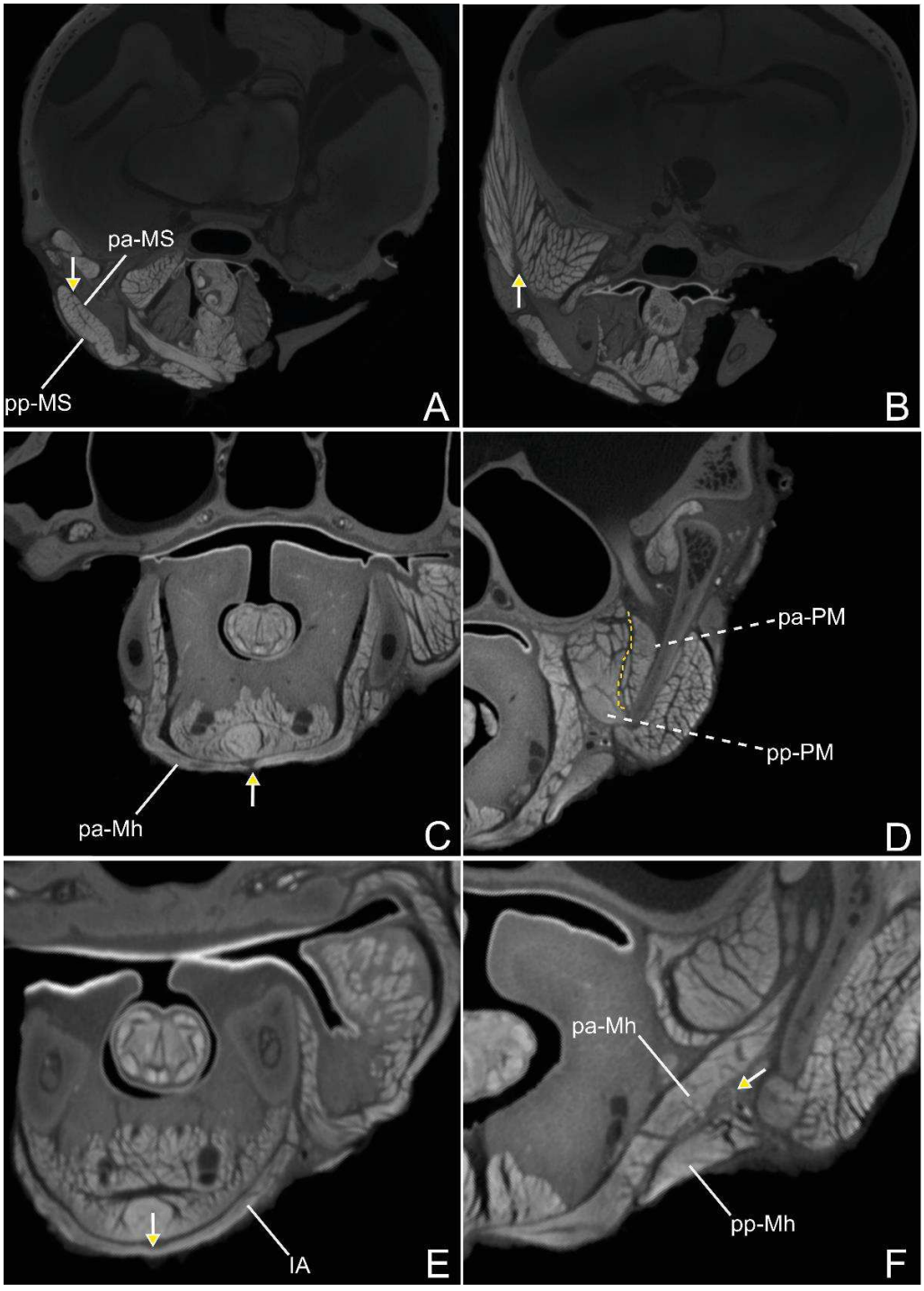

Figure S1 – Coronal sections of the µCT scans of *Cyclopes didactylus* (A, B) and *Tamandua tetradactyla* (C-F). A – the arrow shows the separation between the *pars anterior* (pa-MS) and the *pars posterior* (pp-MS) of the *masseter superficialis*; B – bipennate architecture of the *temporalis superficialis* and axis of pennation indicated by the arrow; C – the arrow points to the midline raphe of the *pars anterior* of the *mylohyoideus* (pa-Mh); D – the dashed yellow line shows the division between the *pars anterior* (pa-PM) and the *pars posterior* (pp-PM) of the *pterygoideus medius*; E – absence of a midline (arrow) raphe on the *intermandibularis anterior* (IA); F – passage of the sublingual artery splitting the *pars anterior* (pa-Mh) and the *pars posterior* (pp-Mh) of the *mylohyoideus*.

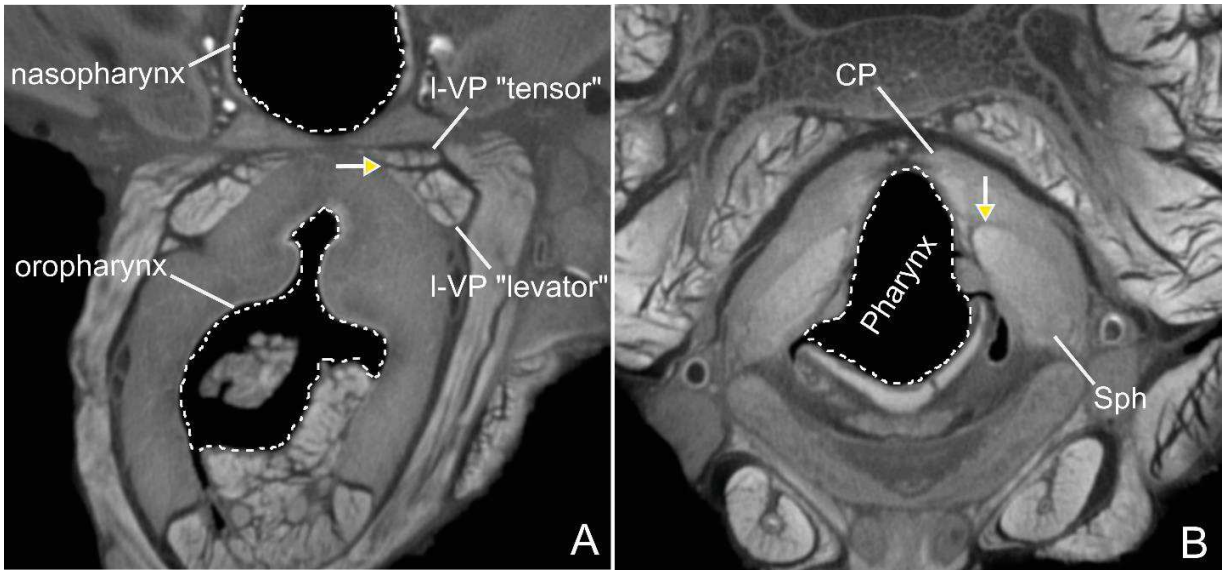

Figure S2 – Coronal sections of the µCT scans of *T. tetradactyla*. A – the arrow shows the separation between the anterior ("tensor") and the posterior ("levator") parts of the *levator veli palatini* (l-VP); B – the arrow indicates the separation between the *constrictores pharyngeus* muscle complex (CP) and the *stylopharyngeus* (Sph).

Table S1 – Weight, in grams, of the muscles of the six dissected specimens. Abbreviations for the muscle names are as in the main text. NA – not weighted.

Muscle	*C. did.*- 1571	*C. did.* - 1525	*T. tet.* - 3075	*T. tet.* - 3074	*T. tet.* - 2813	*M. tri.* - 3023
MS	0.0692	0.0616	0.8789	0.9654	0.9355	6.7043
TS	0.0977	0.098	0.4761	0.3158	0.4062	2.446
pz-TS	0.0071	0.0085	0.0799	0.1093	0.1237	0.7373
pl-TP	0.0156	0.0466	0.1398	NA	0.2594	0.9061
pm-TP	0.0273	0.0207	0.0794	0.0666	0.1104	0.1783
TP	0.0429	0.0673	0.2192	NA	0.3698	1.0844
ps-PE	0.0084	0.0125	0.0837	NA	0.0745	1.2792
pi-PE	0.0117	NA	0.0319	NA	0.0646	0.5529
PM	0.0389	NA	0.3079	NA	NA	1.4173
pe-B	0.0162	NA	0.4135	NA	NA	NA
pi-B	0.0473	0.0301	1.1378	NA	2.3477	9.5742
MA	0.0051	0.0127	0.0874	NA	NA	0.3478
IA	NA	NA	NA	NA	0.3211	NA
Sg	0.0807	NA	NA	NA	NA	NA
Mh	0.1005	0.163	NA	NA	NA	NA
Sm	0.082	0.0787	1.635	NA	NA	5.7758
SM	NA	NA	2.865	NA	NA	NA
DN	0.0051	NA	1.1869	NA	NA	1.9974

6.4-Appendix 4

Supplemental information to Article 4

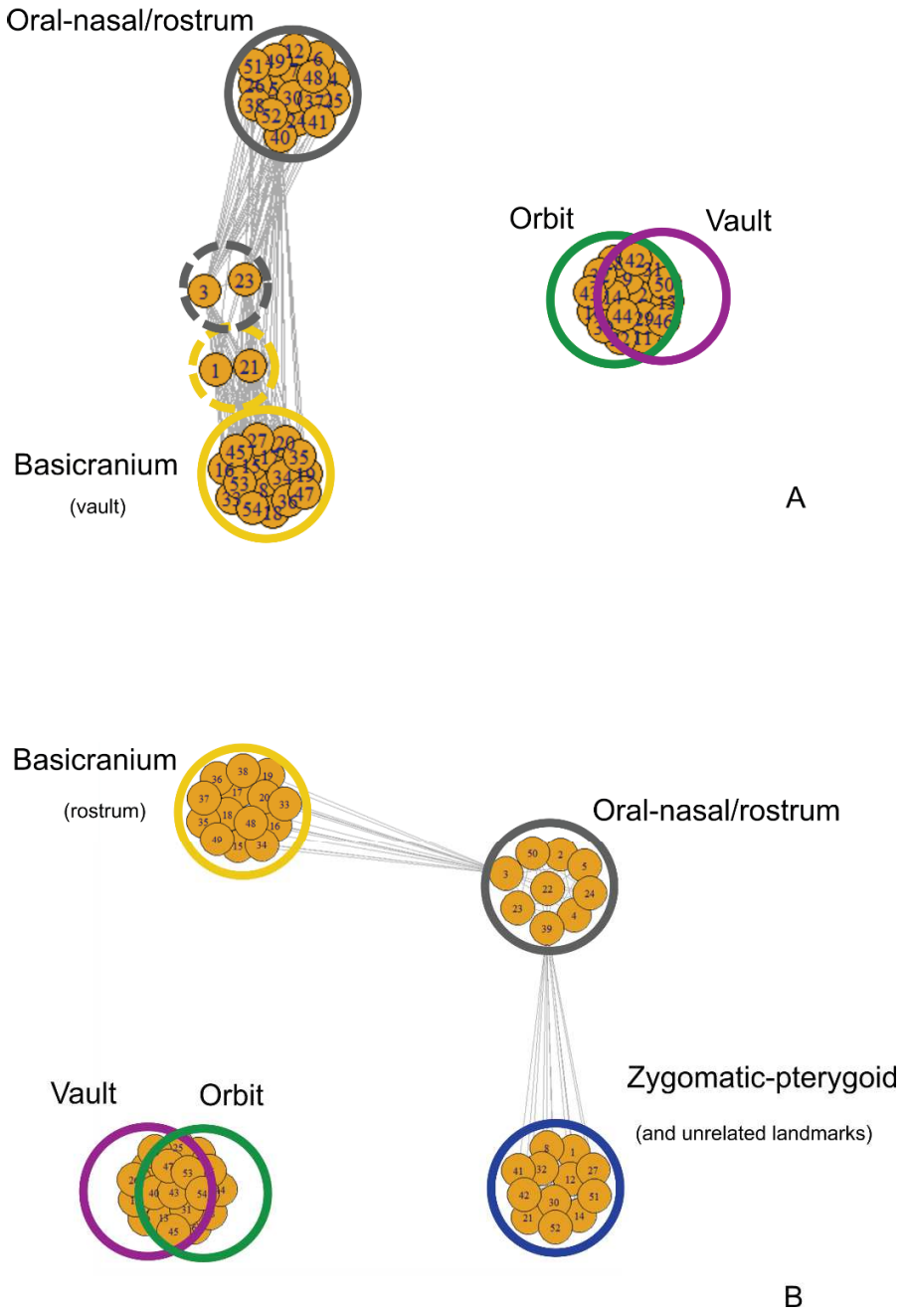

Figure S1 – Networks of skull landmarks of *Cyclopes didactylus* (A; n = 60) and *Orycteropus afer* (B; n = 40). Dashed circles represent separated landmarks that are strongly integrated with the module of the corresponding color.

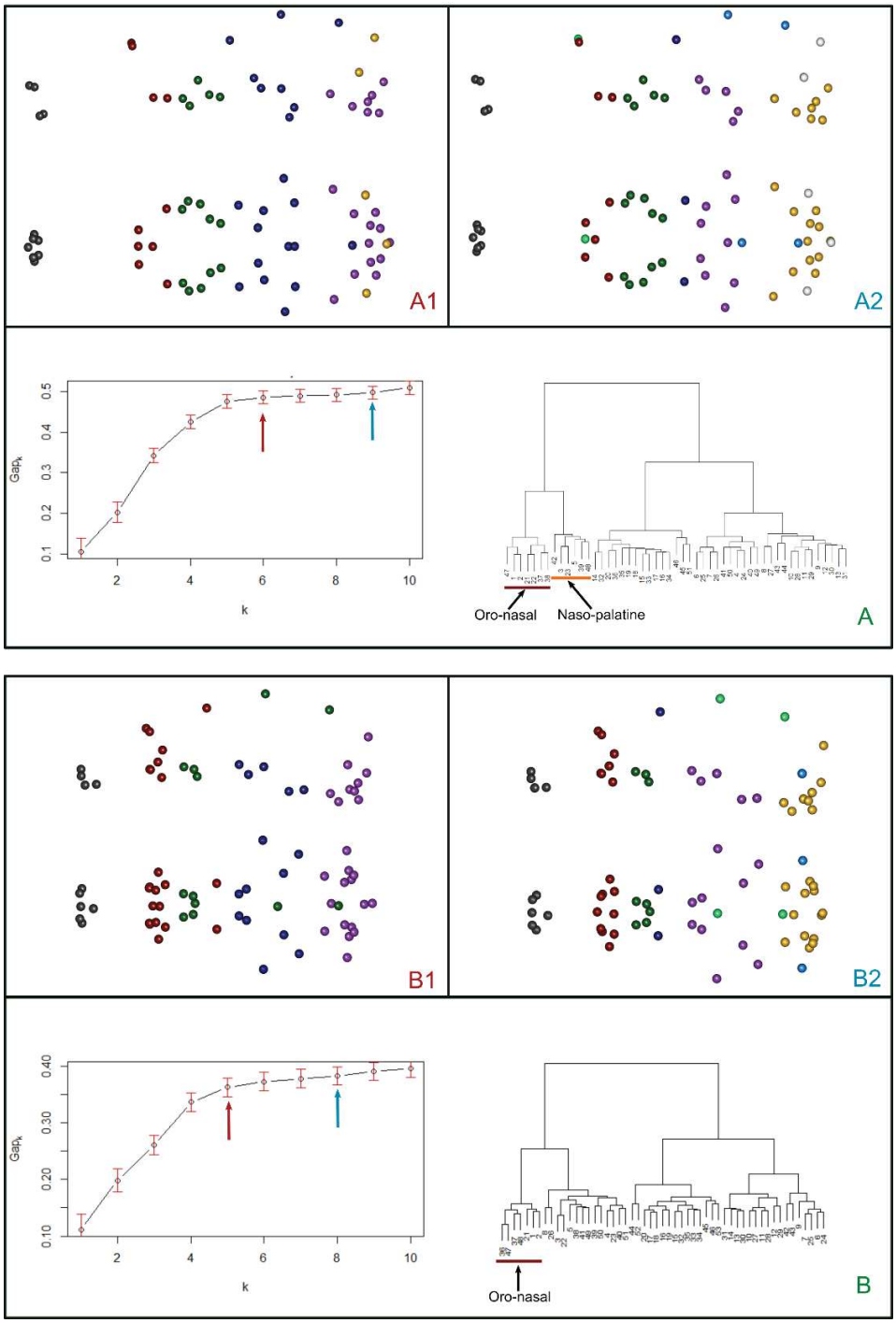

Figure S2 – Modular architectures recovered in the hierarchical clustering result*ing from EDMA performed on two* anteater species. A1 and B1 are lateral (up) and dorsal (down) views of the minimum partitions (see 'Materials and methods') obtained for *Tamandua tetradactyla* and *Cyclopes didactylus*. A2 and B2 are lateral (up) and dorsal (down) views of the partitions obtained from the Gap statistics for the same species as in A1 and B1. Graphs show: left – the variation of the Gap statistics value (y axis) with the number of clusters (x axis), the red arrow representing the minimum number of clusters tested for each species while the blue arrow indicates the original value of the Gap statistics; right – hierarchical clustering resulting from EDMA. Different colors represent different clusters; as the number of clusters is variable, colors are not consistent and do not necessarily represent the same region across species.

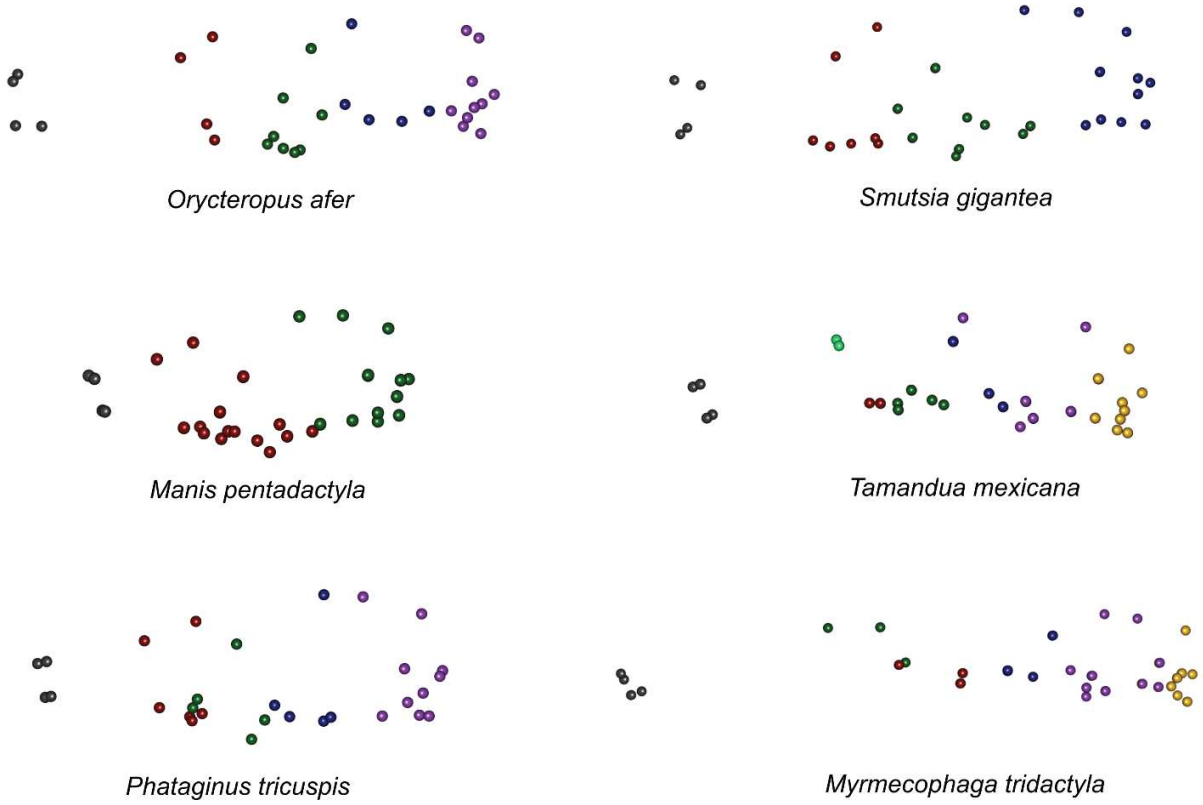

Figure S3 – Modular architectures recovered in the hierarchical clustering resulting from EDMA performed on six myrmecophagous species. Lateral views of modular patterns after removing nonsense clusters (see 'Exploratory analyses of modularity – EDMA'). Different colors represent different clusters; as the number of clusters is variable, colors are not consistent and do not necessarily represent the same region across species

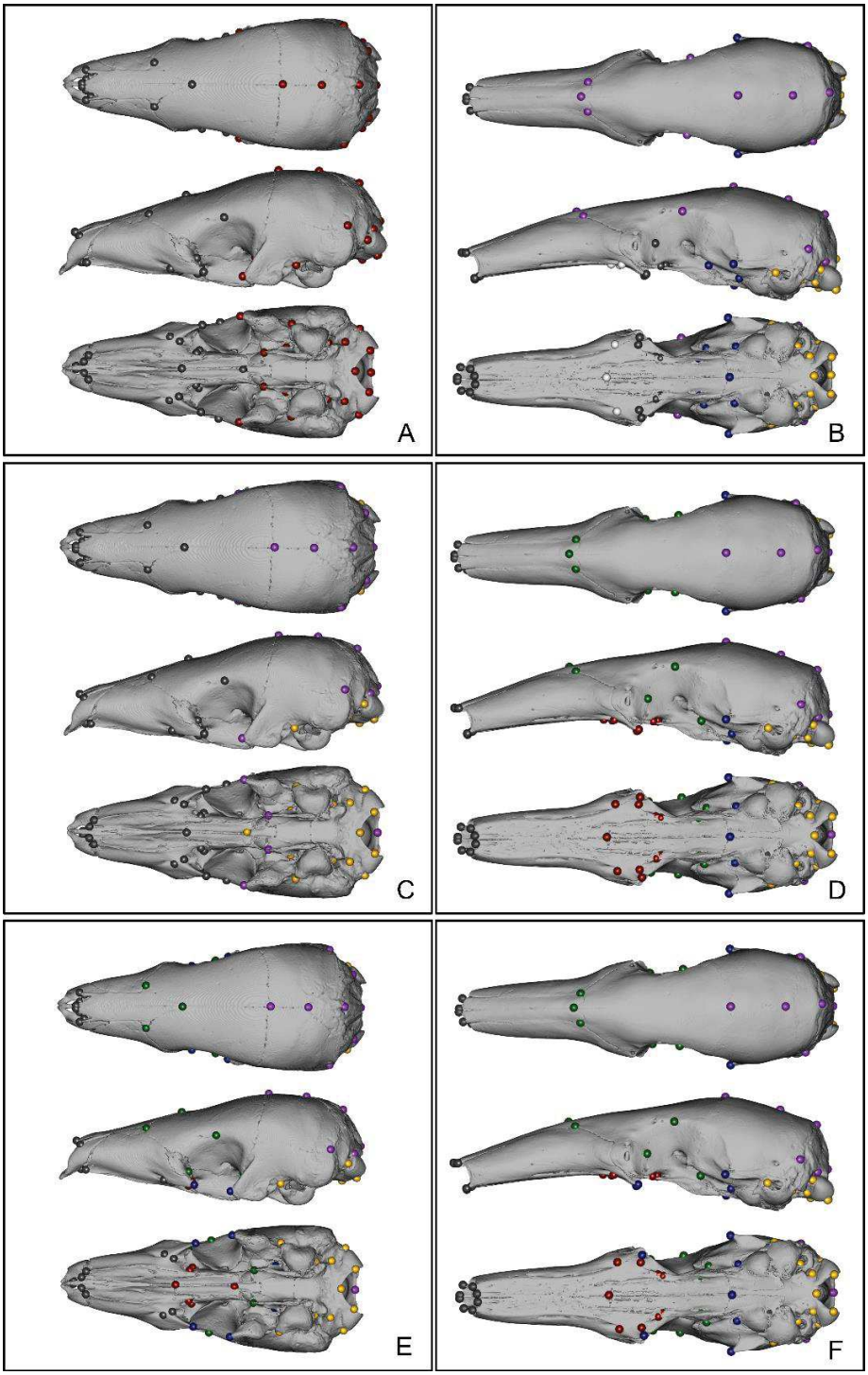

Figure S4 – Six modular architectures tested with EMMLi (Table 1). Landmarks are placed on skulls of *Phataginus tricuspis* (A, C, E, G) and *Tamandua mexicana* (B, D, F, H). Each color corresponds to a module. Architectures IV, IX and X are not represented, as they are based in architectures V (IV, IX) and VIII (X). Architecture VII is shown in Fig. 1. A – I, B – III, C – II, D – Therian 6, E – VIII, F – VI.

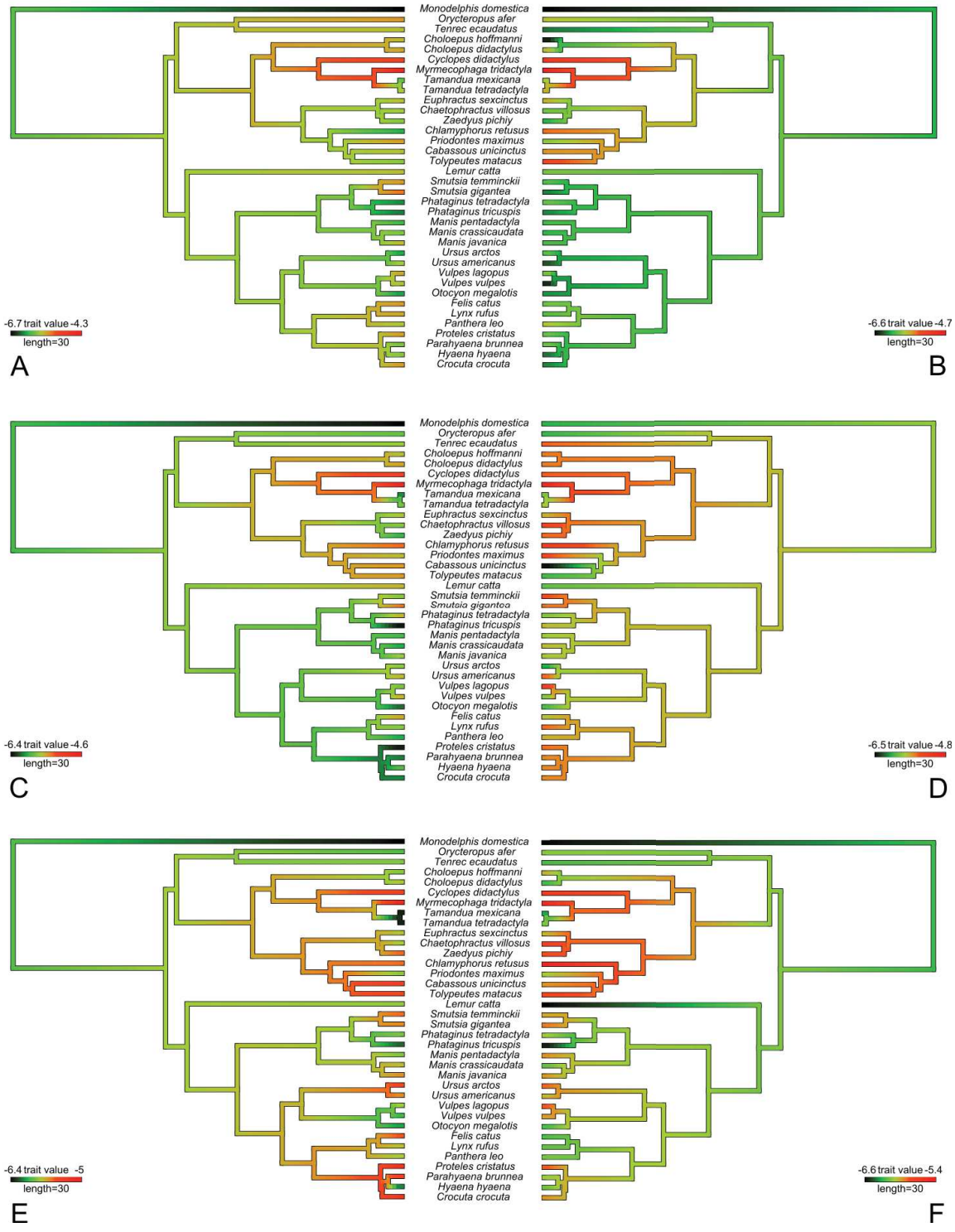

Figure S5 – Morphological evolutionary rates (σ) of six of the seven modules of architecture X for allometry-corrected shape data plotted on a phylogeny. (A) Oro-nasal/rostrum, (B) molar-palate, (C) orbit, (D) zygomatic-pterygoid, (E) vault, (F) basicranium. Black color indicates slow evolutionary rates and red indicates fast evolutionary rates. σ values are $\log_{10}$-transformed.

Table S1 – Landmark descriptions and modular architectures tested in EMMLi.

#	Landmark	I	II	III	IV	V	VI	VII	VII	IX	X
1	Most antero-medial point of the maxilla	1	1	1	NA	1	1	1	1	1	1
2	Most antero-lateral contact of the maxilla	1	1	1	NA	1	1	1	1	1	1
3	Ventral margin of the infraorbital foramen	1	1	NA	2	2	2	2	1	7	8
4	Ventral margin of the maxillary foramen	1	1	1	2	2	2	2	1	2	1
5	Intersection between maxilla and palatine sutures	1	1	NA	2	2	2	2	2	7	8
6	Ventral margin of the sphenopalatine foramen	1	1	1	2	2	2	2	2	2	2
7	Ventral margin of the posterior caudal palatine foramen	1	1	1	2	2	2	2	2	2	2
8	Most dorsal point of the orbit	1	1	5	3	3	3	5	3	3	3
9	Intersection between palatine and pterygoid sutures	1	3	3	4	4	4	2	2	4	2
10	Optic foramen (most postero-ventral point)	2	1	3	3	3	3	3	3	3	3
11	Foramen rotundum (most postero-ventral point)	2	2	3	3	3	3	3	3	3	3
12	Anteriormost point of the zygomatic process of the squamosal	2	2	3	4	4	4	4	4	4	4
13	Most posterior point of the foramen ovale	2	3	3	4	4	4	3	4	4	4
14	Concavity at contact with the tympanic bulla	2	3	6	6	6	6	6	7	6	7
15	Anteriormost point of the jugular foramen	2	3	6	6	6	6	6	7	6	7
16	Posteriormost point of hypoglossus foramen	2	3	6	6	6	6	6	7	6	7
17	Most anterior point of the foramen magnum	2	3	6	6	6	6	6	7	6	7
18	Most postero-dorsal point of the foramen magnum	2	2	6	5	5	5	5	6	5	6
19	Most lateral point of the occipital condyle	2	3	6	6	6	6	6	7	6	7
20	Medial limit of the occipital condyle	2	3	6	6	6	6	6	7	6	7
21	Most antero-medial point of the maxilla	1	1	1	NA	1	1	1	1	1	1
22	Most antero-lateral contact of the maxilla	1	1	1	NA	1	1	1	1	1	1
23	Ventral margin of the infraorbital foramen	1	1	NA	2	2	2	2	1	7	8
24	Ventral margin of the maxillary foramen	1	1	1	2	2	2	2	1	2	1
25	Ventral margin of the sphenopalatine foramen	1	1	1	2	2	2	2	2	2	2
26	Ventral margin of the posterior caudal palatine foramen	1	1	1	2	2	2	2	2	2	2
27	Most dorsal point of the orbit	1	1	5	3	3	3	5	3	3	3
28	Optic foramen (most postero-ventral point)	2	1	3	3	3	3	3	3	3	3
29	Foramen rotundum (most postero-ventral point)	2	2	3	3	3	3	3	3	3	3
30	Anteriormost point of the zygomatic process of the squamosal	2	2	3	4	4	4	4	4	4	4
31	Most posterior point of the foramen ovale	2	3	3	4	4	4	3	4	4	4
32	Concavity at contact with the tympanic bulla	2	3	6	6	6	6	6	7	6	7
33	Anteriormost point of the jugular foramen	2	3	6	6	6	6	6	7	6	7
34	Posteriormost point of hypoglossus foramen	2	3	6	6	6	6	6	7	6	7
35	Most lateral point of the occipital condyle	2	3	6	6	6	6	6	7	6	7
36	Medial limit of the occipital condyle	2	3	6	6	6	6	6	7	6	7
37	Anteriormost point of the nasal	1	1	1	NA	1	1	1	1	1	1
38	Anteriormost point of the suture between nasal and maxilla	1	1	1	NA	1	1	1	1	1	1
39	Intersection mx/nasal/frontal	1	1	5	3	3	3	1	3	7	8
40	Intersection between palatine/lacrimal/frontal	1	1	1	3	3	3	4	3	3	3
41	Zygomatic process of the maxilla	1	1	1	2	2	4	4	4	2	4
42	Intersection between inter-nasal and inter-frontal sutures	1	1	5	3	3	3	1	3	7	8
43	Intersection between inter-parietal fronto-parietal suture	2	2	5	5	5	5	5	6	5	6
44	Intersection between inter-parietal and supraoccipital	2	2	5	5	5	5	5	6	5	6
45	Intersection between squamosal/supraoccipital/parietal	2	2	5	5	5	5	5	6	5	6
46	Posteriormost point of the skull roof on the supraoccipital	2	2	5	5	5	5	5	6	5	6
47	Concavity located above the condyle	2	2	5	5	5	5	6	6	5	6
48	Anteriormost point of the nasal	1	1	1	NA	1	1	1	1	1	1
49	Anteriormost point of the suture between nasal and maxilla	1	1	1	NA	1	1	1	1	1	1
50	Intersection mx/nasal/frontal	1	1	5	3	3	3	1	3	7	8
51	Intersection between palatine/lacrimal/frontal	1	1	1	3	3	3	4	3	3	3
52	Zygomatic process of the maxilla	1	1	1	2	2	4	4	4	2	4
53	Intersection between squamosal/supraoccipital/parietal	2	2	5	5	5	5	5	6	5	6
54	Concavity located above the condyle	2	2	5	5	5	5	6	6	5	6

Table S2 – Number of modules in different architectures obtained from network analysis for 15 myrmecophagous species. Number of specimens (*N*), and number of modules (*x* mod) are given. Numbers in bold represent the most frequent architecture for each species.

	N	2 mod	3 mod	4 mod	5 mod	6 mod	7 mod	8 mod	9 mod	10 mod
T. tetradactyla	74	-	-	-	38	**223**	39	-	-	-
T. mexicana	43	-	-	-	4	**164**	100	30	2	-
M. tridactyla	38	-	**247**	45	8	-	-	-	-	-
C. didactylus	60	-	70	**197**	33	-	-	-	-	-
P. maximus	14	-	**231**	63	6	-	-	-	-	-
O. afer	40	-	-	**183**	82	32	2	1	-	-
M. crassicaudata	7	-	**218**	57	25	-	-	-	-	-
M. javanica	28	-	-	57	**176**	58	9	-	-	-
M. pentadactyla	27	-	-	**163**	36	1	-	-	-	-
S. temminckii	15	-	**230**	61	8	1	-	-	-	-
S. gigantea	12	-	**225**	60	12	3	-	-	-	-
P. tricuspis	72	-	-	-	18	**134**	106	36	5	1
P. tetradactyla	17	-	-	-	**255**	39	6	-	-	-
P. cristata	25	-	-	1	134	**142**	23	-	-	-
O. megalotis	8	-	7	**244**	33	13	3	-	-	-

Table S3 – Modular architectures of the skull of 15 myrmecophagous species. Number of specimens (N), most likely modular architectures (Model), most likely partition of within- and between-module correlation (Part ρ), maximum likelihood value (MaxLik), number of estimated parameters (K), Akaike Information Criterion value (AICc), and posterior probability of the chosen model (PostProb).

Species	**N**	**Model**	**Part ρ**	**PostProb**
T. tet	74	IX (7)	Sep/sep	1.00
T. mex	43	IX (7)	Sep/sep	1.00
M. tri	38	IX (7)	Sep/sep	1.00
C. did	60	IX (7)	Sep/sep	1.00
P. max	14	IX (7)	Sam/sam	0.29
O. afe	40	IX (7)	Sep/sep	0.73
M. cra	7	II (3)	Sam/sam	0.21
M. jav	28	IX (7)	Sep/sep	1.00
M. pen	27	VII (6)	Sep/sep	0.79
S. tem	15	V (6)	Sep/sep	0.65
S. gig	12	VII (6)	Sep/sep	1.00
P. tri	72	VII (6)	Sep/sep	1.00
P. tet	17	X (7)	Sep/sep	0.73
P. cri	25	VII (6)	Sep/sam	0.97
O. meg	8	IX (7)	Sep/sam	0.80

Table S4 – Static allometry-corrected modular architectures of 15 myrmecophagous mammals. Number of specimens (N), most likely modular architectures (Model), most likely partition of within- and between-module correlation (Part ρ), maximum likelihood value (MaxLik), number of estimated parameters (K), Akaike Information Criterion value (AICc), and posterior probability of the chosen model (PostProb).

Species	N	Model	Part ρ	PostProb
T. tet	74	IX (7)	Sep/sep	1.00
T. mex	43	IX (7)	Sep/sep	1.00
M. tri	38	IX (7)	Sep/sep	1.00
C. did	60	IX (7)	Sep/sep	1.00
P. max	14	-	Sam/sam	0.29
O. afe	40	X (7)	Sep/sep	1.00
M. cra	7	-	Sam/sam	0.21
M. jav	28	III (4)	Sep/sep	0.58
M. pen	27	VII (6)	Sep/sep	0.94
S. tem	15	VII* (6)	Sep/sam	0.27
S. gig	12	VII (6)	Sep/sep	1.00
P. tri	72	VII (6)	Sep/sep	1.00
P. tet	17	IX* (7)	Sep/sep	0.42
P. cri	25	-	Sep/sam	0.97
O. meg	8	-	Sep/sam	0.80

Table S5 – Pairtial least-squares analyses between modules in the skull of *Phataginus tricuspis*. *P*-values for the separate (upper triangle) and common superimpositions (lower triangle). Intramodular correlations for the architecture recovered by the MCN analysis. *P*-values are were corrected for multiple comparisons (Benjamini-Hochberg-Yekutieli). Values in bold are significant.

	1	2	3	4	5	6
1	0.23/0.20	0.06	0.12	0.10	0.10	0.24
2	**0.04**	0.21/0.28	**0.02**	**0.01**	0.10	**0.02**
3	**<0.01**	**<0.01**	0.39/0.32	**0.01**	**0.01**	0.12
4	**<0.01**	**<0.01**	**<0.01**	0.27/0.34	**0.01**	0.10
5	**<0.01**	**<0.01**	**<0.01**	**<0.01**	0.17/0.22	0.37
6	**<0.01**	**<0.01**	**<0.01**	**<0.01**	**<0.01**	0.15/0.15

Table S6 – Pairtial least-squares analyses between modules in the skull of *Tamandua tetradactyla*. *P*-values for the separate (upper triangle) and common superimpositions (lower triangle). Intramodular correlations for the architecture recovered by the MCN analysis. *P*-values are were corrected for multiple comparisons (Benjamini-Hochberg-Yekutieli). Values in bold are significant.

	1	4	5	6
1	0.46/0.20	0.37	0.61	0.61
4	**<0.01**	0.30/0.20	0.37	0.61
5	**0.04**	0.10	0.13/0.18	1.00
6	**<0.01**	**<0.1**	**<0.1**	0.43/0.14

6.5-Appendix 5

Book chapter: Gaudin, T.J., Gaubert, P., Billet, G., Hautier, L., Ferreira-Cardoso, S. & Wible, J.R. 2020 *Evolution & morphology. In: Pangolins: Science, Society and Conservation (C. Challender,* D.W.S., Nash, H., Waterman, ed). Academic Press, Cambridge, MA.

CHAPTER

1

Evolution and morphology

Timothy J. Gaudin[1], *Philippe Gaubert*[2,3], *Guillaume Billet*[4], *Lionel Hautier*[5], *Sérgio Ferreira-Cardoso*[5] *and John R. Wible*[6]

[1]Department of Biology, Geology and Environmental Science, University of Tennessee at Chattanooga, Chattanooga, TN, United States [2]Laboratoire Évolution & Diversité Biologique (EDB), Université de Toulouse Midi-Pyrénées, CNRS, IRD, UPS, Toulouse, France [3]CIIMAR, University of Porto, Matosinhos, Portugal [4]Centre de Recherche en Paléontologie-Paris (CR2P), UMR CNRS 7207, Sorbonne Université, Muséum National d'Histoire Naturelle, Paris, France [5]Institut des Sciences de l'Evolution, UMR 5554, CNRS, IRD, EPHE, Université de Montpellier, Montpellier, France [6]Section of Mammals, Carnegie Museum of Natural History, Pittsburgh, PA, United States

OUTLINE

Introduction

Pangolins, or scaly anteaters, comprise the placental mammal order Pholidota, and represent one of the most unusual orders of mammals, morphologically speaking. As implied by the name "scaly anteater," their most noteworthy feature is an external "armor" of overlapping epidermal scales that often earns them colorful nicknames like "walking pinecones" or "perambulating artichokes." They are the only mammals to possess such an armor (although xenarthran armadillos also possess a covering of epidermal scales, these scales are closely associated with underlying bony osteoderms, and as such are organized quite differently; Grassé, 1955a; Vickaryous and Hall, 2006), and pangolins will generally employ this defensive armor by curling up into a ball so that only the scales are exposed (hence the

DOI: https://doi.org/10.1016/B978-0-12-815507-3.00001-0

name "pangolin," derived from the Malay word "peng-goling" meaning "one that rolls up"; Kingdon, 1997). However, in addition to this feature, pangolins are unusual among mammals in their loss not only of teeth, but also of functional enamel genes (Meredith et al., 2009), as well as their extraordinarily elongate tongue (Chan, 1995; Kingdon, 1974), their myrmecophagous diet (Heath, 2013), their pungent anal glands (Kingdon, 1974), and their specializations for digging and climbing (Gaudin et al., 2009, 2016).

The origin and early evolution of Pholidota has been difficult to elucidate. Lacking teeth, the most durable and readily preserved part of the mammalian skeleton, their fossil record is sparse, although, as noted by Gaudin et al. (2016; see also Gaudin et al., 2006, 2009), it includes a number of well-preserved taxa. The scarcity of fossil pangolins is almost certainly exacerbated by their preference for forested habitats and the low population densities at which some species exist in the wild (Gaudin, 2010; Gaudin et al., 2016). Moreover, their relationships to other groups of placental mammals have historically been controversial, although a consensus appears to be emerging (see subsequent discussion). Here too their lack of teeth is a hindrance, because dental morphology has figured importantly in elucidating relationships among mammals in general (Emry, 2004; Ungar, 2010).

The goal of this chapter is to outline the phylogenetic relationships of pangolins as a whole to other groups of mammals, to summarize what is known of their fossil record, and to discuss the historical biogeography of the group. It then explores in more detail the unusual morphological features that characterize this highly distinctive order of mammals.

Pangolin supraordinal relationships

Linnaeus (1758) named *Manis pentadactyla* (Chinese pangolin) and placed it in the order Bruta along with elephants, manatees, sloths, and anteaters, to which he added armadillos in 1766. Storr (1780) removed the elephants and sloths and named the order Mutici for pangolins, anteaters, sloths, and armadillos. The name Mutici forgotten or ignored, the animals included by Storr formed the core of the order Edentati Vicq d'Azyr, 1792, a clade that with various additions and deletions was supported into the 20th century as Edentata Cuvier, 1798. Although not widely recognized, this clade was even raised to the level of sub-class named Paratheria by Thomas (1887) to be counterpart to Eutheria and Metatheria. Undoubtedly the reason Thomas's (1887) hypothesis received little support is the fact that pangolins show clear affinities with other placental mammals, possessing most of the synapomorphic traits of Placentalia, among them a chorioallantoic placenta with a prolonged gestational period, along with the loss of the epipubic bones, a brain with distinct olfactory bulbs, a corpus callosum and a gyrencephalic cerebral cortex, and a bicornuate uterus (Elliot Smith, 1899; Grassé, 1955b; O'Leary et al., 2013).

Weber (1904) gave the pangolins ordinal status as Pholidota, within a supraordinal Edentata, which also included Xenarthra (armadillos, sloths, and anteaters) and Tubulidentata (aardvarks). Xenarthrans and pangolins continued to be linked in supraordinal groupings by various authors in the early 20th century (Rose et al., 2005), but Simpson's (1945) separation of the two in his influential classification of mammals largely ended such claims. For example, in the first cladistic study of placental mammal phylogeny, McKenna (1975) made Pholidota *incertae sedis* within a broad clade including all extant placental orders except Xenarthra, Lagomorpha, and Macroscelidea. However, the association of pangolins and xenarthrans was revived by Novacek and colleagues in the late 1980s and early 1990s (e.g., Novacek, 1986, 1992;

Novacek and Wyss, 1986). They proposed a number of derived resemblances between Pholidota and Xenarthra, including features traditionally used to link the "edentate" mammals to one another, i.e., reduction of the dentition and fossorial specializations (in particular, extensive sacro-innominate fusion), along with several novel cranial features (e.g., reduction of the subarcuate fossa, restriction of the palatine to the ventral orbital wall). These putative synapomorphies have been criticized on morphological grounds (Rose et al., 2005), but perhaps more significantly, not a single molecular analysis (or combined morphological and molecular study) of placental mammal phylogeny published in the last two decades has supported a sister-group relationship between Xenarthra and Pholidota.

Pangolins were first grouped with carnivorans based on DNA sequence data by Shoshani et al. (1985), a result essentially universally accepted since then by additional sequence data (e.g., Murphy et al., 2001a,b; Meredith et al., 2011) and the total evidence analysis of O'Leary et al. (2013). However, it should be noted that the morphology-only results of the latter study yield an "Edentata" grouping of Pholidota+Xenarthra+Tubulidentata. There are several unusual derived features shared by living pangolins and carnivorans, including an ossified tentorium cerebelli and fusion of the scaphoid and lunate bones in the wrist, but these are reduced or absent in the earliest members of each group (Rose et al., 2005), so as yet there are not any identified morphological synapomorphies linking the two taxa.

Several extinct clades have been purported to be closely related to pangolins. The hypothesized relationship that has endured the longest is with palaeanodonts, a small Laurasian group known from the early Paleocene to early Oligocene (Rose, 2006). Palaeanodonts have a reduced dentition, presumably sharing the myrmecophagous diet of pangolins and many xenarthrans, and show adaptations for fossoriality (Rose, 2006). Matthew (1918) was the first to propose close affinities between palaeanodonts, pangolins, and xenarthrans, stating "On the whole, I can find no very conclusive evidence against deriving *Manis* as well as Loricata [=Cingulata] (and through them the remaining Xenarthra) from the primitive type represented by *Palaeanodon*. Just how direct the ancestors may be in each case is a highly speculative matter." Matthew (1918) foretold two schools of thought on the affinities of palaeanodonts: some (e.g., Patterson et al., 1992; Simpson, 1945; Szalay, 1977) supporting closer ties with xenarthrans and others (e.g., Emry, 1970; McKenna and Bell, 1997; Rose et al., 2005) supporting closer ties with pangolins. The latter group has received the most support, with Gaudin et al. (2009) naming a new superorder Pholidotamorpha including Palaeanodonta and Pholidota, which has been supported by the total evidence analysis of O'Leary et al. (2013). Curiously, the Pholidotamorpha of Gaudin et al. (2009) also includes the middle Eocene taxon *Eurotamandua joresi*. The latter, known mostly from a single skeleton from the famed Messel lagerstätten (Storch, 1981), was initially described as a relative of xenarthran anteaters (i.e., vermilinguans), which would make it the only Old World xenarthran. However, more recent studies have disputed this allocation (Rose, 1999; Szalay and Schrenk, 1998), and Gaudin et al. (2009) actually placed *Eurotamandua* within Pholidota proper, in between two other Messel "edentates," *Euromanis krebsi* and *Eomanis waldi*, as a sister taxon to a clade including the latter plus all other undoubted living and fossil pangolins.

Pangolin evolutionary history

It is likely that the Pholidota has its origin in Laurasia, given that the oldest fossil pangolins derive from Europe, and the two possible

closest relatives of Pholidota, Palaeanodonta and Carnivora, originate in North America (Flynn and Wesley-Hunt, 2005; Gaudin et al., 2016; Rose et al., 2005). This pattern of supraordinal relationships implies a substantial ghost lineage for Pholidota at its origin, as both Palaeanodonta and Carnivora date to the early Paleocene (Gaudin et al., 2016; O'Leary et al., 2013), whereas the oldest undoubted fossil pangolins, *Euromanis* and *Eomanis*, are derived from the lower middle Eocene Messel deposits (~45 Ma, Lutetian Age; Gaudin et al., 2009; Rose et al., 2005; Fig. 1.1). Molecular phylogenies imply an even older ghost lineage, extending back into the Cretaceous (Emerling et al., 2018; Meredith et al., 2011).

The pangolins from Messel are clearly fossorial, and share strong resemblances to palaeanodonts. For example, they possess an elongated scapular acromion, a humeral supinator crest with a free-standing proximal extension and an elongated deltopectoral crest that is canted medially at its distal end, short and broad metapodials, and an enlarged third manual ungual (Fig. 1.1; Gaudin et al., 2009; Rose et al., 2005; Storch, 2003). The oldest fossil pangolins are also the smallest fossil

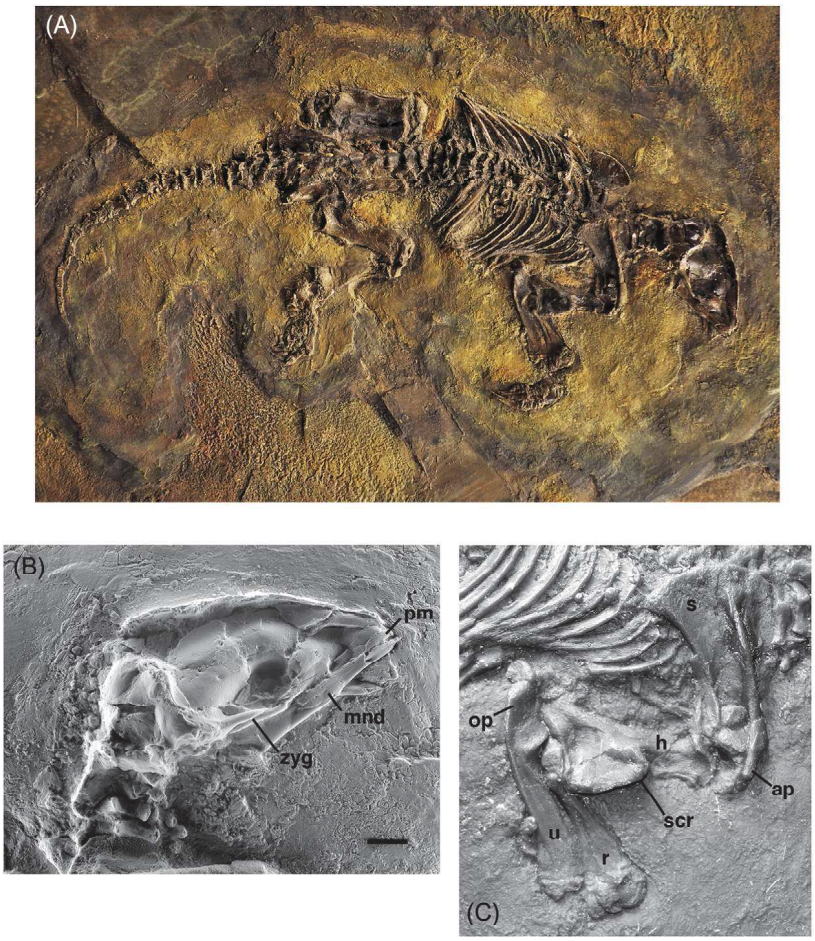

FIGURE 1.1 (A) Skeleton of *Eomanis waldi* in right lateral view. (B) Close-up of the skull of *E. waldi* in right lateral view (SMF MEA 263 cast). (C) Close-up of the right scapula, humerus, radius and ulna of *Eomanis waldi* (SMF MEA 263 cast) in lateral view. Abbreviations: ap, acromion process; h, humerus; mnd, mandible; op, olecranon process; pm, premaxilla; r, radius; s, scapula; scr, supinator crest; u, ulna; zyg, zygomatic arch. *Photos in (A & B) courtesy of Gerhard Storch. Photo in (C) reprinted by permission from Springer/J. Mammal. Evol. Gaudin, T.J., Emry, R.J., Wible, J.R., 2009. The phylogeny of living and extinct pangolins (Mammalia: Pholidota) and associated taxa: a morphology based analysis. J. Mammal. Evol. 16 (4), 235–305. (https://doi.org/10.1007/s10914-009-9119-9).*

pangolins. *Euromanis krebsi* is known from a single incomplete specimen lacking a skull (Gaudin et al., 2009; Storch and Martin, 1994). It is a little larger than *Eomanis waldi*, which is known from multiple specimens, including several nearly complete skeletons (Gaudin et al., 2009; Storch, 1978, 2003), and is smaller than the arboreal African pangolins, the smallest living species (total length of nearly complete skeleton of *E. waldi*, SMF MEA 263, ~ 47 cm; Gaudin et al., 2016). *Eomanis waldi* lacked any clear arboreal adaptations, possessing a rather short tail and short digits. It was edentulous, like living pangolins and other extant myrmecophagous mammals, and thus presumably consumed an ant and termite based diet. It also preserved epidermal scales, though the extent of its scale cover is unknown (Koenigswald et al., 1981). In most respects, however, its skeleton was considerably more primitive than that of other known pangolins, lacking such classic pangolin features as fissured unguals and enrolled lumbar zygapophyses, and retaining a complete zygomatic arch in the skull with a sizable jugal contribution (Gaudin et al., 2009; Rose et al., 2005; the jugal is lost in all extant pangolins except *Manis pentadactyla*, Emry, 2004).

The Paleogene fossil record for pangolins is sparse, but includes several well-known taxa, and is confined to portions of Laurasia outside the range of extant pangolins (Gaudin et al., 2006, 2016). Subsequent to the Messel taxa, only three Paleogene fossil pangolin genera are known. The genus *Cryptomanis* is based on a single partial skeleton lacking a skull, from the late middle Eocene of northern China (*C. gobiensis*; ~40 Ma, Bartonian Age; Gaudin et al., 2006; Fig. 1.2). This taxon had the most robust skeleton of all the Paleogene fossil pangolins, and was likely scansorial like the living Asian pangolins, with elongate digits but lacking a prehensile tail (Gaudin et al., 2006). The genus *Patriomanis* is known from several nearly complete skeletons and some partial remains from two localities in western North America, both latest Eocene in age (~35–37 Ma, Priabonian Age; Gaudin et al., 2016; Fig. 1.2). All the *Patriomanis* material is assigned to a single species, *P. americana*. This species was less robust than *Cryptomanis*, but still showed distinct fossorial adaptations, presumably for excavating ant and termite mounds, as it lacked teeth like *Eomanis*. In comparison to *Cryptomanis*, it had shorter digits but a longer, likely prehensile tail. This tail differed in form but was functionally equivalent to that of the extant prehensile tailed (and arboreal or semi-arboreal) smaller African pangolins (see Chapters 8 and 9), suggesting *Patriomanis* was arboreal (Gaudin et al., 2016). The two genera together comprise the extinct family Patriomanidae (Gaudin et al., 2009, 2016).

The final Paleogene fossil pangolin, the genus *Necromanis*, has the widest stratigraphic and geographic range of any extinct pholidotan, ranging from the middle Oligocene to the middle Miocene (i.e., extending from the late Paleogene into the early Neogene; ~28–14 Ma; Alba et al., 2018; Gaudin et al., 2009; Koenigswald, 1999; Fig. 1.2), and is known from multiple localities in Germany, France and Spain (Alba et al., 2018; Crochet et al., 2015; Koenigswald, 1999). Despite this, the three species in this genus, *N. franconica*, *N. quercyi*, and *N. parva*, remain incompletely known in terms of their skeletal anatomy, though an undescribed skeleton of *N. franconica* from Germany may yet rectify this situation (Hoffmann et al., 2009). The taxonomic affinity of *Necromanis* is also unsettled, with recent phylogenetic analyses allying it either with Patriomanidae (Hoffmann and Martin, 2011), or as the sister taxon to Patriomanidae or to the clade containing all the extant taxa, Manidae (Gaudin et al., 2009).

There is one additional putative Paleogene pangolin record, in the form of several isolated unguals of questionable taxonomic value, from the Oligocene of North Africa

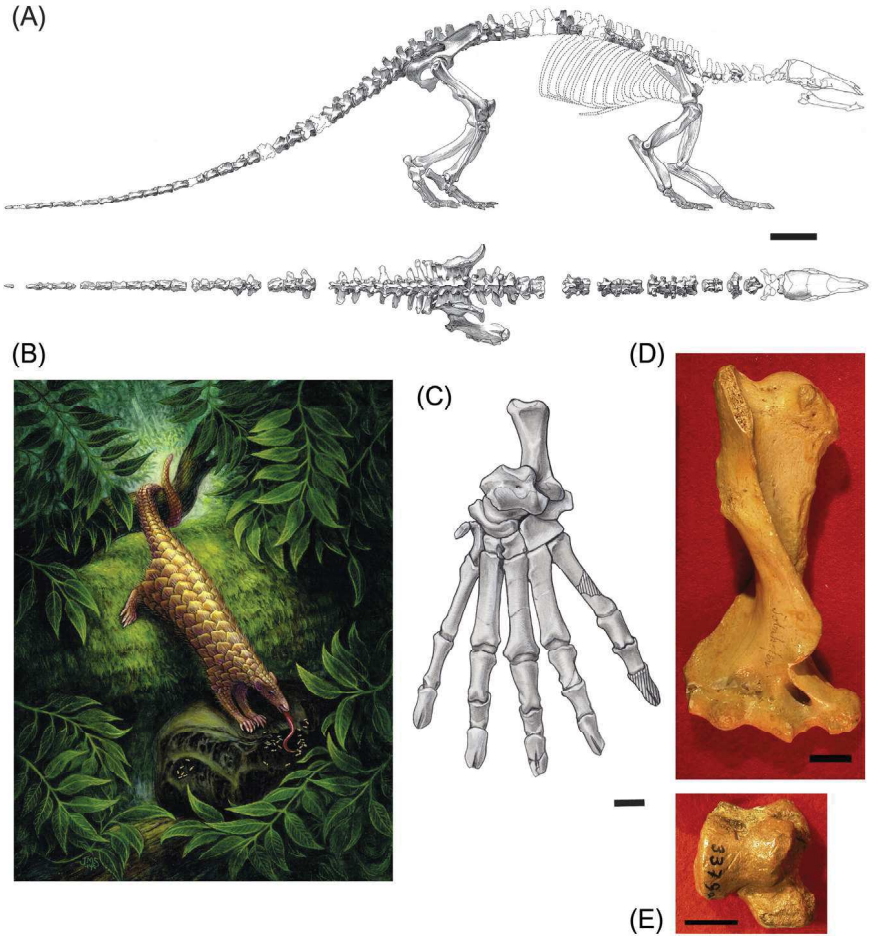

FIGURE 1.2 (A) Skeleton of *Patriomanis* in left lateral (above) and dorsal views (below). (B) Life reconstruction of *Patriomanis*. (C) Left pes of *Cryptomanis* (AMNH 26140) in dorsal view. (D) Right humerus of *Necromanis franconica* in anterior view. (E) Right astragalus of *Necromanis franconica* (SMF M3379a) in dorsal view. Scale bar=1 cm. *(A and B) modified from Gaudin, T.J., Emry, R.J., Morris, J., 2016. Description of the skeletal anatomy of the North American pangolin* Patriomanis americana *(Mammalia, Pholidota) from the latest Eocene of Wyoming (USA). Smithson. Contrib. Paleobiol. 98, 1–102, (C) modified from Gaudin, T.J., Emry, R.J., Pogue, B., 2006. A new genus and species of pangolin (Mammalia, Pholidota) from the late Eocene of Inner Mongolia, China. J. Vertebr. Paleontol. 26 (1), 146–159 (modified by permission from Taylor and Francis Ltd, www.tandfonline.com). Photos in (D and E) by T. Gaudin.*

(Gaudin, 2010; Gaudin et al., 2009; Gebo and Rasmussen, 1985).

The Neogene record of pangolins is little better than the Paleogene record. The group persisted in Europe at least until the middle Miocene (Koenigswald, 1999), and perhaps until the late Pliocene, based on fragmentary material from Hungary (Kormos, 1934), although, as noted above, the early Neogene material of *Necromanis* is not very complete. Undoubted fossil pangolins are known from Africa in the Pliocene and Pleistocene, the Pliocene forms being assigned to the extant giant pangolin species *Smutsia gigantea*, though

their remains are somewhat smaller than those of extant members, and the late Pleistocene record assigned to the living Temminck's pangolin (*Smutsia* cf. *S. temminckii*; Gaudin, 2010). Two of the three records are from South Africa, outside the geographic range of the extant African species, and the Pliocene *S. gigantea* from South Africa is the only African fossil pangolin in which a substantial portion of the skeleton is preserved (Botha and Gaudin, 2007; Gaudin, 2010). Fossil pangolins do not appear in South Asia and the East Indies until the Pleistocene (Emry, 1970). All remains are assigned to extant taxa except for *Manis lydekkeri*, known only from an isolated phalanx, and *M. palaeojavanica*, the giant pangolin from the Pleistocene of Java (Emry, 1970; Gaudin et al., 2009). The latter is known from relatively complete skeletal remains, and is the largest pangolin ever to have lived, with an estimated total length of 2.5 m (Dubois, 1926), roughly one and a half times the length of the largest living form, *S. gigantea*.

Morphological specializations of extant pangolins

Relative to other lineages of mammals, pangolins can be considered a uniform group despite their ancient origin, the adaptive cost of myrmecophagy possibly acting as a strong evolutionary constraint. In fact, a cohort of traits associated with feeding on ants and termites, also observed in South American anteaters, are present in all eight species of extant pangolins (Manidae), including the lack of teeth, weakly developed masticatory muscles, sharp claws, forelegs with strong flexor muscles, thick integument, reduced pinnae and valvular nostrils.

As noted above, the most characteristic feature of pangolins is their scaled armor. It covers the dorsal part of the body, the whole tail and the outer side of the legs (Fig. 1.3). Scales are cornified extrusions of the epidermis, composed of flattened, solid and keratinized cells (Tong et al., 1995; Wang et al., 2016). They do not consist of compressed hairs like in rhino (Rhinocerotidae) horns or echidna (Tachyglossidae) spines, but instead are homologous with primate nails (Spearman, 1967). Pangolins could thus be the only living mammals that have developed nail-like structures on their body.

Wearing a scaled armor may be evolutionarily costly. Indeed, scales are metabolically inactive and represent, together with the thick skin, anywhere from 1/10 to 1/4 or 1/3 of the total body weight of pangolins. Moreover, because scales are made of a significant proportion of scleroprotein (Mitra, 1998), they

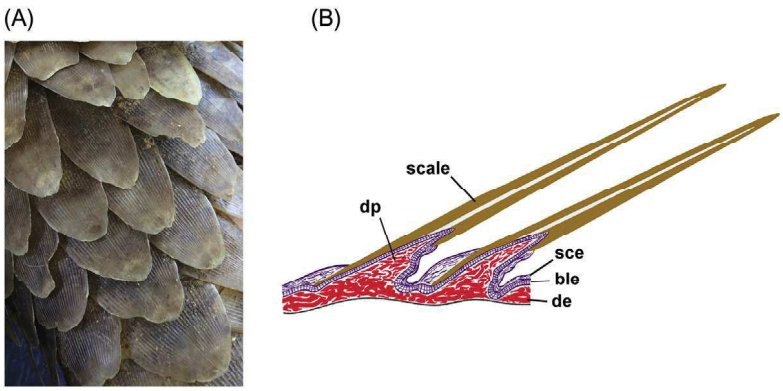

FIGURE 1.3 (A) Close-up photograph of scales at the base of the tail in *Phataginus tricuspis*, in dorsal view. (B) Schematic drawing of pangolin scale histology in *P. tricuspis*. Abbreviations: ble: basal layers of epidermis; de: dermis; dp: dermal papilla; sce, stratum corneum of epidermis. *(B) modified from Grassé, P.-P., 1955b. Ordre des Pholidotes. In: Grassé P.-P. (Ed.), Traité de Zoologie, vol. 17 Mammifères. Masson et Cie, Paris, pp. 1267–1282. Photograph of pangolin scales by T. Gaudin.*

likely require a large consumption of protein for their production (Gaubert, 2011).

Contrary to popular belief, scales contribute little to thermal insulation or protection against ants and termites or dermal parasites (e.g., Heath and Hammel, 1986). Rather, they seem more useful for protecting against injuries from large predators and fossorial activities (e.g., Tong et al., 1995). Scales are sensitive to touch and their orientation is adjustable by dermal muscles. When pangolins roll up into their typical defensive position, the large, salient scales on the sides of the tail are protruded backwards as a threatening series of sharp asperities.

The skull of extant pangolins is very distinctive relative to that of most extant mammals, as it bears many unusual morphological features related to their shift to an almost exclusively myrmecophagous diet. The skull is characterized by its elongated and toothless rostrum, and the incomplete or very slender zygomatic arch. The narrow snout confers a characteristic triangular shape to the skull in dorsal and ventral view (Fig. 1.4). Though lacking teeth, the maxillary bone of pangolins presents sharpened edges that border the palate laterally. The mandible is equally toothless but bears an osseous pseudo-tooth anteriorly. The lower jaw

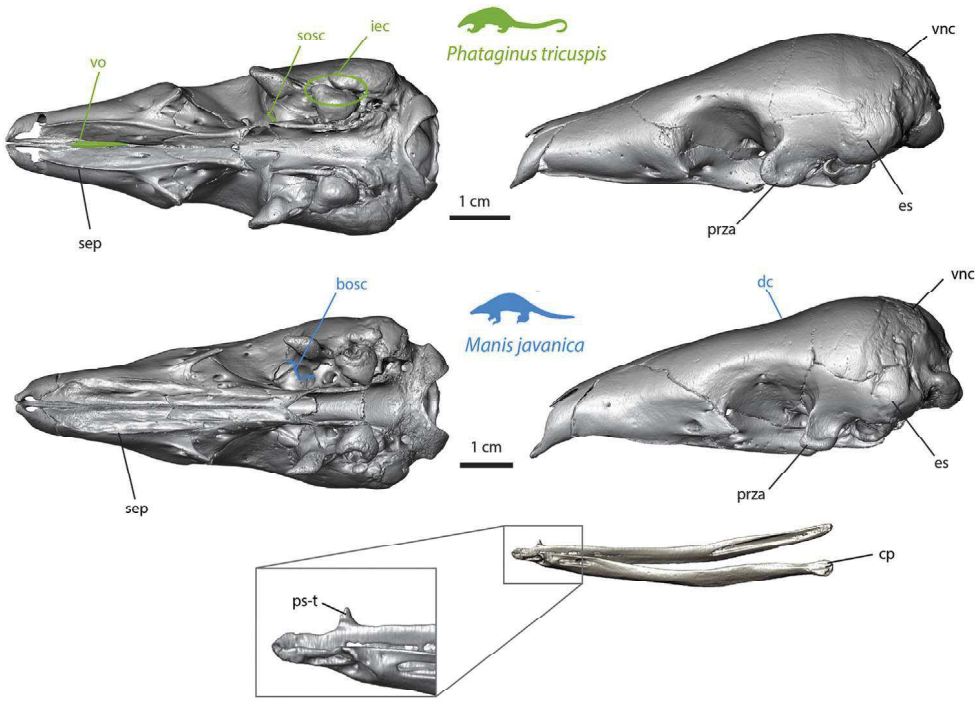

FIGURE 1.4 Cranial characters in extant pangolins. The left part of the figure shows ventral views and the right part lateral views of skulls of *Phataginus tricuspis* (BMNH 12-12-3-3) and *Manis javanica* (BMNH 9-1-5–858). Features labeled in black are shared by all extant pangolins, those labeled in green are typical of African pangolins (*Phataginus* and *Smutsia* spp.), while those labeled in blue characterize Asian pangolins (*Manis* spp.). Abbreviations: bosc: broad orbitosphenoid-squamosal contact; cp: condylar process of the mandible, flat and low-positioned; dc: dorsal constriction; es: inflated epitympanic sinus; iec: inflation of ectotympanic; prza: posterior root of (incomplete) zygomatic arch; ps-t: osseous pseudo-tooth; sep: sharpened edges of the palate; sosc: short orbitosphenoid-squamosal contact; vnc: vestigial nuchal crest; vo: vomer visible in palatal view.

is long and mediolaterally compressed with an ascending ramus consisting solely of a flat and low-positioned condylar process, lacking coronoid and angular processes (Fig. 1.4). Besides these general features, some of which were already present in Paleogene pholidotans (Gaudin et al., 2016), extant pangolins may be further diagnosed by a number of more subtle cranial specializations. The skulls of extant pangolins (Manidae) are unusual and highly diagnostic, characterized by multiple unambiguous cranial synapomorphies, some illustrated in Fig. 1.4 and the remainder listed in Gaudin et al. (2009). As a complement to detailed observation of discrete anatomical characters, recent geometric morphometric analyses highlighted the main patterns of cranial shape variation in seven of the eight extant pangolin species (Fig. 1.5; Ferreira-Cardoso et al., in press). These analyses showed that allometry plays a significant role in shaping intrageneric skull variation, especially among African pangolins, with larger species showing a longer rostrum. The Asian species (*Manis* spp.) generally exhibit more robust (higher and wider) rostra, long zygomatic processes (complete zygomatic arches are rare, but present in some old individuals) and varying degrees of orbital constrictions (Fig. 1.5A, lower left). In contrast, the small African species (*Phataginus* spp.) present narrow and slender rostra, lack orbital and dorsal constrictions, and have relatively wide braincases (Figs. 1.4 and 1.5A (lower right)). Gaudin et al. (2009) stressed similarities between African ground pangolins and their Asian relatives, which partly explains the weak morphological support for the monophyly of the African clade. Ferreira-Cardoso et al. (in press)

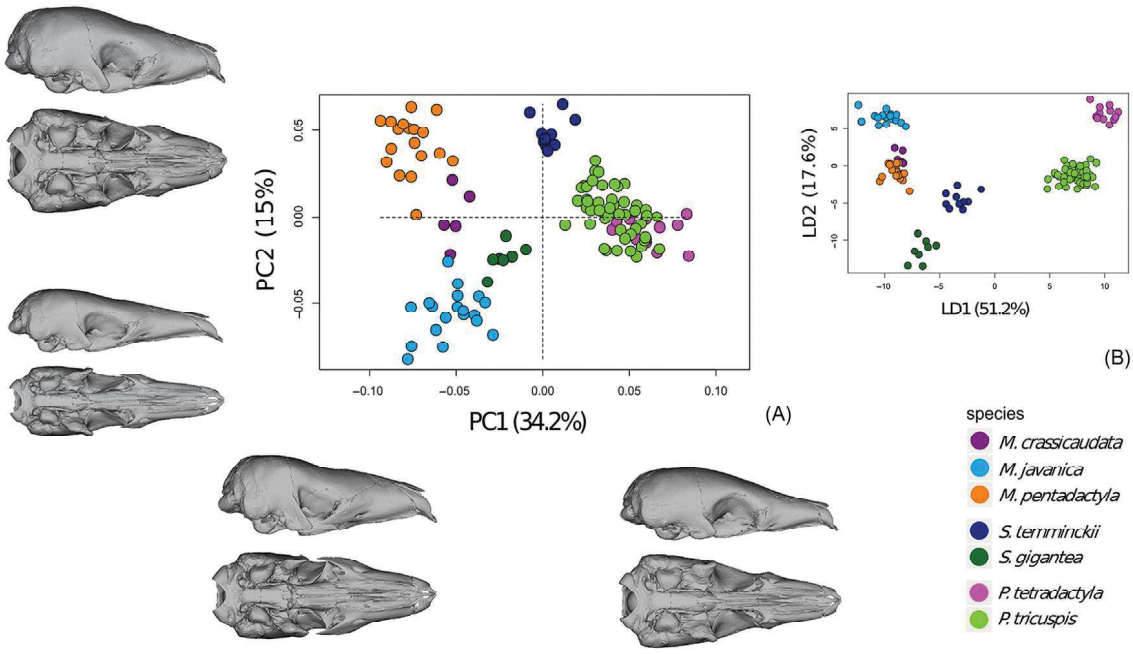

FIGURE 1.5 Morphological variation of the skull of extant pangolins using 3D geometric morphometric methods on a set of 75 anatomical landmarks (Ferreira-Cardoso et al., in press). (A) Principal component analysis and associated patterns of morphological transformation for crania. (B) Linear Discriminant Analysis (LDA) performed on the first principal components explaining 90% of the variance.

confirmed that African ground pangolins (*Smutsia* spp.) display intermediate skull shapes, with the Temminck's pangolin (*S. temminckii*) slightly closer to white-bellied pangolins (*P. tricuspis*), whereas the giant pangolin (*S. gigantea*) resembles the Sunda pangolin (*Manis javanica*). In general, no species represents a clear outlier in the morphospace and the interspecific variation pattern of cranial shape seems to reflect the different geographical distributions (Maninae – Asian; Smutsiinae – African *sensu* Gaudin et al., 2009). Functional correlates of cranial morphology remain to be better assessed for many structures whose shape is unique to pangolins. In this regard, the functional implications of the very thick semicircular canals and the low cochlear spiral of the bony labyrinth in *P. tricuspis* (Ekdale, 2013), as well as the variable morphologies of the epitympanic sinus, posterior root of the zygomatic arch, and glenoid surface (Fig. 1.4) deserve further scrutiny.

Gaudin et al. (2009) noted few postcranial apomorphies that define Pholidota as a whole, among them a triangular subungual process, a prominent ischial spine, and a small obturator foramen. The postcranial skeleton of pangolins has long been considered highly distinctive, due in large part to adaptations for fossoriality and arboreality or scansoriality (Fig. 1.6), and to a lesser degree, myrmecophagy. It should be noted, however, that many of the postcranial skeletal features typically associated with this group are not evident in its earliest members, i.e., in the middle Eocene Messel taxa. However, the Manoidea, the clade including only the extinct Patriomanidae and the Manidae (encompassing all the extant taxa), is diagnosed by a number of distinctive postcranial skeletal features, many linked to fossoriality. These would include fissured ungual phalanges and enrolled or embracing lumbar zygapophyses (for a more complete listing see Figs. 1.7 and 1.8 and Gaudin et al., 2009).

The living pangolins show an additional suite of distinctive postcranial features, including strongly keeled metapodials, a concave astragalar head, and reduction of the crests on the long bones of the hindlimbs (again, for a more complete listing see Figs. 1.7 and 1.8 and Gaudin et al., 2009). According to Gaudin et al. (2006, 2016), many of these features are related to a reduction in fossorial features in the proximal limb elements, and an enhancement in the distal elements, perhaps related to a modified digging style in extant pangolins relative to the extinct forms.

Forefoot claws and powerful forelimbs are used to open termite mounds and ant nests. In arboreal species, forefoot claws are curved and hindfoot claws are longer for moving along tree branches. In terrestrial pangolins, forefoot

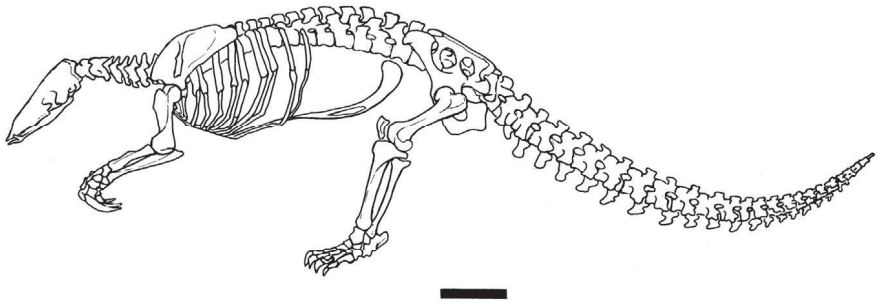

FIGURE 1.6 Skeleton of *Smutsia gigantea* in left lateral view. Scale bar=10 cm. *From Gaudin, T.J., 2010. Pholidota. In: Werdelin, L., Sanders W.J. (Eds.), Cenozoic Mammals of Africa. University of California Press, Berkeley, pp. 599–602.*

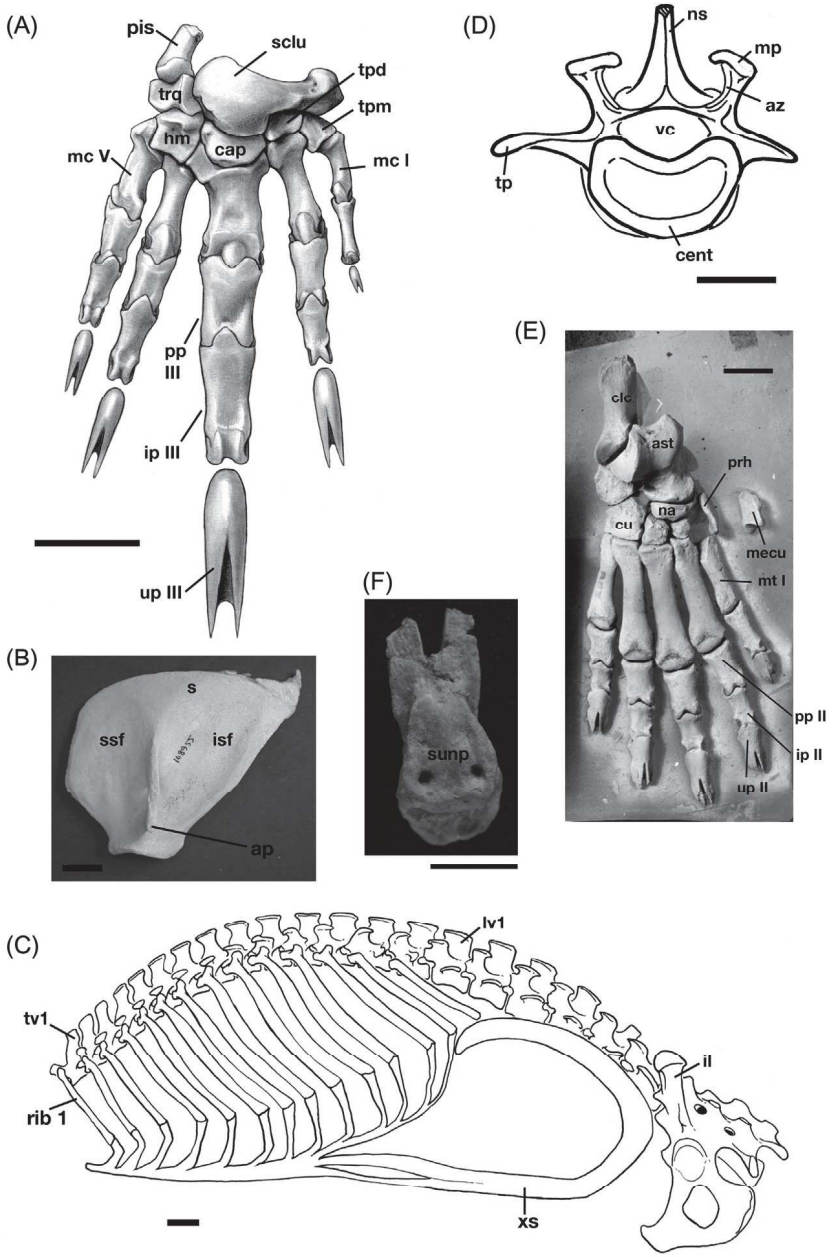

FIGURE 1.7 Pangolin postcranial skeletal features. (A) Right manus of *Phataginus tricuspis* (CM 16206) in dorsal view. (B) Left scapula of *Smutsia temminckii* (AMNH 168955) in lateral view. (C) Dorsal vertebrae, ribcage, sternum, sacrum and pelvis of *Phataginus tricuspis* (CM 16206) in left lateral view. (D) Lumbar vertebra of *Patriomanis americana* (USNM-P 299960) in anterior view. (E) Right pes of *Patriomanis americana* (USNM-P 299960) in dorsal view (the medial cuneiform illustrated is from the left side, as the right one is missing). (F) Ungual phalanx II of right pes of *Patriomanis americana* (USNM-P 299960) in ventral view. The following unambiguous synapomorphies of Manoidea (following Gaudin et al., 2009)

claws are proportionally longer and less curved than in arboreal species, and show greater wear due to their role in supporting the weight of the pangolins while walking and digging in the soil, whereas in arboreal species claws are held perpendicular to the ground and the weight is taken on the folded up wrists. Hindfoot claws are kept short in the plantigrade, terrestrial species by soil abrasion. The forelimbs of terrestrial pangolins, which are predominantly used for burrowing and digging into ant nests, show osteological features reflecting specifically enhanced capacity for shoulder protraction and retraction, strong elbow extension, flexion of the carpus and digits, as well as pronation and supination of the antebrachium (Gaubert, 2011; Kingdon, 1974; Steyn et al., 2018). The clavicle is variably present in extant species regardless of their locomotory mode (Kawashima et al., 2015), which makes its absence difficult to interpret functionally.

The tail of pangolins is very muscular and can be used by members of the larger species as a club to strike predators. It is also used to aid in balance when walking bipedally or to assist climbing in arboreal species. In the semi-arboreal and arboreal African pangolins, the tail is highly prehensile and bears at its ventral tip a touch-sensitive pad impregnated with numerous Pacinian corpuscles (vibration/pressure receptors; Doran and Allbrook, 1973). A similar, but narrower and perhaps less sensitive pad, is also present in the Sunda, Philippine and Chinese pangolins (*Manis javanica*, *M. culionensis*, and *M. pentadactyla*), but not in other species (Pocock, 1924; see Chapters 4, 6–7).

The semi-arboreal and arboreal African pangolins are particularly distinctive in their postcranial anatomy, showing the greatest number of postcranial synapomorphies of any of the pangolin genera in Gaudin et al.'s (2009) phylogenetic analysis, including "more uniform, slender digits . . .[and] more gracile limb elements" (Gaudin et al., 2009). Both species in this genus possess a greatly elongated tail, the black-bellied pangolin (*Phataginus tetradacytla*) having 47–50 caudals, the most of any known extant mammal (Flower, 1885; Gaubert, 2011; Gaudin et al., 2016).

The skeletal musculature in pangolins has been described by numerous authors. Much of the older literature has been summarized admirably by Windle and Parsons (1899). The epaxial musculature has been described by Slijper (1946) for "*Manis* spec.," whereas Jouffroy (1966) and Jouffroy et al. (1975) have published detailed descriptions of the muscles of the distal forelimb, manus, distal hindlimb and pes in the giant pangolin. All the living pangolin taxa show an enlargement of the cartilaginous xiphisternum, where the sternoglossus muscle of the tongue takes its origin

◀ are illustrated: fissured ungual phalanges; fusion of scaphoid and lunate bones; acromion process of scapula rudimentary; neural spines of anterior thoracic vertebrae not dramatically elongated relative to those of more posterior thoracics; embracing lumbar zygapophyses; prehallux present; astragalus/cuboid contact present; triangular subungual process. Abbreviations: ap, acromion process; ast, astragalus; az, anterior zygapophysis; cap, capitate; cent, vertebral centrum; clc, calcaneus; cu, cuboid; hm, hamate; il, ilium; ip, intermediate phalanx; isf, infraspinous fossa; lv, lumbar vertebra; mc, metacarpal; mecu, medial cuneiform; mp, metapophysis; mt, metatarsal; na, navicular; ns, neural spine; pis, pisiform; pp, proximal phalanx; prh, prehallux; s, scapula; sclu, scapholunate; ssf, supraspinous fossa; sunp, subungual process; tp, transverse process; tpd, trapezoid; tpm, trapezium; trq, triquetrum; tv, thoracic vertebra; up, ungual phalanx; vc, vertebral canal; xs, xiphisternum. Scale bars=1 cm. *(A–E) modified from Gaudin, T.J., Emry, R.J., Wible, J.R., 2009. The phylogeny of living and extinct pangolins (Mammalia, Pholidota) and associated taxa: a morphology based analysis. J. Mammal. Evol. 16 (4), 235–305; (F) modified from Gaudin, T.J., Emry, R.J., Morris, J., 2016. Description of the skeletal anatomy of the North American pangolin* Patriomanis americana *(Mammalia, Pholidota) from the latest Eocene of Wyoming (USA). Smithson. Contrib. Paleobiol. 98, 1–102.*

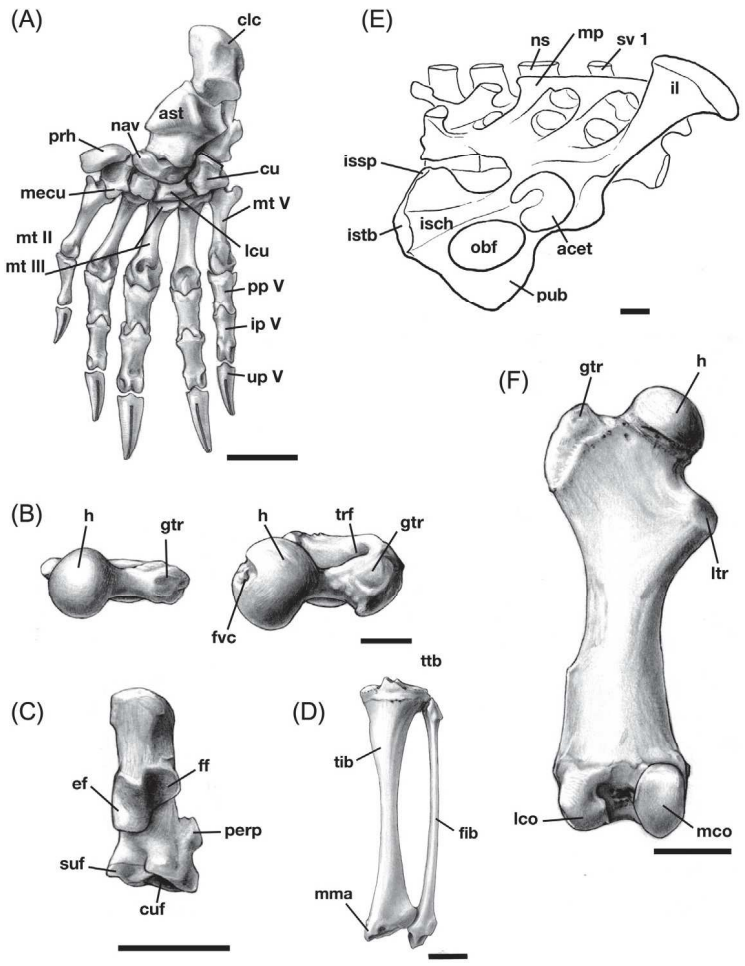

FIGURE 1.8 Postcranial skeletal features of living pangolins. (A) Left pes of *Phataginus tricuspis* (CM 16206) in dorsal view. (B) Left femur of *Phataginus tricuspis* (CM 16206, on left) and *Patriomanis americana* (USNM-P 299960, on right) in proximal view. (C) Left calcaneus of *Phataginus tricuspis* (CM 16206) in dorsal view. (D) Left tibia and fibula of *Phataginus tricuspis* (CM 16206) in anterior view. (E) Pelvis and sacrum of *Smutsia gigantea* (AMNH 53858) in right lateral view. (F) Left femur of *Phataginus tricuspis* (CM 16206) in posterior view. The following unambiguous synapomorphies of Manidae (following Gaudin et al., 2009) are illustrated: distal keel on metatarsals and metacarpals extends along entire dorsoventral length of condyle; proximal end of metatarsal II expanded transversely; proximal articular facet of metatarsal III overlaps dorsal surface of shaft; lateral cuneiform widened transversely, ratio of width to height ≥ 1.4; width of astragalar neck $\geq 60\%$ maximum width of astragalus; astragalar head of navicular with concave distal surface; greater trochanter of femur compressed anteroposteriorly, anteroposterior depth $\leq$ transverse width; fovea capitis absent; sustentacular facet on calcaneus situated well distal to astragalar and fibular facets, contacting distal margin of calcaneus; femoral trochanteric fossa and intertrochanteric ridge rudimentary or absent; sacroiliac attachment fused; metapophyses of sacral vertebrae elongated, >2/3 neural spine height; gluteal fossa poorly demarcated, iliac crest rounded, weak, dorsal flange absent, caudal dorsal iliac spine incorporated in sacroiliac junction; ischial spine situated close to ischial tuberosity, dorsal to posterior portion of obturator foramen; dorsal edge of ischium ventral to transverse processes of sacral vertebrae; cnemial crest of tibia weak, rounded, lacking lateral excavation. Abbreviations: acet, acetabulum; ast, astragalus; clc, calcaneus; cu, cuboid; cuf, cuboid facet; ef, ectal facet; ff, fibular facet; fib, fibula; fvc, fovea capitis; gtr, greater trochanter; h, head; il, ilium; ip, intermediate phalanx; isch, ischium; issp, ischial spine; istb, ischial tuberosity; lco, lateral condyle; lcu, lateral cuneiform; ltr, lesser trochanter; mco, medial condyle; mecu, medial cuneiform; mma, medial malleolus; mp, metapophysis; mt, metatarsal; nav, navicular; ns, neural spine; obf, obturator foramen; perp, peroneal process; pp, proximal phalanx; prh, prehallux; pub, pubis; suf, sustentacular facet; sv, sacral vertebra; tib, tibia; trf, trochanteric fossa; ttb, tibial tuberosity; up, ungual phalanx. Scale bars=1 cm. *Adapted by permission from Springer/J. Mammal. Evol. Gaudin, T.J., Emry, R.J., Wible, J.R., 2009. The phylogeny of living and extinct pangolins (Mammalia: Pholidota) and associated taxa: a morphology based analysis. J. Mammal. Evol. 16 (4), 235–305. (https://doi.org/10.1007/s10914-009-9119-9).*

(Grassé, 1955b), but this takes on extraordinary proportions in the African pangolins, where it extends into the abdominal cavity, actually turning dorsally in front of the pelvis toward the vertebral column (Doran and Allbrook, 1973; Kingdon, 1974; Figs. 1.6 and 1.7). Heath (2013) reviewed various published descriptions of the elongated tongue musculature in African pangolins and the Sunda pangolin. The tongue is enormously elongated (Chan, 1995; Doran and Allbrook, 1973; Heath, 2013; Kingdon, 1974; Fig. 1.9A), and capable of extending nearly half its resting length outside the mouth (Heath, 2013). It extends posteriorly through the neck and thorax to the ventral abdominal wall and beyond. In the thorax and throat region, the tongue is housed in a glossal tube lined by mucous membrane that serves as a guide and facilitates movement. The tongue is stored in a pocket in the throat when retracted (Chan, 1995; Doran and Allbrook, 1973; Heath, 2013). Among the noteworthy features of pangolin musculature are the thickened panniculus and the dramatic reduction of the masticatory muscle (Grassé, 1955b; Windle and Parsons, 1899). Windle and Parsons (1899) listed a variety of distinctive features of the skeletal musculature in pangolins, including the absence of muscles commonly present in other mammals (e.g., cleidomastoid), the enlargement of other muscles (e.g., flexor fibularis, popliteus, gracilis, and supinator brevis, the last of which houses a proximal sesamoid element), modified attachments (e.g., the biceps brachii lacks a long head or radial attachment, whereas the plantaris acquires an attachment to the greater trochanter of the femur), and a variety of muscle fusions

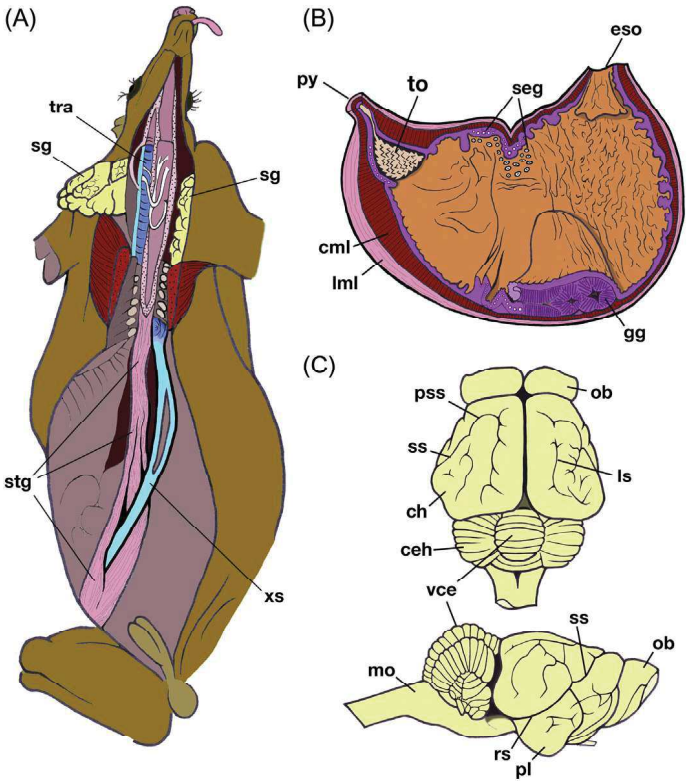

FIGURE 1.9 (A) Dissected *Smutsia gigantea* in ventral view, showing salivary glands, xiphisternum and elongated tongue musculature. (B) Frontal section of stomach of *Manis javanica* shown in ventral view. (C) Brain of *Manis javanica* in dorsal (above) and right lateral (below) views. Abbreviations: ceh, cerebellar hemisphere; ch, cerebral hemisphere; cml, circular layer of smooth muscle fibers; eso, esophagus; gg, gastric glands; lml, longitudinal layer of smooth muscle fibers; ls, lateral sulcus; mo, medulla oblongata; ob, olfactory bulb; pl, piriform lobe; pss, presylvian sulcus; py, pylorus; rs, rhinal sulcus; seg, serous glands; sg, salivary glands; ss, Sylvian sulcus; stg, sternoglossus muscle; to, triturating organ, lined with cornified denticles; tra, trachea; vce, vermis of cerebellum; xs, xiphisternum. *(A) modified from Kingdon, J., 1974. East African Mammals. vol. 1. University of Chicago Press, Chicago. (B, C) Modified from Grassé, P.-P., 1955b. Ordre des Pholidotes. In: Grassé P.-P. (Ed.), Traité de Zoologie, vol. 17. Mammifères. Masson et Cie, Paris, pp. 1267–1282.*

(e.g., spinodeltoid/acromiodeltoid, caudofemoralis/gluteus superficialis, gluteus medius/gluteus minimus/pyriformis, lateral head of gastrocnemius/plantaris). Additionally, Jouffroy (1966) noted that the distal gastrocnemius is fused to the soleus, and the brachioradialis and deltoid abut one another. Pangolins exhibit a number of peculiar myological resemblances to xenarthrans, including the presence of a pterygo-tympanic muscle (Grassé, 1955b), the presence of a rectus thoracis lateralis muscle, a femoral head to the biceps femoris, a strong development of all muscles from the shoulder region (Shrivastava, 1962), and the absence of the sphincter colli muscle (Windle and Parsons, 1899), as well as the presence of a superficial and deep layer in the extensor digitorum breves muscles (Jouffroy, 1966; Jouffroy et al., 1975). Kawashima et al. (2015) proposed that pangolins evolved a unique shoulder girdle musculature in response to the loss of mobility linked to the presence of a continuous hard armor along the body. They showed that the attachments of some shoulder girdle muscles have moved to fully cover the scapula, and suggested that opposite head swinging contributes to the rotation of the shoulder and the protraction of the forelimb.

Like other myrmecophagous mammals (see Gaudin et al., 2018), the salivary glands of pangolins are tremendously enlarged, covering much of the pharyngeal and throat region almost to the shoulder, and secreting a very sticky, alkaline mucus (Fang, 1981; Heath, 2013; Fig. 1.9A). The stomach is comprised of either a single or double chamber (Fang, 1981; Grassé, 1955b; Heath, 2013), with a mass of cornified denticles lining the area near the pylorus to grind up the ants and termites consumed (Krause and Leeson, 1974; Nisa et al., 2010; Fig. 1.9B). Pangolins will also swallow small stones and soil during feeding to facilitate this grinding process in the stomach (Grassé, 1955b). Pangolins lack a cecum, and possess greatly enlarged anal glands that form a projecting perianal ring around the anal opening (Grassé, 1955b; Heath, 2013; Kingdon, 1974).

Female pangolins typically possess two axillary nipples, with a bicornuate uterus and an indeciduate placenta covered by diffuse, villous tufts (Grassé, 1955b; Heath, 2013). The penis in males is described as "petit" by Grassé (1955b), but "well-developed" by Heath (2013), with the corpora cavernosa fused anteriorly (Grassé, 1955b). The testes are housed in a fold of skin in the inguinal area, but there is technically no scrotum, nor do pangolins possess a bulbourethral gland (Grassé, 1955b; Heath, 2013).

The vascular system of the black-bellied pangolin (*Phataginus tetradactyla* [=*Manis macroura*]) was studied by Hyrtl (1854) who found extensive arteriovenous retia mirabilia in the forelimb, hindlimb, and within the vertebral canal in the sacrocaudal region. Along with the black-bellied pangolin, the cranial arteries have been studied in the Sunda pangolin by Bugge (1979) and Wible (1984) and in the Chinese pangolin and white-bellied pangolin by du Boulay and Verity (1973). The pattern in the head was similar in all taxa: the vertebral-basilar arteries are the primary supplier of blood to the brain with supplement from the internal carotids, and most of the stapedial system is obliterated with its end branches annexed to the external carotid system. du Boulay and Verity (1973) reported a rete mirabile on the vertebral artery in white-bellied pangolins, but this was not noted for black-bellied pangolins by Hyrtl (1854). Regarding the arterial supply to the tongue, in white-bellied pangolins and giant pangolins, the left and right lingual arteries join at the base of the tongue to form a central artery that passes through the lyssa (lytta), a supporting fibromuscular cylinder in the tongue apex (Doran and Allbrook, 1973). Union of the lingual arteries has been reported in other mammals with protrusive tongues (e.g., *Tachyglossus* and *Tarsipes*, Doran and Badgett, 1971).

Historically, the most notable contribution on the pangolin brain was by Weber (1894) who illustrated and provided an overview for the Sunda pangolin. A more comprehensive snapshot has been provided recently by Imam et al. (2017) for the white-bellied pangolin. The average encephalization quotient (n = 5) for *P. tricuspis* was 0.844 (average mammalian EQ is 1); however, if the roughly 1/5 of the mass of scales is removed from the calculations, the EQ average is 0.997 (Imam et al., 2017). In general, the gyral and sulcal patterns of the cerebral cortex resemble those in carnivorans, although simpler (Fig. 1.9C). An unusual feature, also reported for the white-bellied pangolin (Chang, 1944), is the position of the pyramidal tract decussation, far rostral to that in other mammals, with apparent association with the hypoglossal nucleus presumably related to the highly modified tongue. Another unusual feature noted by Imam et al. (2017) is a very short spinal cord ending in the thoracic region with an extremely long cauda equina.

Conclusion

Much progress has been made in understanding the relationships of pangolins to other placental mammals, and in reconstructing the morphological evolution and biogeographic history of the Pholidota. A poor fossil record for the group nevertheless remains a significant hindrance in understanding all aspects of pangolin evolutionary history. A better understanding of the anatomy of the oldest fossil pangolins, from the middle Eocene Messel fauna of Germany, would represent an important step forward. Only *Eurotamandua* has received very detailed published treatments (Storch and Habersetzer, 1991; Szalay and Schrenk, 1998), and the only specimen of *Eomanis waldi* that has been described in any detail is the type (Storch, 1978), which is the poorest among multiple known skeletons (T. Gaudin, pers. obs.). Additional finds of new Paleogene fossil pangolin taxa would undoubtedly add much to our knowledge of pholidotan morphological evolution and systematic interrelationships, whereas additional Neogene fossils could clarify the biogeographic origins of the extant forms, which remain poorly understood and reconstructed on fairly scant evidence (Gaudin et al., 2006, 2016). Regarding the morphology of extant forms, interesting studies have been and continue to be published (e.g., Gaubert and Antunes, 2005; Gaudin et al., 2009; Imam et al., 2017; Nisa et al., 2010; Ofusori et al., 2008; Wang et al., 2016), but the group remains significantly understudied. This is no doubt attributable to both the small number of species, and their obscure nature relative to western science, existing as they do largely in Old World tropical forests, at low population densities in some cases, and exhibiting secretive, primarily nocturnal habits. Yet given the distinctiveness of pangolins and the imperative created by their threatened conservation status, additional studies are clearly warranted. It is hoped that this chapter, and this book, will help to spur new investigations of this fascinating group of mammals.

References

Alba, D.M., Hammond, A.S., Vinuesa, V., Casanovas-Vilar, I., 2018. First record of a Miocene pangolin (Pholidota, Manoidea) from the Iberian Peninsula. J. Vertebr. Paleontol. 38 (1), e1424716.

Botha, J., Gaudin, T., 2007. An early pliocene pangolin (Mammalia; Pholidota) from Langebaanweg, South Africa. J. Vertebr. Paleontol. 27 (2), 484–491.

Bugge, J., 1979. Cephalic arterial pattern in New World edentates and Old World pangolins with special reference to their phylogenetic relationships and taxonomy. Acta Anat. (Basel) 105 (1), 37–46.

Chan, L.-K., 1995. Extrinsic lingual musculature of two pangolins (Pholidota: Manidae). J. Mammal. 76 (2), 472–480.

Chang, H.T., 1944. High level decussation of the pyramids in the pangolin (*Manis pentadactyla dalmanni*). J. Comp. Neurol. 81 (3), 333–338.

Crochet, J.-Y., Hautier, L., Lehmann, T., 2015. A pangolin (Manidae, Pholidota, Mammalia) from the French Quercy phosphorites (Pech du Fraysse, Saint-Projet, Tarn-et-Garonne, late Oligocene, MP 28). Palaeovertebrata 39 (2), e4.

Cuvier, G., 1798. Tableau Élémentaire de l'Histoire Naturelle des Animaux. J. B. Baillière, Paris.

du Boulay, G.H., Verity, P.M., 1973. The Cranial Arteries of Mammals. William Heinemann Medical Books Limited, London.

Doran, G.A., Allbrook, D.B., 1973. The tongue and associated structures in two species of African pangolins, *Manis gigantea* and *Manis tricuspis*. J. Mammal. 54 (4), 887–899.

Doran, G.A., Badgett, H., 1971. A structural and functional classification of mammalian tongues. J. Mammal. 52 (2), 427–429.

Dubois, E., 1926. *Manis palaeojavanica*, the giant pangolin of the Kendeng fauna. Proceedings of the Koninklijke Nederlandsche Akademie van Wetenschappen, Amsterdam 29, 1233–1243.

Ekdale, E.G., 2013. Comparative anatomy of the bony labyrinth (inner ear) of placental mammals. PLoS One 8 (6), e66624.

Elliot Smith, G., 1899. The brain in the Edentata. Transactions of the Linnean Society of London. Zoology 7 (7), 277–394.

Emerling, C.A., Delsuc, F., Nachman, M.W., 2018. Chitinase genes (CHIAs) provide genomic footprints of a post-Cretaceous dietary radiation in placental mammals. Sci. Adv. 4 (5), eaar6478.

Emry, R.J., 1970. A North American Oligocene pangolin and other additions to the Pholidota. Bull. Am. Museum Nat. Hist. 142, 457–510.

Emry, R.J., 2004. The edentulous skull of the North American pangolin, *Patriomanis americanus*. Bull. Am. Museum Nat. Hist. 285, 130–138.

Fang, L.-X., 1981. Investigation on pangolins by following their trace and observing their cave. Nat., Beijing Nat. Hist. Museum 3, 64–66. [In Chinese].

Ferreira-Cardoso, S., Billet, G., Gaubert, P., Delsuc, F., Hautier, L., in press. Skull shape variation in extant pangolins (Manidae, Pholidota): allometric patterns and systematic implications. Zool. J. Linn. Soc.

Flower, W.H., 1885. An Introduction to the Osteology of the Mammalia. Macmillan, London.

Flynn, J.J., Wesley-Hunt, G.D., 2005. Carnivora. In: Rose, K. D., Archibald, J.D. (Eds.), The Rise of Placental Mammals. Origins and Relationships of the Major Extant Clades. Johns Hopkins University Press, Baltimore, pp. 175–198.

Gaubert, P., 2011. Family Manidae. In: Wilson, D.E., Mittermeier, R.A. (Eds.), Handbook of the Mammals of the World, vol. 2. Hoofed Mammals. Lynx Edicions, Barcelona, pp. 82–103.

Gaubert, P., Antunes, A., 2005. Assessing the taxonomic status of the Palawan pangolin *Manis culionensis* (Pholidota) using discrete morphological characters. J. Mammal. 86 (6), 1068–1074.

Gaudin, T.J., 2010. Pholidota. In: Werdelin, L., Sanders, W. J. (Eds.), Cenozoic Mammals of Africa. University of California Press, Berkeley, pp. 599–602.

Gaudin, T.J., Emry, R.J., Pogue, B., 2006. A new genus and species of pangolin (Mammalia, Pholidota) from the late Eocene of Inner Mongolia, China. J. Vertebr. Paleontol. 26 (1), 146–159.

Gaudin, T.J., Emry, R.J., Wible, J.R., 2009. The phylogeny of living and extinct pangolins (Mammalia, Pholidota) and associated taxa: a morphology based analysis. J. Mammal. Evol. 16 (4), 235–305.

Gaudin, T.J., Emry, R.J., Morris, J., 2016. Skeletal anatomy of the North American pangolin *Patriomanis americana* (Mammalia, Pholidota) from the latest Eocene of Wyoming (USA). Smithson. Contrib. Paleobiol. 98, 1–102.

Gaudin, T.J., Hicks, P., Di Blanco, Y., 2018. *Myrmecophaga tridactyla* (Pilosa: Myrmecophagidae). Mammal. Sp. 50 (956), 1–13.

Gebo, D.L., Rasmussen, D.T., 1985. The earliest fossil pangolin (Pholidota: Manidae) from Africa. J. Mammal. 66 (3), 538–540.

Grassé, P.-P., 1955a. Ordre des Édentés. In: Grassé, P.-P. (Ed.), Traité de Zoologie, vol. 17, Mammifères. Masson et Cie, Paris, pp. 1182–1266.

Grassé, P.-P., 1955b. Ordre des Pholidotes. In: Grassé, P.-P. (Ed.), Traité de Zoologie, vol. 17, Mammifères. Masson et Cie, Paris, pp. 1267–1282.

Heath, M., 2013. Order Pholidota – Pangolins. In: Kingdon, J., Hoffmann, M. (Eds.), Mammals of Africa, vol. V, Carnivores, Pangolins, Equids and Rhinoceroses. Bloomsbury Publishing, London, pp. 384–386.

Heath, M.E., Hammel, H.T., 1986. Body temperature and rate of O_2 consumption in Chinese pangolins. Am. J. Physiol.-Regul., Integr. Comp. Physiol. 250 (3), R377–R382.

Hoffmann, S., Martin, T., 2011. Revised phylogeny of Pholidota: implications for Ferae. J. Vertebr. Paleontol. 31 (Suppl. 2), 126A–127A.

Hoffmann, S., Martin, T., Storch, G., Rummel, M., 2009. Skeletal reconstruction of a Miocene pangolin from southern Germany. J. Vertebr. Paleontol. 29, 115A–116A.

Hyrtl, J., 1854. Beiträge zur vergleichenden Angiologie. V. Das arterielle Gefäss-system der Edentaten. Denkschriften Akademie der Wissenschaft, Wien, mathematisch-naturwissenschaftliche Klasse 6, 21–65.

Imam, A., Ajao, M.S., Bhagwandin, A., Ihunwo, A.O., Manger, P.R., 2017. The brain of the tree pangolin (*Manis tricuspis*). I. General appearance of the central nervous system. J. Comp. Neurol. 525 (11), 2571–2582.

Jouffroy, F.K., 1966. Musculature de l'avant-bras et de la main, de la jambe et du pied chez *Manis gigantea*, III. Biol. Gabon. 2, 251–286.

Jouffroy, F.K., Lessertisseur, J., Renous, S., 1975. Le problème des muscles extensores breves profundi (manus et pedis) chez les Mammifères (Xenarthra et Pholidota). Mammalia 39 (1), 133–145.

Kawashima, T., Thorington, R.W., Bohaska, P.W., Chen, Y. J., Sato, F., 2015. Anatomy of shoulder girdle muscle modifications and walking adaptation in the scaly Chinese pangolin (*Manis pentadactyla pentadactyla*: Pholidota) compared with the partially osteoderm-clad armadillos (Dasypodidae). Anat. Rec. 298 (7), 1217–1236.

Kingdon, J., 1974. East African Mammals, vol. 1. University of Chicago Press, Chicago.

Kingdon, J., 1997. The Kingdon Field Guide to African Mammals. Academic Press, London.

Koenigswald, W. von, 1999. Order Pholidota. In: Rössner, G.E., Heissig, K. (Eds.), The Miocene Land Mammals of Europe. Verlag Dr. Friedrich Pfeil, Munich, pp. 75–80.

Koenigswald, W. von, Richter, G., Storch, G., 1981. Nachweis von Hornschuppen bei *Eomanis waldi* aus der "Grube Messel" bei Darmstadt (Mammalia, Pholidota). Senckenbergiana lethaea 61, 291–298.

Kormos, T., 1934. *Manis hungarica* n. s., das erste Schuppentier aus dem europäischen Oberpliozän. Folia Zoologica et Hydrobiologica 6, 87–94.

Krause, W.J., Leeson, C.R., 1974. Stomach of pangolin (*Manis pentadactyla*) with emphasis on pyloric teeth. Acta Anat. 88 (1), 1–10.

Linnaeus, C., 1758. Systema Naturæ Per Regna Tria Naturæ, Secundum Classes, Ordines, Genera, Species, Cum Characteribus, Differentiis, Synonymis, Locis. Tomus I. Editio decima, reformata. Salvius, Stockholm.

Matthew, W.D., 1918. Edentata. A revision of the lower Eocene Wasatch and Wind River faunas. Part V—Insectivora (continued), Glires, Edentata. Bull. Am. Museum Nat. Hist. 38, 565–657.

McKenna, M.C., 1975. Toward a phylogenetic classification of the Mammalia. In: Luckett, W.P., Szalay, F.S. (Eds.), Phylogeny of the Primates. Plenum Press, New York and London, pp. 21–46.

McKenna, M.C., Bell, S.K., 1997. Classification of Mammals Above the Species Level. Columbia University Press, New York.

Meredith, R.W., Gatesy, J., Murphy, W.J., Ryder, O.A., Springer, M.S., 2009. Molecular decay of the tooth gene Enamelin (ENAM) mirrors the loss of enamel in the fossil record of placental mammals. PLoS Genet. 5 (9), e1000634.

Meredith, R.W., Janěcka, J.E., Gatesy, J., Ryder, O.A., Fisher, C.A., Teeling, E.C., et al., 2011. Impacts of the Cretaceous terrestrial revolution and KPg extinction on mammal diversification. Science 334 (6055), 521–524.

Mitra, S., 1998. On the scales of the scaly anteater *Manis crassicaudata*. J. Bombay Nat. Hist. Soc. 95 (3), 495–498.

Murphy, W.J., Eizirik, E., Johnson, W.E., Zhang, Y.P., Ryder, O.A., O'Brien, S.J., 2001a. Molecular phylogenetics and the origins of placental mammals. Nature 409 (6820), 614–618.

Murphy, W.J., Eizirik, E., O'Brien, S.J., Madsen, O., Scally, M., Douady, C.J., et al., 2001b. Resolution of the early placental mammal radiation using Bayesian phylogenetics. Science 294 (5550), 2348–2351.

Nisa, C., Agungpriyono, S., Kitamura, N., Sasaki, M., Yamada, J., Sigit, K., 2010. Morphological features of the stomach of Malayan pangolin, *Manis javanica*. Anat. Histol. Embryol. 39 (5), 432–439.

Novacek, M.J., 1986. The skull of leptictid insectivorans and the higher-level classification of eutherian mammals. Bull. Am. Museum Nat. Hist. 183, 1–111.

Novacek, M.J., 1992. Mammalian phylogeny: shaking the tree. Nature 356, 121–125.

Novacek, M.J., Wyss, A.R., 1986. Higher-level relationships of the recent eutherian orders: morphological evidence. Cladistics 2 (4), 257–287.

Ofusori, D.A., Caxton-Martens, E.A., Keji, S.T., Oluwayinka, P.O., Abayomi, T.A., Ajayi, S.A., 2008. Microarchitectural adaptation in the stomach of the African tree pangolin (*Manis tricuspis*). Int. J. Morphol. 26 (3), 701–705.

O'Leary, M.A., Bloch, J.I., Flynn, J.J., Gaudin, T.J., Giallombardo, A., Giannini, N.P., et al., 2013. The placental mammal ancestor and the post-KPg radiation of placentals. Science 339 (6120), 662–667.

Patterson, B., Segall, W., Turnbull, W.D., Gaudin, T.J., 1992. The ear region in xenarthrans (=Edentata, Mammalia). Part II. Sloths, anteaters, palaeanodonts, and a miscellany. Fieldiana, Geology n.s. 24, 1–79.

Pocock, R.I., 1924. The external characters of the pangolins (Manidae). Proc. Zool. Soc. Lond. 94 (3), 707–723.

Rose, K.D., 1999. *Eurotamandua* and Palaeanodonta: Convergent or related? Paläontologische Zeitschrift 73 (3-4), 395–401.

Rose, K.D., Emry, R.J., Gaudin, T.J., Storch, G., 2005. Chapter 8. Xenarthra and Pholidota. In: Rose, K.D., Archibald, J.D. (Eds.), The Rise of Placental Mammals. Origins and Relationships of the Major Extant Clades. Johns Hopkins University Press, Baltimore, pp. 106–126.

Rose, K.D., 2006. The Beginning of the Age of Mammals. Johns Hopkins University Press, Baltimore.

Shoshani, J., Goodman, M., Czelusniak, J., Braunitzer, G., 1985. A phylogeny of Rodentia and other eutherian orders: parsimony analysis utilizing amino acid sequences of alpha and beta hemoglobin chains. In: Luckett, W.P., Hartenberger, J.-L. (Eds.), Evolutionary Relationships Among Rodents: A Multidisciplinary Approach. Plenum, New York, pp. 191–210.

Simpson, G.G., 1945. The principles of classification and a classification of mammals. Bull. Am. Museum Nat. Hist. 85, 1–350.

Slijper, E.J., 1946. Comparative biologic-anatomical investigations on the vertebral column and spinal musculature of mammals. Verhandelingen der Koninklijke Nederlandsche Akademie van Wetenschappen, Afdeeling Natuurkunde, Tweede Sectie 17, 1–128.

Spearman, R.I.C., 1967. On the nature of the horny scales of the pangolin. Zool. J. Linn. Soc. 46 (310), 267–273.

Shrivastava, R.K., 1962. The deltoid musculature of the Edentata, Pholidota and Tubulidentata. Okajimas Folia. Anat. Jpn. 38 (1), 25–38.

Steyn, C., Soley, J.T., Crole, M.R., 2018. Osteology and radiological anatomy of the thoracic limbs of Temminck's ground pangolin (*Smutsia temminckii*). Anat. Rec. 301 (4), 624–635.

Storch, G., 1978. *Eomanis waldi*, ein Schuppentier aus dem Mittel-Eozän der "Grube Messel" bei Darmstadt (Mammalia: Pholidota). Senckenbergiana lethaea 59, 503–529.

Storch, G., 1981. *Eurotamandua joresi*, ein Myrmecophagidae aus dem Eozän der "Grube Messel" bei Darmstadt (Mammalia, Xenarthra). Senckenbergiana lethaea 61, 247–289.

Storch, G., 2003. Fossil Old World "edentates." In: Fariña, R.A., Vizcaíno, S.F., Storch, G. (Eds.), Morphological studies in fossil and extant Xenarthra (Mammalia). Senckenbergiana Biologica 83, 51-60.

Storch, G., Habersetzer, J., 1991. Rückverlagerte Choanen und akzessorische Bulla tympanica bei rezenten Vermilingua und *Eurotamandua* aus dem Eozän von Messel (Mammalia: Xenarthra). Zeitschrift für Säugetierkunde 56, 257–271.

Storch, G., Martin, T., 1994. *Euromanis krebsi*, ein neues Schuppentier aus dem Mittel-Eozän der Grube Messel bei Darmstadt (Mammalia: Pholidota). Berliner geowissenschaftliche Abhandlungen E13, 83–97.

Storr, G.C.C., 1780. Prodromus methodi mammalium. Respondente F. Wolffer, Tubingae.

Szalay, F.S., 1977. Phylogenetic relationships and a classification of the eutherian mammals. In: Hecht, M.K., Goody, P.C., Hecht, B.M. (Eds.), Major Patterns in Vertebrate Evolution. Plenum Press, New York, pp. 315–374.

Szalay, F.S., Schrenk, F., 1998. The middle Eocene *Eurotamandua* and a Darwinian phylogenetic analysis of "edentates". Kaupia: Darmstädter Beiträge zur Naturgeschichte 7, 97–186.

Thomas, O., 1887. On the homologies and succession of the teeth in the Dasyuridae, with an attempt to trace the history of the evolution of mammalian teeth in general. Philos. Trans. R. Soc. Lond. 1887 (B), 443–462.

Tong, J., Ren, L.Q., Chen, B.C., 1995. Chemical constitution and abrasive wear behaviour of pangolin scales. J. Mater. Sci. Lett. 14 (20), 1468–1470.

Ungar, P.S., 2010. Mammal Teeth: Origin, Evolution, and Diversity. Johns Hopkins University Press, Baltimore.

Vickaryous, M.K., Hall, B.K., 2006. Osteoderm morphology and development in the nine-banded armadillo, *Dasypus novemcinctus* (Mammalia, Xenarthra, Cingulata). J. Morphol. 267 (11), 1273–1283.

Vicq d'Azyr, F., 1792. Système anatomique des Quadrupèdes. Encyclopédie méthodique. Vve. Agasse, Paris.

Wang, B., Yang, W., Sherman, V.R., Meyers, M.A., 2016. Pangolin armor: overlapping, structure, and mechanical properties of the keratinous scales. Acta Biomater. 41, 60–74.

Weber, M., 1894. Beiträge zur Anatomie und Entwickelung des Genus *Manis*. Zoologische Ergebnisse einer Reise in Niederländisch Ost-Indien 2, 1–116.

Weber, M., 1904. Die Säugetiere. Einführung in die Anatomie und Systematic der recenten und fossilen Mammalia. Verlag von Gustav Fischer, Jena.

Wible, J.R., 1984. The Ontogeny and Phylogeny of the Mammalian Cranial Arterial Pattern. Ph.D. Dissertation, Duke University, Durham, United States.

Windle, B.G., Parsons, F.G., 1899. Myology of the Edentata. Proc. Zool. Soc. Lond. 314–338, 990–1017.

6.6-Appendix 6

Extended abstract in French.

Extended abstract in French

Introduction - En biologie, la convergence est un phénomène caractérisé par l'évolution de caractéristiques similaires sans ascendance commune directe. Des pressions sélectives similaires peuvent entraîner l'évolution indépendante de phénotypes identiques dans deux ou plusieurs lignées. Autrefois vu comme exceptionnelle, l'évolution convergente est aujourd'hui considérée comme omniprésente (McGhee, 2011). Les cas d'évolution convergence s'expliquent en partie par la façon dont les organismes se développent suivant les lois de la physique, du fait qu'ils proviennent d'une seule cellule et que leur organisation soit codée et transmise à la génération suivante (contraintes développementale). Toutefois, si certains phénotypes sont fonctionnels, d'autres peuvent constituer des conditions létales (contraintes fonctionnelles ; McGhee, 2001, 2006). La vie se cantonne **donc à l'intersection** de formes viables du point de vue du développement et de la fonction (McGhee, 1999), ce qui limite les possibilités de variation phénotypique et conduit à des réponses similaires sous des pressions sélectives convergentes (Losos, 2017).

Parmi les innombrables exemples de convergence évolutive, l'un des plus frappants est celui des mammifères placentaires myrmécophages, se nourrissant presque exclusivement de de fourmis et de termites (Redford, 1987). La convergence écologique vers cette spécialisation alimentaire s'est accompagnée de nombreuses adaptations aux niveaux morphologique, physiologique, comportemental et génétique (Redford, 1981 ; Redford & Dorea, 1984 ; McNab, 1985 ; Rose & Emry, 1993 ; Delsuc et al, 2014 ; Emerling et al, 2018). Les placentaires myrmécophages stricts ; qui mangent plus de 90% des termites et/ou fourmis, se répartissent en cinq lignées : les fourmiliers, le tatou géant, les pangolins, le protèle et l'oryctérope (Redford, 1987). La plupart de ces espèces, historiquement classées dans le groupe des Edentata (à l'exception du protèle ; voir 'Cadre phylogénétique'), présentent de nombreux caractères morphologiques résultant d'évolution convergente, tels que la réduction ou la perte de dents, un museau allongé, une langue collante vermiforme, des griffes et membres antérieurs forts pour creuser dans les nids des insectes sociaux (Rose & Emry, 1993 ; Davit-Béal et al, 2009 ; Casali et al, 2017 ; Goździewska-Harłajczuk et al, 2018 ; Ferreira-Cardoso et al, 2019).

Les traits crâniens constituent l'une des caractéristiques les plus distinctifs des mammifères placentaires myrmécophages (Gaudin et al., 1996 ; Gaudin & Branham, 1998 ; Reiss, 2001). Ceci est principalement dû à la plasticité de l'appareil masticateur des mammifères et au rôle majeur qu'il a pu jouer au cours de plusieurs radiations adaptatives de l'histoire du groupe (Hiiemae, 2000 ; Schwenk,

2000). Cette évolution adaptative des structures crâniennes, combinée à des processus de développement conservés, a entraîné une compartimentation du crâne en petites unités adaptatives, autrement appelé modules (Olson & Miller, 1958 ; Cheverud, 1982a ; Goswami, 2006 ; Porto et al., 2009). Ces modules développementaux correspondent à des ensembles de caractères fortement corrélés (modules phénotypiques), avec un rôle fonctionnel principal, une base génétique et développementale sous-jacente, ainsi qu'un degré d'indépendance qui peut être relativement élevé en fonction de l'organisme (Raff, 1996 ; Wagner, 1996 ; Klingenberg, 2005). Dans un paysage adaptatif (p. ex., la spécialisation alimentaire), des propriétés variationnelles comme la corrélation de caractères et la modularité peuvent accroître un changement directionnel de la sélection (évolutivité ; Riedl, 1978 ; Hansen et Houle, 2008 ; Marroig et al., 2009). Le phénotype crânien unique associé à la myrmécophagie est donc un exemple de compromis entre la facilitation et la contrainte de la variation morphologique dans le contexte d'un régime alimentaire unique sur le plan fonctionnel et physiologique.

Les placentaires myrmécophages ont suscité l'intérêt de plusieurs études depuis plus d'un siècle, portant principalement sur l'étude de leur développement dentaire (Gervais, 1867 ; Rose, 1892 ; Röse, 1892 ; Martin, 1916 ; Anthony, 1934a ; Davit-Béal et al., 2009), de la perte des capacités masticatoires et des modifications de leurs appareils masticateur et hyoide (Owen, 1856 ; Reiss, 1997 ; Endo et al., 1998, 2007, 2017 ; Naples, 1999a). Toutefois, des méthodes de modernes morphométrie géométrique n'ont pas encore ét éutilisées sur le crâne des placentaires myrmécophages, alors qu'elle pourrait permettre de mieux caractériser les variations phénotypiques (Cheverud, 1982, 1995 ; Hallgrímsson et al, 2004 ; Drake & Klingenberg, 2010). De telles méthodes peuvent également fournir de nouvelles perspectives sur les patrons développementaux (Cheverud, 1982b ; Klingenberg, 2016) et la systématique (Palci & Lee, 2018). De plus, l'avènement de la tomographie assistée par ordinateur (μCT) à rayons X et des protocoles de coloration permet étudier les traits ostéologiques et les tissus mous à une échelle et une précision très fines à l'aide de méthodes totalement non destructives.

L'appareil masticateur des mammifères placentaires myrmécophages fournit un cadre particulièrement intéressant pour étudier la convergence morphologique associée à des adaptations écologiques. Les processus développementaux impliqués dans la formation du crâne sont bien documentés, tout comme la modularité et sa relation avec des contraintes fonctionnelles qui sont désormais établies pour plusieurs espèces de placentaires modèles et non modèles. Or, une partie de ces

processus développementaux, comme l'allongement du rostre, le développement des dents ou l'interaction os-muscle, sous-tend la plupart des traits phénotypiques convergents associés à la myrmécophagie. Le crâne myrmécophage offre ainsi un cas d'école de convergence morphologique.

Cadre méthodologique - Différentes méthodes ont été utilisées pour réaliser les quatre études présentées dans les différents chapitres de cette thèse. Une section " Matériels et méthodes " détaillée est fournie pour chaque chapitre et, par conséquent, seules les grandes lignes de mon approche méthodologique seront ici présentées.

Acquisition de données - J'ai visité cinq des plus grandes collections d'histoire naturelle du monde, dont le Natural History Museum (Londres, Royaume-Uni), le Musée Royal de l'Afrique Centrale / *Koninklijk Museum voor Midden-Afrika* (Africa Museum ; Tervuren, Belgique), le *Museum für Naturkunde* (Berlin, Allemagne), *l'American Museum of Natural History* (New York, USA) et le *National Museum of Natural History* (Washington, DC, USA). De plus, j'ai emprunté des spécimens ostéologiques et en fluide au Muséum National d'Histoire Naturelle (Paris, France), au *Museum für Naturkunde* (Berlin, Allemagne), au *Africa Museum* (Tervuren, Belgique) et au *Museum of Vertebrate Zoology* (Berkeley, USA). Chaque visite consistait en un à deux jours de travail d'anatomie comparée, suivi de la pose de points de repères anatomiques homologues en trois dimensions (types I et II). Cette dernière étape a été réalisée avec un numériseur Revware MicroScribe M (précision : 0,0508 mm). Le nombre de points de repère placés varie entre 85 et 119, selon le clade considéré. Au total, j'ai numérisé 703 spécimens appartenant à des espèces myrmécophages et à des groupes non myrmécophages, dont des paresseux, des tatous, des hyènes, des ours et des renards. J'ai utilisé des méthodes de microtomographie à rayons X (µ-CT) pour obtenir des piles d'images à haute résolution des parties squelettiques pour plus de 130 spécimens d'espèces myrmécophages. L'acquisition µ-CT a été réalisé dans deux installations différentes : i) Montpellier Ressources Imagerie (MRI) équipée d'un scanner µ-CT EasyTom 150 à l'Institut des Sciences de l'Evolution (Montpellier, France); et ii) le laboratoire CTscan du *Museum of Natural History* (Londres, Royaume-Uni) équipé d'un Nikon Metrology HMX ST 225. Toutes les données obtenues ont ensuite été traitées avec Avizo (FEI), Fiji (Schindelin et al., 2012) et MorphoDig (Lebrun, 2018). Ces logiciels ont été utilisés pour comprimer les données et générer des surfaces tridimensionnelles (p. ex. Ferreira-Cardoso et al., 2017 ; Martinez et al., 2018).

Enfin, j'ai disséqué les têtes de six spécimens de fourmiliers conservés à l'Institut de Sciences de l'Evolution (Montpellier, France) et à l'Institut Pasteur de Guyane (Cayenne, France). Ces spécimens ont été disséqués à Montpellier et à Cayenne, puis colorés à l'iode afin d'augmenter le contraste des muscles de la tête et de permettre une reconstruction numérique de leur morphologie. Des coupes histologiques ont été également réalisées sur plusieurs de ces spécimens (muscles et mandibules) à l'Institut de Recherche en Cancérologie de Montpellier (IRCM).

Analyse des données - Toutes les données morphométriques ont été traitées et analysées à l'aide du logiciel gratuit d'analyse statistique R (Team, 2013). Des procédures d'analyse de morphométrie géométrique ont été mises en œuvre avec le package geomorph v.3.5.0.0 R (Adams et al., 2017) et le code R fourni dans Claude (2008).. Les packages et fonctions R utilisés sont listés dans chacun des chapitres.

Cadre phylogénétique - En 1742, le médecin et naturaliste français Félix Vicq-d'Azyr publie le deuxième volume de son "Système anatomique : quadrupèdes" (Vicq-d'Azyr, 1742), dans le cadre d'une collection intitulée "Encyclopédie Méthodologique". Dans ce livre, Vicq-d'Azyr nomme un nouveau clade de mammifères qu'il désigne sous le nom d’"édentés/Edentati", le trait diagnostique pour ce groupe étant l'absence d'incisives. Il comprenait quatre groupes, dont les paresseux (Pigri), les tatous (Loricati), les fourmiliers et l'oryctérope (Myrmecophagi), et les pangolins (Squammei) (Vicq-d'Azyr, 1742). Le nom Edentata a été adopté postérieurement par les naturalistes et sa structure a été réorganisée en cinq groupes différents : tatous, fourmiliers, paresseux, oryctéropes et pangolins (p. ex., Cuvier, 1798). Edentata a été utilisé pour désigner ces taxons (Rose, 1892 ; Tims, 1908), sur la base de traits morphologiques communs considérés comme des synapomorphies du groupe.

La diagnose proposée par Huxley (1872) pour les Edentata (ou Bruta, qui se traduit par brut, grossier ou bête) reflétait certains des traits morphologiques convergents liés à la myrmécophagie. Il s'agit notamment de la perte ou de la réduction des dents, de la simplification de la structure dentaire, de l'hypsélodontie, de la monophyodontie (sauf chez certains tatous) et des membres antérieurs adaptés au fouissage (Huxley, 1872). Huxley (1872) divise les Edentata en deux groupes en fonction de leur alimentation : à base de plantes (paresseux ; Phytophaga) ou d’insectes (Entomophaga). Ce dernier groupe comprend les fourmiliers, les pangolins, les tatous et les oryctéropes. Chacun de ces taxons a été placé

séparément dans son propre taxon, pour qui aucune affinité provisoire n'a été proposée. Au moment où Huxley publie ses travaux, un peu plus d'un siècle après la formalisation du groupe des Edentata, une somme croissante de connaissances sur l'anatomie et la physiologie de ces mammifères permet désormais aux chercheurs d'interroger la pertinence d'un tel regroupement. Huxley (1872) lui-même précède sa diagnose et sa description des Edentata en déclarant que le groupe était "mal défini" et hétérogène.

Cependant, il faudra attendre le début des années 1900 pour voir apparaître la première division officielle en trois ordres clairement différents. Weber (1904, p. 412) soutient que, bien qu'il soit devenu habituel de regrouper ces taxons dans le même ordre, les différences morphologiques sont trop nombreuses pour qu'une telle classification soit cohérente. Simultanément, Weber fait référence à la réduction de la dentition et à la simplification de la structure dentaire comme à une "réduction et transformation multiples" (traduit de l'allemand) qui ne pouvait être utilisée comme facteur de regroupement (voir ci-dessous). Weber (1904) considérait les Edentata comme un groupe "inférieur" au sein des mammifères thériens, les Paratheria, ne décrivant pas pour autant ses relations avec les autres mammifères. Weber (1904) a divisé les Edentata en deux groupes : i) les Nomarthra comprenant deux ordres d'espèces à articulation vertébrale normale (pangolins et oryctéropes); ii) les Xenarthra possédant des articulations accessoires anormales dans les dernières vertèbres thoraciques et lombaires (fourmiliers, paresseux et tatous). De plus, Weber (1904) a inventé le terme Pholidota, l'ordre dans lequel les pangolins sont toujours classés, remplaçant ainsi la désignation Squamata qui était synonyme de clade de reptiles. Au sein de Xenarthra, il a maintenu les divisions précédemment utilisées entre les fourmiliers (Myrmecophagidae), les paresseux (Bradypodidae) et les tatous (Dasypodidae).

Depuis le début du XXe siècle, le nom Edentata a été utilisé pour désigner les Xenarthra, les similitudes entre ces derniers et les Pholidota et Tubulidentata ayant été attribuées à une évolution convergente vers la myrmécophagie (par exemple, Rose & Emry, 1993 ; McGhee, 2011). Cette classification a été largement acceptée, avant même l'avènement des méthodes de phylogénie moléculaire, les Xenarthra étant considérés comme un clade séparé au sein des Eutheria, divisé en deux ordres : les Cingulata (armadillos) et les Pilosa (paresseux et fourmiliers) (McKenna, 1975). McKenna (1975) a considéré les Pholidota comme un clade *incertae sedis*, tandis que les Tubulidentata ont été regroupés avec les ongulés avec un rang similaire aux ordres des artiodactyles, proboscidiens ou siréniens. Ces propositions n'ont toutefois pas été corroborées par les analyses phylogénétiques moléculaires les plus récentes (voir ci-dessous).

Depuis les années 1980-1990, les phylogénies moléculaires ont fourni de plus en plus de preuves confirmant la polyphylie des Edentata (De Jong et al., 1985 ; Springer et al., 1997 ; de Jong, 1998 ; Murphy et al., 2001b). Les pangolins sont désormais reconnus come le groupe frère des carnivores au sein des Laurasiatheria (Sarich, 1993 ; Murphy et al., 2001b ; a ; Meredith et al., 2011). Les oryctéropes forment un sous-clade (Afroinsectiphilia) avec les tenrecs, les taupes dorées et les rats à trompes, au sein du super-ordre des Afrotheria (Waddell et al., 1999 ; Asher et al., 2009 ; Meredith et al., 2011). La position phylogénétiques des xénarthres au sein des placentaires restent mal définie (Nishihara et al., 2009 ; Teeling & Hedges, 2013 ; Foley et al., 2016), leur position changeant dans chacune des trois hypothèses proposées : i) Atlantogenata-Boreoeutheria (Fig. 1); ii) Afrotheria-Exafroplacentalia; iii) Xenarthra-Epitheria. Jusqu'à présent, la racine de l'arbre placentaire n'est toujours pas résolue, et les trois hypothèses sont actuellement considérées comme équiprobables (Nishihara et al., 2009 ; Teeling & Hedges, 2013). Néanmoins, tous fournissent des preuves non équivoques de la polyphylie des Edentata (*sensu* Cuvier), pointant du doigt le haut degré de convergence morphologique résultant d'une sélection directionnelle vers un régime alimentaire myrmécophage.

Objectifs de la thèse - Dans cette thèse, j'ai combiné des méthodes d'anatomie comparée et de morphométrie géométrique, en utilisant des techniques modernes de microtomographie assistée par ordinateur et des vastes collections muséales, afin de mieux comprendre l'évolution convergente de la tête, du crâne et des muscles des mammifères placentaires myrmécophages. Les études présentées ici se concentrent sur le crâne de 15 espèces myrmécophages, incluant les fourmiliers, le tatou géant, les pangolins, les oryctéropes et le protèle, ainsi que leurs groupes frères.

Dans le premier chapitre, j'ai utilisé une approche basée sur des points homologues pour décrire et quantifier les variations interspécifiques et intraspécifiques de la forme du crâne, ainsi que les modèles allométriques des pangolins (Pholidota), les mammifères les plus braconnés au monde.

Dans le deuxième chapitre, j'ai analysé l'anatomie interne de la mandibule de toutes les espèces placentaires myrmécophages et je l'ai comparée à des taxons non myrmécophages afin de ré-interpréter les patrons de convergence phénotypique et de discuter des aspects fonctionnels de la régression dentaire. J'ai également utilisé des spécimens de collection et des données CTscans pour effectuer une description anatomique comparée des musculatures masticatoire, hyoïde, linguale et faciale des trois genres de fourmiliers (Vermilingua, Xenarthra).

Enfin, j'ai évalué et comparé les modèles de covariation phénotypique intra- et interspécifique chez les placentaires myrmécophages, en utilisant une approche de morphométrie géométrique. J'ai utilisé des méthodes exploratoires et confirmatoire pour comprendre l'impact de l'acquisition d'un mode de vie myrmécophage sur la modularité et l'intégration du crâne.

Principaux résultats - Dans le premier chapitre, j'ai montré que la forme du crâne peut permettre de différencier sept des huit espèces de pangolins actuelles. Mes résultats ont montré que les pangolins africains et asiatiques se distinguent par des trajectoires allométriques différentes au cours de l'ontogénie. J'ai montré que la taille influence largement la forme du crâne ce qui représente un effet confondant pour déterminer des distances phénétiques entre groupes. J'ai également étudié la variation intraspécifique de la forme du crâne chez deux espèces à large répartition géographique, *Phataginus tricuspis* et *Manis javanica*. Bien qu'aucune discrimination n'ait été trouvée entre les différentes populations de *M. javanica*, j'ai montré qu'il existe un certain degré de différenciation morphologique entre les espèces cryptiques récemment proposées sur la base de données moléculaires.

Dans le deuxième chapitre, j'ai développé deux axes de recherche. Tout d'abord, j'ai décrit la morphologie mandibulaire interne des espèces actuelles de mammifères myrmécophages. En utilisant des méthodes de microtomographie à rayons X, j'ai montré que des structures supposément associées à l'innervation de la dent (canalicules dorsaux) sont présentes chez les fourmiliers, pourtant dépourvus de dents, alors qu'elles sont absentes chez les pangolins également édentés. L'anatomie comparative intra- et interspécifique permet de : i) montrer que les canalicules dorsaux sont invariablement présents chez les fourmiliers; ii) confirmer la relation entre les canalicules dorsaux et le développement dentaire précoce; iii) montrer l'évolution indépendante des canalicules dorsaux chez les fourmiliers et les baleines à fanons. De plus, j'ai pu montrer que, malgré la perte des dents, les canalicules dorsaux sont vascularisés et innervés.

Toujours dans mon deuxième chapitre, j'ai produit une description anatomique comparaée de la musculature de la tête des trois genres de fourmiliers actuels (*Myrmecophaga*, *Tamandua* et *Cyclopes*). J'ai pu confirmer que les muscles adducteurs mandibulaires sont réduits chez les fourmiliers, tandis que les muscles intermandibulaires et de la langue sont bien développés. J'ai montré que l'appareil masticateur du fourmilier pygmée présente des proportions volumiques musculaires différentes de celles du tamanoir et des tamanduas. De plus, j'ai montré que la perte de l'os jugal chez le fourmilier pygmée est

probablement liée à l'absence d'un muscle masséter profond et d'une partie du *zygomaticomandibularis*. J'ai ensuite comparé les musculatures des fourmiliers à celles des pangolins et des oryctéropes et montré que l'anatomie musculaire de leur appareil masticateur est très différente, malgré des régimes alimentaires similaires.

Dans le troisième chapitre, j'ai décrit la quantité et la répartition des corrélations entre différents traits ostéologiques sur le crâne de 15 espèces myrmécophages. J'ai montré que les modèles de modularité ressemblent globalement à ceux des mammifères placentaires non myrmécophages et que l'allongement du crâne a pu entraîner un léger remodelage des patrons de modularité dans la région du rostre. Mes résultats montrent un découplage apparent entre la fonction masticatrice et les patrons de modularité. J'ai notamment pu démontrer que les patrons de covariance changent significativement au cours de l'ontogenèse, au sein d'une même espèce. Des résultats préliminaires permettent également de discuter de l'effet de la superposition Procrustes sur des ensembles de données biologiques.

Discussion - Les résultats de mes recherches confirment que l'évolution adaptative vers la myrmécophagie a eu un impact majeur sur la forme du crâne. Les recherches incluses dans les chapitres 1 et 3 révèlent à quel point les axes de variation du crâne des mammifères placentaire sont conservés. Ils montrent que l'allométrie évolutive et ontogénétique sont des axes principaux de variation morphologique qui peuvent facilement répondre aux pressions de sélection (Cardini & Polly, 2013 ; Cardini, 2019). Dans le premier chapitre, nous avons montré que l'allométrie peut avoir un effet confondant dans certains axes de l'espace morphologique crânien des pangolins (Gaudin et al, 2009 ; Ferreira-Cardoso et al, 2019a). Si l'allométrie est génératrice de covariance phénotypique entre les caractères crâniens (Hallgrimsson *et al*., 2007 ; Porto *et al*., 2013), nous avons montré que les interactions fonctionnelles, comme celles entre muscle et os, n'ont pas un effet également évident sur les patrons de covariance. Nos résultats du chapitre 3 suggèrent que les modèles de modularité sont relativement inchangés chez les mammifères myrmécophages par rapport aux autres placentaires (Cheverud, 1982a ; Goswami, 2006 ; Parr et al, 2016 ; Heck et al, 2018). Ceci peut s'expliquer par des phénomènes de canalisation de la variation phénotypique du crâne (Dworkin, 2005). La sélection naturelle aura tendance à agir sur des ensembles de caractères fortement corrélés, maximisant ainsi l'évolvabilité des caractères (Riedl, 1978). Par conséquent, les changements morphologiques associés à la myrmécophagie sont probablement liés à la présence modules conservés au cours de l'évolution.

Si les patrons de variation phénotypique n'ont pas montré de changement commun associé à la myrmécophagie, les résultats des recherches présentés dans le chapitre 2 ont montré que certains aspects de l'anatomie des espèces myrmécophages pourraient être très distincts malgré une ressemblance globale. L'anatomie interne des mandibules des pangolins et des fourmiliers est différente, ce qui suggère les processus induisant une perte des dents sont distincts dans chacun de ces groupes**.** Ces différences anatomiques pourraient être en outre liées à des différences fonctionnelles, impliquant en particulier la biomécanique de leur appareil masticateur. La musculature masticatrice, intermandibulaire et de la langue des fourmiliers, des pangolins et des oryctéropes présente quelques similitudes mais aussi des différences significatives. Il en va de même au sein même des fourmiliers, le fourmilier pygmée présentant des proportions musculaires et un nombre de muscles masticateurs différents, qui pourraient expliquer des variations significatives de leur biomécanique masticatrice.

Conclusion

Pour conclure, les approches utilisées dans cette thèse montrent que l'utilisation combinée de la morphométrie géométrique, de la microtomographie à rayons X et de l'histologie m'a permis d'étudier dans le détail un exemple classique de convergence morphologique. Ces techniques ont permis de mieux appréhender la complexité qui sous-tend l'évolution du crâne des mammifères myrmécophages. Les contraintes de développement sont omniprésentes chez les mammifères (McGhee, 2001), tout comme les phénomènes de convergence (McGhee, 2011). En agissant sur des systèmes intégrés d'un point de vue développemental, la sélection conduit des sous-unités morphologiques à évoluer dans des directions qui sont plus susceptibles de produire des phénotypes « mieux » adaptés (Riedl, 1978). Cette thèse a permis de comprendre que cette hypothèse théorique ne se traduit pas toujours par l'acquisition de morphologies exactement identiques chez des organismes considérés comme convergents. L'exposition à certains stimuli environnementaux se traduira donc par le meilleur compromis disponible à un instant donné (Bock, 1959). "*La vie trouve toujours un chemin*", comme l'a dit un célèbre chaoticien de fiction, mais ce chemin peut être différent, en fonction des conditions de départ. J'ai montré que ce fut le cas avec l'exemple de l'évolution convergente des mammifères édentés.

7-Acknowledgements

First of all, I would like to thank Lionel and Fred for having trusted me with this thesis subject and for giving the opportunity to grow, professionally and personally, surrounded by mind-blowingly bizarre organisms (special mention to anteaters). I appreciate their willingness to let me explore the amazing world of cranial anatomy in whichever directions chance led me to (and it sometimes led me as far as North Korea). Lionel and Fred's patience and criticism during my PhD were priceless and I will be forever thankful to them for tempering and guiding my thoughts (and for playing 'Queen' during dissections; I give it up for Fred).

I want to leave a word of gratitude to my office mate during these three years, on whom I relied daily for all aspects of the PhD life. With him I shared most of my first thoughts, my joy, as well as my disappointments. Myself having a slight tendency towards pessimism, it took him a big deal of Buddhism (not the Rohingya massacre part) to be able to share the same work space with me. In a time in which technique is more valued than science, and in which curiosity tends to be replaced by business-like entrepreneurship, I was extremely lucky to have an office mate that was so excited about the complex simplicity of a skull, a tooth, or a vertebra. I will be thankful to him *ad vitam aeternam* for showing me the beauty of comparative anatomy and of the anatomist profession, and for being a perfect model of how a top researcher should think and work. Lastly, I apologize to him for keeping all those skins in the office. Thank you, Lionel.

All ISEMers, especially the ground floor teams (molecular phylogeneticists and paleontologists), are to be thanked. I owe Pierre-Henri, for his warm welcome from day one, his never-ending jokes, and his enthusiasm for natural history. Cheers, PH. Special thanks to Mélanie, who was my first PhD supervisor (!), and shared the office with me for around one year, and the dissection room for another iodine-stinking year. I want to thank Renaud, for all his help with the µCT scan and 3D modelling, to Julien and Allowen for their help with morphometrics and modularity. Special thanks to Hélder for all discussions and encouragement during the last days of his post-doc life at Montpellier. I also want to thank Ricardo, my master's mentor in Portugal and colleague at the lab for two years. Lastly, but most importantly, I want to thank to all PhD students and post-docs from the lab, mainly those in Phyl Evol Mol.

I have to give a special mention to my collaborators, colleagues, and museum curators who made my work possible. Guillaume, Vielen Dank für all Ihre Hilfe, Ihren Rat und Ihre Merkelness. Thanks to Philippe, for his help with pangos, to Benoit for all the help in French Guiana, and to Anthony for bringing the anteater heads to this side of the pond. To Kévin, I thank very much for our friendly discussions, for the debates about modularity, and for the priceless favor you did to me by bringing me specimens from Paris. I immensely appreciate all the help provided by the collection curators of the AMNH (New York), USNM (Washington; thanks Louise Emmons), MfN (Berlin), MNHN (Paris), KMMA/Africa Museum (Tervuren), JAGUARS, and Institut Pasteur (French Guiana). Special thanks to Roberto and to the NHM collections (London) for the warm receptions and valuable help in London.

Fortunately, a good part of the three-year period of the PhD was filled with non-working hours. Part of that time was spent with friends from ISEM. Being a foreigner, getting to know everyone's names took a few more days than expected… So thanks Paul, for having an easy name to memorize, for showing me OSS 117, and for accepting the death of your computer that I inadvertently anticipated. Thank you Manon, Marjo, Clémentine des Vosges, Yoann (le petit), Yoann (le grand), Corentin for warmly welcoming this migrant. After proving that I pay taxes and explaining that I am into anatomy (and therefore will be no threat in the race for a permanent position, other than at McDonald's), you have all welcome me to Montpellier and filled a very special place in my life. I also thank to all the friends from the French classes, Heliana, Clarissa, Charlotte, Oscar, and especially Valerio, with whom I co-celebrated the end of the PhD, and who I almost killed during our bike ride to the Pic St. Loup. Of the many people with whom I had the privilege to spend time with, while at Montpellier, I would like to make a special mention to Andrea, Pauline, Marina, Clémentine de Bretagne, Louise-Anne, Blaise, Emeric, Jihad, and Kévin. Many thanks to Laure, Elodie, Camille, Julien, Brice, and Nicolas (and Mathys, whose neocortex recently started to work) for all our weekends, games, and discussions about why surgeons are good doctors. I would briefly like to mention all the cool people that I met in France, especially from Lyon and French Texas (Nîmes).

From the latter come people to whom I need to show my immense appreciation for all the moments we spent together during the last two years and who made the thesis redaction time more bearable. Therefore I thank to Quentin, for our wonderings in the maze of size correction, all those coffee breaks that overboosted our heart rates, and all those dance floor dominations. Rémi, thank

you for all the encouraging words during my third year of PhD, for never telling Fred that I left the car in the middle of the main road of Cayenne with the keys on it, and for all the gamelles that either saved me, but most often made me lose during our “meetings”. I owe you a run to the Pic St. Loup, and you guys owe me a Monopoly night.

Gostaria de agradecer à minha familia, à minha mãe (Ana), ao meu pai (Sérgio), à minha irmã (Jéssica), aos meus avós (Lourdes e Duarte), e ao meu padrinho (Zeca). Obrigado por todo o apoio, não só durante o doutoramento, mas principalmente durante todos os anos que o precederam. Esta tese também é um pouco vossa. Uma menção à Sacha e à Cuca, por estarem lá a cada vez que regresso a casa. Gostava também de agradecer aos meus amigos em Lisboa, do liceu e da FCUL, nomeadamente ao Ruben e ao Miguel pelas sessões de descontração no Steam e pelas deficiências do costume since D. Dinis, e ao João, com quem partilhei a minha primeira visita aos Alpes.

I would like to thank Denise and Alex for their kindness, but mainly for giving birth to Laura. She was part of the best moments for the last three years and was there for me during the worst. When I look back, I couldn’t be happier (and feel luckier) that she accidentally had to come get her keys from her house mate after a busy day, which ultimately led us to meet. Thank you, Laura, for changing my life, for coming to visit me when I was working in collections abroad, for being so patient, and for making the good days immensely better and bringing a spark to the gloomy ones.

I want to dedicate this thesis to my patrons, the tax-payers of the European Union, especially those who always pay, never default, and rarely benefit: the proletariat.

Abstract

The subject of this thesis is the morphological convergence in the skull of ant- and termite-eating placentals. Its goals are to characterize tooth reduction, covariance patterns, and morphological variation of the skull, and explore their link to the selective pressures associated to myrmecophagy.

The first chapter focuses on the evolutionary, ontogenetic, and static variations of the skull in pangolins, a group of myrmecophagous animals that include the most threatened mammalian species on Earth. The morphological delimitation between seven of the eight species is demonstrated. Their ontogenetic allometric trajectories are described and the implications of the size variation on systematics are discussed. Additionally, intraspecific variation was partly associated to molecular distinctiveness of recently diverged cryptic species within the white-bellied pangolin. These results were obtained with the use of three-dimensional geometric morphometric methods.

The second chapter was dedicated to the comparative anatomy of the mandible and masticatory apparatus. First, I investigate the internal mandibular anatomy on a comparative sample of placental mammals using μ-CT tomography and histology. Structures putatively associated to tooth innervation (dorsal canaliculi) are present in toothless anteaters, while they are absent in pangolins, which are equally toothless. Comparative anatomy performed intra- and interspecifically allowed to: i) show that dorsal canaliculi are invariably present in anteaters; ii) confirm the relationship between dorsal canaliculi and early tooth development; iii) show the independent evolution of dorsal canaliculi in anteaters and toothless whales. Dorsal canaliculi are vascularized and innervated in the collared anteater, despite its tooth loss. This suggests that despite tooth loss, tooth pulp innervation likely maintained its sensorial role on the dorsal part of the mandible of anteaters. The second part of chapter 2 is devoted to the comparative anatomy of the head musculature of the three extant anteater genera. Classical and digital dissections confirmed the reduction of the masticatory apparatus in anteaters. The masticatory apparatus of the pygmy anteater is found to significantly differ from that the other two genera. A comparison with the head musculatures of pangolins and aardvarks was done, based on previously published studies. Despite being myrmecophagous, the head musculature of aardvarks and pangolins shows some key differences from that of anteaters. This suggests that the feeding apparatus of ant- and termite-eating placentals varies at the functional level.

The last chapter of this thesis covers the patterns of phenotypic covariance of the skull of 15 myrmecophagous species. A geometric morphometrics approach is used in order to explore and confirm hypotheses of modularity. Results show that patterns of modularity in myrmecophagous mammals resemble those of other placentals mammals. No common shift in the parcellation was found, other than that expected from the null hypothesis. Results suggest instead that skull elongation might have resulted on a slight remodeling of modularity patterns on the rostrum region in myrmecophagid anteaters. A preliminary analysis of ontogenetic trajectories of phenotypic covariance matrices in two myrmecophagous species shows that covariance patterns significantly change during ontogeny. This indicates that functional interpretations of static modularity and integration must be taken with caution.

Résumé
Cette thèse porte sur la convergence morphologique du crâne des mammifères placentaires myrmécophages, qui se nourrissent principalement de fourmis et de termites. Les objectifs ici sont de caractériser la réduction dentaire, les patrons de covariance et la variation morphologique du crâne, et d'explorer leur lien avec les pressions sélectives associées à la myrmécophagie.

Le premier chapitre se concentre sur les variations évolutives, ontogénétiques et statiques du crâne des pangolins, un groupe d'animaux myrmécophages qui comprend les espèces de mammifères les plus menacées sur Terre. La délimitation morphologique entre sept des huit espèces de pangolins est démontrée. Leurs trajectoires allométriques ontogénétiques sont décrites et l'influence des variations de taille sur la systématique du groupe sont discutées. De plus, la variation intraspécifique était en partie associée au caractère distinctif moléculaire d'espèces cryptiques récemment divergentes au sein du pangolin à petites écailles. Ces résultats ont été obtenus à l'aide de méthodes morphométriques géométriques tridimensionnelles.

Le deuxième chapitre était consacré à l'anatomie comparée de la mandibule et de l'appareil masticateur. Tout d'abord, l'anatomie interne de la mandibule a été étudiée sur un échantillon comparatif de mammifères placentaires par microtomographie et histologie. Les structures supposément associées à l'innervation des dents (canalicules dorsaux) sont présents chez les fourmiliers édentés, alors qu'elles sont absentes chez les pangolins également édentés. L'anatomie comparative intra- et interspécifique permet de : i) montrer que les canalicules dorsaux sont invariablement présents chez les fourmiliers ; ii) confirmer la relation entre les canalicules dorsaux et le développement dentaire précoce ; iii) montrer l'évolution indépendante des canalicules dorsaux chez les fourmiliers et les baleines à fanons. Les canalicules dorsaux sont vascularisés et innervés chez le fourmilier à collier, malgré la perte de ses dents. Ceci suggère, qu'en dépit de la perte des dents, l'innervation de la pulpe dentaire a probablement gardé un rôle sensoriel sur la partie dorsale de la mandibule des fourmiliers. La deuxième partie du chapitre 2 est consacrée à l'anatomie comparée de la musculature de la tête des trois genres de fourmiliers actuels. Les dissections classiques et numériques ont confirmé la réduction de l'appareil masticateur des fourmiliers. L'appareil masticateur du fourmilier pygmée est très différent de celui des deux autres genres. Une comparaison avec les musculatures crânienne des pangolins et des oryctéropes a été faite, uniquement basée sur des études publiées précédemment. Bien que myrmécophages, la musculature de la tête des oryctéropes et des pangolins présente quelques différences importantes avec celle des fourmiliers. Cela suggère que l'appareil masticateur des mammifères placentaires myrmécophages varie au niveau fonctionnel.

Le dernier chapitre de cette thèse couvre les modèles de covariance phénotypique du crâne de 15 espèces myrmécophages. Une approche de morphométrie géométrique est utilisée afin d'explorer et de confirmer les hypothèses de modularité. Les résultats montrent que les patrons de modularité chez les mammifères myrmécophages ressemblent à ceux des autres mammifères placentaires. Aucun changement commun dans la parcellisation du crâne n'a été détecté, autre que celui attendu de l'hypothèse nulle. Les résultats suggèrent plutôt que l'allongement du crâne a pu entraîner un léger remodelage des patrons de modularité dans la région du rostre des fourmiliers myrmécophagidés. Une analyse préliminaire des trajectoires ontogénétiques des matrices de covariance phénotypique chez deux espèces myrmécophages montre que les patrons de covariance changent significativement pendant l'ontogenèse. Cela indique que les interprétations fonctionnelles de la modularité statique et de l'intégration doivent être effectuées avec prudence.